Degree PhD Year 2006 Name of Author HUI BIN

Imperial College
London

Experimental and Theoretical Investigation of Phase Inversion in Liquid-liquid Dispersions

Bin HU

A thesis submitted to University of London in fulfilment of the requirements for the degree of Doctor of Philosophy

Department of Chemical Engineering
University College London
London WC1E 7JE
&
Department of Chemical Engineering
Imperial College London
London SW7 2AZ

December 2005

ProQuest LLC
789 East Eisenhower Parkway
P.O. Box 1346
Ann Arbor, MI 48106-1346

Abstract

This thesis describes an experimental and theoretical investigation of phase inversion in concentrated liquid-liquid dispersions, as part of a joint project between University College London (UCL) and Imperial College London (ICL).

Experimental studies of phase inversion behaviour and associated phenomena in pipeline flows were carried out on the Water-Oil Liquid Flow (WOLF) facility at the Department of Chemical Engineering at UCL. Two inversion routes (w/o to o/w and o/w to w/o) were followed to elucidate the hysteresis effect in pipeline flows in both upward and downward flows at either constant or increased mixture velocity. System parameters, such as frictional pressure gradient, in-situ holdup, velocity ratio, drop velocity and drop size distribution were studied for flows before and after phase inversion. The velocity ratio of two liquid phases was shown to play a key role in the phase inversion process. A hot-film anemometer (HFA) was also employed in this work to measure the mean and turbulent fluctuation velocities of the continuous phase at different dispersed phase input fraction. Enhancement or attenuation of turbulence level of the continuous phase was found to depend on a number of parameters such as local concentration, drop size, flow direction and velocity. It is evident that high concentrations and large drops of the dispersed phase are likely to increase local turbulence.

An improved analytical method was also developed to derive stable drop size distributions (DSD) from the distributions of chord lengths (CLD), measured by an impedance probe. The effect of biased sampling towards larger drops was included while smoothing equations were introduced to eliminate the negative DSD values that can arise from direct backward transformation of CLD.

Two PBEs models were developed for liquid-liquid dispersions formed in stirred vessels and pipeline flows, respectively. A novel combination of population balance equations (PBEs) model with studies of phase inversion was presented in this work, which provided further understanding of the influence of breakage and coalescence of dispersed drops on the process of phase inversion. PBEs model indicated that there is a difference in the distance required to achieve the fully-developed state for different inversion routes, which suggests the existence of an ambivalent region in terms of location rather than input oil fraction in pipeline flow; this distance from the inlet where inversion occurs depends on the initial

conditions, mixture velocity and fluid physical properties. Also, modelling of phase inversion and the ambivalent region in stirred vessels with heterogeneous and homogeneous distribution on turbulent energy were presented. To achieve better predictions for stirred vessels, a 'two-region' model was postulated which assumed that drop breakup and coalescence take place preferentially in the vicinity of the impeller and away from that region, respectively. The predictions from the two-region model were found to be in good agreement with experimental data.

Finally, a framework of studying the behaviour of secondary dispersions was developed and incorporated into a PBEs model, by taking into account the inclusion and escape of secondary droplets.

Acknowledgement

Firstly, I would like to express my sincere gratitude and acknowledgment to my supervisors, Dr. P. Angeli at University College London (UCL), Dr. O.K. Matar and Prof. G.F. Hewitt (FRS, FREng) at Imperial College London (ICL), who introduced me to a very interesting research area – phase inversion in multiphase flow. Their insightful guidance, invaluable suggestions and infinite enthusiasms have enriched me not only in terms of technical aspects, but also in terms of my personal development. It would have been impossible to complete my Ph.D. study without their endless efforts and help. Words cannot express my deep-heartfelt appreciation of their laborious work and help over the past three years.

I would also like to thank Prof. C.J. Lawrence (ICL) who has also been a source of inspiration for me and helped me in solving many practical problems, particularly on converting chord length distributions to drop size distributions where many stimulating and instructive discussions were raised.

I am also greatly indebted to all the members of electronics, technicians and Workshops, especially Alan, Martin and Jone at UCL and Malcolm Dixon at ICL, who all kindly offered me help whenever I needed it.

I also wish to thank all my friends and colleagues, both past and present, who made my abroad life so memorable and enjoyable. Firstly, special appreciations go to Jason Lum who was one of my best friends at UCL, not only for his unforgettable helps but also for his optimism and braveness during his fight for life. He will be deep in my heart forever. Great thanks are also due to: Karolina, Talal, Jonathan, Wael, Prim, Carlos, Andrea, Shao Nan, Xiuyan, Sarah, Zhichao Florence, Colin Hale, Priscilla, Prash, Zuu, Wai-Lid, Tahsin, Ngugi, Toni, Liyun, Lina, Salihu, Jin, Colin Stewart, Jerry, James, Pooiling, Da Bao. I wish you all the best in your future life!

Finally, I would like to give my special thanks to my wife, Lan, for her endless love and support, to my lovely daughter, Naizhuo, for all the pleasure and excitement she brings to my life, and to my parents and my elder sister for their persistent encouragement and unconditional support.

Contents

List of Figures

Chapter 4

Chapter 5

Chapter 7

Chapter 8

Chapter 9

Appendix

List of Tables

Nomenclature

Roman Symbol

a	Constant in Eq. (2-1), (2-7), dimensionless
a, b	Parameters that control the distribution shape in Eq. (2-45), dimensionless
A	Interfacial areas of dispersion in Eq. (7-23), [m^2]
A, R	Pipe cross-sectional area ([m^2]) and pipe radius ([m]) in Eq. (3-1)
A, B, n	Parameters in Eq. (3-2), dimensionless
$A, B, n, C_0, C_1, C_2, C_3, C_4$	Calibration constants in Eq. (3-6), dimensionless
$\dot{b}(d/D)$, $\dot{d}(d/D)$	Birth and death rates of secondary droplets of diameter d in the host drop of diameter D, respectively, dimensionless
B	Birth rate in Eq. (2-15), (2-17), dimensionless
$\dot{B}(D)$, $\dot{D}(D)$	'Birth' and 'death' rates of a host drop of size D, respectively, dimensionless
c_f	Surface increase fraction, dimensionless
c_1	Drag coefficient in Eq. (2-69), dimensionless
c_1, c_2	Coefficients dependent on the bubble Reynolds number and the Bond number in Eq. (2-67), dimensionless
$c(v,V')$	Escape frequency of secondary droplets of volume v from host drop of volume V', dimensionless
$C(i, j)$	Element of matrix [**C**] in Eq. (4-16), dimensionless
C_1, C_2	Empirical constants to be found experimentally in Eq. (2-27), dimensionless
C_{AM}	Added mass coefficient by the bubbles in Eq. (2-66), dimensionless
C_D	Drag coefficient, dimensionless
C_H	Tunable constant, dimensionless
C_w, C_o	Multiplier in the Blasius type equation described in Eq. (2-11), dimensionless
C^*	Ratio of mass of the dispersed phase to the carrier phase in Eq. (2-71), dimensionless
C', C'', C'''	Constants in Eq. (2-25), dimensionless
d	Drop diameter, [m]

d, D	Diameters of secondary droplets and host drop, respectively, in Eq. (9-9), (9-10), [m]
d_{32}	Drop Sauter mean diameter, [m]
d_e	Eddies size, [m]
d_{min}, d_{max}	Minimum and maximum drop diameter, [m]
D	Death rate in Eq. (2-15), (2-17), dimensionless
D	Pipe diameter, [m]
D	Diameter of drop or bubble in Eq. (4-2), [m]
$D_F(\varphi)$	Turbulence damping factor due to the presence of dispersed phase at volume fraction φ, dimensionless
D_I	Impeller diameter in Eq. (2-63), [m]
e_k	Kinetic energy, [$m^2 s^{-2}$]
e_{min}	Minimum turbulence energy in Eq. (7-14), [$m^2 s^{-2}$]
E, E_C, E_s	Surface energy, [$m^2 s^{-2}$]
$\overline{E}$	Mean turbulent kinetic energy, [$m^2 s^{-2}$]
ΔE_k	Turbulent kinetic energy, [$m^2 s^{-2}$]
E_w, E_{corr}	Voltage acting on the sensor which is also the output of the CTA and the corrected voltage in Eq. (3-2), (3-4), [V]
f	Volume fraction in Eq. (2-40), dimensionless
f_S	Ratio of particle drag to Stokes drag in Eq. (2-70), dimensionless
f_V	Dimensionless variable describing the sizes of daughter drops
$f(l_w)$	Length function in Eq. (2-69) representing a measure of the region behind the particle where the fluid velocity is close to that of the particle, dimensionless
$f(L_{i-1}, L_i)$	Function defined in Equation (4-13), [m^2]
F	Force compressing the drops together in Eq. (2-59), (2-60), [N]
Fr	Froude number, dimensionless
g	Gravity acceleration, [$m s^{-2}$]
$g(v)$	Break-up frequency of drops of volume v, dimensionless
$G(d)$	Breakage rate, dimensionless
$G(i)$	Discrete chord length distribution of i^{th} category, dimensionless
$G(L)$	Probability of cutting chord of length L, [m^{-1}]
$\hat{G}$	Noise-added discrete chord length distribution, dimensionless
h	Film thickness, [m]
$h(v, v')$	Collision frequency, dimensionless
$\hbar_i$, $\hbar$	Turbulence intensities in particle-free (single-phase) and particle-laden flows
I	Normalization coefficient in Eq. (2-45), (2-46), dimensionless

k	Wave number in Eq. (2-32), dimensionless
k_1, k_2	Parameter in Eq. (2-11), dimensionless
$\widetilde{k}_i$, $\widetilde{k}$	Turbulence kinetic energy in particle-free and particle-laded flows, [m^2 s^{-2}]
k_i, l_i	Turbulence intensity ([-]) and length scale ([m]) for the corresponding single-phase flow in Eq. (2-70)
$k(v/V')$	Average number of secondary droplets of volume v within a host drop of volume V', dimensionless
K_a	Constant in Eq. (2-6), dimensionless
l_{hl}	Hybrid turbulence length scale, [m]
l_k	Kolmogorov length scale,[m]
L	Length scale of the energy containing eddies[m]
L	Chord length in Eq. (4-2), [m]
L	Pipe length in Eq. (7-12), [m]
M	Number of chord-length groups, dimensionless
$m(V')$	Number of drops formed from the breakage of a drop volume V', dimensionless
n, K	Constants in Eq. (2-65), dimensionless
n_e	Number density of eddies in the size range of interest, dimensionless
$n(d)$	Number density of droplets of diameter d, dimensionless
n_l	Noise level, dimensionless
n_w, n_o	Multiplier in the Blasius type equation described in Eq. (2-11), dimensionless
$n^0(v)$	Initial droplet number at $t = 0$ in Eq. (9-7), dimensionless
N	Number of drop-size groups, dimensionless
N	Rotation speed of impeller, [rpm]
N_T	Total number of drops per unit volume, [m^{-3}]
$N(v)$	Total number of particles of volume v per unit volume, [m^{-3}]
$p_v(V, V')$	Probability to entrap secondary droplets of volume v inside the host drop if secondary droplets are formed, dimensionless
P	Power input, [W]
P_E	Escape probability in Eq. (9-7), dimensionless
ΔP	Pressure difference, [Pa]
$\overline{P}$	Drop size distribution over the whole pipe cross-section area, dimensionless
$P(D)$	Probability density function of drop diameter D, [m^{-1}]
$P(j)$	Number density of drops in j^{th} group, dimensionless
$P(L)$	Probability of intersecting chord of length L, [m^{-1}]

$P(L\|R)$	Conditional probability of intersecting chord of length L from drop of size R, [m^{-1}]
$P(R)$	Probability density function of drop radius R, [m^{-1}]
$P(v)$	Initial number density of drops of volume v, dimensionless
$P_B(v: f_v v)$	Probability for a particle of size v to break into two particles, one with volume of $f_v v$, when the particle is hit by an arriving eddy of size λ, dimensionless
Q	Volumetric flow rate, [m^3/s]
r	Drop radius in Eq. (6-10), [m]
R	Pipe radius, [m]
Re	Reynolds number, dimensionless
RHS_k, RHS_{kj}	Rate of change of the k^{th} group of host drop and the rate of change of the j^{th} group of secondary droplets whose host drops are in the size group k, respectively, in Eq. (9-19), dimensionless
R_w, R_o	Wire resistances at the temperature T_w and reference temperature T_o, respectively, in Eq. (3-2), [Ω]
s	Solid surface area per unit volume in Eq. (2-12), [m^3]
s_f	Smoothing factor, dimensionless
$S(d,e)$	Collision cross-sectional area between particles of radius, $d/2$, and eddies of size, r_e, [m^2]
t_c	Circulation time of the secondary droplet inside the host drop in Eq. (9-7) [s]
t_d	Film drainage time, [s]
t_i	Drop interacting time, [s]
T_w, T_o	Wire working temperature and reference temperature, [°C]
u	Fluctuating velocity in Eq. (2-65), [m s^{-1}]
u	Relative velocity of drops in Eq. (2-61), [m s^{-1}]
$\overline{u^2}$	Mean square turbulent velocity fluctuation, [m s^{-1}]
$\overline{u}$	Average turbulent fluctuating velocity, [m s^{-1}]
U	Fluid (mean) velocity of phase, [m s^{-1}]
$\mathbf{U}$	Mean velocity of all drops, [m s^{-1}]
U_∞	Terminal velocity of a single bubble in an infinite liquid, [m s^{-1}]
$U(r)$	Local velocity at radius r, [m s^{-1}]
$\tilde{U}$	Instantaneous velocity at the pre-set sampling frequency in Eq. (6-1), (6-2), [m s^{-1}]
U_R	Relative velocity in Eq. (2-65), [m s^{-1}]
U_{rel}	Relative velocity in Eq. (2-69), [m s^{-1}]
U_{sw}, U_{so}	Water and oil superficial velocities, respectively, [m s^{-1}]

v, v'	Drop volume,
$\bar{v}$	Average size of included secondary droplets by coalescence of V and V' in Eq. (9-16), [m^3]
V	Volume of a single drop, [m^3]
V_I	Mixture volume in Eq. (2-63), [m^3].
V_I, V_T	Volumes of the impeller region and total volume of the vessel in Eq. (8-4), [m^3]
W_A	Width of the ambivalent region, dimensionless
We	Weber number, dimensionless
x	Axial distance from the entrance in Eq. (7-8), [m]
$X(r,D)$	Frequency density for drop of size D intersecting probe at centre distance r, [$s^{-1}m^{-2}$]
$X(L,D)$	Frequency density of cutting chord length L from drop of size D, [$s^{-1}m^{-2}$]
X_T	Total frequency of chords intersected by probe, [s^{-1}]
Y, Ω	Parameters in Eq. (2-22) fitted from experiments and representing the coalescence kernel and breakage kernel, respectively, dimensionless

Greek letters

α	Constant in Eq. (2-58), dimensionless
α_{cr}	Critical volume fraction in Eq. (9-7), dimensionless
α_R	Overheat ratio for a thin wire (or fibre film) sensor, in Eq. (3-3), dimensionless
α_p	Dispersed phase volume fraction in Eq. (2-71), dimensionless
β	Daughter drop size distribution, dimensionless
γ	Coefficient of virtual mass in Eq. (2-64), dimensionless
ϵ	Turbulent energy dissipation rate, [$m^2\ s^{-3}$]
ϵ	Phase holdup or volume fraction., dimensionless
η	Kolmogorov length scale, [m]
$\eta(V,V')$	Fraction of the coalescence events which do not involve secondary droplet inclusion in the formed drops (which is called 'pure' coalescence), dimensionless
θ	Contact angle, [rad]
κ	Viscosity ratio of the dispersed to the continuous phase, dimensionless

λ	Eddy size, [m]
$\lambda(V,V')$	Coalescence efficiency once a collision occurs between drops of volume V and V', dimensionless
λ_{SF}	Smoothing function defined by Eq. (4-18), dimensionless
μ	Liquid viscosity, [Pa s]
$\dot{\gamma}$	Shear rate defined by the stirrer spin rotation frequency, [s^{-1}]
ξ	Collision frequency in Eq. (2-39), dimensionless
ξ	Size ratio (λ/d) between an eddy and a drop, dimensionless
ρ	Density, [kg m^{-3}]
$\Delta\rho$	Density difference, [kg m^{-3}]
σ	Interfacial tension or surface tension, [N m^{-1}]
τ	Particle-eddy interaction time in Eq. (2-69), [s]
τ_c	Coalescence time or drainage time, [s]
$\bar{\tau}_I$	Interaction or contact time, [s]
τ_p	Characteristic time of the particle (relaxation time) in Eq. (2-69), [s]
ϕ	Phase holdup, dimensionless
ϕ_0	Asymptotic phase inversion holdup at high agitation speed in Eq. (2-1), dimensionless
φ^I	Phase inversion holdup, dimensionless
ϕ	Dispersed phase volume fraction, dimensionless
χ_c	Critical dimensionless energy for break-up, dimensionless
$\dot{\omega}_{B,\lambda}(v)$	Arrival (bombarding) frequency of eddies of size (length scale) between λ and $\lambda+d\lambda$ on particles of size v, [s^{-1}]
Γ	Viscosity ratio of the dispersed to the continuous phase, dimensionless
$\psi(L,D)$	Function defined by Eq. (4-16), dimensionless

Subscript

B	Breakup
c	Continuous phase
C	Coalescence
d	Dispersed phase
d	Drop in Eq. (2-29)

e	Eddy in Eq. (2-29), (2-30), (2-36)-(2-38)
f	Carrier fluid in Eq. (2-68), (2-69)
i, j	Group *i* and *j* of drop size or chord length
i,c	Impeller and circulation regions, respectively in Eq. (8-1)
I	Impeller, Eq. (2-10) –(2-11)
L	Liquid in Eq. (3-5)
m	Mixture liquids or dispersion
o/w, w/o	Oil-in-water dispersion and water-in-oil dispersion
o	Oil phase or organic phase
p	Particle in Eq. (2-68)
w	Water phase

Chapter 1

Introduction

1.1 Liquid-liquid Flows and Phase Inversion

Liquid-liquid systems, involving an aqueous phase (e.g. water) and an organic phase (e.g. oil), are found in a wide range of applications either in continuous flow (e.g. production wells and pipeline transportation) or in batch systems (e.g. two-phase reactors, separators). Compared to gas-liquid flows, which have received considerable attention, the experimental and theoretical studies involving liquid-liquid flows have covered only a restricted range of flow configurations and fluid properties. Much of the previous work has been devoted to liquid-liquid dispersions in agitated vessels, while only limited amount of work exists on liquid-liquid pipeline flows. According to Trallero (1995) and Angeli (1996), the following regimes for liquid-liquid flows in horizontal pipes have been identified:

- ❖ Segregated flow:
  - Stratified flow [ST (Trallero, 1995), SW (Angeli, 1996)]
  - Stratified flow with mixing at the interface
    [ST & MI (Trallero, 1995), SWD (Angeli, 1996)]
- ❖ Dispersed flow:
  - Water dominated
    - Dispersion of oil in water and water
      [Do/w & w (Trallero, 1995), M (Angeli, 1996)]
    - Oil in water dispersions [o/w (Trallero, 1995), M (Angeli, 1996)]
  - Oil dominated
    - Dispersions of water in oil and oil in water
      [Dw/o & Do/w (Trallero, 1995), 3L (Angeli, 1996)]
    - Water in oil dispersions [w/o (Trallero, 1995), M (Angeli, 1996)]

In dispersions of two immiscible liquids, for example oil and water, both water-in-oil (w/o) and oil-in-water (o/w) configurations can be obtained depending on operational factors such as dispersed liquid volume fraction, liquid properties (e.g. viscosity, interfacial tension and density), initial conditions and wall-wetting characteristics. For a given system, there is a transition between these two dispersions under certain conditions. Phase inversion is then defined as a phenomenon of phase interchange, whereby the continuous phase changes to become dispersed and the dispersed phase becomes continuous (Selker & Sleicher, 1965; Yeo et al., 2000). This phenomenon often occurs spontaneously at some critical operational condition, for example volumetric phase fraction or power input (e.g. velocity for pipeline systems or agitation speed for stirred vessels).

Phase inversion has been regarded as a spontaneous process associated with an abrupt change in drop sizes, affecting the rates of momentum, heat and mass transfer between the continuous and dispersed phases. A large number of studies on phase inversion have been carried out for dispersions generated with mechanically agitated impellers in batch or semi-batch systems. The results clearly indicated that the critical volume fraction of the dispersed phase where inversion appears (phase inversion point), varies with the system and is affected by a number of physical and operational parameters, such as properties of liquids, the container geometry and the initial conditions. In contrast to stirred vessels, significantly less work has been carried out on phase inversion during pipeline flows.

The experimental results clearly show the existence of a hysteresis effect between inversion from an organic and from an aqueous continuous solution, which manifests itself by the formation of a so-called *ambivalent* region, i.e. the range of organic (or dispersed) phase volume fraction wherein either the organic or the aqueous phase can be continuous. This ambivalent range is presented as a plot of the holdup of either the organic (Selker & Sleicher, 1965) or the dispersed phase (Kumar et al., 1991; Deshpande & Kumar, 2003) at inversion against agitation speed. Most recent studies in agitated vessels have suggested that the width of such an ambivalent range is dependent on initial conditions, viscosity ratio and wall material.

Knowing when phase inversion appears is important in industrial application since the change in phase continuity will lead to a system with different properties (e.g. rheology). In many cases phase inversion is part of the process (e.g. in the production of margarine or polymerisation). Of significance to transportation of dispersions is the observed increase in pressure gradient accompanying phase inversion (Ioannou et al., 2005). In the petroleum industry, for example, where crude oil and water need to be transferred from seabed to

offshore to plant, failure to predict this phenomenon can result in substantial decrease of oil productivity and pipeline capacity.

Prediction of phase inversion is therefore essential in many industries. Since the observation of this phenomenon, several physical mechanisms and some empirical correlations have been postulated to explain phase inversion and the existence of the ambivalent range (Yeh et al., 1964; Luhning & Sawistowski, 1971; Arashmid & Jeffreys, 1980; Brauner & Ullman, 2002; Sajjadi et al., 2002; Liu et al., 2005). In spite of many studies on phase inversion, however, the mechanism underlying phase inversion is still not well understood. The agreement between theory and experiment in terms of phase inversion point and the width of the ambivalent region is generally rather poor.

1.2 Objectives of the Study

The work presented in this thesis was carried out as part of a joint project between University College London (UCL) and Imperial College London (ICL). The main aim of this work is to gain a fundamental understanding of phase inversion at the mesoscale level and to derive models for its predictions. To this end, both theoretical and experimental studies were undertaken in this study, with the main objectives being described as follows:

Objectives of the experimental work:

(1) To investigate phase inversion and its associated phenomena (e.g. pressure drop, drop size distribution, ambivalent region and in-situ holdup) in vertical pipeline flows, where inhomogeneities in phase distribution due to gravity are eliminated.

(2) To understand the modifications of the continuous phase turbulence by the presence of dispersed phase in two-phase flow pre- and post-inversion. Here, an advanced instrument, hot-film anemometer (HFA), was employed for the measurements of the turbulence structure.

Objectives of the theoretical work:

(1) To derive a population balance equations (PBEs) model to predict drop size distribution and phase inversion for dispersions in stirred vessels and pipeline flow systems. To achieve this, a methodology is developed for transforming the measured

chord length distributions (CLD) to drop size distributions (DSD) used in the above model.

(2) To develop a model to simulate the ambivalent region widely found to accompany phase inversion in stirred vessels.

(3) To develop a framework of population balance modelling for simulating the dynamic evolution of concentrated dispersions containing secondary droplets.

1.3 Structure of the Thesis

The remainder of this thesis is organised as follows. A literature review is given in Chapter 2, which covers previous studies on phase inversion and its associated phenomena (e.g. the ambivalent range), population balance equations (PBEs), continuous phase turbulence modifications due to the presence of a dispersed phase and the application of a hot-film anemometer to turbulence measurements in two-phase flows.

Chapter 3 describes the experimental facilities, instrumentations and methods used in the present work; the techniques for measuring drop size and turbulence in oil-water dispersed flows are presented in detail. In Chapter 4, the relationship between the chord length distribution (CLD) obtained by an impedance probe and the drop size distribution (DSD) in a liquid-liquid dispersion is investigated. A new algorithm is also introduced to solve the problem of noisy or even apparently negative DSD values while performing the backward conversion (i.e. from CLD to DSD).

In Chapter 5, experiments on phase inversion and its associated phenomena in co-current upward and downward oil-water flow are described. Two inversion routes (w/o→ o/w and o/w→ w/o) are followed in dispersions with either constant or increasing power input (given by the mixture velocity). Parameters such as frictional pressure gradient, in-situ holdup, ratio of the oil and water phase velocity (U_o/U_w) and drop size distribution were also studied for flows pre- and post-phase inversion. Chapter 6 describes the experimental results on the modification of turbulence structure (mean and fluctuating turbulent velocities) in these flows, the information being obtained by a hot-film anemometer (HFA). Comparisons are also given in this Chapter between experimental findings and theoretical models suggested previously for predicting turbulence enhancement or attenuation.

In addition to the above experimental investigations, theoretical studies of phase inversion were also carried out in the work described in this thesis. Chapter 7 describes a population balance model, developed to predict phase inversion in liquid-liquid dispersions in stirred vessels and pipe flows; this is based on the assumption that the dispersion and the turbulent energy are homogeneously distributed. A further study of phase inversion in stirred vessels is reported in Chapter 8; this study developed a model that can predict ambivalent region based on the assumption that breakup only occurs in the impeller region and coalescence away from that region (two-region model). The predictions from the two-region model are then compared with experimental data (Norato et al., 1998).

In Chapter 9, preliminary work on the inclusion of secondary dispersion into population balance equations modelling is described. Secondary dispersion, wherein part of the continuous phase is entrapped into the dispersed phase, has been suggested as another important factor for phase inversion (Groeneweg et al., 1998; Sajjadi et al., 2002). However, the understanding of the mechanism of inclusion and escape of continuous phase droplets within dispersed drops is still rather limited due to the complicated nature of this phenomenon and the difficulties associated with experimental measurements. Even though a few experiments have been conducted to quantitatively investigate some parameters associated with such complex dispersions, no modelling work on dispersed systems containing secondary dispersions has been reported in the literature. Chapter 9, therefore, aims to outline a framework for simulating the dynamic evolution of dispersions containing secondary droplets.

Finally, conclusions and recommendations for future studies are presented in Chapter 10.

Chapter 2

Literature Survey

Previous work on phase inversion in agitated vessels and pipeline flows is reviewed in this Chapter. Section 2.1 mainly focuses on the experimental studies of phase inversion carried out in liquid-liquid pipeline flows, though studies of phase inversion in agitated vessels are also briefly discussed. More details of phase inversion and associated parameters in agitated vessels can be found in the reviews given by Yeo (2002) and Liu (2005). The postulated models to predict phase inversion in agitated vessels and pipeline flows are summarized in Section 2.2. The studies of drop size distribution in liquid-liquid dispersions via the population balance equations method (PBEs) are then reviewed in Section 2.3. The previous theoretical models of drop breakage and coalescence in turbulent flows are discussed in Section 2.4. In Section 2.5, studies of turbulent flow modifications by the dispersed phase in two-phase flow are reviewed. Section 2.6 describes the application of hot-film anemometer to turbulence measurement in air-liquid and liquid-liquid dispersed flows. Finally, a short summary is given in Section 2.7.

2.1 Experimental Studies of Phase Inversion

2.1.1 Phase Inversion Process

In liquid-liquid two-phase flow systems, usually consisting of an aqueous liquid (e.g. water) and an organic liquid (e.g. oil), there are two general types of dispersions in which either oil drops are dispersed in water phase (oil-in-water) or water drops are dispersed in oil phase (water-in-oil) respectively. Often, at certain conditions, either type of dispersion can be obtained. Phase inversion is then defined as a phenomenon whereby the phases of a liquid-liquid dispersion interchange such that the dispersed phase spontaneously inverts to become the continuous phase and vice versa. In general, for dispersions formed in agitated

vessels phase inversion will take place at a critical impeller speed for a certain phase fraction, or a critical phase concentration for a certain impeller speed.

For liquid-liquid dispersions with a constant turbulent power input (e.g. agitation speed or mixture velocity), phase inversion was found to occur at a certain critical volume fraction of the dispersed phase. As liquid-liquid dispersions have wide applications in industries, a well controlled phase inversion is a desirable and essential step whereas uncontrolled phase inversion is undesirable. As a result (since the first report of phase inversion by Rodger et al., 1956), much of the experimental and modelling work has been directed towards finding the critical phase volume fraction. The experiments have indicated that this critical volume fraction is system-specific and can be affected by a number of physical and physicochemical parameters, such as liquid properties, container geometry and initial conditions.

Figure 2.1 shows the schematic diagram postulated by Arirachakaran et al. (1989) to illustrate the phase inversion process in oil-water pipe flow. For small water volume fractions, the mixture forms a stable dilute water-in-oil dispersion where there is equilibrium between break-up and coalescence of water drops. As the water fraction increases, the rate of coalescence increases and water drops become larger. The system then becomes unstable if the water fraction continues to increase. Beyond a critical value of the volume fraction, rapid coalescence of the dispersed water drops occurs which dominates over their break-up, leading to catastrophic phase inversion, that is the dispersed phase spontaneously inverts to become continuous.

Recently, however, Liu et al. (2005) applied a non-intrusive dye tracing technique, laser-induced fluorescence (LIF), to visualize the phase inversion process in concentrated immiscible organic-aqueous liquid dispersions in a stirred vessel. Their experimental results, as shown in Figure 2.2, clearly demonstrated that phase inversion is a *gradual* rather than a catastrophic phenomenon: the process occurs over 1–2 s, may not occur globally and depends on the local phase distribution. During phase inversion, two opposing pairs of processes, drop coalescence and break-up, and the inclusion and escape of small droplets in larger drops, play a key role in the inversion process. The structure of the dispersion is extremely complex and a great number of secondary dispersions and multi-dispersions appear during phase inversion, which include water–in–oil–in–water secondary dispersions (which are notoriously difficult to observe).

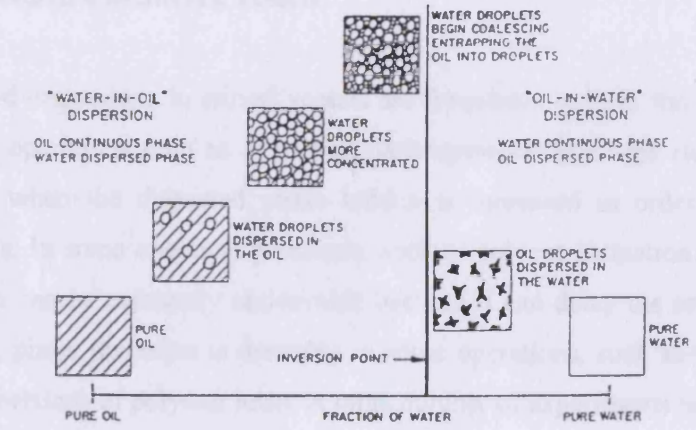

Figure 2.1: A schematic of phase inversion process in an oil-water dispersed pipe flow, postulated by Arirachakaran et al. (1989).

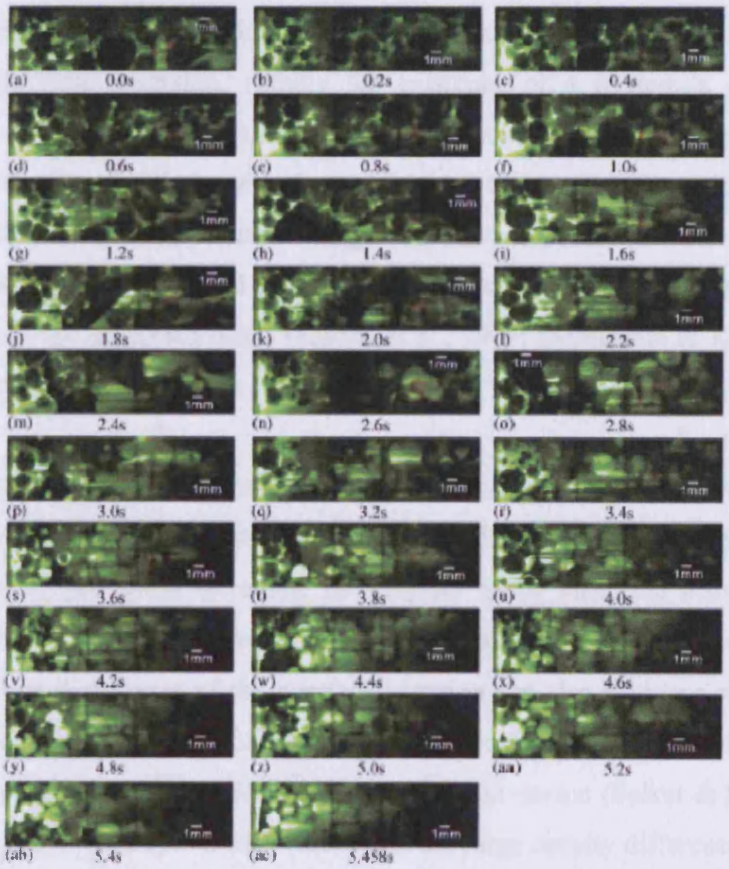

Figure 2.2: A time-series of photographs taken over 5.458 s, showing the dynamic evolution of an o/w emulsion (45% aqueous solution holdup) to a w/o emulsion, visualized by Liu et al. (2005) using laser-induced florescence. The experiments were conducted in a stirred vessel. Here, the black regions designate the organic phase and the lighter regions designate the aqueous phase.

2.1.2 Phase Inversion in Stirred Vessels

Liquid-liquid dispersions in stirred vessels are frequently used in the chemical industry for conducting operations such as extraction, heterogeneous reactions etc. Phase inversion mostly occurs when the dispersed phase holdup is increased in order to obtain higher interfacial areas. In some chemical processes, such as solvent extraction, in mixer-settlers, phase inversion can be extremely undesirable because it can delay the settling process. On the other hand, phase inversion is desirable in some operations, such as the preparation of waterborne dispersions of polymer resin. A large number of experiments have been reported, aimed at studying phase inversion and associated phenomena in agitated vessels. Table 2.1 lists the previous experimental investigations and their focal aspects in stirred vessel systems. Comprehensive reviews of the work conducted in stirred vessels have been given by Yeo et al. (2000) and Liu (2005).

Many of the experiments listed in Table 2.1 found an interesting additional phenomenon associated with phase inversion, namely the existence of a hysteresis effect between inversion from an organic and from an aqueous continuous solution, which manifests itself by the formation of a so-called *ambivalent region*, i.e. the range of organic (or dispersed) phase volume fraction wherein either the organic or the aqueous phase can be continuous. This ambivalent region is presented as a plot of the holdup of either the organic (Selker & Sleicher, 1965) or the dispersed phase (Kumar et al., 1991; Deshpande & Kumar, 2003) at inversion against agitation speed.

Generally in stirred vessels, it has been found that phase inversion and the ambivalent region can be affected by various factors. For example, Selker & Sleicher (1965) found that as the viscosity of one phase increases, its tendency to be dispersed also increases and ascribed this observation to be the result of the lower coalescence rates caused by the longer film drainage time. A decrease of the interfacial tension can also lead to a widening of the ambivalent region (Luhning & Sawistowski, 1971; Norato et al., 1998). Low density contrast between liquid pairs seem to show little effect on phase inversion (Selker & Sleicher, 1965, Norator et al., 1998), while systems in which there are large density differences between the phases were found to show an increased tendency to invert (Rodger et al., 1956; Kumar et al., 1991). However, it was also found recently that, for a specific system under sufficiently intense turbulence (i.e. high agitation speed), the inversion holdup is independent of any operational and geometric parameters and only affected by the liquid properties; the limits of the ambivalent region do not change with agitation speed (Deshpande & Kumar, 2003).

A number of alternative mechanisms for phase inversion have been postulated. Phase inversion was regarded, for example, as an instability between breakup and coalescence of dispersed drops (Arashmid & Jeffreys, 1980; Groeneweg et al., 1998), as a match of the system free energy (Luhning & Sawistowski, 1971; Tidhar et al., 1986; Yeo et al., 2002; Brauner & Ullman, 2002), as a point where zero shear stress exists between phases (Yeh et al., 1964; Nädler & Mewes, 1995) and as a result of the severe inclusion of the continuous phase into the dispersed drops (Groeneweg et al., 1998; Liu et al., 2005). Despite of the above efforts on phase inversion, the understanding on the mechanism of phase inversion and the existence of the ambivalent region is still fairly limited.

Table 2.1: Lists of previous experimental studies carried out in agitated vessels.

Author (year)	Parameters Studied & Focal points	Range or Material	Technique for Determining Phase Inversion	Impeller Type (Agitation Speed, r.p.m.)	Impeller Diameter (cm)	Tank Dia. (cm) or Vol. (L)
Quinn & Sigloh (1963)	1. Impeller Type & Size 2. Interfacial Tension	1: 7.94 ~ 9.37 cm 2: 0.0037 ~ 0.0511 N/m	Conductivity Probe	4-Flat Bladed Paddle & Double Paddles* (150 ~ 900)	7.94, 8.57, 9.37, 7.78*	14.29
Selker & Sleicher (1965)	1.Viscosity Ratio 2.Impeller Material 3.Tank Size and Shape	1: 0.02 ~ 130 2: Glass, Brass, Stainless Steel, Polyethylene	Conductivity Probe, Visualization (Dyes and Settling of Dispersion)	2-Blade Vertical Paddles & Three-Blade Axial-Flow Propellers (420 ~ 2000)	4.5 ~ 10.3	200ml~4L
Luhning & Sawistowski (1971)	1. Interfacial Tension 2. Ambivalent region 3. Mass Transfer	1: 0.0157 ~ 0.0511 N/m	Conductivity Probe	4-Bladed Turbine (300 ~ 1500)	6.65	15.3
Clarke & Sawiskowski (1978)	1. Mass Transfer	–	Conductivity Probe	4-Bladed Turbine (500 ~ 1500)	–	–
McClarey & Mansoori (1978)	1.Viscosity Difference	–	Conductivity Probe	2-Pitch Bladed Turbine (120 ~ 600)	–	–
Arashmid & Jeffreys (1980)	1. Fluid pairs 2. Ambivalent region	1. Toluene-water & Carbon tetrachloride-water	Conductivity Probe	4-Bladed Open Turbine (300 ~ 800)	5.0	10.2 (0.8 L)
Guilinger et al. (1988)	1.Tank Geometry 2.Dispersed Phase Viscosity 3.Impeller Wetting Characteristics	1.Stainless Steel & Plexiglass	Conductivity Probe & Visualization	4, 6 & 8-Bladed Turbines (300 ~ 600)	4.4~16.5	11.3 & 33.9
Kumar et al. (1991)	1. Impeller Materials	1.Stainless Steel & Glass	Conductivity Probe	Rushton Turbine (600 ~ 1250)	–	10.5

Author (year)	Parameters Studied	Range or Material	Technique for Determining Phase Inversion	Impeller Type (Agitation Speed, r.p.m.)	Impeller Diameter (cm)	Tank Dia. (cm) or Vol. (L)
Nienow et al. (1994)	1. Viscosity 2. Delay time 3. Batch & Semi-batch	1. 0.78 ~ 48 mPa S 2. 300 ~ 700 rpm	Conductivity Probe & Visualization	4-Pitch Bladed Turbine (400 ~ 700)	7.5	15.0
Chiang & Chen (1994)	1. Density Ratio 2. Surfactants 3. Mass Transfer	1: 0.6 ~ 1.6	Conductivity Probe	6-Flat Bladed Turbine (600 ~ 1400)	4.7	10.5
Brooks & Richmond (1994 abc)	1. Oil Viscosity 2. Drop Size	1. 0.7 ~ 200 mPa S	Visualization	6-Bladed Rushton Turbine (200 ~ 5000)	4.0	10.0
Pacek et al. (1994a)	1. Drop Size 2. Secondary Dispersion 3. Batch & Semi-batch	–	Conductivity Probe & Visualization	4- Bladed (60°-Pitch) Turbine (400 ~ 700)	7.5	15.0
Pacek et al. (1994b)	1. Viscosity 2. Ambivalent region 3. Delay Time 4. Density, Surface Tension	1. 0.59 ~ 48.0 mPa S	Conductivity Probe & Visualization	4- Bladed (60°-Pitch) Turbine (400 ~ 700)	7.5	15.0
Groeneweg et al. (1998)	1. Interfacial Tension 2. Agitation Time 3. Inclusion & Escape 4. Size of Included Droplet	–	Conductivity Probe& Visualization	6- Bladed Turbine (200 ~ 900)	4.8	8.9

Author (year)	Parameters Studied	Range or Material	Technique for Determining Phase Inversion	Impeller Type (Agitation Speed, r.p.m.)	Impeller Diameter (cm)	Tank Dia. (cm) or Vol. (L)
Norato et al. (1998)	1. Density 2. Viscosity 3. Interfacial Tension 4. Impeller Type & Size	1: 867 ~ 1180 Kg/m^3 2: 0. 96 ~ 3.78 mPa S 3: 0.0089 ~ 0.0323 N/m	Conductivity Probe	6-Bladed Rushton Turbine [1] Marine Propeller [2] (400 ~ 2000)	4.234 [1], 5.061 [1], 6.294 [1], 5.080 [2]	10.2
Tsouris & Dong (2000)	1. Electric Fields	59 ~ 1200 V	Conductivity Probe	6-Bladed Rushton Turbine (600 ~ 1050)	5.0	10.2
Sajjadi et al. (2002)	1. Inclusion & Escape 2. Size of Included Droplet 3. Drop Size Distribution	–	Conductivity Probe	4-Flat Bladed Turbine (500)	5.0	10.0
Deshpande & Kumar (2003)	1.Impeller Type 2.Tank Geometry 3.Ambivalent region	2. 0.9 L & 1.58 L 3. 600 ~ 2000 rpm	Conductivity Probe	6-Bladed Rushton Turbine[1] 6-Bladed Paddle[2] 4-Bladed Propeller[3] Disk with 21-Teeth Saw[4]	4.5, 5.5[1] 5.0[2] 6.75[3] 4.8[4]	10.2 & 12.7
Liu et al. (2005)	1. Inclusion & Escape 2. Coalescence & Breakage 3. Phase Inversion Process 4. Ambivalent Region 5. Complex Structure 6. Phase Inversion Time	–	Visualization	Magnetic Stirrer	2.0	80×25×25 mm square crosssection cell

2.1.3 Phase Inversion in Pipeline Flows

One of the most common but least understood types of multiphase flow is that of pipeline transportation of two immiscible liquids. In the petroleum industry, mixtures of oil and water are transported over long distances in pipelines from offshore to plant. Water is often introduced in controlled amounts into the pipeline in order to reduce the pressure gradient and hence pumping power required to transport the oil through the pipelines. However, at high volume fractions of oil phase, the oil-in-water dispersion has a strong tendency to invert to a water-in-oil dispersion. In addition, in the phase inversion region an abrupt increase of pressure gradient may occur. Failure to account for the abnormally high-pressure drops may result in substantial decreases of oil productivity and of pipeline capacity. Therefore, the design of pipelines as well as of pumping equipment requires knowledge of the critical volume fraction where phase inversion happens, and therefore an understanding of the inversion mechanism.

Experiments on a two-phase liquid-liquid flow in horizontal pipes (Russell et al., 1959; Charles et al., 1961; Guzhov et al., 1973; Arirachakaran et al., 1989; Nädler & Mewes, 1997) indicated that the pressure drop of the pipeline flow strongly depends on the flow regime and hence the distribution of the two liquids in the cross-sectional area of the pipe. The largest reduction in the pressure drop was expected when water, which is the less viscous liquid phase, forms a uniform annulus along the pipe wall, while the more viscous oil phase flows within the pipe core. Russell et al. (1959) suggested that the turbulent mixing in the pipeline can be sufficient to disperse the initially separated phases, so that dispersions are formed resulting in higher pressure drops. A reduction in the pressure drop is possible in oil-in-water dispersions (e.g. Sanchez & Zakin, 1994) and water-in-oil dispersions (Angeli, 1996). In addition, for water-in-oil dispersions the pressure drop can be significantly higher than the pressure drop for the pure oil flowing alone in the pipeline (Rose & Marsden, 1970; Nädler & Mewes, 1997). The flow behaviour of the oil and water dispersions is dependent on the input volume fraction and drop size distribution of the dispersed phase (Pilehvari et al. 1988). An abrupt increase of the pressure drop in dispersed flow to a value higher than that of pure oil flow is also observed in the region of phase inversion (Pan et al., 1996; Angeli, 1996; Nädler & Mewes, 1997; Ioannou et al., 2004&2005). Being complicated and undesirable, phase inversion becomes a key phenomenon in the design of oil-water pipelines since the rheological characteristics of the dispersion (e.g. wettability and conductivity) and the associated pressure drop change abruptly and significantly at or near the phase inversion point.

Despite the importance of phase inversion in pipelines, less work has been carried out in contrast to the studies in stirred vessels. Some researchers (Arirachakanran et al., 1989; Pal et al., 1986; Nädler & Mewes, 1995&1997; Ioannou et al., 2004; Liu et al., 2004; Liu, 2005) have investigated phase inversion and associated phenomena from experiments carried out in oil-water two-phase pipe flow, to characterize the dependence of the critical volume fraction on the various system parameters, e.g. viscosity ratio, velocity and pipe materials. The studies of phase inversion in oil-water flows are summarized in Table 2.2. The experimental data from pipe flows suggested that the more viscous oil tends to form the dispersed phase and water is likely to be continuous. The critical input water fraction required to invert a water-in-oil dispersion decreases as the oil viscosity increases. Recently Ioannou et al. (2005) investigated the influence of pipe wettability on phase inversion by using stainless steel and plastic pipes. The results showed that phase inversion of oil-in-water flows would happen at a higher input oil fraction when using the plastic pipe, than in the stainless steel pipe at the same velocity.

Table 2.2: Main aspects of studies of phase inversion in liquid-liquid pipe flows.

Author (Year)	**Main Aspects**
Tidar et al. (1986)	1.Surface energy.
Arirachakaran et al. (1989)	1.Pressure drop; 2.Phase inversion point; 3.Pipe diameter; 4.Temperature 5.Viscosity
Pal (1993)	1.Surfactants; 2.Drag Reduction.
Luo et al. (1997)	1.Mixture velocity; 2.Temperature; 3.Pressure; 4.Dispersion viscosity; 5. Pressure drop.
Nädler & Mewes (1997)	1.Oil viscosity; 2.Temperature; 3.Pressure drop.
Angeli & Hewitt (1998,2000a)	1.Wettability; 2.Mixture velocity; 3.Pressure gradient.
Soleimani (1999)	1.Pressure drop; 2.Flow pattern.
Gillies et al. (2000)	1.Surfactants; 2.Intensity and nature of shear process; 3.Solids content of oil.
Ioannou et al. (2004&2005)	1.Wettability; 2.Pipe diameter and material; 3.Pressure drop; 4.Phase distribution.
Liu et al. (2004) & Liu (2005)	1.Flow structure; 2.Drop size; 3.Phase inversion point.

Compared to investigations of phase inversion in horizontal flows, only limited work has been reported for vertical pipe flows (Govier et al., 1961; Luo et al., 1997; Liu et al., 2004; Liu, 2005). Luo et al. (1997) studied the oil-water upward flows in a stainless steel pipe of I.D. 44mm, using an oil with viscosity 452.6 cP. From the measured frictional pressure drops, they obtained the effective emulsion viscosity in the pre- and post-inversion regions and correlated it to water fraction, temperature, pressure and velocity. They found that phase inversion is affected by the mixture velocity while the emulsion becomes unstable probably due to phase inversion when the mixture velocity exceeds 0.8 m/s. The phase inversion point was not measured directly but calculated from a correlation by Yeh et al. (1964) though it was also associated with the pressure drop change observed. Recently, Liu et al. (2004) used a laser-induced florescence (LIF) technique to directly visualize the dynamic evolution of the dispersion and the internal flow structure in concentrated liquid-liquid downward flows. It was found that there is an unstable region between the two possible dispersions (o/w and w/o), wherein complex flow structures (i.e. multiple dispersions) are often observed. Phase inversion for a given well-established dispersion is suggested as a transitional process of crossing this unstable region.

Information on phase distribution in a horizontal pipe cross-section obtained by gamma densitometry (Soleimani, 1999; Hussain, 2004) and by high frequency impedance probe measurement (Angeli & Hewitt, 2000b; Ioannou et al., 2004) indicated mixture inhomogeneity and suggested that phase inversion could occur at different cross-sectional locations even in fully dispersed flow. For example, the inversion of a water-in-oil dispersion could take place first at the bottom part of the pipe, where water tends to accumulate. Local rather than global appearance of phase inversion was also found by Liu et al. (2005) in agitated systems using the LIF technique.

The studies reviewed above were of *unstable* dispersions (no added surfactants) in pipeline flow; Pal et al. (1986) and Pal (1993) also investigated phase inversion during *stable* emulsion pipe flow where non-ionic surfactants had been added. The viscosity of the emulsion (measured by a coaxial cylinder viscometer) was found to increase as the dispersed phase concentration increased and, as in the case of unstable dispersions, there was a sudden increase in the viscosity when inversion occurred. Furthermore, secondary and multiple emulsions (continuous phase is entrapped in dispersed drops) were widely observed in the water-in-oil emulsion before inversion. Due to the large number of secondary continuous phase drops a dramatic increase in the dispersed phase drop size was also observed before inversion, which has not been reported for pipe flow of unstable dispersions.

2.1.4 Ambivalent Region

Many experiments in liquid-liquid dispersions showed that there is a wide region of volume fractions, over which either liquid phase can be the stable dispersed phase (Selker & Sleicher, 1965; Clarke & Sawistowski, 1978; McClarey & Mansoori, 1978; Arashmid & Jeffrey, 1980; Tidhar et al., 1986; Dong & Tsouris, 2001; Deshpande et al., 2003). This region is known as ambivalent region, and the extent of this range depends on how the dispersion is produced and its subsequent history (Arashmid & Jeffrey, 1980).

The ambivalent region can be illustrated by plotting the dispersed phase volume fraction, ϕ_d, or organic phase volume fraction, ϕ_o, against the turbulent power input (e.g. agitation speed or mixture velocity). Figures 2.3 a&b show a typical ambivalent region obtained in a stirred vessel system by Kumar et al. (1991) and in horizontal pipeline flows by Ioannou et al. (2005). For example in the system described by Figure 2.3a, the dispersion can exist only as benzene-in-water dispersion below the lower ambivalent curve and only as water-in-benzene dispersion above the upper ambivalent curve. In between the two curves, namely within the ambivalent region, depending on initial conditions and dispersion history both water and benzene can be continuous.

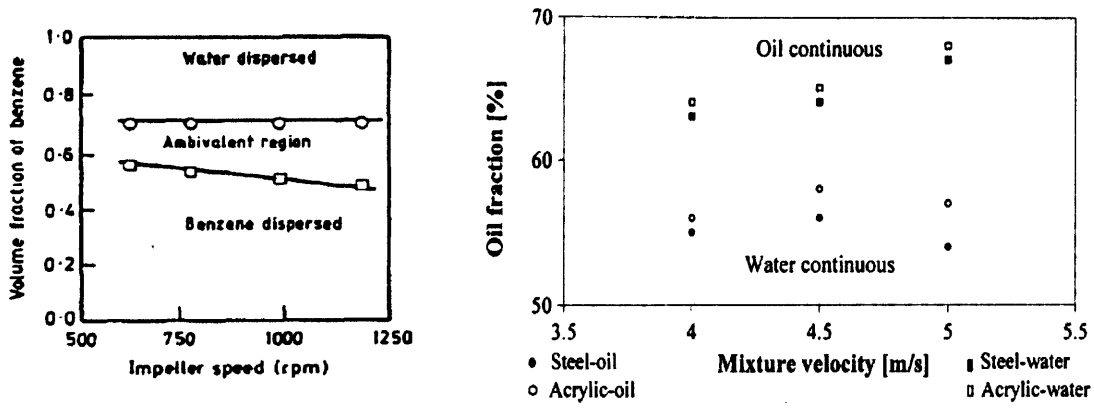

(a) (b)

Figure 2.3: The ambivalent region observed in (a) the benzene-water stirred vessel system (Kumar et al., 1991), and (b) the oil-water horizontal pipeline flow system (Ioannou et al., 2005)

Based on their experimental findings in stirred vessels, Clarke & Sawistowski (1978) suggested that the ambivalent region is a metastable region and any perturbations to the system will lead to the instability of the dispersion producing phase inversion at the boundaries of this region. The factors influencing the ambivalent region have been examined by many investigators. Previous experiments have found that the width of this range is a function of physical properties and system construction, such as wall wettability, impeller material, impeller type and container geometry (Guilinger et al., 1988; Kumar et al., 1991; Pacek et al., 1994b; Norato, et al., 1998; Tsouris & Dong, 2000; Deshpande, et al., 2003). However, for dispersions at high turbulent power input, several investigators found that the dispersed phase volume fraction at phase inversion saturates with increasing the agitation speed or mixture velocity (Tidhar et al., 1986; Brauner & Ullmann 2002; Deshpande et al., 2003). Under these conditions, the ambivalent region is only determined by the physical properties of the liquid pair.

Pacek et al. (1994b) and Kumar (1996) also attributed the ambivalent region to the effect of secondary dispersion where the continuous phase is trapped in the dispersed drops as small droplets. Their experiments showed the secondary dispersion to be present in water-in-oil dispersions but absent from oil-in-water dispersions. They claimed that since a small volume of the continuous phase is trapped in the oil drops, the effective holdup of the continuous phase decreases and that of the dispersed phase increases. Kumar (1996) took a further step and considered the differences of dielectric constants of two immiscible phases. The oil drops in water experience repulsive forces due to the overlapping of the electrical double layers and have low coalescence efficiency, whereas the water drops in oil do not experience such repulsion and have high coalescence efficiency. These charged drops would also give rise to hysteresis and an ambivalent region.

In contrast to the large number of studies reporting ambivalent region in stirred vessels, only a few such observations have been reported for pipeline flow systems. Ioannou et al. (2005) investigated the effect of pipe diameter and wettability on phase inversion in horizontal pipeline flows by using different sizes of stainless steel and acrylic pipes. Their experiments clearly showed the existence of an ambivalent region in both steel and acrylic pipes in terms of the input oil fractions as a function of the mixture velocity, shown in Figure 2.3b. However, these authors have also noticed in their system that the ambivalent region was only obtained for mixture velocities higher than 4 m/s in large pipes (60 mm ID), whereas ambivalent region was not found for flows in a small diameter acrylic pipe (32 mm ID). These findings indicated that the flows of concentrated dispersions in pipeline are very complex.

2.2 Theoretical Studies of Phase Inversion

Although the detailed mechanisms of phase inversion in liquid-liquid dispersions are still not well understood, extensive research has been carried out leading to some empirical and semi-empirical relationships for predicting phase inversion of dispersed flows in stirred vessels and pipelines.

2.2.1 Prediction of Phase Inversion in Stirred Vessels

Quinn & Sigloh (1963) found the phase inversion holdup obtained in oil-in-water dispersion decreases with the increase of the agitation speed before reaching a constant value at higher agitation speeds. Their experiments showed the organic phase holdup at phase inversion is inversely proportional to the energy input rate when water is continuous. They suggested the phase inversion holdup φ^I can be found as follows:

$$\varphi^I = \varphi_0 + \frac{a}{P} \tag{2-1}$$

where ϕ_0 is the asymptotic phase inversion holdup at high agitation speed, (N, revolutions per second) P is the power input ($\propto \rho_m N^3$) for mixture density ρ_m, and a is a constant determined by the physical properties of the system which could be approximately related to Weber number.

Yeh et al. (1964) studied the relationship of the phase inversion holdup to the system characteristics of a hand shaken flask, e.g. fluid viscosities and container geometries. They correlated the critical phase inversion holdup as a function of the viscosities of the liquids, which has the form of

$$\varphi_w^I = \frac{1}{1+\left(\frac{\mu_O}{\mu_W}\right)^{0.5}} \tag{2-2}$$

where φ_w^I is the critical water volume fraction at phase inversion and μ_O, μ_W are the oil and water viscosities, respectively.

Luhning & Sawistowski (1971) experimentally investigated the effect on the phase inversion and ambivalent region of various parameters, such as interfacial tension and agitation speed. The results showed that the inversion curve tends asymptotically to a constant value with increasing agitation speed. The organic phase holdup, φ_o^I, at phase inversion was found to be a linear function of the Weber number. They therefore correlated the curves of the ambivalent region as follows,

$$\varphi_O^I = 0.16 + 6.0\times10^{-5} We \qquad \text{for the upper inversion curve} \qquad (2\text{-}3a)$$

$$\varphi_O^I = 0.47 + 2.0\times10^{-5} We \qquad \text{for the lower inversion curve} \qquad (2\text{-}3b)$$

Here, $We = \rho_c N_I^2 D_I^3 / \sigma$ where ρ_c is the density of continuous phase, N_I is the agitation speed, D_I is the impeller diameter and σ is the interfacial tension. In addition, they found that interfacial tension is one of the principal factors affecting the width of the ambivalent region, W_A, which was correlated by their experimental data as

$$W_A = (5.64N_I - 64)(1.0\times10^{-3}\sigma)^{-(0.82+3.96\times10^{-2}N_I)} \qquad (2\text{-}4)$$

In later work, Fakhr-Din (1973) who conducted experiments in stirred vessels reported that there was always a reduction in the interfacial energy when phase inversion appeared. The magnitude of surface energy change was found to be close to the total system energy change, while the kinetic energy variation was considered to be negligible. Taking into account the fact that phase inversion is a spontaneous process, he suggested that the total system energy would be at its lowest level at the phase inversion point. Hence, according to this criterion he correlated the curves of ambivalent region as a function of appropriate dimensionless numbers as follows:

$$\varphi_O^I = 1.32\times10^6\left(\frac{\mu_d}{\mu_c}\right)^{0.32}\left(\frac{\Delta\rho}{\rho_c}\right)^{-0.11} Fr^{0.71}\,\mathrm{Re}^{1.06}\,We^{-0.25} \qquad \text{for upper inversion curve} \qquad (2\text{-}5a)$$

$$\varphi_O^I = 12.2\times\left(\frac{\mu_d}{\mu_c}\right)^{0.31}\left(\frac{\Delta\rho}{\rho_c}\right)^{0.04} Fr^{0.13}\,\mathrm{Re}^{0.22}\,We^{-0.03} \qquad \text{for lower inversion curve} \qquad (2\text{-}5b)$$

where μ_d, μ_c are the dispersed and continuous phase viscosities, respectively; ρ_c is the continuous phase density and $\Delta\rho$ is the density differences between the dispersed and

continuous phase; Fr is the Froude number (defined by $Fr=N_I^2D_I/g$) where g is the gravitational acceleration, Re is the impeller Reynolds number (defined by $Re= \rho_m N_I D_I^2/ \mu_c$) and We is the Weber number. This criterion of minimal or equal system energy at phase inversion was also suggested by Tidhar et al. (1986).

An attempt was made by Arashmid & Jeffreys (1980) to understand the phase inversion phenomenon by considering drop collision and coalescence frequencies. They proposed that when the dispersion is agitated, the drops will collide and some will coalesce. As the dispersed phase holdup increases, at constant agitation speed, the proportion of the pairs of drops coalescing at each collision will increase until, at phase inversion coalescence will occur for every collision. In other words, when the frequencies of drop collision and coalescence become equal, phase inversion occurs. Then by using the collision frequency model developed by Levich (1962) and the coalescence frequency model given by Howarth (1967), they derived the following equation for dispersed phase holdup, φ_d^I, at phase inversion,

$$\frac{K_a}{\varphi_d^I D_I^2 N_I^{0.48}} = 1 \tag{2-6}$$

where D_I is the impeller diameter, N_I is the agitation speed and K_a is a constant that was found dependent on the system and physical properties, varying from 10^{-3} to 10^7.

In contrast to the mechanism postulated by Arashmid & Jeffreys (1980) which attributed phase inversion only to drop coalescence, Vaessen et al. (1996) investigated the dynamic balance of drop breakage and coalescence rates within a dispersion in which one of the phases contained a surfactant. Droplets made up of the phase containing surfactant are much less stable than droplets surrounded by the phase with surfactant, they suggested that there are two types of inversion: *easy inversion* where initially the surfactant is present in the dispersed phase and *difficult inversion* where initially the surfactant is in the continuous phase. Easy inversion will involve rapid film drainage where the coalescence rate could be regarded equal to the drop collision frequency, whereas difficult inversion will involve slow film drainage where the coalescence efficiency must be taken into account. They also inferred that these two different inversions may be the reason for the occurrence of hysteresis phenomenon in phase inversion. The coalescence rate before inversion was then expressed by the product of collision frequency (Saffman & Turner, 1956) and coalescence efficiency (Chesters, 1991):

$$\Lambda(d) = 6.87\varepsilon^{1/3}d^{7/3}n(d)^2 \exp(-\frac{at_d}{t_i}) \tag{2-7}$$

where $\Lambda(d)$ is the coalescence rate of drops with mean diameter d, ϵ is the average energy dissipation rate, *n(d)* represents the number density of droplets of diameter d, t_d and t_i are the film drainage time and drop interacting time, respectively. The constant a=0 for easy inversion and a=1 for difficult inversion. The formation postulated by Delichatsios & Probstein (1976) was used for breakage rate, *G(d)*:

$$G(d) = 1.37\sqrt{\frac{2}{\pi}}\varepsilon^{1/3}d^{-2/3}\exp(\frac{\sigma}{1.88\varepsilon^{2/3}d^{5/3}})n(d) \tag{2-8}$$

From Equations (2-7) and (2-8), an estimate of the stationary drop size at a given dispersed phase volume fraction could then be calculated, namely the drop size at which the coalescence and breakage do not change the number mean diameter. Vassen et al. (1996) then suggested a criterion for phase inversion, in which phase inversion will occur at the dispersed phase volume fraction where the stationary drop size from the above equations starts diverging. Furthermore, using this criterion they studied the delay time of phase inversion. However the results from this model showed underestimation of the phase inversion point when compared to the one measured in water and *n*-hexane dispersion.

Recently, Juswandi (1995) and Yeo et al. (2002) studied the drop size distribution in dense dispersions using Monte Carlo method, which employed drop breakage and coalescence models suggested by Sovová (1981). To identify the dispersed phase volume fraction at phase inversion, ϕ^I, the criterion of equal surface energy was applied (Luhning and Sawistowski, 1971; Tidhar et al., 1986). Therefore the following equation at phase inversion was derived (Yeo et al., 2002),

$$\frac{\varphi_o^I}{1-\varphi_o^I} = \frac{d_{32\,O/W}}{d_{32\,W/O}} \tag{2-9}$$

where φ_o^I is the oil holdup at phase inversion and $d_{32_{O/W}}$ and $d_{32_{W/O}}$ are the Sauter mean diameters in oil-in-water and water-in-oil dispersions, respectively.

2.2.2 Prediction of Phase Inversion in Pipeline Flows

Based on a number of experimental data from various investigators on the phase inversion point in pipe flow, Arirachakanran et al. (1989) correlated the critical input water fraction, φ_w^I, as follows,

$$\varphi_w^I = \frac{U_{sw}}{U_{sw}+U_{so}} = 0.5 - 0.1108 \log \frac{\mu_O}{\mu_W} \tag{2-10}$$

where μ_O and μ_W are the oil and water viscosities, respectively; U_{sw} and U_{so} are the water and oil superficial velocities, respectively. For a highly viscous oil (~ 0.2 Pa s), a constant value of $\varphi_w^I = 0.15$ has been reported (Brooks & Richmond, 1994).

Nädler & Mewes (1995) postulated another correlation on the basis of momentum equations for stratified flow. They assumed a negligible interfacial shear and no-slip between the two layers at phase inversion, and the following correlation was obtained:

$$\varphi_w^I = \frac{1}{1+k_1\left(\frac{C_O}{C_W}\frac{\rho_O^{1-n_O}}{\rho_W^{1-n_W}}\frac{\mu_O^{n_O}}{\mu_W^{n_W}}(DU_m)^{n_W-n_O}\right)^{1/k_2}} \tag{2-11}$$

where D is the pipe diameter; U_m is the mixture velocity; $\rho_{O,W}$ and $\mu_{O,W}$ are the densities and viscosities of the oil and water phases, respectively; $C_{O,W}$ and $n_{O,W}$ are the parameters of the Blasius equation for the friction factor, $C\mathrm{Re}^{-n}$; k_1 and k_2 are empirical constants. They suggested that k_1 reflects the wall-liquids contact perimeter and k_2 accounts for the flow regime in each phase. For laminar flow in both phases, where $k_1 = 1$ and $k_2 = 2$, Equation (2-11) is identical to the model postulated by Yeh et al. (1964) based on studies in hand-shaken flasks [see Equation (2-2)].

Recently Brauner & Ullmann (2002) employed the criterion of minimum system free energy to predict conditions under which phase inversion will occur in dispersed liquid-liquid pipe flows. They assumed that the initial dispersion and the dispersion after inversion are stable within a range of operational conditions. After postulating that the system free energy should be represented by the total surface energy, they suggested that phase inversion will occur under the critical condition, where the sums of the wall-liquid and liquid-liquid

surface energies in either of two possible dispersions are equal. After expressing the interfacial area by means of Sauter mean diameter, d_{32}, the following equation was produced:

$$\varepsilon_w^I = \frac{\left(\frac{\sigma}{d_{32}}\right)_{W/O} + \frac{s}{6}\sigma\cos\theta}{\left(\frac{\sigma}{d_{32}}\right)_{W/O} + \left(\frac{\sigma}{d_{32}}\right)_{O/W}} \tag{2-12}$$

where σ is the oil-water surface tension; s is the solid surface area per unit volume, where $s = 4/D$ for flow in a smooth pipe of diameter D; $(d_{32})_{O/W}$ and $(d_{32})_{W/O}$ represent the Sauter mean diameter in a dispersion of oil-in-water and water-in-oil, respectively; θ is the liquid-solid wall contact angle, where $0 \le \theta < 90^o$ corresponds to a surface which is preferentially wetted by water (hydrophilic surface) and $90^o < \theta \le 180^o$ corresponds to a surface which is preferentially wetted by oil (hydrophobic surface). They also assumed that in concentrated dispersed flow the Sauter mean diameter, d_{32}, is proportional to the maximum drop size, d_{max}. Hence, if the oil-water surface tensions in the pre-inversion and post-inversion dispersions are the same (no surfactants or surface contaminants are involved), and solid-liquid wettability effects can be neglected, Equation (2-12) then becomes similar to Equation (2-9),

$$\varphi_w^I = \frac{(d_{\max})_{O/W}/(d_{\max})_{W/O}}{1+(d_{\max})_{O/W}/(d_{\max})_{W/O}} \tag{2-13}$$

where $(d_{\max})_{O/W}$ and $(d_{\max})_{W/O}$ are the maximum drop sizes in oil-in-water and water-in-oil dispersion, respectively. As shown in the above equations, this model requires the prediction of the characteristic drop size in dense dispersions. Brauner & Ullmann (2002) evaluated the maximum drop size based on a local energy balance for dense dispersions, which yields the following expression for $d_{\max}$:

$$\frac{(d_{\max})_{d/c}}{D} = 7.61 C_H \left(\frac{\sigma}{\rho_c D U_m^2}\right)^{0.6} \left(\frac{\rho_c D U_m}{\mu_c}\right)^{0.08} \left(\frac{\rho_c}{\rho_m}\right)^{0.4} \frac{\varphi_d^{0.6}}{(1-\varphi_d)^{0.2}} \tag{2-14}$$

where subscript d, c, m refer to the dispersed, continuous, and mixed phase and $C_H = O(1)$ is the tunable constant.

Brauner & Ullmann (2002) also discussed the influence of contaminants on the ambivalent region. They reported that for a pure liquid-liquid system the interfacial tension, σ, in the initial dispersion and in the post-inversion dispersion is the same. However, for dispersions containing contaminants or surfactants, the contaminants or surfactants could cause the decrease of the surface tension, σ. After phase inversion, where new interfaces have been created, the surface tension will be different and equal to that of a pure system. Using Equation (2-12) under this assumption in an o/w and a w/o system would give different inversion points and therefore an ambivalent range.

2.3 Population Balance Equations Method

The essential characteristic of a dispersion is the drop size distribution. Knowing the drop size distribution of the dispersed phase is very important in a variety of practical problems, such as the design of physical and chemical processes, the transportation of oil-water mixtures and emulsion separation. Many researchers experimentally measured the dispersed phase drop size via several different techniques, e.g. photography (Pal et al., 1986; Pacek et al., 1994a; Angeli & Hewitt, 2000b; Sajjadi et al., 2002), impedance probes (Kurban, 1997; Lovick, 2004), and laser backscattering optical techniques (Simmons & Azzopardi, 2001). On the basis of these experimental data a number of correlations have been postulated to estimate the maximum drop size (d_{max}) and Sauter mean diameter (d_{32}) for dispersions in agitated vessels (Zhou & Kresta, 1998) and pipeline flows (Angeli & Hewitt, 2000b). In addition to the experimental correlations another advanced technique, namely the population balance equations method (PBEs), has also been broadly employed in studies of drop size evolution in liquid-liquid dispersions. In what follows, the general equations of a PBEs model are reviewed.

The drop size distribution within a particular region in two-phase liquid-liquid dispersions is basically determined by various phenomena, which can be divided into the following:

- Feed or discharge of drops;
- Nucleation and growth of drops due to mass transfer or chemical reactions between dispersed and continuous phases;
- Breakage and coalescence of drops affected by the turbulent flows and physical properties.

If the drops are assumed to be spherical and $n(\mathbf{X},v,t)d\mathbf{X}dv$ represents the number of drops of volume from v to $v+dv$ per unit volume at time t in the spatial range $d\mathbf{X}$ at $\mathbf{X}$, the general population balance equations can then be written in the following form:

$$\frac{\partial n(\mathbf{X},v,t)}{\partial t}+\frac{\partial[\dot{v}\cdot n(\mathbf{X},v,t)]}{\partial v}+\nabla_{\mathbf{X}}\cdot[\mathbf{U}(\mathbf{X},v,t)]=B(\mathbf{X},v,t)-D(\mathbf{X},v,t) \tag{2-15}$$

where $\dot{v}=dv/dt$ is the drop growth rate, $\mathbf{U}$ is the mean velocity of all drops of volume v at location $\mathbf{X}$ and time t, B and D are the birth and death rates, respectively, of drops of volume v due to drop breakage and coalescence.

Generally for liquid-liquid dispersions, the changes of dispersed drop size are regarded as resulting only from breakage and coalescence rather than mass transfer or reaction ($\dot{v}=0$). Thus in flows where the drops can be assumed uniformly dispersed in a turbulent field, e.g. in batch stirred vessels, the population balance equations for a unit volume are given by (Valentas et al., 1966; Coulaloglou & Tavlarides, 1977; Hsia & Tavlarides, 1980; Alopaeus, et al., 1999)

$$\frac{dn(v,t)}{dt}=\frac{1}{\tau}[n_{in}(v,t)-n_{out}(v,t)]+B(v,t)-D(v,t) \tag{2-16}$$

where τ is the drop residence time, $n_{in}(v,t)$ and $n_{out}(v,t)$ are the number rate of drops flowing into and out of the volume of interest. In the batch agitated vessels widely used in chemical engineering, flows into and out of the vessels are negligible and Equation (2-16) can be simplified to (Sovová, 1981; Lasheras et al., 2002; Hagesaether et al., 2002)

$$\frac{dn(v,t)}{dt}=B(v,t)-D(v,t) \tag{2-17}$$

For drops of volume v at a given time t, the death term consists of breakage to smaller drops and coalescence with other drops to form a larger drop, and similarly the birth term consists of breakage of larger drops into drops of volume v and coalescence of smaller drops leading to a product drop of volume v. Therefore, the following expressions for the birth and death rates are given:

$$B(v,t) = B_B(v,t) + B_C(v,t) \tag{2-18}$$

$$D(v,t) = D_B(v,t) + D_C(v,t) \tag{2-19}$$

where $B_B(v)$ and $D_B(v)$ are the birth rate and death rate of volume v due to drop breakage, respectively; $B_C(v)$ and $D_C(v)$ are the birth rate and death rate of group v due to drop coalescence, respectively. For a given time t their values can be calculated by

$$B_B(v) = \int_v^\infty m(v')\beta(v,v')g(v')n(v',t)dv' \tag{2-20a}$$

$$D_B(v) = g(v)n(v,t) \tag{2-20b}$$

$$B_C(v) = \int_0^{v/2} \lambda(v-v',v')h(v-v',v')n(v-v',t)n(v',t)dv' \tag{2-20c}$$

$$D_C(v) = n(v,t)\int_0^\infty \lambda(v,v')h(v,v')n(v',t)dv' \tag{2-20d}$$

Here, $m(v')$ is the number of daughter drops formed due to breakage of a drop volume v'; $\beta(v, v')$ is the probability density function of the daughter drops which represents the probability of forming drops of volume v from breakage of drops of volume v'; $g(v')$ is the breakage frequency of drops of volume v'; $\lambda(v, v')$ is the coalescence frequency between drops of volume v and drops of volume v'; $h(v, v')$ is the collision frequency of drops of volume v and v'.

Although PBEs modelling has been widely applied to drop size studies in stirred vessels, little work exists in pipeline flows. Kostoglou & Karabelas (1998) employed 1-D PBEs model to investigate the maximum drop size (d_{max}) in oil-water pipe flows at dilute dispersions where coalescence can be ignored. They considered the oil-water dispersion moving as a plug flow while the gravitational and axial turbulent diffusion effects were ignored. By assuming that the drops of the dispersed phase are homogeneously distributed over the pipe cross-section area at any axial location, the following population balance equations were derived:

$$\frac{dn(v,t)}{dt} = B_B(v,t) - D_B(v,t) \tag{2-21}$$

where $n(v,t)$ represents the number density of drops of volume v at time t in a controlled volume moving at the mixture velocity. A simple power law breakage rate and a U-shaped daughter drop distribution postulated by Kostoglou et al. (1997) were used in Equation (2-20a&b) to calculate the r.h.s of Equation (2-21).

Following the above work, Kostoglou & Karabelas (1998 & 2001) also applied PBEs to study the drop size distribution when coalescence cannot be ignored. Again, assuming the mixture moving like a plug at the same velocity along the pipe, a similar expression to that in stirred vessels (Equation 2-17) was derived. However, in contrast to the PBEs method suggested by Kostoglou & Karabelas (1997, 1998, 2001), Gnotke et al. (2003) deduced a different equation for gas-liquid bubbly pipeline flows. They studied the axial evolution of bubble size distribution in a vertical pipe via PBEs by assuming that the dispersed flows are in steady state at all axial locations along the pipe [$\partial n(v,x)/\partial t = 0$]. Taking into account that the mixture velocity is the same in the whole pipe, the following 1-D population balance equation was derived,

$$U_m \frac{\partial n(v,x)}{\partial x} = Y \cdot n(v,x)^2 + \Omega \cdot n(v,x) \tag{2-22}$$

where U_m is the mixture velocity along axial direction, Y and Ω are two parameters fitted from experiments and representing the coalescence kernel and breakage kernel, respectively.

Using Equation (2-21), Kostoglou & Karabelas (1998 & 2001) analysed the axial evolution of drop sizes in a dilute dispersion where coalescence of drops is negligible. Their computational results suggested that the maximum stable drop size (d_{max}) may not be attainable within a time period of practical interest if much larger particles undergo breakage in a limited developing distance. Extra care should be exercised in evaluating data, reported to be representative of the steady state. Since the time required to reach steady state is unknown a priori, one naturally attempts to obtain d_{max} by comparing several (often closely spaced in time) measured distributions; a tendency to obtain nearly identical distributions (within the accuracy limits of the experimental technique) may be interpreted as evidence of the attainment of steady state (e.g. Hesketh et al., 1991). Kostoglou & Karabelas (1998 & 2001) argued that their PBEs model suggested that this may lead to incorrect results if the rate of change is small and reliance on a critical droplet size in apparatus design (as is often done) may not be warranted.

2.4 Drop Breakage & Coalescence Models

In order to solve population balance equations the rates of drop breakage and coalescence in turbulent flow are required. Many models for drop (or bubble) break-up and coalescence have been proposed in literature and these are reviewed below.

2.4.1 Breakage Models

In turbulent flow, it has been recognized that there are at least three possible breakage mechanisms for drops or bubbles. These are turbulent (deformation) breakage, viscous shear (tearing) breakage and elongation flow breakage in accelerating flow (Hagesaether et al., 2002). In multiphase reactors or pipeline flows, breakage due to turbulence has been considered as the dominant mechanism, since viscous shear breakage often happens in laminar flow and elongation flow breakage always takes place at a liquid acceleration region (e.g. the area close to impeller). Hence, most postulated models are primarily concerned with the turbulent breakage mechanism. It is also generally assumed that breakage mechanism is that of binary breakage, namely two droplets are formed in one breakage. In what follows, four widely used models for breakage are described, namely those of Coulaloglou & Tavlarides (1977), Prince & Blanch (1990), Tsouris & Tavlarides (1994) and Luo & Svendsen (1996).

Coulaloglou & Tavlarides (1977) initially postulated a phenomenological model to calculate drop breakage rate, which was defined as

$$g(v)=\left(\frac{1}{\text{breakup time}}\right)\left(\begin{matrix}\text{fraction of}\\ \text{drops breaking}\end{matrix}\right)=\frac{1}{t_b}\frac{\Delta N(v)}{N(v)} \tag{2-23}$$

where $N(v)$ is the total number of particles of volume v per unit volume. They modeled the fraction of drops breaking as

$$\frac{\Delta N(v)}{N(v)}=\exp\left(-\frac{E_c}{\overline{E}}\right) \tag{2-24}$$

$E_C=C'\sigma d^2$ is the surface energy and $\overline{E}$ is the mean turbulent kinetic energy. For a homogeneous and isotropic turbulence, if a drop diameter d is within the inertial turbulent subrange, the mean turbulent kinetic energy, $\overline{E}$, can be expressed as (Batchelor, 1956):

$$\overline{E} = C''\rho d^3\overline{\Delta u^2} = C'''\rho d^3\left(\frac{\varepsilon}{d}\right)^{2/3} \tag{2-25}$$

where ϵ is the energy dissipation rate per unit mass. Here, C', C'' and C''' are constants obtained from experiments. Coulaloglou & Tavlarides (1977) further suggested that the time scale of break-up is determined by the turbulent (eddy) turnover time, which is

$$t_b \propto \frac{d^{2/3}}{\varepsilon^{1/3}} \tag{2-26}$$

Finally they deduced the following function for the break-up frequency of drops of volume v,

$$g(v) = C_1 \frac{\varepsilon^{1/3}}{(1+\varphi)v^{2/9}} \exp\left(-\frac{C_2\sigma}{\rho\varepsilon^{2/3}v^{5/9}}\right) \tag{2-27}$$

Here C_1 and C_2 are empirical constants to be found experimentally. Several investigators have determined these two constants from their experimental data. Table 2.3 lists the suggested values of C_1 and C_2 (Alopaeus *et al.*, 1999)

Table 2.3: Empirical constants of C_1 and C_2.

Author (year)	C_1	C_2
Coulaloglou & Tavlarides (1977)	0.00487	0.0552
Ross et al. (1978)	0.00487	0.08
Hsia et al. (1980)	0.01031	0.06354
Bapat & Tavlarides (1985)	0.00481	0.08

Following arguments from the kinetic theory of gases, Prince & Blanch (1990) postulated another model where particle break-up is the result of collisions between particles and turbulent eddies. Their break-up frequency of drops of size d, therefore, is given by a collision rate with eddies, $h(d,e)$, multiplied by a break-up efficiency, $p(d)$,

$$g(d) = h(d,e)p(d) \tag{2-28}$$

where the collision rate is given by

$$h(d,e) = n_e S(d,e)(u_d^2 + u_e^2)^{1/2} \tag{2-29}$$

Here n_e is the number density of eddies in the size range of interest; u_d^2 and u_e^2 are the average mean square turbulent velocities of particles (or drops) and eddies, respectively, that follow the relationship of $u^2 \propto (\varepsilon l)^{2/3}$ for distance l; *S(d,e)* is the collision cross-sectional area between particles of radius, *d/2*, and eddies of size, r_e, given by

$$S(d,e) = \frac{\pi}{4}(d/2 + r_e)^2 \tag{2-30}$$

The number density of eddies within a given size range is obtained by integrating the energy spectrum, $dn_e(k)/dk = 0.1k^2$. Prince and Blanch noted that this integration would give an infinite number of eddies as the wave number k goes to infinity (small-size eddies). To avoid this problem, they arbitrarily chose a minimum eddy size equal to 20% of the particle diameter, suggesting that eddies with a characteristic length equal to 20% of the drop diameter contain only 0.5% of the kinetic energy associated with an eddy of the size of the particle (this point will be further discussed later on). A breakage efficiency function, similar to Equation (2-24) by Coulaloglou and Tavlarides (1977), was also used.

$$p(d) = \exp\left(-\frac{E_c}{E}\right) \tag{2-31}$$

Prince and Blanch (1990) hence expressed the breakage frequency of drops of size d as an integral form,

$$g(d) = \int_0^{10\pi/d} \frac{0.14\pi}{16}\left(d + \frac{2\pi}{k}\right)^2 \left(d^{2/3} + \left(\frac{2\pi}{k}\right)^{2/3}\right)^{1/2} \varepsilon^{1/3} \exp\left(-\frac{1.18}{(2\pi)^{2/3}} \frac{\sigma k^{2/3}}{\rho d \varepsilon^{2/3}}\right) k^2 dk \tag{2-32}$$

Here, an arbitrarily chosen value of $k_{max} = 10\pi/d$ was taken to be the maximum wave number. Although the authors claimed that eddies with lengths less than 20% of the particle sizes do not have enough energy to break up the particle, it has been shown that Equation (2-32) is very sensitive to the upper limit of integration (Lasheras et al., 2002).

The models proposed by Coulaloglou & Tavlarides (1977) and later Konno et al. (1983) showed a maximum in the breakage frequency as the drop diameter increases. This fact is not as evident in the model proposed by Prince & Blanch (1990) for low values of ϵ; their model suggests that the break-up frequency increases monotonically with the drop diameter. On the other hand, at higher ϵ values, the model of Prince & Blanch (1990) also shows a maximum in the breakage frequency as the drop diameter increases.

In later work, Tsouris & Tavlarides (1994) questioned the existence of the maximum breakage frequency predicted by Coulaloglou & Tavlarides (1977) and Prince & Blanch (1990). They suggested that the breakage frequency would show a monotonic increase with the drop diameter. Hence they corrected the minimum surface energy, E_c in Equation (2-31), by using the mean of the surface energy increase resulting from breakage into two equal-sized drops, and the surface energy increase caused by breakage into a smaller drop (d_{min}) and a larger one (d_{max}). This gives

$$E_c = \frac{\pi\sigma}{2}\left[2\left(\frac{d}{2^{1/3}}\right)^2 + d_{\max}^2 + d_{\min}^2 - 2d^2\right] \tag{2-33}$$

Thus, the break-up frequency becomes

$$g(d) = C_3 D_F(\varphi)\varepsilon^{1/3}\int_{k_{\min}}^{k_{\max}} k^2\left(d+\frac{2}{k}\right)\left(1.07d^{2/3}+\frac{8.2}{k^{2/3}}\right)^{1/2}\exp\left[-\frac{C_4 E_c}{\rho k^{-11/3}\varepsilon^{2/3}}\right]dk \tag{2-34}$$

Here they defined $k_{\min} = 2/d$ and $k_{\max} = 2/\eta$ where η is the Kolmogorov length scale; $D_F(\varphi)$ is the turbulence damping factor due to the presence of dispersed phase at volume fraction φ, expressed by

$$D_F(\varphi) = \left(1 + 2.5\varphi\frac{\mu_d + 0.4\mu_c}{\mu_d + \mu_c}\right)^2 \tag{2-35}$$

However, as in the model of Prince & Blanch (1990), the breakage frequency from Equation (2-34) is dependent on the lower limit of the integration (Lasheras et al., 2002).

Luo & Svendsen (1996) proposed a breakage model based on principles of molecular collision and isotropic turbulence. As in the work by Prince & Blanch (1990), the breakage

frequency was also defined as the product of the collision frequency between eddies and particles and collision efficiency. However, Luo and Svendsen (1996) suggested that the collision frequency of eddies of size between d_e and $d_e+d(d_e)$ with a particle of size d is represented by

$$h(d,e)=\frac{\pi}{4}(d+d_e)^2 u_e \frac{dn_e}{d(d_e)} \tag{2-36}$$

where u_e is the fluctuation velocity expressed as Equation (2-37) and n_e is the number density of eddies per unit volume, given by Equation (2-38)

$$u_e^2 = 2.045(\varepsilon d_e)^{2/3} \tag{2-37}$$

$$\frac{dn_e}{d(d_e)} = \frac{0.822(1-\varphi)}{d_e^4} \tag{2-38}$$

Here ϕ is the dispersed phase volume fraction. After introducing $\xi = d_e/d$, the collision frequency of eddies of size between d_e with a particle of size d can then be expressed by

$$h(d,\xi d) = 0.923(1-\varphi)(\varepsilon d)^{1/3}\frac{(1+\xi)^2}{d^2\xi^{11/3}} \tag{2-39}$$

To derive the breakage efficiency, Luo & Svendsen (1996) suggested that when a drop of size d breaks into two smaller drops, one with a given volume fraction f and the other with 1-f, the minimum breakage energy, E_c, should be:

$$E_c = [f^{2/3}+(1-f)^{2/3}-1]\pi d^2\sigma = c_f \pi d^2\sigma \tag{2-40}$$

where σ is the surface tension and c_f [$=f^{2/3}+(1-f)^{2/3}-1$] is the fractional increase in surface area resulting from the breakup, which Luo and Svendsen (1996) suggested lies in the range 0 to 0.26. Consequently, the frequency for a drop of volume v (or size d) breaking into two droplets of volume of fv and 1-fv is

$$g(v:fv) = 0.923(1-\varphi)\left(\frac{\varepsilon}{d^2}\right)^{1/3}\int_{\xi_{\min}}^{1}\frac{(1+\xi)^2}{\xi^{11/3}}\exp\left(-\frac{12C_f\sigma}{2.045\rho\varepsilon^{2/3}d^{5/3}\xi^{11/3}}\right)d\xi \tag{2-41}$$

where $\xi_{min} = d_{min;e}/d$, $d_{min;e}/\eta \approx 11.4 - 31.4$ in which $d_{min,e}$ is the minimum eddy size. Hence, the global breakage frequency of particles of size d can be calculated from the integration of the above equations in the range of

$$g(v) = \frac{1}{2}\int_0^1 g(v : fv)df \tag{2-42}$$

Luo and Svendsen (1996) argued that, in contrast to previous models, this model had no adjustable parameters and all constants were calculated from isotropic theory. The daughter size distribution was derived directly from the breakage rate model. Furthermore, their model gave a monotonic increase of breakage frequency with the bubble (or drop) size, which is consistent with the prediction of the model suggested by Tsouris & Tavlarides (1994).

Another model on air bubble breakage rate was proposed by Martínez-Bazán et al. (1999) based purely on kinematic ideas. The basic premise of this model is that for a particle to break, its surface has to be deformed, and further, that this deformation energy must be provided by the turbulent stresses produced by the surrounding fluid. Although their model was initially developed for the particular simulation of the breakage of air bubbles in turbulent water flow, it was also shown to be able to predict the drop sizes in liquid–liquid systems (Eastwood et al., 2000). Recently, Hagesaether et al. (2002) argued that Luo & Svendsen's (1996) model contains an inherent weakness regarding the breakup rate for small particles and small daughter particle fragments. They introduced a new particle breakage criterion based on the requirement that there is no energy density increase as a result from the collision and breakage. It was found that the new energy density criterion is more effective in finding the breakage rate for large eddies colliding with particles than is the surface energy criterion. However, for small particles the surface energy criterion becomes dominant. However, Hagesaether et al. (2002) stated that validation of this model was required by incorporating it into a suitable CFD package and comparing the prediction with experimental data.

2.4.2 Daughter Drop Size Distribution Functions

Another factor that affects the breakage kernel is the daughter drop size distribution, β. For binary break-up, two approaches have been used for the calculation of the probability density function (PDF) of the daughter drop size distribution. In the first approach, a PDF is developed from statistical models, such as normal distribution (Valentas et al., 1966), truncated normal distribution (Coulaloglou & Tavlarides, 1977; Chatzi et al., 1989, 1992), uniform distribution (Prince & Blanch, 1990), β distribution (Hsia & Tavlarides, 1980; Alopaeus, et al., 1999) and U-shaped distribution (Hesketh et al., 1991; Kostoglou et al., 1997). In the second, a PDF is derived from surface energy models which are based on either drop-eddy collision (Tsouris & Tavlarides, 1994; Luo & Svendsen; 1996) or stress balances (Martínez-Bazán et al., 1999).

Coulaloglou & Tavlarides (1977) firstly proposed the truncated normal distribution after setting the variance of the normal distribution function given by Valentas et al. (1966) to a value so that more than 99.7% drops are within the volume range from 0 to v. For a drop of volume v_0 breaking into a daughter drop of volume v, the distribution function is defined as

$$\beta(v,v_0)=\frac{6}{\sqrt{2\pi}v_0}\exp\left[-\frac{4.5(2v-v_0)^2}{v_0^2}\right] \tag{2-43}$$

Hsia & Tavalrides (1980) modified the previous function and proposed a β distribution for daughter drop size distribution, which is

$$\beta(v,v_0)=30\left(\frac{v}{v_0}\right)^2\left[1-\frac{v}{v_0}\right]^2 \tag{2-44}$$

Following the work of Hsia & Tavalrides (1980), Lee et al. (1987) further developed this β distribution to multi-breakage model.

Hesketh et al. (1991) investigated the particle breakage in turbulent pipe flow and compared the results with the above daughter drop size distribution functions. They found that the experimental data were best fitted to the predictions by $1/X$-shaped distribution. It was then suggested that the energy required for break-up into two equally sized drops is greater than the energy requirement for break-up into two unequally sized drops (a smaller and a larger drop). Therefore breakage into two equal sized daughter drops should have the

lowest probability. However, both truncated normal and β distributions showed a bell shape with a peak for equal sized breakage. Following the studies of Hesketh et al. (1991), Kostoglou et al. (1997) proposed an expression with two adjustable parameters that describes a U-shaped daughter drop distribution function with a minimum at equal size breakage. This U-shaped distribution defines the probability for a drop of volume v_0 breaking into a smaller drop of volume v as follows,

$$\beta(v,v_0)=\left(\frac{1}{\frac{v}{v_0}+b}+\frac{1}{1-\frac{v}{v_0}+b}+\frac{2(z-1)}{b+0.5}\right)\cdot\frac{I}{v_0} \tag{2-45}$$

I is the normalization coefficient defined as:

$$I=\frac{0.5}{\ln(1+b)-\ln(b)+\frac{z-1}{b+0.5}} \tag{2-46}$$

and z is given by:

$$z=\frac{0.5a}{2b(1+b)(1-a)} \tag{2-47}$$

where a and b are the parameters that control the distribution shape.

In contrast to the above daughter drop distributions derived from statistical functions, several researchers developed some distribution functions based on phenomenological models. Tsouris & Tavlarides (1994) proposed a surface energy model for binary breakage. They postulated that the formation of a daughter particle of size d is inversely proportional to the energy required to split a mother drop of size d_0 into a drop size of d. The energy requirement is proportional to the excess surface area produced when the mother drop splits, which is given as

$$E(d)=\pi\sigma d_0^2\left[\left(\frac{d^2}{d_0^2}\right)+\left(1-\frac{d^3}{d_0^3}\right)^{2/3}-1\right] \tag{2-48}$$

The surface energy excess reaches its maximum when the two daughter drops are the same and gets to minimum when the mother drop does not break. Thus,

$$E_{\max} = \pi\sigma d_0^2\left(2^{1/3} - 1\right) \tag{2-49}$$

$$E_{\min} = \pi\sigma d_{\min}^2 \tag{2-50}$$

where d_{min} is the minimum size of the daughter drop. The daughter size distribution function is therefore expressed by

$$\beta(d,d_0) = \frac{E_{\min} + [E_{\max} - E(d)]}{\int_{d_{\min}}^{d_0} \{E_{\min} + [E_{\max} - E(d)]\} d(d)} \tag{2-51}$$

This distribution follows a U-shaped curve, with a minimum probability for the formation of two equally sized daughter particles and a maximum probability for the formation of a very large daughter particle and its complement of size d_{min}. However, this model does not show dependence on either energy dissipation rate or initial drop size, both of which have been experimentally observed to affect the daughter drop distribution (Lasheras et al., 2002).

Another model was presented by Luo & Svendsen (1996) to obtain the daughter drop distribution using a similar method to that used by Tsouris & Tavlarides (1994). The prediction of breakage of a drop of volume v_0 into daughter drops of size $v_0 f$ and $v_0(1-f)$, was calculated by normalizing the partial breakage rate by the overall breakage rate, leading to

$$\beta(v_0 f, v_0) = \frac{2\int_{\xi_{\min}}^{1} (1+\xi)^2 \xi^{-11/3} e^{-\chi_c} d\xi}{v_0 \int_0^1 \int_{\xi_{\min}}^{1} (1+\xi)^2 \xi^{-11/3} e^{-\chi_c} d\xi df} \tag{2-52}$$

where χ_c is the dimensionless energy required for breakage, which is defined as

$$\chi_c = \frac{12 c_f \sigma}{2.04 \rho \varepsilon^{2/3} d^{5/3} \xi^{11/3}} \tag{2-53}$$

Luo & Svendsen's (1996) model can also predict a U-shaped daughter drop size distribution function. Most importantly, compared with Tsouris & Tavlarides's (1994) model

their function incorporated the turbulent flow information, e.g. energy dissipation rate and fluid density.

Figure 2.4 illustrates the comparisons of the daughter drop distributions for breakage of a mother drop of diameter of 3 mm at ε = 1 m^2s^{-3}, calculated from the various models described above.

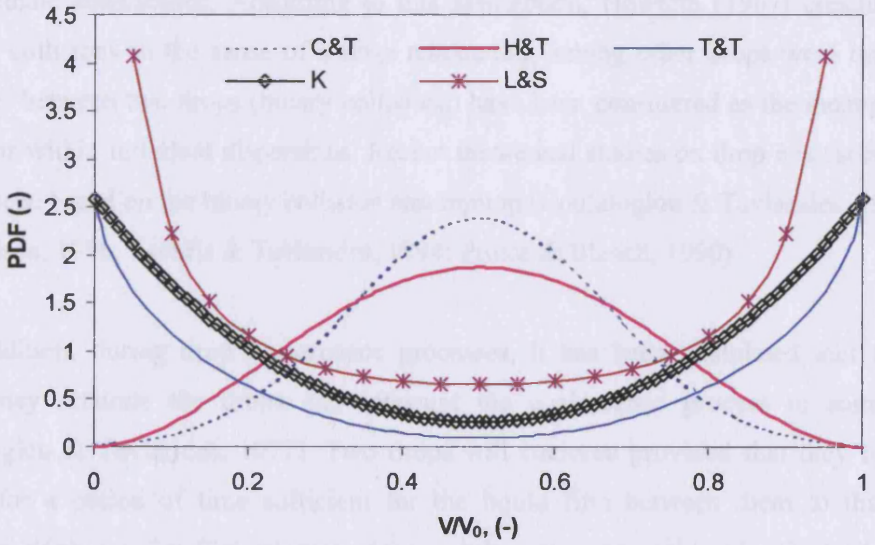

Figure 2.4: Comparisons on the daughter drop size distributions for breakage of a mother drop of size of 3mm at ε = 1 m^2s^{-3}, calculated from the models suggested by Coulaloglou & Tavlarides (1977) (C&T), Hsia & Tavlarides (1980) (H&T), Kostoglou et al. (1980) (K) for a=0.1 and b=1.0 in Equation (2-45), Tsouris & Tavlarides (1994) (T&T) and Luo & Svendsen (1996) (L&S).

2.4.3 Coalescence Models

In an isotropic turbulence, the drops are carried in random motion by the turbulent eddies and continually collide with one another; these collisions may result in drop coalescence. Drop coalescence coexists with drop breakage in a dispersion system. For coalescence of drops to occur the drops must first collide and then remain in contact for sufficient time so that the processes of film drainage, film rupture and coalescence may occur. Firstly, drops collide trapping a small amount of liquid between them. Then, while the two drops approach each other, this liquid film drains out. Finally when the trapped liquid film reaches the

critical film thickness, film rupture occurs resulting in coalescence. Therefore, coalescence is intimately dependent on drop collisions.

Howarth (1963) suggested that lower energetic collisions would result in the droplets colliding being held together by certain cohesive forces whilst the film between them drained, leading to coalescence. In contrast, the higher energetic collisions will result in immediate coalescence. It was also said that most collisions would result in either cohesion or immediate coalescence. According to this assumption, Howarth (1967) concluded that multiple collisions in the sense of a drop rebounding among other drops were rare. Thus, collisions between two drops (binary collisions) have been considered as the most prevalent behaviour within turbulent dispersions. Recent theoretical studies on drop coalescence have mostly been based on the binary collision assumption (Coulaloglou & Tavlarides, 1977; Luo & Svendsen, 1996; Tsouris & Tavlarides, 1994; Prince & Blanch, 1990).

In addition, during drop coalescence processes, it has been postulated that turbulent eddies may separate the drops and interrupt the coalescence process to some extent (Coulaloglou & Tavlarides, 1977). Two drops will coalesce provided that they remain in contact for a period of time sufficient for the liquid film between them to thin to the necessary thickness for film rupture. As a result, not every collision will lead to drop coalescence. The coalescence rate is not only dependent on drop-drop collision frequency but also on drop coalescence efficiency. For drops of volume v and v', the coalescence rate, $\Lambda(v,v')$, has been expressed as the product of the collision frequency, $h(v, v')$, and the coalescence efficiency, $\lambda(v,v')$.

$$\Lambda(v,v') = h(v,v') \times \lambda(v,v') \tag{2-54}$$

Figure 2.5 illustrates the conceptual framework for modelling the coalescence frequency, postulated by Chesters (1991). He concluded that there are two kinds of flows, external flow and internal flow, during drop coalescence. The continuous phase flow that carries drops, defined as the external flow, determines drop collision frequency, approaching force and duration of drop contact. The liquid film drainage between two drops, defined as the internal flow, is characterised by deformation of the approaching interfaces and by film rupture and drop coalescence if sufficient time is provided. The approaching force (or velocity) and duration of drop contact due to external flow define the boundary conditions for internal flow.

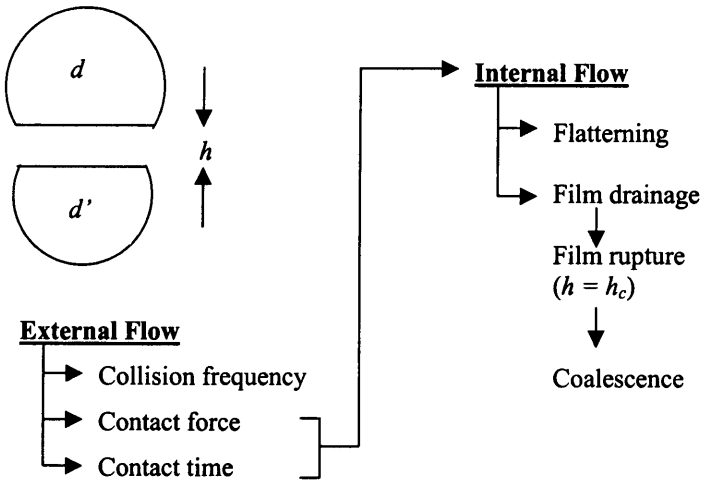

Figure 2.5: Conceptual framework for coalescence modelling (Chesters, 1991)

Collision frequency, *h(v, v')*

With regard to the coalescence of air bubbles in turbulent flows, Prince & Blanch (1990) concluded that collisions could occur due to a variety of mechanisms, arising from turbulence, buoyancy and laminar shear. In addition to collisions arising from random motion of bubbles due to turbulence, bubbles of different sizes will have different rise velocities and thus may lead to collision. However, in liquid-liquid dispersion systems collisions due to buoyancy can be neglected, since the density difference between the fluids is small compared to air-liquid systems. Therefore, the primary cause of liquid drop collision in an isotropic and homogeneous turbulent system is from the fluctuating turbulent velocity of the continuous liquid phase.

Since little is known about the mechanism of drop collision in turbulent flow, no exact expression has been derived to calculate drop collision frequency. Despite this difficulty, two approximate mechanisms have been proposed in previous studies to describe drop collision.

The first mechanism (Howarth, 1964), namely the collision between randomly moving drops, whose sizes are assumed to be smaller than the microscale of turbulence, is analogous to the collision between particles encountered in coagulation of smokes and colloidal suspensions. Howarth then applied Taylor's theory of diffusion to obtain an expression for the average collision frequency of drops of size *d*, *h(d)*, which is

$$h(d) = \frac{(24\overline{u^2}\varphi)^{1/2}}{d} \tag{2-55}$$

where ϕ is the volume fraction of dispersed phase and $\overline{u^2}$ is the mean square turbulent velocity fluctuation. Following this analogy, Das et al. (1987) further developed an expression to calculate the collision frequency for drops whose sizes are larger than the microscale of turbulence.

The other proposed theory to calculate collision frequency is that assuming the collision mechanism of drops within an isotropic flow field is analogous to that of molecules in an ideal gas. Then drop collision frequency is calculated based on the kinetic theory of gases (Kennard, 1938). Accordingly, the collision frequency between drops of volume v and v' is defined as (Coulaloglou & Tavlarides, 1977; Prince & Blanch, 1990; Tsouris & Tavlarides, 1994):

$$h(v,v') = S(v,v')[\overline{u^2}(v) + \overline{u^2}(v')]^{1/2} n(v)n(v') \tag{2-56}$$

where $n(v)$ and $n(v')$ are the concentrations of drops of volume v and v' respectively, $\overline{u}(v)$ and $\overline{u}(v')$ are the average turbulent fluctuating velocities and $S(v,v')$ is the collision cross-sectional area of drops, which is defined as

$$S(v,v') = \frac{3^{2/3}\pi^{1/3}}{8 \cdot 2^{1/3}}(v^{1/3} + v'^{1/3})^2 \tag{2-57}$$

To obtain the turbulent velocity fluctuation of a drop, it has been assumed that the eddy motions of the same length scale as the drop are primarily responsible for the drop relative motion. Very small eddies do not have sufficient energy to significantly affect drop motion, while eddies larger than the drop size transport groups of drops without leading to significant relative motion (Prince & Blanch, 1990). In addition, drops are assumed to lie in the inertial subrange of turbulence. This is defined by considering that drop size d satisfies $L >> d >> \eta$, where L is the length scale of the energy containing eddies (usually related to the scale of the tank or pipe, e.g. impeller diameter or 0.1×pipe diameter) and η is the Kolmogorov microscale (the scale of the smallest eddies of the turbulent motion) and is equal to $(\upsilon^3/\epsilon)^{1/4}$, where υ is the kinematic viscosity. Thus, the average turbulent velocity of drops in the inertial subrange of isotropic turbulence is (Hinze, 1959; Rotta, 1972):

$$u = \alpha \varepsilon^{1/3} d^{1/3} \tag{2-58}$$

where ϵ is the turbulent energy dissipation rate per unit mass, d is the drop diameter and α is a constant that was set to 1.4 (Rotta, 1972; Kuboi et al., 1972ab) or 1.03 (Tsouris & Tavlarides, 1994).

Consequently, the expressions of collision frequency of drops of size d and d' that have been proposed following the above theories are summarized in Table 2.4.

Table 2.4: Lists of expressions for collision frequency of drops of size d and d'

Authors (year)	Expression of collision frequency, $h(d,d')$	Constant c
Howarth (1967)	$c(\overline{u^2}\varphi)^{1/2}/d$	4.90
Das et al. (1987)	$c\varphi^{0.5} N_I D_I^{2/3} d^{-2/3}$	-
Delichatsios & Probstein (1976)	$c\varepsilon^{1/3}(d+d')^{7/3} n(d)n(d')$	0.8524
Coulaloglou & Tavlarides (1977)	$c\varepsilon^{1/3}(d+d')^2(d^{2/3}+d'^{2/3})^{1/2} n(d)n(d')/(1+\varphi)$	2.17×10^{-4}
Prince & Blanch (1990)	$c\pi\varepsilon^{1/3}(d+d')^2(d^{2/3}+d'^{2/3})^{1/2} n(d)n(d')$	0.089
Tsouris & Tavlarides (1994)	$c\pi\varepsilon^{1/3}(d+d')^2(d^{2/3}+d'^{2/3})^{1/2} n(d)n(d')$	0.2675

Coalescence efficiency, $\lambda(v,v')$

On the basis of the coalescence theory (Coulaloglou & Tavlarides, 1977; Ross et al., 1978; Sovová, 1981; Prince & Blanch, 1990; Chesters, 1991; Luo & Svendsen, 1996), once the drops collide they will stay together for a characteristic time, called interaction or contact time ($\bar{\tau}_I$), and coalescence will occur if this contact time is long enough for the liquid film between two drops to drain out. The required time for film drainage to a critical rupture thickness is defined as the 'coalescence time' or 'drainage time' ($\bar{\tau}_C$). Ross (1971) proposed an expression for coalescence efficiency by considering the contact time and coalescence

time to be randomly distributed, and the contact time to follow a normal distribution. Building upon this work, Coulaloglou & Tavlarides (1977) introduced the following relation for $\lambda(v,v')$ by assuming that the coalescence time ($\bar{\tau}_C$) is not randomly distributed unlike the contact time ($\bar{\tau}_I$):

$$\lambda(v,v') = \exp\left[-\frac{\bar{\tau}_C}{\bar{\tau}_I}\right] \tag{2-59}$$

According to the above, several expressions have been derived based on phenomenological analyses to calculate the coalescence time and contact time. Although little is known about drop coalescence mechanism, most studies show that the coalescence time and contact time are dependent on collision forces (or approaching velocity), the liquid properties and the interfacial characteristics (e.g. deformable or rigid interface). In addition, their values also depend on the colliding drop sizes (or size ratio). In a system where Van der Walls and double layer forces can be neglected, the coalescence time ($\bar{\tau}_C$) for two non-deformable solid drops is given by Jeffreys & Davies (1971) as:

$$\bar{\tau}_C = t_2 - t_1 = \frac{3\pi\mu_c}{2F}\left(\frac{dd'}{d+d'}\right)^2 \ln\left(\frac{h_1}{h_2}\right) \tag{2-59}$$

where d and d' are the drop diameters, μ_c is the continuous phase viscosity, F is the force compressing the drops together, h_1 and h_2 are the intervening film thicknesses at the initial contact time t_1, and when spontaneous film rupture occurs at time t_2, respectively. The drops are assumed to collide in a fluid eddy of size $d + d'$. The compressing force, F, is then regarded as being proportional to the mean square velocity difference at either end of the eddy (Coulaloglou & Tavlarides, 1977), which is expressed as

$$F \propto \rho_c \overline{u^2}\left(\frac{dd'}{d+d'}\right)^2 \tag{2-60}$$

Given the initial film thickness h_1, Equations (2-59) and (2-60) can predict a finite coalescence time for the cases that the film is not completely drained out ($h_2 > 0$). However, it will give an infinite coalescence time if it is assumed that drops coalesce when zero film thickness is reached ($h_2 = 0$). Thus the choices of rupture film thickness, h_2, as well as the initial film thickness, h_1, become important.

Previous studies follow two methods for estimating h_1 and h_2, assuming them to be either equal to two independent constants or, dependent on drop pair sizes. Coulaloglou & Tavlarides (1977) assumed that h_1 and h_2 are two universal constants and their influences could be represented by one parameter that was decided by experiments. Prince & Blanch (1990), on the other hand, estimated the initial film thickness, h_1, to be 100 μm and the final rupture film thickness is typically taken as 0.01 μm in air-water systems. In contrast to choosing two constants, Tsouris & Tavlarides (1994) applied a relation of drop pair sizes to the initial film thickness, h_1, although a constant value 0.05 μm was set to the rupture film thickness, h_2. They suggested that $h_1 = k(dd'/d+d')$, where k was arbitrarily set to 0.1 for aqueous-organic liquid dispersions.

In addition to the above, other researchers (Chesters, 1991; Oolman & Blanch, 1986) developed different expressions to calculate the coalescence time between equal size drops with deformable and fully mobile interfaces. Chesters (1991) developed an expression for equal size drops and Luo & Svendsen (1996) assumed that this is also suitable for the unequal size cases. Hence, considering drop diameters d and d', the coalescence time is written as

$$\bar{\tau}_C = 0.5\frac{\rho_c u(dd')^2}{\sigma(d+d')^2} \tag{2-61}$$

where ρ_c is the continuous liquid density, σ is the interfacial tension and u is the relative velocity of drops.

The contact time (or interaction time), $\bar{\tau}_I$, has also been calculated in different ways by various authors. An estimate was made by Coulaloglou & Tavlarides (1977) assuming the average contact time to be proportional to the characteristic period of velocity fluctuation of an eddy of size $(d + d')$. In other words, the contact time of two approaching drops can be related to the average life of eddies whose sizes equal $(d + d')$. According to dimensional analysis suggested by Levich (1962) the average contact time can be written as follows (Coulaloglou & Tavlarides, 1977; Lee et al., 1987; Prince & Blanch, 1990)

$$\bar{\tau}_I \propto \frac{(d+d')^{2/3}}{\varepsilon^{1/3}} \tag{2-62}$$

Tsouris & Tavlarides (1994) suggested that the contact time could be considered as the reciprocal of the frequency of fluid velocity fluctuations. For liquid-liquid dispersions in a stirred vessel, this time is given as

$$\bar{\tau}_I = 0.03468 \frac{V_I^{1/3}}{N_I D_I} \tag{2-63}$$

where N_I is the agitation speed, D_I is the impeller diameter and V_I is the mixture volume. Luo & Svendsen (1996) developed a simple film model based on conservation of energy so as to obtain the contact time for two equal or unequal sized fluid particles. From this model the following contact time was derived that is independent of the initial approach velocity.

$$\bar{\tau}_I = \left(1 + \frac{d}{d'}\right)\left[\frac{(\rho_d/\rho_c + \gamma)}{3(1 + d^2/d'^2)(1 + d^3/d'^3)} \frac{\rho_c d}{\sigma}\right]^{1/2} \tag{2-64}$$

where ρ_d is the dispersed phase density and γ is the coefficient of virtual mass that is a constant between 0.5 and 0.8.

A summary of coalescence efficiency for drops of size d and d' is listed in Table 2.5.

Table 2.5: Lists of expressions for coalescence efficiency.

Authors (year)	Coalescence efficiency, $\lambda(d,d')$	Constant, c
Coulaloglou & Tavlarides (1977)	$\exp\left[-c\frac{\rho_c\mu_c\varepsilon}{\sigma^2(1+\varphi)^3}\left(\frac{dd'}{d+d'}\right)^4\right]$	2.28×10^{13}
Sovová (1981)	$\exp\left[-c\frac{\sigma(v^{2/3}+v'^{2/3})(v+v')}{\rho_d N_I^2 D_I^{4/3} vv'(v^{2/9}+v'^{2/9})}\right]$	0.5×10^{-3} ~ 11.0×10^{-3}
Prince & Blanch (1990)	$\exp\left[-c\frac{\rho_c^{1/2}\varepsilon^{1/3}(dd')^{3/2}}{\sigma^{1/2}(d+d')^{13/6}}\ln\frac{h_0}{h_1}\right]$	0.14038
Tsouris & Tavlarides (1994)	$\exp\left[-c\frac{6\pi\mu_c\zeta}{\rho_c\varepsilon^{2/3}(d+d')^{2/3}}\frac{28.83N_ID_I}{V_I^{1/3}}\right]$ †	3.44 or 28.1
Luo & Svendsen (1996)	$\exp\left[-c\sqrt{\frac{0.75(1+d^2/d'^2)(1+d^3/d'^3)\rho_c\overline{u^2}d}{(\rho_d/\rho_c+\gamma)\sigma}}\frac{1}{(1+d/d')^3}\right]$	~O(1)
Alopaeus et al. (1999)	$(0.26144\frac{\mu_d}{\mu_c}+1)^{-c\frac{\mu_c}{\rho_c\varepsilon^{1/3}(d+d')^{2/3}D_I^{2/3}}}$	5889.28 or 48107.2
Liu & Li (1999)	(immobile interface): $\exp\left[-0.0272\frac{\mu_c\rho_c^{0.84}\varepsilon^{0.89}}{\sigma^{1.38}B_w^{0.46}}\left(\frac{dd'}{d+d'}\right)^{3.11}\right]$ (mobile interface): $\exp\left\{\left[-1363.3\frac{\sigma^{1.29}\mu_c^{0.02}B_w^{0.26}}{E^{1.7}\mu_d^{1.02}\rho_c^{0.55}\varepsilon^{0.7}}\left(\frac{dd'}{d+d'}\right)^{-2.03}-217.3\frac{\sigma^{1.38}B_w^{0.46}}{E^{0.7}\mu_c\rho_c^{0.84}\varepsilon^{0.89}}\left(\frac{dd'}{d+d'}\right)^{-3.11}\right]^{-1}\right\}$ ††	$B_w=10^{-28}$ Jm

† V_I is the effective volume of total liquid in agitated vessels;

†† $E=12.61+2.16\arctan\left[2.19\left(\frac{\mu_c}{\mu_d}\right)^{0.8}\left(\frac{\pi\sigma}{\rho_c\varepsilon^{2/3}}\right)^{0.4}\left(\frac{dd'}{d+d'}\right)^{-2/3}\right]$ is the dimensionless curvature radius of the liquid film.

2.5 Turbulent Modification and Measurement in Two-Phase Flow

Turbulence is an important phenomenon in most fluid flows and contributes significantly to the transport of mass, momentum and energy. Turbulence in two-phase flows for both gas/liquid and liquid/liquid two-phase flow systems also plays a key role in the velocity distribution, phase distribution, mixing and other phenomena such as dispersed phase breakage and coalescence. It is therefore essential to investigate the modification of turbulence in the presence of the second phase in order to optimize the system performance. Many experimental investigations have been carried out to measure the local turbulence structure in two-phase systems by means of suitable instrumentation, such as impact pressure probes, hot-wire/film anemometers (HFA), laser-Doppler anemometers (LDA) and, more recently, particle-imaging velocimetry (PIV). The results from these turbulence measurements have been widely employed for the validation of theoretical modelling approaches in computational fluid dynamics (CFD) simulations. Compared to the large amount of work on gas-liquid flows, experimental data on liquid-liquid flows only cover a restricted range and the available literature is fairly limited. In what follows, the experimental studies on turbulence modification in gas-liquid and liquid-liquid flows are reviewed in Section 2.5.1, with an emphasis on highly turbulent systems. Section 2.5.2 briefly reviews the application and signal-processing algorithms for one of the major techniques, hot-film anemometry which was employed in the work described in this thesis.

2.5.1 Turbulence modification in two-phase bubbly/dispersed flows

Based on the source of turbulence generation, turbulent two-phase flow can be classified into gravity or buoyancy driven flow (pseudo-turbulence) and highly turbulent flow. The relevant literature on both regimes is reviewed below.

2.5.1.1 Gravity or Buoyancy Driven Flow

Pseudo-turbulence in gravity or buoyancy driven flow, where the turbulence of the continuous phase is mainly induced by the dispersed phase (i.e. bubble or droplet), has been investigated for many years. Generally, the fluctuating velocity of the continuous liquid phase is found to be dependent on the slip velocity and the fraction of the dispersed phase, which leads to the following correlation (Parthasarathy & Faeth, 1990; Mizukami et al., 1992; Garnier et al., 2002; Augier et al., 2004):

$$\frac{u_c^2}{U_R^2} = K\varphi C_D^n \tag{2-65}$$

where u_c is the fluctuating velocity of the continuous phase, U_R is the relative velocity, ϕ is the dispersed phase volume fraction, C_D is the drag coefficient for a single dispersed particle or bubble in an infinite medium of continuous phase and n and K are the constants. The values of n and K are found to be a function of the system components and phase fraction. Table 2.6 lists those values suggested by previous studies.

Table 2.6: Suggested parameters in Equation (2-65).

Authors (Year)	System	n	K	ϕ
Lance & Bataille (1991)	Air-water	2/3	0.862	<4%
Cartellier & Riviere (2001)	Solid-water & Solid-air	4/3	17.5	<0.01%
Haam & Brodkey (2000)	Solid-water	4/3	50	<8%
Augier et al. (2004)	Liquid-liquid	2/3	0.2	<40%

Lance & Bataille (1991) used a LDA technique to measure the pseudo-turbulence in water induced by air bubbles at a very low void fraction (ϕ <4%). By comparing the spectrum of the bubble wake-induced turbulence and the shear-induced turbulence, they suggested that the contribution of the wakes to the turbulent kinetic energy is small compared to the irrotational pseudo-turbulence in their conditions. The turbulent velocity field was found to be homogeneous and isotropic, with the fluctuating kinetic energy (e_k) being proportional to the void fraction and the square of the relative velocity, as expressed by

$$e_k = 0.5C_{AM}\varphi U_R^2 \tag{2-66}$$

where C_{AM} is the added mass coefficient by the bubbles. Also, they found that the integral length scale of the pseudo-turbulence was weakly dependent on ϕ, and apparently only determined by the bubble size and was approximately 0.8×bubble diameter.

Parthasarathy & Faeth (1990) and Mizukami et al. (1992) studied the fluctuating motion of the continuous phase induced by the settling of glass particles in dilute regimes (ϕ <0.01%). They measured the axial and transverse fluctuating velocity components; both components were found to be proportional to the energy dissipation rate and solid phase

fraction. However, the fluctuating field was strongly anisotropic with the ratio of the axial to transverse components being of the order of 4, which is contrary to what was observed in air-water system by Lance & Bataille (1991).

Using an HFA technique, Garnier et al. (2002) measured the mean and fluctuating velocity of the water phase in buoyancy-driven air-water flow in an 80×310 mm glass cylindrical column, at a superficial water velocity less than 0.062 m/s, bubble Reynolds number of 300-500 and void fractions in the range of 0.01-0.4. The relative velocity of the air bubbles to the water phase was found to follow a power law similar to that in particle laden flows. Based on this they postulated that the relevant turbulent length scale is the distance between bubbles. From the experimental data they suggested the following expression:

$$u_c^2 = c_1 U_\infty^2 \varphi (1 - c_2 \varphi^{1/3})^2 \tag{2-67}$$

where u_c is the axial fluctuating velocity, U_∞ is the terminal velocity of a single bubble in an infinite liquid, ϕ is the void fraction and c_1 and c_2 are coefficients dependent on the bubble Reynolds number and the Bond number. However, they also noticed that the above expression does not agree with their experimental observations for void fractions larger than 0.2. This discrepancy was then attributed to the spatial heterogeneities of the void fraction in the high void fraction cases.

Augier et al. (2004), using a PIV technique, investigated the velocity fluctuations at high phase fraction in a liquid-liquid gravity-driven upward flow. The measurements were carried out in a rectangular cross-section channel with matched refractive index liquids, which were 48.5% by mass glycerol and water solution as the continuous phase and n-heptane as the dispersed phase, respectively. Their results showed a strong anisotropy for dispersed phase fractions 0.01–0.4. The axial component of the fluctuating energy of the continuous phase was 4-5 times larger than the transverse component which is similar to the findings in solid settling experiments (Parthasarathy & Faeth, 1990; Mizukami et al., 1992). Also the axial component of the normalized fluctuating energy of the continuous phase follows a 2/3 power law in relation to the product of phase fraction and local drag coefficient. They argued that this finding is in agreement with the hypothesis of a local equilibrium between the dissipation of turbulent fluctuations at a non resolved length scale (0.12×drop diameter) and the production rate induced by the average drag force, even though this relationship cannot be directly compared with those for dilute dispersed systems. Their experimental results also

suggested that the instantaneous fluctuating velocity of the continuous phase can be locally correlated to the dispersed phase distribution, which was found to have a mean inter-drop spacing $3d/8\phi$ at the flow stream direction, and to follow a Poisson distribution for drop size d and volume fraction ϕ. However, the dispersion of their system (and drop size) was generated by injecting the dispersed liquid through 1.1 mm capillary tubes and the interactions between phases (i.e. breakage and coalescence) were hardly allowed to happen, although their work was carried out at fairly high phase fraction.

2.5.1.2 Highly Turbulent Bubbly/Dispersed Flow

(1) Gas-liquid systems

Serizawa et al. (1975abc) studied the turbulence structure in an air-water bubbly upward flow in a 60 mm ID (D) Lucite tube using an HFA. Measurements were taken at three axial positions ($10D$, $20D$ and $30D$). They found that over a large portion of fully developed bubbly flow, the velocities of each phase, and the velocity ratio between phases showed fairly flat radial profiles, which, they suggested, may be due to the accumulation of bubbles at the wall region leading to an increase of the liquid phase velocity. The experimental data also showed a trend for the turbulent intensity to decrease first with increasing gas flow rate for constant water velocity, and to increase again with a further increase in the gas flow rate. This behaviour was found to become more accentuated at higher water velocities.

Theofanous & Sullivan (1982) experimentally investigated air-water vertical upwards flow in a 57 mm ID (D) glass pipe using an LDV technique with the measurements taken at $24D$ downstream of the entrance. Their results showed that turbulence production and dissipation depend on bubble concentration. The authors noted that their two-phase flow results show a large augmentation of the turbulence intensity for all axial positions, which is contrary to the trends observed in previous experiments by Serizawa et al. (1975bc) where turbulence intensity was found to be weakly-dependent on the amount of gas bubbles. They also found that at the wall region the relative turbulence intensity in two-phase flow is higher than in single-phase flow, which was attributed to the additive effect of bubble induced turbulence on the wall shear-generated turbulence. To further clarify and examine their experimental findings, they developed a theoretical model based on the assumption that the turbulence level in the liquid phase is the sum of wall-induced and bubble-induced turbulence.

Liu & Bankoff (1993a) investigated the turbulent structure of an air-water upward bubbly flow in a 38mm ID and 2.8m long acrylic pipe. Liquid phase local velocities and turbulent Reynolds stresses were simultaneously measured using both one- and two-dimensional hot-film anemometer probes. The relationship of turbulence intensity with the phase flowrate was then examined. It was found that increasing the gas flowrate at a fixed liquid flowrate not only increases the total turbulence but also increases the turbulence intensity in both axial and lateral directions and the Reynolds stress. However, increasing the liquid flow at constant gas flowrate reduces the liquid phase turbulence in the core region, but increases the turbulence in the wall region, which results in an overall decrease of turbulence intensity. Similar trends were exhibited by bubble-induced turbulent intensity, which increases with increasing gas flowrate and decreases with increasing liquid flowrate. They also reported that in the pipe core area most of the turbulent energy is from bubble-induced turbulence, constituting 90% of total energy at superficial liquid velocity 0.376 m/s. The profile of bubble-induced turbulent energy indicated that this local turbulent energy at the pipe centre due to bubble agitation is reduced as the wall is approached. Later, Liu & Bankoff (1993b) studied the local parameters (i.e. void fraction, bubble velocity and bubble size distribution), and suggested that the turbulence could be affected by the local bubble size distribution. However, no quantitative conclusion on turbulence modification by bubble size was drawn in their work.

Another significant study of turbulence modification in air-water bubbly vertical flow using hot-film anemometry technique was carried out by Hogsett & Ishii (1997) and Hibiki et al. (1998) in similar systems. A TSI Flowpoint system and a 1-D conical velocity probe (TSI 1231W), which has a sensor with diameter 1.27mm and sensor length 1mm (operated at 66.7 °C), were used to measure the axial velocity with the probe calibrated by a Pitot-static tube. Hibiki et al. (1998) reported that the probe sensor is small enough to give nearly a point velocity measurement and has a good response to the individual bubble phase as the diameters of injected air bubbles are in the range of 3 – 5mm which are much larger than the probe sensor length. The two-phase signals, recorded at maximum sampling frequency 5 kHz with maximum 16284 data points, were then processed by a threshold scheme to remove the depressions and spikes due to the passage of air bubbles. By comparing the time-averaged void fraction with that from a conductivity probe the authors concluded that the hot-film anemometer can give a reasonably consistent prediction by setting the minimum amplitude threshold near the zero liquid velocity voltage. In the experiments conducted by Hogsett & Ishii, (1997) and Hibiki et al. (1998), the fluctuating velocities at 12 different radial points and 3 axial positions (2*D*, 32*D* and 62*D* from inlet) in a 50.88 mm ID (*D*) vertical acrylic tube were measured. The maximum void fraction and liquid velocity were

10% and 1.147 m/s, respectively, for the studies of Hogsett & Ishii (1997), and are 6.99% and 1.3763 m/s, respectively, for the studies of Hibiki et al. (1998). Both studies suggested that the bubble-induced turbulence at a water superficial velocity 0.6 m/s dominates the shear-induced turbulence, even for the lowest void fractions; these effects were then found to dissipate with increasing liquid velocity. Hibiki et al. (1998) analysed the turbulence energy production in the pipe and found that only small amount of shear-induced turbulence is produced in the core region because the liquid velocity profile is flat in that region. Therefore, the turbulence energy in the core region may arise mainly by the generation near the wall followed by diffusion into the core region. Experimental data showed that there was a reduction of turbulence generation in the wall region in the presence of bubbles. Since turbulence induced by the air bubbles tends to increase with void fraction or bubble size, it was suggested whether the turbulence was augmented or attenuated in bubbly pipe flow depended on the balance between direct turbulence generation by the bubble and the action of the bubbles in reducing other-generated turbulence.

Iskandrani & Kojasoy (2001) used an HFA technique to investigate the velocity and turbulence profile of air-water bubbly flow in a 50.3 mm ID, 15.4 m long horizontal Pyrex glass tube. The mean axial liquid velocities were found to show a relatively uniform distribution except near the upper pipe wall, where a sharp reduction in velocity was observed. The local mean liquid velocity and turbulence fluctuations increased with gas flow rate. It was noted that the liquid velocity forms a fully developed turbulent pipe flow profile in the lower part of the pipe. At very low local void fractions the turbulent intensity consistently tended to be slightly lower than in single-phase flow. However, at high void fractions, introduction of gas phase strongly enhanced the turbulence fluctuating velocity and intensity. They consequently concluded that the turbulence intensity is mainly a function of the local void fraction in pipe flow.

Cui & Fan (2004) investigated the turbulence energy distribution of air-water bubbly flow in 10.2×10.2×150 cm Plexiglas square column system. LDA was employed to measure the liquid phase turbulence velocity, and a PIV system was applied to measure the bubble size and rise velocity. They found that the liquid axial velocity (i.e. 23.9 cm/s) is much larger than that the radial velocity (i.e. 0.6 cm/s), and the average size of the bubble wake region is 6.5 mm which is of the same order of magnitude as that of the rising bubbles, 5.34-5.52 mm, in their experiments. The turbulence in the bubble wake was much stronger (more than 200%) than that in the main flow stream and the ratio of radial to axial turbulence energy was approximately 1, implying a strong mixing in the bubble wakes. The turbulence energy in the wall region was found to be only 10% of that in the central region, although the

Kolmogorov $-5/3^{th}$ law was obeyed in both regions. Cui & Fan (2004) therefore suggested that the bubble-induced turbulence is dominant in turbulence production under their flow conditions, compared to the liquid shear-induced turbulence.

Fujiwara et al. (2004) studied the effect of bubble size on turbulence modification in dilute vertical bubbly flow (0.5%-1% void fraction). Experiments were conducted in 44 mm ID FEP pipe and the liquid phase velocities were measured by PIV with fluorescent tracer particles. Their experimental data indicated that the bubble size has little effect on the liquid phase mean streamwise velocity, even though the average bubble rise velocity is 1.5 times higher than the liquid phase velocity in the core area. For locations near the wall (r/R>0.9), the axial turbulence intensity in the case of large bubbles (2 mm mean size) was nearly the same or even larger compared to that in single-phase flow, however, the axial turbulence intensity in the case of small bubbles (1 mm mean size) was always lower than the single phase value. Also the levels of turbulence in both size cases were found to be suppressed in the pipe core region. They suggested that the turbulence enhancement in wall region in the large bubble case is due to the wake structure of large bubbles accumulating near the wall and the local shear flow induced by these bubbles. Radial fluctuation velocity profiles were also measured and compared with those in single-phase flow. Radial turbulence in both the small and large bubble size cases was enhanced near the wall and reduced in the pipe core region. This enhanced region near the wall was then seen to depend on the bubble diameter, which was accordingly attributed to the bubble wake size and the length scale of vortices at high intensity. Fujiwara et al. (2004) further suggested that negligible turbulence is produced in the pipe by the shear flow because of the fairly small mean velocity gradient as was also suggested by Hibiki et al, 1998); however, in this region the bubble motion is expected to contribute to the turbulent energy production.

Apart from the above work focusing on turbulence studies in gas-liquid co-current upward flows, a few studies were also conducted in co-current downward flows. Wang et al. (1987) investigated the three-dimensional turbulence structure (3-D) and phase distribution in air-water upward and downward bubbly flows. To measure the liquid velocity and Reynolds stresses, a 1-D and a special 3-D conical-shaped hot-film anemometer probes were used and mounted in a 57.15 ID circular pipe. The void fraction in upward and downward flows showed two distinctive profiles: for upward flow a sharp peak is exhibited near the wall, while for downward flow the bubbles migrate towards the centre of the pipe and form a pronounced gas core with the wall region almost free of gas. The maximum liquid velocity in downward flow was found to occur away from the pipe centreline and sometimes even close to the wall, which was ascribed to the gas core (or 'chimney') effect by the authors.

The fluctuating velocities at three normal directions were seen to increase non-monotonically with the void fraction for both upward and downward flows. The authors suggested that the previous postulated hypothesis, that the turbulence level in two-phase flow is the sum of wall-shear induced and bubble induced turbulence, is invalid because the presence of bubbles in turbulent flow also enhances the dissipation rate of turbulent kinetic energy. Therefore, the overall turbulence augmentation or suppression will be determined by the balance of turbulence dissipation and production induced by bubbles. The turbulence fluctuations in the core region in the experiments of Wang et al. (1987) also exhibited flat profiles, consistent with other studies.

Sun et al. (2004) compared the mean and fluctuating liquid velocity in air-water co-current upward and downward flows using the LDA technique. Experiments were carried out in a 50.8mm ID acrylic pipe of an overall length 3.81m, with bubbles generated uniformly by a sparger unit with a mean pore size of 10 μm. After optimising the LDA operation procedure, they measured the turbulence structure at a high area-averaged void fraction reaching up to 8.5%. The experimental data indicated that the liquid velocity profile in downward flow is flatter than that in upward flow and may have the maximum peak value off the centreline. This feature became less pronounced with increasing velocity, which is consistent with the findings by Wang et al. (1987). However, the liquid turbulence was observed to be higher generally compared to that in single-phase flow in both upward and downward flows, especially in the core region. They argued that this observation of turbulence increase is different from other findings by Serizawa et al. (1975c), Tsuji et al. (1984), Michiyoshi & Serizawa (1986) and Wang et al. (1987) which showed a reduction of the axial liquid turbulence in some conditions. The authors attributed it to the bubble size in their system that was larger than in the other studies and resulted in significant increase of bubble-induced turbulence.

(2) Liquid-liquid Systems

Compared to the amount of work in air-water systems, only a limited number of studies have been performed for liquid-liquid systems. So far, most of the work in liquid-liquid flows was published by researchers at Bradford University, with the measurements conducted in kerosene-water systems in a 77.8 mm ID acrylic tube using hot-film anemometry (Farrar et al., 1995; Farrar & Bruun, 1996; Al-Deen & Bruun, 1997; Al-Deen et al., 1998).

Using a normal cylindrical hot-film probe, Farrar et al. (1995) carried out a set of experiments in a kerosene-water upward flow to measure local void fraction and average mean and fluctuating velocities at different input oil fractions (β<70%). The local volume fraction profiles in dispersed flows were found to depend significantly on the input flow configuration. For example, they found uniform profiles with no wall peak for β<20%, centrally uniform with a small wall peak at about 0.9R for 20%<β<40% and centre peak with a small wall peak for 40%<β<70%. For β=70% the small wall peak almost vanishes. The average streamwise velocity profiles were almost flat for β=10, 20, 30%, and then exhibit a steep centre peak at β=40%. In addition, their data indicated that the axial velocity profile is considerably flattened change at β = 5%, compared to single-phase flow. Farrar et al. (1995) also observed that the turbulence intensity profiles generally become flat as β increases, changing from a wall peak in single-phase flow to a more uniform profile. In agreement with the observations on average velocity profiles, a substantial increase in the core area was found to occur at β=5%.

Farrar & Bruun (1996) studied both the turbulence structure and other local parameters (e.g. volume fraction, velocity and drop size profiles) in an oil-in-water dispersed upward flow. Their measurements were conducted at a mixture velocity of 0.65 m/s (185 l/min) and input oil fractions 5%< β <30%. The experimental data, as illustrated in Figure 2.6, showed the local oil volume fraction profile to be very uniform at low oil fractions but becomes wall peaked as β increases. For β < 15%, the average drop size is almost independent of position and β, but above 15% the drop size at the pipe centreline was found to increase significantly with β. The authors attributed this to the flow regime change from drop flow to spherical cap drop flow. The mean velocity profile was also found to be flat up to 15%, but showed a steep central peak for β >15%. The turbulence intensity was seen to increase with β up to 15% and then drop at 20% over the complete cross-section. It was suggested that the decrease was a result of the accumulation of large drops in the pipe centre. However, as β increases to β=25% and 30%, the turbulence intensity profile becomes centrally peaked in association with the behaviour of mean velocity. Farrar & Bruun (1996) inferred that the steep central peak velocity and turbulence intensity is due to the appearance of large drops in the pipe centre which drive the continuous phase at a higher velocity. However, the input oil fractions, where the profiles are changed from flat to central peak, were lower than those observed by Farrar et al. (1995). The turbulence intensity profile was also found to become much more uniform for β=5% compared to single-phase flow. Furthermore, based on the assumption that the overall turbulence in a pipe consists of drop-generated and wall shear-generated turbulence, they found the former to increase monotonically with β, but the latter showed a minimum at β=15~20%. Their experimental data also indicated that the integral

turbulent length scale and the microscale of the continuous water phase decrease rapidly with increasing β, which highlighted the increasing importance of drop generated turbulence and its associated higher frequency fluctuations.

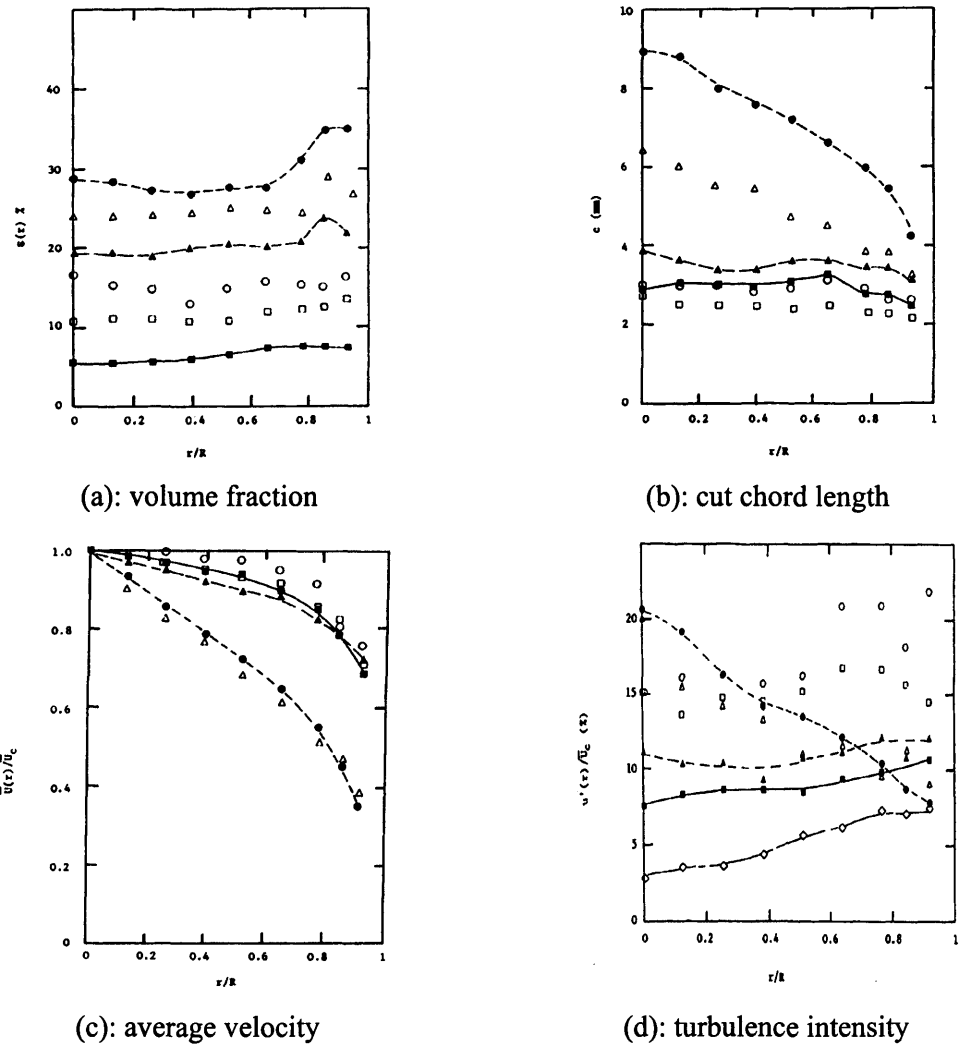

(a): volume fraction

(b): cut chord length

(c): average velocity

(d): turbulence intensity

Figure 2.6: Experimental data in kerosene-in-water vertical pipe flow with various input oil fraction: ◊: 0%; ■: 5%; □: 10%; ○: 15%; ▲: 20%; Δ: 25%; ●: 30% (Farrar & Bruun, 1996).

Al-Deen & Bruun (1997) performed a comparative study of different hot-film probes in vertical kerosene-water dispersed flow. Results from three probe types, single normal, X type and split-film, were compared for a mixture velocity 0.55 m/s and β<40%. Experimental data from all probe measurements were in agreement and the turbulence

structure (mean and fluctuating velocities) was found to be similar to that obtained by Farrar et al. (1995).

In addition to the above studies in vertical pipe flow of two-immiscible liquids, Al-Deen et al. (1998) further investigated the turbulence structure in inclined pipes for β=10% and 18%. It was found that at large inclination (30° from vertical) the kerosene-water bubbly flow became unstable and some large scale structures were seen visually. The authors argued that as there was no obvious drop coalescence under their experimental conditions, the observed swarms of drops must be carried by some underlying instability from the continuous water phase. However, no detailed analysis was conducted regarding this phenomenon. The mean and fluctuating velocities in inclined pipes were found to show skewed characteristics compared to vertical flow because of the migration of the majority of kerosene drops towards the top of the pipe; higher values were obtained at the lower part of the pipe.

2.5.2 Turbulence Modification (Augmentation or Attenuation?) in Two-Phase Dispersed Flows

There is extensive discussion in the literature on turbulence generation and suppression by the presence of the second phase in bubbly, dispersed and particle loaded flows. Generally, turbulence generation involves perturbation of the continuous-phase flow by the wake of each dispersed-phase element and is most important when the velocity fluctuation within the wake of a bubble or particle is larger than the background continuous-phase velocity fluctuations. These effects of turbulence generation are most significant in nearly homogeneous flows and where other sources of turbulence production are weak. On the other hand, turbulence suppression by the bubbles in bubbly flow may be due to the following phenomena (Serizawa et al., 1974 abc; Wang et al., 1987): work done to provide buoyancy to the bubbles, energy dissipation associated with the lateral relative motion or rotation of the bubbles, energy-absorbing characteristics of bubbles. Similar effects would presumably occur in dispersed liquid-liquid and particle loaded flows. However, the understanding of such fundamental phenomena, such as how the turbulence level is changed in two-phase flow and whether the turbulence is enhanced or suppressed, is still limited and inconclusive.

Theofanous & Sullivan (1982) proposed a theoretical basis for the prediction of turbulence levels in two-phase bubbly flows and derived an expression of the turbulence

intensity at the pipe centerline as a function the dispersed phase volume fraction, by assuming that the turbulence level in the liquid phase is the sum of shear-induced and bubble-induced turbulence. They discussed this theoretical model in certain asymptotic limits, such as in gas/liquid and gas/particle systems. Later, Liu & Bankoff (1993a) compared this model with their experimental data in air-water bubbly flow and found fairly good agreement. However, Wang et al. (1987) questioned the validity of this model in flows where the bubble-dominated effects dissipate, as the turbulence may also be suppressed by the presence of the bubble phase.

Gore and Crowe (1989) reviewed the available experimental data on turbulence modulation in particle-laden flows and suggested that the turbulence increase or decrease is dependent on the ratio of particle diameter (d_p) to the Eulerian turbulence length scale (l_e). After plotting the turbulence intensity data of previous experiments as a function of this length ratio, they postulated that there is a critical value of d_p/l_e=0.1, above which the turbulence intensity of the carrier phase is increased and below which it is suppressed by the addition of particles. However, no detailed study was made on the magnitude of turbulence modulation by the particle-fluid interactions.

Hetsroni (1989) performed an order of magnitude analysis on experimental data available in the literature and found that the turbulence increase or decrease in two-phase flow appears to be dependent on the particle Reynolds number (based on relative velocity and particle size):

$$\mathrm{Re}_P = \frac{\rho_p d_p (u_f - v_p)}{\mu_f} \tag{2-68}$$

where ρ_p and d_p are the density and diameter of the particle, respectively; u_f and v_p are the velocity of the carrier fluid and particle, respectively, and μ_f is the viscosity of the carrier fluid. Particles with Reynolds numbers greater than 400 would augment turbulence due to vortex shedding and those with Reynolds numbers less than 400 would suppress turbulence of the carrier fluid.

Yuan & Michaelides (1992) proposed a mechanistic model based on wake shedding for turbulence generation and developed a simplified theory for the modification of turbulence intensity due to the existence of particles in dilute gas-solid flows. It was assumed in this model that the damping motion of an individual particle was responsible for turbulence attenuation and that the wake behind the particle was responsible for turbulence generation.

Accordingly, the following equation was derived for the total time-average change in turbulent kinetic energy (ΔE_k):

$$\Delta E_k = -\frac{\pi}{12} d_p^3 \rho_p U_{rel}^2 \left[1 - \exp\left(-\frac{2c_1 \tau}{\tau_p} \right) \right] + \frac{\pi}{12} d_P^2 \rho_f f(l_w) U_{rel} (2u_f - U_{rel}) \qquad (2\text{-}69)$$

where $U_{rel}=u_f - v_p$ is the relative velocity, c_1 is the drag coefficient, $\tau_p = \rho_p d^2_p/18\mu$ is the characteristic time of the particle (relaxation time), τ is the particle-eddy interaction time, and $f(l_w)$ is a length function representing a measure of the region behind the particle where the fluid velocity is close to that of the particle. They suggested that the total turbulence augmentation or suppression is determined by the combinations of these two effects. Kim et al. (2004), however, suggested that this model should be modified in order to yield a positive value independent of the relative velocity magnitude.

Yarin & Hetsroni (1994) developed a theory which accounted for turbulence production due to velocity gradients both in the carrier fluid and the turbulent wakes behind the particles. They used the modified mixing length theory to calculate the effect of the particle size distribution on the turbulence of the carrier fluid. Their model appears to work well for fluid-particle flows in which the turbulence is generated solely by the particles. Later, Kim et al. (2004) applied a similar theory using mixing lengths, but taking into account the effect of the wakes induced by the dispersed phase, the drag force between the particle and liquid, and the velocity gradient in the wake, to estimate the production of turbulence. The simulation results showed turbulence attenuation at a relatively small particle size and low loading ratio, and turbulence augmentation at a large particle size and high loading ratio, both qualitatively and quantitatively. The calculated critical particle size was found to agree with the value suggested by Gore and Crowe (1989), namely d_p/l_e=0.1.

Kenning and Crowe (1997) presented a new idea on the modulation of the carrier phase turbulence based on a simple physical model for turbulence generation and dissipation by particles. The turbulence length scale (l_h) in a particle-loaded flow was assumed to depend on a combined length between integral (dissipation) length scale (l_d) in a particle free flow and the inter-particle spacing (l_p), $2l_p l_d/(l_p+l_d)$. They developed the following relation for the change in turbulence intensity.

$$\frac{\hbar-\hbar_i}{\hbar_i}=\left[\frac{l_h}{l_i}+\frac{l_h}{k_i^{3/2}}\frac{f_S(u_f-v_p)^2}{\tau_p}\frac{\rho_p}{\rho_f}\right]^{1/3}-1 \tag{2-70}$$

where $\hbar_i$ and $\hbar$ are the turbulence intensities in particle-free (single-phase) and particle-laden flows, respectively; k_i and l_i are the turbulence intensity and length scale for the corresponding single-phase flow; f_S is the ratio of particle drag to Stokes drag, and ρ_p is the density of the particles. The model successfully predicts that the inter-particle spacing is important in establishing a turbulence length scale, which was consistent with the experimental findings in a particle-gas suspension.

Recently, Crowe (2000) proposed another model for the turbulence modification of a carrier phase in a two-phase flow based on the volume averaged equations for the kinetic energy of the carrier phase. A hybrid turbulence length scale (l_{hl}) in two-phase flow, given by $l_p l_d/(l_p+l_d)$, was used; this is different from the function suggested by Kenning & Crowe (1997). The following relation was derived for the modification of the turbulence kinetic energy:

$$\left(\frac{\tilde{k}}{\tilde{k}_i}\right)^{3/2}=\frac{1+\frac{1}{18}C^*(gD/u_f^2)^2\rho_p u_f D/\mu_f(l_{h1}/D)^3 f_S\hbar_i^3(d_p/l_{h1})^2}{1+\alpha_p^{1/3}(l_{h1}/d_p)} \tag{2-71}$$

where $\tilde{k}_i$ and $\tilde{k}$ are the turbulence kinetic energy in particle-free and particle-laden flows, respectively, C^* is the ratio of mass of the dispersed phase to the carrier phase, D is the pipe diameter, and α_p is the dispersed phase volume fraction. He showed that the change in the turbulence intensity can be correlated with the particle loading and the ratio of the particle diameter to the turbulence length scale. However, it was assumed in the model that the production term due to velocity gradient in two-phase flow is the same as that of the particle free flow.

Yuge & Hagiwara (2004) applied a direct numerical simulation based on a finite difference scheme in a liquid-liquid upward channel flow to elucidate the near-wall turbulence structure. After tracking the interface using a modified volume-of-fluid (VOF) method, they found that the secondary flows around a dispersed droplet increase the Reynolds shear stress production, and can be attenuated in the flow direction by an adjacent droplet. The small-scale streamwise vortices were found to be attenuated near the droplet; however, the large-scale vortices developed were deformed by the droplet. They further

suggested that there is an enhancement of the turbulent heat transfer due to the presence of the droplets, as the product of lateral velocity production is increased by the secondary flows in the proximity of the droplets.

2.6 Application of Hot-Film Anemometer in Two-Phase Flow Measurements

The hot-film anemometer (HFA) is an instrument for measuring local velocity which is based on determining the convective heat transfer from a heated sensor to the surrounding fluid, the heat transfer being primarily related to the fluid velocity. Typical hot-film sensors are nickel films placed on quartz substrates of different shapes that give high temperature coefficients of resistance and possess sufficient mechanical and electrical stability. They are protected by a sputtered quartz coating, which protects against electrolysis, when used in liquids, and protects against wear and oxidization in gas applications. By using very fine sensors placed in the fluid and electronics with servo-loop technique, it is possible to measure velocity fluctuations of fine scales and of high frequencies. There are many advantages of the HFA over other flow measuring techniques (i.e. LDA and PIV), for example HFA has a very high temporal resolution ideal for measuring spectra, less limitations for the second phase volume fraction (can be used up to 70% unlike LDA or PIV which are limited to a very low volume fraction due to the requirement of a free optical path), higher signal-to-noise level.

Following its successful application in single-phase flow measurements, this technique has recently been applied to two-phase flow, i.e. in particle-liquid flow (Ljus et al., 2002), air-water bubbly flow (Liu & Bankoff, 1993a&b; Shaha, 1999; Wang & Ching, 2001), oil-water dispersed flow (Farrar & Bruun, 1996; Al-Deen et al., 1997; Hamad & Bruun, 2000) and vapour-liquid R134A bubbly flow (Trabord & Kumar, 2000). In the case of two-phase flows the output voltages from the HFA normally give an abrupt change when the probe encounters interfaces and is exposed to the second phase, due to the different cooling rates of the two phases. Provided that the signals related to the dispersed phase are well removed, the probe is capable of providing information on the turbulence structure (i.e. intensity and Reynolds stresses) of the continuous phase. Table 2.7 lists experimental investigations carried out recently in fluid-liquid pipeline flows using hot-film anemometry.

Table 2.7: Application of HFA to two-phase flow measurements.

(* SR is the sampling rate and ϕ_{max} is the maximal local or input fraction of dispersed phase).

Authors (year)	Fluids & flow patterns	Probe type	Fluid temp. (°C)	SR* (kHz)	ϕ_{max}*
Wang et al. (1986)	Vertical bubbly (air-water) U_{air}=0~0.4m/s; U_{water}=0.4~0.9 m/s	Single sensor hot-film probe (TSI 1218-20W)	–	10	48%
Hagiwara et al. (1989)	Horizontal wavy flow (air-water)	Glue-on hot-film (TSI 1268W); hot-wire (Kanomax 1011)	–	4	–
Liu & Bankoff (1993a, b)	Vertical bubbly flow (air-water)	Boundary layer (TSI 1218-20W, 1D) Dual-sensor X-type (TSI 1246-60, 2D)	10±0.1	5 – a; 10 – b	50%
Farrar et al. (1995)	Vertical dispersed flow (kerosene-water)	Single fibre sensor (Dantec 55R11)	16±0.1	4	70%
Farrar & Bruun (1996)	Vertical dispersed flow (kerosene-water)	Single fibre sensor (Dantec 55R11)	16±0.1	1.667	30%
Al-Deen & Bruun (1997)	Vertical dispersed flow (kerosene-water)	Single fibre sensor (Dantec 55R15); Dual-sensor X (Dantec 55R61); Boundary layer split-fibre (55R58 sepcial)	16±0.1	–	40%
Hogsett & Ishii (1997)	Bubbly flow (air-water)	Conical shape (TSI 1231-W)	16±0.1	5	10%
Al-Deen et al. (1998)	Vertical and inclined dispersed flow (kerosene-water)	Single fibre sensor (Dantec 55R15);	16±0.1	–	18%
Hibiki et al. (1998)	Bubbly flow (air-water)	Conical shape (TSI 1231-W)	16±0.1	5	6.99%
Sharma et al. (1998)	Slug/plug flow (air-water) U_{gas} = 1.1~2.2m/s; U_{water} = 0.27~2.2m/s	Conical miniature platinum hot-film probe (TSI 1264 AW)	20~22	5	–
Hamad & Bruun (2000)	Vertical bubbly flow (water-kerosene)	SN boundary layer (Dantec 55R15)	16±0.1	–	10%

Authors (year)	**Fluids & flow patterns**	**Probe type**	**Fluid temp. (°C)**	**SR* (kHz)**	ϕ_{max}*
Iskandrani & Kojasoy (2001)	Horizontal bubbly flow (air-water) U_{water}=3.8~5m/s; U_{air}=0.25-0.8m/s	Conical shape (TSI 1231-W)	20~22	20	65%
Trabold & Kumar (2000)	Vertical annular flow (vapor- liquid 134A)	Dual fibre sensor probe	–	50	0.92
Wang & Ching (2001)	Slug and bubbly flow (air-water)	Single fibre sensor (Dantec 55R11)	–	7	17.4%
Ljus et al. (2002)	Horizontal dispersed flow (air-particle) U_{air}=12, 19 m/s	Wedge-shape probe (Dantec 55R31)	–	10	10% (m_p/m_l)
Garnier et al. (2002)	Vertical buoyancy-driven bubbly flow (air-water) U_{water}=0.016-0.062m/s	Miniature conical probe (TSI 1264 AW-BR)	T_{op}±0.1	–	40%
Sun et al. (2002)	Vertical bubbly flow (air-water)	Conical miniature platinum (TSI 1264 AW)	20±0.5	5	20%

Despite the many advantages and wide applications of this technique, some limitations still remain. For example, the fibre probe is extremely fragile which requires specially care. The probe is also prone to contamination by a liquid phase, especially in oil-water flows; however, Al-Deen & Bruun (1997) suggested that the contamination problem can be solved by using deionised water and installing 8 and 2 μm filter units, and by regular cleaning with dilute acid (i.e. 2-propanol alcohol or fresh lemon juice). Also, HFA was found not to be applicable for measuring very small or backwards liquid velocity (Garnier et al., 2002). For very low velocity the calibration curve of the hot-film probe is very sharp and small temperature variations can lead to large errors. It has also been reported that there could be measurement errors of 25% ~ 40% if the fluid temperature shifts by 1°C (Samways et al., 1994; Bruun, 2004). For application in two-phase flows, a significant amount of work is required for signal separation; for example, in order to obtain the true turbulence structure of the continuous phase it is necessary to eliminate any part of the HFA signals which does not correspond to the continuous phase velocity.

Identifying the signal of each phase is particularly important when a hot-film anemometer probe is used to measure local void fraction. Wang et al. (1987) applied the single sensor cylindrical hot-film probe (TSI-1218-20W) to measure local void fraction in a vertical pipe and found that the measured local void fraction normally underestimates the actual value, as the eliminated sharp change in the signal only spans part of the duration of bubble passage. This error was then determined and corrected by using a single-beam γ-ray desitometer as a standard. However, the void fraction was also sometimes overestimated which may be due to the signal discrimination algorithm. Even when a well-developed separation method was used, Hibiki et al. (1998) still noted that the void fractions measured by hot-film anemometry tend to be overestimated by about 10-20% when compared with those measured by a conductivity probe, due to the bubble interface deformation during entry into and exit out of the probe.

To gain further understanding of the HFA probe behaviour in two-phase flows, some elaborate work has been carried out. Figure 2.7 elucidates the 'U' shape effect on the output voltage during bubble or drop passage through the probe sensor (Abel & Resch, 1978; Bruun, 1995; Farrar et al., 1995; Al-Deen & Bruun, 1997). A number of algorithms have thus been proposed in the past to eliminate the part not representing the continuous phase, like amplitude threshold voltage (Jones & Zuber, 1978), slope threshold voltage (Abel & Resch, 1978) and combined amplitude and slope threshold method (Wang et al., 1987; Liu & Bankoff, 1993 a&b; Farrar et al., 1995; Garnier et al., 2004). The combined amplitude and slope threshold method has been extensively employed recently as the separated signals are not crucially dependent on the threshold values. In addition, Farrar et al. (1995) pointed out that a method based only on slope could introduce errors, because the water film formed between two prongs of the probe may be heated up and broken when the probe sensor is immersed in the bubble (see point F in Figure 2.7b). When this water film breaks an abrupt change in the signal will occur which will be interpreted as another bubble by the slope discrimination method.

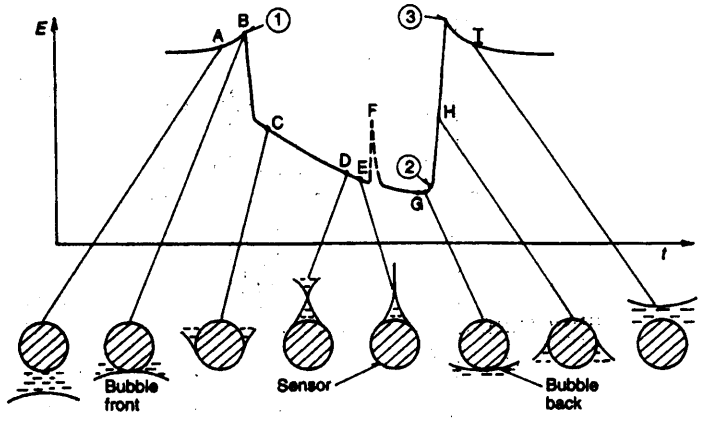

Figure 2.7: The response of a cylindrical probe to the passage of an air bubble/oil drop (Farrar et al., 1995; Bruun, 1995).

One of the well known signal discrimination algorithms based on amplitude and slope threshold method and used broadly in two-phase flow measurements was developed by Liu & Bankoff (1993a). In their method, eight simple conditions covering normal and closely-spaced bubble-probe interactions are proposed. According to the criteria listed as follows, if $R_i > T$ and any one of them are satisfied, the current point is in the continuous water phase:

Case (i): if at least two liquid data points lie between two successive bubbles.

(1) $R_b < S$ and $R_f < S$ (remain in liquid);

(2) $R_b < S$ and $P_f > S$ (entering bubble);

(3) $R_{i+1} > T$ and $P_b > S$ and $R_f < S$ (entering liquid);

(4) $P_f < 0$ and $R_b < S$ and $R_f < 1.5S$ and $R_{i+2} < R_{i+1}$ and $|R_{i+2} - R_{i+1}| > S$ (overshooting due to bubble approaching);

(5) R_{i-1} in gas and $R_{i+1} > T$ and $P_f > 0$ and $P_b > S$ and $R_f < 1.5S$ (overshooting due to detaching)

Case (ii): if only one liquid data point lies between two consecutive bubbles.

(6) $P_b > 2S$ and $P_f > S$

(7) $P_b > S$ and $P_f > 2S$

(8) $R_{i-1} < T$ and $R_{i+1} < T$

where T is the level threshold, S is the slope threshold, R_i is the i^{th} data sample voltage (or velocity) value, $P_b=R_i-R_{i-1}$ is the backward slope, $P_f=R_i-R_{i+1}$ is the forward slope, R_b is the magnitude of P_b, $R_b=|P_b|$, and R_f is the magnitude of P_f, $R_f=|P_f|$.

Although the amplitude threshold, T, depends on the flow conditions, Liu & Bankoff (1993a) found that this value is not necessarily close to the continuous phase when a slope threshold is used as well.

2.7 Summary

A number of topics were reviewed in this Chapter, namely previous studies of phase inversion in liquid-liquid dispersed flows in stirred vessel and pipeline flow systems, studies of drop size distribution using population balance equations modelling in dispersed flow, the postulated models for drop/bubble breakage and coalescence rates in turbulent flow, the current views on turbulence modification of a fluid by the addition of a secondary dispersed phase, and the application of hot-film anemometry to turbulence measurement in two-phase flows. Particular emphasis was placed on the investigations of phase inversion, the subject of this thesis. Although a large number of studies have been carried out in the past decades, the understanding of phase inversion and its associated phenomena is still fairly limited. Furthermore, fewer studies have been conducted on phase inversion in pipeline flows than for agitated vessels, and most of the previous work concentrated on understanding phase inversion at the macroscale (characterised by the phase inversion point and width of ambivalent region affected by various parameters, such as viscosity ratio, interfacial tension, and container material etc.). There is a dearth for studies at the mesoscale level, for example turbulence and its modification of dense dispersions where inversion occurs. As it is particularly important in industrial applications to control dispersion behaviour under operational conditions, comprehensive understanding of phase inversion is urgently required. The prime aim of the work described in this thesis therefore was to achieve such an understanding.

Chapter 3

Experimental Facilities, Instruments and Methods

This Chapter describes the experimental facilities, instruments and methods used. The main objective is to present descriptions for the techniques employed in the work described in this thesis in sufficient detail to promote a clear understanding of the experimental processes. Both horizontal and vertical experiments were carried out; the basic flow system is described in Section 3.1. The instruments and techniques used to measure flow parameters, i.e. pressure drop, drop size distribution, drop velocity and phase continuity are described in Section 3.2. Section 3.3 discusses the application of the hot-film anemometer technique for the turbulence measurements. A short summary is finally given in Section 3.4.

3.1 The WOLF Facility

In the work described in this thesis, all the experiments were carried out on the Water-Oil Liquid Flow (WOLF) facility, at the Chemical Engineering Department, University College London, which is designed for studies of horizontal, inclined (maximum inclined angle $\pm 10^{o}$) and vertical liquid-liquid flows. The facility has been used to investigate phase inversion and associated phenomena in horizontal and vertical flows. Figure 3.1 illustrates the system used for current studies in horizontal flow, while the systems for upward and downward vertical flows are shown in Figure 3.2 and 3.3, respectively.

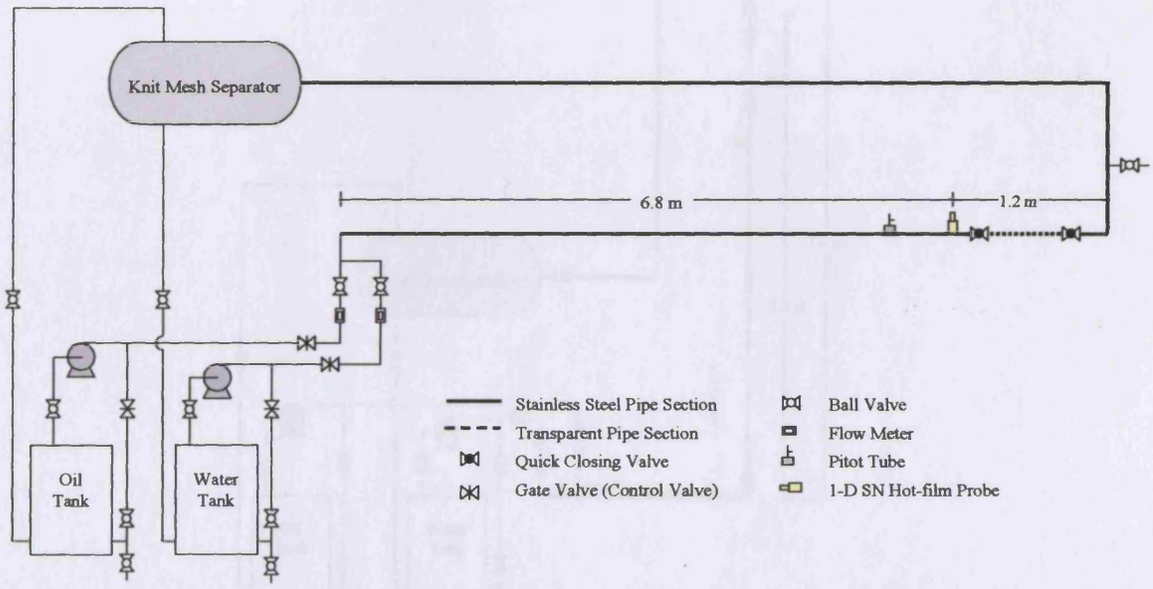

(a)

(b)

Figure 3.1: Schematic (a) and photograph (b) of the WOLF facility for horizontal flows.

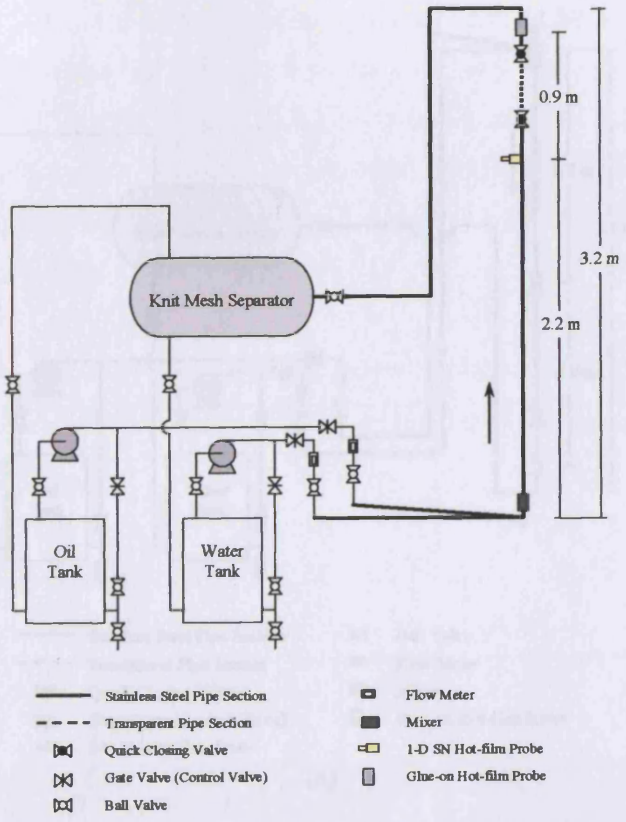

(a)

(b)

Figure 3.2: Schematic (a) and photograph (b) of the WOLF facility for upward flows.

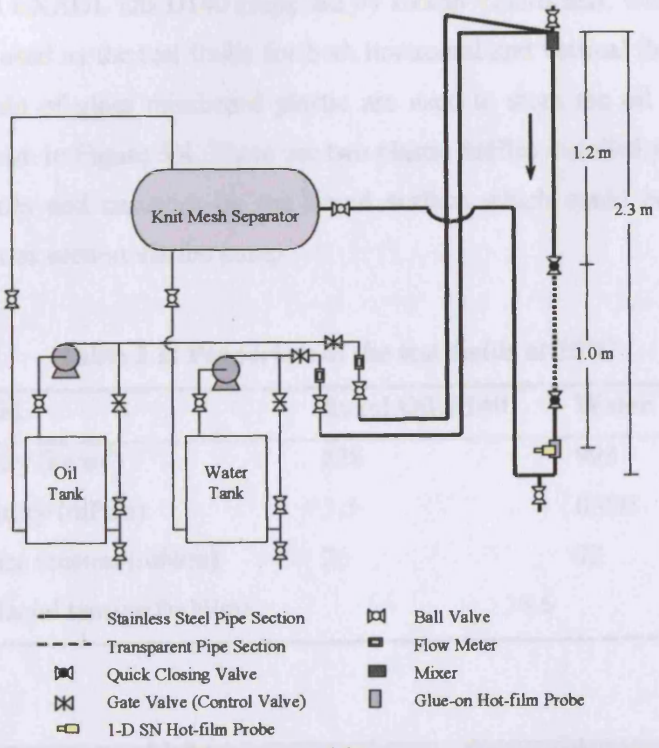

(a)

(b)

Figure 3.3: Schematic (a) and photograph (b) of the WOLF facility for downward flows.

Tap water and EXXOL Oil D140 (supplied by Exxon Chemicals), with properties given in Table 3.1, are used as the test fluids for both horizontal and vertical flows. Two 0.88 m^3 storage tanks made of glass reinforced plastic are used to store the oil and water phases separately, as shown in Figure 3.4. There are two plastic baffles installed within each tank to reduce any vortices and cascades on the liquid surface which could entrain air into the reservoir and the test section via the pump.

Table 3.1: Properties of the test fluids at 25°C

Liquid	Exxol Oil D140	Water
Density (kg/m^3)	828	998
Viscosity (mPa s)	5.5	0.993
Surface tension (mN/m)	20	72
Interfacial tension (mN/m)	36.6	

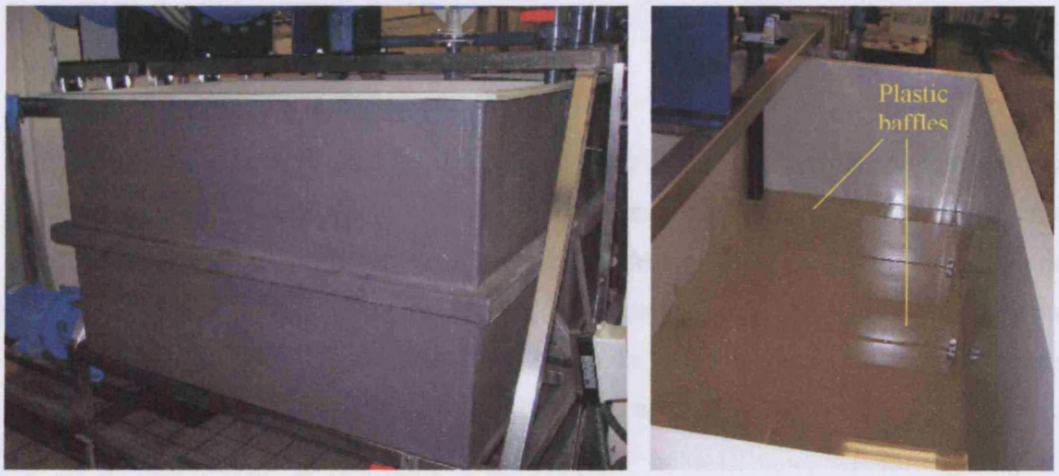

Figure 3.4: Photographs of the storage tanks (side and top views).

Two 7.5 KW centrifugal pumps (Ingersoll-Dresser, 40-25CPX200) are used to pump separately the oil and water phases. Each pump can supply the maximum output volumetric flowrate of 240 l/min (approximate 3.5 m/s superficial velocity) at 45 kPa. Armoured variable area flowmeters (ABB Instrumentation 10A5400) are mounted at the beginning of the flow loop to measure the oil and water flowrates and the signals are recorded into a PC for analysis. Four different flowmeters have been used to ensure better measurement accuracy: two with a range of 10-240 l/min and ±1% full scale accuracy, and two with a

range of 0-10 l/min and ±2% full scale accuracy. The choice between the large and small range flowmeters is determined by the experimental conditions.

After exiting the test section the oil-water mixture is delivered into a 0.8 m^3 separator unit which contains a KnitMesh (DC 9201/SS/PPL) coalescer (see Figure 3.1b). The coalescer consists of wired meshes made of two materials (one plastic and the other metal) with different free surface energies, which allows rapid separation of dispersed drops of size down to 50μm. The separated oil and water are then passed back to their respective storage tanks to ensure the continuous operation of the system. Also, there are two ball valves installed at the feedback passage to water and oil storage tank so that the interface level between phases in the separator can be maintained approximately in the middle in order to avoid the over flow of one phase into the reservoir of the other phase.

3.1.1 WOLF Setup in Horizontal Flows

3.1.1.1 The Inlet Section

For the horizontal flow studies, the oil and water phases are introduced into the test section via the inlet section shown in Figure 3.5. Oil and water are joined together in a short distance before a 90° elbow which leads into the straight horizontal test section. Although no particular mixer is used at the inlet section in the current studies, visualizations of the mixture have indicated that dispersed flows can be obtained at the measuring points (between 4 m and 7 m from inlet) under the conditions used.

Figure 3.5: The inlet section of the rig in horizontal flows.

3.1.1.2 The Test Section

The test section is a 16 m long pipe which consists of two parallel 8 m long pipes of 38 mm I.D. connected through a U-bend (see Figure 3.1b). The test section is made of stainless steel, except for a 54-cm long transparent acrylic section installed for flow visualization purposes.

Experimental studies of drop velocity, drop size distribution and turbulence modification, were carried out for horizontal flow. For the drop velocity and drop size distribution studies, a dual-impedance probe (see Section 3.2.1) was used and the measurements were conducted at two positions: 4 m (105*D*) and 7 m (184*D*) from the entrance, respectively. For the turbulence modification studies, a hot-film anemometer (see Section 3.3.1) is employed and the velocity probe is mounted at 6.8 m (179*D*) from the entrance.

3.1.2 WOLF Setup in Vertical Flows

3.1.2.1 The Inlet Section

Figure 3.6 illustrates the inlet section of the vertically upward and downward flows. After leaving the storage tanks, the oil and water phases join together right before the entrance of the vertical test section via a 'Y' junction. The oil-water mixture then flows through a 90° elbow before passing through a coarse mixer (see Figure 3.7) which is located next to the entrance. The objective of having the inlet mixer is to premix the fluids and shorten the length needed to achieve fully-developed conditions so that fully-dispersed flows can be obtained at the downstream measuring point for the given length of the test section.

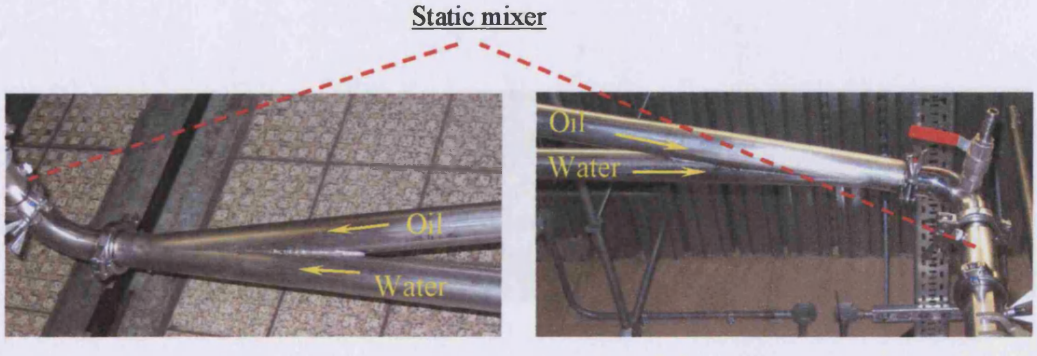

(a) (b)

Figure 3.6: The inlet section of the rig in vertical flows. (a): upward and (b): downward.

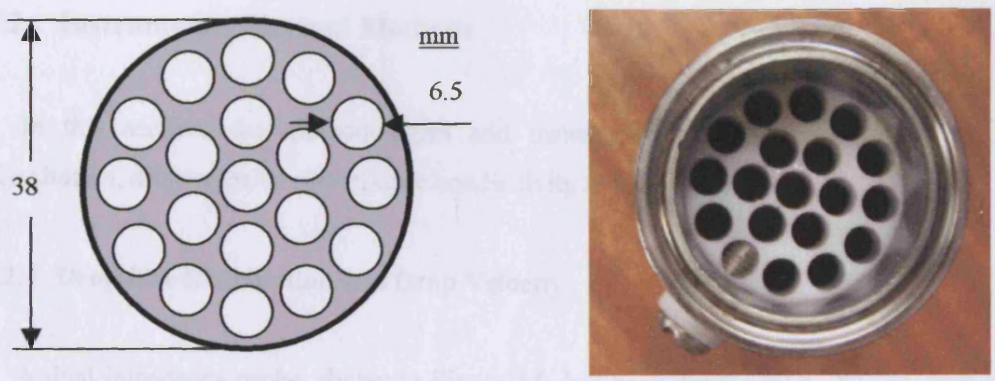

Figure 3.7: The static mixer used in vertical flows.

3.1.2.2 The Test Section

The vertical test sections were a 38 mm I.D. stainless steel pipes having a total lengths of 3.2 m and 2.3 m for upward and downward flows, respectively, as shown in Figures 3.2 and 3.3. Pressure drop, drop size distribution, drop velocity, mixture conductivity, holdup and turbulence were measured for both upward and downward flows. Pressure drop is measured with a Validyne DP103 differential pressure transducer, which is connected to the test section between the positions 42*D* and 81*D* for upward flow, and 16*D* and 55*D* from the inlet for downward flow. Drop size (and velocity) and conductivity are measured at an axial distance from the inlet of 81*D* and 58*D* for upward and downward flow, respectively; turbulence velocity is measured at an axial distance of 58*D* from the inlet for both upward and downward flow. A transparent section with rapid closing valves installed at both sides is used at the end of each test section replacing a section of steel pipe to measure the average holdup and visualize the flow behaviour (see Figure 3.8).

Figure 3.8: Photograph of the transparent acrylic pipe section for holdup measurements and visualization.

3.2 Instrumentations and Methods

In this section, the methodologies and instruments used for measuring drop size distribution, drop velocity and mixture conductivity are described.

3.2.1 Drop Size Distribution and Drop Velocity

A dual impedance probe, shown in Figure 3.9, has been developed by Lovick (2004) and installed in the WOLF rig at UCL. In the work described in this thesis, this dual impedance probe is also employed to measure drop velocity and drop size distributions. The detailed descriptions of the probe setup, operation and working principles can be found in detail in the Lovick (2004) thesis.

Briefly, the dual impedance probe consists of two impedance sensors working independently, each measuring the instantaneous impedance of the liquid contacting the sensitive probe tip. In a two-phase flow, the signals obtained by each impedance probe are primarily dependent on the conductivity of the liquid that the probe is in contact with. For the probe immersed in oil, a substantially higher voltage value is expected than for the probe immersed in water. These two impedance probes are set 10 mm away and their mountings are designed in a way that allows them to move together at the same height in the pipe cross-section. Alternating current with frequencies of 2 ~ 45 kHz can be applied to each probe via a signal control box. The frequency of 35 kHz was applied in the present study in order to ensure the capture of drops as small as 200 μm. In a given test, 120,000 successive values of voltage were recorded, at time interval of typically 29 μs for each probe, the value being logged in a PC. Typical output signals from the dual impedance probe are presented in Figure 3.10a, which was obtained in horizontal flows at 3.0 m/s mixture velocity and 10% input oil fraction.

The drop velocity can therefore be estimated by cross-correlating the experimental data from the two sensors; this gives the average delay time for drops passing through the two sensors of 10 mm distance. The details on the cross-correlation function and implementation can be found in Jonathan (2004). Figure 3.10b illustrates the plots of the cross-correlation density function based on the raw signals of Figure 3.10a. The peak in the cross-correlation function is observed for a time lag is approximately 2.8 ms. Furthermore, the average drop velocity can be obtained by dividing the distance by this lag time between the two sensors. Following the determination of the drop travelling velocity, the chord length can be found from the signals of either sensor by multiplying this average drop velocity by the duration of

each drop passage. To obtain the durations of each dispersed drop passage, a square wave model based on level and slope threshold values developed by Lovick (2004), is used here. Finally, chord length distributions for each location are found by summarizing all the drops in recorded signals, as shown in Figure 3.10c. It is worth noting that this chord length distribution is biased since bigger drops have a higher probability of being captured by the probe than smaller drops (see also Chapter 4).

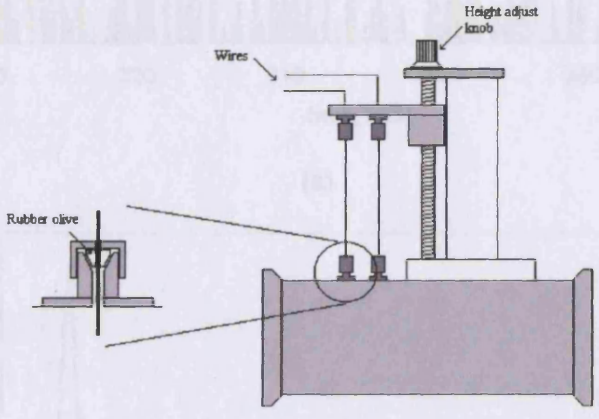

(a)

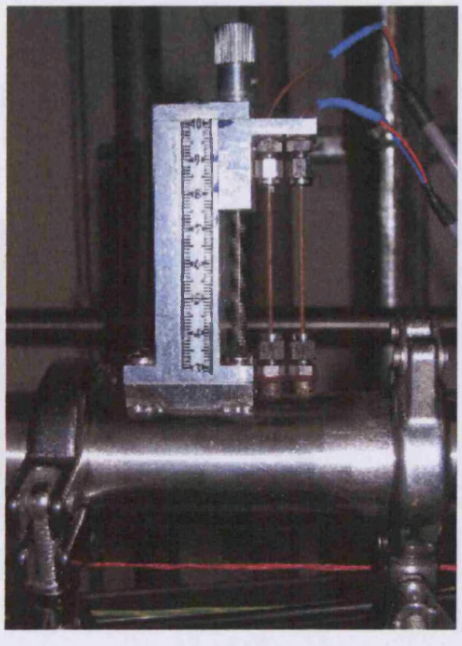

(b)

Figure 3.9: Schematic (a) (Lovick, 2004) and photograph (b) of the dual impedance probe.

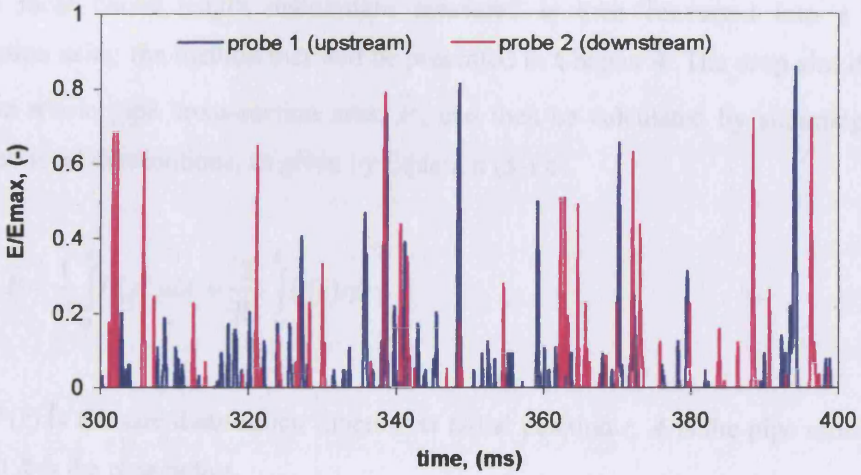

(a)

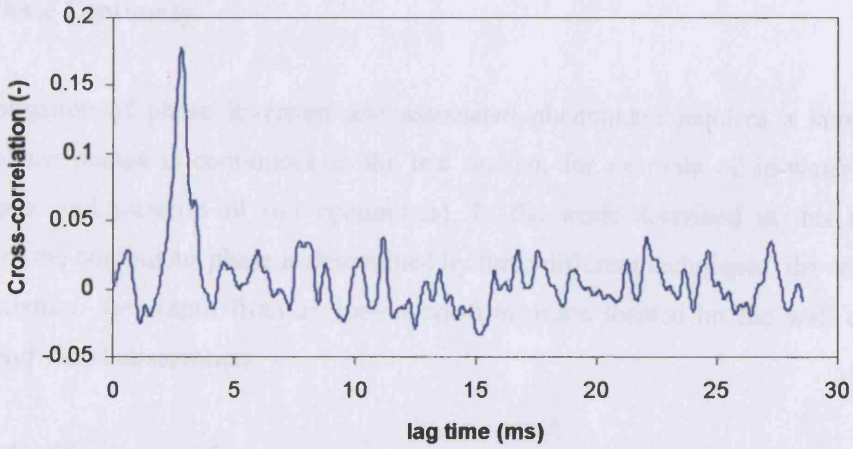

(b)

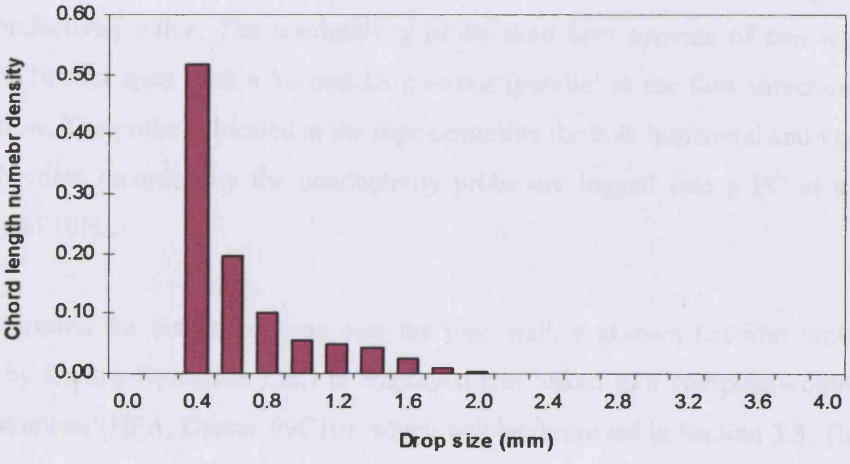

(c)

Figure 3.10: (a): Signals from dual impedance probe, (b): cross-correlation function plot and (c): chord length number density, obtained at 7 m from the inlet and 2 mm from pipe centre, under conditions of 3.0 m/s mixture velocity and 10% input oil fraction.

The local chord length distribution measured is then converted into a drop size distribution using the method that will be presented in Chapter 4. The drop size distribution over the whole pipe cross-section area, $\overline{P}$, can then be calculated by summing the area-weighted local distributions, as given by Equation (3-1):

$$\overline{P} = \frac{1}{A}\int_0^A P(A')dA' = \frac{2}{R^2}\int_0^R P(r)rdr \tag{3-1}$$

where $P(r)$ is the size distribution function at radial position r, A is the pipe cross-sectional area and R is the pipe radius.

3.2.2 Phase Continuity

Investigation of phase inversion and associated phenomena requires a knowledge of which of the phases is continuous in the test section, for example oil-in-water (or water continuous) and water-in-oil (oil continuous). In the work described in this thesis, the identity of the continuous phase is determined by three different techniques: the conductivity of the mixture, the output from a glue-on hot-film probe located on the wall of the test section and visual observation.

The identification of phase continuity by conductivity is based on the fact that water-continuous dispersions have a high conductivity value while oil-continuous dispersions have a low conductivity value. The conductivity probe used here consists of two wire sensors which are 10 mm apart with a 10 mm long sensor (parallel to the flow direction) exposed into the flow. The probe is located at the pipe centreline for both horizontal and vertical flow cases. The data recorded by the conductivity probe are logged into a PC at a sampling frequency of 10Hz.

To determine the dispersion type near the pipe wall, a glue-on hot-film probe (55R47 supplied by Dantec Dynamics Ltd.) is employed and linked to a computer-controlled hot-film anemometer (HFA, Dantec 99C10), which will be discussed in Section 3.3. The glue-on hot-film probe, as shown in Figure 3.11a, is a special version of the flush-mounting probe, where the sensor is deposited on a Kapton™ foil, 50 μm thick. The sensor is 0.9 mm ×0.1 mm and connected to gold-plated lead areas. It is primarily intended for qualitative measurements of points of flow transition and separation. Copper wires soldered to the leads constitute the electrical connection between probe cable and probe. The sensor is oriented

perpendicular to the flow direction. The details of the technical data for this probe are listed in Table 3.2.

The probe is then glued to an acrylic block by Perspex glue. This acrylic block, as seen in Figures 3.11b&c, has a surface which is flush with the inner wall of the pipe and is inserted into a 10 cm long section. The whole section is sealed by a rubber o-ring. The probe cannot normally be removed when glued in place. The test section with glue-on probe is positioned in a distance of 81*D* from the inlet for upward flow and at a distance of 58*D* for downward flow. The glue-on hot-film probe is primarily designed for measurements in air flows. In the present experiments when the probe was operated in contact with water, it corroded very rapidly (see Figure 3.12) and broke down, giving no signal, within 5 minutes. However, the corrosion was avoided, and useful results obtained, by gluing the inner side of the probe to the acrylic block, i.e. operating the probe upside down!

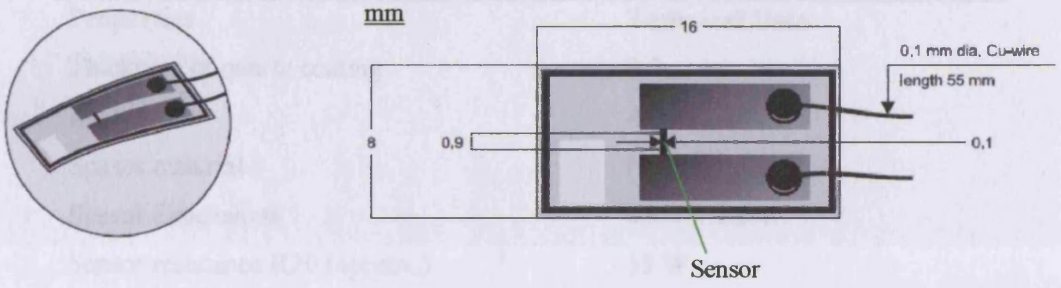

(a) Schematic of the probe

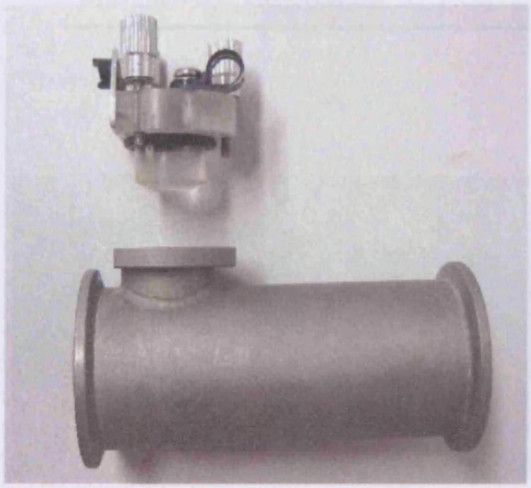

(b) Side view

(c) Top view

Figure 3.11: Schematic of the Dantec 55R47 glue-on probe (a) and the photographs of the test section mounted with the glue-on probe (b&c).

In spite of the probe being used with the sensor facing away from the fluid, it was found that the probe still showed high enough sensitivity to distinguish between the cooling effects of oil and water respectively in contact with the non-sensor side. For example, for fully dispersed oil-in-water flows where water wets the wall surface and the probe, a high voltage signal is expected due to the fast cooling effect of the water phase. Alternatively, in a water-in-oil dispersion the HFA system gives a low voltage output as oil has reduced cooling effect. It was found, therefore, that the probe could give a fast and reliable indication of which phase was in contact with the wall. Because of its location this probe, however, can only detect the continuous phase in the vicinity of the wall. Although this technique has not been used before to identify phase inversion, the results from the present study show the good stability and accuracy of this methodology.

Table 3.2: Technical data of the glue-on hot-film probe, Dantec 55R47.

Properties	**Technical Data**
Thickness of quartz coating	0.5 μm
Medium	Air
Sensor material	Nickel
Sensor dimensions	0.9 × 0.1 mm
Sensor resistance R20 (approx.)	15 W
Temperature coefficient of resistance (TCR)	0.40%/°C
Max. ambient temperature	120°C

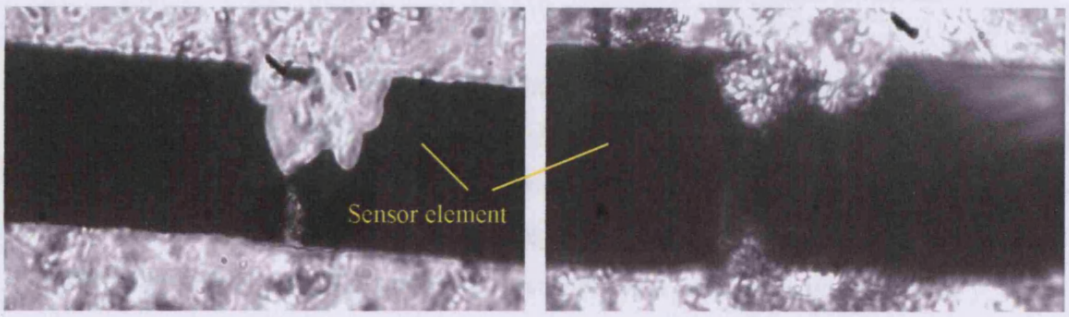

Figure 3.12: Microscope view of two broken sensors due to water corrosion found in Dantec 55R47 probes.

In addition to the above techniques, the phase inversion point can also be identified by observing the dispersion through the transparent test sections using a Kodak digital camera. Water-in-oil dispersions appear more opaque than oil-in-water ones while there is also a major visual difference between water and oil drops. A set of photographs in o/w and w/o dispersions is presented in Appendix A.

3.3 Turbulence Structure

Phase inversion often occurs in dense dispersions where only limited techniques can be employed for turbulence measurement. This section describes the application in the WOLF rig of the hot-film anemometer, which had been used successfully in highly concentrated systems (Farrar & Bruun, 1996).

3.3.1 Hot-Film Anemometer (HFA)

Working Principle

An HFA is basically a thermal transducer where the probe forms one arm of a Wheatstone bridge, which is the kernel of the anemometer. An electric current heats a fine filament in the probe which is exposed to a cross flow. As a result, heat is transferred from the hot filament to the ambient fluid. Any variation in fluid properties (e.g. velocity and temperature) will cause a change in the heat transfer rate from the sensor. The hot-film anemometer monitors this variation and gives signals relating to the velocity or temperature changes. The hot-film (or hot-wire) anemometer can thus be used to measure instantaneous velocities (and velocity derivatives, such as shear stress) and temperatures in a flow.

There are two operation modes for a hot-film anemometry system according to its functionality: Constant Current Anemometry (CCA) where a constant current is passed through the sensor (also termed *cold-wire anemometry*), and Constant Temperature Anemometry (CTA) where the sensor is kept at constant temperature (also termed *hot-wire/film anemometry*). A CTA system (Dantec 90C10) is used in the present work.

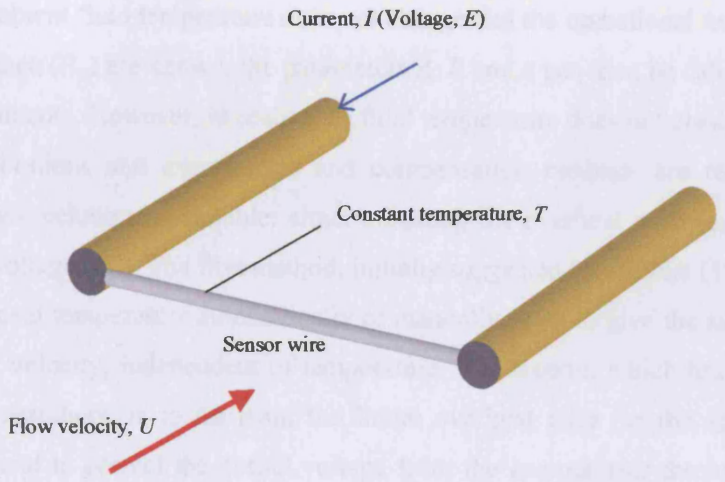

Figure 3.13: Schematic diagram of the heated sensor of a hot-film probe for a constant temperature hot-film anemometer.

Figure 3.13 schematically depicts a heated hot-film sensor immersed in an ambient fluid. The convective heat transfer between a heated sensor and the fluid passing by the probe sensor is described by relations which are parameterized by the Nusselt (*Nu*), Reynolds (Re), Prandtl (*Pr*) and Grasshof (*Gr*) numbers. For a constant temperature hot-film anemometer working at steady state, the heat transfer relationship can be expressed by the following function, known as King's Law,

$$\frac{E_w^2}{R_w(T_w - T_o)} = (A + B \cdot U^n) \tag{3-2}$$

where E_w is the voltage acting on the sensor which is also the output of the CTA, T_w is the wire working temperature, T_o is a reference temperature (such as initial fluid temperature), U is the velocity of fluid flow, R_w is the wire resistance at the temperature T_w, and A, B and n are parameters. For a thin wire (or fibre film) sensor, its resistance can be estimated by the overheat ratio α_R.

$$\alpha_R = \frac{(R_w - R_o)}{R_o} \tag{3-3}$$

where R_o is the resistance at a reference temperature T_o.

If the ambient fluid temperature does not change and the operational temperature (T_w) and wire resistance (R_w) are known, the parameters A, B and n can then be calibrated as constants from experiments. However, in reality the fluid temperature does not always remain constant during calibrations and experiments and compensation methods are required. Generally, there are two techniques available: either adjusting the overheat ratio (α_R) or by correcting the output voltage (E_w). The first method, initially suggested by Drubka (1977), is to alter the sensor filament temperature automatically or manually so as to give the same output voltage at the same velocity, independent of temperature. The second, which has been widely used by other researchers, is to maintain the initial overheat ratio (or the sensor temperature) unchanged and to correct the output voltage from the anemometer through an independent measurement of fluid temperature (Bearman, 1971; Perry, 1982). In the studies presented here, the latter compensation technique was applied.

If variances of fluid properties can be ignored within a small range of temperature change, the following expression (Bearman, 1971) can be used to compensate for the temperature shift,

$$E_{corr} = \left(\frac{T_w - T_o}{T_w - T_a} \right)^{0.5} \cdot E_w \tag{3-4}$$

where E_w is the acquired voltage from anemometer, E_{corr} is the corrected voltage, T_w is the sensor operating temperature during acquisition, T_o is the ambient fluid temperature related to the last overheat setup before calibration, T_a is the ambient fluid temperature during acquisition.

System Component

The system for a constant temperature anemometer (CTA 90C10, Dantec Dynamics Ltd.), shown in Figure 3.14, consists of a *Probe* with *Probe support* and *Cabling*, a *CTA anemometer*, a *signal conditioner*, an *A/D converter*, and a *computer with data processing software.* These items form a measuring chain illustrated in Figure 3.15. The film sensor immersed into the fluid transfers the velocity information to the constant temperature anemometer, which gives an analogue voltage output of 0~10 V to an A/D converter. Subsequently, the digital signals are logged into a computer and are processed by the Dantec *Stream-Ware* software package.

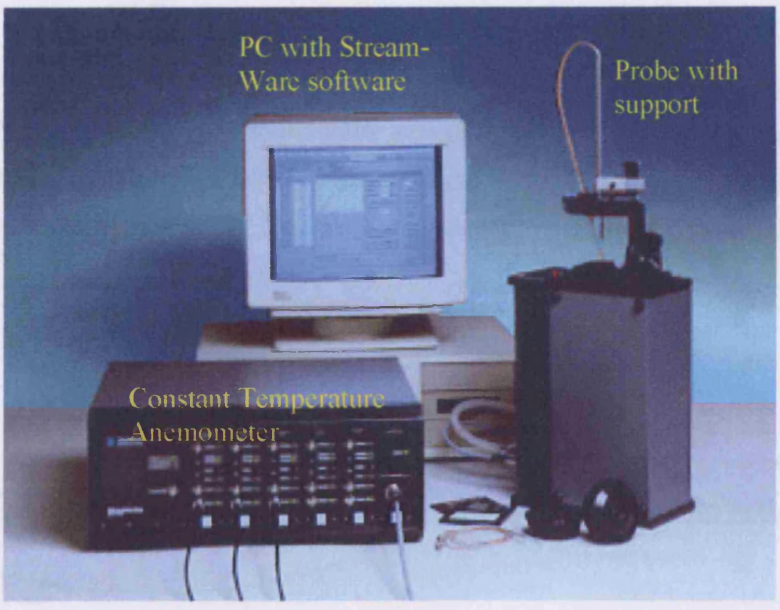

Figure 3.14: Photograph of a constant temperature anemometry system (90C10 Dantec Dynamics Ltd.).

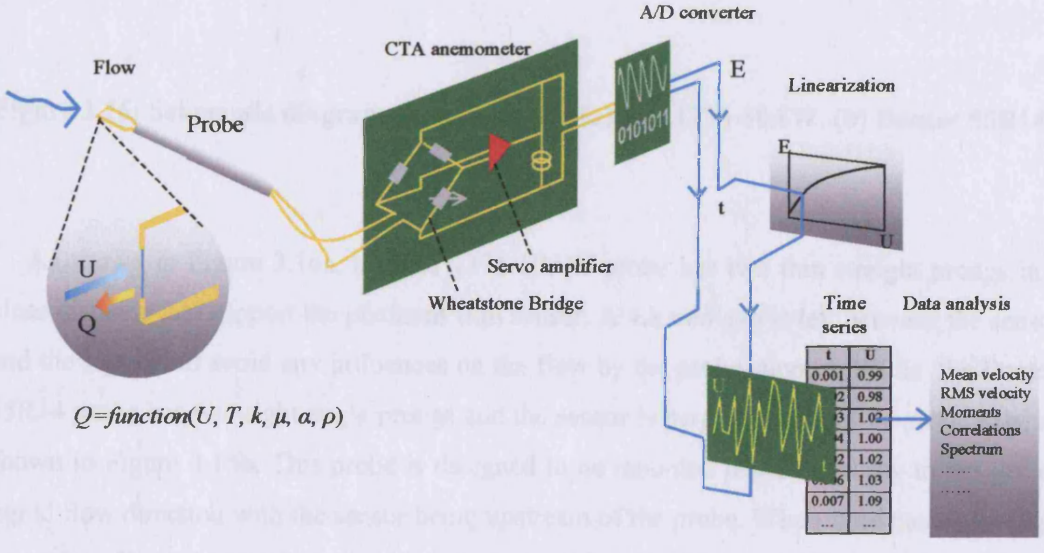

Figure 3.15: Typical measuring chain of a CTA system.

Single Fibre Probe Structure

In the present experiments carried out in this thesis, two 1-D velocity probes are used to measure the turbulence: a subminiature straight platinum film probe supplied by TSI Incorporated (Model 1276-10AW) and a single fibre film probe supplied by Dantec Dynamics Ltd. (Model 55R14). The probe geometries are schematically illustrated in Figure 3.16.

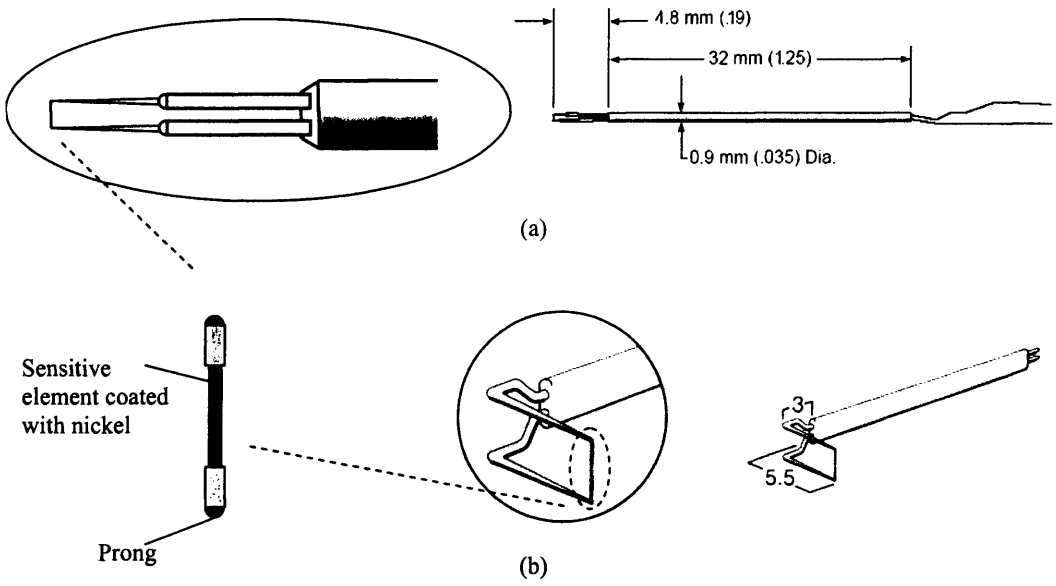

Figure 3.16: Schematic diagrams of the probes: (a) TSI 1276-10AW, (b) Dantec 55R14.

As shown in Figure 3.16a, the TSI 1276-10AW probe has two thin straight prongs in a close distance that support the platinum film sensor. A 4.8 mm gap is left between the sensor and the support to avoid any influences on the flow by the probe support. While, the Dantec 55R14 probe has two right angle prongs and the sensor is perpendicular to the probe axis, as shown in Figure 3.16b. This probe is designed to be mounted perpendicularly to the gas or liquid flow direction with the sensor being upstream of the probe. When fluid passes through the sensor filament, therefore, the flow cannot be affected by the probe support.

In the Dantec 55R14 probe the film sensor is a 70 μm diameter quartz fibre, 3 mm long, covered by a nickel thin film approximately 2 μm thick. This layer guards against electrolysis when used in liquids and protects against wear and oxidization in gas

applications. The actual active sensitive element is 1.25 mm long. The sensor ends are copper- and gold- plated. The fibre is soldered onto the probe ends. The probe has lacquer-coated soldered joints and the prongs are insulated from the surrounding liquid or gas. The probe is then mounted in a long straight probe support (Dantec 55H21), shown in Figure 3.17. The support consists of a coupling ring that provides a water- and pressure-tight sealing, and one set of contacts embedded in a cylindrical body that end in Teflon™-coated cables with detachable BNC connector. The outside probe support diameter is 4 mm.

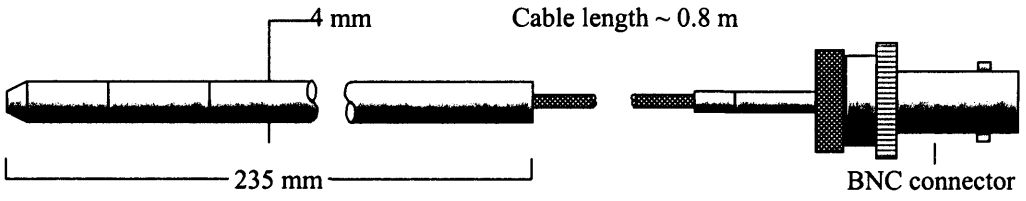

Figure 3.17: Long straight probe support (Dantec 55H21) for Dantec 55R14 probe.

In the TSI 1276-10AW probe the sensor is constructed of a high purity anticorrosive platinum film on a fused-quartz substrate which provides high strength and low thermal conductivity. The sensor has a diameter of 25.4 μm and is 0.76 mm long with 0.25 mm long actual active sensor element. To use the same test section designed for Dantec 55R14 probe, a stainless steel tube with 4mm O.D. is used as the support for TSI 1276-10AW probe, and was sealed with Perspex glue.

The details of the technical data for the two probes are listed in Table 3.3

Table 3.3: Technical data of the 1-D velocity hot-film probes.

Properties	**TSI 1276-10AW**	**Dantec 55R14**
Sensor material	Platinum	Nickel
Sensor diameter	25.4 μm	70 μm
Sensor length (active sensor length)	0.76 (0.25) mm	3 (1.25) mm
Sensor resistance (20°C)	~ 5 Ω	~ 6 Ω
Temperature coefficient of resistance (20°C)	~ 0.24 % / °C	~ 0.40 % / °C
Maximum sensor temperature	67 °C	150 °C
Maximum ambient fluid temperature	30 °C	100 °C

Data Acquisition

The 0~10 V analogue signal from the anemometer box is converted to digital signal via a National Instruments A/D box (Mode AT/PCI-MIO-16E-1). The time history signals are then stored into a PC (P4 2.6 GHz and 256M RAM) at a 10~30 kHz sampling frequency for further processing and analysis.

3.3.2 Test Section

The special test spool, of the same diameter as the stainless steel test section pipe, was designed to accommodate the mounting and calibration of the 1-D hot-film velocity probe and a temperature probe. In order to measure local turbulence at different radial positions in the test section, the hot-film probe sensor should be able to move between the pipe centre and wall. However, to avoid breaking the fragile probe sensor at locations near the wall, a minimum distance was set between the probe and the wall, 0.5 mm for the TSI 1276-10AW probe and 2 mm for the Dantec 55R14 probe. The temperature probe supplied by Dantec Dynamics Ltd. (Model 99P10) is used to record the fluid temperature, as shown in Figure 3.18. A Pitot tube is chosen to calibrate the hot-film probe, as in previous work (Farrar & Bruun, 1996; Shaha, 1999). The details on the probe calibration will be given in Section 3.3.3.

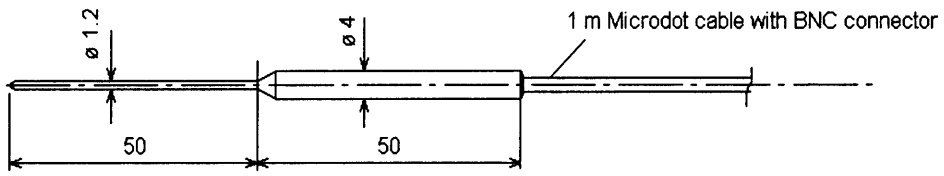

Figure 3.18: The temperature probe 99P10, supplied by Dantec Dynamics Ltd.

The test section design is shown in Figure 3.19. The hot-film probe, temperature probe and Pitot tube are installed in a 1 m long and 38 mm I.D. stainless steel tube in successive downstream position. The velocity and temperature probes are mounted on a mobile metal block, which is inserted into another steel block welded on the tube and flush with the inner tube wall. The two probes are kept at the same horizontal level and stay approximately 10 mm apart, while the Pitot tube is further downstream. The method of fixing the hot-film and

temperature probe positions is schematically represented in Figure 3.20. The radial positions of the hot-film probe and temperature probe can be adjusted together by a fine micrometer with a precision of 0.1 mm. These two probes can move freely between the pipe centre and 0.5 mm away from the pipe wall. Their actual probe radial positions are indicated by one external pointer through a ruler of effective range 19~36 mm ($0 \leq r/R \leq 0.895$). The hot-film probe could be easily removed from the test section by unscrewing the supporting steel body; this enables easy regular cleaning of the probe.

A 4mm O.D. Pitot tube supplied by Airflow Developments Ltd. is used in this study for calibration of the hot-film probe. The Pitot tube is mounted on a stainless steel block, with the bottom being machined at the same curvature as the inner pipe wall (see Figure 3.21). Rubber O-ring seals are used to seal the steel block and Pitot tube. The Pitot tube is positioned exactly at the pipe centre to measure pipe centreline flow velocities for the hot-film probe calibration. The two pressure outlets of the Pitot tube are then connected to a differential pressure transducer (Validyne DP103 differential pressure transducer), which has a maximum pressure rating of 22 kPa and an accuracy of 0.25% of full scale

In addition, when hot-film probe is used in conducting liquids the system has to be grounded to avoid excessive voltage between the probe and the liquid, as this will break down the insulating quartz coating and the thin film will be etched away. Therefore, a metal ring strip linked to the anemometer ground port is located adjacent to the hot-film probe to ground the liquid.

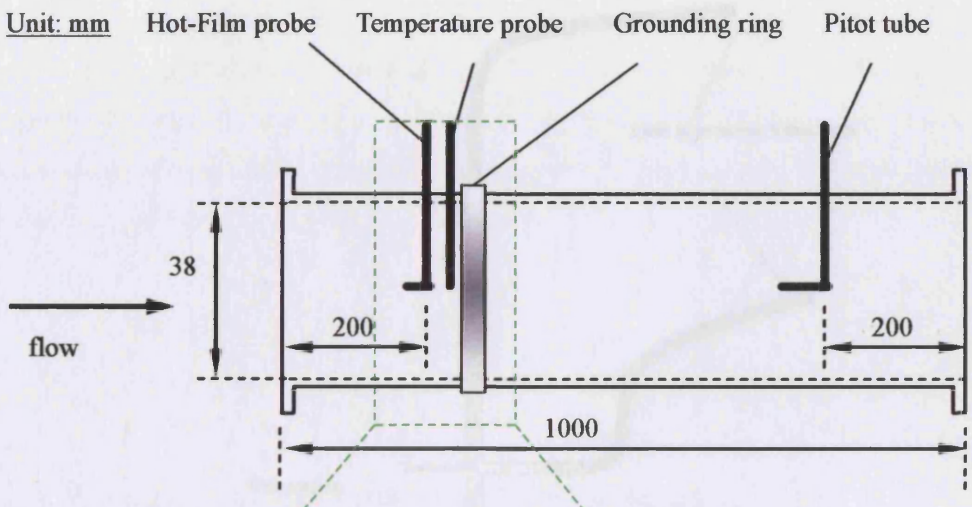

Figure 3.19: Schematic diagram of the test section designed for axial turbulence velocity measurements (not to scale).

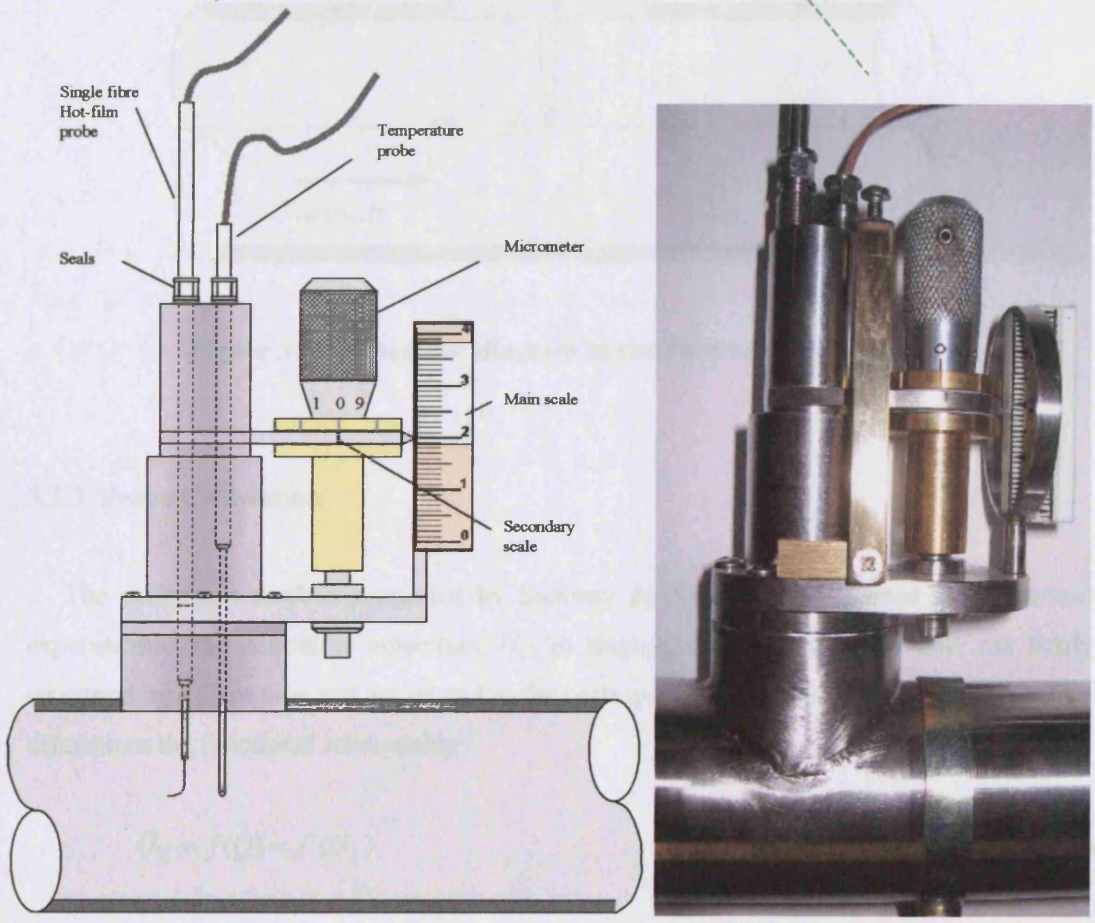

Figure 3.20: Schematic and photograph of the section for mounting the hot-film probe and temperature probe.

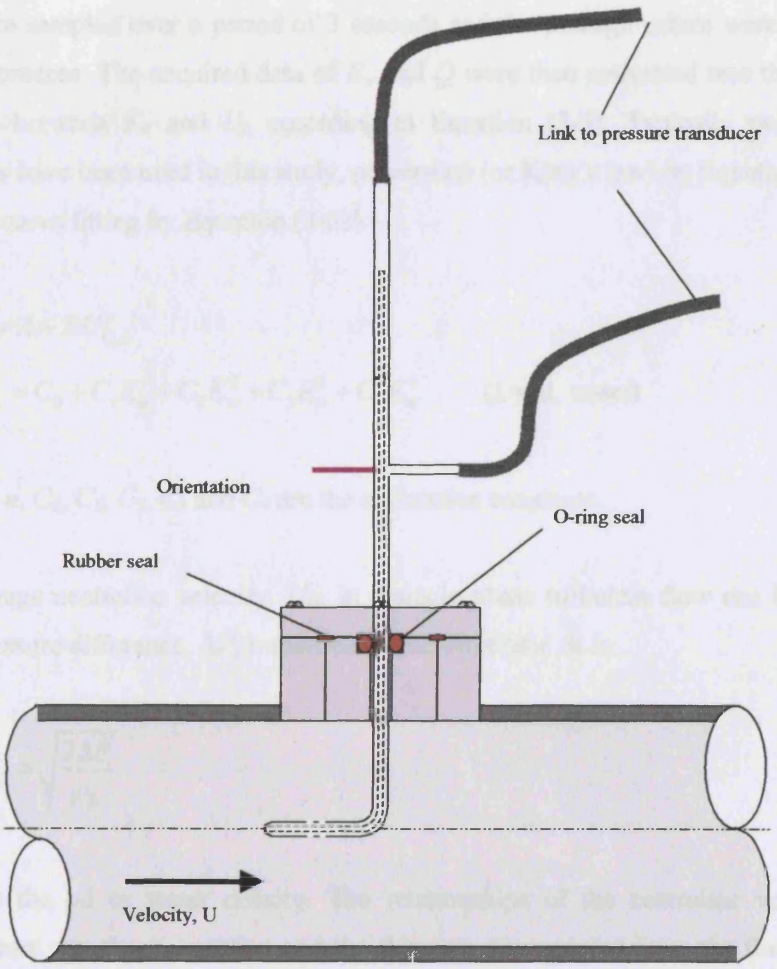

Figure 3.21: Schematic diagram of the Pitot tube installation.

3.3.3 Probe Calibration

The calibration method suggested by Samway & Bruun (1994) is used in the current experiments. The centreline velocities, U_C, in single-phase oil and water flow are firstly measured by a Pitot tube and are related to the corresponding flowrate of each phase, Q. This determines the functional relationship

$$U_C = f(Q) = f'(U_L) \tag{3-5}$$

where U_L is the superficial liquid velocity. Knowing the functional form of Equation (3-5) enables a complete computer-based calibration for the single fibre velocity probe. After selecting 6 or more points covering the expected velocity range, the anemometer output voltage, E_w, and the flowrate, Q, are acquired digitally. Here, E_w and Q values at each flow

condition are sampled over a period of 3 seconds and the average values were used for the calibration process. The acquired data of E_w and Q were then converted into the calibration relationship between E_w and U_L according to Equation (3-5). Typically two calibration relationships have been used in this study, power-law (or King's law) by Equation (3-6a) and polynomial curve fitting by Equation (3-6b)

$$E_w^2 = A + BU_{C,L}^n \tag{3-6a}$$

$$U_{C,L} = C_0 + C_1 E_w + C_2 E_w^2 + C_3 E_w^3 + C_4 E_w^4 \qquad (L\text{=oil, water}) \tag{3-6b}$$

where A, B, n, C_0, C_1, C_2, C_3 and C_4 are the calibration constants.

The average centreline velocity, U_C, in a single phase turbulent flow can be calculated from the pressure difference, ΔP, measured by the Pitot tube. It is

$$U_C = \sqrt{\frac{2\Delta P}{\rho_L}} \tag{3-7}$$

where ρ_L is the oil or water density. The relationships of the centreline velocities, U_C, calculated from the above equation and the flowrate, Q, recorded from the flowmeter have been plotted in Figure 3.22. Two linear functions are correlated for water and oil single phase flow, respectively.

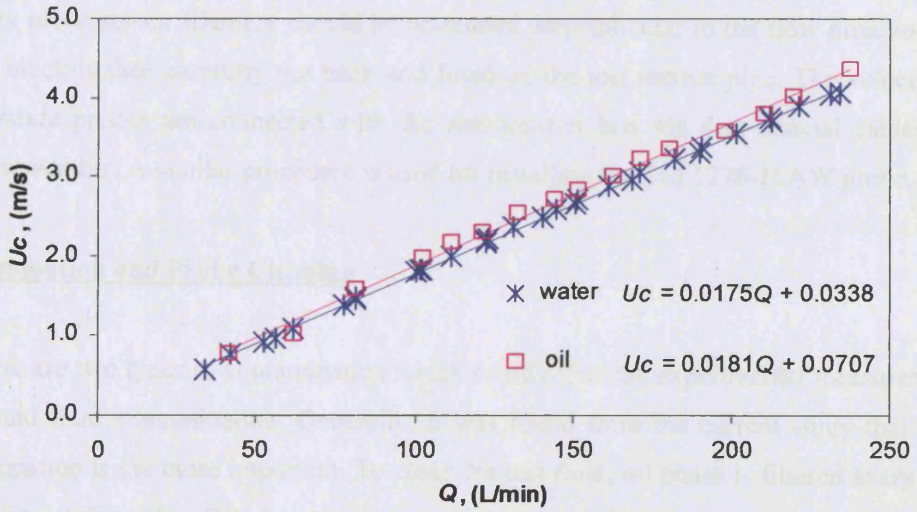

Figure 3.22: Relationship between the centreline velocity U_C and the liquid flow rate Q.

3.3.4 Operation

The hot-film anemometer is without doubt a delicate instrument that requires a lot of attention during operation and setup. Most importantly, the velocity probe is extremely fragile and past experience shown that the sensor filament could be broken quite easily. Actually, two probes broke during the period of this study. However, with care the duration of the probe life can be extended. This section describes the need for the probe installation and cleaning.

Installation of Probes

The hot-film velocity and temperature probes are used together to measure the local fluid velocity and temperature. For a Dantec 55R14 probe, the probe sensor and the long straight probe support are separated and need to be assembled prior to each experiment. To do this, the mobile steel block must first be taken out of the test section. The probe support and the temperature probe are then each inserted into this steel body from its top until the ends are exposed on the other side. The velocity probe is then plugged into the support at the right electrical connection position and is firmly held by tightening the O-ring seals inside the support body. Then, the velocity probe sensor and the temperature probe tip are carefully adjusted at a distance of 19 mm from the wall (namely at the pipe centre) using a Vernier Calliper; the external pointer is then also set at the 19 mm position (see Figure 3.20). Once the two probes are set at the right position and matched with the pointer scale, the two nuts on the top are tightened firmly to hold them and seal the metal block. During this process the velocity probe sensor filament should be orientated perpendicular to the flow direction. The whole block is then carefully put back and fitted on the test section pipe. The velocity and temperature probes are connected with the anemometer box via 4-m coaxial cables with BNC connectors. A similar procedure is used for installing the TSI 1276-10AW probe.

Contamination and Probe Cleaning

There are two types of contamination which could affect the experimental measurements: probe and fluid contamination. Generally, it was found from the current study that probe contamination is the more important. To clean the test fluid, oil phase is filtered every week by flowing it through a 'Y' shape hygienic stainless steel filter (supplied by PCI-Memtech Ltd., Model 854-5XX-010) with a maximum 10 μm passage allowance, as shown in Figure 3.23. The water phase is filtered through this unit all the time during the experiments. This filter is also used to remove any possible solid particles in the fluids which could potentially

destroy the fragile probe sensor. Usage of this 10 μm filter was shown to be sufficiently effective to maintain the fluids reasonably clean. However, it is also found that there is often a 'fine emulsion' growing at the interface between oil and water phases in the separator unit and at the bottom of the oil reservoir. This fine emulsion looks like thread (or gel) which can wind around the probe sensor easily (see Figure 3.24) reducing its sensitivity. Although Bruun (1995) suggested that the probe can be cleaned by immersing the sensor into a solvent, it is found that this layer of fine emulsion is difficult to remove using this method. Instead, a soft sable hairbrush dipped into 15% acetic acid solution or still water was used in order to clean the probe thoroughly. It is important to execute very carefully so as not to crack the fragile fibre coating.

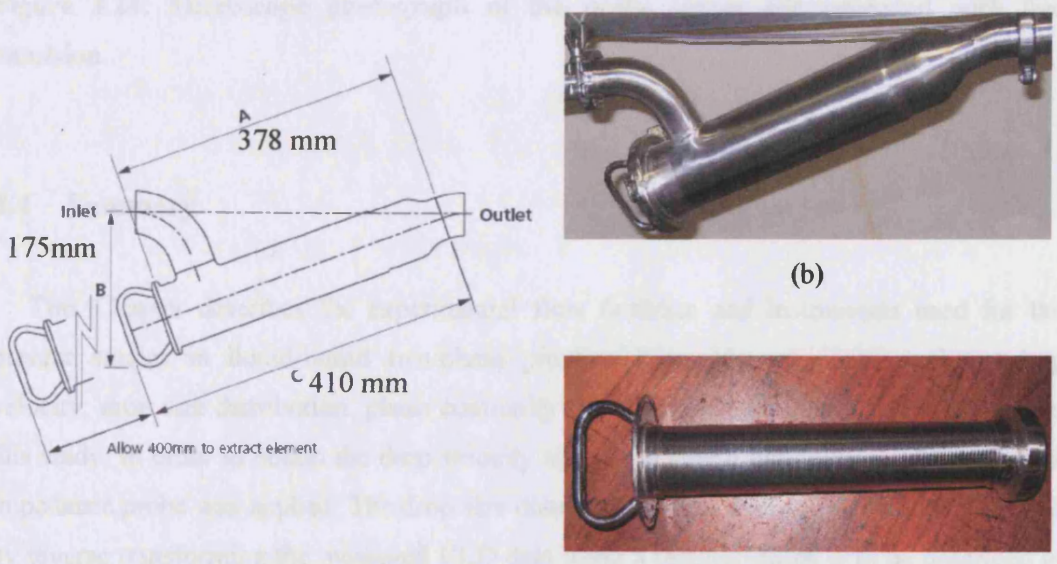

Figure 3.23: The schematic and photographs of the 10 μm Y-shape stainless steel filter supplied by PCI-Memtech Ltd. (854-5XX-010), (a) dimensional sketch, (b) filter housing, (c) filter element.

Figure 3.24: Microscope photograph of the probe sensor contaminated with fine emulsion.

3.4 Summary

This Chapter describes the experimental flow facilities and instruments used for the present studies in liquid-liquid two-phase pipeline flow. Measurements, such as drop velocity, drop size distribution, phase continuity and turbulence needed to be carried out in this study. In order to obtain the drop velocity and chord length distribution (CLD), a dual-impedance probe was applied. The drop size distribution in the system can also be estimated by inverse transforming the measured CLD data using a method which is to be described in Chapter 4. Three different methods were used in this thesis to identify the phase inversion point: by using a conductivity probe in the pipe centre, a glue-on hot-film probe mounted at the pipe inner wall and visualization over the transparent part of the test section. Finally, the working principle, application and operation of a hot-film anemometer were discussed in detail to elucidate the measurements of the turbulence of the continuous phase in oil-water dispersions.

Chapter 4

Evaluation of Drop Size Distribution from Chord Length Measurements

The relationship between the chord length distribution (CLD) obtained by a point sensor and the drop size distribution (DSD) in a liquid-liquid dispersion was investigated as part of the work described. Section 4.1 introduces the previously developed methods and their associated problems during implementation. In Section 4.2, based on analysis of the frequency of drop-cutting by the sensor, a physical model is built to derive the probability density function of chord lengths for a given DSD, and *vice versa*. A new algorithm is also introduced in Section 4.2 to solve the problem of noisy or even negative DSD values by adding smoothing equations while performing the backward conversion. In Section 4.3, both forward and backward transforms are shown to be in good agreement with ideal data when using continuous (e.g. log-normal, normal, uniform) distributions and with data obtained from Monte-Carlo simulations. In addition, the effect of parameters such as the number of drop size groups used, the noise level and the smoothing factor value on the backward transform is discussed in Section 4.3. Finally a summary is given in Section 4.4.

4.1 Introduction

One important characteristic of flow behaviour in dispersed systems is the distribution of drop (or bubble) sizes, which has been found to affect significantly the heat/mass transfer and turbulence characteristics. Many experimental techniques for drop size measurement have been developed for air-liquid and liquid-liquid systems: photographic and video recording techniques (Kubie & Gardner, 1977), sometimes coupled with an endoscope to

obtain local measurements (Angeli & Hewitt, 2000a); resistance or impedance probes (Serizawa et al., 1975a; Lovick & Angeli, 2004); hot-film anemometry (Wang & Ching, 2001); and optical probes, such as the Par-Tec 300, Lasentec Ltd. (El-Hamouz & Stewart, 1996; Simmons et al., 1999). However, while photographic and video recording techniques give the drop diameter distribution directly, other techniques involving point sensor probes provide only a distribution of the chord lengths intersected by the probe. It is therefore necessary to convert a measured chord length distribution (CLD) to the relevant drop size (diameter) distribution (DSD).

Consider a dispersed system where the drops (or bubbles) are uniformly distributed in space and the distribution of drop size R is described by $P(R)$. The chord length distribution $P(L)$, defined as the likelihood of finding chords of length L among all the intersected chords, will be determined by the following factors:

(A): the size distribution function $P(R)$ of drops in the system;

(B): the conditional probability function $P(L|R)$ of cutting a chord of length L from a drop intersected by the probe with a specific size R;

(C): the biased sampling probability function $P_B(R)$, which describes the likelihood that a drop of size R will be sampled by the probe if a uniform spatial distribution is assumed. This is known as biased sampling because the probe is more likely to sample large drops than small ones, as will be shown in Section 4.2.1. $P_B(R)$ is determined by the probe and drop geometries and the flow characteristics in a given system.

Knowing the above functions, the distribution function of the measured chords $P(L)$ for any system can generally be written as follows

$$P(L) = \int_0^\infty P(L \mid R) P_B(R) P(R) dR = \int_{L/2}^\infty P(L \mid R) P_B(R) P(R) dR \tag{4-1}$$

where the latter equality follows since $P(L|R)$ is zero for $R<L/2$. Note that the probability functions $P(L|R)$, $P_B(R)$ and $P(R)$ are independent of each other, while the values of $P(L|R)$ and $P_B(R)$ depend on the sensor geometry (e.g. needle-tip probe, optical sensor or laser sheet), the drop shape and the drop motion (e.g. uni- or multi-directional flow), and can be calculated accordingly, while $P(R)$ is a property of the dispersion. The function $P(L|R)$ has been calculated by Clarke & Turton (1988) for various bubble shapes in a uni-directional flow. In the present work, we consider only spherical drops and point probes, for which

$P(L|R)$ is independent of the details of the flow. In this case $P_B(R)$ is independent of the directionality of the flow; it could be influenced by a variation of the droplet speed with R, but we shall assume that all drops have the same speed. These assumptions are consistent with the analysis of drop size distribution in dispersed oil/water pipe flows.

Equation (4-1) describes the forward transformation from DSD to CLD. It can also be used to obtain the system DSD from an experimentally measured CLD (known as backward transformation). To the best of the author's knowledge Equation (4-1) has not been used explicitly before, although the concept of biased sampling with respect to larger drops has been considered by other investigators and expressions similar to Equation (4-1) have been reported in some studies which combined $P_B(R)$ and $P(R)$ into a sampling distribution function $P_P(R)$ (Clarke & Turton, 1988; Liu & Clarke, 1995; Liu et al., 1998). Langston et al. (2001) also mentioned that the probability of a particle being detected depends on its size. Wynn (2003) derived a relationship between DSD and CLD that included the effect of biased sampling based on geometrical arguments that related the drop position to that of the probe.

The backward transform from CLD to DSD is usually achieved by discretizing Equation (4-1) in a matrix form and directly solving it (e.g. Clarke & Turton, 1988; Wynn, 2003). In addition a number of methodologies have been suggested for finding the DSD from the CLD such as the peeling method (PM) (Hobbel et al., 1991), the probability apportioning method (PAM) (Simmons et al., 1999) (which was found to be in error and was later improved to PAM2 by Langston et al., 2001) and the finite element method (FEM) (Simmons et al., 1999). Recently, techniques that describe more complicated systems, such as ellipsoidal bubbles with multi-dimensional motion (Santana & Macias-Machin, 2000) and spherical bubbles with size-dependent velocity (Kulkarni et al., 2004) have also been proposed. However, neither of these works have fully incorporated the effect of $P_B(R)$.

Apart from the form of the relation between CLD and DSD, previous studies have also been concerned with the stability of the backward transformation (from measured CLD to system DSD). Clarke & Turton (1988) assessed the backward-calculated $P(R)$ using the CLD $P(L)$ generated by Monte-Carlo simulations from a given DSD and found that the results are sensitive to the number of groups (bins) that the drop diameter data are divided into. If the number of groups is increased beyond some value, the backward transform becomes unstable, yielding irregular and sometimes negative $P(R)$ values. For the 'peeling' method suggested by Hobbel et al. (1991), Simmons et al. (1999) found that the converted $P(R)$ is very sensitive to the 'noise' in the population of the largest size. Their own PAM model was

found to be always stable and agree reasonably well with simulated drop size data but inaccurate for unknown drop diameters. The improved PAM2 model (Langston et al., 2001) was found to be more accurate and robust when applied to the experimental data measured from a Lasentec ™ Par-Tec optical instrument. Simmons et al. (1999) also noted that the FEM model is robust in general cases when the drop diameters are not known but inaccurate for discontinuous CLD data due to overshoot in the numerical integration and, consistent with the findings by Clark & Turton (1988), negative values were often observed.

Recently Wynn (2003) proposed a model to study the relationship between drop size and chord length measured by a Lasentec™ focused beam reflectance instrument. By integrating the probability that the beam cuts chords of one size from the passing drops of various sizes, a matrix equation was deduced. The drop size distribution was then calculated by solving this equation. However, as the method of solving the matrix equation is equivalent to the earlier 'peeling' method; it is very sensitive to errors in the counting of large drops and negative results are unavoidable. After testing the matrix equation it was suggested that the model may show reasonable stability if the drop size intervals are chosen to be very small. In addition, Liu et al. (1998) developed a 2-D conversion relationship in a heterogeneously dispersed system based on the assumption that the DSD can be represented as the product of two functions which are only dependent on drop size and chord length. Interestingly, they also observed that the accuracy of the numerical backward transform was increased as the drop classification group number increased, which differs from the observation of Clark & Turton (1988).

In most of the previous work, biased sampling has not been properly considered while conceptual mistakes have sometimes been present. The backward transforms also suffer from stability problems. In this Chapter, we revisit the problem of inferring the DSD from the CLD and investigate the relationship through a direct method, as suggested by Wynn (2003), to include the effect of biased sampling. To this end, both forward and backward calculations are carried out and a new algorithm is introduced for eliminating the previous problem of sensitivity to noise and negative DSD values. In what follows, a dispersed system is considered with spherical drops that move at a constant speed.

4.2 Mathematical Relationship between DSD and CLD

4.2.1 Models and Equations

In this Section, the relationship between DSD and CLD is investigated and deduced for two-phase systems where the chord lengths are obtained by a 'needle' (point sensor) probe, for example an impedance or conductivity probe. Here, it is assumed that drops with spherical shapes are homogeneously distributed and that drops of all sizes move with the same velocity. The dimension of the probe sensor tip is negligible compared to the drop size, and drops are assumed not to deform while passing across the probe and are not interfered by the probe. Therefore, the maximum chord length (L_{max}) will be equal to the maximum drop diameter (D_{max}). Figure 4.1(a) illustrates a drop of radius R intersected by the probe in such way that the perpendicular between the chord intersected by the probe and centre of the drop has a length r, "closest-approach distance", to the probe tip. In the diagram, the needle probe is oriented in the z-direction and the drop moves into the plane of the paper in the y-direction; r is the distance of closest-approach between the particle centre and the probe tip, measured in the x-z plane. The arising chord length can then be calculated from the Pythagoras Theorem, as shown in Figure 4.1(b), which leads to:

$$L = \sqrt{D^2 - 4r^2} \tag{4-2}$$

where L is the chord length intersected by the probe and $D=2R$ is the drop diameter.

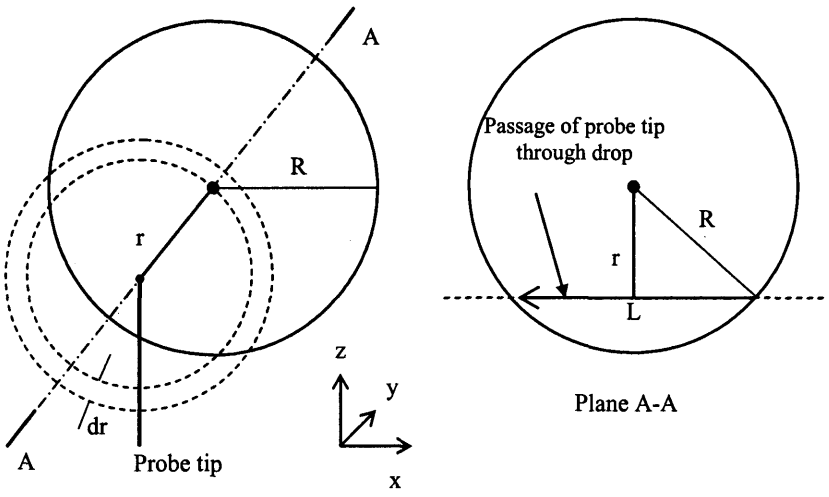

Figure 4.1: Diagram of drop sampled by 'needle' probe, (a): view of x-z plane at point of closest approach; (b): intersecting path with chord length L in plane A-A.

Here, the drop size distribution (DSD) of the system is defined as a relative number density per unit volume, $P(D)$, where for drops with sizes between D and $(D+dD)$ the number density is $N_T P(D)dD$, in which N_T is the total number of drops per unit volume. Similarly, $X(r,D)dDdr$ is defined as the sampling frequency of drops of size between D and $D+dD$ at a central distance between r and $r+dr$, (see Figure 4.1a), which is given by:

$$X(r,D)dDdr = 2\pi r dr \cdot N_T \cdot P(D)dD \cdot U \tag{4-3}$$

where U is the velocity at which drops pass the probe. From Equation (2) one also has:

$$r = \frac{\sqrt{D^2 - L^2}}{2} \qquad \text{and for fixed } D, \qquad dr = \frac{-L}{4r}dL \tag{4-4}$$

The frequency of cutting chords of length L from drops of size D is therefore calculated as

$$X(L,D) = X(r,D)\left|\frac{dr}{dL}\right| \tag{4-5}$$

According to Equations (4-3) and (4-4), Equation (4-5) will lead to the following expression:

$$X(L,D) = \frac{\pi}{2} N_T \cdot U \cdot L \cdot P(D) \tag{4-6}$$

Then the frequency of measuring chord length L from all drops can be calculated by integrating Equation (4-6) with respect to the drop diameter, D. One can observe that chords of length L cannot be detected from drops whose sizes are smaller than L. So it also follows that

$$X(L) = \frac{\pi U N_T}{2}\int_L^{D_{max}} L \cdot P(D)dD = \frac{\pi U N_T}{2}\int_0^{D_{max}} L \cdot P(D)\psi(L,D)dD \tag{4-7}$$

where $\psi(L,D)$ is defined as

$$\psi(L,D) = \begin{cases} 1 & , \quad (L \le D) \\ 0 & , \quad (L > D) \end{cases} \tag{4-8}$$

Consequently, the frequency for the probe to measure chords of any length can be expressed by

$$X_T = \int_0^{L_{max}} X(L)dL = \int_0^{D_{max}} X(L)dL \tag{4-9}$$

where L_{max} is the maximum chord length and, according to the assumption that drops are spherical and their deformations are negligible, L_{max} is set equal to D_{max}. Here, X_T represents the overall chord frequency detected by the probe. The total number of drops per unit volume, N_T, is a constant provided that the dispersed phase volume fraction and drop size distribution function, $P(D)$, are fixed. Thus, for a given maximum drop size, D_{max}, and average drop velocity, U, the total chord frequency detected by the probe, X_T, will also be a constant. Define $G(L)$ as the chord length distribution function (CLD) so that the number density of detected chords whose lengths are between L and $(L+dL)$ is $G(L)dL$. If $G(L)$ is estimated from measurements within a time interval Δt, one has

$$G(L)dL = \frac{X(L)dL \cdot \Delta t}{X_T \cdot \Delta t} \tag{4-10}$$

Hence, the number fraction of measured chord lengths between L_1 and L_2 can be expressed by the following integral:

$$\int_{L_1}^{L_2} G(L)dL = \alpha \int_{L_1}^{L_2} \int_0^{D_{max}} L \cdot P(D)\psi(L,D)dDdL \tag{4-11}$$

where $\alpha = \pi UN_T/2X_T$ is a constant parameter. Equation (4-11) has the same form as Equation (4-1) for $P(L|R)=L/2R^2$ and $P_B(R) \propto R^2$.

Equation (4-11) can be used to find the likelihood of cutting chord length L ($L_1 \leq L \leq L_2$) for continuous distribution functions. In discrete analysis, if drop sizes are grouped into N categories and chord lengths are grouped into M categories, discretization of Equation (4-11) will lead to

$$G(i) = \alpha \sum_{j=1}^{N} f(L_{i-1} : L_i)P(j)\psi(L_i, D_j) \qquad (i = 1,2 \cdots M) \tag{4-12}$$

where $G(i)$ is the number density of chords in the i^{th} chord group; L_{i-1} and L_i are respectively the minimal and maximal chord lengths in the i^{th} chord group (L_0 is equal to 0); D_j is the average drop diameter in the j^{th} drop group; $P(j)$ is the fraction of drops in the j^{th} drop group; and the function f is defined by

$$f(L_{i-1}:L_i)=\frac{L_i^2-L_{i-1}^2}{2} \tag{4-13}$$

Note that the number of chord-length groups, M, is not required to match the number of drop-diameter groups, N, and that in general $D_i \neq L_i$. Equation (4-12) can then be written in the following matrix form,

$$\begin{pmatrix} C(1,1) & \cdots & C(1,N-1) & C(1,N) \\ C(2,1) & \cdots & C(2,N-1) & C(2,N) \\ \vdots & \ddots & \vdots & \vdots \\ C(M-1,1) & \cdots & C(M-1,N-1) & C(M-1,N) \\ C(M,1) & \cdots & C(M,N-1) & C(M,N) \end{pmatrix} \begin{pmatrix} P(1) \\ P(2) \\ \vdots \\ P(N-1) \\ P(N) \end{pmatrix} = \begin{pmatrix} G(1) \\ G(2) \\ \vdots \\ G(M-1) \\ G(M) \end{pmatrix} \tag{4-14}$$

In compact form, Equation (4-14) is written as

$$[\mathbf{C}][\mathbf{P}]=[\mathbf{G}] \tag{4-15}$$

where the matrix **[C]** contains the coefficients $C(i,j)$, which are given by

$$C(i,j)=\alpha \cdot f(L_{i-1}:L_i)\psi(L_i,D_j) \tag{4-16}$$

The forward calculation of the CLD, **[G]**, can then be performed directly using Equation (4-15), provided that the DSD, **[P]**, is known. For the backward calculation of the DSD from the CLD, **[G]**, which is given by the experimental data, the number density function, **[P]**, can be found from

$$[\mathbf{P}]=[\mathbf{C}]^{-1}[\mathbf{G}] \tag{4-17}$$

where the inverse matrix $[\mathbf{C}]^{-1}$ can be obtained directly for $M=N$. However, for cases of $M \neq N$, a singular value decomposition (SVD) algorithm (Press et al., 1992) must be used to compute a pseudo-inverse of the non-square matrix **[C]**, which minimizes the quadratic form $([\mathbf{G}]-[\mathbf{C}][\mathbf{P}])^{T}([\mathbf{G}]-[\mathbf{C}][\mathbf{P}])$.

4.2.2 Smoothing Equations

As with the methods suggested by previous investigators, Equation (4-17) was found sometimes to give negative solutions when applied to experimental CLDs that included noisy errors. To reduce this sensitivity resulting from noisy experimental data, a technique was applied which has been widely used for solving other inverse problems. Additional smoothing equations are imposed into matrix **[C]** and the inverse of the combined matrix is solved by Tikhonov Regularization (Groetsch, 1984; Nguyen et al., 1999; Yeow et al., 2000, Hu et al., 2005).

If one knows beforehand that the DSD follows a continuous function (such as a log-normal or β distribution, for instance), the drop size number densities between adjacent groups can be assumed to be similar. Hence the following additional equations can be added into Equation (4-15):

$$\lambda_{SF,i}[P(i)-P(i-1)]=0 \quad , \quad i=2\cdots N \tag{4-18}$$

where $\lambda_{SF,i}$ is the *weighting function* for $P(i)$, which controls the extent to which noise in the experimental data is filtered out and the converted DSD curve is rendered smooth. The relationships in Equation (4-18) are not enforced as equations, but are enforced in a least square sense by the pseudo inverse. The appropriate choice of $\lambda_{SF,i}$ has been found to depend on several factors, such as the noise level in the experimental data, the number of groups (M and N) and the actual DSD of the system (Yeow et al., 2000). The following function is employed for $\lambda_{SF,i}$ in this study:

$$\lambda_{SF,i}=s_f N D_i / D_{\max} \quad , \quad i=2\cdots N \tag{4-19}$$

where s_f is an adjustable dimensionless smoothing factor. The form of Equation (4-19) was chosen to ensure that accurate results are obtained for the largest drop sizes. Expressing Equation (4-18) in compact form leads to

$$[\mathbf{C}^{\mathbf{S}}][\mathbf{P}] = [\mathbf{0}] \tag{4-20}$$

where $[\mathbf{C}^{\mathbf{S}}]$ is the coefficient matrix of the smoothing equations with elements given by Equation (4-18). Thus, after adding these additional smoothing equations, Equation (4-15) is replaced by the following expression:

$$\begin{bmatrix} \mathbf{C} \\ \mathbf{C}^{\mathbf{S}} \end{bmatrix}[\mathbf{P}] = \begin{bmatrix} \mathbf{G} \\ \mathbf{0} \end{bmatrix} \tag{4-21}$$

The backward conversion from CLD to DSD can therefore be obtained in the form

$$[\mathbf{P}] = \begin{bmatrix} \mathbf{C} \\ \mathbf{C}^{\mathbf{S}} \end{bmatrix}^{-1}\begin{bmatrix} \mathbf{G} \\ \mathbf{0} \end{bmatrix} \tag{4-22}$$

where the pseudo-inverse is again used.

4.3 Results and Discussion

4.3.1 Forward Transform from DSD to CLD

Given the system DSD, the CLD can be calculated directly according to Equation (4-15). Figure 4.2 illustrates the forward transform from two continuous DSD functions, the log-normal and uniform distributions, respectively. Here, to maintain the same resolution in the DSD and the CLD, the number of groups of drop diameters and chord lengths are both chosen to be 40. The CLD from the log-normal DSD shows a higher probability at the large sizes (chords) compared to the original DSD, reflecting the sampling bias, while for the system with a uniform DSD a parabolic CLD is obtained.

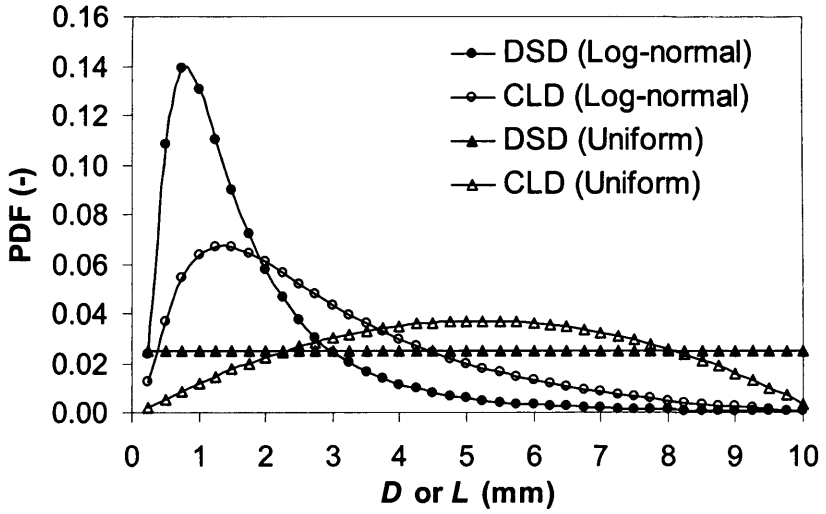

Figure 4.2: Forward CLD transforms of a log-normal and a uniform DSD.

It is useful to compare the CLD predicted by Equation (4-15) with CLD simulated by a Monte-Carlo method. 10^6 drops with a known size distribution were employed within a Monte-Carlo simulation to generate intersected chord lengths. The probability density functions of the chord lengths are shown in Figure 4.3, where 20 groups of chord lengths are used for drops within the size range of 0-10 mm. Figures 4.3(a) and (b) illustrate the results obtained from uniform and (truncated) normal DSDs of the system, respectively. As can be seen, the predictions of Equation (4-15) are in good agreement with the Monte-Carlo calculations.

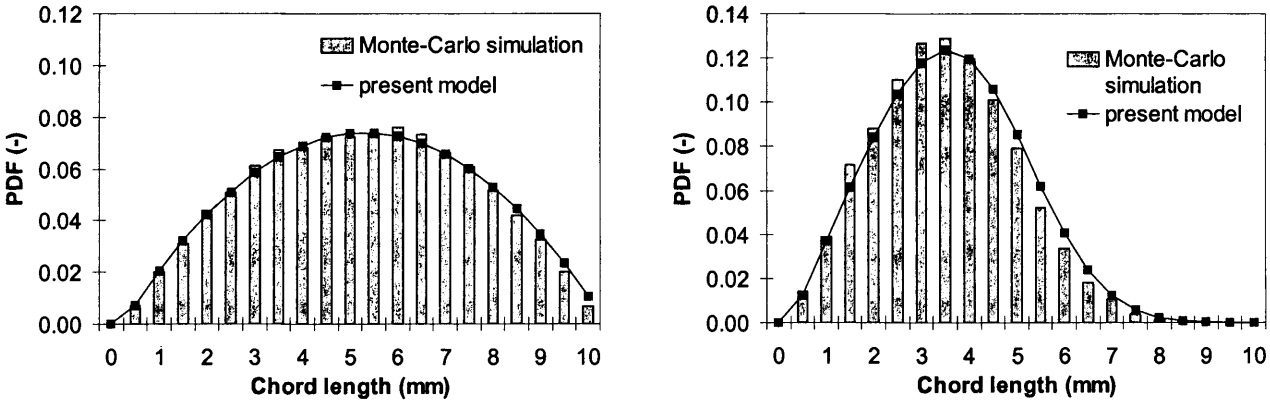

Figure 4.3: Comparison of CLD from a Monte-Carlo simulation and prediction by Equation (4-16), (a): Uniform DSD; (b): Truncated normal DSD.

4.3.2 Backward Transform from CLD to DSD

While visualization techniques (e.g. endoscopes) can give drop size distribution information directly, other instruments (e.g. impedance or optical probes and PIV) will produce only chord length distributions. It is, therefore, necessary to perform the backward calculation to derive the DSD which is more useful in practice (for example, when the interfacial area of the system is investigated). In this section, two simulations are used to evaluate the method developed above; CLD data are generated either from continuous DSD functions or from Monte-Carlo simulations.

In order to simulate CLD data obtained from experiments, a known DSD was firstly used to produce an 'ideal' CLD, $G(i)$. Then the 'ideal' CLD was modified by imposing noise, which leads to

$$\hat{G}(i) = \zeta[1 + n_l \cdot \kappa]G(i) \tag{4-23}$$

where n_l is the noise level parameter, κ is a (uniformly distributed) random value between 0 and 1, $G(i)$ is the ideal CLD of the i^{th} group, ζ is a normalisation constant to maintain $\sum \hat{G}(i) = 1$ and $\hat{G}(i)$ is the noise-added CLD of the i^{th} group.

The CLDs generated from two different continuous distribution functions, the log-normal and uniform distribution (shown in Figure 4.2), were used first to perform backward transform calculations. Noisy perturbations with n_l=1 were added into the ideal data, as shown in Figures 4.4(a) and (c). The corresponding backward conversions, using Equation (4-17) without smoothing and Equation (4-22) with smoothing, are shown in Figures 4.4(b) & (d) and compared with the original DSD. The DSD obtained from Equation (4-17) gives many negative values for both log-normal and uniform distributions. However, after adding the smoothing equations, the DSD results obtained from the noisy CLD data showed good agreement with the ideal DSD for the log-normal distribution when smoothing factor s_f=0.3 or 1.0 was applied (see Figure 4.4b), and for the uniform distribution when s_f=3.0 or 5.0 was applied (see Figure 4.4d). As pointed out by others (Nguyen et al., 1999; Yeow et al., 2000), the appropriate value of the adjustable parameter s_f was found to depend on the noise level and the distribution type; higher noise and smoother DSD curves require much larger value of s_f. Although the value of s_f is important in obtaining the DSD curve, the converted curve is not sensitive to s_f once the curve is smooth. For example, in Figure 4.4d there is a large difference between the results for s_f=1.0 and 3.0, but a much smaller difference between

s_f=3.0 and 5.0. In addition, and most importantly, incorporating smoothing into Equation (4-22) eliminates the negative DSD values which often occur if the DSD is directly converted from the CLD using Equation (4-17). Furthermore, no instability is found in Equation (4-22) when the number of size groups is varied.

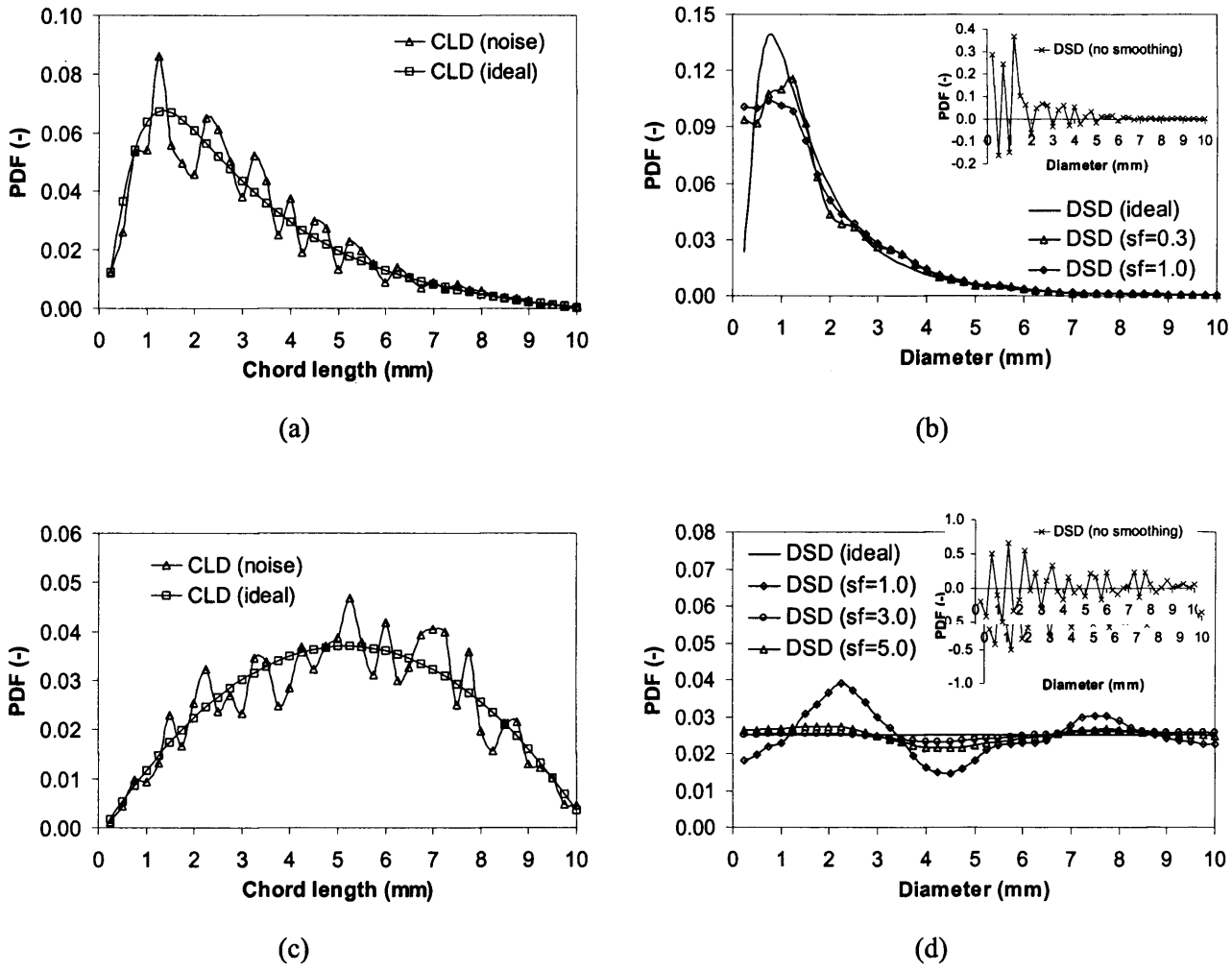

Figure 4.4: Noise-added CLD and comparison of backward transform, (a): CLD from log-normal DSD; (b): Converted DSD from (a); (c): CLD from uniform DSD; (d): Converted DSD from (c).

The Monte-Carlo method was further employed here to evaluate the behaviour of the backward transform. Initially a CLD was generated for a given DSD, either the truncated normal or the uniform distribution (shown in Figure 4.3), and the backward transform on the CLD was then performed. Figure 4.5 illustrates the DSD obtained using Equations (4-17) and (4-22), respectively without smoothing and with smoothing. As mentioned before,

negative values are unavoidable when using direct conversion even if 'near ideal' CLD data are used (some differences can be seen between the generated CLD and the ideal CLD in Figure 4.3). However, when the smoothing equations are added, the converted DSD presents rather good agreement with the original distribution, as can be seen in Figure 4.5.

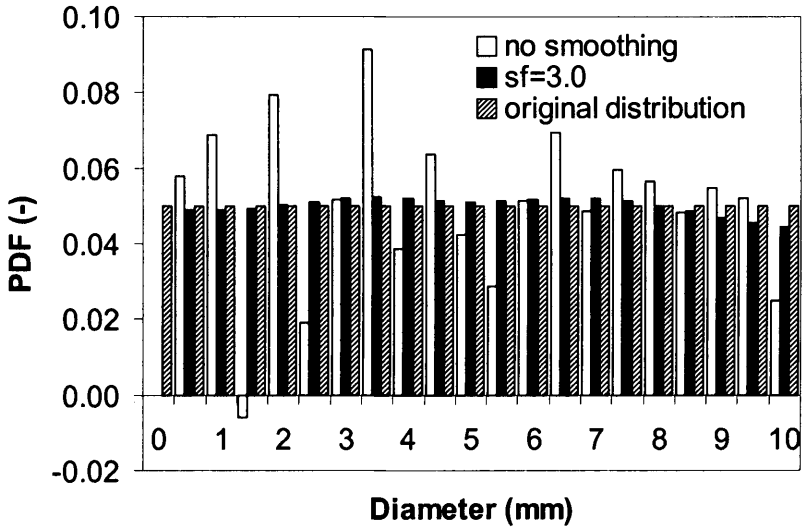

(a) uniform distribution

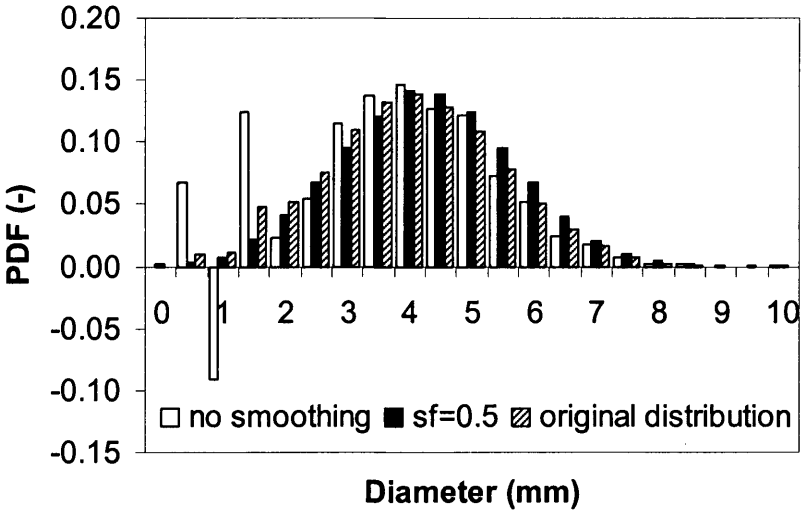

(b) normal distribution

Figure 4.5: Backward transform of the CLD generated by the Monte-Carlo method, (a): Truncated normal DSD; (b): Uniform DSD.

4.3.3 Sensitivity Studies

As mentioned above, the DSD obtained from the backward transformation of a given CLD using the method proposed here depends on several factors, such as the noise level (n_l), the number of DSD groups (N) chosen, and the smoothing factor (s_f). In this section the sensitivity of the converted DSD to these parameters is further investigated. Figure 4.6 shows the effect of the number of DSD groups, N, on the generated drop size probability density function. Here, the DSD is obtained by backward transforming noise-loaded CLD data distributed in 40 groups (n_l=1, M=40), originating from a log-normal distribution as shown in Figure 4.4(a), with s_f=0.2. As can be seen in Figure 4.6, the error in the converted DSD data (open symbols) compared to the ideal distribution (solid symbols) is not strongly dependent on the number of DSD groups used (N) in the range from 40 to 5. This is to be expected because the number of groups N is explicitly factored into the definition of $\lambda_{SF,i}$ in Equation (4-19). The quality of the backward transforms shown in Figure 4.6 can be further evaluated by the root-mean-square (r.m.s) error, shown in Figure 4.7, which shows the residual between the ideal and converted DSD values, and the relative deviation of a characteristic length scale, in this case the Sauter mean diameter, $D_{32}=\sum D^3/\sum D^2$. The r.m.s. and D_{32} deviation are found to increase with decreasing N, indicating a reduction in the quality of the conversion. This discrepancy is also understandable, because the width of the bin becomes larger when N is reduced, so each point represents a wide range of sizes. It can be concluded that in the method described here, a reduction in the DSD resolution does not necessarily improve the estimation of the DSD although it may lead to a smoother DSD curve. It is suggested therefore that a DSD resolution is used that is at least the same as the CLD resolution, namely N=M.

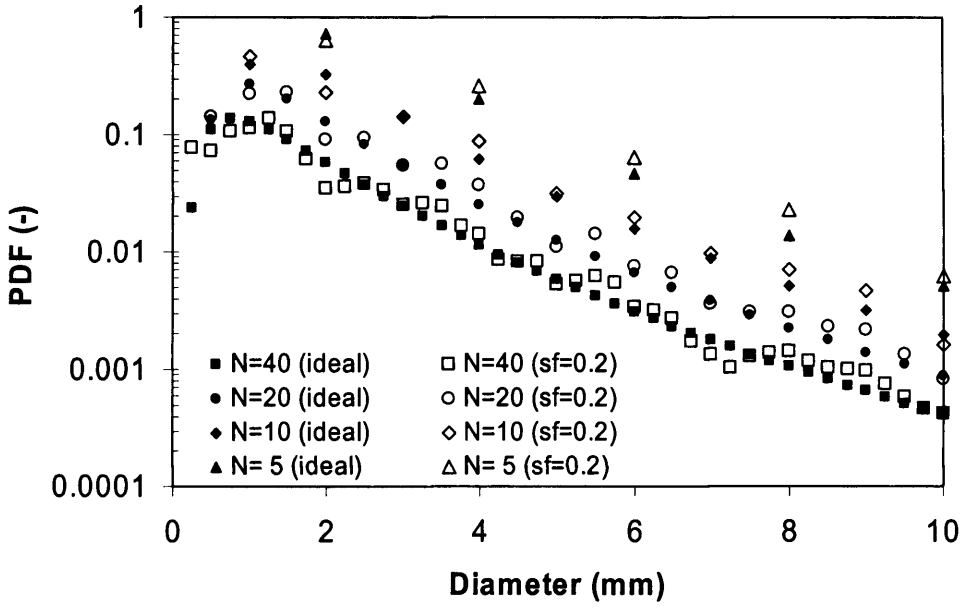

Figure 4.6: The effect of the number of DSD groups (N) on the converted drop size probability density function.

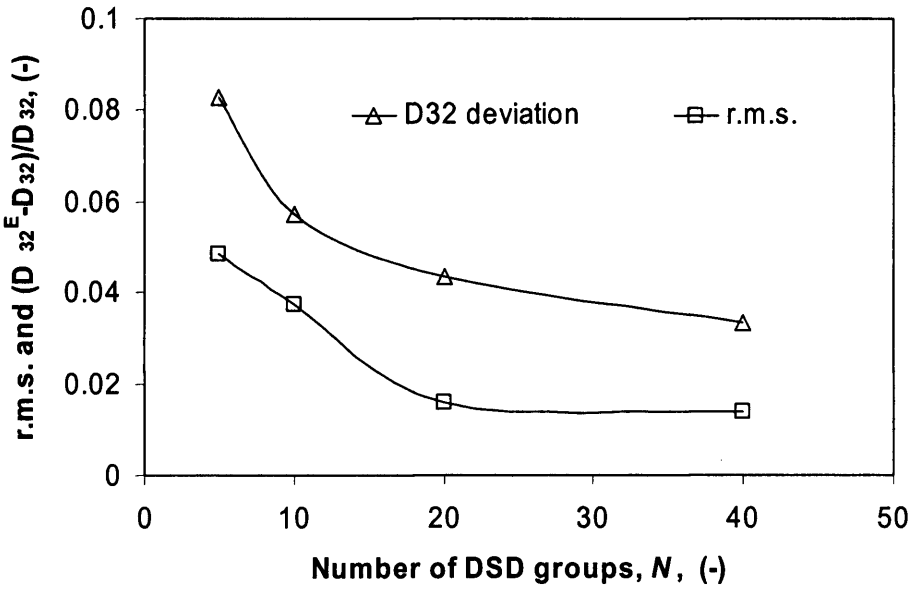

Figure 4.7: R.m.s. and D_{32} deviations between ideal and converted drop size distributions for the data shown in Figure 4.6. The D_{32} deviation is defined as $(D_{32}^E - D_{32})/D_{32}$, where D_{32} and D_{32}^E are the true and estimated values, respectively.

The effect of the smoothing factor value (s_f) on the converted DSD was also investigated. Figure 4.8 shows the r.m.s. of the residual between the true DSD and the estimated DSD transformed from the CLD with various noise levels and smoothing factors (s_f). The CLD data shown in Figure 4.4(a) with N=40 are used. As expected, the results in Figure 4.8 indicate that a larger s_f is required for the CLD data with higher noise level to reach the same r.m.s. level as the less noisy CLD data. Note that even when the ideal CLD data are used, the conversion method developed introduces small errors to the DSD, due to the additional smoothing equations (see n_l=0 in Figure 4.8). For the noise-loaded CLD data, three distinctive regions can be seen in Figure 4.8. In the *less-controlled region*, a significant decrease in the r.m.s. value is observed with increasing s_f, but the smoothing equations are less effective in suppressing the noise in the CLD and negative values are often found on the backward transformation. In the *well-balanced region* the r.m.s. errors for different noise levels drop down to a low level and reach a minimum at some value of s_f. In this region, the noise in the DSD curve is damped without destroying the form of the curve. Finally in the *over-controlled region* the r.m.s. value increases with s_f. At these high values of the smoothing factor, smoothing controls the backward transform so that the noise in the CLD data has negligible effect (the r.m.s. values at different n_l coincide).

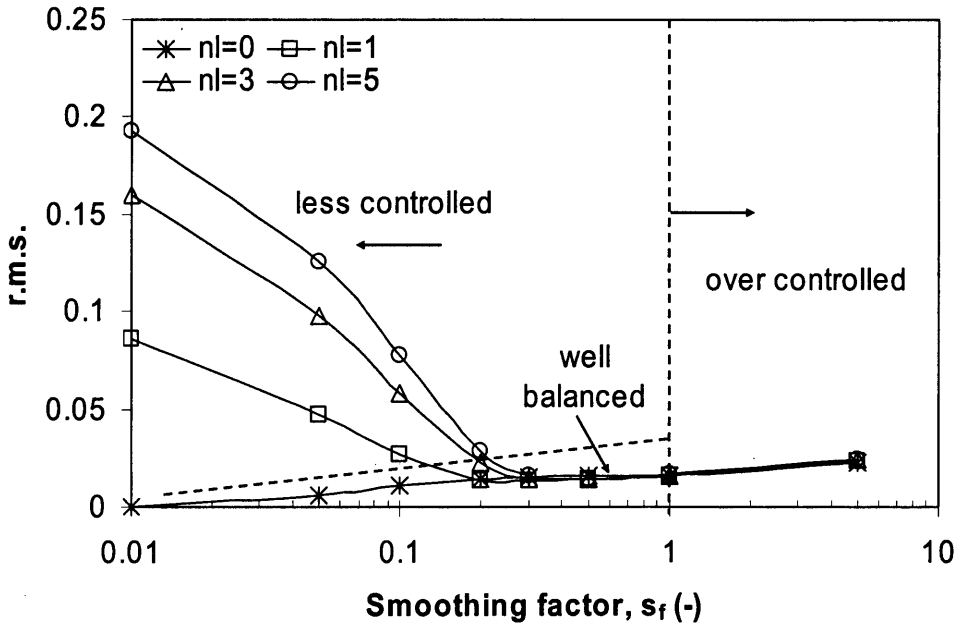

Figure 4.8: Effect of the noise levels (n_l) and smoothing factors (s_f) on the r.m.s. values for the converted DSD (N=40, CLD shown in Figure 4.4a).

For the backward transforms given in Figure 4.8 the corresponding deviations in D_{32} are shown in Figure 4.9. Except for the cases in the less controlled region where meaningless negative DSD data are obatined, the other two regions show that the error in D_{32} increases as a result of imposing the smoothing equations. Two trends can however be seen. In the *well-balanced* region the D_{32} deviation is almost constant for a given level of noise in the CLD, while in the *over-controlled* region there is a significant increase in the D_{32} deviation with the smoothing factor. A smoothing factor in the *well-balanced* region should therefore be chosen to get a minimal error in the converted DSD. In practice, however, Figures 4.8 and 4.9 are not available unless a direct drop size measuring technique, such as an endoscope, is also used. A good choice of the smoothing factor (s_f) can still be made by plotting the estimated D_{32}^E against s_f, which would show a trend similar to Figure 4.9. The conversion can start with large s_f that decreases gradually until the DSD becomes reasonably smooth and D_{32}^E reaches an approximately constant value.

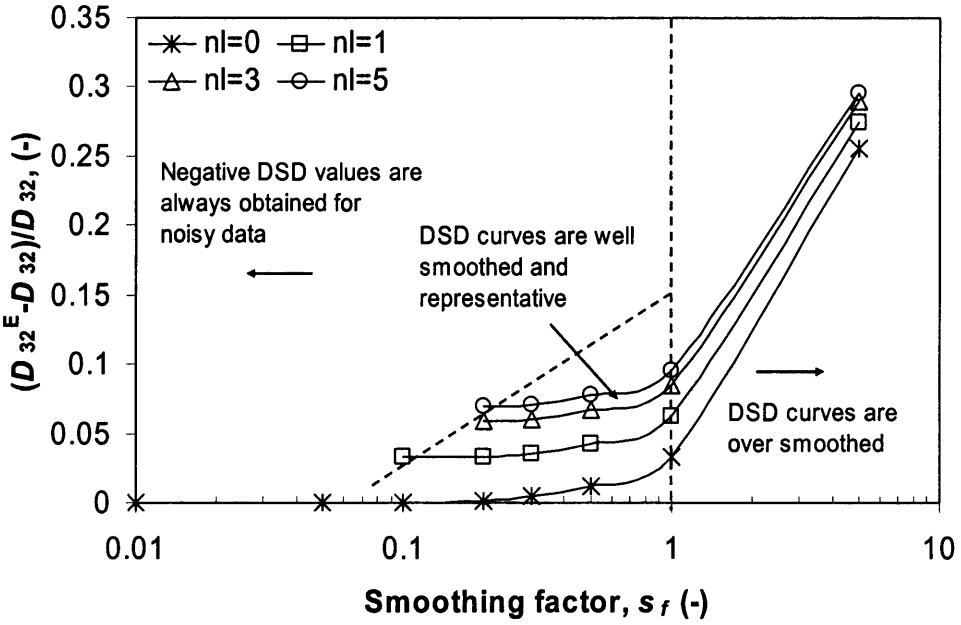

Figure 4.9: Effect of the noise level (n_l) and smoothing factor (s_f) on the relative deviation of the Sauter mean diameter, estimated from the backward transform (same data as for Figure 4.8).

4.3.4 Backward Transform from Experimental Data

The methodology developed in this Chapter was applied to experimental data. The results were compared with direct drop diameter distribution (number-basis) measurements obtained from photography.

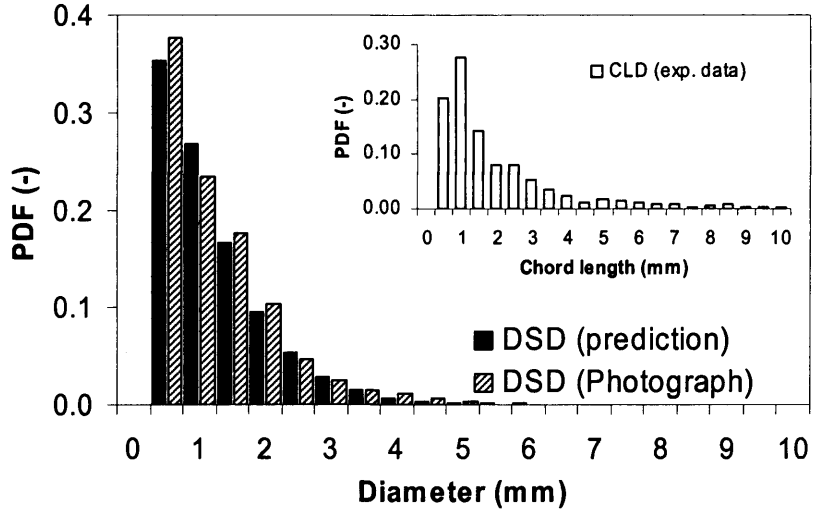

(a) upward flow

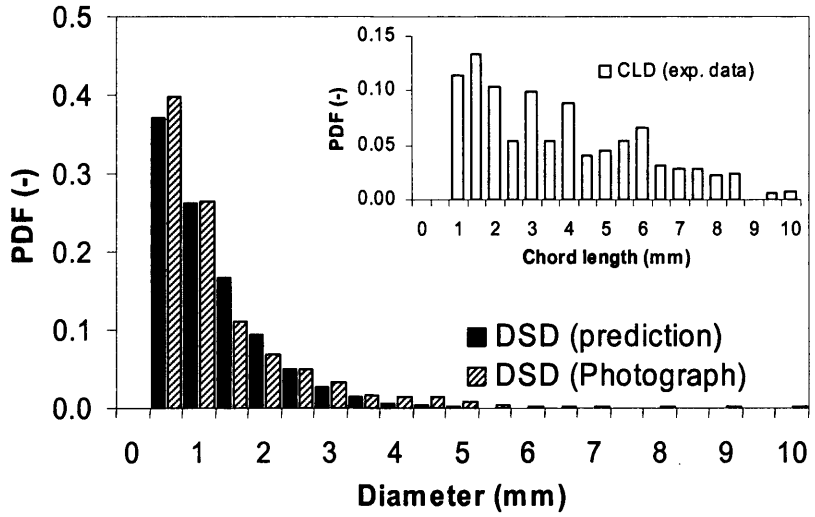

(b) downward flow

Figure 4.10: Experimental CLD data measured using an impedance probe in liquid-liquid dispersions and the corresponding DSD obtained by backward transform with s_f=1.0, in comparison with those from photographic observations. (a) upward flow and (b) downward flow.

The experiments were carried out in vertical dispersed flow of oil and water at 1.5 m/s mixture velocity and 20% oil input volume fraction in a 38 mm I.D. stainless steel tube. The dual impedance probe (see Section 3.2.1) was employed to measure the chord length distribution. Simultaneously a digital camera at shutter speed 1/2000 sec was applied to visualize the flow behaviour through an acrylic transparent section and the drop size distribution was measured directly from the video images. Figure 4.10 shows the cross-sectional averaged CLD obtained from experimental measurements in upward and downward flows, the corresponding DSD estimated by backward transformation with s_f=1.0 (selected using the procedure described in Section 4.3.3), and the DSD obtained directly from visualization. As can be seen, the predicted DSD obtained from Equation (4-22) is closely consistent with the findings from photographic analysis. A large number of small drops (<1.5 mm) were found in the mixture with large drops observed only occasionally.

4.4 Summary

In the work described in this Chapter, the relationship between the distribution of chord lengths obtained by a needle probe and the distribution of drop sizes in a liquid-liquid dispersion was determined analytically and a rigorous relationship given by Equation (4-15) was developed for spherical drops in uniform motion. The effect of biased sampling towards larger drops, relevant to point sensors, which has often been ignored by other investigators, was included in this relationship. In order to eliminate the negative DSD values that can arise from direct inversion of Equation (4-17), smoothing equations were introduced for the DSD functions. Both forward and backward transforms were shown to be in good agreement with ideal data when using continuous (e.g. log-normal and uniform) distributions, and with data obtained from Monte-Carlo simulations. The effect of parameters such as the noise level, the number of drop size groups used and the value of the smoothing factor on the backward transform were further studied. It was found that the number of drop size groups used can be taken the same as the number of chord length groups to ensure good resolution of the DSD without deterioration of the accuracy; a method for choosing an appropriate smoothing factor, s_f, was also suggested. Finally, drop size distributions converted from experimentally measured chord length distributions showed good agreement with experimental data obtained directly via photography.

The methodology presented in this Chapter could be generalized to more complicated systems with various dispersed phase shapes and more than one flow direction, for which more complex expressions for $P(L|R)$ and $P_B(R)$ would be needed.

Chapter 5

Experimental Investigation of Phase-Inversion and Associated Phenomena in Oil-Water Vertical Pipeline Flow

In this Chapter, the results from experimental investigations of phase inversion and its associated phenomena in co-current upward and downward oil-water vertical pipeline flow are reported. Two inversion routes (w/o→ o/w and o/w→ w/o, respectively) are followed with either constant power input or increasing power input. Parameters such as frictional pressure gradient, in-situ holdup, velocity ratio (U_o/U_w) and drop size distribution were studied experimentally for the regimes before and after phase inversion, respectively. The experimental procedures used in the work described in this Chapter are given in Section 5.1. Section 5.2 presents the results and findings from experiments with constant power input (type I) and with increasing power input (type II). A phase inversion process for vertical pipeline flows is subsequently suggested in Section 5.3. Finally, a summary is given in Section 5.4.

5.1 Experimental Procedure

In the studies described in this Chapter, two types of experiments were carried out in both upward and downward flows to observe phase inversion and its associated phenomena. In the first one (type I), phase inversion is achieved by varying the input superficial velocities of both oil and water phases, while keeping the total mixture velocity constant at each run (e.g. 1.5, 2.0 and 2.5 m/s). The velocity of the initial continuous phase is reduced while that of the dispersed phase is increased until phase inversion is achieved. Within the type I

experiments more detailed studies of pressure drop, in-situ holdup and drop size were carried out. In the second type (type II) of experiments, phase inversion is obtained by increasing the input superficial velocity of the initial dispersed phase, either oil or water, while maintaining that of the other, continuous, phase unchanged. Type I and II experiments are analogous to those experimental work conducted in stirred vessels (i.e. changing the volume fraction of one phase at a constant impeller speed or changing the impeller speed at a constant volume fraction).

In the type I experiments, the pressure gradient was measured with a differential pressure transducer between the positions 42D and 81D for upward flow, and 16D and 55D from the inlet for downward flow. The drop velocity profile and drop size distribution were measured by a dual impedance probe at an axial distance from the inlet of 81D and 58D for upward and downward flow, respectively. In total, 12 different radial locations in the pipe cross-section were sampled. The average in-situ holdup of each phase was also measured by simultaneously shutting two quick-closing valves, installed at the two ends of each transparent pipe section. The details of the measurement techniques are given in Section 3.2.

For both type I and type II experiments, phase inversion has been approached from two different routes, from oil to water continuous dispersions (denoted by w/o→ o/w) and from water to oil continuous dispersions (denoted by o/w→ w/o), respectively. In the o/w→ w/o experiments, for example, the test section is filled initially with either pure water or oil-in-water dispersion such that the inner wall is wetted only by water phase.

5.2 Results and Discussion

5.2.1 Type I experiments

5.2.1.1 Phase Inversion Point

Figure 5.1 illustrates the average dimensionless conductivity value of the mixture at the pipe centre obtained by the conductivity probe in upward vertical flows at 2.0 and 2.5 m/s mixture velocity. The conductivity values are plotted as a function of input oil fraction and are compared for the two different routes used to approach phase inversion, namely o/w→ w/o and w/o→ o/w, respectively. Here, the input oil fraction is defined as $\epsilon_o=Q_o/(Q_o+Q_w)$ where Q_o and Q_w are the volumetric flowrates of oil and water phases. The curve of conductivity versus ϵ_o is similar independent of the route followed (w/o→ w/o or w/o→ o/w) and shows a characteristic shape. The conductivity decreases slowly with input oil fraction until a critical input oil fraction, ϵ^I_o, is reached. Beyond input oil fraction, ϵ^I_o, the

conductivity probe falls rapidly until a second critical input oil fraction, ϵ^2_o, after which it is close to zero. At lower oil input fractions ($\epsilon_o < \epsilon^1_o$) the water phase is continuous, though the conductivity falls with ϵ_o due to intermittent bridging between the two probe tips by large oil drops. At high input oil fraction ($\epsilon_o > \epsilon^2_o$), the oil phase is continuous. The results indicate that between the two types of dispersions there exists a transitional region ($\epsilon^1_o < \epsilon_o < \epsilon^2_o$) since the two critical oil fractions are not the same, i.e. ϵ^1_o =74% and ϵ^2_o =84% for 2.5 m/s (Figure 5.1b). In this transitional region the two phases seem to compete to become continuous. This is similar to the transitional region between the two types of dispersions observed visually by Liu et al. (2004) and Liu (2005) with the Laser Induced Fluorescence (LIF) technique. Their work indicated that within the transitional region (also called the "unstable" region) the flow structure is very complex, where secondary and multiple dispersion are frequently seen, and both o/w and w/o dispersions can co-exist in the pipe. The unstable characteristics of the transitional region can also be seen from the time history plot of the conductivity signals for volume fractions before and after phase inversion, as illustrated in Figures 5.2a-f for 2.5 m/s mixture velocity. High values can be seen for 70% and 74% oil fraction indicating a water continuous phase interrupted by the many oil drops existing in these dense dispersions, while low values are seen for an oil continuous dispersion at 84% oil fraction. In the intermediate range of volume fraction, the signals shift between these two limits reflecting the fact that the dispersion is neither clearly water-continuous nor clearly oil-continuous but that complex structures may exist.

The identity of the continuous phase in contact with the wall was also identified with the hot-film anemometer (HFA) probe glued on the wall and the results are illustrated in Figure 5.3 for all cases studied in this work, namely both upward and downward flows at 1.5, 2.0 and 2.5 m/s mixture velocity. The high values recorded by the HFA at lower ϵ_o values indicate that water is in contact with the probe and therefore the pipe wall while low values indicate that oil is in contact with the wall. Since visual observations showed that the flow regime was fully dispersed, it can be assumed that the phase in contact with the wall is the continuous phase of the dispersion. As can be seen from Figure 5.3, the HFA output illustrates a clear and abrupt transition between o/w and w/o dispersions which is in contrast to the results from the conductivity probe.

A possible explanation is that even when the flow at the centre of the pipe has started to invert and create complex structures, as indicated by the changing conductivity values, the region close to the wall will preserve the continuous phase until phase inversion is complete and the new continuous phase is established everywhere in the pipe and at the wall, which is the point detected by the HFA probe. This difference in behaviour at different pipe locations

results probably from the smaller size of the drops close to the wall (see Section 5.2.1.4) that reduces their likelihood of forming multiple dispersions with coalescence. Therefore, the phase inversion detected by the glue-on HFA probe is the point of *complete phase inversion*. These complete phase inversion points are found to match those observed visually.

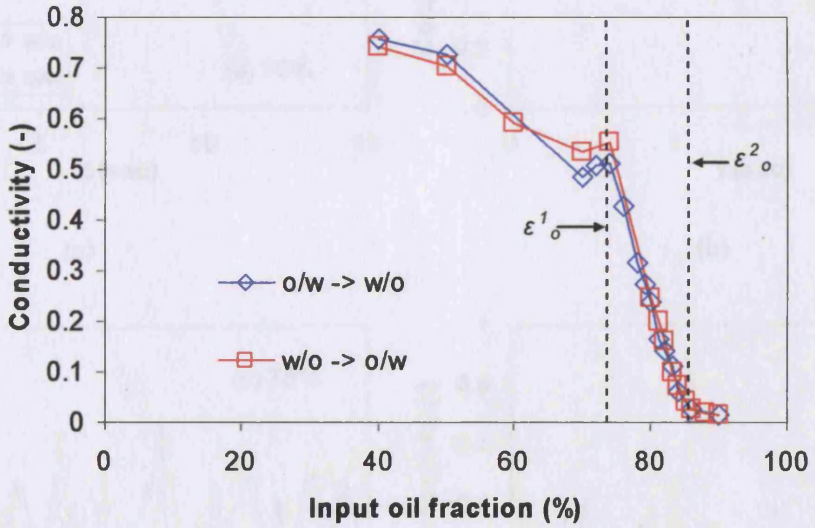

(a) 2.0 m/s

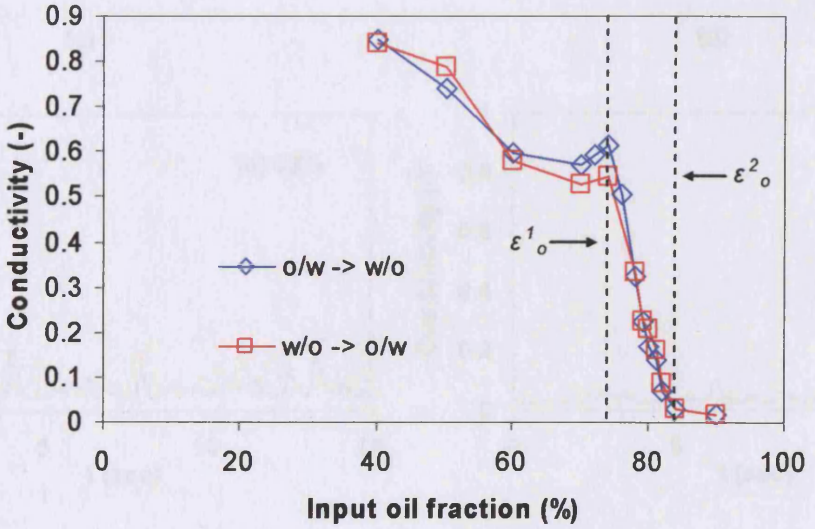

(b) 2.5 m/s

Figure 5.1: Relative mixture conductivity value in the pipe centre at various input oil fractions in upward flow for mixture velocities (a) 2.0 m/s and (b) 2.5 m/s.

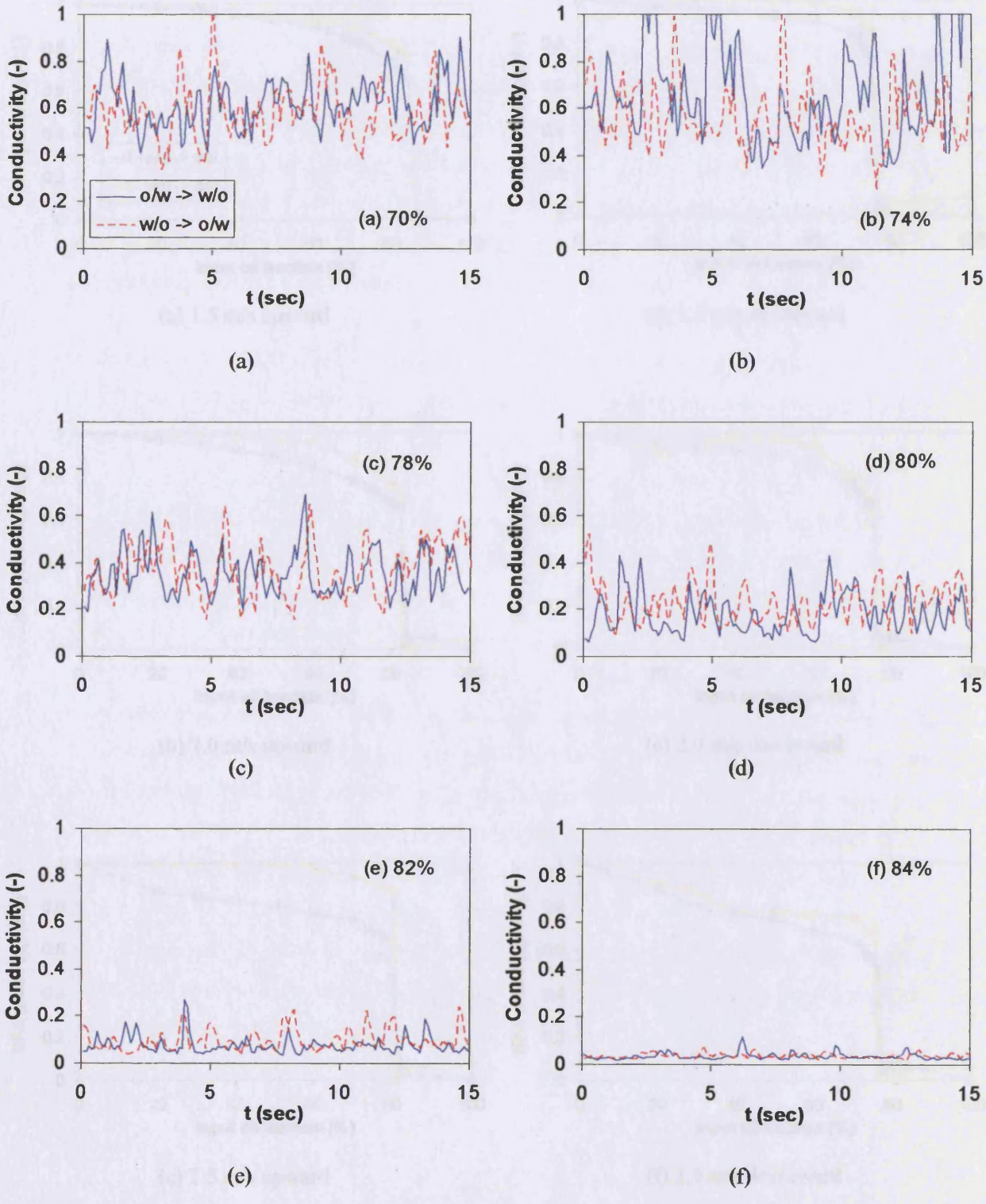

Figure 5.2: Time history plot of conductivity signals (normalized to single-phase water value) at different input oil fractions (%) measured at 2.5m/s upward flow. The HFA probe indicates complete phase inversion at 81% input oil fraction (see Figure 5.3c).

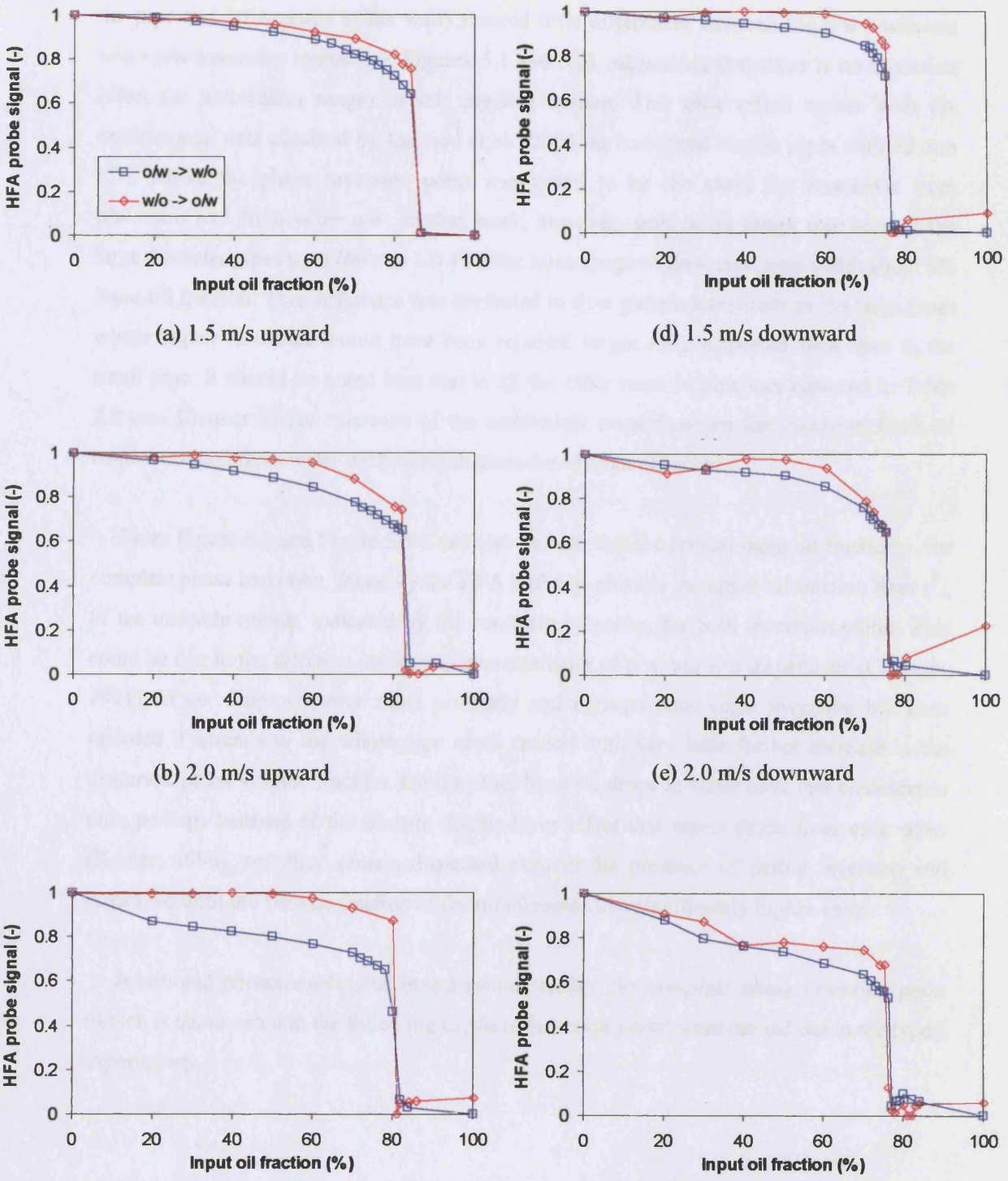

Figure 5.3: Change of hot-film anemometer (HFA) output signal obtained at the pipe wall at complete phase inversion in upward and downward flows.

Both types of measurement of phase inversion (the conductivity probe at the middle of the pipe and HFA probe at the wall) showed little differences between the o/w→ w/o and w/o→ o/w inversion routes (see Figures 5.1 and 5.3), suggesting that there is no hysterisis effect (or ambivalent range) in this pipeline system. This observation agrees with the experimental data obtained by Ioannou et al. (2005) in horizontal acrylic pipes with 32 mm I.D., where the phase inversion point was found to be the same for inversions from o/w→ w/o and from w/o→ o/w. In that work, however, ambivalent range was seen in the large diameter pipes used (60 mm I.D.) for the same range of flowrates, with width about 6% input oil fraction. This difference was attributed to flow pattern transitions in the large pipes where higher flowrates would have been required to get fully dispersed flow than in the small pipe. It should be noted here that in all the other work in pipelines reported in Table 2.2 (see Chapter 2) the existence of the ambivalent range between the inversion from oil continuous and from water continuous dispersions was not observed.

From Figure 5.1 and Figure 5.3 it can also be seen that the critical input oil fraction ϵ_o for complete phase inversion, found by the HFA probe, is close to the upper oil fraction limit ϵ^2_o, of the unstable region, indicated by the conductivity probe, for both inversion routes. This could be due to the different coalescing characteristics of o/w and w/o dispersions (Chesters, 1991). Water drops coalesce more promptly and perhaps once some inversion has been initiated it spreads to the whole pipe cross section with very little further increase in the dispersed phase volume fraction. On the other hand oil drops in water have low coalescence rate, perhaps because of the electric double-layer effect that repels drops from each other (Kumar, 1996), and they remain dispersed even in the presence of partial inversion and remain so until the volume fraction of the oil increases to a significantly higher value.

Additional phenomenological investigations around the *complete phase inversion point* (which is abbreviated in the following to *phase inversion point*) were carried out in the type I experiments.

5.2.1.2 Frictional Pressure Drop

Equation (5-1) is used to calculate the frictional pressure gradient in the vertical pipeline flows:

$$\left(\frac{dp}{dx}\right)_f = \left(\frac{dp}{dx}\right)_m \pm (\rho_w - \rho_o)\phi_o g \tag{5-1}$$

where $(dp/dx)_f$ is the frictional pressure gradient, $(dp/dx)_m$ is the pressure gradient measured by the pressure transducer, ρ_w and ρ_o are the densities of water and oil phase, ϕ_o is the average in-situ holdup of the oil phase that is obtained by the quick-closing valves, g is the gravitational acceleration and the '±' sign corresponds to upward or downward flow, respectively. In the current experiments, based on the uncertainty analysis for the pressure gradient and holdup measurements, the maximum and average errors in obtaining the frictional pressure gradient are 6.0% and 4.6%, respectively.

In horizontal pipeline flow, phase inversion is often accompanied by a peak in pressure drop, which suggests a maximum of the dispersion viscosity (Arirachakaran et al., 1989; Angeli & Hewitt, 1998; Soleimani, 1999; Ioannou et al., 2005). This increase in pressure drop is more noticeable at high mixture velocities. The frictional pressure gradients measured in the current work are shown in Figures 5.4a-c for vertical upward flow and in Figures 5.4d-f for downward flow. Interestingly there is no peak in the pressure gradient data during phase inversion. In contrast, comparisons with the change in phase continuity shown in Figure 5.3 indicate that at the phase inversion point pressure gradient seems to have its lowest value. For both routes of approaching phase inversion starting from a high water fraction, the pressure gradient decreases slightly with increasing oil fraction. At higher oil fractions, and especially in upward flow, the pressure gradient seems to increase and then sharply decrease before phase inversion. After the inversion point it increases again with further increase in the oil volume fraction towards the single-phase oil value. The region of sharp increase and decrease in pressure drop is within the transitional region given by the conductivity probe (see Figure 5.1) while the minimum in this region matches exactly the boundary identified by the glue-on hot-film probe (see Figure 5.3).

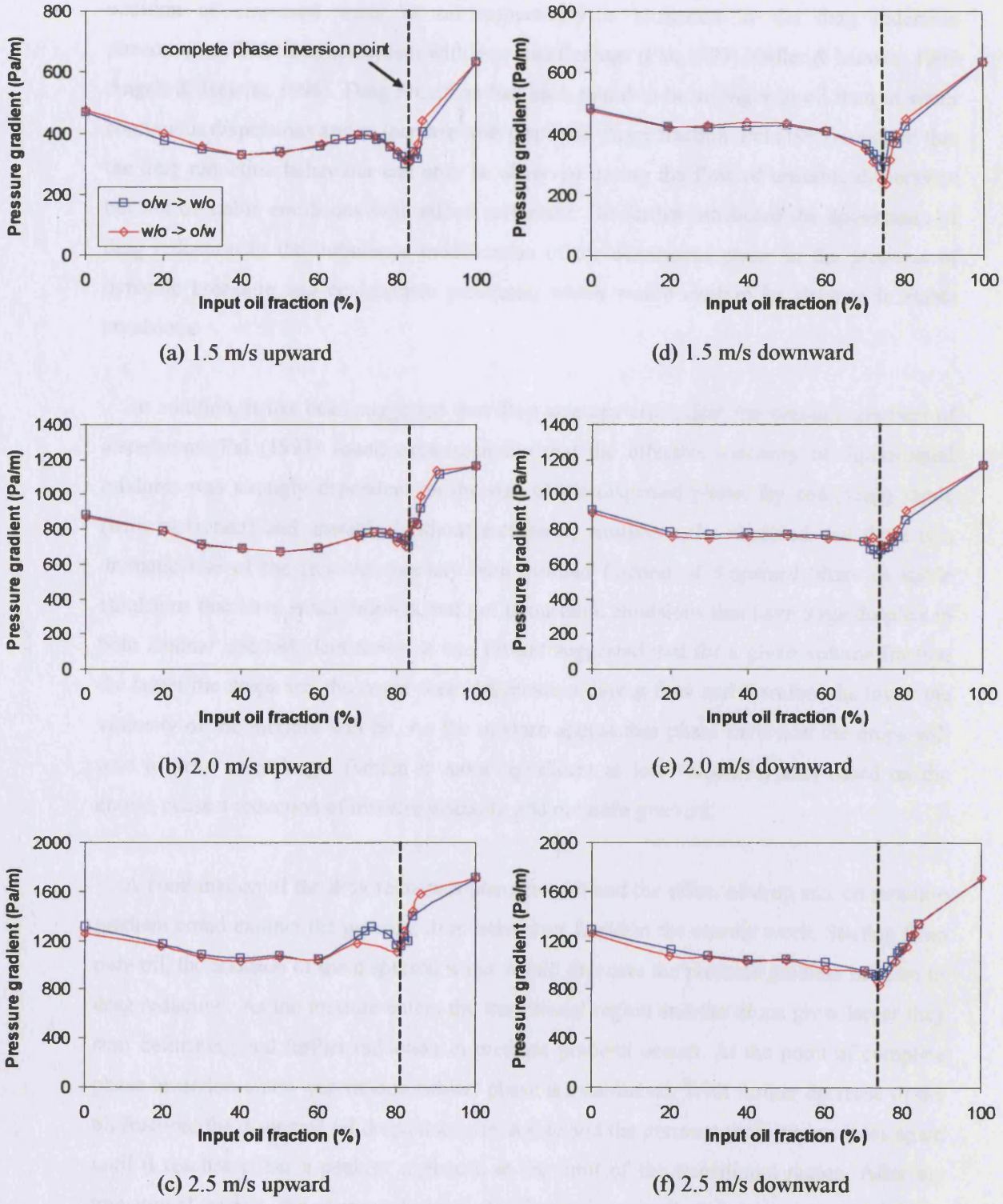

(a) 1.5 m/s upward

(d) 1.5 m/s downward

(b) 2.0 m/s upward

(e) 2.0 m/s downward

(c) 2.5 m/s upward

(f) 2.5 m/s downward

Figure 5.4: Frictional pressure gradient at different input oil fractions and mixture velocities for upward and downward flows. The vertical line indicates the phase inversion given by the hot film probe.

The reduction in pressure gradient from the single-phase oil or water values with the addition of dispersed water or oil respectively is attributed to the drag reduction phenomenon. This is in agreement with previous findings (Pal, 1993; Nädler & Mewes, 1997; Angeli & Hewitt, 1998). Drag reduction has been found to be stronger in oil than in water continuous dispersions and to increase with dispersed phase fraction. Pal (1993) reported that the drag reduction behaviour can only be observed during the flow of unstable dispersions but not of stable emulsions with added surfactant. He further attributed the appearance of drag reduction to the turbulence modification of the continuous phase in the presence of dynamic breakage and coalescence processes, which would explain its absence in stable emulsions.

In addition, it has been suggested that drop size can also affect the pressure gradient of dispersions. Pal (1993) found experimentally that the effective viscosity of liquid-liquid mixtures was strongly dependent on the size of the dispersed phase. By comparing stable (with surfactant) and unstable (without surfactant) emulsions, he observed that there is a dramatic rise of the relative viscosity with volume fraction of dispersed phase in stable emulsions that have small droplets, but not in unstable emulsions that have large droplets in both laminar and turbulent flows. It was further suggested that for a given volume fraction the larger the drops are, the easier their deformation during flow and therefore the lower the viscosity of the mixture will be. As the mixture approaches phase inversion the drops will tend to grow even larger (which is more significant at low velocities) and, based on the above, cause a reduction of mixture viscosity and pressure gradient.

A combination of the drag reduction phenomenon and the effect of drop size on pressure gradient could explain the pressure drop behaviour found in the current work. Starting from pure oil, the addition of the dispersed water would decrease the pressure gradient because of drag reduction. As the mixture enters the transitional region and the drops grow larger they start deforming and further reduction in pressure gradient occurs. At the point of complete phase inversion a new continuous (water) phase is established. With further decrease of the oil fraction, the dispersed oil drops decrease in size and the pressure gradient increases again until it reaches either a peak or a plateau at the limit of the transitional region. After the transitional region the dispersed drops are becoming small and less easy to deform. Combined with the reduced effect of drag reduction in water continuous dispersions the pressure gradient is much closer to the single phase water value and approaches it as the dispersed phase oil fraction further decreases. A lower drag reduction is observed in the water than in the oil continuous dispersions perhaps due to the reduced deformability of more viscous oil drops.

A possible reason for the different behaviour of the pressure gradient during phase inversion between vertical and horizontal flows could be the difference of drop sizes in the two conditions. Because of the orientation of the flow, in vertical flows gravity does not promote phase separation in a pipe cross section as in horizontal flows and dispersed flow can be achieved easily at much lower mixture velocities, such as 1.0 m/s in the current case, at which the flow in a horizontal pipe of the same size, the flow is not fully dispersed at this mixture velocity. As a result larger drops, that deform more easily, will be present in vertical flow compared to those in horizontal flows. Perhaps with a further increase in the mixture velocity a peak in pressure gradient can also appear in vertical flow during phase inversion. In fact there are some small peaks close to the phase inversion point in upward flows (see Figure 5.4), which could become more prominent as the mixture velocity further increases. It should also be pointed out that in the previous investigations, where both changes in phase continuity and pressure gradient were studied (Pal, 1993; Nädler & Mewes, 1995, 1997; Ioannou et al., 2005), phase inversion was identified at only one location in the pipe and the increase in pressure gradient was not matched with the change in phase continuity throughout the pipe cross section. In other studies the peak in pressure drop was used as an indication of phase inversion but was not related to phase continuity measurements. It is possible, therefore, that a maximum in pressure gradient appears not at the exact point of complete phase inversion but close to it, as the location of the small peaks in upward flow suggest.

Figure 5.5 shows the friction factor (f) at different mixture Reynolds numbers ($\mathrm{Re}=\rho_m U_{mix} D/\mu_m$) calculated from the data in Figure 5.4, against the predictions of the Blasius equation ($f = 0.079\mathrm{Re}^{-0.25}$). Here, the Taylor equation (Taylor, 1932) for the dispersion viscosity is employed to calculate the Re number [see Equation (5-2)].

$$\mu_m = \mu_c \left[1 + 2.5\varphi \frac{\mu_d + 0.4\mu_c}{\mu_d + \mu_c} \right] \tag{5-2}$$

where μ_d, μ_c and μ_m are the viscosities of dispersed phase, continuous phase and mixture, respectively, and ϕ is the in-situ volume fraction of the dispersed phase measured by using the quick-closing valves (see Section 5.2.1.3 below). As shown in Figure 5.5, the experimental values obtained from the current upward and downward flows are lower than those calculated from the Blasius equation which affirms the existence of drag reduction in pure (or unstable) oil-water flow.

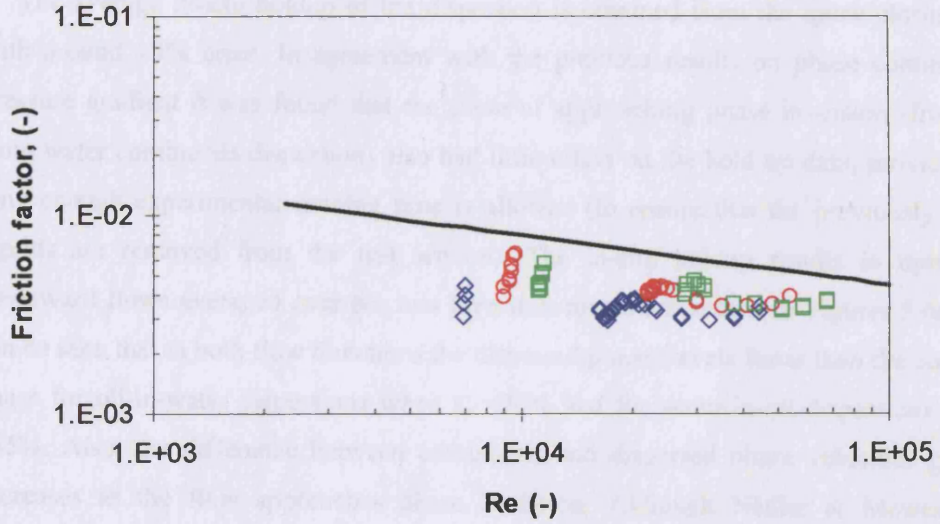

(a): upward flow

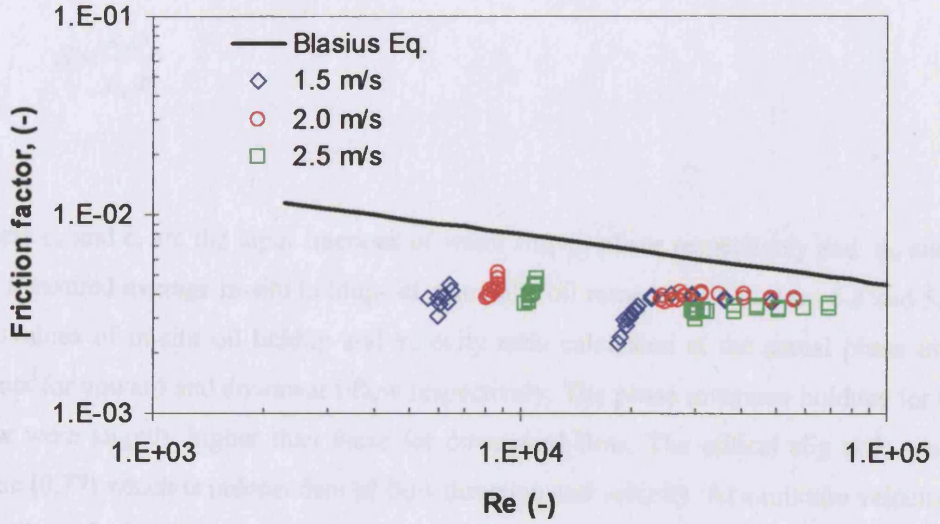

(b): downward flow

Figure 5.5: Experimentally measured friction factor (*f*) as a function of mixture Reynolds (Re) number, compared with Blasius equation.

5.2.1.3 In-situ Holdup and Velocity Ratio

The average in-situ holdup of the dispersion is obtained from the quick-closing valves with around ±3% error. In agreement with the previous results on phase continuity and pressure gradient it was found that the route of approaching phase inversion (from oil or from water continuous dispersion) also had little effect on the hold up data, provided that a long enough experimental running time is allowed (to ensure that the previously stagnant liquids are removed from the test section). The in-situ holdup results in upward and downward flows averaged over the two inversion routes are shown in Figures 5.6a & b. It can be seen that in both flow directions the dispersed phase travels faster than the continuous phase for oil-in-water dispersions when ϵ_o <70% and for water-in-oil dispersions when ϵ_o >85%. Also, the difference between continuous and dispersed phase velocities gradually decreases as the flow approaches phase inversion. Although Nädler & Mewes (1995) suggested that at phase inversion the velocities of two phases are same, the current work suggests that this is not the case. Figure 5.7 presents the data on velocity ratio (slip ratio) in the vicinity of phase inversion point ($S=U_o/U_w$), calculated by Equation (5-3).

$$S = \frac{\varepsilon_o \varphi_w}{\varepsilon_w \varphi_o} \tag{5-3}$$

where ϵ_w and ϵ_o are the input fractions of water and oil phase respectively and ϕ_w and ϕ_o are the measured average in-situ holdups of water and oil respectively. Figures 5.8 and 5.9 show the values of in-situ oil holdup and velocity ratio calculated at the actual phase inversion points for upward and downward flow respectively. The phase inversion holdups for upward flow were slightly higher than those for downward flow. The critical slip ratio tends to a value (0.77) which is independent of flow direction and velocity. At a mixture velocity of 1.5 m/s, the velocity ratio at phase inversion was higher (i.e. close to unity); visual observation showed that at high oil fractions at this mixture velocity, very large oil drops (similar to plugs) appeared in the middle of the pipe.

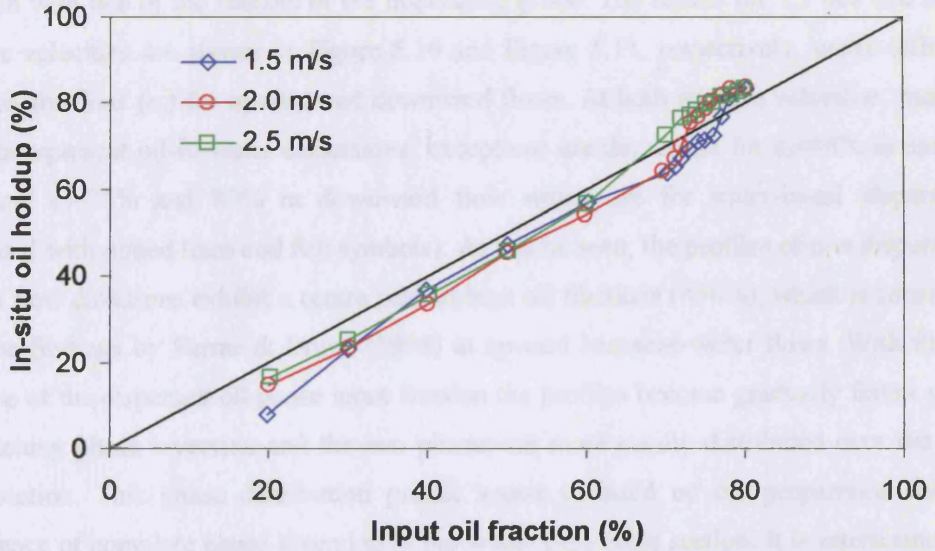

(a): upward flow

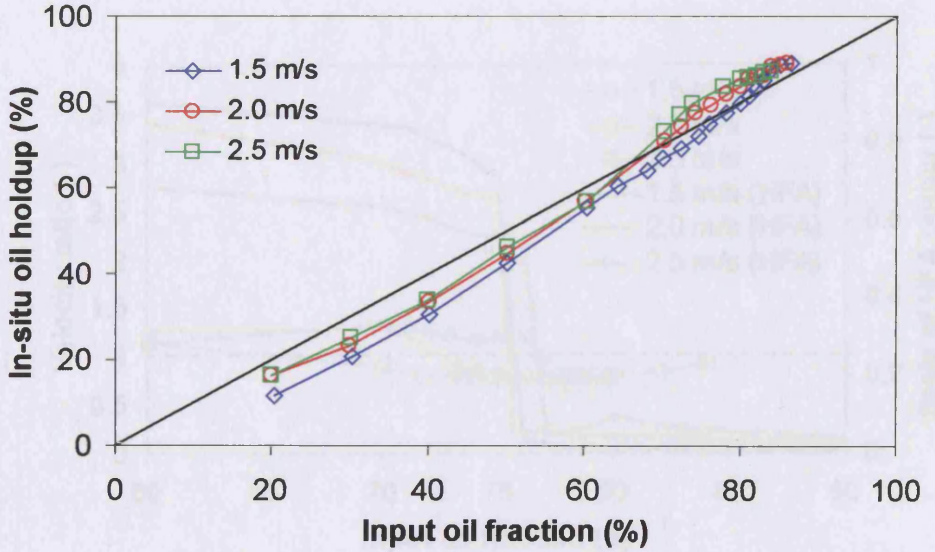

(b): downward flow

Figure 5.6: Average in-situ holdup at different input oil fractions in upward (a) and downward (b) flows.

Detailed measurements of the in-situ hold-up profile in a pipe cross section were also obtained with one of the sensors of the impedance probe. The results for 1.5 m/s and 2 m/s mixture velocities are shown in Figure 5.10 and Figure 5.11, respectively, under different input oil fractions (ε_o) for upward and downward flows. At both mixture velocities, most of the data represent oil-in-water dispersions; exceptions are the results for ε_o=86% in upward flow and ε_o=76% and 80% in downward flow which are for water-in-oil dispersions (indicated with dotted lines and full symbols). As can be seen, the profiles of o/w dispersions in both flow directions exhibit a centre peak at high oil fractions (<50%), which is consistent with the findings by Farrar & Bruun (1996) in upward kerosene-water flows. With further increase of the dispersed oil phase input fraction the profiles become gradually flatter while approaching phase inversion and the two phases are more evenly distributed over the pipe cross-section. This phase distribution profile seems to build up the preparation for the occurrence of complete phase inversion in the whole pipe cross section. It is interesting that although there are differences in the local holdup between upward and downward flows for a given ε_o, as illustrated in Figure 5.10, which would explain the differences in the complete phase inversion points between the two directions, phase inversion does happen at the higher velocities at both directions at nearly the same slip ratio (see Figure 5.9).

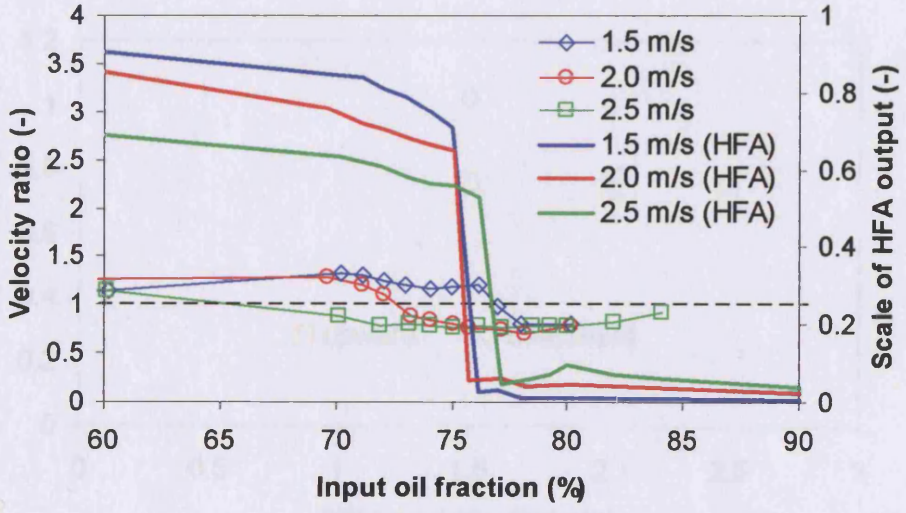

Figure 5.7: Velocity ratio (U_o/U_w) and output of hot-film probe (which indicates the complete inversion point) measured at different mixture velocities in downward flow.

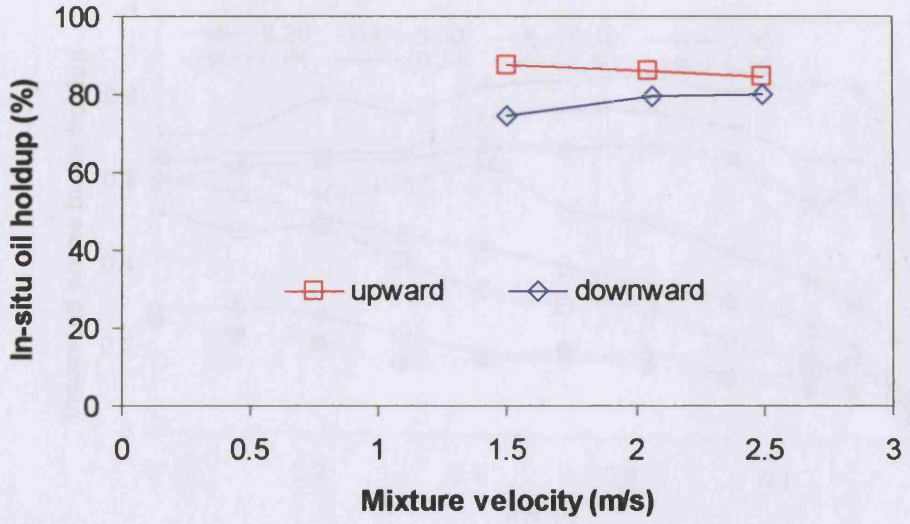

Figure 5.8: Average in-situ oil holdup at complete phase inversion obtained in upward and downward flows.

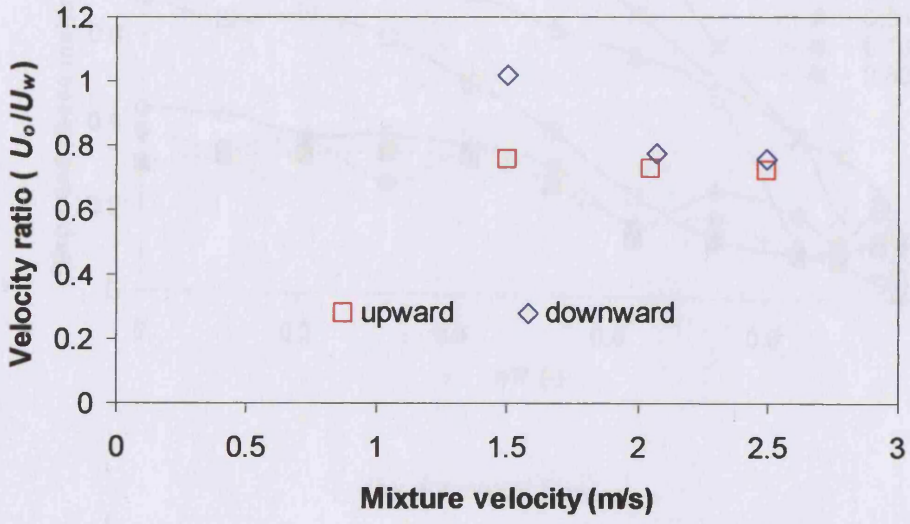

Figure 5.9: Slip velocity ratio (U_o/U_w) at complete phase inversion obtained in upward and downward flows.

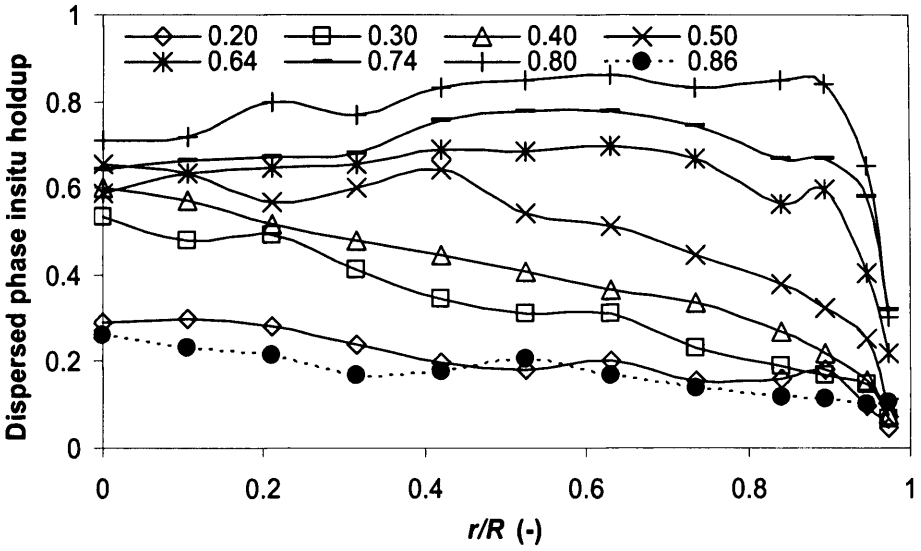

(a): upward flow

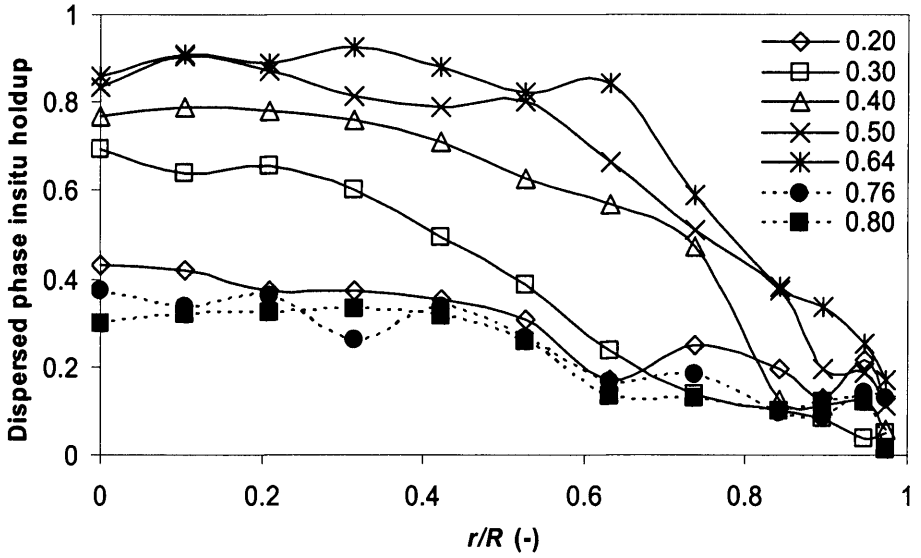

(b): downward flow

Figure 5.10: In-situ holdup profiles of the dispersed phase at 1.5 m/s mixture velocity at various input oil fractions (ϵ_o) for (a) upward and (b) downward flow. Here, w/o dispersions are obtained for ϵ_o=86% in upward flow and ϵ_o=76% and 80% in downward flow.

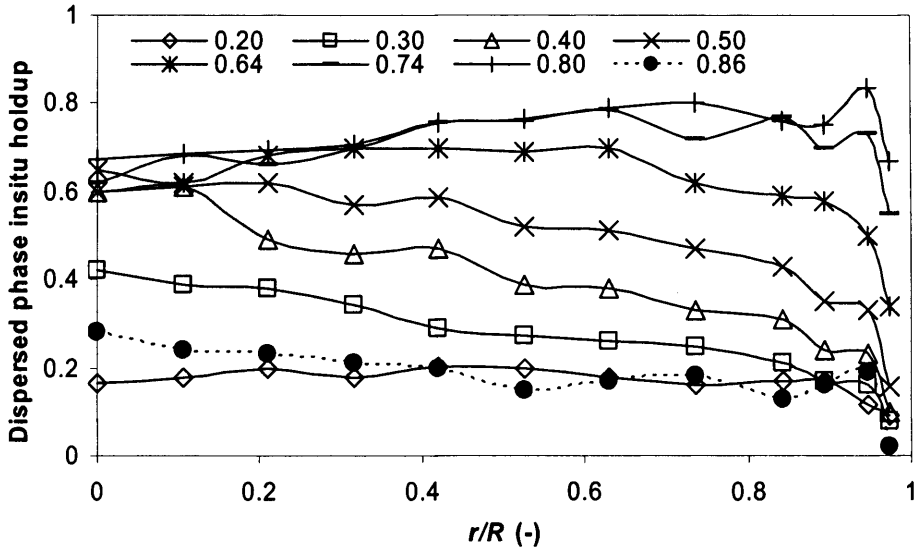

(a): upward flow

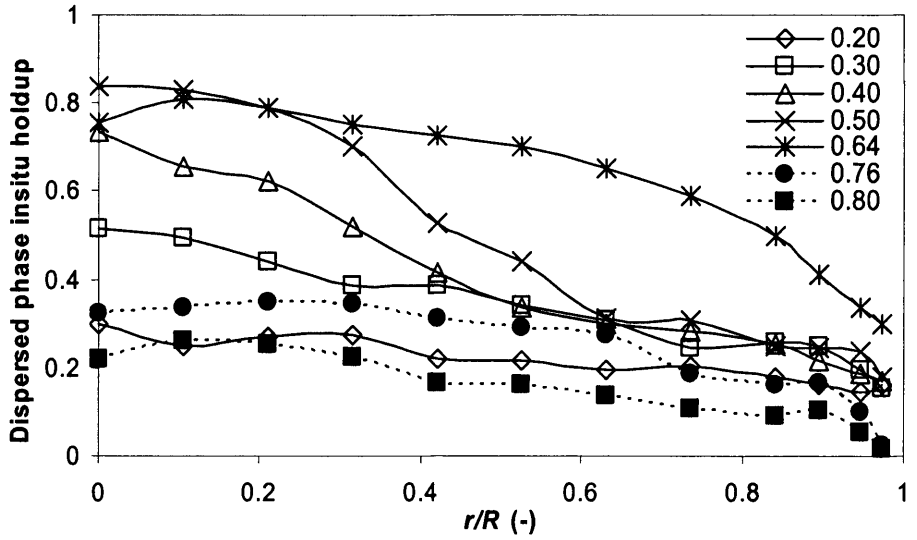

(b): downward flow

Figure 5.11: In-situ holdup profiles of the dispersed phase at 2.0 m/s mixture velocity at various input oil fractions (ϵ_o) for (a) upward and (b) downward flow. Here, w/o dispersions are obtained for ϵ_o=86% in upward flow and ϵ_o=76% and 80% in downward flow.

To generate further confidence in the experimental results obtained in this study, mass (or volume) conservation was checked for all the above cases. Figure 5.12 shows the dispersed phase volumetric flowrate (Q_d^m), calculated by Equation (5-4) using the measured holdup and the drop velocity data (to be presented in Section 6.4).

$$Q_d^m = 2\pi \int_0^R U_d(r)\varphi_d(r) r dr \tag{5-4}$$

where $U_d(r)$ is the average velocity of dispersed phase at radius r which is obtained by the dual impedance probe, $\varphi_d(r)$ is the local holdup of dispersed phase at radius r and $R=D/2$ is the pipe radius. As can be seen from Figure 5.12, the dispersed phase volumetric flowrates calculated in this way are generally less than the input value; this may reflect the fact that the impedance probe used in this study is unlikely to capture drops smaller than 150 μm due to probe geometry limitations (see Chapter 3). This would result in some underestimation of the local holdup of the dispersed phase. However, reasonably good agreement can still be found in Figure 5.12 for all the cases studied.

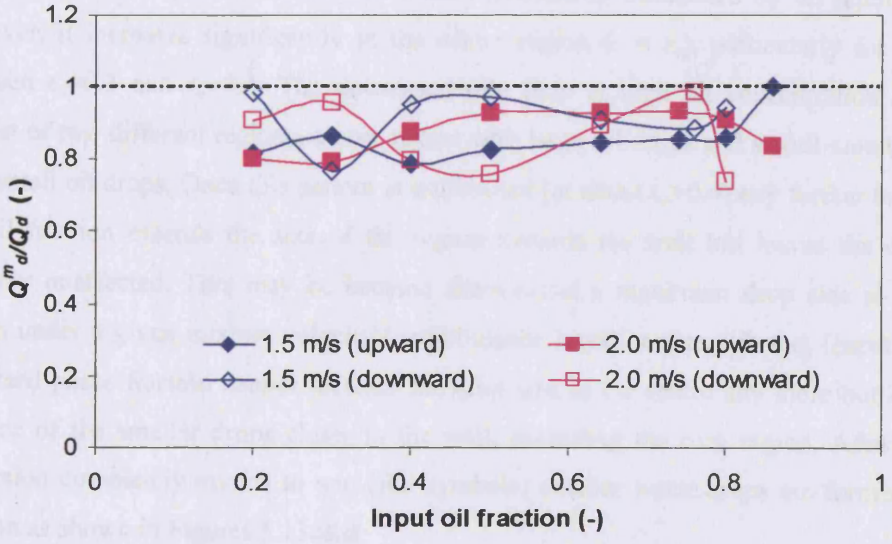

Figure 5.12: Ratio of the measured dispersed phase volumetric flowrate (Q_d^m) to the input value (Q_d) at various input oil fractions.

5.2.1.4 Chord Length and Drop Size Distribution

By cross-correlating the signals of the two sensors of the dual impedance probe the velocity of the dispersed phase drops can be found. This velocity can then be combined with the time duration of the interactions between the dispersed phase and either of the two probe sensors to provide a distribution of the drop chord lengths that have been intersected by the sensor. A Sauter mean chord length is defined as $L_{32}= \sum[P(L)L^3]/ \sum[P(L)L^2]$ where $P(L)$ is the number density of chord length L, and Figures 5.13a-d show the radial profile of L_{32} measured at 1.5 and 2.0 m/s mixture velocity in upward and downward flows respectively for different input oil fractions before and after phase inversion, following the w/o→ o/w inversion route. Again, most lines represent o/w dispersions apart from ϵ_o=86% in upward flow and ϵ_o=76% and 80% in downward flow which represent w/o dispersions (indicated by dotted lines and full symbols).

As can be seen from Figures 5.13 c&d for downward dispersions, in the o/w dispersions (denoted by open symbols) L_{32} has a peak at the pipe centre, which becomes particularly prominent at oil fractions 40% and above. In other words, there are more large drops in the pipe central region (defined as lying within a certain pipe radius r_c) than in the wall area. The L_{32} profile for dense dispersions also shows a significant decrease at pipe radius r_c. for the case shown in Figure 5.13d, r_c increases from $0.3R$ for ϵ_o=0.4 to $0.78R$ for ϵ_o=0.64. The dispersed phase drop size at the wall is not significantly influenced by oil input fraction; however, it increases significantly in the centre region ($r < r_c$), particularly for fractions between ϵ_o=0.3 and ϵ_o=0.4. The downward o/w flow at high oil concentration seems to consist of two different regions, a core region with large oil drops and a wall-annular region with small oil drops. Once this pattern is established (at about ϵ_o=0.4) any further increase in the oil fraction extends the size of the region towards the wall but leaves the drop size virtually unaffected. This may be because there exists a maximum drop size in the core region under a given mixture velocity (or turbulence level), and any further increase in the dispersed phase fraction cannot increase the drop size in the centre any more but increases the size of the smaller drops closer to the wall, extending the core region. After the o/w dispersion completely inverts to w/o (full symbols) smaller water drops are formed due to dilution as shown in Figures 5.13c&d.

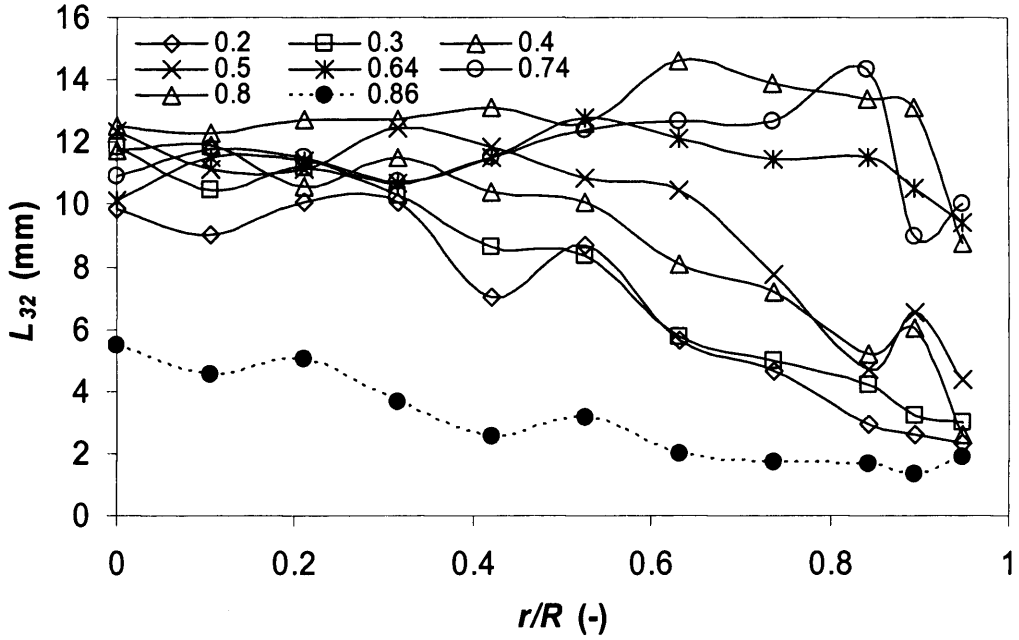

(a) 1.5 m/s upward flow

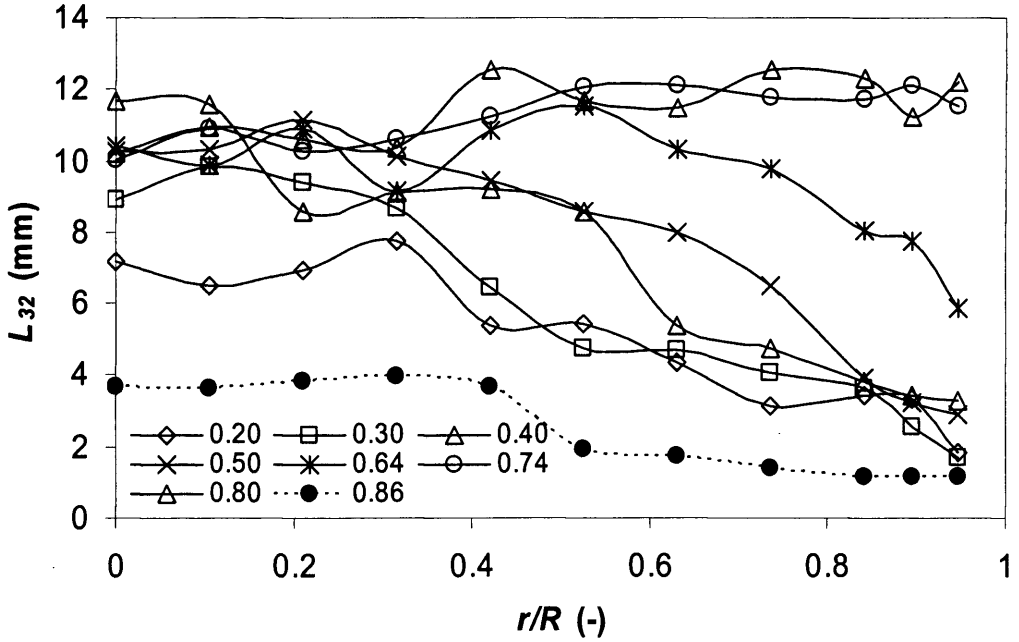

(b) 2.0 m/s upward flow

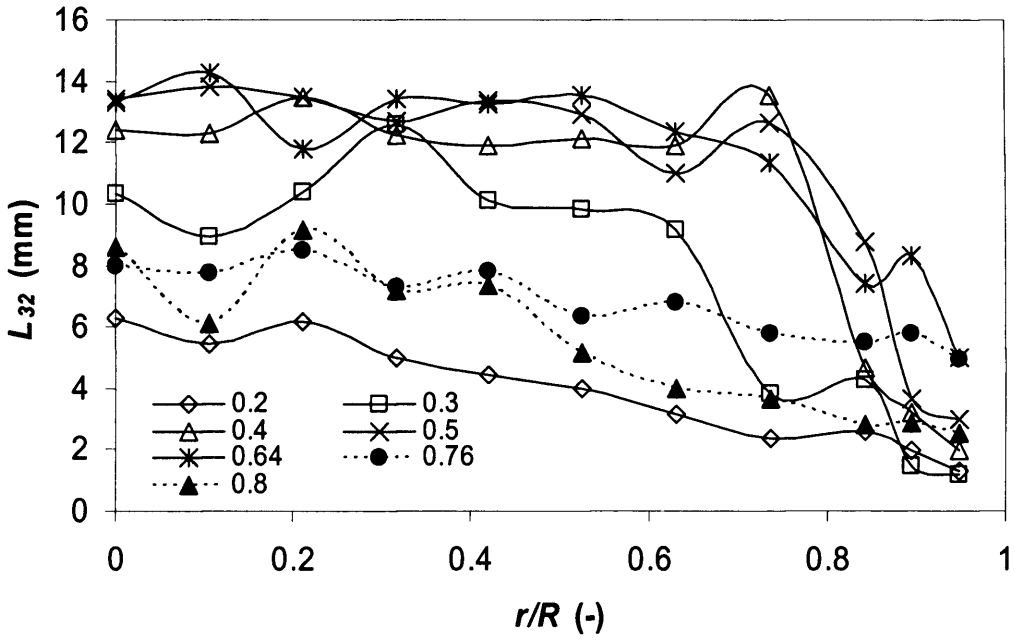

(c) 1.5 m/s downward flow

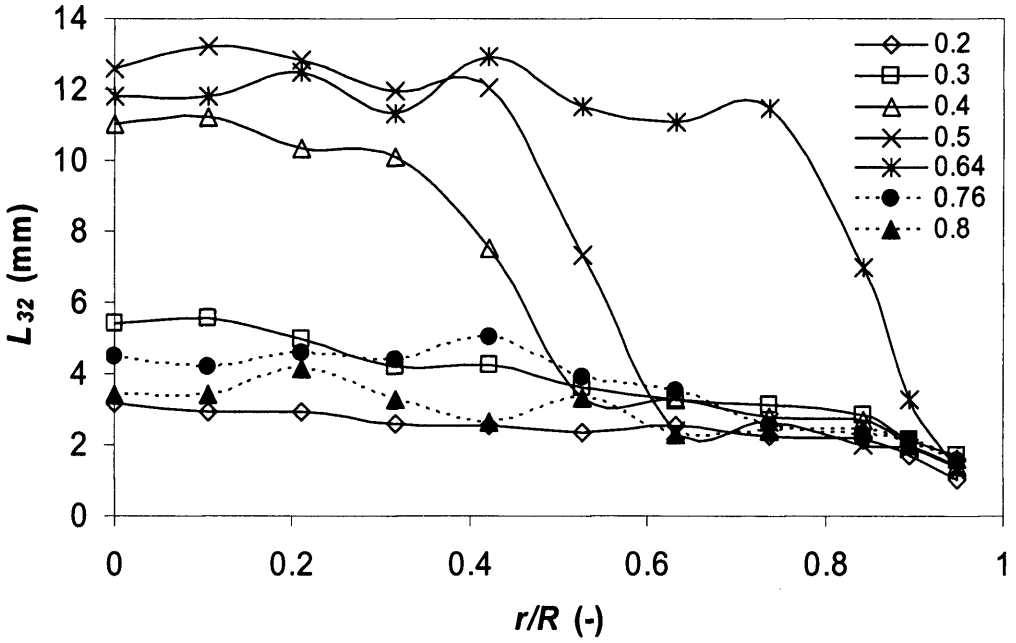

(d) 2.0 m/s downward flow

Figure 5.13: Average chord length L_{32} profiles: (a) 1.5 m/s upward flow, (b) 2.0 m/s upward flow, (c) 1.5 m/s downward flow and (d) 2.0 m/s downward flow. The empty markers are o/w dispersions while the solid markers are w/o dispersions.

In both upward and downward flows of o/w dispersions, L_{32} has large values in the pipe centre. L_{32} reduces to low values after inversion to w/o mixtures (see Figures 5.13 a&b), reflecting the fact that the water drops in oil have a smaller size than the oil drops in water before inversion. However, the L_{32} profiles in o/w dispersions at the highest oil fractions (ϵ_o=0.74 and 0.8) seem to be almost uniform across the pipe or slightly increase closer to the wall. In addition, the differences in drop size between the pipe centre and wall regions are not as great in upward as in downward flow, even for the lower oil fractions.

This disagreement between upward and downward flow dispersed phase size and distribution (also reflected in the hold-up profiles, see Figures 5.10 and 5.11) may suggest that the process of approaching phase inversion in the two flow directions is different. It is interesting, however, that despite these differences in the dispersed phase size and distribution, phase inversion appears at the same velocity ratio in both directions. Perhaps a mechanism based on the momentum of the two phases during inversion is more relevant to phase inversion in pipeline flow. This would agree with the theory proposed by Yeh et al. (1964) and Nädler & Mewes (1995) of zero interfacial shear stresses during inversion.

From the local measurements of drop chord length the area-weighted integrated distributions of chord length (L) over the pipe cross-section can be obtained and are shown in Figures 5.14a-f for different input oil fractions (ϵ_o) at 2.0 m/s downward flow. In o/w flows (see Figures 5.14a-d), as the dispersions become denser, the likelihood of the probe intersecting large chords rises. This is understandable since the coalescence rate of oil drops will increase with oil concentration which will result in many large drops in the flow. Particularly for ϵ_o=64%, before the phase inversion point (74%), intersected chords as long as 19mm (=D/2) can frequently be seen. These would originate either from large spherical drops or from smaller drops that have deformed in the dense dispersion. The distributions after phase inversion to w/o (Figures 5.14d & e) confirm the presence of many small water drops.

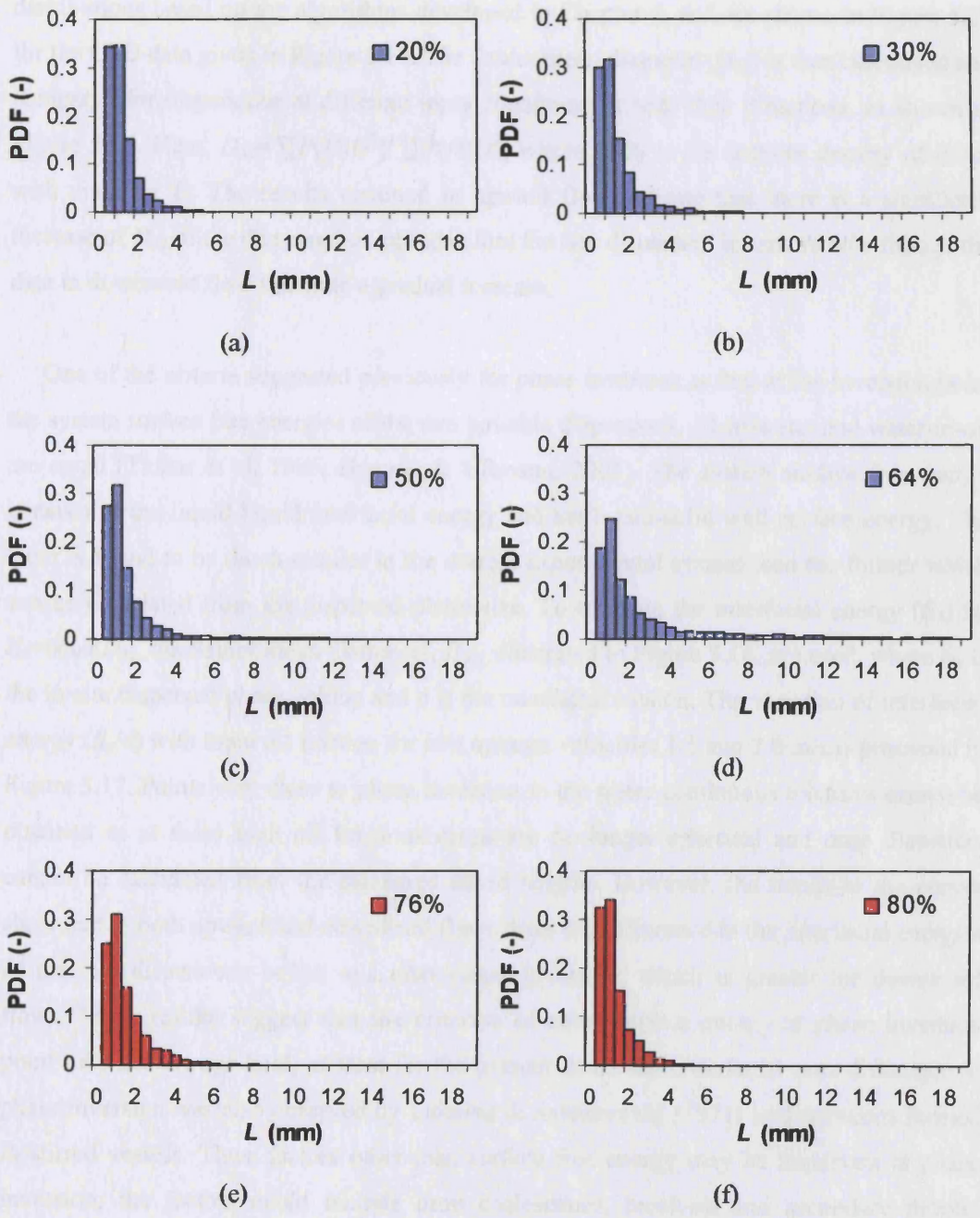

Figure 5.14: Cross-sectionally averaged chord length (L) distribution at 2.0 m/s mixture velocity and different input oil fractions (ε_o=20% – 80%) in downward flow. Blue colours represent water continuous while red colours represent oil continuous dispersions.

Additionally, the measured chord length distributions were further converted to drop size distributions based on the algorithms developed in Chapter 4, and are shown in Figure 5.15 for the CLD data given in Figure 5.14. The Sauter mean diameter (D_{32}) is then calculated and compared for dispersions at different input conditions in both flow directions, as shown in Figure 5.16. Here, $D_{32}=\sum[P(D)D^3]/\sum[P(D)D^2]$ where $P(D)$ is the number density of drops with diameter D. The results obtained in upward flow indicate that there is a significant increase of D_{32} of the dispersed oil phase before the o/w dispersion inverts to w/o, though the data in downward flow illustrate a gradual increase.

One of the criteria suggested previously for phase inversion is that at the inversion point the system surface free energies of the two possible dispersions, oil-in-water and water-in-oil are equal (Tidhar et al. 1986; Brauner & Ullmann, 2002). The system surface free energy consists of the liquid-liquid interfacial energy and the liquid-solid wall surface energy. The latter is found to be much smaller in the current experimental system than the former which can be calculated from the dispersed phase size. To estimate the interfacial energy (E_S) by $E_S=6\phi_d\sigma/D_{32}$, the Sauter mean diameters, D_{32}, illustrated in Figure 5.16, are used, where ϕ_d is the in-situ dispersed phase holdup and σ is the interfacial tension. The variation of interfacial energy (E_s/σ) with input oil fraction for two mixture velocities 1.5 and 2.0 m/s is presented in Figure 5.17. Points very close to phase inversion in the water continuous mixtures cannot be obtained as at these high oil fractions drops are no longer spherical and drop diameters cannot be calculated from the measured chord lengths. However, the trends in the curves show that in both upward and downward flows there is a difference in the interfacial energies of the two dispersions before and after phase inversion, which is greater for downward flows. These results suggest that the criterion of equal surface energy at phase inversion point may not always hold, at least for the present data. This interfacial area difference at phase inversion was also observed by Luhning & Sawistowski (1971) in dispersions formed in stirred vessels. Thus, factors other than surface free energy may be important in phase inversion; the factors could include drop coalescence, break-up and secondary droplet inclusion.

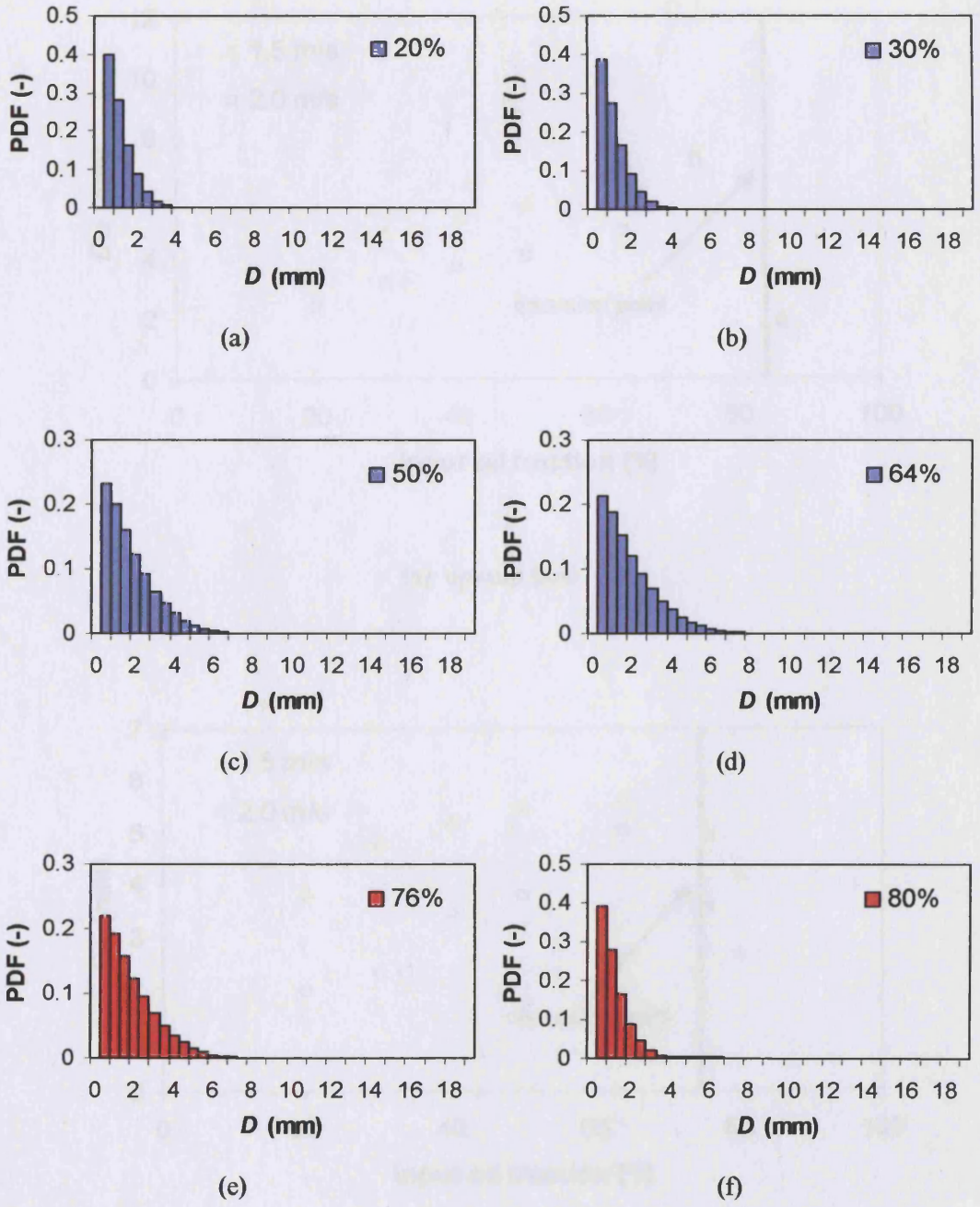

Figure 5.15: Cross-sectionally averaged drop size (D) distribution at 2.0 m/s mixture velocity and different input oil fractions (ε_o=20% – 80%) in downward flow. Blue colours represent water continuous while red colours represent oil continuous dispersions.

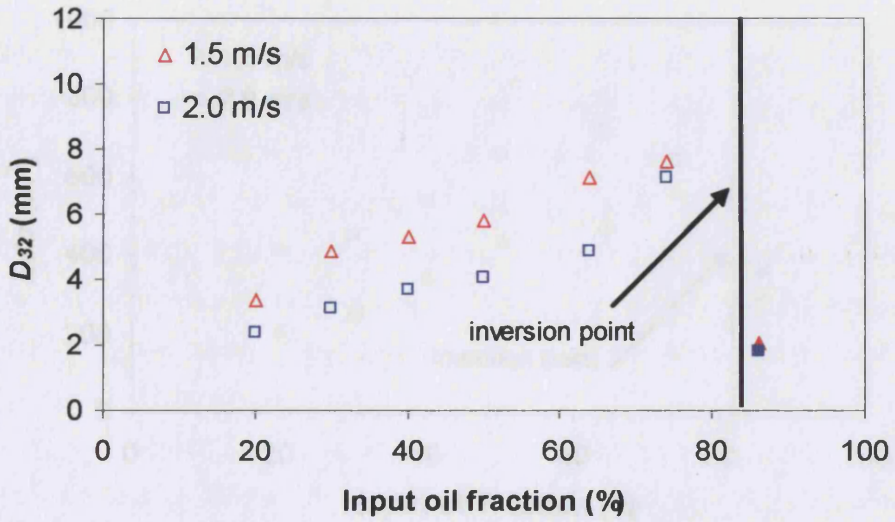

(a): upward flow

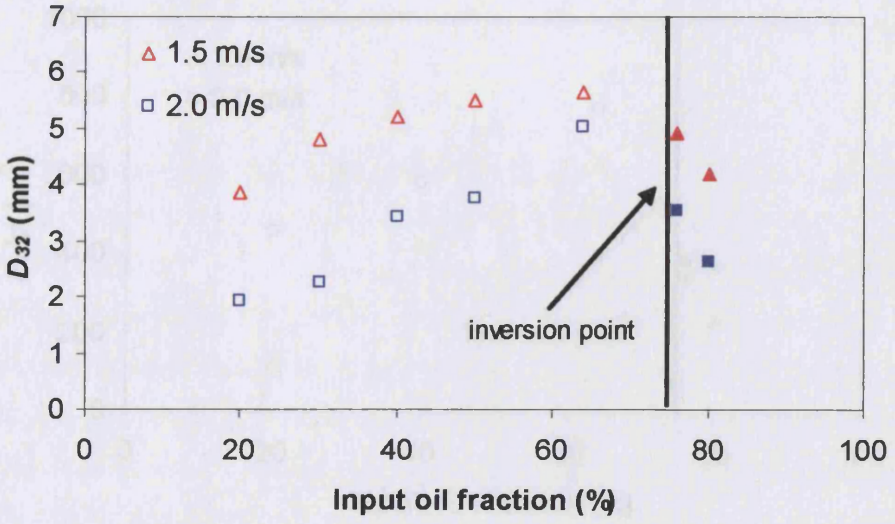

(b): downward flow

Figure 5.16: Sauter mean diameter (D_{32}) vs. the input oil fraction for oil drops (empty markers) and water drops (solid markers) at different mixture velocities in (a) upward flow and (b) downward flow.

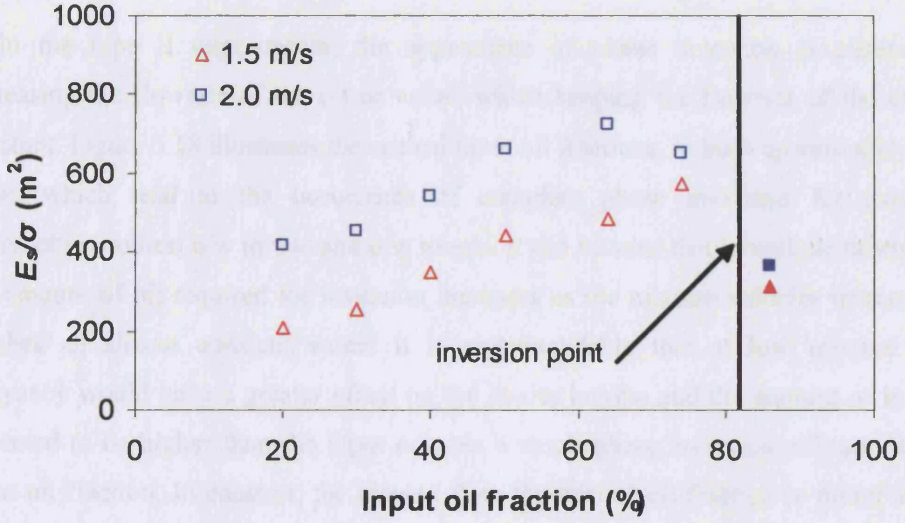

(a): upward flow

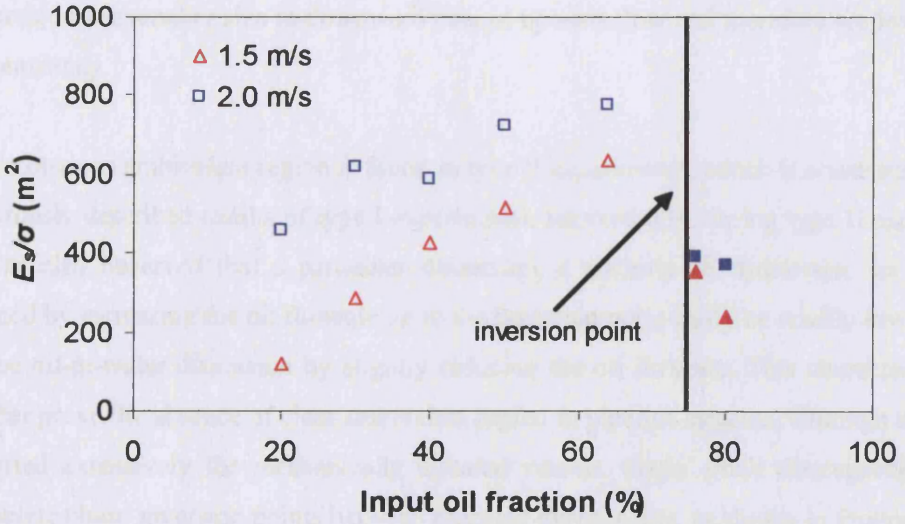

(b): downward flow

Figure 5.17: Interfacial energy (E_s/σ) vs. input oil fraction for oil-in-water (empty markers) and water-in-oil (solid markers) dispersions at different mixture velocities for (a) upward flow and (b) downward flow.

5.2.2 Type II Experiments

In the type II experiments, the appearance of phase inversion is observed whilst increasing the flowrate of the oil or water, whilst keeping the flowrate of the other phase constant. Figure 5.18 illustrates the critical input oil fractions, in both upward and downward flows which lead to the occurrence of complete phase inversion for two different approaching routes, o/w to w/o and o/w to w/o. It can be seen that in vertical downward flow the amount of oil required for inversion increases as the mixture velocity increases until it reaches an almost constant value. It is understandable that at low mixture velocities buoyancy would have a greater effect on the in-situ holdup and the amount of in-situ oil is expected to be higher than the input one. As a result phase inversion will appear at lower input oil fraction. In contrast, for upward flow the critical oil fraction is found to decrease with the mixture velocity. The opposite will happen in the upward flow where buoyancy will now favour lower in-situ oil hold up than the input one. As shown in Figure 5.18, when the mixture velocity increases above 3.5 m/s the buoyancy effect seems to be negligible and the critical oil fraction for inversion becomes less dependent on mixture velocity. This is more obvious for downward than for upward flow, perhaps because the dispersed drops close to inversion have smaller size in downward than in upward flow and therefore are less affected by buoyancy.

No obvious ambivalent region is found in type II experiments, which is consistent with the previously described results of type I experiments. Interestingly, during type II experiments, it was also observed that a particular dispersion, a water-in-oil dispersion, for example, formed by increasing the oil flowrate up to the inversion point could be readily inverted back to the oil-in-water dispersion by slightly reducing the oil flowrate. This characteristic may further prove the absence of clear ambivalent region in pipeline systems, although it has been reported extensively for mechanically agitated vessels. Some small discrepancies of the complete phase inversion points between repeated experiments, as shown in Figure 5.18, are attributed to the differences that can experimentally exist in the system set-up and operating conditions as well as contamination and temperature variation.

Previous works have indicated that the phase inversion point is independent of mixture velocity (Arirachakaran et al., 1989; Soleimani, 1999; Ioannou et al., 2004) which would agree with the current findings for the higher mixture velocities used.

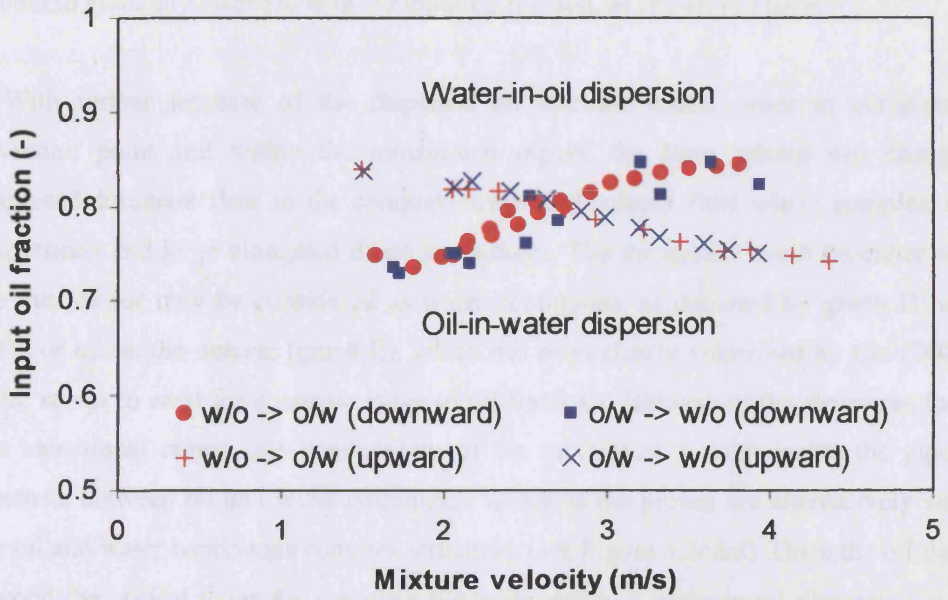

Figure 5.18: Critical input oil fraction for complete phase inversion at different mixture velocities obtained from type II experiments for both inversion routes in upward and downward flows.

5.3 Phase Inversion Process

On the basis of the visual observations in this work, supported by the experimental work carried out by Liu (2005) in a project linked to the present one, a sequence of flow patterns before and after phase inversion is proposed, which is schematically shown in Figure 5.19 for an o/w to w/o transition. In the o/w dispersion at low oil fractions, oil is present in the water continuum in the form of spherical drops (graph A). As the input oil fraction increases a relatively dense dispersion with larger drops is formed due to drop coalescence (graph B). If more oil is fed into the pipe the drops will be more closely packed and the dispersion will become more concentrated. Although the close packing would occasionally force the drops, especially the larger ones, to deform into various shapes (e.g. ellipsoidal and more complex and elongated shapes as shown in graph C), the majority of the dispersed drops would still be spherical. At this stage, drops can stay together exhibiting negligible coalescence even for systems with no added surfactants, as shown by Figure 5.20. The formation of such concentrated o/w dispersions is attributed to the electrical double-layer effect around the oil drops because of preferential adsorption of ions from the continuous water phase, which was found to significantly suppress coalescence in both less dense (<10%, Collins & Knudsen,

1970) and dense dispersions (< 45%, Pal, 1993). The conductivity of the dispersion is then shown to gradually decrease with the input oil fraction, as shown in Figure 5.1.

With further increase of the dispersed oil fraction, much closer to complete phase inversion point and within the transitional region, the flow pattern can change from dispersed-dominant flow to the complex-structure-dominant flow where complex multiple dispersions and large elongated drops are present. The dispersion could be either water on the outside (or may be considered as water continuous, as depicted by graph D in Figure 5.19) or oil on the outside (graph E), which has been clearly visualized by Liu (2005). The latter seems to exist for a narrow range of oil fractions. Because of the structures formed in the transitional region, the conductivity of the mixture at a point inside the pipe would fluctuate between oil and water continuous values as the probes are alternatively wetted by the oil and water continuous complex structures (see Figure 5.2c&d). Once the oil fraction is beyond the critical value for complete phase inversion, a water-in-oil dispersion is formed (graph F in Figure 5.19). The rather low conductivity value that corresponds oil continuous is found (see Figure 5.1 and Figure 5.2e). The transitional region is found in this study to be over 4-6% input oil fraction and is expected to narrow down with an increase in the mixture velocity.

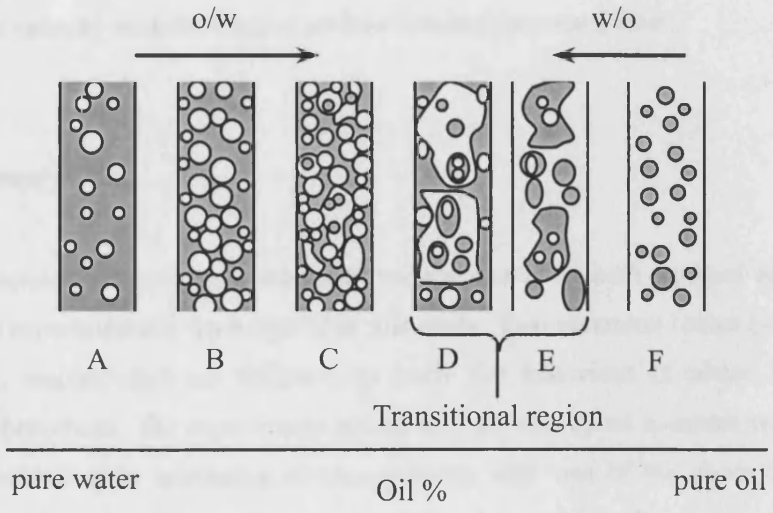

Figure 5.19: Schematic of the phase inversion process in vertical oil-water pipeline flow in either upward or downward direction (not to scale).

The above process would also describe the w/o to o/w inversion. In this case, however, the continuous oil phase is non-polar and there is a higher possibility of water drops to

coalesce due to the absence of the double-layer effect. This would justify the lower dispersed water fraction required to invert an oil continuous dispersion, compared to the dispersed oil fraction required to invert a water continuous dispersion.

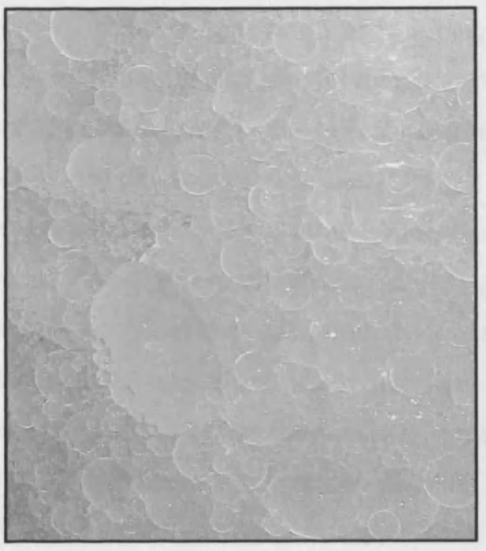

Figure 5.20: Photograph of highly concentrated oil-in-water dispersion observed at 1.5 m/s mixture velocity and 60% input oil fraction in downward flow.

5.4 Summary

Phase inversion in co-current oil-water vertical flows in both upward and downward directions is experimentally investigated in this study. Two inversion routes (w/o to o/w and o/w to w/o, respectively) are followed to study the behaviour of phase inversion and associated phenomena. The experiments are carried out with either constant mixture velocity (type I experiments) or increasing mixture velocity with one of the phase flowrate fixed (type II experiments). A conductivity probe at the pipe centre and a glue-on HFA probe at the pipe wall indicate that phase inversion initially takes place at the pipe centre via the formation of complex structures, before it reaches the wall. The input oil fraction at which inversion is detected at the wall signifies the fact that the new continuous phase has spread into the whole pipe cross section and is defined as the 'complete phase inversion point'.

Based on the above experimental investigations around the complete phase inversion point, the following conclusions can be drawn:

- The results from type I experiments in both upward and downward flow indicate that frictional pressure gradient reaches a minimum at the complete phase inversion point. Drag reduction as well as the effect of drop size on mixture viscosity are suggested as possible reasons for this behaviour;
- No obvious ambivalent region is found in either type I and type II experiments nor in either flow direction. There is however, a narrow range of input phase fractions ($\Delta\epsilon_o$<4%- 6%) where the flow is unstable and complex structures are formed;
- The phase inversion point is found by the type II experiments to depend on mixture velocity for low and medium mixture velocities;
- The phase inversion points were found to be different for the two flow directions. However, the velocity ratios where complete inversion appeared, acquired the same constant value in both flow directions apart from the lowest velocity investigated;
- In contrast to the previously postulated phase inversion mechanisms, it was found, based on drop size measurements, that the interfacial energies of the dispersions just before and after phase inversion are not necessarily equal. Other phenomena, such as increased coalescence rate before inversion, supported by the large drops observed, could also be responsible for the appearance of the phenomenon.

A number of issues still need to be resolved in order to establish a mechanism of phase inversion, such as turbulence modification as the system approaches phase inversion and during the phenomenon and the existence (or absence) of ambivalent range. More work is also necessary to understand the effect of complex structures and multiple dispersions on the velocity and momentum of each phase.

Chapter 6

Mean Velocity and Turbulent Velocity Fluctuation in Oil-Water Dispersed Pipeline Flows

This Chapter describes the experimental results on turbulence structure measured with the hot-film anemometer (HFA) at an axial distance of 58*D* from the inlet. The objective was to investigate the modifications of turbulence in the presence of dispersed phase in both oil-in-water and water-in-oil dispersed flows, so as to promote a further understanding on the behaviour of the turbulence structure associated with phase inversion. Section 6.1 introduces the background of this experimental work and the experimental procedure. Section 6.2 briefly presents measurements of mean and turbulent velocity in single-phase flows, which are compared with those reported in previous studies. Section 6.3 illustrates the application of the signal separation algorithms (introduced in Section 2.6) to measurements in the two-phase flow case. In Section 6.4, the profiles of average velocity and turbulence intensity of the continuous phase and the average velocity of the dispersed phase at pre- and post-phase inversion conditions, in vertical upward and downward flows are presented and discussed. Section 6.5 describes the effects of such factors as mixture velocity, flow direction and drop size on changes of the turbulence velocity profiles. Section 6.6 compares the experimental observations with some theoretical models, suggested previously to predict turbulence enhancement or attenuation. In addition to studies in vertical flows, some experiments were also carried out in oil-water horizontal pipe flows, and the results are shown in Section 6.7. A short summary is finally given in Section 6.8.

6.1 Experimental Procedure

In addition to the experimental studies in vertical dispersed flows described in Chapter 5 on macroscale flow parameters, such as pressure drop and holdup, some work was also conducted on the WOLF rig to measure the turbulence structure in the continuous phase over a range of flow conditions. This part of experimental work aims at understanding the inherent flow characteristics in concentrated liquid-liquid dispersed flows and in two different types of emulsions (i.e. o/w and w/o). For this purpose, the hot-film anemometer (Dantec 99C10) connected with a 1-D velocity probe was used.

As discussed in Section 3.3, HFA is an extremely delicate and sensitive instrument. Small changes of ambient fluid temperature and probe contamination during the experiments could potentially lead to a big error into the measured results. For example, it has been reported that up to a 40% error could be introduced if the fluid temperature shifts ±1°C (Bruun, 2004). It is therefore imperative to conduct the measurements with HFA with extra care. Based on what has been reported in previous studies as well as experience gained during this work, the following procedure was applied to the current experiments to ensure better measurement accuracy:

(1) The oil phase is cleaned before each set of experiments to remove large solid particles and possible contaminants, by passing it through a filter with maximum 10 μm passage tolerance; the water phase is continuously cleaned during runs by mounting the filter on the water circuit.
(2) The 1-D velocity hot-film probes are cleaned daily before experimental runs by using a soft sable hairbrush to maintain a high and stable sensitivity.
(3) It was found difficult to maintain the temperature of the liquids at a constant value by the available heat exchanger. An alternative method was therefore applied. The mixture of cold fresh water and oil was passed through the loop until a near equilibrium state (where the mixture temperature changes only very slowly with time) is reached. The probe is then calibrated and a set of experiments conducted. The fluid temperature is normally limited in the range of 19~23°C, however, the temperature will gradually increase as the fluids pass through the pumps. If the mixture temperature goes above 23°C, part of the water in the system is drained away and fresh (cold) tap water is introduced so that the water in the loop has a low enough temperature. Once the cold water is introduced, the two fluids are run together again to achieve an equilibrium temperature.

(4) Generally, calibration of the hot-film probe is carried out at time intervals of 1 hour or immediately before a set of experiments. However, it is found necessary to repeat the calibration if the temperature of the mixture shifts by more than 1°C.

(5) Due to the frequent changing of the water phase and the limited amount of available deionised water, tap water is used here instead of deionised water. Also, to minimize the bubble formation on the heated sensor surface, air-saturated tap water is left to stand alone for 1 hour before the experiments and also several baffles are inserted in the water tank to avoid any air entrapment.

(6) An overheat ratio of 1.10 is applied to the setup of the hot-film anemometer, which gives ~25 °C temperature difference between the film sensor and test water.

(7) The experimental data for each test are acquired over a sampling time of 1 sec and at a sampling frequency of 30 ~ 50 kHz. The higher sampling frequency is used for highly concentrated dispersed flows (i.e. 40~50%).

(8) Experimental measurements are repeated twice for each probe position and flow conditions in order to obtain better measurement accuracy and reduce the experimental errors, and the average values are then used for further analysis.

Two single-fibre 1-D velocity probes were employed, namely a Dantec 55R14 probe with 1.25 mm long sensor and a TSI 1276-10AW subminiature probe with 0.25 mm long sensor. The conditions used in the experiments are listed in Table 6.1. Here, Re_{oil} and Re_{water} are the Reynolds numbers calculated for the given velocity assuming the physical properties of the oil and water phases, respectively.

Table 6.1: Experimental conditions on turbulence structure studies.

U_{mix} (m/s)	Flow Direction	Sampling Location*	Probe(s)	Re_{oil} & Re_{water}
1.0	Upward	58*D*	Dantec & TSI	5520 & 38000
1.5	Upward	58*D*	Dantec & TSI	8280 & 57000
1.5	Downward	58*D*	Dantec	11040 & 76000
2.0	Downward	58*D*	Dantec	13800 & 95000
3.0	Horizontal	182*D*	Dantec	16560 & 114000
3.5	Horizontal	182*D*	Dantec	19320 & 133000

*: Value indicates the relative distance from the inlet of the test section where *D* is the pipe internal diameter.

6.2 Single-phase Flow Measurements

Before conducting two-phase flow measurements, certain single-phase flow studies were carried out to calibrate the probe, to compare the findings with other published data and to serve as reference for later comparisons with the two-phase flow results. The process of calibrating the hot-film probe with a Pitot tube was introduced in Section 3.3.3. Given the calibration relationship between the velocity and the voltage, the output of HFA is a set of discrete time-history values of instantaneous velocity ($\tilde{U}$) at the pre-set sampling frequency. The mean and turbulence fluctuation velocities can then be calculated from simple statistical analysis, as given by Equations (6-1) and (6-2), respectively:

$$U = \frac{\sum_{i=1}^{N} \tilde{U}(i)}{N} \tag{6-1}$$

$$u = \sqrt{\frac{\sum \tilde{U}^2 - \frac{(\sum \tilde{U})^2}{N}}{N-1}} \tag{6-2}$$

where U is the average axial velocity, u is the axial velocity fluctuation and N is the number of sampling data.

The radial profiles of the measured mean axial velocity (U) for the cases listed in Table 6.1, normalized to the mean axial velocity at the pipe centreline (U_c), are presented in Figures 6.1 a & b for pure oil and water flows, respectively. The experimental data are also compared with the empirical correlation for fully developed turbulent flow in smooth pipes which is assumed to follow the $1/7^{th}$ power law curve, as expressed by Equation (6-3):

$$\frac{U(r)}{\overline{U}} = \frac{60}{49}\left(1 - \frac{r}{R}\right)^{1/7} \tag{6-3}$$

where $U(r)$ is the local velocity at radius r, $\overline{U}$ is the average flow velocity in a pipe and R is the pipe radius. As can be seen in Figure 6.1, the mean velocity data obtained in both single-phase water and oil flows are in fairly good agreement with the empirical correlation. This agreement also supports the choice of the operational methods as described in Section 6.1.

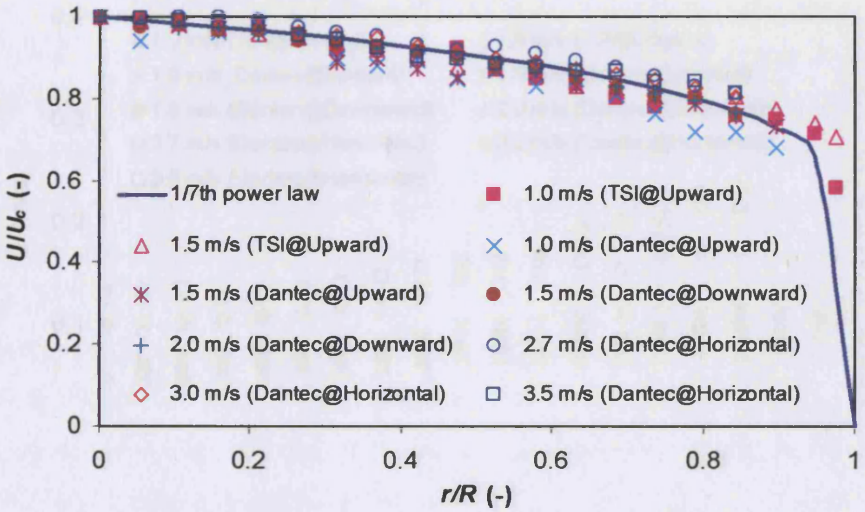

(a)

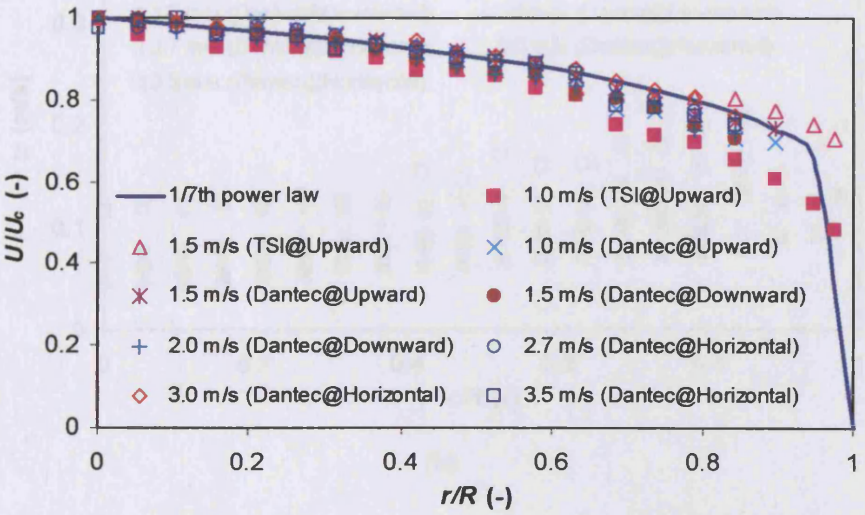

(b)

Figure 6.1: Radial profiles of the average axial velocity (U), normalized to the velocity at pipe centre (U_c), in single-phase flows compared with the 1/7th Power law curve, (a) water flow and (b) oil flow.

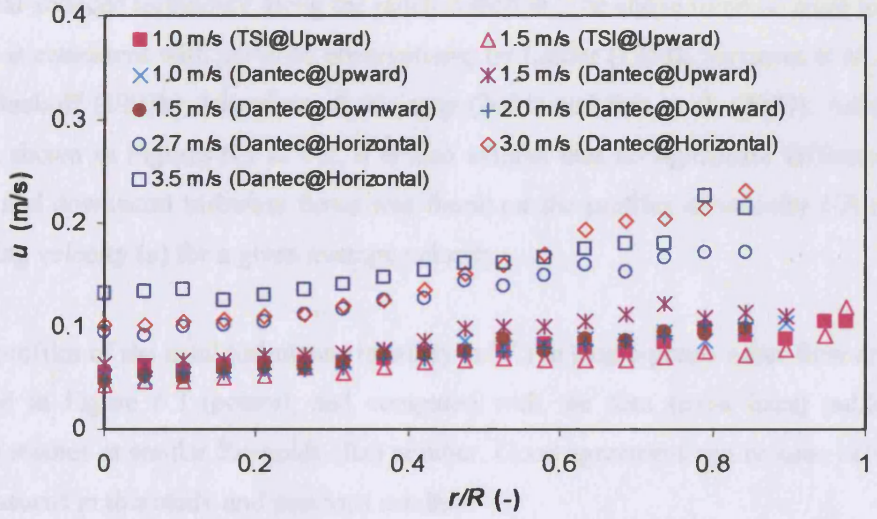

(a)

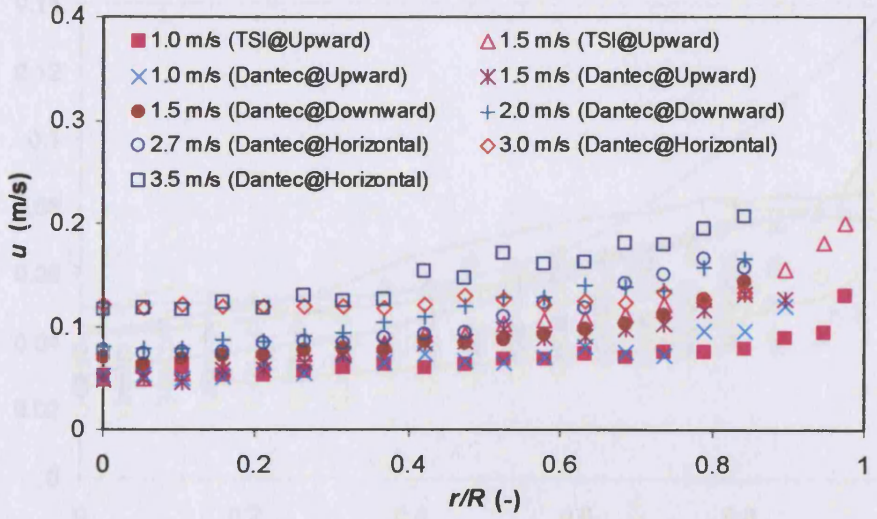

(b)

Figure 6.2: Radial profiles of axial fluctuation velocity (u) in single-phase flows, (a) water flow and (b) oil flow.

Figure 6.2 illustrates the radial profiles of the axial fluctuation velocity (u) obtained at different flow conditions. The experimental data for both single-phase water and oil flows indicate that the flows have large velocity fluctuations at the wall area. For a given radial position r, the axial fluctuation velocity is found to increase with the mixture velocity. The results in Figure 6.2 suggest that the axial turbulence level decreases gradually from the wall

area to the pipe centre where a minimum value is found, which indicates a dissipation of the wall-shear-induced turbulence along the radial direction. The above trend on axial turbulence velocity is consistent with previous observations, by Laufer (1954), Serizawa et al. (1975b), Liu & Bankoff (1993b), Iskandrani & Kojasoy (2001) and Sun et al. (2004). According to the data shown in Figures 6.1 & 6.2, it is also evident that no significant difference in the upward and downward turbulent flows was found on the profiles of velocity (U) and axial fluctuating velocity (u) for a given average velocity.

The profiles of the axial turbulence intensity (u/U_c) in single-phase water flow are further presented in Figure 6.3 (points), and compared with the data (solid lines) published by previous studies at similar Reynolds (Re) number. Good agreement can be seen between the data measured in this study and previous results.

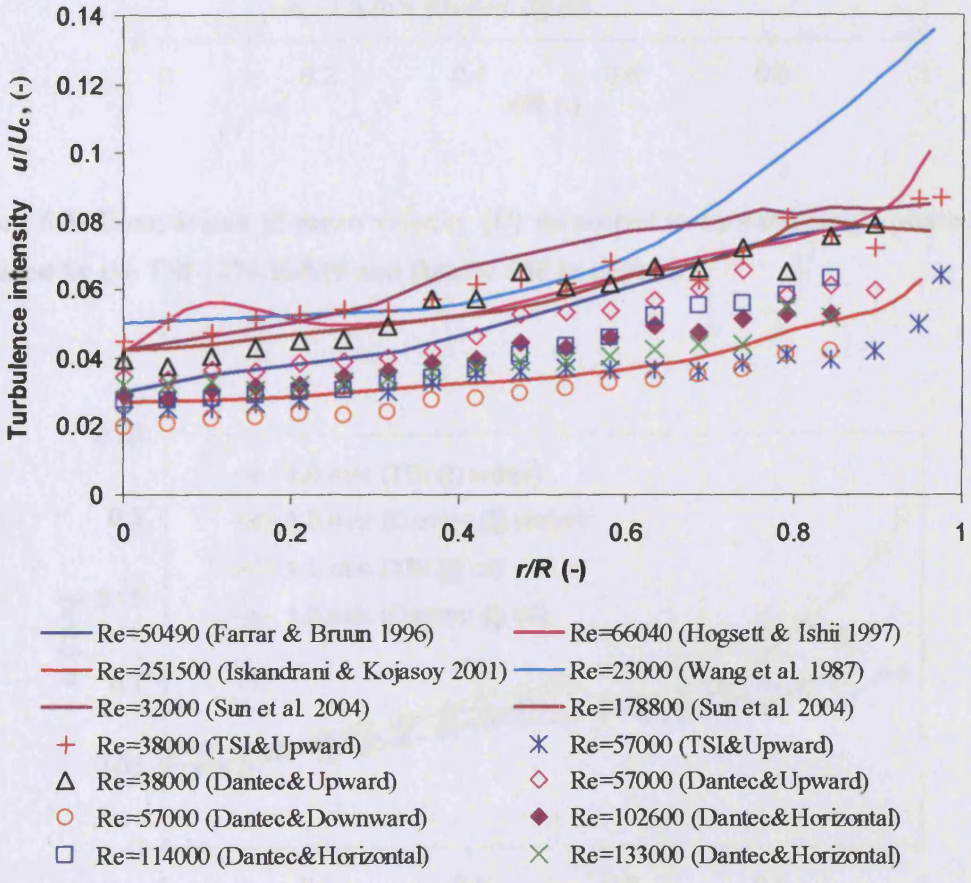

Figure 6.3: Profiles of the axial turbulence intensity (u/U_c) in single-phase water flows compared with published data in similar conditions.

Figures 6.4 and 6.5 illustrate the mean and turbulent velocities, respectively, obtained by the Dantec 55R14 and TSI 1276-10AW probes in single-phase water or oil upward flows. As can be seen, the results between the two probes are in good agreement. Due to its small size, the TSI 1276-10AW probe could be located closer to the wall and data obtained from that region.

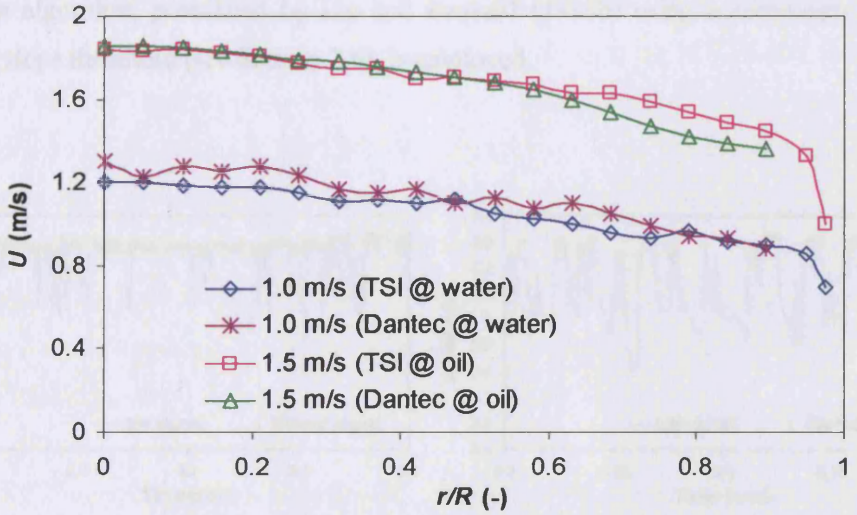

Figure 6.4: Comparison of mean velocity (U) measured in upward single-phase flows obtained by the TSI 1276-10AW and Dantec 55R14 probes.

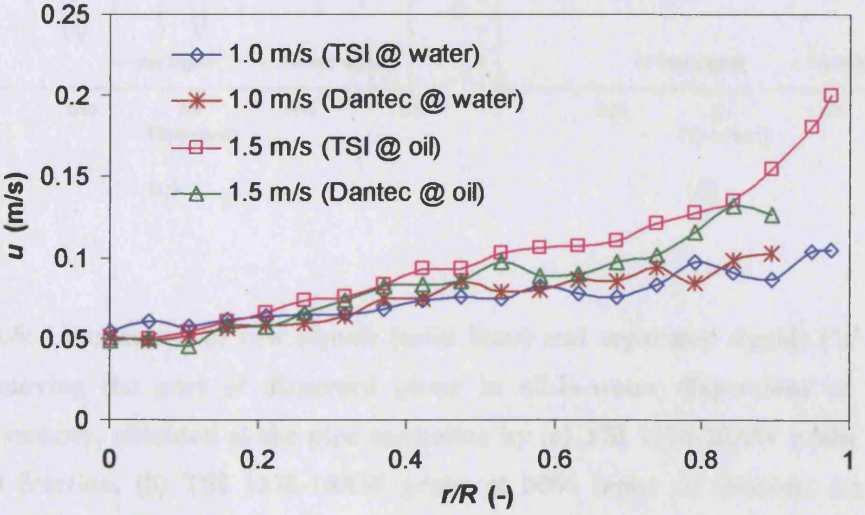

Figure 6.5: Comparison of turbulent velocity (u) measured in upward single-phase flows obtained by the TSI 1276-10AW and Dantec 55R14 probes.

6.3 Signal Processing

As described in Section 2.6, measuring turbulence structure of the continuous liquid in two-phase flows with the hot-film anemometer requires a precise signal separation process, so that the sections corresponding to the dispersed fluid in the output signals can be removed and only leave the part indicating the continuous phase for analysis. In this study, the signal separation algorithm, postulated by Liu and Bankoff (1993b) using a combination of the level and slope threshold (see Section 2.6), is employed.

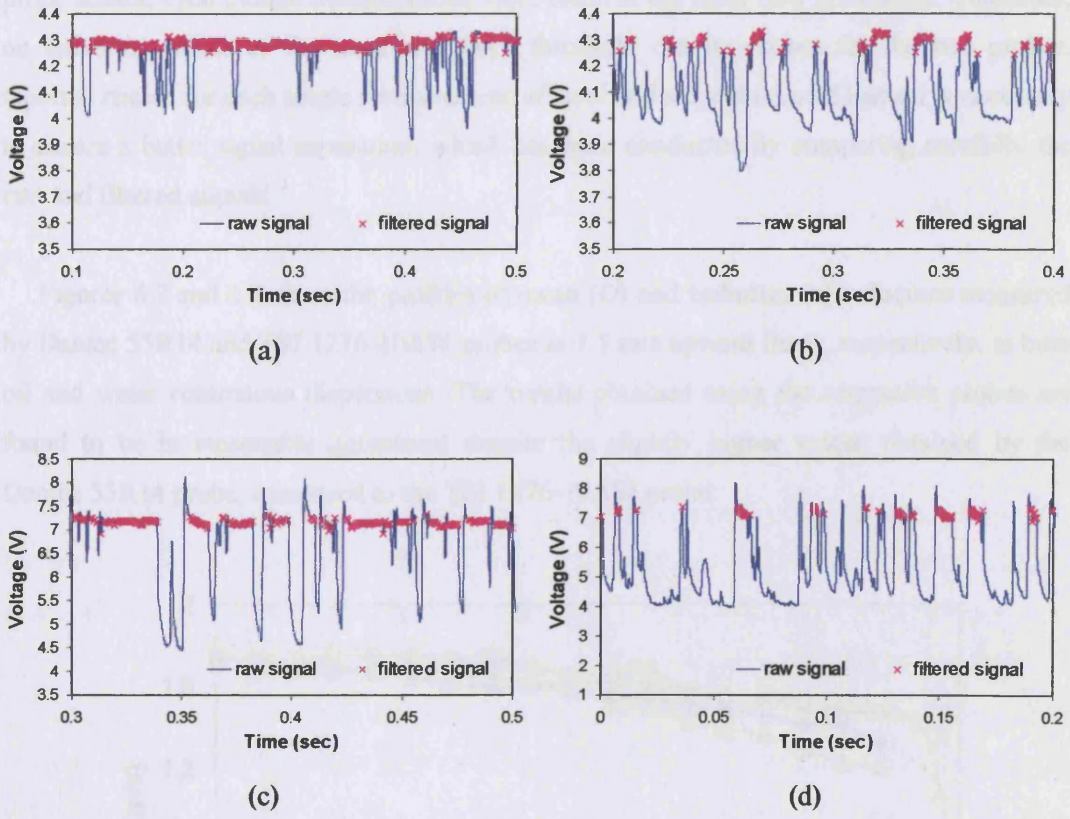

Figure 6.6: Comparison of raw signals (solid lines) and separated signals ('x' marks) after removing the part of dispersed phase in oil-in-water dispersions at 1.5 m/s mixture velocity, obtained at the pipe centreline by (a) TSI 1276-10AW probe at 20% input oil fraction, (b) TSI 1276-10AW probe at 50% input oil fraction, (c) Dantec 55R14 probe at 20% input oil fraction, (d) Dantec 55R14 probe at 50% input oil fraction.

Figure 6.6 shows the processed signals after filtering the dispersed phase and the raw output signals, obtained at the pipe centreline from 1.5 m/s upward flow at 20% (a&c) and 50% (b&d) input oil fractions with TSI 1276-10AW (a&b) and Dantec 55R14 (c&d) probes. Here, the dispersed phase (oil) is expected to give lower voltage due to its lower heat transfer capacity than the continuous phase (water), and produce 'spikes' as a result in the output signals that are to be eliminated. As can be seen, the algorithm employed works generally well for the two different probe type and can effectively identify the dispersed phase section for all conditions, even at highly concentrated dispersions (such as 50%, Figure 6.6 b&d). It should also be noted that, as shown in Figure 6.6, the Dantec 55R14 probe is more likely to have overshoot effects than the TSI 1276-10AW probe when an oil drop detaches from the probe sensor, even though measurements were taken at the same flow conditions. Therefore, no universal values of the level and slope threshold can be chosen for the two probes. Optimal choice for each single measurement of level and slope threshold instead is necessary to ensure a better signal separation, which has been conducted by comparing carefully the raw and filtered signals.

Figures 6.7 and 6.8 show the profiles of mean (U) and turbulent (u) velocities measured by Dantec 55R14 and TSI 1276-10AW probes in 1.5 m/s upward flows, respectively, at both oil and water continuous dispersions. The results obtained using the respective probes are found to be in reasonable agreement despite the slightly higher values obtained by the Dantec 55R14 probe, compared to the TSI 1276-10AW probe.

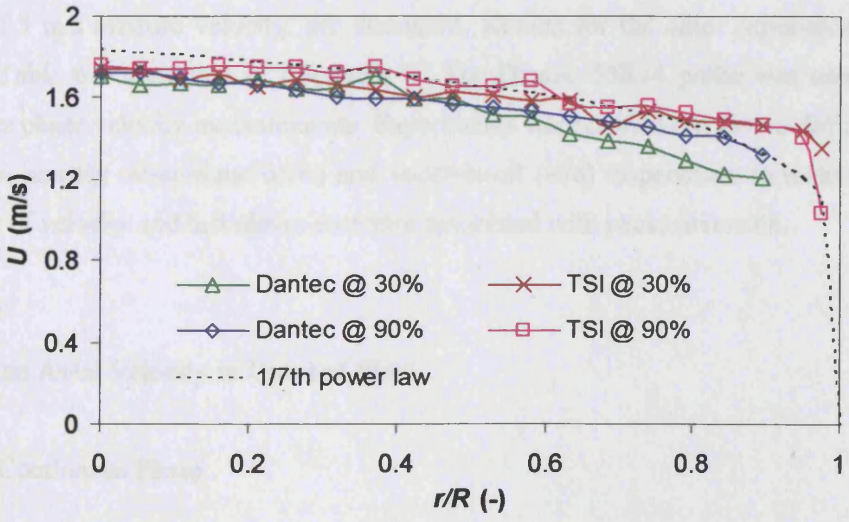

Figure 6.7: Axial mean velocity (U) profiles obtained by Dantec 55R14 and TSI 1276-10AW probe at 1.5 m/s mixture velocity in o/w (30%) and w/o (90%) upward flows.

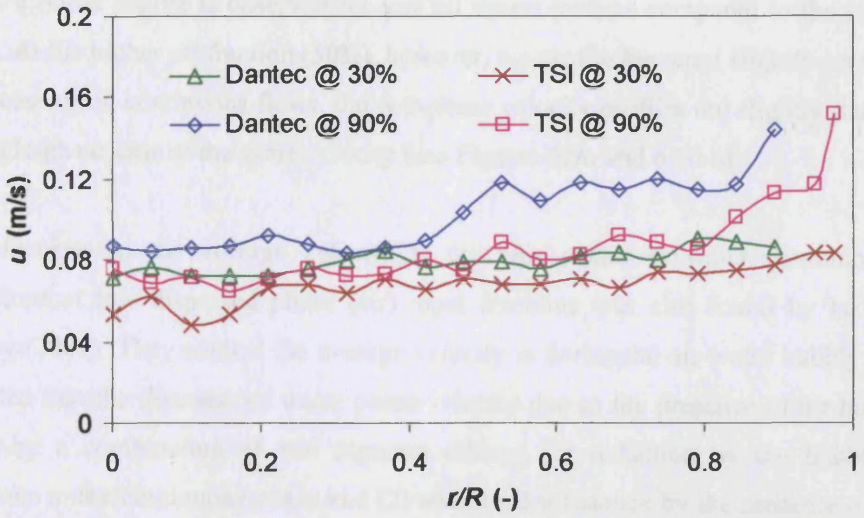

Figure 6.8: Axial turbulent velocity (u) profiles obtained by Dantec 55R14 and TSI 1276-10AW probe at 1.5 m/s mixture velocity in o/w (30%) and w/o (90%) upward flows.

6.4 Mean and Turbulence Velocity Profiles in O/W and W/O Dispersions

In this Section, the average axial velocity profiles of continuous and dispersed phases and the fluctuating velocity of the continuous phase, obtained in vertical upward and downward flows at 1.5 m/s mixture velocity, are discussed. Results for the other experimental cases listed in Table 6.1 are given in Appendix B. The Dantec 55R14 probe was used for the continuous phase velocity measurements. Experiments were carried out in two different flow conditions, namely oil-in-water (o/w) and water-in-oil (w/o) dispersions, to understand the behaviour of velocity and turbulence structure associated with phase inversion.

6.4.1 Mean Axial Velocity in Upward Flow

6.4.1.1 Continuous Phase

Figures 6.9 and 6.10 illustrate the radial profiles of actual velocity (U) and relative velocity (U/U_c), respectively, at 1.5 m/s mixture velocity and a range of input oil fractions. As can be seen, the introduction of the second phase has only a small effect on the profiles of

mean continuous phase velocity. In the case of water continuous flows (Figures 6.9a and 6.10a), a flatter profile is observed for low oil concentrations compared to the single-phase values. At the higher oil fraction (50%), however, the profile becomes slightly centre peaked. In the case of oil continuous flows, the two-phase velocity profiles are slightly flatter than in the single-phase case at the same velocity (see Figures 6.9b and 6.10 b).

A decrease in the average velocity at the pipe centre in water continuous bubble dispersions at low dispersed phase (air) input fractions was also found by Iskandrani & Kojasoy (2001). They studied the average velocity in horizontal air-water bubbly flows and suggested that the decrease of water phase velocity due to the presence of air bubbles was caused by a combination of two separate effects: (1) reduction by the bubble-induced turbulence to the continuous phase and (2) additional resistance by the presence of the large population of bubbles. They also reported that in air-water upward bubbly flows, the higher bubble concentration near the wall tends to increase the liquid velocity, as shown by Wang et al. (1987), which seems to contradict their second suggestion. In the present studies, more oil drops are in the pipe centre (as shown in Section 5.2.1.3) which could increase the local velocity of the carrier fluid. Because of the reduced buoyancy effect in oil-water flows and the small amount of oil drops present at these oil fractions, this effect may not be as significant. The continuous phase velocity is therefore possibly decreased because of the drop turbulent fluctuations following the first suggestion by Iskandrani & Kojasoy (2001).

For the water continuous cases shown in Figure 6.9a, the velocity profiles are found to become slightly more centre-peaked with further increase in the input oil fraction. The increased concentration of oil drops at the pipe centre relative to that close to the wall (as shown in Section 5.2.1.3), combined with the effect of buoyancy, would have contributed to this. This profile change agrees with the findings of a number of investigations, i.e. by Liu & Bankoff (1993a) in air-water upward flow at low liquid velocity, Sun et al. (2004) in air-water upward flow and Farrar & Bruun (1996) in kerosene-water upward flow; however, it is in contrast to some observations in air-water upward flows. Thus, Liu & Bankoff (1993a) found an opposite tendency at high liquid velocity and Wang et al. (1987) found that the maximum liquid velocity could occur away from the pipe centreline at high gas velocity. According to Farrar and Bruun (1996), the reasons for this centre peaked behaviour may be that, in oil-in-water flows, many drops in the centre region are much larger than in the wall region (a centre peak holdup and drop size profile can also be found, see Section 5.2.1.3). Large oil drops at the pipe centre would travel at a higher velocity and cause the carrier fluid to move faster due to drop-induced drag. This does not necessarily happen in air-water upward flows where the bubble size profiles can be fairly uniform over most of the pipe

cross-section (Wang et al., 1987). In fact, maxima in dispersed phase size and holdup near the wall have been observed (Liu & Bankoff, 1993b) which could explain the higher continuous phase velocities away from the pipe centre.

A decrease of the average velocity at the pipe centre and a flatter profile, on the other hand, is always seen in oil continuous dispersions (Figure 6.9b). Buoyancy effect as well as reduction of the velocity by the fluctuation of the drops, as suggested by Iskandrani & Kojasoy (2001), would contribute to this.

The changes on velocity profiles at different input oil fractions observed in this study were found to be less significant than those reported by Farrar & Bruun (1996) in their kerosene-water system. This is probably due to the low velocity used in their experiments (~0.6 m/s), which would result in flow transition from bubbly to cap bubbly to churn flow as the input oil fraction increases. In the present study, fully dispersed flow is maintained at all oil fractions used.

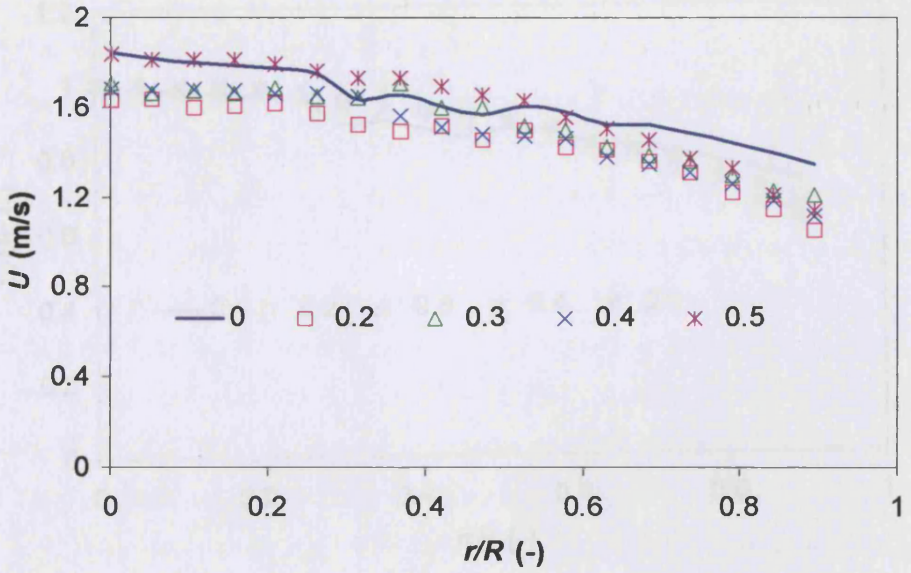

(a) o/w

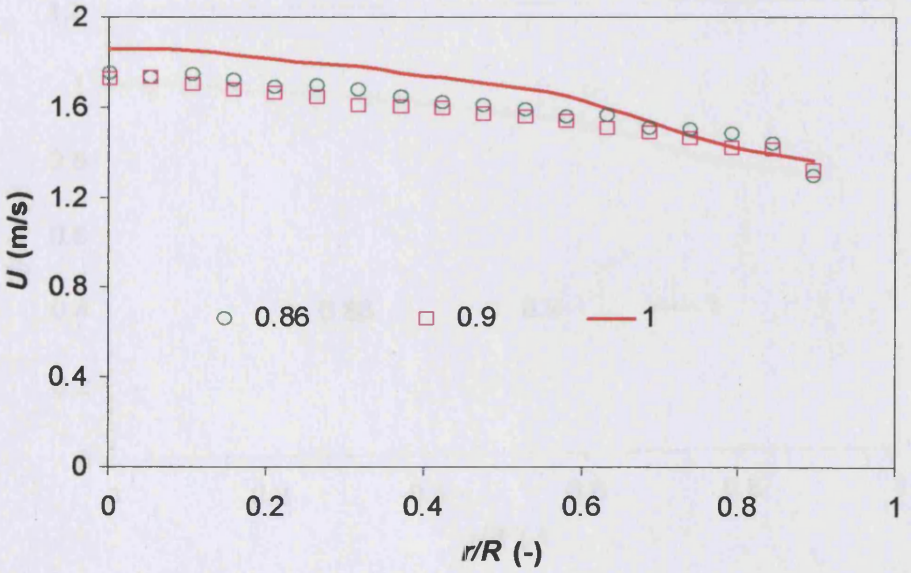

(b) w/o

Figure 6.9: Mean axial velocity (*U*) profiles of the continuous phase at different input oil fractions measured with Dantec 55R14 probe at 1.5 m/s mixture velocity in upward flow. (a): water continuous, (b): oil continuous.

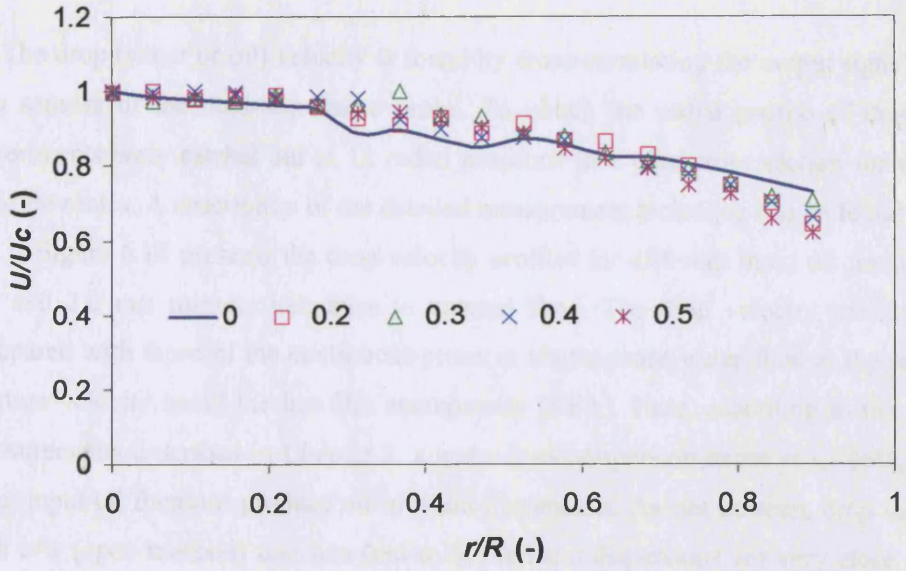

(a) o/w

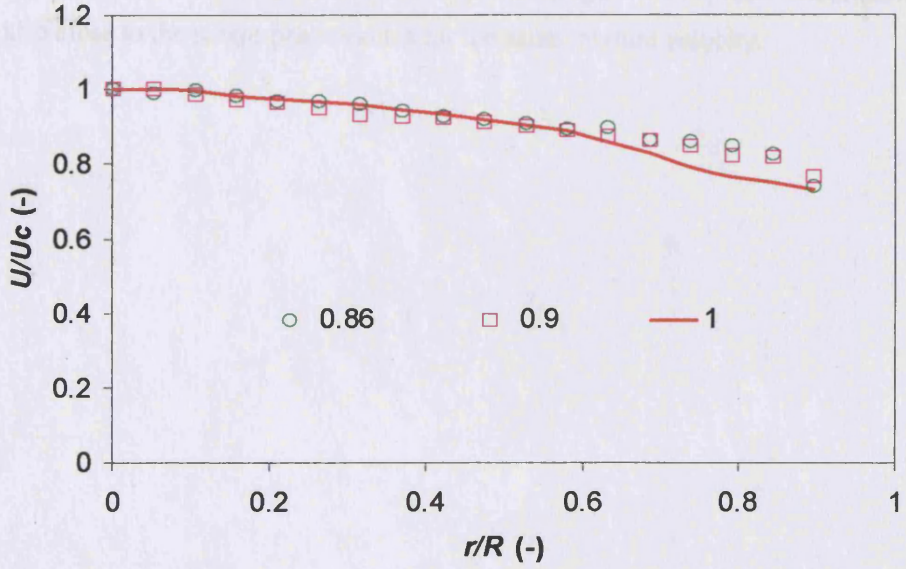

(b) w/o

Figure 6.10: Relative mean axial velocity (U/U_c) profiles of the continuous phase at different input oil fractions measured with Dantec 55R14 probe at 1.5 m/s mixture velocity in upward flow. (a): water continuous, (b): oil continuous.

6.4.1.2 Dispersed Phase

The drop (water or oil) velocity is found by cross-correlating the output signals from the two sensors of the dual-impedance probe. To obtain the radial profile of drop velocity, experiments were carried out at 12 radial positions in a pipe cross section for each set of fluid flowrates. A description of the detailed measurement technique can be found in Section 3.2.1. Figure 6.11 presents the drop velocity profiles for different input oil fractions (ϵ_o) at 1.5 and 2.0 m/s mixture velocities in upward flow. The drop velocity profiles are also compared with those of the continuous phase in single-phase water flow at the same as the mixture velocity using the hot-film anemometer (HFA). Here, according to the continuity measurements described in Chapter 5, a water-in-oil dispersion exists at ϵ_o=86%, while the other input oil fractions produce oil-in-water dispersions. As can be seen, drop velocities in both o/w (open markers) and w/o (red-solid markers) dispersions are very close. A centre-peaked profile is obtained in this study, which is similar to those reported in gas-liquid systems (Liu & Bankoff, 1993b, Farrar & Bruun, 1996). Moreover, the drop velocity profiles are found to match fairly well the single-phase profile, in particular at the higher mixture velocity of 2.0 m/s. It appears that because of the small density difference between the phases, both continuous (Figure 6.9) and dispersed (Figure 6.11) phase velocities are similar and also close to the single-phase values for the same mixture velocity.

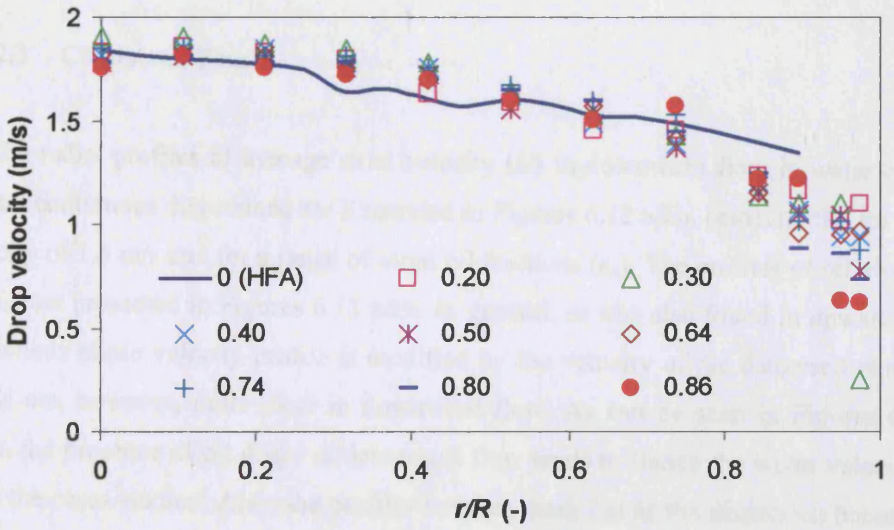

(a) 1.5 m/s

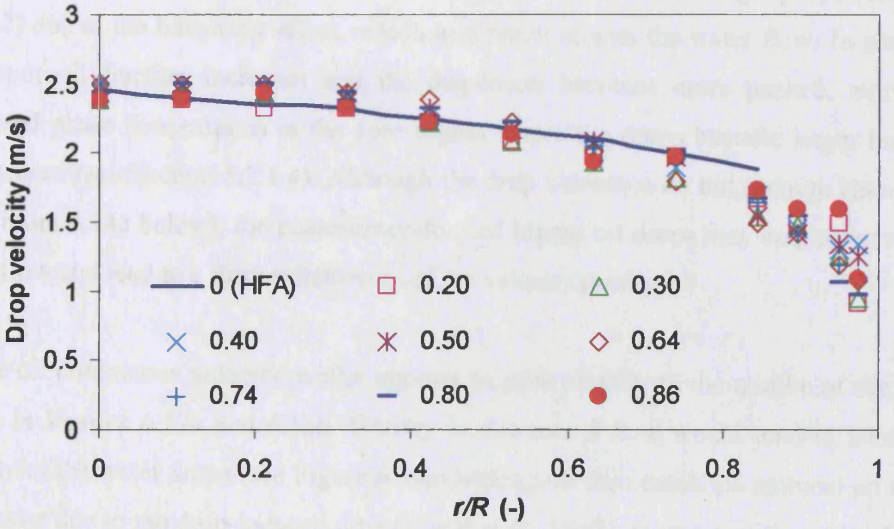

(b) 2.0 m/s

Figure 6.11: Mean axial velocity (U_{drop}) profiles of the dispersed phase at different input oil fractions measured with the dual-impedance probe at (a) 1.5 and (b) 2.0 m/s mixture velocity in upward flow, in comparison with the single-phase velocity profile at the same as the mixture velocity obtained by the HFA. The open marks denote water continuous and the red-solid marks denote oil continuous flow.

6.4.2 Mean Axial Velocity in Downward Flow

6.4.2.1 Continuous Phase

The radial profiles of average axial velocity (U) in downward flow in water continuous and oil continuous dispersions are illustrated in Figures 6.12 a&b, respectively, for a mixture velocity of 1.5 m/s and for a range of input oil fractions (ϵ_o). The profiles of relative velocity (U/U_c) are presented in Figures 6.13 a&b. In general, as was also found in upward flow, the continuous phase velocity profile is modified by the velocity of the dispersed phase. Some trends are, however, more clear in downward flow. As can be seen in Figures 6.12a and 6.13a, the presence of oil drops in downward flow tends to flatten the water velocity profile in all the cases studied. Also, the profiles become more flat as the dispersion becomes more concentrated. This behaviour in downward flow seems to be different from the findings in upward flow, as shown in Section 6.4.1, which suggested that the velocities in upward flow are flattened first and then change to centre peaked as the input oil fraction increases. This could be because the oil drops move noticeably slower than the single-phase (see Section 6.4.2.2) due to the buoyancy effect, which as a result retards the water flow. In addition, as the input oil fraction increases and the dispersion becomes more packed, more of the dispersed phase concentrates in the core region where the drops become larger because of coalescence (see Section 5.2.1.4). Although the drop velocities do not seem to change much (see Figure 6.14a below), the coalescence-formed bigger oil drops may counteract more the water flow and lead to a further flattening of the velocity profile.

The oil continuous velocity profile appears to peak slightly in the middle of the pipe, as shown in Figures 6.12b and 6.13b. Gravity in downward flow would tend to increase the velocity of the water drops (see Figure 6.14a) which will then cause the ambient oil phase to flow faster due to the drop-induced drag (Wang et al., 1987). As most of the water drops are in the pipe core region as shown in Section 5.2.1, the oil phase velocity will be affected more in the pipe centre resulting in the centrally peaked profile.

Previous studies in air-water downward flow have suggested that the maximum velocity is likely to occur off the pipe centreline (Wang et al., 1987; Sun et al., 2004). Wang et al. (1987) found a 'chimney effect' in their experimental cases (U_{mix}<1.11 m/s) and attributed this to the void fraction distribution. The high void fraction at the core region tended to retard the liquid flow due to buoyancy, while its effect was less in the wall region where the void fraction is low and the liquid is diverted. Sun et al. (2004) observed this phenomenon only at low velocities (i.e. U_{mix}=0.669 m/s and 1.331 m/s) but not at high ones. They

attributed this off-centreline occurrence of maximum velocity to the liquid velocity depression in the wake region of the bubbles, which becomes less significant at high velocities. However, this characteristic is not seen in the present oil-water downward flows. The reason could be the smaller buoyancy effect in oil-water than in air-water flow as well as the relatively high mixture velocities (i.e. U_{mix} ≥1.5m/s) used in the current study.

6.4.2.2 Dispersed Phase

Figures 6.14 a&b present the drop velocity profiles in downward flow for different input oil fractions (ϵ_o) at 1.5 and 2.0 m/s mixture velocities, respectively; the drop velocities are also compared with the single-phase value at the same as the mixture velocity measured by the HFA. Here, as found in Chapter 5, water-in-oil dispersions are produced in the pipeline for input oil fractions ϵ_o=76% and 80% while all the other fractions result in oil-in-water dispersions. It can be seen from Figures 6.14 a&b that, in downward flow, oil drops in water generally show a flatter velocity profile with smaller values at the pipe core region, compared to water drops in oil and the single-phase profile. This contrasts with the profiles shown in upward flows where there is no obvious difference between o/w and w/o flows (see Figure 6.11 a&b); the velocities of oil drops in all cases are lower than those of water drops. This behaviour is expected based on buoyancy effects. It is also evident that this velocity difference is more pronounced at the lower mixture velocity (i.e. 1.5 m/s, see Figure 6.14a) than at the higher one (2.0 m/s, Figure 6.14b). This behaviour of drop velocity in o/w and w/o vertical downward flows suggests that drop velocity may become another method of identifying phase inversion in systems where gravitational effects cannot be neglected.

The velocities of both water and oil drops in downward flow do not exhibit any obvious centre-peak profile which is also different from upward flow. Instead, the locations of maximum values are sometimes seen to occur off the pipe centreline in the range $0.4<r/R<0.6$.

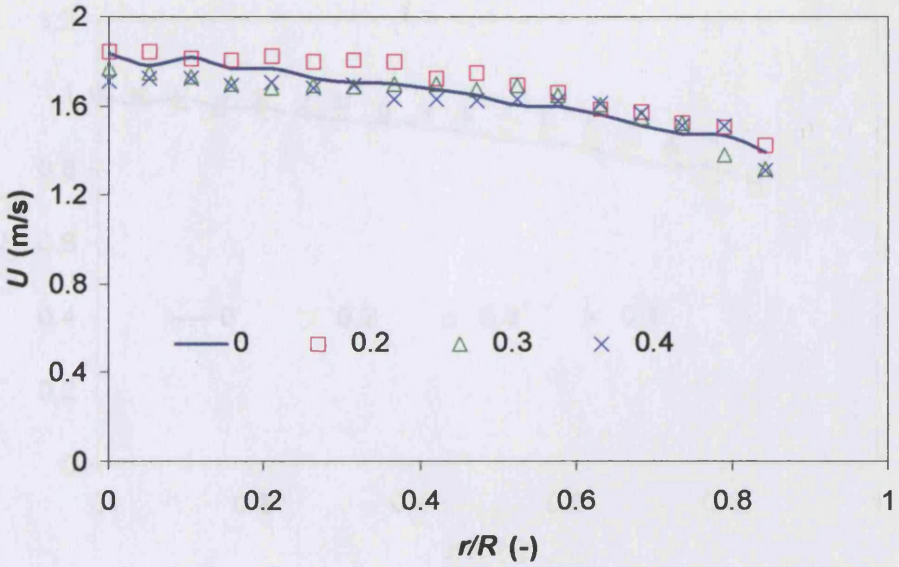

(a) o/w

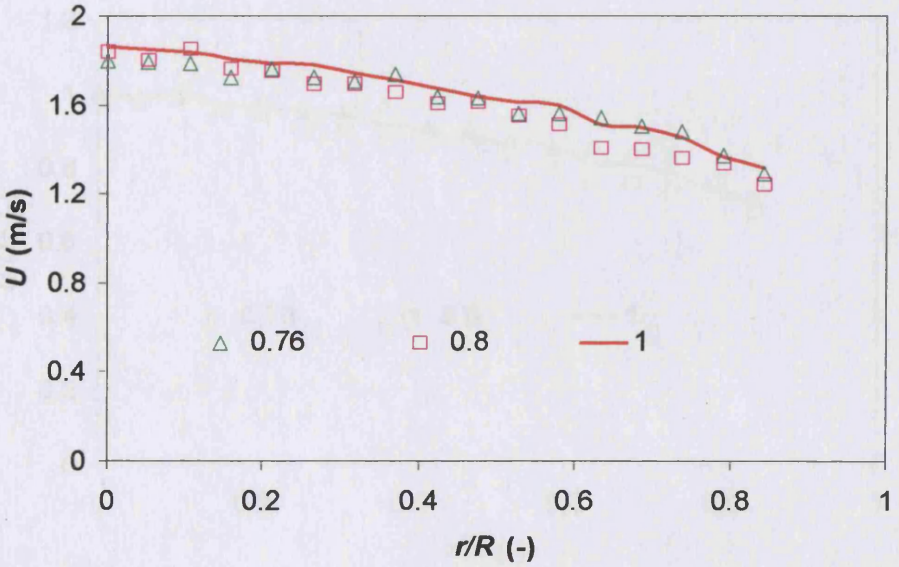

(b) w/o

Figure 6.12: Mean axial velocity (*U*) profiles of the continuous phase at different input oil fractions measured with Dantec 55R14 probe at 1.5 m/s mixture velocity in downward flow. (a): water continuous, (b): oil continuous.

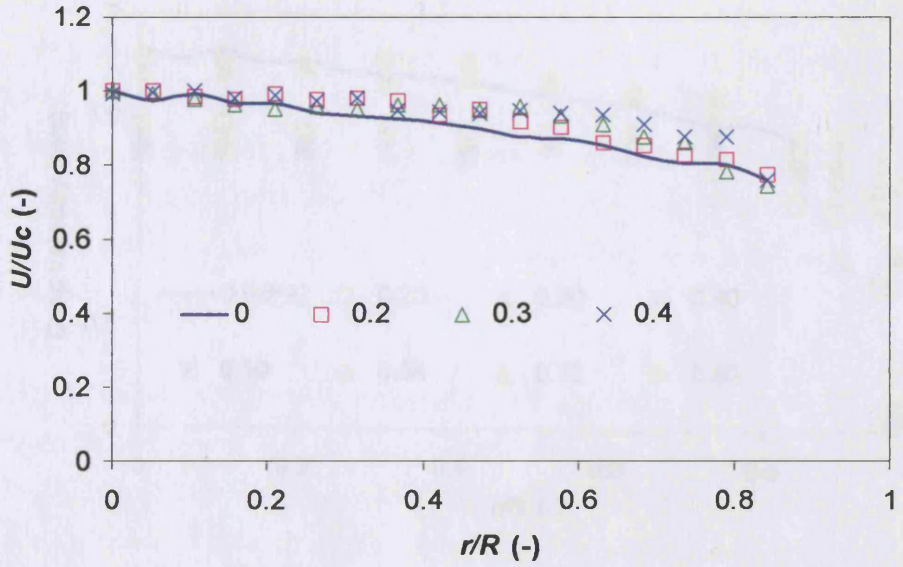

(a) o/w

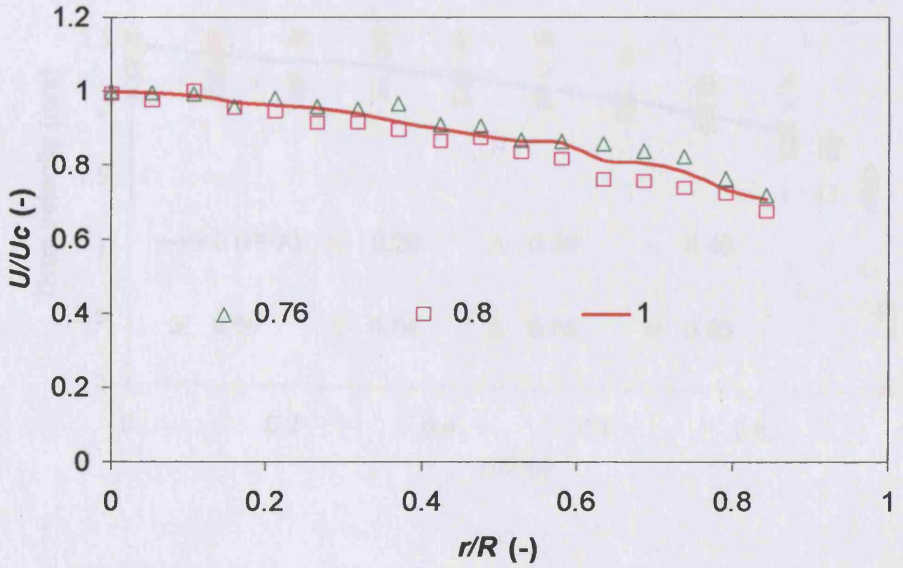

(b) w/o

Figure 6.13: Relative mean axial velocity (U/U_c) profiles of the continuous phase at different input oil fractions measured with Dantec 55R14 probe at 1.5 m/s mixture velocity in downward flow. (a): water continuous, (b): oil continuous.

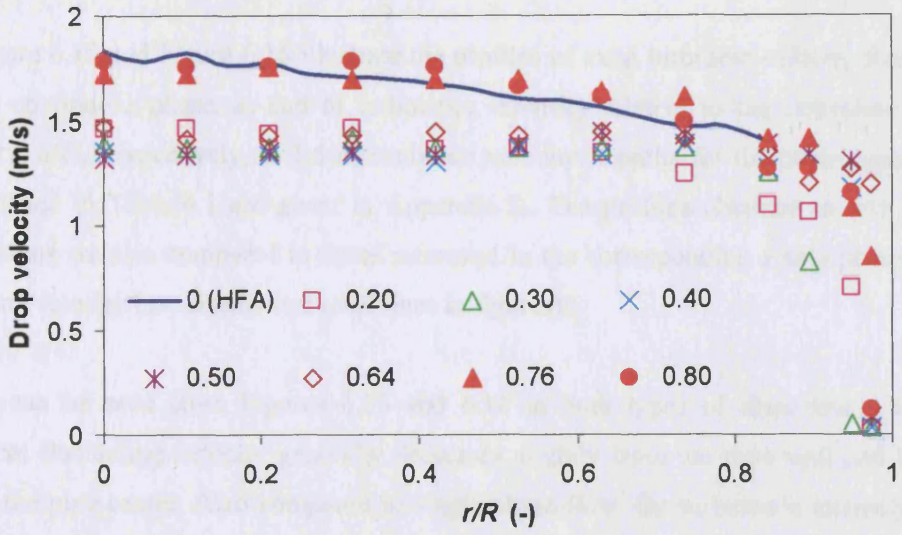

(a) 1.5 m/s

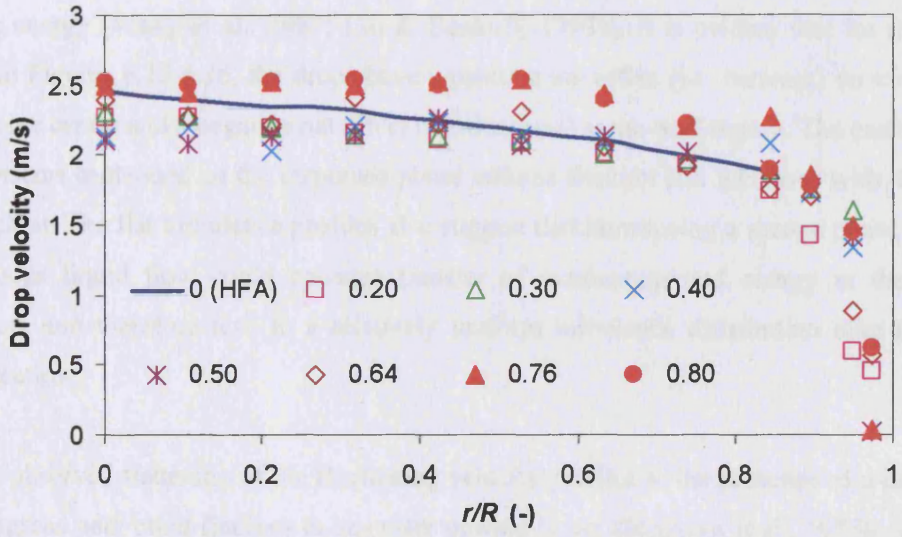

(b) 2.0 m/s

Figure 6.14: Mean axial drop velocity profiles of the dispersed phase at different input oil fractions, measured with the dual-impedance probe at (a) 1.5 and (b) 2.0 m/s mixture velocity in <u>downward</u> flow, in comparison with the single-phase velocity profile at the same as the mixture velocity obtained by the HFA. The open marks denote water continuous and the red-solid marks denote oil continuous flow.

6.4.3 Axial Turbulent Fluctuating Velocity in Upward Flow

Figure 6.15 and Figure 6.16 illustrate the profiles of axial turbulent velocity fluctuations of the continuous phase, u, and of turbulence intensity relative to the centreline average velocity, u/U_c, respectively, at 1.5 m/s mixture velocity. Results for the other experimental cases listed in Table 6.1 are given in Appendix B. The profiles obtained in o/w and w/o dispersions are also compared to those measured in the corresponding single-phase flow at the same velocity (see continuous solid lines in figures).

As can be seen from Figures 6.15 and 6.16 in both types of dispersions, the axial turbulent fluctuating velocity generally decreases slightly from the pipe wall and becomes flat at the pipe centre. Also compared to single-phase flow, the turbulence intensity profile becomes generally flatter when the second phase is introduced. This flattering is more pronounced as the input oil fraction increases. In the pipe centre region, the turbulence level is increased by the presence of dispersed drops for both water continuous and oil continuous dispersions. As the dispersed drops in turbulent two-phase flow can enhance both dissipation (e.g. by absorbing energy) and production (e.g. by bubble-induced turbulence) of turbulent kinetic energy (Wang et al., 1987; Liu & Bankoff, 1993a), it is evident that for the cases given in Figures 6.15-6.16, the drops have a positive net effect (i.e. increase) on turbulence at the pipe centre and a negative net effect (i.e. decrease) at the wall region. The extent of the effect seems to depend on the dispersed phase volume fraction and increases with the input oil fraction. The flat turbulence profiles also suggest that introducing a second phase into the continuous liquid flow could enhance transfer of momentum and energy in the lateral direction, and therefore lead to a relatively uniform turbulence distribution over the pipe cross-section.

The observed flattening of the fluctuating velocity profiles in the presence of a dispersed phase agrees with other findings in air-water upward flows (Serizawa et al., 1975b; Wang et al., 1987; Liu & Bankoff, 1993a; Sun et al. 2004) and in oil-water upward flow (Farrar & Bruun, 1996). However, in oil-water flows, Farrar & Bruun (1996) reported that the turbulent fluctuating velocity profiles change to be centreline peaked at high dispersed phase fraction (see Figure 2.6d), which they attributed to the flow pattern transition from bubbly to cap flow. Sun et al. (2004) also observed a higher turbulence fluctuation in air-water upward flows in the whole pipe cross-section than in single-phase flow and attributed this to the relative large drop sizes in their system. As dispersed flow with relatively small droplets is always obtained in the present experiments, it is therefore not surprising that their observations are not found here.

Another interesting phenomenon in pipeline flow is the reduction of frictional pressure gradient compared to single-phase flow, known as drag reduction, when another phase (e.g. polymer or dispersed phase) is introduced into the initial single-phase flow. It has been suggested that drag reduction may be due to the interference with the continuous phase turbulent structure of the additives or the second phase, which somehow absorb energy bursts from the near-wall region and reduce the transport of both vorticity and momentum to the pipe core (Wilson, 1989). Pal (1993) further suggested that in liquid-liquid pipeline flow, the breakage and coalescence of dispersed drops is responsible for drag reduction, as they will promote turbulent energy dissipation. According to the above suggestions, it could be inferred that the near-wall turbulence can influence drag reduction. Drag reduction, observed in the current oil-water pipeline flows (as discussed in Section 5.2.1.2), may be seen as a result of the damping of turbulence at the wall region (see Figure 6.15a&b) in both o/w and w/o dispersions.

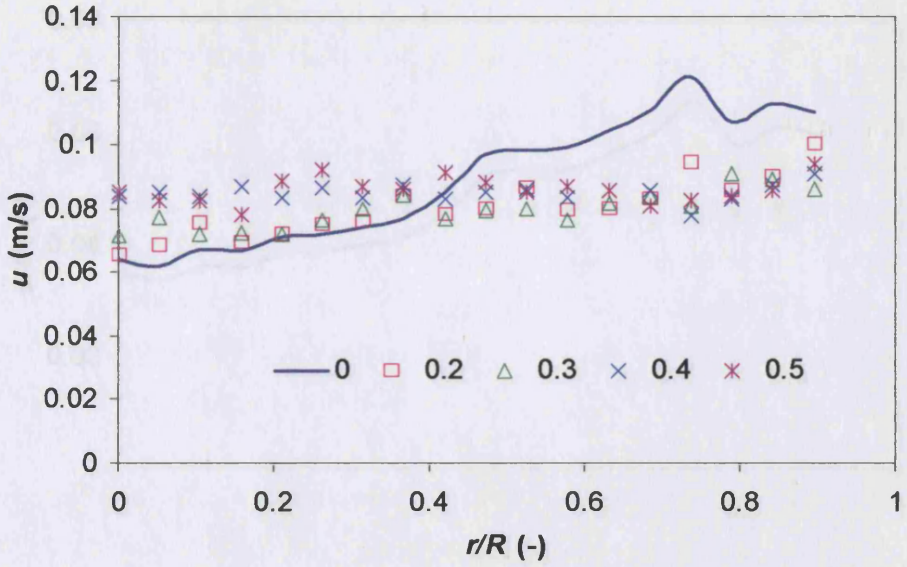

(a) o/w

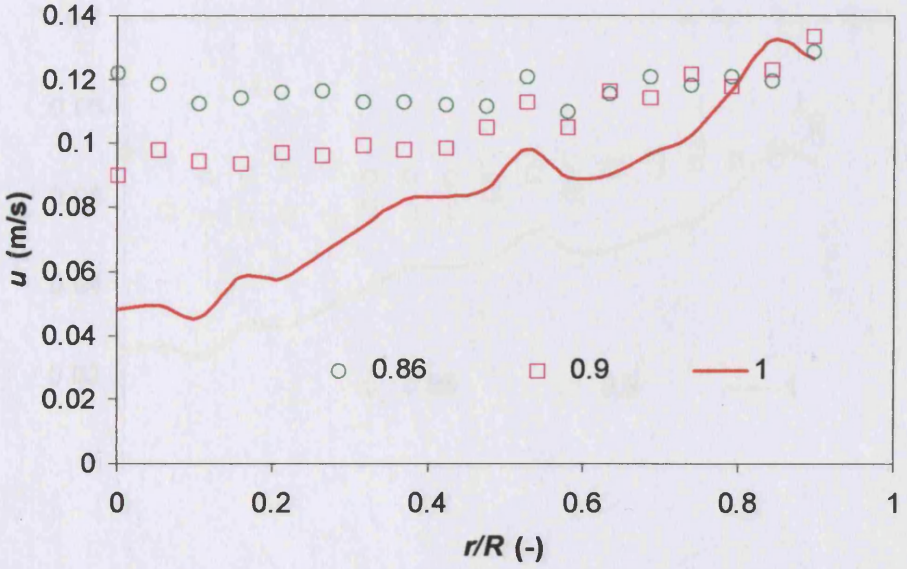

(b) w/o

Figure 6.15: Axial turbulent fluctuating velocity (u) profile of the continuous phase at different input oil fractions measured with Dantec 55R14 probe at 1.5 m/s mixture velocity in upward flow. (a): water continuous, (b): oil continuous.

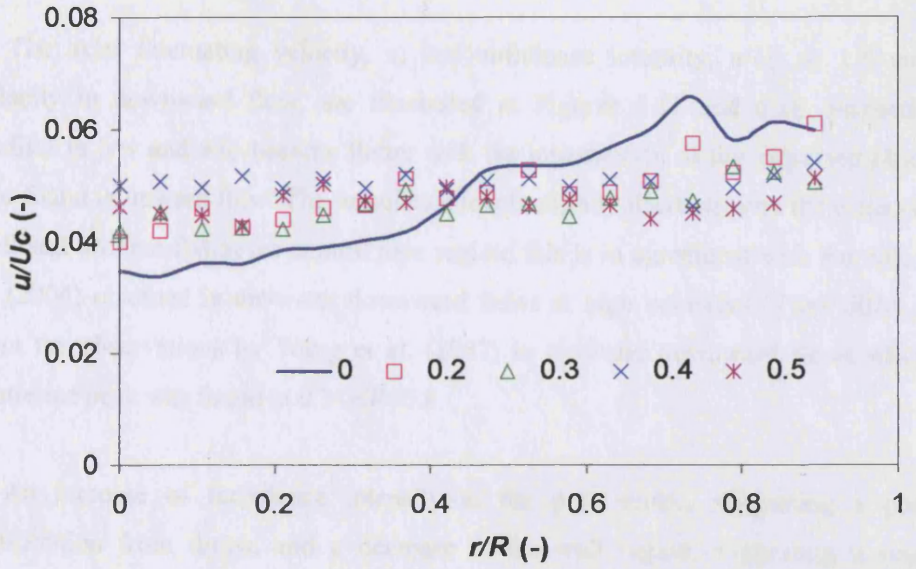

(a) o/w

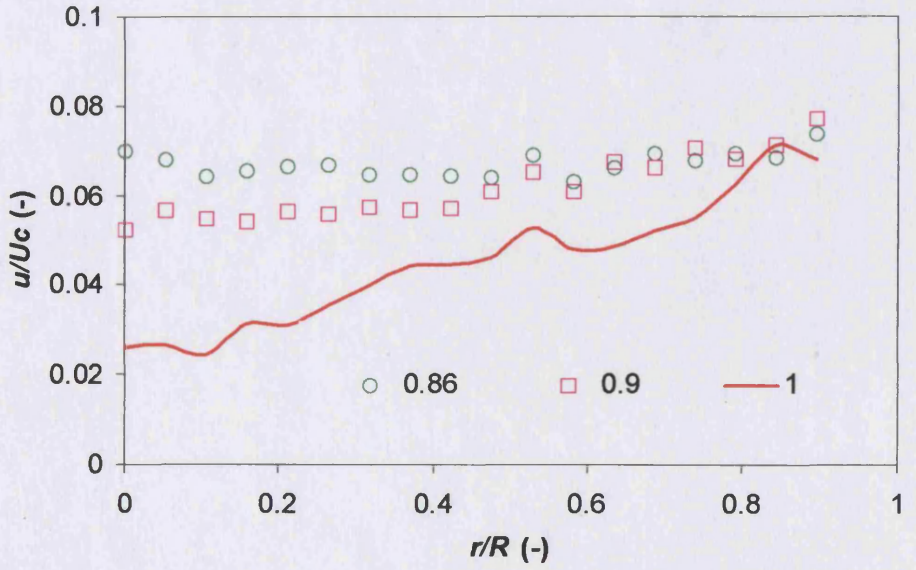

(b) w/o

Figure 6.16: Axial turbulent intensity (u/U_c) profiles of the continuous phase at different input oil fractions measured with Dantec 55R14 probe at 1.5 m/s mixture velocity in upward flow. (a): water continuous, (b): oil continuous.

6.4.4 Axial Turbulent Fluctuating Velocity in Downward Flow

The axial fluctuating velocity, u, and turbulence intensity, u/U_c, at 1.5 m/s mixture velocity in downward flow, are illustrated in Figures 6.17 and 6.18, respectively. The profiles in o/w and w/o become flatter with the introduction of the dispersed phase; as was also found in upward flow. The turbulence levels slightly decrease with the distance from the wall and become flat at the central pipe region; this is in agreement with the data by Sun et al. (2004) obtained in air-water downward flows at high velocities. They differ, however, from the observations by Wang et al. (1987) in air-water downward flows where an off-centreline peak was found at $0.7<r/R<0.8$.

An increase of turbulence intensity at the pipe centre, suggesting a positive net contribution from drops, and a decrease at the wall region, suggesting a negative net contribution, can be seen in Figures 6.17 and 6.18. As in upward flow, drops at the pipe centre in downward flow seem to enhance turbulence while they suppress it at the wall region. In addition, according to the results in Sections 6.4.3 and 6.4.4, no significant differences on the shape of turbulence intensity profiles for o/w and w/o dispersions can be seen between upward and downward flows.

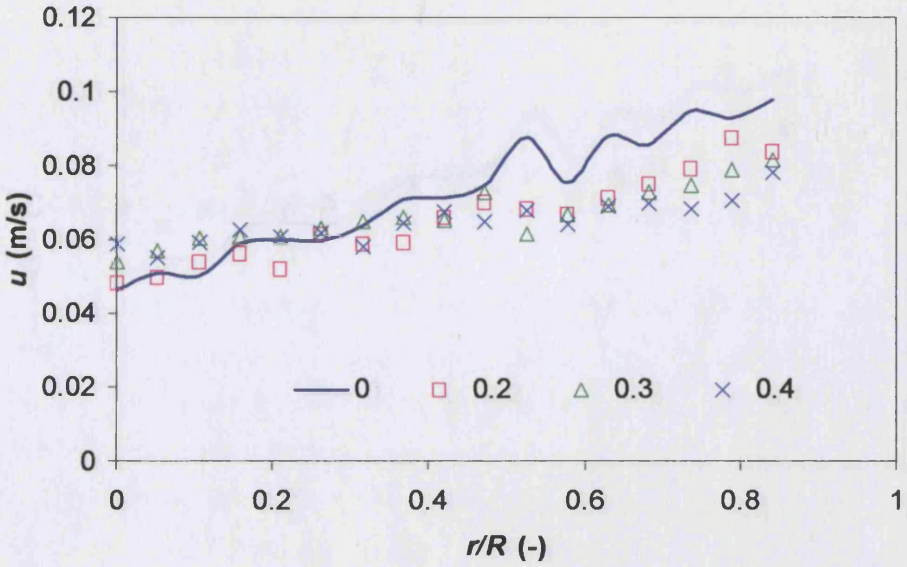

(a) o/w

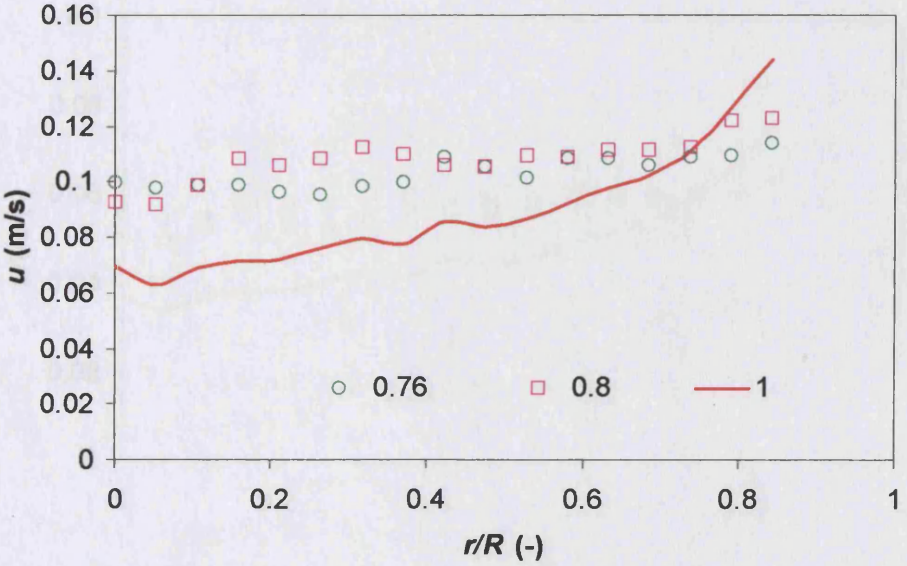

(b) w/o

Figure 6.17: Axial turbulent fluctuating velocity (u) profiles of the continuous phase at different input oil fractions measured with Dantec 55R14 probe at 1.5 m/s mixture velocity in downward flow. (a): water continuous, (b): oil continuous.

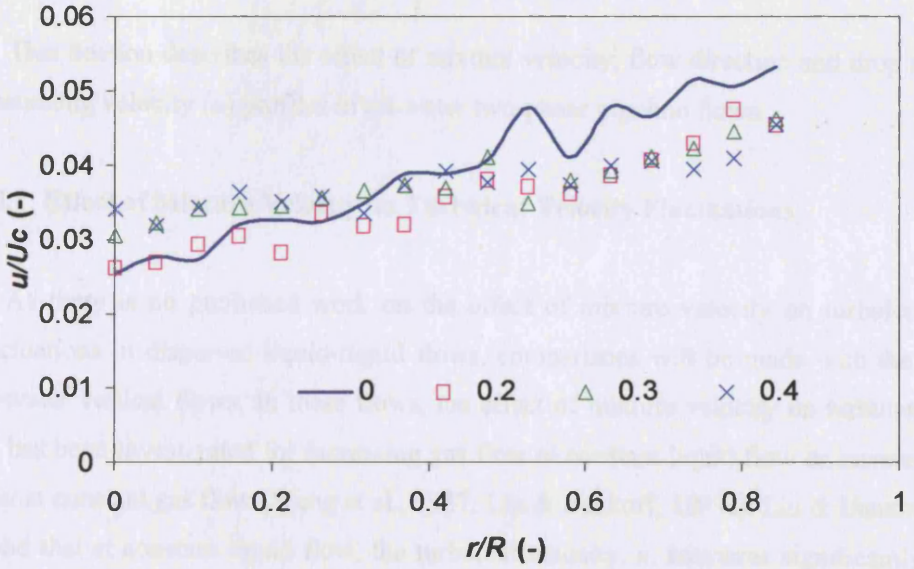

(a) o/w

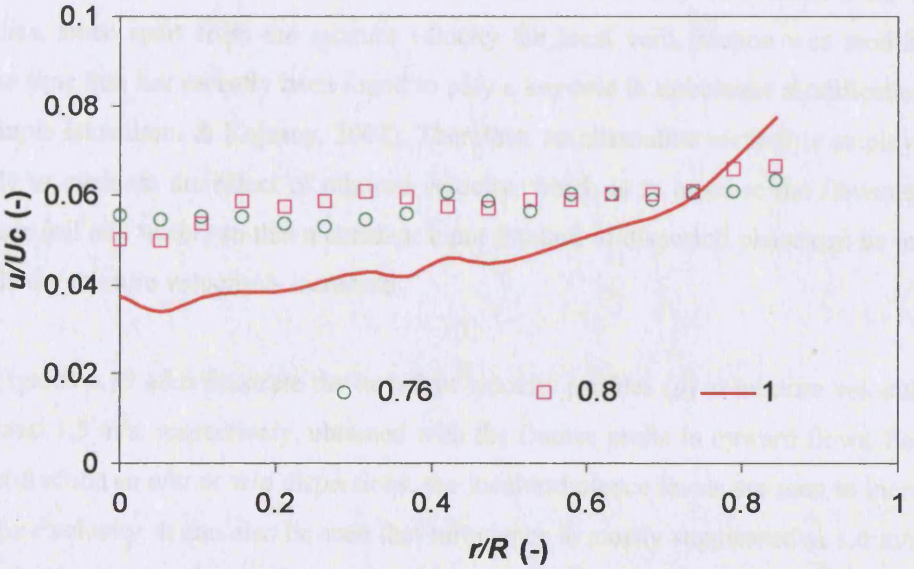

(b) w/o

Figure 6.18: Axial turbulent intensity (u/U_c) profiles of the continuous phase at different input oil fractions measured with Dantec 55R14 probe at 1.5 m/s mixture velocity in downward flow. (a): water continuous, (b): oil continuous.

6.5 Factors that Influence the Turbulence Velocity Profiles

This Section describes the effect of mixture velocity, flow direction and drop size on the fluctuating velocity (u) profiles in oil-water two-phase pipeline flows.

6.5.1 Effect of Mixture Velocity on Turbulent Velocity Fluctuations

As there is no published work on the effect of mixture velocity on turbulent velocity fluctuations in dispersed liquid-liquid flows, comparisons will be made with the results in air-water vertical flows. In these flows, the effect of mixture velocity on turbulent velocity (u) has been investigated for increasing gas flow at constant liquid flow or increasing liquid flow at constant gas flow (Wang et al., 1987; Liu & Bankoff, 1993a). Liu & Bankoff (1993a) found that at constant liquid flow, the turbulent velocity, u, increases significantly with the increase of gas flow in the pipe core region, especially at low liquid flow. In contrast, increasing water flow at constant gas flow decreases the liquid turbulent velocity over most of the pipe cross-section, apart from the wall region where the reverse was observed. Sun et al. (2004) concluded that high velocity of the liquid phase reduces the bubble effect on turbulence modification. However, it is difficult to draw any conclusion from the above studies, since apart from the mixture velocity the local void fraction was modified at the same time that has recently been found to play a key role in turbulence modification (see for example Iskandrani & Kojasoy, 2001). Therefore, an alternative method is employed in this study to evaluate the effect of mixture velocity, which is to increase the flowrates of both phases (oil and water) so that a constant input fraction of dispersed phase can be maintained while the mixture velocity is increased.

Figures 6.19 a&b illustrate the turbulent velocity profiles (u) at mixture velocities of 1.0 m/s and 1.5 m/s, respectively, obtained with the Dantec probe in upward flows. For a given input fraction in o/w or w/o dispersions, the local turbulence levels are seen to increase with mixture velocity. It can also be seen that turbulence is mostly suppressed at 1.0 m/s mixture velocity in o/w flows, and slightly enhanced in w/o flows. At the higher velocity (1.5 m/s), turbulence is increased in the core and attenuated close to the wall region for o/w flows, while an overall increase is observed for w/o flows. In general, turbulent fluctuations seem to increase more in the centre with increasing mixture velocity than at the wall. Since turbulent eddies in a pipe are considered to be generated from both wall-shear induced and bubble/drop induced turbulence, Figure 6.19 seems to suggest that the drop-induced turbulence becomes more pronounced as the mixture velocity increases, in particular in the core region where drops are relatively large and closely packed.

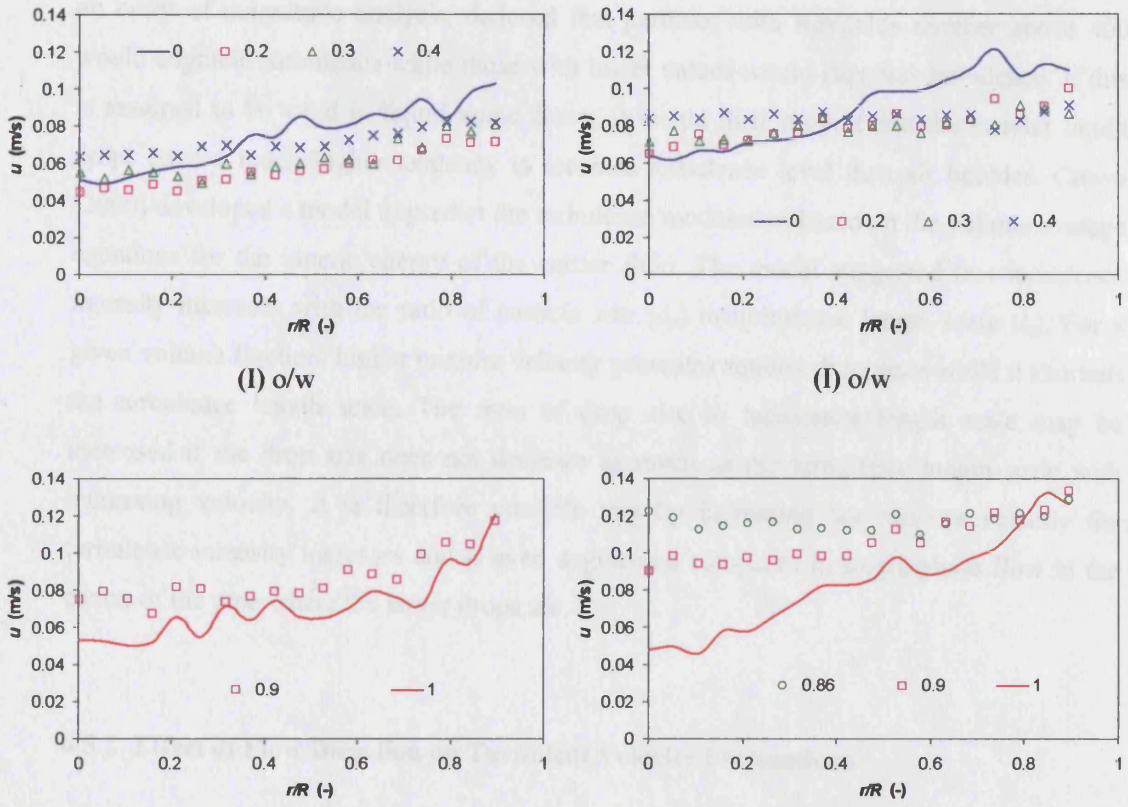

(I) o/w (I) o/w

(II) w/o (II) w/o

(a): 1.0 m/s **(b): 1.5 m/s**

Figure 6.19: Fluctuating turbulence velocity (u) profiles at mixture velocities of (a) 1.0 m/s and (b) 1.5 m/s, measured in upward flow by Dantec 55R14 probe.

In air-water flows, turbulent fluctuations were found to decrease significantly with increasing water (continuous phase) velocity at a constant air velocity (Liu & Bankoff, 1993a). The present investigation, however, shows either an increase or no change of the continuous phase turbulent velocity with mixture velocity even when the dispersed phase fraction is slightly decreased. One possible reason for this disagreement could be that there is a significant decrease in the void fraction observed in the air-water flows when increasing the water velocity at a constant air velocity (Liu & Bankoff, 1993b). In addition, the large difference in the dispersed phase density between the work of Liu and Bankoff ($\rho_d \approx 1$) and the present work ($\rho_d > 828$ kg/m^3) could also contribute to the differences. In oil-water flow,

the dispersed drops would exhibit a much stronger inertial effect than air bubbles. More intensive vortex shedding is therefore expected behind liquid drops. Hetsroni (1989), from an order of magnitude analysis, deduced that particles with Reynolds number above 400 would augment turbulence while those with lower values would suppress turbulence. If this is assumed to be valid in liquid-liquid flows, it would then suggest that the heavier liquid drops have a much higher tendency to increase turbulence level than air bubbles. Crowe (2000) developed a model to predict the turbulence modulation based on the volume average equations for the kinetic energy of the carrier fluid. The model suggested that turbulence intensity increases with the ratio of particle size (d_p) to turbulence length scale (l_e). For a given volume fraction, higher mixture velocity generates smaller drop sizes while it shortens the turbulence length scale. The ratio of drop size to turbulence length scale may be increased if the drop size does not decrease as much as the turbulence length scale with increasing velocity. It is therefore possible that by increasing the mixture velocity the turbulence intensity increases and is even augmented compared to single-phase flow in the centre of the pipe where the larger drops are.

6.5.2 Effect of Flow Direction on Turbulent Velocity Fluctuations

Figure 6.20 illustrate the turbulence velocity profiles in upward and downward flows at various input oil fractions, measured by the Dantec 55R14 probe at 1.5 m/s mixture velocity. In both directions the profiles are flatter compared to single-phase flow while turbulence is augmented in the core region of the pipe and suppressed close to the wall. For a given input oil fraction, the turbulence level in upward flow is found slightly higher than in downward flow, especially in o/w flows. Similar findings were also reported by Sun et al. (2004) for gas-liquid flows. This effect is more evident at the pipe core region for the oil-in-water dispersions. The differences in the velocity of the dispersed drops relative to the continuous phase velocity in upward and downward flow may be responsible for this phenomenon; oil drops travel slower than the continuous phase in downward flow and slightly faster than it in upward flow (see Figures 6.11a and 6.14a). The results for oil continuous flow cannot be directly compared as they refer to different dispersed phase fractions; this is because of the different inversion points in the two directions, 82% and 75% in upward and downward flows, respectively.

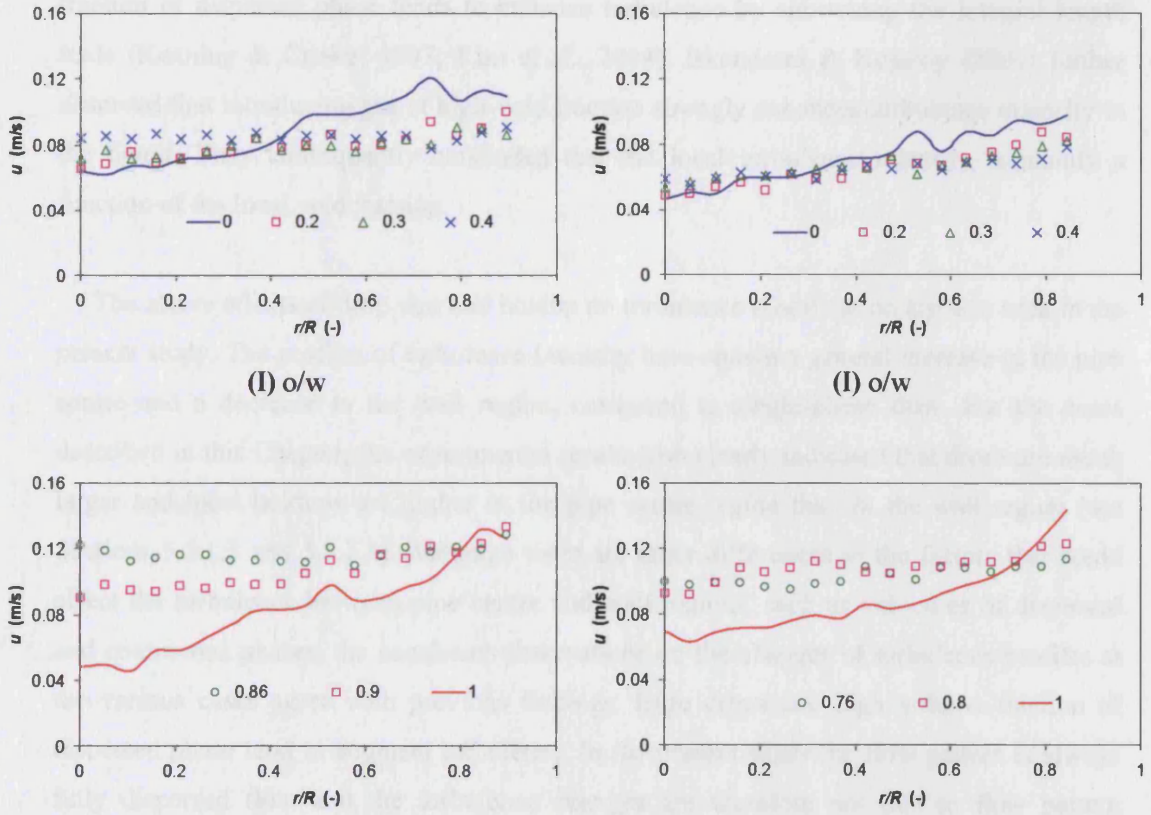

(I) o/w (I) o/w

(II) w/o (II) w/o

(a): upward flow **(b): downward flow**

Figure 6.20: Comparisons of turbulence velocity (u) profiles in (a) upward and (b) downward flows, measured by Dantec 55R14 probe at 1.5 m/s mixture velocity.

6.5.3 Effect of Holdup and Drop Size on Turbulent Velocity Fluctuations

In air-liquid and liquid-liquid flows, the augmentation and attenuation of turbulence have been found to strongly depend on the bubble or drop size (Liu & Bankoff, 1993b; Farrar & Bruun, 1996; Sun et al., 2004) and the holdup of dispersed phase (Kashinsky & Randin, 1999; Iskandrani & Kojasoy, 2001). Experimental data generally indicated that large drops tend to enhance turbulent velocity whereas small drops are more likely to suppress the turbulence of the carrier fluid. Bubble or drop size distributions were also found to play a key role in local turbulent structure by changing the flow regimes, as suggested by Liu &

Bankoff (1993b) and Farrar & Bruun (1996). In addition to size distribution, high volume fraction of dispersed phase tends to enhance turbulence by shortening the integral length scale (Kenning & Crowe, 1997; Kim et al., 2004). Iskandrani & Kojasoy (2001) further observed that introducing gas at high void fraction strongly enhances turbulence intensity in the liquid. They consequently concluded that the local turbulence intensity is mainly a function of the local void fraction.

The above effects of drop size and holdup on turbulence modification are also seen in the present study. The profiles of turbulence intensity have shown a general increase in the pipe centre and a decrease in the wall region, compared to single-phase flow. For the cases described in this Chapter, the experimental results also clearly indicated that drops are much larger and local holdups are higher in the pipe centre region than in the wall region (see Sections 5.2.1.3 and 5.2.1.4). Although there are other differences in the factors that could affect the turbulence between pipe centre and wall regions, such as velocities of dispersed and continuous phases, the consistent observations on the changes of turbulence profiles at the various cases agree with previous findings: large drops and high volume fraction of dispersed phase tend to augment turbulence. In the present study the flow pattern is always fully dispersed flow and the turbulence changes are therefore not due to flow pattern transition as was found by Farrar & Bruun (1996) where the turbulence velocity at the pipe core region was significantly increased because of the flow pattern transition from bubbly to cap bubbly and to churn flow.

Note that, unlike solid-fluid systems wherein the effect of particle size and concentration on the turbulence structure of the carrier fluid can be investigated independently, in air-liquid or liquid-liquid flows changing the holdup of the dispersed phase also affects the bubble or drop size and vice versa. It is difficult therefore to isolate one parameter from the other.

6.6 Comparisons with the Postulated Models

Several mechanisms have been proposed to explain the effect of dispersed phase on the modification of turbulence intensity of the continuous phase (or carrier fluid). Based on the experimental data in particle-laden systems, Gore & Crowe (1989) suggested that the augmentation or suppression of turbulence depends on the ratio of particle size to the integral length scale of turbulence (d_p/l_e): when this ratio is greater than 0.1 an increase of turbulence was observed, whereas values below this result in suppression. Azzopardi & Teixeira (1994a and 1994b) however additionally noticed an enhancement of turbulence intensity in the droplet-laden core of an air-liquid annular flow even though this ratio was below 0.1. Hetsroni (1989) conducted an order of magnitude analysis and stated that particles with Reynolds number greater than 400 would augment turbulence due to vortex shedding behind them and those with Reynolds number less than 400 would attenuate turbulence. Here the Reynolds number is defined as

$$\mathrm{Re} = \frac{\rho_p U_{rel} d_p}{\mu_f} \tag{6-4}$$

where ρ_p is the particle density, U_{rel} is the relative velocity between particle and carrier fluid and μ_f is the viscosity of the carrier fluid.

Kenning & Crowe (1997) suggested that the level of turbulence would be determined by the balance among the production of inherent turbulence (particle-free), the production due to the presence of dispersed phase, the loss of turbulence energy from viscous dissipation and the retransmission of energy to the motions of solid particles. By using a hybrid turbulence length scale, they derived the following equation to describe the change of turbulence intensity.

$$\frac{\hbar - \hbar_i}{\hbar_i} = \left[\frac{l_h}{l_i} + \frac{l_h}{k_i^{3/2}} \frac{f_S (u_f - v_p)^2}{\tau_p} \frac{\rho_p}{\rho_f} \right]^{1/3} - 1 \tag{6-5}$$

where $\hbar_i$ and $\hbar$ are the inherent and particle-laden turbulence intensities, respectively, k_i is the inherent turbulence kinetic energy, l_i is the length scale for the corresponding single-phase flow, u_f and v_p are the continuous and dispersed phase velocities, respectively, f_S is the ratio of particle drag to Stokes drag, τ_P is the particle aerodynamic response time (or

relaxation time), ρ_p and ρ_f are the densities of particle and carrier fluids, respectively, and l_h is the hybrid length scale defined as:

$$l_h = \frac{2 l_i l_S}{l_i + l_S} \tag{6-6}$$

For a single phase pipe flow, the length scale of turbulence is approximated as l_i=0.1D where D is the pipe diameter (Hutchinson et al., 1971). l_S is the average distance between dispersed phase particles. The drops were assumed to be spherical and the following expression for inter-particle spacing was used (Kenning & Crowe, 1997; Kim et al., 2004)

$$\frac{l_S}{d_p} = \left(\frac{\pi}{6\varphi_d} \right)^{1/3} - 1 \tag{6-7}$$

where ϕ_d is the local volume fraction of the dispersed phase.

The inherent turbulence kinetic energy, k_i, is determined by the viscous dissipation rate per unit mass, ϵ, which takes the form:

$$\varepsilon = \frac{k_i^{3/2}}{L_i} \tag{6-8}$$

In pipe flow, the energy dissipation rate per unit mass, ϵ, is (Karabelas, 1978):

$$\varepsilon = \frac{f U^3}{2D} \tag{6-9}$$

where f is the friction factor and U is the average axial velocity.

In vertical pipeline flow, the relative velocity between dispersed and continuous phases was assumed to be the terminal velocity (Crowe, 2000; Kim et al., 2004). For the spherical or nearly spherical drops at low Reynolds number, Hetsroni (1982) suggested the following expression for the terminal rise or fall velocity:

$$U_{rel} = | u_f - v_p | = \frac{2}{3} \frac{g r^2 \Delta\rho}{\mu_c} \frac{\kappa + 1}{3\kappa + 2} \tag{6-10}$$

where $\kappa = \mu_d / \mu_c$ is the viscosity ratio of the dispersed to the continuous phase, r is the drop radius and $\Delta\rho$ is the density difference.

The particle relaxation time, τ_p, which describes the time for a particle at rest to be accelerated within ~63% of the carrier fluid velocity, has been suggested (Crowe, 2000; Kim et al., 2004):

$$\tau_p = \frac{f_S U_{rel}}{g} \tag{6-11}$$

The first step was to compare the results with the suggestion of Hetsroni (1989) that turbulence would be enhanced for Reynolds numbers (defined by Equation (6-4)) greater than 400 and suppressed for Reynolds numbers below this. Here, a Reynolds number similar to that given by Equation (6-4) is defined as

$$\mathrm{Re}_d = \frac{\rho_p d_{32} \mid u_c - v_d \mid}{\mu_c} \tag{6-11}$$

where d_{32} is the Sauter mean diameter found from experiments (see Chapter 5), and u_c and v_d are the measured continuous and dispersed phase velocities, respectively. Figures 6.21a and 6.21b show the values of Re_d calculated from Equation (6-11) for o/w and w/o dispersions, respectively. The values are plotted against dimensionless radius (r/R). As will be seen, the results are extremely complex and the following main points emerge:

(1) For o/w dispersions, and for $r/R < 0.8$, the values of Re_d fall with increasing r/R. In the centre region of the pipe ($r/R < 0.4$), augmentation of the turbulence was observed and for $0.4 < r/R < 0.8$, there is attenuation of the turbulence. The transition corresponds to Re_d ~300, a value of the same order of magnitude as that suggested by Hetsroni (1989).

(2) For w/o dispersions, the values of Re_d are much lower than those for o/w dispersions (reflecting the fact that the continuous phase has a higher viscosity and the droplets are generally smaller). Despite the fact that Re_d is an order of magnitude less than the transition values of 400, turbulence enhancement persists up to $r/R \sim 0.8$.

(3) In the near-wall region (i.e. the regions of data surrounded by dotted lines), the values of Re_d increase for both o/w (Figure 6.21a) and w/o (Figure 6.21b) dispersions. In contrast to the suggestions by Hetsroni (1989), these regions of higher Re_d near the wall are ones in which the turbulence was found to be suppressed in the present study.

It will be seen from these findings that turbulence in liquid-liquid systems is much more complex than in the solid particle dispersions addressed in the study by Hetsroni (1989). This additional complexity probably arises from the deformability of the interfacial in liquid-liquid flow.

The experimental data are also compared with the predictions of Equation (6-5), as suggested by Kenning & Crowe (1997). Figure 6.22 shows the predicted curves (solid lines) and the experimental data (points) at various radial positions measured at 1.5 m/s mixture velocity in upward (U) and downward (D) flows. The open symbols in Figure 6.22 represent local turbulence augmentation, while the solid markers represent turbulence attenuation. According to Kenning & Crowe, drops tend to enhance turbulence if they are above the predicted curve, and suppress turbulence if they are below the curve. As can be seen in Figure 6.22a for o/w dispersions, both turbulence enhancement conditions (denoted by the open symbols) and turbulence attenuation conditions (denoted by the solid symbols) tend to lie above the predicted curve. For w/o flows as shown in Figure 6.22b, the model gives more reasonable predictions. One possible reason for the different performance of this model in o/w and w/o dispersions may be that the model used was mainly developed for dilute dispersions; the w/o dispersions encountered in this study are much less concentrated than o/w dispersions because of the oil fraction where phase inversion occurs. Furthermore, in oil-water flows other phenomena may also contribute to turbulence change, such as drop break-up and coalescence which could potentially accelerate the turbulence energy dissipation.

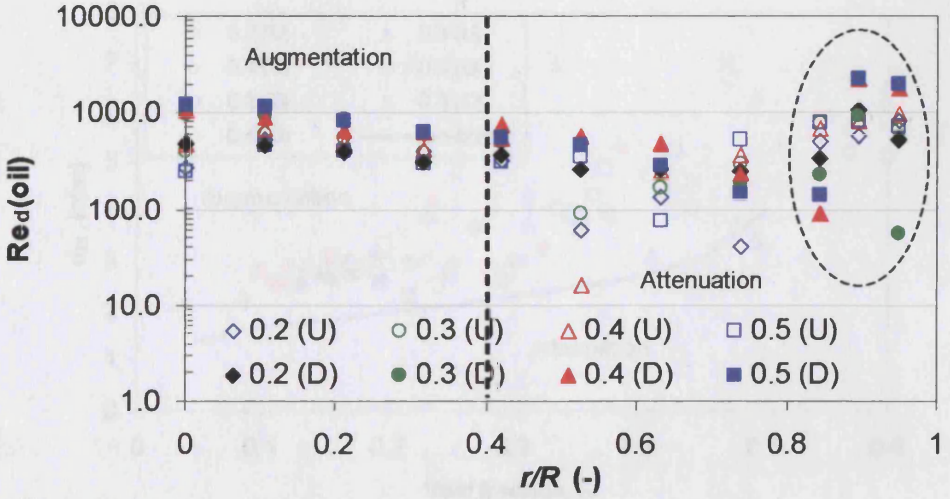

(a) o/w

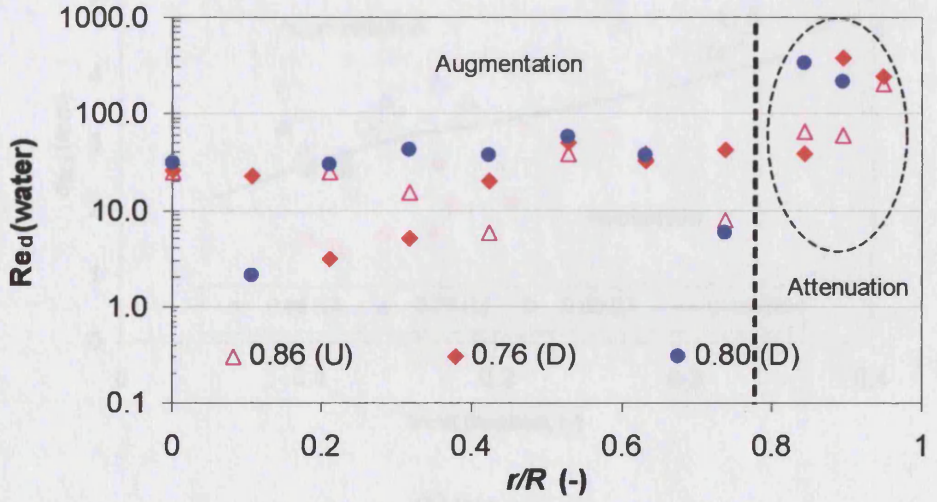

(b) w/o

Figure 6.21: Reynolds number, Re_d, of the dispersed phase profiles in (a) o/w and (b) w/o dispersed flows, calculated by Equation (6-4) for various input oil fractions at 1.5 m/s mixture velocity in upward (U) (open marks) and downward (D) (solid marks) flows.

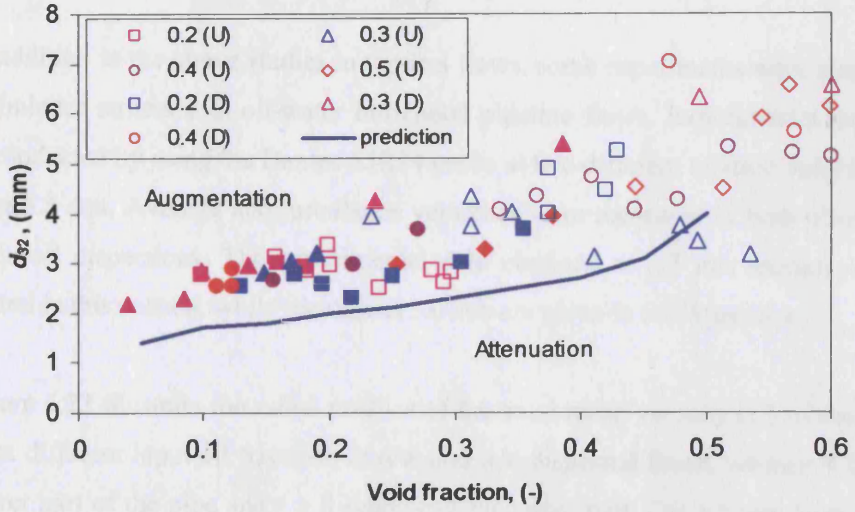

(a) o/w

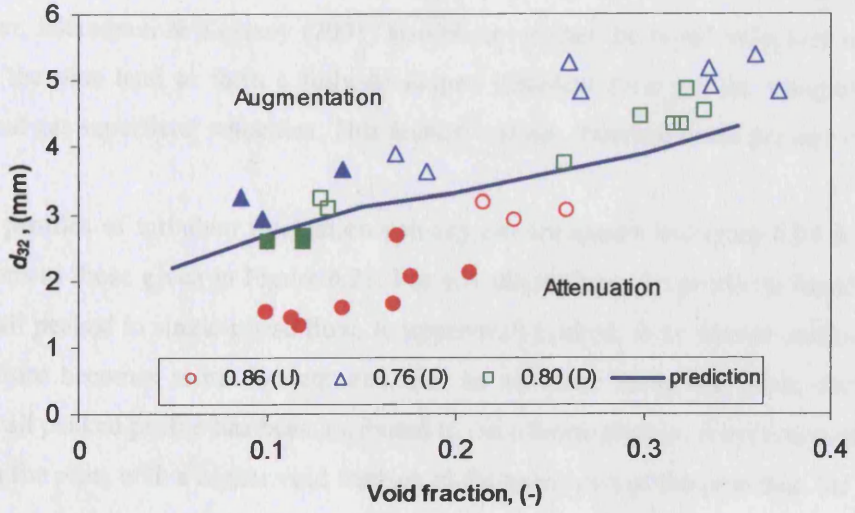

(b) w/o

Figure 6.22: Comparisons between the predictions of Equation (6-5) and the experimental data in (a) o/w and (b) w/o dispersed flows, at various input oil fractions and 1.5 m/s mixture velocity in upward (U) and downward (D) flows. Here, the open marks indicate turbulence enhancement and the solid marks indicate turbulence attenuation.

6.7 Modification of Turbulence Structure in Horizontal Pipeline Flow

In addition to the above studies in vertical flows, some experiments were also carried out on turbulence structure in oil-water horizontal pipeline flows. Experimental measurements were conducted by using the Dantec 55R14 probe at two different mixture velocities, namely 3.0 and 3.5 m/s. Average and turbulence velocities were measured in both oil-in-water and water-in-oil dispersions. The experimental data obtained at 3.5 m/s mixture velocity are presented in this section, while the data at 3.0 m/s are given in the Appendix C.

Figure 6.23 illustrate the radial profiles of the axial mean velocity (U) of the continuous phase at different input oil fractions in o/w and w/o dispersed flows, where $r < 0$ represents the lower part of the pipe and $r > 0$ represents the upper part. For 3.5 m/s mixture velocity, phase inversion has been found to occur at 72% input oil fraction in the current system according to Ioannou et al. (2004). As can be seen, in both dispersions the axial liquid mean velocity shows a more uniform distribution, compared to the $1/7^{th}$ Power law. This agrees with the results by Iskandrani & Kojasoy (2001) for air-water horizontal pipe flows. However, Iskandrani & Kojasoy (2001) also observed that the liquid velocities in the lower part of the pipe tend to form a fully-developed turbulent flow profile, irrespective of the water and gas superficial velocities. This feature was not observed in the present study.

The profiles of turbulent fluctuation velocity (u) are shown in Figure 6.24 for the same conditions as those given in Figure 6.23. For o/w dispersions, the profile is found to change from wall peaked in single-phase flow, to upper-wall peaked, to an almost uniform curve as the mixture becomes more concentrated. For an air-water horizontal flow, occurrence of upper-wall peaked profile has been attributed to the inhomogeneous distribution of dispersed phase in the pipe, with a higher void fraction at the upper part of the pipe than the lower part (Iskandrani & Kojasoy, 2001). This can also be the reason for the upper wall peaked profile in the current experiments at medium oil fractions. The flat turbulence profile in the pipe centre region at high input oil fractions could, therefore, suggest a relatively uniform distribution of the holdup. For w/o dispersions a wall-peaked turbulence velocity profile is always observed, but in this case the input fraction of the dispersed phase is generally low (i.e. does not exceed 28%).

The turbulence levels in o/w and w/o dispersed flows are shown to generally increase with the input oil fraction. This is consistent with the findings by Iskandrani & Kojasoy (2001) for air-water flows; they found that at high void fraction (i.e. high bubble population), introduction of gas strongly enhances the turbulence level and suggested that the local

turbulence intensity is mainly determined by the local void fraction. In contrast to vertical flows, there is no obvious turbulence suppression found in horizontal flows, which may be due to the high velocities used in the current studies.

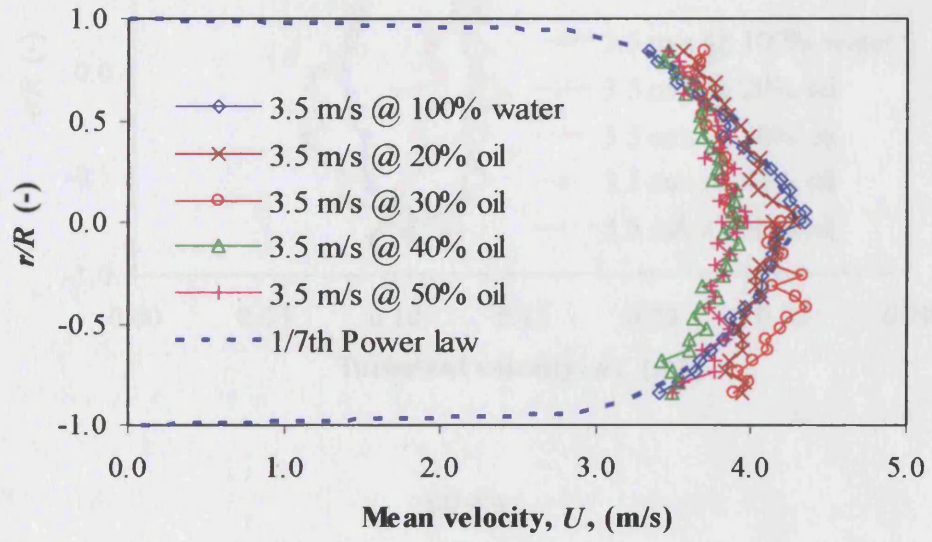

(a) o/w

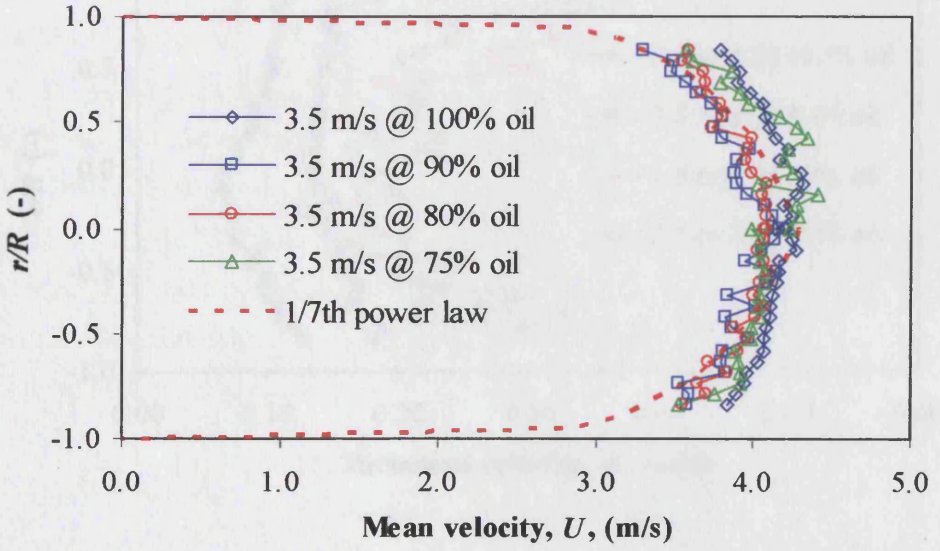

(b) w/o

Figure 6.23: Axial mean velocity (*U*) profiles of the continuous phase at different input oil fractions measured with Dantec 55R14 probe at 3.5 m/s mixture velocity in horizontal flows obtained at 7 m from the pipe inlet, against the predictions of the 1/7th Power law (dot line). (a): water continuous, (b): oil continuous.

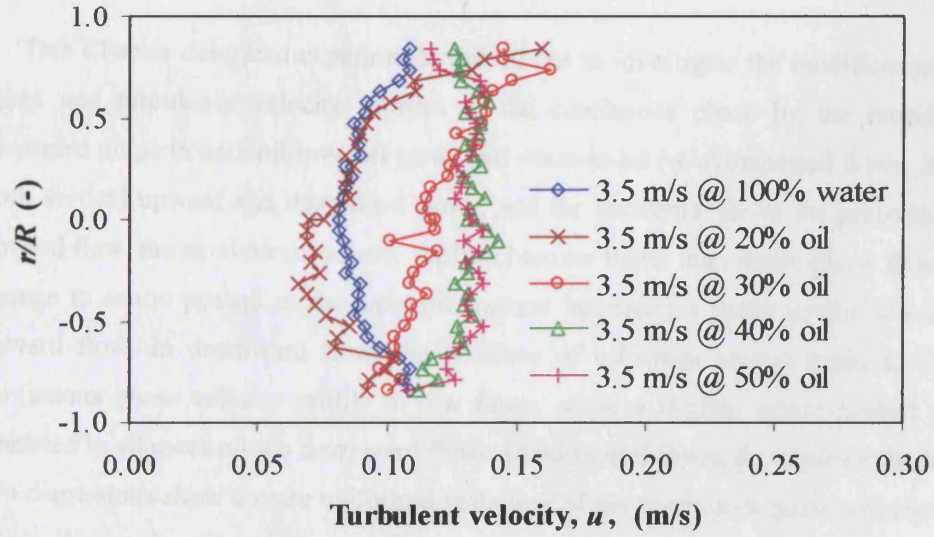

(a) o/w

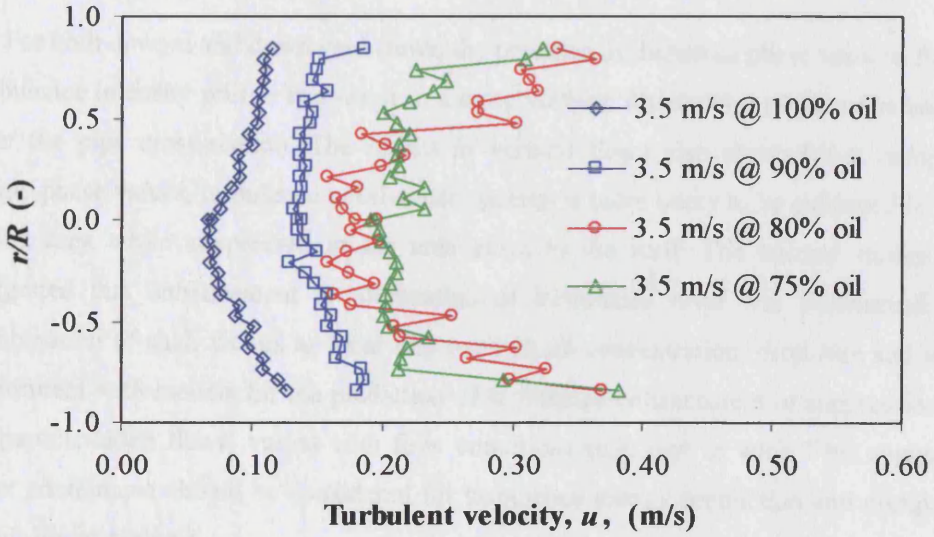

(b) w/o

Figure 6.24: Axial turbulence velocity (u) profiles of the continuous phase at different input oil fractions measured with Dantec 55R14 probe at 3.5 m/s mixture velocity in horizontal flow obtained at 7 m from the pipe inlet. (a): water continuous and (b): oil continuous

6.8 Summary

This Chapter described experiments carried out to investigate the modifications of axial mean and turbulence velocity profiles of the continuous phase by the introduction of dispersed phase in both oil-in-water (o/w) and water-in-oil (w/o) dispersed flows. Results for both vertical upward and downward flows, and for horizontal flows are presented. In o/w upward flow, the axial mean velocity profiles become flatter than single-phase flow and then change to centre peaked as the input oil fraction increases; a flatter profile is seen in w/o upward flow. In downward flow, the presence of oil drops always tends to flatten the continuous phase velocity profile in o/w flows, while a slightly centre peaked profile is observed in all cases of w/o downward flows. In horizontal flows, the results in both o/w and w/o dispersions show a more uniform distribution of the continuous phase velocity than the single-phase values. In addition to factors such as effect of the turbulent fluctuations of the dispersed phase and local dispersed phase fraction (or population) suggested in previous studies (e.g. by Iskandrani & Kojasoy, 2001), the present study also suggests that local velocity of the dispersed phase could play a further key role in changing the continuous phase velocity.

For both upward and downward flows, the presence of dispersed phase tends to flatten the turbulence intensity profile and result in a more uniform distribution of the turbulent energy over the pipe cross-section. The results in vertical flows also showed that compared to single-phase values, turbulence in oil-water systems is more likely to be enhanced in the pipe centre area while suppressed in the area close to the wall. The current studies further suggested that enhancement or attenuation of turbulence level was determined by the combination of such factors as local dispersed phase concentration, drop size and velocity. Agreement with models for the prediction of turbulence enhancement or suppression, based on particle-laden flows, varied with flow conditions (e.g. o/w or w/o). This suggests that other phenomena should be considered for turbulence energy production and dissipation in liquid-liquid systems.

Chapter 7

Theoretical Predictions of Phase Inversion with Population Balance Equations (PBEs) Model in Liquid-Liquid Dispersed Flows

In this Chapter, a population balance equations (PBEs) model is developed to predict phase inversion in liquid-liquid dispersions in stirred vessels and pipe flows. Breakage and coalescence models previously used in the literature are implemented. A short introduction of previous methods and the criteria used for phase inversion in previous investigations is presented in Section 7.1. The basic PBEs model is described in Section 7.2. Section 7.3 presents the breakage and coalescence functions used in the current study. Section 7.4 discusses the criterion used to predict phase inversion. Section 7.5 describes the implementation of the PBEs model in stirred vessel and pipeline systems. The results are then presented and discussed in Section 7.6. Finally, a summary is given in Section 7.7

7.1 Introduction

As described in Section 2.2, several theoretical models have been proposed to predict the phase inversion point in stirred vessels and pipe flows based on some suggested mechanisms, for example, equal surface energy and inclusion of secondary droplets. However, in order to implement the above criteria an estimate of the average drop size in dispersions is required. Some correlations have been postulated for predicting the maximum drop size and Sauter mean diameter (D_{32}) in dispersions (Zhou & Kresta, 1998). These have mainly evolved from drop break-up theory in a turbulent field. In dense dispersions,

however, such as those close to phase inversion, coalescence is also important and these sizes may not be representative averages. Techniques such as the Monte-Carlo method (Juswandi, 1995; Yeo et al., 2002) and population balance equations (PBEs) (Tsouris & Tavlarides, 1994; Alopaeus et al., 1999), that can predict drop size distribution where both coalescence and break-up are taken into account, would be more appropriate.

PBEs techniques have been extensively used to predict the evolution of drop size distribution. However, little work has been reported to apply this technique to systems at highly dense dispersions (>40%) and to phase inversion studies. In this Chapter, the PBEs model is implemented in concentrated dispersions and is further used to predict phase inversion in stirred vessels and pipeline flows.

7.2 Population Balance Equations (PBEs) Model

The PBEs model is a well-established method in computing the particle/drop size distribution and evolution in various systems, such as dispersed flows, crystallization and particle sedimentation. More details of the PBEs can be found in Section 2.3. The PBEs model has been widely used to simulate drop size distributions in liquid-liquid dispersions in agitated vessels (Valentas et al., 1966; Tsouris & Tavlarides, 1994; Alopaeus et al., 1999) and pipeline flows (Hesketh et al., 1991; Kostoglou & Karabelas, 1997 & 1998; Gnotke et al., 2003).

For a system without chemical reactions, heat transfer and mass transfer, the change of drop number is only dependent on breakage and coalescence. Hence, a general form of the population balance equation is given by

$$\frac{\partial n(v)}{\partial t} + \nabla \cdot \vec{V} n(v) = B_B(v) - D_B(v) + B_C(v) - D_C(v) \tag{7-1}$$

where $n(v)$ is the number of drops of volume v per unit volume, t denotes time, $\vec{V}$ is the velocity vector; $B_B(v)$ and $D_B(v)$ are the 'birth' rate and 'death' rate of drops of volume v due to drop breakage, respectively; $B_C(v)$ and $D_C(v)$ are the birth rate and death rate of drops of volume v due to drop coalescence, respectively.

For drops of volume v at a given time t, the death term consists of breakage to smaller drops and coalescence with other drops to form a larger drop, and similarly the birth term

consists of breakage of larger drops into drops of volume v and coalescence of smaller drops leading to a product drop of volume v. Therefore, the terms on the r.h.s. of Equation (7-1) can be given by the following expressions:

$$B_B(v) = \int_v^\infty m(v')\beta(v,v')g(v')n(v',t)dv' \tag{7-2}$$

$$D_B(v) = g(v)n(v,t) \tag{7-3}$$

$$B_C(v) = \int_0^{v/2} \lambda(v-v',v')h(v-v',v')n(v-v',t)n(v',t)dv' \tag{7-4}$$

$$D_C(v) = n(v,t)\int_0^\infty \lambda(v,v')h(v,v')n(v',t)dv' \tag{7-5}$$

Here, $m(v')$ is the number of daughter drops formed due to breakage of a drop volume v'; $\beta(v, v')$ is the probability density function of the daughter drops which represents the probability of forming drops of volume v from breakage of drops of volume v'; $g(v')$ is the breakage frequency of drops of volume v'; $\lambda(v, v')$ is the coalescence frequency between drops of volume v and drops of volume v'; $h(v, v')$ is the collision frequency of drops of volume v and v'.

7.2.1 Application of PBEs to Stirred Vessel Systems

To develop the population balance equations in stirred vessels, it is assumed that the drops are uniformly dispersed in a homogeneous turbulent flow field within a given volume, and that the drops are spherical and the changes in their size are only a result of breakage and coalescence rather than mass transfer or reactions. According to Equation (7-1), the population balance equations for drops in stirred vessels can then be expressed by

$$\frac{\partial n(v)}{\partial t} = B_B(v) - D_B(v) + B_C(v) - D_C(v) \tag{7-6}$$

Discretization of Equation (7-6) yields a set of non-linear integro-differential equations where drops are categorised into discrete size groups. Recognizing that the r.h.s. of Equation (7-6) can be calculated from drop breakage and coalescence functions and an initial drop size distribution, these integro-differential equations can then be solved numerically (Tsouris & Tavlarides, 1994; Alopaeus et al., 1999). In the studies described in this Chapter, a variable

coefficient ordinary differential equation solver (DVODE) package is implemented into a Fortran 90 program to solve the differential equations generated from the PBEs (Brown et al., 1989).

For a system that has a dispersed phase volume fraction ϕ, the initial number, $n(v)$, of drops of volume v in a unit volume can be calculated from

$$n(v) = \frac{\varphi P(v)}{\int_0^{v_{max}} vP(v)dv} \tag{7-7}$$

where $P(v)$ represents the initial number density of drops of volume v, which can be found either from experimental data or set according to some type of statistical distribution, such as uniform distribution or normal distribution.

7.2.2 Application of PBEs to Pipeline Flow Systems

For the development of population balance equations in oil-water pipe flow, it is assumed that the drops of dispersed phase are homogeneously distributed over the pipe cross-section area at any axial location. The mixture is assumed to flow with uniform turbulence, namely energy dissipates at the same rate for the whole pipe. Again, drops are regarded to be spherical and the changes in their size results from breakage and coalescence only rather than heat and mass transfer or reaction. The dispersed flow is also assumed to be one dimensional. Thus, the evolution of the drop size distribution can be expressed by 1-D macroscopic population balance equation, which leads to Equation (7-8).

$$\frac{\partial n(v,x)}{\partial t} + U_m \frac{\partial n(v,x)}{\partial x} + n(v,t)\frac{\partial U_m}{\partial x} = B_B(v,x) - D_B(v,x) + B_C(v,x) - D_C(v,x) \tag{7-8}$$

where U_m is the mixture velocity and x is the axial distance from the entrance.

In recent studies, Kostoglou & Karabelas (1998, 2001) assumed that there is no axial change in the drop size distribution in Equation (7-8) and the mixture moves like a plug at the same velocity along the pipe. As a result, Equation (7-8) reduces to

$$\frac{\partial n(v,x)}{\partial t} = B_B(v,x) - D_B(v,x) + B_C(v,x) - D_C(v,x) \tag{7-9}$$

In contrast, Gnotke et al. (2003) studied the axial development of drop size distribution in a vertical pipe by assuming that the dispersed flows are in steady state at all axial locations along the pipe. Considering the mixture velocity to be constant leads to the following population balance equations.

$$U_m \frac{\partial n(v,x)}{\partial x} = B_B(v,x) - D_B(v,x) + B_C(v,x) - D_C(v,x) \tag{7-10}$$

In realistic situations, however, the oil-water mixture is neither flowing like a plug nor is it in a steady state, especially in regions close to pipe entrance. Therefore, in contrast to the previous models, that can only determine either the spatial or temporal evolution of the drop size distribution, a more advanced PBEs method is proposed in this Chapter.

Here, it is assumed that the drops have the same distribution over the pipe cross-sectional area and there is no slip between the drops and the continuous phase at high velocity. The mixture velocity (U_m) is constant along the pipe and represents the drop velocity in the axial direction. Hence, Equation (7-8) becomes

$$\frac{\partial n(v,x)}{\partial t} + U_m \frac{\partial n(v,x)}{\partial x} = B_B(v,x) - D_B(v,x) + B_C(v,x) - D_C(v,x) \tag{7-11}$$

Discretization of the above equation yields a group of non-linear integral-differential equations, when categorising drops into some discrete size groups. To solve the above discrete equations the boundary conditions at pipe inlet and outlet, and initial drop size distributions for the pipe are also required. In this work, the drops at the inlet are set to follow either a uniform or a normal distribution. By using a sufficiently long pipe the drops at the outlet are then assumed to be in a fully developed state, namely

$$\frac{\partial n(v,L)}{\partial x} = 0, \tag{7-12}$$

where L is the pipe length. On the basis of the PDECOL solver developed by Madsen & Sincovec (1979), a Fortran 90 program has been written to solve the non-linear integral-differential equations arising from Equation (7-11).

7.3 Drop Breakage and Coalescence Models

7.3.1 Drop Breakage Model

7.3.1.1 Drop Breakup Frequency

In general three mechanisms can lead to drop breakage, namely turbulent (deformation) breakage, viscous shear (tearing) breakage and elongation flow breakage. However, viscous shear breakage tends to happen mainly in laminar flow and elongation flow breakage always takes place at a liquid acceleration region, such as the area close to impeller in stirred vessels. For dispersions in stirred vessels and pipe flows, turbulent breakage has been regarded as the most prevailing mechanism, the elongation breakage region near the stirrer in stirred vessels being regarded as insignificant. Many investigators have developed models based on different mechanisms of drop breakage and several breakage frequency functions have been proposed in the literature (Coulaloglou & Tavlarides, 1977; Prince & Blanch, 1990; Tsouris & Tavlarides, 1994; Luo & Svendsen, 1996). In the studies described in this Chapter, the breakage model proposed by Luo & Svendsen (1996) is used.

Luo & Svendsen (1996) postulated a general rate model for fluid particle (drop or bubble) breakage in turbulent flows as follows:

$$g(v:f_v v) = \int_{\lambda_{\min}}^{d} P_B(v:f_v v)\dot{\omega}_{B,\lambda}(v)d\lambda \tag{7-13}$$

where $\dot{\omega}_{B,\lambda}(v)$ is the arrival (bombarding) frequency of eddies of size (length scale) between λ and $\lambda+d\lambda$, on particles of size v; $P_B(v:f_v v)$ is the probability for a particle of size v to break into two particles, one with volume of $f_v v$, when the particle is hit by an arriving eddy of size λ.

Luo & Svendsen (1996) suggested that at a given volume fraction, f_v, there is the minimum turbulence energy, e_{min}, for a drop of diameter of d to break into two smaller drops. This minimum turbulent energy, e_{min}, is defined as the increase of interfacial energy:

$$e_{\min} = [f_v^{2/3} + (1-f_v)^{2/3} - 1]\pi d^2\sigma = c_f \pi d^2\sigma \tag{7-14}$$

where σ is the interfacial tension and c_f represents the surface increase fraction. The probability $P_B(v:f_v v)$ was then expressed as an exponential function of the ratio of this

minimum surface energy and average kinetic energy of an eddy of size λ. Consequently the following equation was derived to calculate $g(v:f_v v)$:

$$g(v:f_v v) = 0.923(1-\varphi)\left(\frac{\varepsilon}{d^2}\right)^{1/3}\int_{\xi_{min}}^{1}\frac{(1+\xi)^2}{\xi^{11/3}}\exp\left(-\frac{12c_f\sigma}{\alpha\rho_c\varepsilon^{2/3}d^{5/3}\xi^{11/3}}\right)d\xi \qquad (7\text{-}15)$$

where φ is the dispersed phase volume fraction, ε is the energy dissipation rate per unit volume, α=2.04 is a constant, ρ_c is the continuous phase density, ξ is the ratio (λ/d) between length scale of the eddy λ and the drop diameter d. ξ_{min} is the minimum value of ξ, corresponding to a length scale λ_{min} which is set equal to the Kolmogorov length scale. The total breakage rate of particles of size v or d can be obtained by integrating this equation over the whole fraction interval, which is expressed as

$$g(v) = \frac{1}{2}\int_0^1 g(v:f_v v)df_v \qquad (7\text{-}16)$$

where the factor 1/2 takes into account that the effective range of f_v is either 0-0.5 or 0.5-1 (the integrand is symmetrical with f_v=0.5).

Figure 7.1 shows the effect of drop size and energy dissipation rate on the specific breakage rate, $g(v:f_v v)/(1-\varphi)$, for an oil-water system with σ = 0.05 N/m. As shown in Figure 7.1 increasing ε results in an increase of the drop break-up rate for a given size.

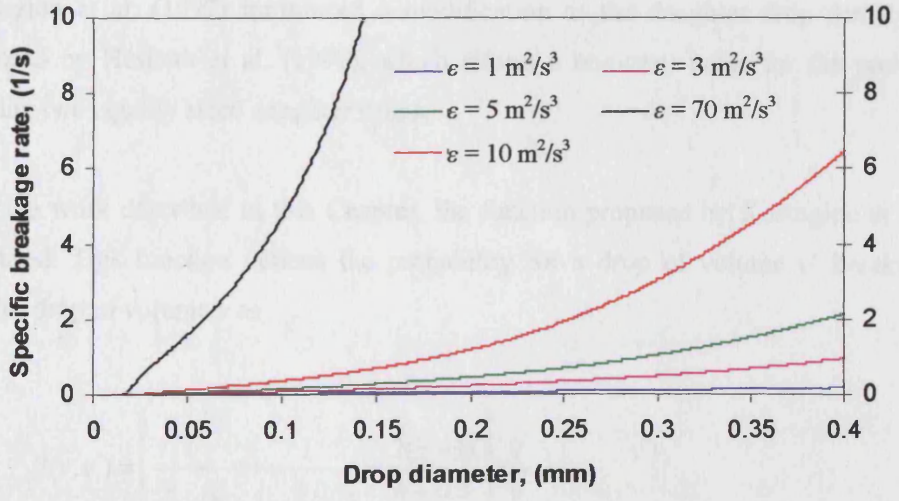

Figure 7.1: Effect of drop size and energy dissipation rate on the specific breakage rate, $g(v:f_v v)/(1-\varphi)$, in an oil-in-water dispersion (ρ_w=1000 Kg/m^3 and ρ_o=828 Kg/m^3)

7.3.1.2 Daughter Drop Size Distribution Function

Another factor that affects the breakage kernel is the daughter drop size distribution, β. Many investigators have proposed a model for β based on the assumption of binary break-up, i.e. that two daughter drops are formed from one breakage. This assumption is also used in the current studies.

In case of binary break-up, two typical methods have been used to calculate the size distribution function of the formed daughter drops. In the first, the daughter drop size distribution is considered to follow certain statistical models, such as truncated normal distribution (Valentas et al., 1966; Coulaloglou & Tavlarides 1977; Chatzi et al., 1989; Ribeiro et al., 1995; Maggioris et al., 2000), uniform distribution (Narsimham et al, 1979; Prince & Blanch, 1990), β distribution (Hsia & Tavlarides, 1980; Lee et al., 1987) and 'U' shape distribution (Hesketh et al., 1991; Kostoglou et al., 1997). The other approach used is to derive the daughter drop size distribution from surface energy models, which are based on either drop-eddy collision (Tsouris & Tavlarides, 1994; Luo & Svendsen; 1996) or stress balances (Martínez-Bazán et al., 1999).

Recently, it has been shown that the energy required for break-up into two equally sized drops is greater than the energy requirement for break-up into two unequally sized drops (a smaller and a larger drop). Taking this fact into account, Hesketh et al. (1991) suggested a U-shaped daughter density function with a zero probability of forming two exactly equal bubbles, based on their experimental results concerning bubbles flowing in a pipe. Later Kostoglou et al. (1997) introduced a modification to the daughter drop density function proposed by Hesketh et al. (1991), which allows a non-zero value for the probability of forming two equally sized daughter drops.

In the work described in this Chapter, the function proposed by Kostoglou et al. (1997) was used. This function defines the probability for a drop of volume v' breaking into a smaller drop of volume v as

$$\beta(v,v') = \left(\frac{1}{\frac{v}{v'}+b} + \frac{1}{1-\frac{v}{v'}+b} + \frac{2(z-1)}{b+0.5} \right) \cdot \frac{I}{v'} \tag{7-17}$$

where I is the normalization coefficient defined as:

$$I = \frac{0.5}{\ln(1+b) - \ln(b) + \dfrac{z-1}{b+0.5}} \tag{7-18}$$

and z is given by:

$$z = \frac{0.5a}{2b(1+b)(1-a)} \tag{7-19}$$

where a and b are the parameters that control the distribution shape (shown in Figure 7.2).

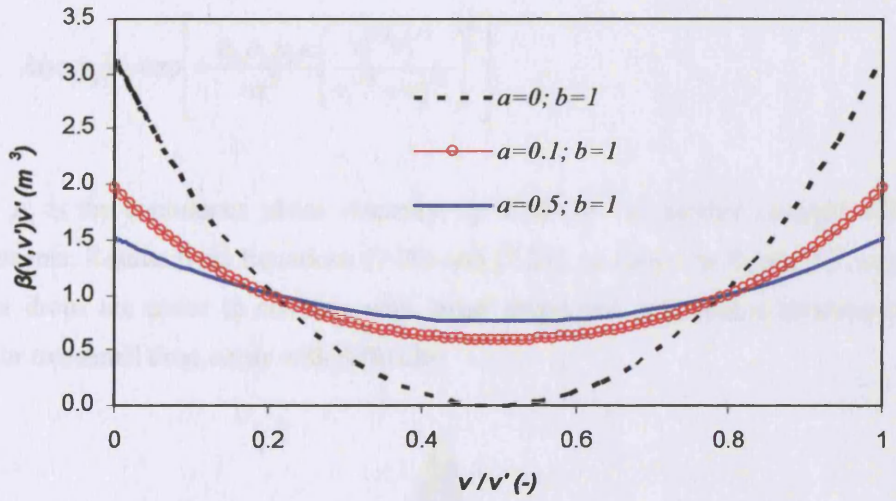

Figure 7.2: Variation of the daughter drop size distribution with the parameters *a* and *b* which appear in Equation (7-17).

7.3.2 Drop Coalescence Model

The model postulated by Coulaloglou & Tavlarides (1977) is used in this Chapter to calculate the coalescence rate between drops of volume of v_i and v_j. Coulaloglou & Tavlarides (1977) suggested that the coalescence rate for drops of volume of v_i and v_j can be expressed as the product of collision frequency, $h(v_i, v_j)$, and coalescence efficiency, $\lambda(v_i, v_j)$. The drop-drop collision frequency in a turbulent flow is assumed to be analogous to that in gas molecular collisions, which can be calculated from

$$h(v_i, v_j) = c_1 \frac{\varepsilon}{1+\varphi} (v_i^{1/3} + v_j^{1/3})^2 (v_i^{2/9} + v_j^{2/9})^{1/2} \tag{7-20}$$

where $c_1 = 2.17 \times 10^{-4}$ is a constant obtained from experiments.

The two drops are assumed to coalesce only if the contact time is greater than the time for the draining film between them to reach a critical thickness for film rupture. By viewing the film drainage under a constant squeezing turbulent force, Coulaloglou & Tavlarides (1977) proposed a model to calculate the coalescence efficiency, which was expressed by an exponential function relating the film drainage time to the drop contact time. For two drops of volume of v_i and v_j, the coalescence efficiency $\lambda(v_i, v_j)$ was given by

$$\lambda(v_i, v_j) = \exp\left[-\frac{c_2 \rho_c \mu_c \varepsilon}{\sigma^2} \left(\frac{v_i^{1/3} v_j^{1/3}}{v_i^{1/3} + v_j^{1/3}} \right)^4 \right] \tag{7-21}$$

where μ_c is the continuous phase viscosity; $c_2 = 2.28 \times 10^{13}$ is another constant found from experiments. Results from Equations (7-20) and (7-21), as shown in Figure 7.3, suggest that smaller drops are easier to coalesce with larger drops and coalescence between two large drops or two small drop occur with difficulty.

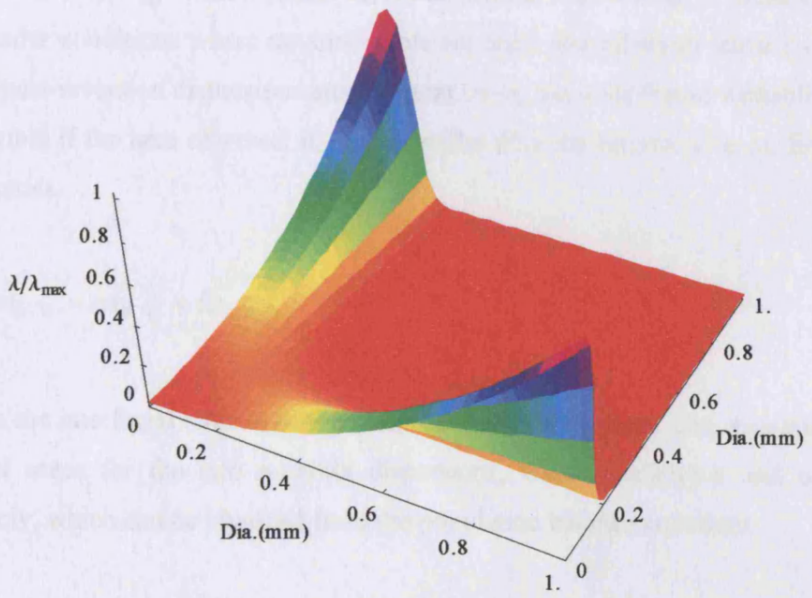

Figure 7.3: Normalised coalescence frequency calculated using Equations (7-20) and (7-21) in a benzene-in-water system.

7.4 Criterion for Phase Inversion

For oil-water systems, many investigators have suggested that phase inversion occurs when the total free energies from oil-in-water and water-in-oil configurations are equal (to a critical value) after assuming the two possible dispersions are stable. For each dispersed system, the total free energy consists of the continuous phase free energy, the dispersed phase free energy and the free energy of the interfaces. In the case of constant system temperature and composition for a given mixture velocity, the free energy of the continuous and dispersed phases have been assumed to remain the same during phase inversion (Yeo et al., 2002; Brauner & Ullman, 2002). Thus, the phase inversion criterion is only dependent on the free energy of interfaces, which include the interfacial energy between the oil and water phases, and between the continuous phase and the solid wall. Therefore, the criterion can be expressed as:

$$Es_{O/W} + Es_{WS} = Es_{W/O} + Es_{OS} = Es^{*}_{Crit} \tag{7-22}$$

where $Es_{O/W}$ and $Es_{W/O}$ are the interfacial energy per unit volume in the oil-in-water (o/w) and water-in-oil (w/o) dispersions, respectively; Es_{OS} and Es_{WS} are the wall surface energy per unit volume when oil and water are the continuous phases, respectively, and Es^{*}_{Crit} is the critical surface energy where phase inversion occurs. According to Brauner & Ullmann (2002) under conditions where no surfactants are used, the oil-water surface tensions in the pre- and post-inversion dispersions are the same. Also, the solid-liquid wettability effects can be negligible if the area of vessel is much smaller than the interfacial area. Equation (7-22) then becomes

$$\sigma A_{O/W} = \sigma A_{W/O} = Es_{Crit} \tag{7-23}$$

Here, σ is the interfacial tension between the oil and water phases, and $A_{O/W}$ and $A_{W/O}$ are the interfacial areas for the two possible dispersions, water continuous and oil continuous respectively, which can be obtained from the population balance equations.

$$A_K = \pi \int_0^{\infty} n_K(x) x^2 dx \quad , \quad (K = o/w, \quad w/o) \tag{7-24}$$

where $n_K(x)$ is the number of drops of diameter x in a unit volume.

The above criterion of equal surface energy has been used recently for phase inversion studies in stirred vessel systems by Juswandi (1995) and Yeo et al. (2002), using the drop size distributions simulated by the Monte-Carlo method, whereas Brauner & Ullmann (2002) applied this criterion to liquid-liquid pipe flow using correlations for average drop sizes. Brauner & Ullmann (2002) also attributed the ambivalent range to the interfacial tension changes (due to contaminants) pre- and post-phase inversion in liquid-liquid pipe flows and stirred vessels. However, assuming no changes in interfacial tension and negligible wall surface energy, the criterion of equal interfacial energy cannot predict the existence of an ambivalent range.

7.5 Model Implementation

Although the non-linear partial differential equations given by Equation (7-6) or (7-11) can be solved numerically, there are two other aspects which need to be considered. Firstly, the drops are divided into different classes of equally separated sizes. The minimum drop class is set to have the size of Kolmogorov length scale, $l_k = (\nu^3/\varepsilon)^{1/4}$ (Alopaeus et al., 1999). The size of the largest class, d_{max}, has been suggested for stirred vessels to follow Equation (7-25) by Tsouris & Tavlarides (1994):

$$d_{\max} = 0.125We^{-0.6}D_I\left[1+2.5\varphi\frac{\mu_d+0.4\mu_c}{\mu_d+\mu_c}\right]^{1.2} \tag{7-25}$$

where $We=N_I^2D_I^3\rho_c/\sigma$ is the Weber number in which ρ_c is the continuous phase density, N_I is the impeller speed, σ is the interfacial tension and D_I is the impeller diameter; ϕ is the dispersed phase volume fraction, μ_d and μ_c are the viscosity of dispersed and continuous phases, respectively. For pipe flow, d_{max} is set equal to $0.1\times D$, where D is the pipe diameter, which represents the integral turbulence length scale (Hutchinson et al., 1971). In addition, it is also assumed that there is no breakage of the lowest class as no other class can contain its daughter drop size; similarly coalescence forming a drop larger than the maximum size is also not allowed.

Secondly, because the daughter drop size or coalescence-formed drop size cannot match exactly the discrete characteristic class sizes, the mass (or volume) of the total dispersed phase is unlikely to remain constant with time. It is, therefore, necessary to use complementary methods to conserve mass. In this Chapter, two algorithms are applied

respectively for drop breakage and coalescence. For drop breakage, the daughter drop size distribution function β is scaled at each time step, such that the total mass of daughter drops formed from larger drop breakages equals the total mass of drops that break up at the same time. For drop coalescence when two drops coalesce, the drop produced is split into the two nearest drop classes according to the ratio of the third moment of the diameters. The sum of the split fractions into each of the two consecutive classes should be equal to unity.

7.6 Results and Discussion

7.6.1 Simulations in Stirred Vessels

Before studying phase inversion, the sensitivity of population balance equations to the initial distribution conditions of dispersed phase drops is investigated. Three different initial distributions, shown in Figure 7.4, namely two normal distributions with different mean values and one uniform distribution, are used. The results of steady state drop distribution at 800 rpm impeller speed are also presented in Figure 7.4. It is clearly shown that the distribution finally formed in the stirred vessel when the dispersion reaches steady state is essentially independent of the initial conditions; the initial condition will, however, affect the time required to reach the steady state. As also shown in Figure 7.4, dispersions having an initially uniform distribution require more time than those with normal distribution to reach the steady state. A normal distribution therefore has been used in this study in order to obtain the steady state in shorter time.

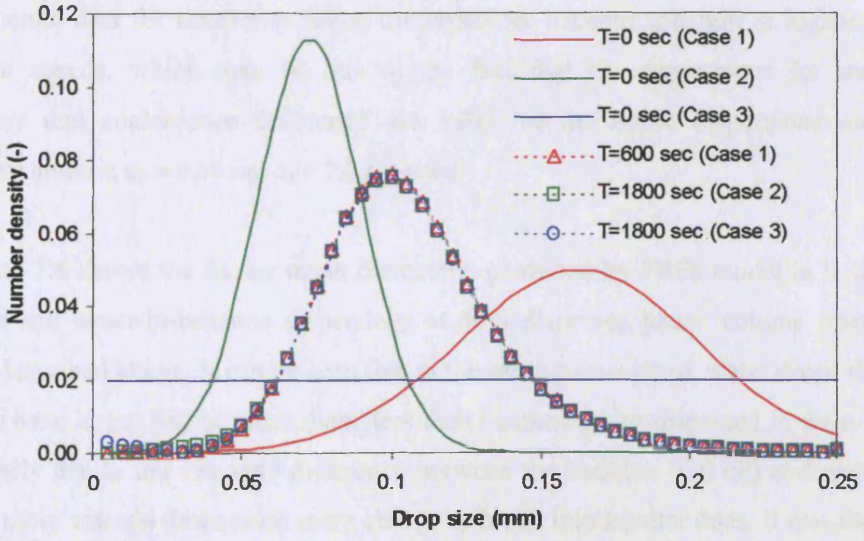

Figure 7.4: Equilibrium drop size distributions obtained from three different initial distributions at 800 rpm agitation speed in a benzene-in-water system.

Benzene-water dispersions in a stirred vessel with 100 mm diameter and 110 mm height were simulated using the present PBEs model. This system is characterized by the following parameter values (o and w denote benzene and water, respectively): ρ_w=996 Kg/m^3, ρ_o=867 Kg/m^3, μ_w=1.0 cP, μ_o=0.6 cP and σ=0.0323 N/m. A normal drop size distribution with 200 μm mean diameter is used as the initial condition. The Sauter mean diameter (D_{32}), calculated by Equation (7-26) for a benzene-in-water dispersion at different dispersed phase volume fractions and agitation speeds, is shown in Figure 7.5.

$$D_{32} = \frac{\sum n(d_i) d_i^3}{\sum n(d_i) d_i^2} \tag{7-26}$$

The results are also compared with the correlation of Equation (7-27) suggested in previous studies (e.g. Zhou & Kresta, 1998; Pacek et al., 1998).

$$\frac{D_{32}}{D_I} = c_3 We^{-0.6}(1 + c_4 \varphi) \tag{7-27}$$

In Equations (7-26) and (7-27), c_3 and c_4 are constants that can be obtained by fitting experimental data. For c_3, most of the previous experimental data can be fitted using values within the range of 0.05~0.06, while c_4 varies more widely in the range of 3 – 10. Here c_3 and c_4 are given at the values of 0.06 (0.05*) and 7.0 (10.0*), respectively. As can be seen in Figure 7.5, the predictions of the PBEs model are in good agreement with the correlation of experimental data for smaller ϕ. Some discrepancies become apparent at higher ϕ and low agitation speeds, which may be due to the fact that the expressions for the collision frequency and coalescence efficiency are valid for the dilute dispersions only. In the following studies, c_3 = 0.06 and c_4 = 7.0 are used.

Figure 7.6 shows the Sauter mean diameters, predicted by PBEs model in both benzene-in-water and water-in-benzene dispersions at 50% dispersed phase volume fraction in the system described above. It can be seen that at the same power input, water drops dispersed in benzene have larger Sauter mean diameters than benzene drops dispersed in water. This may be partially due to the viscosity difference between the benzene (0.6 cP) and water (1.0 cP) phases: more viscous drops need more energy to break into smaller ones. It can also be noted that the differences tend to become smaller as the agitation speed increases.

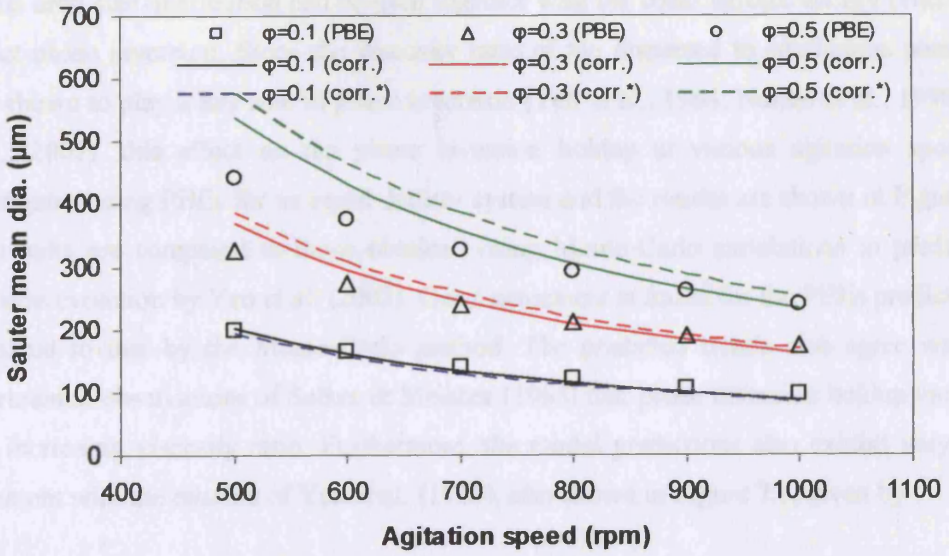

Figure 7.5: Comparisons on the Sauter mean diameters between the PBEs predictions and the correlation given by Equation (7-27) in benzene-in-water dispersions. Here, c_3 and c_4 are given at the values of 0.06 (0.05*) and 7.0 (10.0*), respectively.

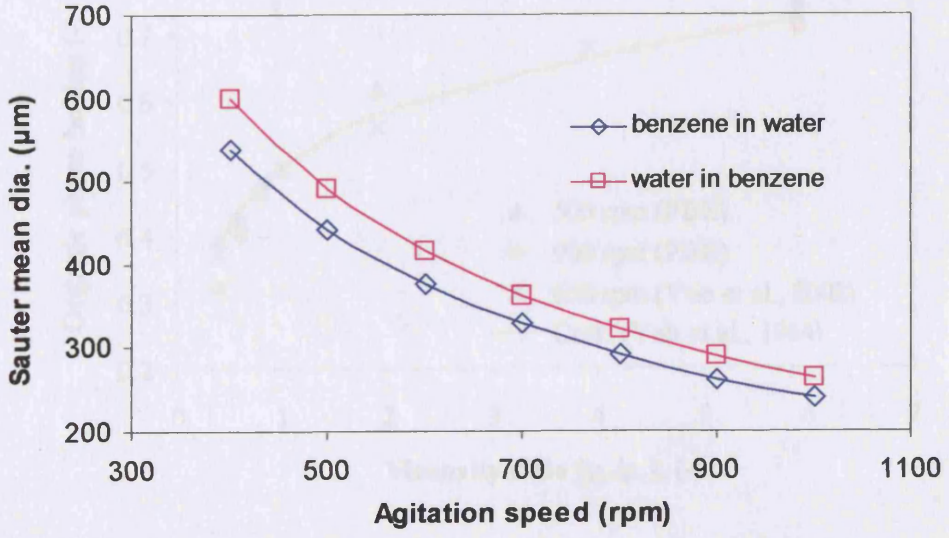

Figure 7.6: The Sauter mean diameters predicted by the PBEs model for benzene-in-water and water-in-benzene systems at various agitation speeds and φ=0.5.

The drop size distribution can be used together with the equal surface energy criterion to predict phase inversion. Since the viscosity ratio of the dispersed to continuous phase has been shown to play a key role in phase inversion (Yeh et al., 1964; Norato et al., 1998; Yeo et al., 2002), this effect on the phase inversion holdup at various agitation speeds is investigated using PBEs for an equal density system and the results are shown in Figure 7.7. The results are compared to those obtained using Monte-Carlo simulations to predict the drop size evolution by Yeo et al. (2002). Good agreement is found for the PBEs prediction in compared to that by the Monte-Carlo method. The predicted trends also agree with the experimental observations of Selker & Sleicher (1965) that phase inversion holdup increases with increasing viscosity ratio. Furthermore, the model predictions also exhibit very good agreement with the relation of Yeh et al. (1964), also shown in Figure 7.7, given by

$$\frac{\varphi}{1-\varphi} = \sqrt{\frac{\mu_d}{\mu_c}} \tag{7-28}$$

The results shown in Figure 7.7 also provide a check on the performance of the numerical procedure used to solve the PBEs equations.

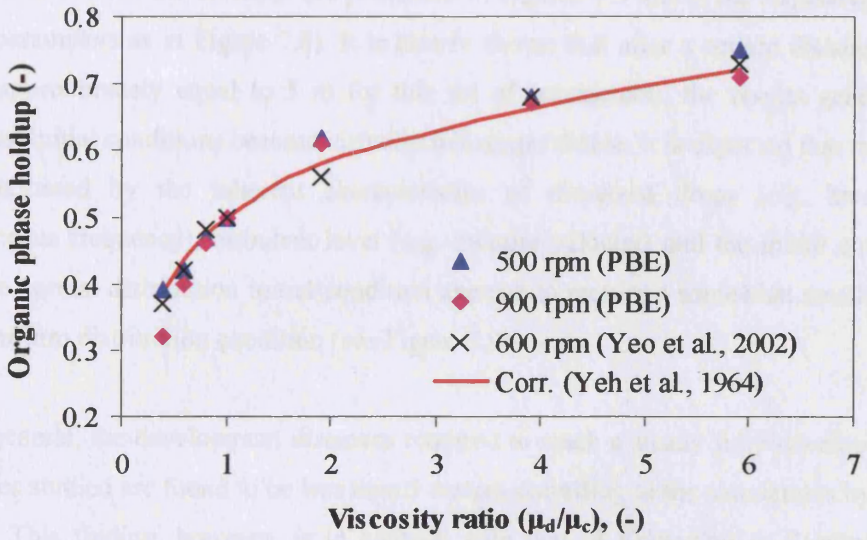

Figure 7.7: Effect of viscosity ratio on phase inversion point in an equal density system.

7.6.2 Simulations of Pipeline Flow

7.6.2.1 Sensitivities to the Inlet (and Initial) Drop Size Distribution

Evolution of drop sizes along the pipeline was studied as a precursor to the predictions of phase inversion with the PBEs model. Dispersed flows of oil and water in a 38mm ID pipe are considered in this study. Dispersed phase are introduced into a 15 m long straight pipe in two known distributions, a uniform distribution and a truncated normal distribution which are shown in Figure 7.8(a) and Figure 7.8(d), respectively; Figure 7.8 illustrates the evolution of drop size distributions at different axial locations for 3.0 m/s mixture velocity (U_{mix}) and 30% input oil fraction. The axial profiles at 0 sec, 1sec and 5 sec are shown (the profile changes are found to be negligible after 5 seconds for this case). It can be seen that the drop sizes injected at the entrance have a strong impact on the distribution of drops near the inlet (i.e. at distance less than about 5m), but a much less noticeable effect on drops far downstream. These results suggest that the distribution become fully developed and independent of the initial conditions used.

To better elucidate the independence of downstream drop size distribution on the initial conditions, the axial profiles of the Sauter mean diameter (D_{32}) and the drop size distribution curve at 8 m from the entrance are presented in Figures 7.9 and 7.10, respectively (for the same parameters as in Figure 7.8). It is clearly shown that after a certain distance from the inlet (approximately equal to 5 m for this set of parameters), the results generated with different initial conditions become virtually indistinguishable. It is expected that this distance is determined by the inherent characteristics of dispersed drops (e.g. breakage and coalescence frequency), turbulent level (e.g. mixture velocity) and the initial conditions in that the normal distribution initial condition appears to require a somewhat smaller distance than uniform distribution condition (see Figure 7.9).

In general, the development distances required to reach a steady fully-developed state in the cases studied are found to be less than 5 meters according to the simulations by the PBEs model. This finding, however, is in contrast with that of Kostoglou & Karabelas (1998) based on a simplified PBEs model (see Equation 7-9). They investigated the attainment of steady state in turbulent pipe flow of dilute dispersions and their theoretical evidence showed that an unrealistic long pipe is required to achieve the steady state. The reason for this discrepancy may be because of the following two aspects. Firstly, the work of Kostoglou & Karabelas (1998) was concentrated on dilute dispersions where only drop breakages are

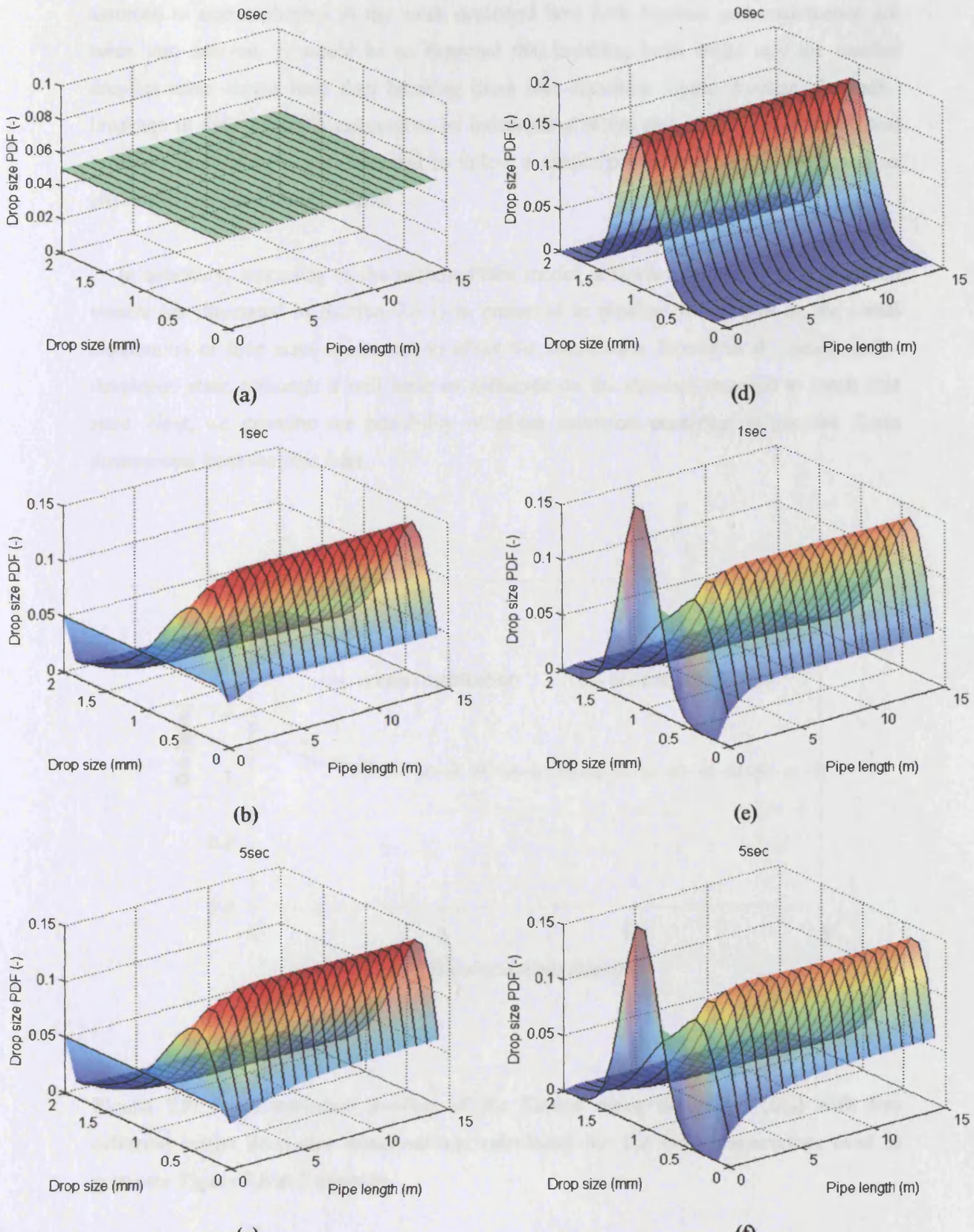

Figure 7.8: Spatio-temporal evolutions of drop size distributions for 3.0 m/s mixture velocity and 30% input oil fraction with an initially uniform (a-c) and a truncated normal distribution (d-f).

assumed to occur whereas in the work described here both breakup and coalescence are taken into account. It would be as expected that breaking large drops into the smaller droplets takes longer time than breaking those into somehow bigger droplets. Secondly, breakage in their model is assumed to be independent of the size of the parent drops, and breakage probability is also assumed to follow a simple power form and is not based on physically well-developed models.

In summary, according to the present PBEs model, a similar finding to that in stirred vessels (as illustrated in Section 7.6.1) is presented in pipeline flows, that is, the initial distribution of drop sizes seems not to affect the distribution formed at the steady fully-developed state, although it will have an influence on the distance required to reach that state. Next, we examine the possibility of phase inversion occurring in pipeline flows downstream from the pipe inlet.

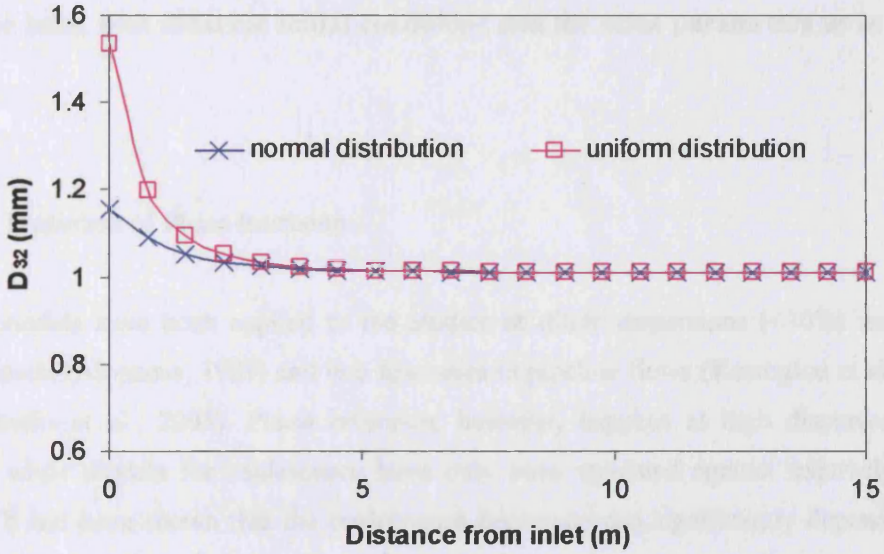

Figure 7.9: Axial variation profiles of the Sauter mean diameters (D_{32}) with two different initial drop size distributions, calculated for the same parameters used to generate Figure 7.8 at 5 seconds.

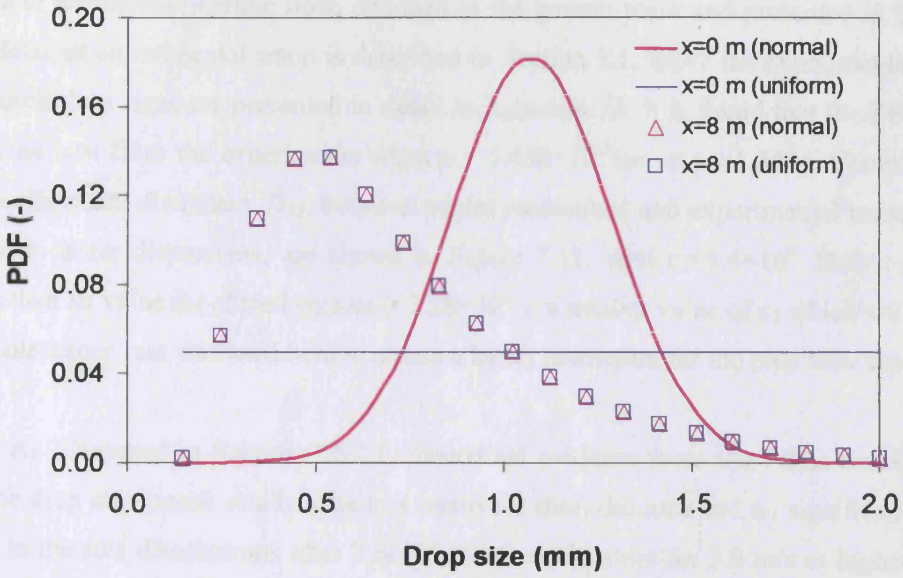

Figure 7.10: Comparisons of the predicted drop size distributions at a distance of 8.0 m from pipe inlet, with different initial conditions and the same parameters as in Figure 7.9.

7.6.2.2 Prediction of Phase Inversion

PBEs models have been applied to the studies of dilute dispersions (<30%) mainly in stirred vessels (Alopaeus, 1999) and in a few cases in pipeline flows (Kostoglou et al., 1998, 2001; Gnotke et al., 2003). Phase inversion, however, happens at high dispersed phase fractions while models for coalescence have only been validated against relatively dilute systems. It has been shown that the coalescence frequency can significantly depend on the dispersed phase volume fraction. To account for this in the current work parameter c_1 in Equation (7-20) is considered as a function of the dispersed phase fraction. As was suggested by Desnoyer et al. (2003), c_1 is assumed to be given by the following relationship:

$$c_1 = p\varphi^m \tag{7-29}$$

where p and m are empirical constants.

The constants p and m are correlated from the experimental data on average drop size distributions, measured at positions 4 m (105D) and 7 m (184D) from the test section inlet in

oil-water horizontal pipeline flow, obtained in the present work and presented in Chapter 3. The detailed experimental setup is described in Section 3.1, while the experimental data for measured drop sizes are presented in detail in Appendix D. It is found that the PBEs model gives the best fit to the experiments when $p = 5.458\times10^{-3}$and $m = -1.3404$. Comparisons of the Sauter mean diameters, D_{32}, between model predictions and experimental measurements for oil-in-water dispersions, are shown in Figure 7.11, with $c_2=5.4\times10^{8}$. Here c_2 is much lower than its value for stirred vessels ($=2.28\times10^{13}$); a smaller value of c_2 which will enhance the coalescence rate was used here to obtain a better prediction for the pipe flow case.

As illustrated in Section 7.6.2.1, theoretical evidence from the PBEs model showed that the drop sizes reach steady state in a relatively short distance and no significant changes occur in the size distributions after 7 m (184*D*) from the inlet for 3.0 m/s or higher mixture velocities. Therefore, the predictions of phase inversion at 7 m were compared with the experimental observations. The equal surface energy criterion (Brauner & Ullman, 2002) was used to predict phase inversion in pipe flow, as given by Equation (7-23). Thus, the interfacial energies of the two possible dispersions (oil-in-water and water-in-oil) are equal at the phase inversion point. The simulated results are shown in Figure 7.12 for 3.5 m/s mixture velocity. The interfacial energy of each dispersion (oil continuous or water continuous) increases with increasing dispersed phase fraction (continuous lines). At 71% oil fraction the two curves cross. At this phase fraction, where the two possible dispersions have the same interfacial energy, phase inversion is predicted to occur. For each mixture, any further increase in the dispersed phase fraction (represented by the dotted lines) is not possible. The dispersed phase will therefore become continuous and the interfacial energy will follow the continuous line of the inversed dispersion. The results of the model are in very good agreement with the experimental data for the same flow conditions as found by Ioannou et al. (2004), which also showed that phase inversion occurs at about 70~72% input oil fraction.

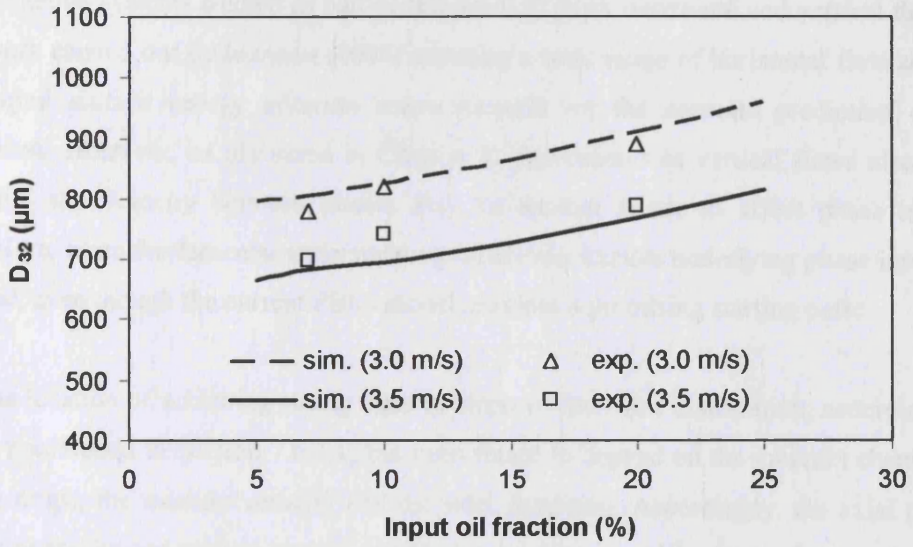

Figure 7.11: Comparison of the predictions of the PBEs model and experimental data of the Sauter mean diameter (D_{32}) at 3.0 m/s and 3.5 m/s mixture velocity obtained in horizontal oil-in-water dispersed pipeline flows at 7 m from the pipe inlet.

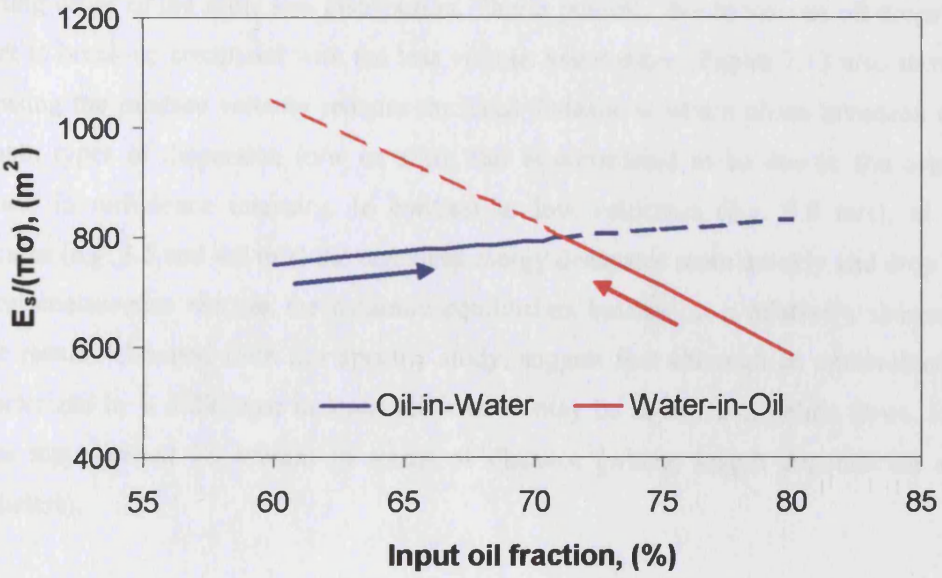

Figure 7.12: Interfacial energy of oil-in-water and water-in-oil dispersions calculated at a distance of 7 m from the entrance for 3.5 m/s mixture velocity. The solid (dashed) lines represent stable (unstable) dispersions.

Since no clear experimental evidence points to the existence of an ambivalent range in the experimental systems studied as part of this work (in both horizontal and vertical flows) and the work carried out by Ioannou (2004) covering a wide range of horizontal flow situations, the equal surface energy criterion seems suitable for the accurate prediction of phase inversion. However, as discussed in Chapter 5, experiments in vertical flows also implied that the slip velocity between phases may be another factor to affect phase inversion. Therefore, more fundamental understanding on the mechanism underlying phase inversion is needed, even though the current PBEs model provides a promising starting point.

The location of achieving steady state in terms of drop size distribution, according to the PBEs predictions in Section 7.6.2.1, has been found to depend on the inherent characteristic of the drops, the mixture velocity and the inlet condition. Accordingly, the axial positions where phase inversion first occurs would also be determined by those factors. A specific study for this characteristic has been conducted in this Chapter. Figure 7.13 presents the inversion point simulated by PBEs model at different mixture velocities; here the same initial drop distribution condition, i.e. a truncated normal distribution, is used for both o/w and w/o dispersions at all velocities. It is clearly illustrated that for the same mixture velocity the inversion location from oil-in-water to water-in-oil dispersion is further away from the entrance compared to the inversion from water-in-oil (w/o) to oil-in-water (o/w), when injecting drops of the same size distribution. This is possibly due to viscous oil drops taking longer to break-up compared with the less viscous water drops. Figure 7.13 also shows that increasing the mixture velocity reduces the axial distance at which phase inversion occurs, for both types of dispersion (o/w or w/o); this is considered to be due to the associated increase in turbulence intensity. In contrast to low velocities (e.g. 3.0 m/s), at higher velocities (e.g. 3.5 and 4.0 m/s) the turbulent energy dissipates more quickly and drop break-up and coalescence reaches the dynamic equilibrium balance in a relatively shorter time. These results, obtained from this specific study, suggest that although an ambivalent range characterized by a difference in input oil fraction may be absent in pipeline flows, such as region may instead be present in terms of distance (whose length depends on system parameters).

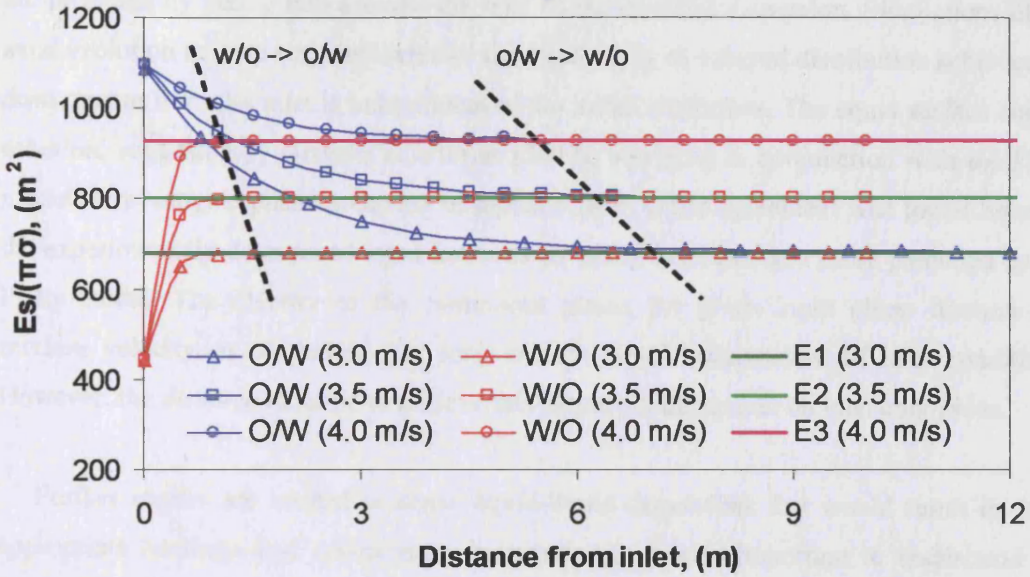

Figure 7.13: A specific case study on the predicted locations for the occurrence of phase inversion in pipeline flows, demarcated by dashed lines, at various mixture velocity and inlet dispersion morphology. Here, O/W (W/O) refers to oil-in-water (water-in-oil) dispersions as the initial conditions; *E* represents the critical level leading to phase inversion as predicted by Equation (7-23).

7.7 Summary

The application of a PBEs model for predicting phase inversion in liquid-liquid dispersed systems, formed in stirred vessels and in pipelines, is described in this Chapter. For stirred vessel systems, the drop size distribution predicted by the PBEs model in dilute dispersions shows good agreement with experimental correlations. However, discrepancies appear for dense dispersions, which were attributed to the modification of coalescence efficiency and collision frequency in dense dispersions. According to the equal surface energy criterion, the predictions from the PBEs model agree with the results by a Monte-Carlo method (Yeo et al., 2002) and the correlation of Yeh et al. (1964). However, this criterion fails to predict the width of ambivalent range, which indicated that a better understanding of the mechanism underlying phase inversion process is needed.

For pipeline flow systems, more advanced PBEs models than those available in literature are proposed by taking into account the flow of the resultant dispersion. Simulations of the axial evolution in drop sizes indicate that the steady fully-developed distribution achieved far downstream from the inlet is independent of the initial conditions. The equal surface energy criterion, suggested by Brauner & Ullman (2002), was used in conjunction with the PBEs model to investigate phase inversion in pipeline flow. Good agreement was found between the experimentally determined input fractions for phase inversion and those predicted by the PBEs model. The identity of the continuous phase, for given input phase fraction and mixture velocity, is ultimately (for long enough pipes) independent of inlet conditions. However, the *distance* required to achieve this identity *is* dependent on inlet conditions.

Further studies are needed in dense liquid-liquid dispersions that would result in more appropriate breakage and coalescence frequencies. It is also important to understand the underlying physical mechanism of phase inversion that would indicate a more suitable criterion for the appearance of an ambivalent region.

Chapter 8

Theoretical Simulation of Phase-Inversion and Ambivalent Range in Stirred Vessels Using a Two-Region Model

Phase inversion in agitated vessels was studied using a two-region model. In this model, breakup and coalescence are assumed to take place in the vicinity of the impeller and away from that region, respectively. The mechanism of phase inversion is regarded as the result of an imbalance between the breakup and coalescence processes. A brief introduction is given in Section 8.1 on the basis for the model developed in the present work. The mathematical equations and model development are presented in Section 8.2. Section 8.3 describes the criterion suggested in the current study for prediction of phase inversion in stirred vessels. A comparison of the predicted ambivalent ranges under various conditions with experimental data is discussed in Section 8.4. Finally, a summary is given in Section 8.5.

8.1 Introduction

Despite the postulation of a number of physical mechanisms to explain phase inversion and the existence of the ambivalent range, as described in Section 2.1.4, very few studies have reported good agreement between theory and experiment in terms of the width of the ambivalent region has proved elusive. The studies described in this Chapter reconsider the problem of predicting phase inversion in an agitated vessel and propose a model that compares breakup and coalescence in the impeller and circulation regions, respectively, to

predict the ambivalent range as a function of system parameters. The predictions are found to be in good agreement with experimental data.

8.2 Model Development

In this section, details of the problem formulation are provided. Details of the procedure used to solve the relevant equations are also given.

8.2.1 Energy Dissipation Rate

For systems (e.g. agitated vessels) where the flow is turbulent but anisotropic and inhomogeneous, the rates of drop breakup and coalescence are spatially dependent; this is because drops tend to breakup and coalesce under high and low turbulence, respectively (Brown & Pitt, 1972). Although phase inversion in agitated vessels has been studied by using the homogeneous turbulence assumption (Juswandi, 1995; Yeo et al., 2002), in order to be able to predict ambivalent range it is necessary to include the flow inhomogeneity, which arises naturally in agitated vessels, in any predictive models. In general, the flow in an agitated vessel exhibits two distinct regions: a region near the impeller in which the flow is highly turbulent and a circulation region away from the impeller where the turbulence intensity is less. This feature of the flow was incorporated in the two-region model described below.

A number of investigators have measured the energy dissipation rates as a function of position in an agitated vessel (see, for instance, Cutter, 1966; Placek & Tavlarides, 1985) and confirmed that the turbulence in these systems is highly inhomogeneous. The following relationships have been postulated to describe the ratio of the local to mean energy dissipation rate,

$$\frac{\varepsilon_i}{\bar{\varepsilon}} = \begin{cases} 7.26 & \text{(Coulaloglou, 1975)} \\ 5.16 & \text{(Placek \& Tavlarides, 1985)} \end{cases} \tag{8-1a}$$

$$\frac{\varepsilon_c}{\bar{\varepsilon}} = 0.26 \quad \text{(Coulaloglou, 1975; Placek \& Tavlarides, 1985)} \tag{8-1b}$$

where ε_i and ε_c are the energy dissipation rates in the impeller and circulation regions, respectively, and $\bar{\varepsilon}$ is the mean energy dissipation rate which in stirred vessels can be estimated by

$$\bar{\varepsilon} = C_1 N_I^3 D_I^2 \tag{8-2}$$

where N_I is the impeller agitation speed, D_I is the impeller diameter and C_1 is a constant for which values of 0.99 (Schwartzberg & Treybal, 1968) and 0.81 (Tsouris & Tavlarides, 1994) have been suggested. Equation (8-2) is valid for a single phase and a dilute dispersion, while for non-dilute dispersions, the use of an effective mixture viscosity was suggested to account for turbulence damping due to the presence of drops (Doulah, 1975):

$$\frac{\bar{\varepsilon}_m}{\bar{\varepsilon}_c} = \left(\frac{\mu_c \cdot \rho_m}{\mu_m \cdot \rho_c} \right)^3 \tag{8-3}$$

where $\bar{\varepsilon}_c$ and $\bar{\varepsilon}_m$ are the energy dissipation rates for the pure continuous phase and the dispersion, respectively; μ_c and μ_m, and ρ_c and ρ_m are the viscosities and densities of the pure continuous phase and dispersion, respectively. A number of expressions have been suggested for the viscosity of liquid-liquid dispersions, μ_m, and they are listed in Table 8.1. Guilinger et al. (1988) applied an indirect method to measure the mixture viscosity during the inversion process in water-kerosene dispersions and found that the predictions by Vermuelen et al. (1955) agree well with the experiments. The expression given by Vermuelen et al. (1955) was used in the present work.

By using the above energy dissipation rate in the circulation region (Equation 8-1b) to calculate maximum stable drop size in a toluene-water dispersion, Tsouris & Tavlarides (1994) found the predicted average drop size to be much larger than that measured experimentally. They concluded that drop breakup occurs only in the impeller region where energy dissipation is higher. Based on an energy balance inside the vessel, the volume of the impeller region, V_I, can be calculated as follows:

$$\frac{V_I}{V_T} = \frac{\bar{\varepsilon}_m - \varepsilon_c}{\varepsilon_i - \varepsilon_c} \tag{8-4}$$

where V_T is the total volume of the vessel. In the present study, $\varepsilon_i = 5.16\bar{\varepsilon}_m$ and C_1=0.99 were used, and $\bar{\varepsilon}_m$ is given by Equation (8-3).

Table 8.1: Expressions for the viscosity of liquid-liquid dispersions. Here, ϕ and μ_d are the dispersed phase volume fraction and viscosity, respectively.

Author (year)	Mixture Viscosity
Taylor (1932)	$\mu_m = \mu_c\left[1+2.5\phi\left(\frac{\mu_d+0.4\mu_c}{\mu_d+\mu_c}\right)\right]$
Vermuelen et al. (1955)	$\mu_m = \frac{\mu_c}{1-\phi}\left(1+\frac{1.5\phi\mu_d}{\mu_d+\mu_c}\right)$
Laity & Treybal (1957)	$\mu_m = \frac{\mu_c}{1-\phi}\left(1+\frac{6\phi\mu_d}{\mu_d+\mu_c}\right)$
Furuse (1972)	$\mu_m = \mu_c\left[\frac{1+0.5\phi}{(1-\phi)^2}\right]$
Barnea & Mizrahi (1976)	$\mu_m = \mu_c \exp\left[2.5(\phi+\phi^{5/3}+\phi^{11/3})\left(\frac{\mu_d+0.4\mu_c}{\mu_d+\mu_c}\right)\right]$
Bedeaux (1983)	$\frac{\mu_d-\mu_m}{\mu_d+1.5\mu_m}\phi+\frac{\mu_c-\mu_m}{\mu_c+1.5\mu_m}(1-\phi)=0$

8.2.2 Sauter Mean Diameter (d_{32})

Drop size measurements in liquid-liquid dispersions in agitated vessels have been carried out for decades. Many correlations have been postulated for the relationship between the Sauter mean diameter (d_{32}) and the physical properties of the fluids, e.g. dispersed phase fraction, viscosity, density and interfacial tension. A comprehensive review is given by Godfrey et al. (1989) and Zhou & Kresta (1998). Generally, in dilute dispersions where the drop size is determined by the turbulent breakup, the Sauter mean diameter, d_{32}, is given by:

$$d_{32} = C_2 We_I^{-n} D_I \tag{8-5}$$

where $We_I = \rho_c N_I^2 D_I^3 / \sigma$ is the Weber number representing the ratio of the external distorting (or deforming) force over the restoring surface tension force, ρ_c is the density of continuous phase and σ is the interfacial tension. However, correlations similar to that given by Equation (8-5) are only valid for dilute dispersions with an inviscid dispersed phase so that the viscous energy within a drop is negligible compared to its surface energy.

As phase inversion often takes place in concentrated dispersions where drop sizes are determined by both breakup and coalescence processes, the influence of drop coalescence must be considered. One common method is to modify Equation (8-5) to take into account the dispersed phase fraction and the viscosity of the dispersed phase as follows:

$$d_{32} = C_2(1+C_3\phi)We_I^{-n} D_I \left(\frac{\mu_d}{\mu_c}\right)^{C_4} \tag{8-6}$$

where C_2, C_3, C_4 and n are adjustable constants, varying with the nature of the dispersed system. Previous experiments have indicated that $0.05 \leq C_2 \leq 0.08$, $0.48 \leq C_3 \leq 22$ (Godfrey et al., 1989; Pacek et al., 1994a; Desnoyer, et al., 2003), n=0.6 in the breakup region and n=3/8 in the coalescence region (Roger et al., 1956; Shinnar, 1961; Nishikawa et al., 1987), and $0.2 \leq C_4 \leq 0.25$ (Zhou & Kresta, 1998). Recently, Desnoyer et al. (2003) investigated drop sizes in two concentrated liquid-liquid dispersed systems (up to 60%), one liquid pair with high coalescence rate and the other with low coalescence rate. They reported that the classical Hinze-Kolmogorov theory (Hinze, 1955) with n=0.6 failed to provide an accurate fit for the drop size in highly concentrated dispersions. Instead, the following polynomial relationships were proposed for n in order to fit their experimental data:

$$n = \begin{cases} -0.425\phi + 0.598 & \text{(at low coalescence rate)} \quad \text{(8-7a)} \\ -\phi^2 + 0.1625\phi + 0.5962 & \text{(at high coalescence rate)} \quad \text{(8-7b)} \end{cases}$$

In the present study, n was given different values for the impeller and circulation regions but was considered independent of the volume fraction. For baffled systems, the parameters used to calculate the drop size in these regions in o/w and w/o dispersions, respectively, are summarised in Table 8.2.

Table 8.2: Values of the parameters in Equation (8-6).

Regions	Impeller Region		Circulation Region	
Dispersions	**o/w**	**w/o**	**o/w**	**w/o**
C_2	0.07	0.07	0.07	0.07
C_3	9.0	9.0 or 0.5	2.0	2.0
n	0.6	0.6 or 3/8	3/8	3/8
C_4	0.25	0.25	0.25	0.25

8.2.3 Breakage and Coalescence Frequency

This chapter focuses mainly on studies in pure liquid-liquid systems in the absence of surfactants and therefore the expressions developed for drop breakage and coalescence are those for dispersions without surfactant. Modification of the present model would be required if surfactants are present. In general three mechanisms are associated with drop breakup, namely turbulent (deformation), viscous shear (tearing) and elongation flow breakup. For dispersions in agitated vessels, turbulent breakup is regarded as the most dominant mechanism (Lasheras et al., 2002). Several functions have been suggested for the turbulent breakup rate. In this paper, the binary breakup frequency, $g(d)$, for drops of diameter d is calculated by the following equation (Luo & Svendsen, 1996):

$$g(d) = 0.4615(1-\phi)\left(\frac{\varepsilon_B}{d^2}\right)^{1/3} \int_0^1 \int_{\xi_{\min}}^1 \frac{(1+\xi)^2}{\xi^{11/3}} \exp\left(-\frac{12C_5\sigma}{2.04\rho_c\varepsilon_B^{2/3}d^{5/3}\xi^{11/3}}\right) d\xi df \qquad (8\text{-}8)$$

where $\varepsilon_B = \varepsilon_i$ is the energy dissipation rate in the breakup region, ξ is the size ratio (l/d) between a turbulent eddy and a drop, σ is the surface tension, and $C_5 = f^{2/3} + (1-f)^{2/3} - 1$ represents the surface increase due to drop breakup given the daughter drop volume fraction f. Note that Equation (8-8) does not need any adjustable parameters for a known drop size in a given turbulent flow.

The drop coalescence rate has been expressed as the product of collision frequency and coalescence efficiency (Coulaloglou & Tavlarides, 1977; Prince & Blanch, 1990; Tsouris & Tavlarides, 1994). Collisions of drops in a turbulent flow were assumed to be analogous to those of gas molecules. Coalescence occurs only when the drop contact time exceeds the time needed by the liquid film trapped between the colliding drops to drain. Accordingly, the

coalescence efficiency was represented by an exponential function of the film drainage time and the drop contact time. A frequently used expression for coalescence frequency, $\lambda(d_1,d_2)$, for drops with diameters d_1 and d_2 was given by Coulaloglou and Tavlarides (1977):

$$\lambda(d_1,d_2)=C_6\frac{\varepsilon_O}{1+\phi}(d_1+d_2)^2(d_1^{2/3}+d_2^{2/3})^{1/2}\exp\left[-\frac{C_7\rho_c\mu_c\varepsilon_O}{\sigma^2(1+\phi)^3}\left(\frac{d_1d_2}{d_1+d_2}\right)^4\right] \qquad (8\text{-}9)$$

where $\varepsilon_O=\varepsilon_c$ is the energy dissipation rate in the coalescence region, $C_6 = 2.17\times10^{-4}$ and $C_7 = 2.28\times10^{13}$ from experimental measurements conducted in dispersions of volume fraction less than 15% (Coulaloglou & Tavlarides, 1977). However, in Equation (8-9) the collision rate between drops is calculated from gas molecular collision theory, which may not be applicable to dense dispersions in which drops are closely packed.

In the present work, the collisions of drops of various sizes are assumed to be analogous to molecular interactions in a fluid of hard spheres that are close together. Therefore, given a drop of size d_1, the possibilities of finding drops of size d_2 at a distance between r and $r+dr$ (see Figure 8.1) can be expressed by a radial distribution function, $h_{12}(r)dr$, where r represents the distance between the drop centres.

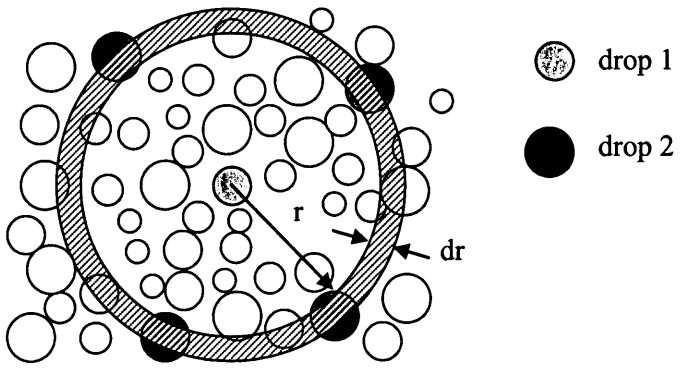

Figure 8.1: A schematic showing drops of various sizes in a concentrated dispersion.

In addition, in order for coalescence to occur, two liquid drops have to stay sufficiently close so that the liquid film between them can be drained off over a short period of time.

Accordingly, the possibility for drops of size 1 'seeing' drops of size 2 can be estimated by the *radial distribution function* when the distance $r \approx (d_1+d_2)/2$. Many expressions have been proposed for the radial distribution function for hard spheres with multi-components (i.e. multi-sized particles) (see, for instance, Percus-Yevick theory (PY), Oden & Henderson theory (OH) and Carnhan & Starling's equation (CS)). The CS equation was found to give better predictions at $r = (d_1+d_2)/2$ and was used here (McQuarrie, 2000):

$$h_{12}(r=\frac{d_1+d_2}{2}) = \frac{1}{1-\chi_3} + \frac{3d_1d_2}{d_1+d_2}\frac{\chi_2}{(1-\chi_3)^2} + 2\left(\frac{d_1d_2}{d_1+d_2}\right)^2 \frac{\chi_2^2}{(1-\chi_3)^3} \tag{8-10}$$

where

$$\chi_i = \frac{\pi}{6}\int_0^\infty N(k)d(d_k^i) \qquad i = 2 \text{ and } 3 \tag{8-11}$$

and $N(k)$ is the number density of drops of size d_k. Therefore, the following coalescence frequency was used, where the right hand side of Equation (8-9) is multiplied by the radial distribution function $h(r)$:

$$\lambda^*(d_1,d_2) = h_{12}(r=\frac{d_1+d_2}{2})\lambda(d_1,d_2) \tag{8-12}$$

8.3 Criterion for Phase Inversion

As discussed above, there is a dynamic balance between drop breakup and coalescence in dispersions, and phase inversion follows when this balance is destroyed. In inhomogeneous systems, such as agitated vessels, the processes of drop breakup and coalescence take place in different regions. In this study, the assumption was used that drops break in the impeller region in which the flow is highly turbulent, and coalesce in the circulation region in which the flow is much less turbulent. Figures 8.2 a&b present a comparison of breakup and coalescence frequencies calculated from Equations (8-8) and (8-12), in which $\varepsilon_B = \varepsilon_i$ and $\epsilon_O = \epsilon_c$, respectively for ρ_c = 998 Kg/m^3, μ_c = 0.96 cP, σ = 0.0323 N/m, $\phi = 0.5$ and $\bar{\varepsilon} = 0.1\,\text{m}^2/\text{s}^3$. The result further illustrates that the breakup frequency in the impeller region is much higher than that in the circulation region; the opposite is true for coalescence frequency, particularly for larger drops.

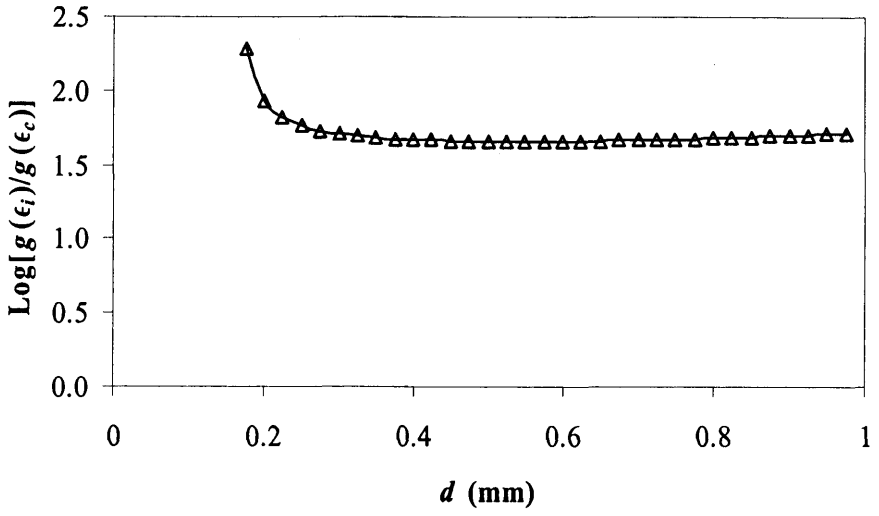

(a)

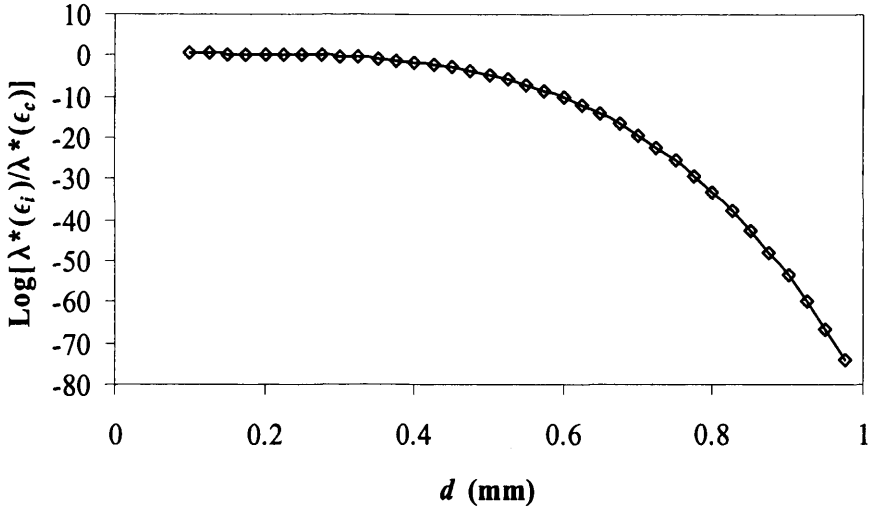

(b)

Figure 8.2: Comparisons of (a) coalescence and (b) breakup frequencies in the impeller and circulation regions with $\bar{\varepsilon} = 0.1$ m^2s^{-3} for $\phi = 0.5$.

From the above description, phase inversion is expected to occur when the coalescence rate exceeds the breakup rate, or:

$$[N(d_{32,c})(V_T - V_I)]^2 \lambda^*(d_{32,c}, d_{32,c}) > N(d_{32,i}) V_I g(d_{32,i}) \tag{8-13}$$

where N is the drop number density per unit volume, $d_{32,c}$ and $d_{32,i}$ are the Sauter mean diameters in the circulation and impeller regions, respectively. Equation (8-13) can then be solved for the only unknown variable, namely the volume fraction of the dispersed phase, ϕ.

8.4 Results and Discussion

Given the above models and criterion for phase inversion, simulations were performed to simulate experiments by Norato et al. (1998) who used a stirred vessel of 10.2 cm in height (H) and 10.2 cm in diameter (T). A Rushton impeller of 5.0 cm diameter was used to agitate the dispersion of two immiscible liquids. Figure 8.3 illustrates the predicted ambivalent range for phase inversion (solid lines) in the toluene/water system using the parameters listed in Table 8.2. The properties of the fluids used in the experiments are shown Table 8.3. As can be seen in Figure 8.3 the prediction of the upper curve of the ambivalent range (from o/w to w/o) is in fairly good agreement with the experimental data of Norato et al. (1998). The organic phase volume fraction required for phase inversion decreases with increasing agitation speed. However, the lower curve (solid line) representing inversion from w/o to o/w shows an opposite trend compared with the experiments. It is proposed that this may be due to the fact that water drops in an oil medium can coalesce more efficiently due to the relative absence of repulsive electrostatic forces; that is, water drops do not experience similar repulsive forces to oil drops in an aqueous environment where the electrical double layers around oil drops that approach each other can overlap (Kumar, 1996). This means that some coalescence of water drops in oil can also appear in the impeller region which will modify the average drop size. This effect may be taken into account by setting n = 3/8 and C_3 = 0.5 in the impeller region. As shown in Figure 3, the prediction of the model with the revised constants (dashed line) agrees reasonably well with the experimental data and the modified parameters are then used to generate the rest of results shown in this work.

Table 8.3: Physical properties of the liquid-liquid systems used in the experiments of Norato et al. (1998).

Liquid-liquid system	ρ_o (kg/m^3)	ρ_w (kg/m^3)	μ_o (Pa s)	μ_w (Pa s)	σ (N/m)
Toluene/Water	867	996	0.00057	0.00096	0.0323
Toluene+CCl4(4.54 wt%) /Water	900	995	0.00059	0.00101	0.0299
Toluene+CCl4(23.8 wt%) /Water	1040	996	0.00065	0.00097	0.0277
Toluene+CCl4(43.1 wt%) /Water	1180	996	0.00073	0.00100	0.0263
Methyl Isobutyl Ketone /Water	805	977	0.00061	0.00102	0.0089

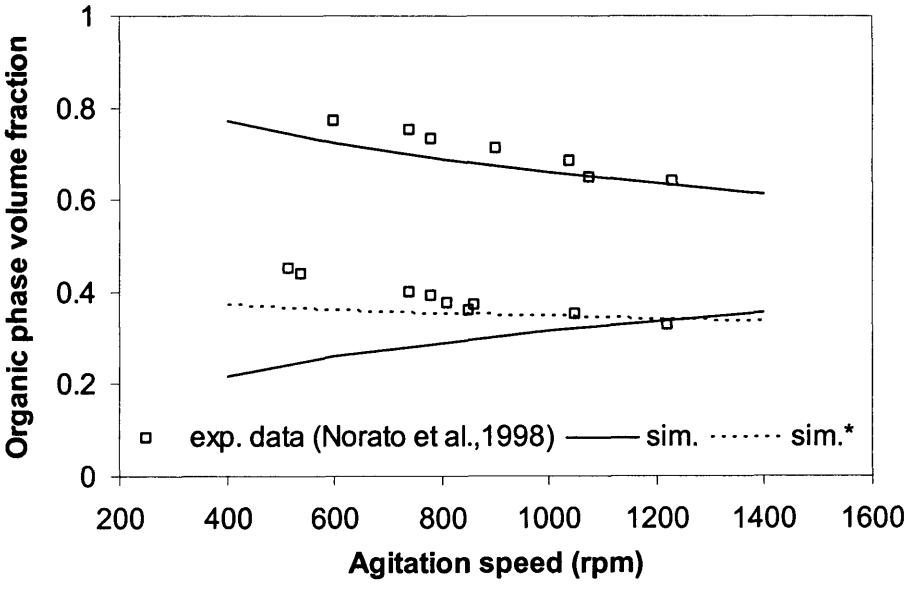

Figure 8.3: Comparison of the predicted ambivalent range with the experimental data by Norato et al. (1998). Here, for the impeller region C_3=9 and n=0.6 (solid line); C_3=0.5 and n=3/8 (dashed line); the rest of the parameters are as listed in Table 8.2.

Figure 8.4 presents a comparison between model and experiments (by Norato et al., 1998) of the ambivalent range in a toluene/water system with and without the use of the radial distribution function [Equation (8-10)], which was adopted to better describe the drop collision behaviour in concentrated dispersions. As shown in Figure 8.4, the width of the ambivalent range is over-predicted in the absence of the radial distribution function. This illustrates the fact that the coalescence rates obtained for dilute dispersions provide a poor approximation to those of dense dispersions, and Figure 8.4 also provides a motivation for the use of the radial distribution function in the rest of the work.

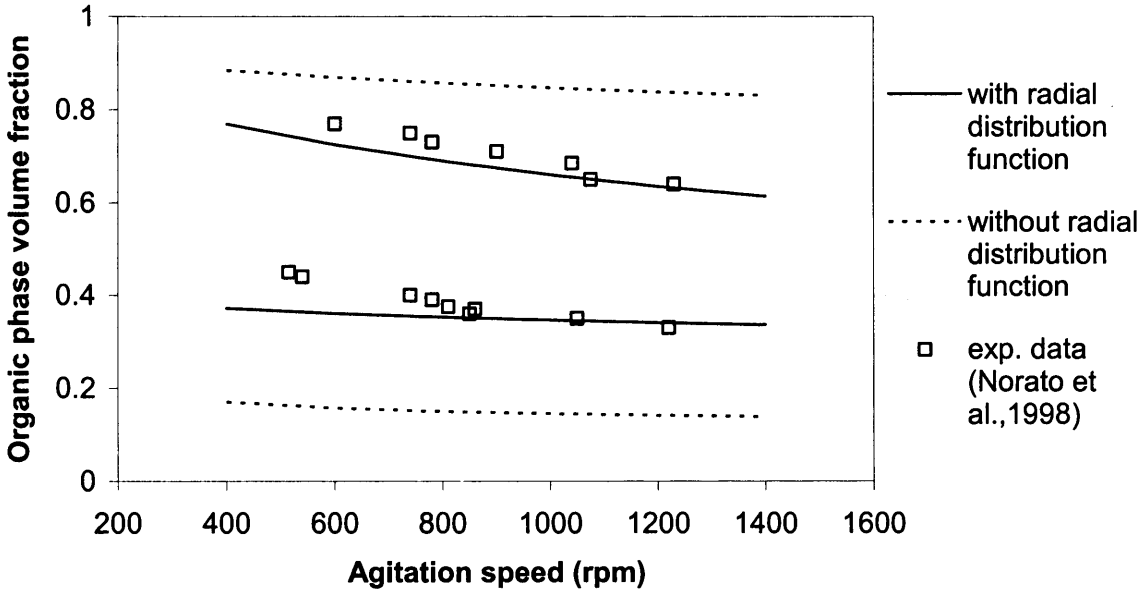

Figure 8.4: Effect of the radial distribution function on the model predictions for a toluene/water system; the experimental data is taken from the work by Norato et al. (1998).

Figure 8.5 illustrates the predicted phase inversion ambivalent ranges for a toluene/water system, with an interfacial tension of 0.0323 N/m, and a methyl isobutyl ketone (MIBK)/water system, with a lower interfacial tension of 0.0089 N/m. The predictions are compared with the experimental data of Norato et al. (1998). Both prediction and experimental data indicate a shift to lower organic phase fractions of the lower and upper inversion curves. As shown in Figure 8.5, the predicted upper curve of the ambivalent range of both systems shows good agreement with the experimental data. The organic phase

volume fraction at phase inversion from o/w to w/o dispersion decreases gradually with increasing agitation speed. The predicted lower curves are also in good agreement with the experimental data for the toluene/water system which has a relatively high interfacial tension; the agreement for the lower interfacial tension system, MIBK/water, is not as good. The experimental results of Norato et al. (1998) show that the lower curve of the ambivalent range undergoes a significant drop as the interfacial tension decreases. Similar investigations were also carried out by Reeve & Godfrey (2002) in a square cross-section tank; their experiments show that the width of the ambivalent range is unchanged with variation of the interfacial tension. The simulations from our two-region model, shown in Figure 8.5, seem to agree better with the findings of Reeve & Godfrey (2002).

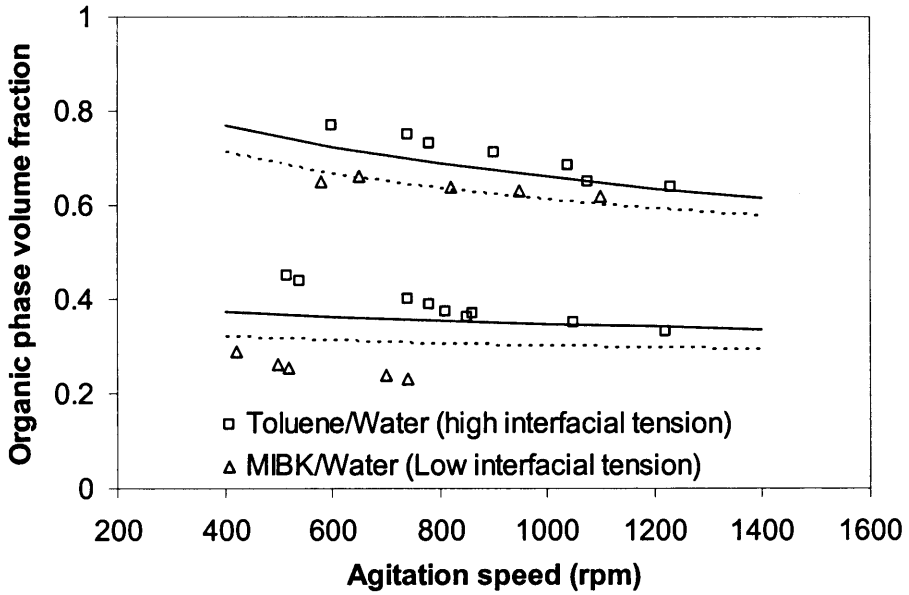

Figure 8.5: Effect of interfacial tension on phase inversion; comparison of predicted ambivalent ranges for toluene/water (solid lines) and MIBK/water (dashed lines) with the experimental data by Norato et al. (1998).

Figure 8.6 shows the influence of the organic phase density on the predicted ambivalent range; the predictions are again compared with the experimental data of Norato et al. (1998) where the organic phase density is varied by adjusting the concentration of CCl_4 in toluene+CCl_4/water system. To truly compare with the experiments, the simulation has also taken into account the slight changes of other parameters (e.g. interfacial tension and

viscosity) due to the variation of the CCl_4 concentration. The agreement between the model predictions and the experimental results shows that the density differences between organic and aqueous phase do not affect significantly the phase inversion point and ambivalent range. These results are also in agreement with those reported by previous investigators (Selker & Sleicher, 1965; McClarey & Mansoori, 1978).

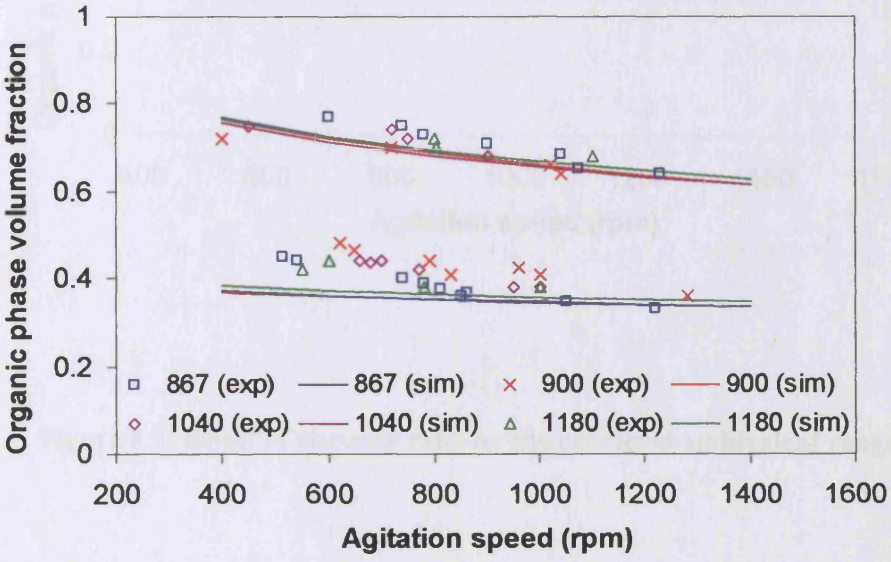

Figure 8.6: Effect of organic phase density (in Kg/m^3) on phase inversion; comparison of predicted ambivalent ranges with the experimental data by Norato et al. (1998).

Viscosity has been shown to play an important role in determining phase inversion point and to affect directly the width of the ambivalent range. In general, it has been found that as the viscosity of a liquid phase increases its tendency to be the dispersed phase also increases (Selker & Sleicher, 1965). Figure 8.7 illustrates the predicted effect of the viscosity ratio (μ_d/μ_c) on the ambivalent range. The simulation shows that the upper and lower curves of the ambivalent range move towards higher and lower organic phase volume fractions, respectively, with increasing viscosity ratio; in other words, more dispersed phase is required to invert a dispersion as its viscosity increases. This trend is in agreement with previous experimental observations (Selker & Sleicher, 1965). The trend is due to the fact that the coalescence probability increases with decreasing viscosity of dispersed phase (Chesters, 1991). Similar trends were also found by Yeh et al. (1964) and Yeo et al. (2002).

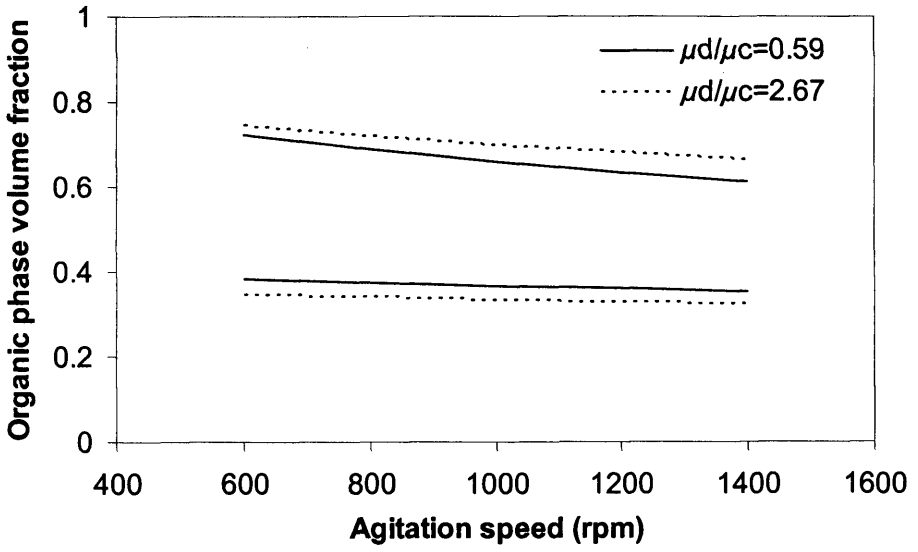

Figure 8.7: Effect of viscosity ratio on the predicted ambivalent range.

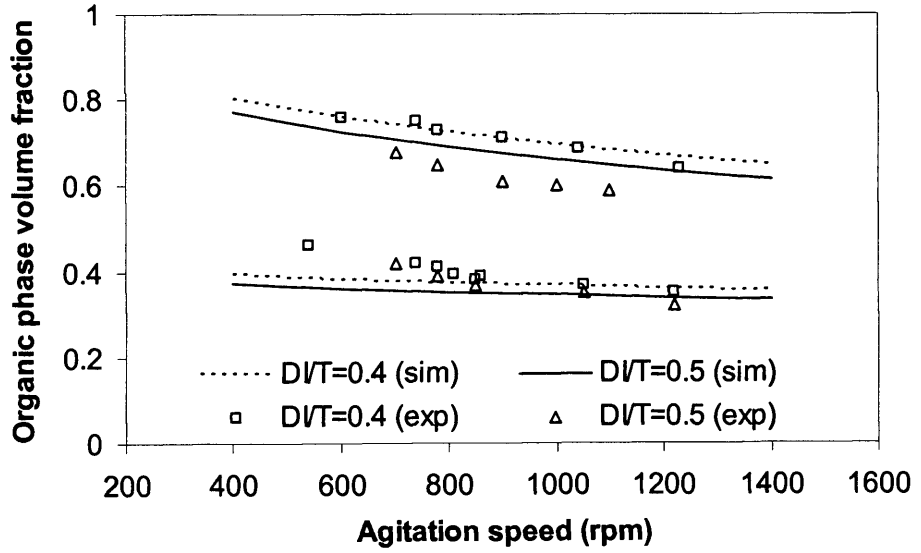

Figure 8.8: Effect of impeller to tank diameter ratio on phase inversion; comparison between model predictions and the experimental data by Norato et al. (1998).

Apart from liquid physical properties (e.g. viscosity, interfacial tension and density), the effect on phase inversion of tank geometry and materials has also been studied (Quinn & Sigloh, 1963; Selker & Sleicher, 1965; Kumar et al., 1991; Deshpande & Kumar, 2003). The experiments of Norato et al. (1998) showed that the ambivalent range is not strongly influenced by varying the ratio of impeller size to tank diameter (in the range 0.417 ~ 0.619), although both curves shift downwards slightly with impeller speed. Moreover, it was found that for a given system and a fixed volume fraction, a small impeller needs higher agitation speed to reach inversion (Quinn & Sigloh, 1963; Deshpande & Kumar, 2003). In this study the effect of impeller size on phase inversion and ambivalent range is simulated for a toluene/water system and the results are presented in Figure 8.8. The predictions are in good agreement with the experimental data by Norato et al. (1998). Both curves of the ambivalent range are found to shift to slightly lower values of organic phase fraction as the impeller size increases and more energy input is required to invert the dispersion under a given volume fraction for a smaller size impeller.

8.5 Summary

In this Chapter, a model to predict the phase inversion volume fraction and the width of the ambivalent range of concentrated liquid-liquid dispersions in agitated vessels is described. This so-called 'two-region' model is based on the assumption that rates of breakup and coalescence are relatively high in the impeller and circulation regions, in which the turbulence intensity is high and low, respectively. Phase inversion was assumed to take place when the drop coalescence rate in the circulation region exceeds that of breakup in the impeller region. In order to extend the validity of the coalescence frequency expressions available in the literature which have been determined for dilute dispersions, the concept of a radial distribution function was used. The model predictions were found to be in good agreement with experimental observations, particularly for the upper curve of the ambivalent range (inversion from o/w to w/o). The agreement between the predictions of the lower ambivalent range curve (inversion from w/o to o/w) and experimental data, however, were not as good. This may be due to the formation of secondary dispersions, which have been observed experimentally to accompany the inversion from w/o to o/w (Pal, 1993; Pacek et al., 1994b; Liu et al., 2005). Their formation would mean less effective continuous phase volume for the same dispersed phase fraction and the appearance of phase inversion at higher continuous (organic) phase fraction. A PBEs-based framework to account for the presence of secondary dispersions and the inclusion and escape of secondary droplets is presented in the following chapter.

Chapter 9

Frame Work for Simulating Secondary Dispersions Using Population Balance Equations (PBEs) Model

As discussed in previous chapters, the formation of secondary dispersions was suggested as another important factor that could significantly affect the stability of a dispersion and the occurrence of phase inversion. Moreover, despite the fact that secondary dispersions have been observed for several decades, the understanding of the mechanism of inclusion and escape is still rather limited due to the complicated nature of this phenomenon and the difficulties associated with experimental measurements. Even though a few experiments have been conducted to quantitatively investigate some parameters associated with such complex dispersions, no modelling work on dispersed systems containing secondary dispersions has been reported in the literature. This Chapter, therefore, outlines a framework, developed in the present work, for simulating the dynamic evolution of dispersions containing secondary droplets, using a population balance equations (PBEs) model.

The rest of this Chapter is organised as follows. Section 9.1 summarizes previous experimental observations and postulated mechanisms for inclusion and escape processes of secondary droplets. The models and equations used to develop the present modelling framework are given in Section 9.2, and Section 9.3 describes the implementation methods. Section 9.4 illustrates the simulated results on the evolution of secondary droplets and dispersed drops. Finally a short summary is given in Section 9.5.

9.1 Introduction

In a liquid-liquid dispersion (normally involving an organic and an aqueous phase) it is possible for the dispersed phase to entrain some of the continuous phase forming a droplets-in-drop structure, termed 'secondary' dispersion or 'multiple' dispersion, as shown in Figure 9.1. The enclosed continuous phase droplets can also escape from the dispersed drops. The formation of secondary dispersions is a common phenomenon which can impact a number of processes in chemical and process industries, such as the production of fine emulsions and phase separation. It is therefore necessary, in order to optimise the system performance, to understand the dynamic evolution of these two processes (i.e. secondary droplet entrainment and escape, and the distribution of secondary droplets). However, so far not much attention has been paid to achieving fundamental understanding of the dynamic behaviour of secondary droplets in the literature.

To describe clearly what follows in this Chapter, the structure of a secondary dispersion is hence defined in terms of '*host drop*' (or '*drop*') which is dispersed in the continuous phase, and '*secondary droplet*' (or '*droplet*') which is the part of the continuous phase entrapped inside the 'host drop'.

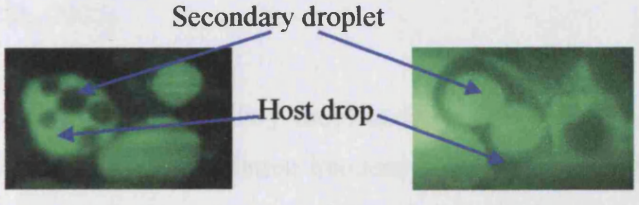

Figure 9.1: Secondary dispersions of o/w/o (a) and w/o/w (b) structures visualized by laser induced florescence technique (Liu et al., 2005). Green and black regions correspond to water solution and oil phase, respectively.

9.1.1 Mechanisms of Inclusion

A number of mechanisms have been proposed in the literature to interpret the formation of secondary droplets (Pacek et al., 1994a; Groeneweg et al., 1998; Sajjadi et al., 2002; Liu et al., 2005), which could be summarized as follows:

Binary coalescence Inclusion could occur during coalescence following an intense collision between two drops, which gives rise to 'dimple' formation followed by film rupture, that causes entrapment of a droplet of the continuous phase in the resultant coalesced 'host' drop. This mechanism is often regarded valid at low volume fractions of dispersed phase (Kumar, 1996).

Multi-body coalescence Inclusion could also occur during multi-drop collision and subsequent coalescence, e.g. by three or more adjacent drops, which entrains the interstitial continuous phase into the newly formed drop. The secondary droplets formed by multi-body collision are likely, as expected, to occur in highly concentrated emulsions where drops are closely packed.

Large drop deformation Inclusion could occur if a large drop of dispersed phase under a high shear rate is severely deformed, and then engulfs the continuous liquid inside. After analysing the size of secondary droplets formed in a polymer/water/surfactant system, Sajjadi et al. (2002) suggested that drop deformation was the main mechanism for generating secondary dispersions at a low dispersed phase fraction. However, it was also found that there is a large contribution of this mechanism to the formation of secondary droplets as phase inversion is approached, where the flow becomes highly viscous and drops are very elongated (Liu et al., 2005).

The rates of formation of secondary droplets from binary coalescence and large drop engulfment may depend on the circulation frequency of drops passing through the region of high shear rate, such as the impeller region in agitated vessels. Groeneweg et al. (1998) measured the inclusion frequency both by microscopic observations and by measuring the conductance of the dispersion, and found only a few inclusions per drop are occurring in their system during each circulation. They then pointed out that collisions of drops with sufficient intensity leading to coalescence and possibly secondary dispersions only occur in a small volume just outside the impeller region. The inclusion rates at two different initial dispersed phase volume fractions, 20% and 40% respectively, were also compared and accordingly they suggested that the inclusion frequency is not necessarily proportional to the coalescence frequency, as a similar number of inclusion events are shown for both cases. It was further reported that the inclusion frequency reaches its maximum at one critical volume fraction; no further increase in the inclusion frequency will occur with increasing volume fraction of the dispersed phase.

9.1.2 Mechanisms of Escape

According to Groeneweg et al. (1994), Sajjadi et al. (2002) and Klahn et al. (2002), the following two mechanisms lead to the escape of entrapped small droplets:

Passive escape The escape of included droplets could occur if the surrounding host drop becomes sufficiently deformed by the external flow, such that the film between the secondary droplet and the continuous phase might rupture and the droplet will subsequently escape.

Active escape The enclosed droplet actively moves within the surrounding drops and when it reaches the boundary of the host drop and remains there for a sufficiently long time, the film between the enclosed droplet and the continuous phase might become so thin that it ruptures, leading to the coalescence of droplet and continuous phase and the escape of the entrapped droplet.

Klahn et al. (2002) recently developed a model to calculate the rate from active escape, by assuming that motions of secondary droplets are driven by the flow within the host drop exposed to an external shear flow and that the entrapped droplets can escape provided that they contact the boundary of host drop for a sufficiently long time. A modified coalescence model of drop-drop interaction was then used to express the escape process. The escape rate function derived was then incorporated into a CFD model and the theoretical predictions showed good agreement with their experimental data. However, the fundamental expression of the escape rate postulated in their paper [see Eq. (2) of Klahn et al. (2002)] may be in error (as will be discussed below). A modified escape function is applied in this work.

9.1.3 Asymmetric Characteristic

Interestingly, previous experiments have shown that oil droplets are likely to be entrapped by water drops in water-in-oil dispersions (o/w/o), but water droplets are seldom included within oil drops in oil-in-water dispersions (w/o/w), even in the case of systems with equal densities and viscosities. There have been a large number of visual observations of o/w/o dispersions in the past [see, for instance, of Pal (1993), Pacek et al. (1994 a,b), Pacek & Nienow (1995a,b), Pacek et al. (1994b), Sajjadi et al. (2002), and Liu et al. (2005)]. However, only few experiments have captured the formation of w/o/w structures in pure (no surfactant) liquid-liquid dispersions (Luhning & Sawistowski, 1971; Groeneweg et al., 1998; Liu et al., 2005). Although some suggestions have been postulated to elucidate the reason for

this asymmetric behaviour, i.e. overlapping of electrical double layers of oil drops (Kumar 1996) and purity of the oil phases (Groeneweg et al., 1994), complete understanding of this has not yet been achieved. Recently, Groeneweg et al. (1998) also argued that the inclusion does occur in both o/w and w/o dispersions, but in the case of o/w emulsions, inclusion of secondary droplets is counterbalanced by their fast escape, making w/o/w dispersions difficult to observe.

9.1.4 Effect on Phase Inversion

The occurrence of secondary dispersion will increase and decrease the effective volume fractions of the dispersed and continuous phases, respectively. As expected, the effective volume fraction of the dispersed phase is determined by the balance between the rate of inclusion of droplets of the continuous phase into host drops of the dispersed phase and the rate of escape of the enclosed droplets to the continuous phase. In a system where inclusion is preferable initially, there can either be a gradual increase of the effective volume fraction until a steady state is reached in which the inclusion is in balance with the escape, or a large increase in the effective volume fraction to the point where drop break-up can no longer counterbalance coalescence and phase inversion occurs. In addition, increases in the effective volume fraction of the dispersed phase also lead to damping of turbulence levels and the enhancement of drop coalescence, both of which promote phase inversion. In fact, it has been suggested that, in an agitated system, the time for increasing the effective volume fraction via inclusion corresponds to the majority of the total stirring time, as the actual inversion occurs rapidly soon after the critical effective volume fraction is reached (Groeneweg et al., 1998; Sajjadi et al., 2002).

The formation of secondary dispersions may also be partly responsible for the appearance of the 'ambivalent' region, a well-documented phenomenon which accompanies phase inversion in agitated vessels (Pacek et al., 1994b; Kumar, 1996). As discussed above, there is an asymmetry of secondary liquid-liquid dispersions: o/w/o are more likely to be formed than w/o/w. The effective dispersed phase volume fraction is, therefore, higher in w/o dispersions than o/w dispersions for a given initial volume fraction. The asymmetric existence of secondary dispersion is then invoked to interpret why the critical dispersed phase holdups for phase inversion from o/w dispersion to w/o dispersion are higher than in the reverse case.

9.2 Model and Equations

The details of population balance-based models and equations adopted in this work are presented in the following Section.

9.2.1 Population Balance Equations (PBEs)

A surfactant-free liquid-liquid dispersion is considered wherein the turbulence fluctuations and energy dissipation rate are isotropic and uniform. Drops of the dispersed phase, which are assumed to be spherical, can break into two smaller daughter drops or coalesce with another drop to form a large drop; droplets of the continuous phase, also assumed to be spherical, can be included into and released from host drops. Only the multiple dispersion structure of o/w/o or w/o/w is considered, while the rate of formation of more complex structures, such as w/o/w/o, is assumed to be negligibly small. It is also assumed that all drops (including secondary droplets) are distributed homogeneously in terms of size and space. Therefore, the time evolution of drop and droplet distribution can be described by the dynamic balance of processes, such as coalescence and breakage of host drops, inclusion and escape of secondary droplets, coalescence and breakage of secondary droplets in a given host drop. However, since the secondary droplets are surrounded by a relatively passive ambient fluid whose flows are driven mainly by external shear stresses, it could then be expected that the breakage rate of small droplets is negligible as compared to that of the escape and inclusion processes. Similarly, the coalescence of small droplets is also assumed to be negligible in the current model, despite the results of Sajjadi et al. (2002) who observed an increase in the size of secondary droplets with volume fraction which they attributed to their coalescence.

If $N(D)$ describes the number density (defined as the number per unit volume) of host drops for a given size D, and $n(d/D)$ describes the number density [defined similarly to $N(D)$] of secondary droplets of diameter d in the host drop of size D, then the equations governing the population of host drop (D) and its included secondary droplets (d) can be expressed as

$$\frac{dN(D)}{dt} = \dot{B}(D) - \dot{D}(D) \tag{9-1}$$

$$\frac{dn(d/D)}{dt} = \dot{b}(d/D) - \dot{d}(d/D) \tag{9-2}$$

where t denotes time, and $\dot{B}(D)$ and $\dot{D}(D)$ are the 'birth' and 'death' rates of a host drop of size D, respectively; while, $\dot{b}(d/D)$ and $\dot{d}(d/D)$ are the birth and death rates of secondary droplets of diameter d in the host drop of diameter D, respectively. Note that in Equations (9-1) and (9-2), the precise number of secondary droplets within a host drop (for example how many host drops, D, only include three secondary droplets) is unknown in the current framework. Instead, an average number of secondary droplets of size d in a host drop of given size D is used in the current work.

As far as the inclusion and escape processes are concerned, it is assumed that any two events (such as breakage and escape, escape and inclusion, escape of secondary droplets of two different sizes etc.) could not take place simultaneously for a given drop or droplet but could happen in a finite sequence. The inclusions of secondary droplets are assumed only as a result of intensive coalescence of two drops. It is also assumed that only one droplet can be entrapped into a host drop formed via coalescence of two drops if coalescence leads to the occurrence of an inclusion event. The secondary droplets of a given size d are assumed to be distributed equally among the host drops of diameter D, so that the decrease in the number of host drops due to an escape event could be estimated by knowing the total number of escape events and the average droplet number per host drop.

Therefore, for the system studied, the increases in the number of drops of volume V will be dependent on the following factors:

- Breakage of large (host) drop ($>V$) which leads to one of the daughter drops having a volume V;
- Escape of secondary droplet(s) in a large host drop ($>V$) which leads to formation of a new host drop of volume V;
- Pure coalescence of small (host) drops without entrapping the secondary droplets, forming a big (host) drop of volume V;
- Coalescence of small (host) drops, in the presence of inclusion of secondary droplet, to form a host drop of volume V.

Accordingly, the birth rate of drops of size D (volume V) in Equation (9-1) can be given by the following expression:

$$\dot{B}(V) = \int_{V}^{\infty} m(V')\beta(V,V')g(V')N(V')dV' +$$
$$\int_{V}^{\infty}\int_{0}^{V'-V} S(v,V')\frac{c(v/V')n(v/V')}{k(v/V')}dvdV' +$$
$$\int_{0}^{V/2} \eta(V-V',V')\lambda(V-V',V')h(V-V',V')N(V-V')N(V')dV' + \quad (9\text{-}3)$$
$$\int_{0}^{v_{max}}\int_{0}^{(V-v)/2} [1-\eta(V-V'-v,V')]p_v(V-V'-v,V')\lambda_v(V-V'-v,V')\times$$
$$h(V-V'-v,V')N(V-V'-v)N(V')dV'dv$$

The terms on the right-hand-side of Equation (9-3) represent the contributions of *breakage, escape, pure coalescence, and inclusion* events, respectively, to the increase in population of a given (host) drop size, as discussed above. Here, $m(V')$ is the number of drops formed from the breakage of a drop volume V', which is set to 2 for the binary break-up assumed in the present model; $\beta(V,V')$ is the probability density of the daughter drops which represents the likelihood of forming drops of V from breakage of drops of V'; $g(V')$ is the breakage frequency of the drops of volume V'; and $c(v,V')$ is the escape frequency of secondary droplets of volume v from host drop of volume V'. $k(v/V') = n(v/V')/N(V')$ is the average number of secondary droplets of volume v within a host drop of volume V'; $S(v,V')$ is a sign function which is 1 if $V=V'-k(v/V')v$, 0 otherwise; $h(V,V')$ is the collision frequency of drops of volumes of V and V'; $\lambda(V,V')$ is the coalescence efficiency once a collision occurs between drops of volume V and V'; $\eta(V,V')$ is the fraction of the coalescence events which do not involve secondary droplet inclusion in the formed drops (which is called 'pure' coalescence); v_{max} is the maximum volume of secondary droplets entrapped by coalescence; $\lambda_v(V,V')$ is the efficiency for drops of volume V and V' to coalesce and include the secondary droplet and $p_v(V, V')$ is the probability to entrap secondary droplets of volume v inside the host drop if secondary droplets are formed. Note that the efficiency $\lambda_v(V,V')$ could depend on $p_v(V, V')$, since the size of an entrapped droplet can depend on the drainage dynamics accompanying coalescence (Yeo et al., 2002). However, in this study they are assumed to be two independent functions. During the escape process, also, the release of secondary droplets of different sizes is assumed not to occur simultaneously to a single host drop; in other words, at a given time one host drop could only allow its internal droplets of one fixed size to escape.

Similarly, the decreasing number of (host) drops of volume V at a given time t depends on the following factors:

- Breakup into smaller drops;
- Coalescence with other drops to form larger (host) drops (with and without droplet inclusion);
- The release of internal secondary droplets which leads to the formation of smaller drops;

According to above description, the death rate in Equation (9-1) can then be given by the following expression:

$$\dot{D}(V) = g(V)N(V) + N(V)\int_{o}^{\infty} \{\eta(V,V')\lambda(V,V') + [1-\eta(V,V')]\int_{0}^{v_{max}} P_v(V,V')\lambda_v(V,V')dv\} \times h(V,V')N(V')dV' + \int_{0}^{v_{max}} \frac{c(v/V)n(v/V)}{k(v/V)}dv \quad (9\text{-}4)$$

where the terms on the right-hand-side of Equation (9-4) show the contributions from the phenomena of *breakage*, *coalescence* and *escape*, respectively.

Here, it is assumed that the birth of secondary droplets of volume v in host drop V will be determined by the following factors:

- Breakup of a droplet-carrying host drop of volume larger than V to form a host drop of volume V containing a secondary droplet of volume v;
- Coalescence of host drops of volume smaller than V to form a host drop of volume V which contains a secondary droplet of volume v; this may be formed during the coalescence process or may have existed in either one of the mother host drops ;
- Release of secondary droplet from a host drop of volume larger than V that contains droplets of volume v to form a host drop of volume V containing a secondary droplet of volume v;

The expression of birth rate of secondary droplets of volume v in host drops of volume V can then be written as

$$\dot{b}(v/V) = V\int_{V}^{\infty}\frac{k(v/V')}{V'}m(V')\beta(V,V')g(V')N(V')dV' +$$
$$\int_{0}^{V/2}\eta(V-V',V')\lambda(V-V',V')h(V-V',V')N(V-V')N(V')\times$$
$$\left[k(v/V')+k(v/(V-V'))\right]dV' +$$
$$\int_{0}^{(V-v)/2}[1-\eta(V-V'-v,V')]p_v(V-V'-v,V')\lambda_v(V-V'-v,V')\times \quad (9\text{-}5)$$
$$h(V-V'-v,V')N(V-V'-v)N(V')dV' +$$
$$\int_{V}^{\infty}k(v/V')\times\left[\int_{0}^{V'-V}S(v',V')\frac{c(v'/V')n(v'/V')}{k(v'/V')}dv'\right]dV'$$

where the terms on the right-hand-side represent the contributions by the processes of *breakage*, *pure coalescence*, *inclusion* and *escape*, respectively.

The death of secondary droplets of volume v in host drops of volume V depends on the following factors:

- Breakup of a host drop of volume V to form a drop of a smaller volume containing a secondary droplet;
- Coalescence of a drop of volume V carrying secondary droplets with another drop (in the presence or absence of inclusion events);
- Release of secondary droplets by their hosts into the continuous phase to form smaller host drops;

The expression for the death rate of secondary droplets of volume v in host drops of volume V can be finally written as:

$$\dot{d}(v/V) = k(v/V)g(V)N(V) +$$
$$k(v/V)N(V)\int_{o}^{\infty}\{\eta(V,V')\lambda(V,V') +$$
$$[1-\eta(V,V')]\int_{0}^{v'_{max}}P_v(V,V')\lambda_v(V,V')dv\}h(V,V')N(V')dV' + \quad (9\text{-}6)$$
$$c(v/V)k(v/V)N(V)$$

Equations (9-1) – (9-6) constitute the basic population balance equations and will be used to track the distributions of host drops and secondary droplets. Equations (9-1) and (9-2) generate a group of integral differential equations which could only be solved if the functions expressing the inclusion and escape rate of secondary droplets are specified. However, with the exception of the work of Klahn et al. (2002) on droplet escape, very few relevant studies exist in the literature. Here, the model of Klahn et al. (2002) on droplet escape is used and some approximate closure representations for the remaining functions are adopted.

9.2.2 Escape Rate of Secondary Droplets

The model developed by Klahn et al. (2002) is used here to derive the escape rate of secondary droplets from the host drop. It was presumed that the instability of a secondary dispersion is governed by the external flow of the continuous fluid, which generates an internal flow within the host drop. This internal flow drives the included droplets into contact with the interface of the host drop, which could result in an escape event provided that the film between the droplets and the continuous fluid drains sufficiently quickly. Also, Klahn et al. (2002) suggested that, for an inner droplet to escape, it must be transported to the critical volume near the boundary of host drop (see Figure 9.2). Only droplets in this outer shell region only would have an opportunity to escape, while those in the core region cannot be released.

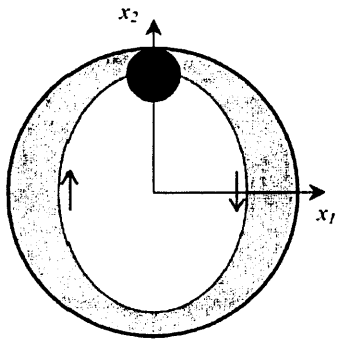

Figure 9.2: Diagram of critical volume (shaded region) determined by the internal fluid flow streamlines (Klahn et al., 2002).

The change of internal droplet number, $n(v)$, was accordingly expressed as follows

$$\frac{dn(v)}{dt} = -\frac{2P_E}{t_c}[n(v) - (1-\alpha_{cr})n^0(v)] \tag{9-7}$$

where P_E is the escape probability which was assumed to be analogous to the probability of coalescence of the entrapped droplet with the outer continuous phase; α_{cr} is the critical volume fraction; t_c is the circulation time of the secondary droplet inside the host drop and $n^0(v)$ is the initial droplet number at $t = 0$. Klahn et al. (2002) then developed the following functions to describe the above variables:

$$t_c = \frac{4\pi m}{\dot{\gamma}} \tag{9-8}$$

$$P_E = \left(\frac{\pi\sigma d^2}{8A_H}\right)^{\frac{-4(1+\Gamma)}{9\pi \cdot m}} \tag{9-9}$$

$$\alpha_{cr} = 1 - \exp\left\{-\left[2.22 + 1.51 \cdot \Gamma^{-0.57}\right]\frac{d}{D}\right\} \tag{9-10}$$

in which

$$m = \frac{1+\Gamma}{\sqrt{\Gamma(1+\Gamma)}} + \frac{95\Gamma(19\Gamma+16)}{4[(19\Gamma)^2 + (40/C_a)^2]}\left[5 - \frac{(1+\Gamma)(25\Gamma^2+50\Gamma-31)}{5[\Gamma(\Gamma+2)]^{3/2}}\right] \tag{9-11}$$

Here, the capillary number (C_a) is defined as

$$C_a = \frac{d\dot{\gamma}\mu_c}{\sigma} \tag{9-12}$$

In Equations (9-8) – (9-12), m is the dimensional circulation time, given by Equation (9-11); $\dot{\gamma}$ is the shear rate defined by the stirrer spin rotation frequency in Klahn's work; d and D are the diameters of secondary droplets and host drop, respectively; $A_H = 4.88\times10^{-21}$ J is the Hamaker constant; Γ is the viscosity ratio of the dispersed (μ_d) to the continuous phase (μ_c); σ is the interfacial tension.

Recently, the above escape model has also been incorporated into the CFD code, STAR-CD, by Agterof et al. (2003) to predict the drop size distribution in oil-water dispersions.

However, note that in the work of Klahn et al. (2002) and Agterof et al. (2003), the formula for escape rate was incorrectly derived. [§] The current study revises their expression resulting in the correct form of Equation (9-7).

Equation (9-7) can be solved for a given host drop according to the above definitions for circulation time, coalescence probability and critical volume fraction. However since, in the current PBEs model, the number and details of secondary droplets within each host drop are not considered (an average value is used instead), another simplification is therefore necessary before Equation (9-7) can be used. Here, the secondary droplets in each individual host drop are assumed to be redistributed uniformly in space following an escape event. This, of course, implies that the droplets in the core region will travel outside this region over a short time to compensate for the release of a secondary droplet, which violates the main assumption underlying the work of Klahn et al. (2002). Accordingly, in this study the escape rate of secondary droplet is then written as

$$c(v/V) = \frac{2P_E(v/V)}{t_c(v/V)} \tag{9-13}$$

Figure 9.3 shows the relationship of $c(d/D)$ with the size of secondary droplet and host drop in a water-in-toluene system with $\dot{\gamma} = 20\,\mathrm{s}^{-1}$.

Another mechanism for secondary droplet escape is the host drop deformation; the inside droplet is gripped in the narrow neck region of a deformed drop and is then released. However, by comparing their prediction with experimental data, Klahn et al. (2002) suggested that the escape from deformation is negligible compared to the active escape. Hence, deformation-induced escape (or 'passive' escape) of secondary droplets is not considered here.

[§] The escape rate of inner droplets in a host drop was expressed as $-dn_i/dt = 2n_i^{cr}P_E/t_c$ by Klahn et al. (2002), where n_i is the number of inner droplets and n_i^{cr} is the number of inner droplets in the critical area. According to their assumption that secondary droplets further away from host drop surface (see white area in Figure 9.2) cannot escape from the host drop due to the slow motion, for a given time, t, one can write $n_i^{cr}(t) = n_i(t) - (1-\alpha_{cr})n_i^0$. Hence, the final expression for the escape rate would be $-dn_i(t)/dt = 2P_E[n_i(t) - (1-\alpha_{cr})n_i^0]/t_c$, as given by Equation (9-7), instead of Equation (2) in the paper of Klahn et al. (2002) which is $-dn_i(t)/dt = 2P_E[n_i(t) - (1-\alpha_{cr})n_i^0]/(\alpha_{cr}t_c)$.

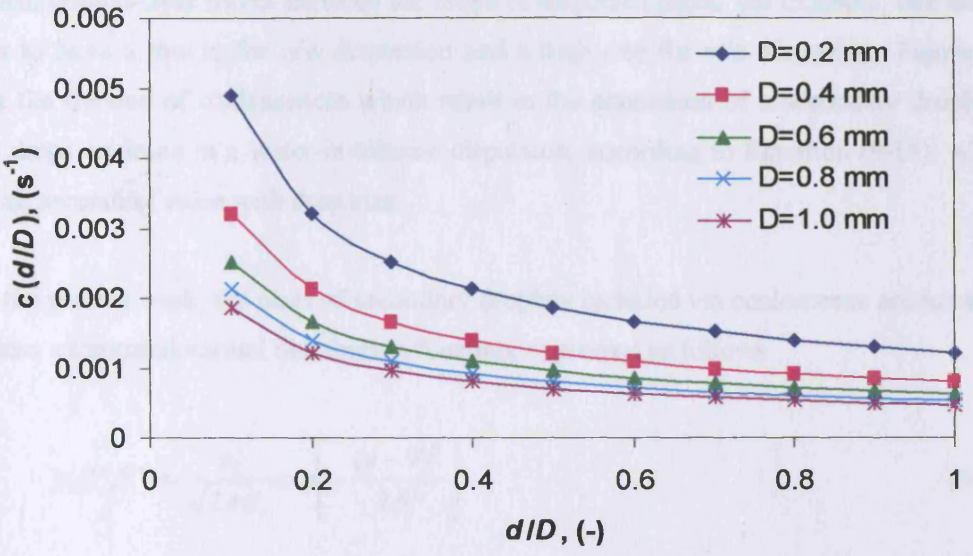

Figure 9.3: Escape rate of secondary droplet (d) from different sizes of host drops (D), calculated from Equation (9-13).

9.2.3 Inclusion Rate

In this study, the appearance of secondary droplets is presumed to be the consequence of intense drop-drop coalescence that entraps continuous phase into the newly formed host drop. The frequency of entrapping droplet of volume v by coalescence of drops of volume V and V', $\omega_v(V,V')$, can therefore be expressed by

$$\omega_v(V,V') = [1-\eta(V,V')]p_v(V,V')\lambda_v(V,V')h(V,V')N(V)N(V') \tag{9-14}$$

where $\eta(V,V')$, $p_v(V,V')$, $\lambda_v(V,V')$, $h(V,V')$ and $N(V)$ have been previously defined. In the absence of any available functional forms for $\eta(V,V')$, $p_v(V,V')$ and $\lambda_v(V,V')$, suitable closure expressions are adopted. For the fraction $\eta(V,V')$, analogous to the coalescence efficiency of drops suggested by Coulaloglou and Tavlarides (1977), Equation (9-15) is assumed,

$$\eta(V,V') = \exp\left[-x_0\left(\frac{VV'}{V+V'}\right)^{x_1}\frac{\Gamma^{x_2}\varepsilon^{x_3}}{\sigma^{x_4}}\right] \tag{9-15}$$

where x_0, x_1, x_2 x_3 and x_4 are the assumed empirical parameters; ε is the energy dissipation rate per unit mass; note that x_0 is dimensional and its value is assumed to be dependent on the

electrical double-layer forces between the drops of dispersed phase, for example, one would expect to have a low x_0 for o/w dispersion and a high one for w/o dispersion. Figure 9.4 shows the fraction of coalescences which result in the generation of a secondary droplet if water drops coalesce in a water-in-toluene dispersion, according to Equation (9-15), which gives an ascending value with drop size.

In the present work, the sizes of secondary droplets included via coalescence are assumed to follow a truncated normal distribution function, expressed as follows

$$p_v(V,V') = \frac{x_5}{\sqrt{2\pi}\delta_v}\exp\left[-\frac{(v-\bar{v})^2}{2\delta_v^2}\right] \tag{9-16}$$

where $\bar{v}$ is the average size of included secondary droplets by coalescence of V and V', which is set arbitrarily equal to half the volume of the maximum droplet staying in the host drop V or V'; δ_v is the standard deviation, where $\delta_v = \bar{v}/3$ in this study; x_5 is the scale constant to ensure the sum of distribution is equal to 1.

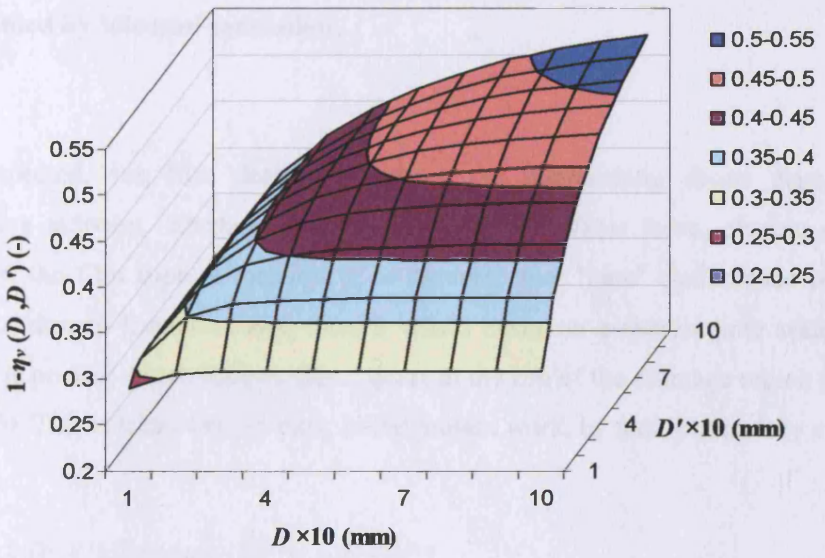

Figure 9.4: Fraction of entrapping droplet inclusion, if water drops coalesce, in a water-in-toluene system. Here, $x_0 = 0.5$, $x_1 = 1/9$, $x_2 = 0.2$, $x_3 = 1/3$, $x_4 = 1$ and $\varepsilon = 0.1$ m^2s^{-3} are used.

The efficiency of coalescence in the presence of inclusion is also taken to be an exponential function of the ratio of the coalescence time (t_d) to the contact time (t_i), in a manner similar to that postulated for pure coalescence (i.e. Coulaloglou & Tavlarides, 1977; Chester, 1991; Tsouris & Tavlarides, 1994):

$$\lambda(V,V') = \exp\left(-\frac{t_d}{t_i}\right) \tag{9-17}$$

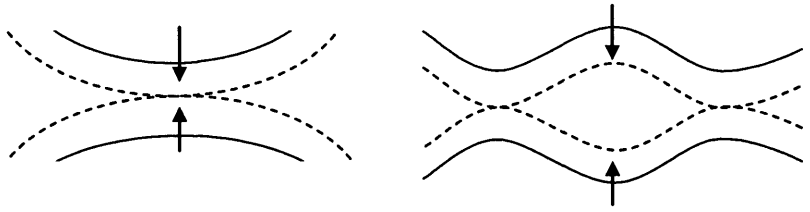

Nose-nose coalescence (a)

Dimple formation coalescence (b)

Figure 9.5: Schematic of (a) 'pure' coalescence (i.e. in the absence of an inclusion event) with nose-nose coalescence and of (b) secondary droplet inclusion via coalescence accompanied by 'dimple' formation.

As expected, the film drainage between the approaching drops depends on the approaching velocity, interface deformability, van de Waals force, electric double-layer forces and the film rupture location. It is assumed that 'pure' coalescence occurs in the absence of dimple formation and, thus, it would occur on a shorter time scale than when inclusion is present which follows film rupture at the rim of the drainage region (as shown in Figure 9.5). This is taken into account, in the present work, by multiplying λ by a factor x_6.

$$\lambda_v(V,V') = x_6 \exp\left(-\frac{t_d}{t_i}\right) = x_6\lambda(V,V') \tag{9-18}$$

Equations (9-15), (9-16) and (9-18) are then applied to the population balance equations, as given in Section 9.2.1

9.3 Model Implementation

In order to obtain the distributions of host drops and secondary droplet within given-size host drop, it is necessary to solve Equations (9-1) and (9-2) simultaneously. In this study, the integro-differential equations generated from Equations (9-1) and (9-2) are combined together to form a new set of equations, such that, if host drops are categorized by K groups and secondary droplets inside one category of host drops are categorized by J groups, one has

$$\begin{bmatrix} \dot{N}_1 \\ \vdots \\ \dot{N}_K \\ \dot{n}_{1,1} \\ \dot{n}_{1,2} \\ \vdots \\ \dot{n}_{K,J} \end{bmatrix} = \begin{bmatrix} RHS_1 \\ \vdots \\ RHS_K \\ rhs_{1,1} \\ rhs_{1,2} \\ \vdots \\ rhs_{K,J} \end{bmatrix} \tag{9-19}$$

where RHS_k is the rate of change of the k^{th} group of host drop, $RHS_{k,j}$ is the rate of change of the j^{th} group of secondary droplets whose host drops are in the size group k. Equations (9-19) are numerically solved using a FORTRAN program, variable-coefficient ordinary differential equation solver (DVODE) (Tsouris & Tavlarides, 1994).

However, several other aspects need to be specified prior to the numerical solution of the above equations. Firstly, the drops and secondary droplets are divided into equally separated classes according to their sizes. The minimum group size of drops is set equal to the Komolgroff length scale. Neither breakage of drops of the smallest size group nor coalescence of drops of the largest group can be allowed. For a host drop of volume V, the maximum volume of the secondary droplet it can accommodate is assumed proportional to its own volume:

$$v_{k,\max} = x_7 V_k \tag{9-20}$$

where $0 < x_7 < 1$.

Secondly, during coalescence, breakage, inclusion and escape processes, the formed host drop or secondary droplets cannot match exactly the discrete characteristic group sizes. The mass (or volume) of each phase is then unlikely to remain constant with time. The methods

suggested in Chapter 7 to conserve mass are also adopted here for the host drops and the secondary droplets: drops formed by coalescence or escape, and secondary droplets generated by coalescence are split into two adjacent groups nearest to their size, on the basis of conservation of mass (or volume) and number; for drops generated by breakage of large drops, the mass is balanced by scaling the daughter drop distribution function of the large drops. We also assume that the secondary droplets are distributed evenly in the host drops. Thus, breakup or coalescence of a host drop in a given class will result in the loss of the secondary droplet associated with this host drop. For example, if for a given class, one has 4 host drops and 4 secondary droplets of given size, it is assumed that each host drop contains one secondary droplet. Breakup or coalescence of one of these hosts results in three hosts and three secondary droplets in this class.

Thirdly, it is assumed that the effect of the secondary droplets inside a host drop on the breakage frequency of the host drop and its daughter drop distribution is negligible; in other words the functions derived for a pure drop are presumed to be still valid for host drops containing secondary droplets. The breakage rate function of Luo & Svendsen (1996) and the U shaped daughter drop size distribution function of Kostoglou et al. (1997) are employed in the current work; details of these expressions can be found in Section 7.3.1.2 (see Equation 7-11). Again, the coalescence function with radial distribution function used in Chapter 8 (Equation 8-12) is also employed in this Chapter.

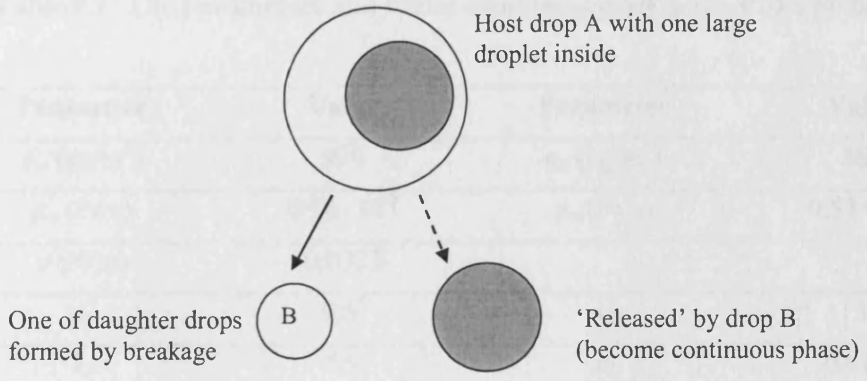

Figure 9.6: Schematic diagram showing the immediate 'release' of a secondary droplet by its 'host' drop in a breakage process.

Yet, another consideration is necessary while simulating the process of breakage of a host drop and escape of secondary droplets. For example, if a host drop (A) breaks into two smaller host drops (B and B'), the secondary droplets in host drop A may sometimes be larger than the maximum size of droplets that host drops B or B' can accommodate. To compensate for this, it is assumed that such droplets (say in drops B) are immediately 'released' by their host drop (B) and become part of the continuous phase, as shown in Figure 9.6. The above compensation method is also applied to the escape process.

9.4 Results and Discussion

A water-in-toluene system is studied to assess the PBEs model presented above. Initially, drops of dispersed phase (water) are assumed to follow a truncated normal distribution in terms of size, and it is assumed that there are no secondary droplets in the dispersion. Secondary droplets, however as expected, will appear as a consequence of coalescence and also some will escape from host drops. The system under given operating conditions will evolve until an equilibrium state is reached, should one exist, in which a balance is present between coalescence, break-up, inclusion and escape. The system may also not reach such a steady state if phase inversion occurs. In the results presented below, two different cases are discussed: one with an ultimate equilibrium state formed (case I), and the other showing no existence of this equilibrium state (case II).

Table 9.1: The parameters and initial conditions used in the PBEs model.

Parameter	Value	Parameter	Value
ρ_w (kg/m^3)	996	ρ_o (kg/m^3)	867
μ_w (Pa s)	0.96×10^{-3}	μ_o (Pa s)	0.57×10^{-3}
σ (N/m)	0.0323		
x_0	0.5*	x_4	1
x_1	1/9	x_5	0.8328
x_2	0.2	x_6	0.9
x_3	1/3	x_7	0.8
ϵ (case I)	0.1 (m^{2}s^{-3})	ϕ_i (case I)	0.5
ϵ (case II)	0.05 (m^{2}s^{-3})	ϕ_i (case II)	0.8

*: Suggested absolute value of x_0 without considering its unit, as the unit will change with the other parameters, i.e. x_1, x_2 and x_3 etc.

Simulations are carried for the parameters shown in Table 9.1, which lists the values of the parameters described above and initial operation conditions (such as energy dissipation rate ϵ and dispersed phase holdup ϕ_i) for the two cases. Note that the energy dissipation rate (ϵ) has been suggested to decrease with the increase of dispersed phase volume fraction due to increase of mixture viscosity (Taylor, 1932; Tsouris & Tavlarides, 1994); a 50% decrease has been assumed here accordingly for the holdup rising from 0.5 to 0.8.

Figure 9.7 shows the evolution of the effective volume fraction (ϕ_{eff}) simulated for the two cases, where $\varphi_{eff} = \int_0^V N(V)VdV$. As can be seen, for case I where $\phi_i = 0.5$ and $\epsilon = 0.1$ m^2s^{-3}, ϕ_{eff} gradually increases due to the inclusion of secondary droplets until it reaches a constant value where an equilibrium state is formed. A similar trend is also shown by the Sauter mean diameter (D_{32}) of the host dispersed drops for case I, as illutrated in Figure 9.8. However, for case II when a higher ϕ_i (=0.8) and a lower ϵ (=0.05 m^2s^{-3}) are used, the effective volume fraction does not reach a constant value, but goes up to its maximum condition $\phi_{eff} = 1$ in approximate 220 seconds due to the associated increase in coalescence efficiency and that of secondary droplet formation entrapping continuous phase. If the frequency of escape does not balance that of inclusion of secondary droplets (as is evident in case II), then ultimately the majority of the continuous phase will become trapped within the dispersed phase leading to ϕ_{eff}=1. The evolution of Sauter mean diameter in case II illustrates that a gradual increase before $\phi_{eff} = 1$ is achieved (see Figure 9.8), which indicates that net-entrapment of the continuous phase into the dispersed drops. According to Sajjadi et al. (2002) and Liu et al. (2005), phase inversion can be defined as a phenomenon where all of the continuous phase is entrapped into the dispersed phase and become secondary droplets, namely, $\phi_{eff} = 1$. Hence, the non-existence of equilibrium state shown by case II could suggest a necessary condition/criterion for emulsion invert to the opposite one (toluene-in-water).

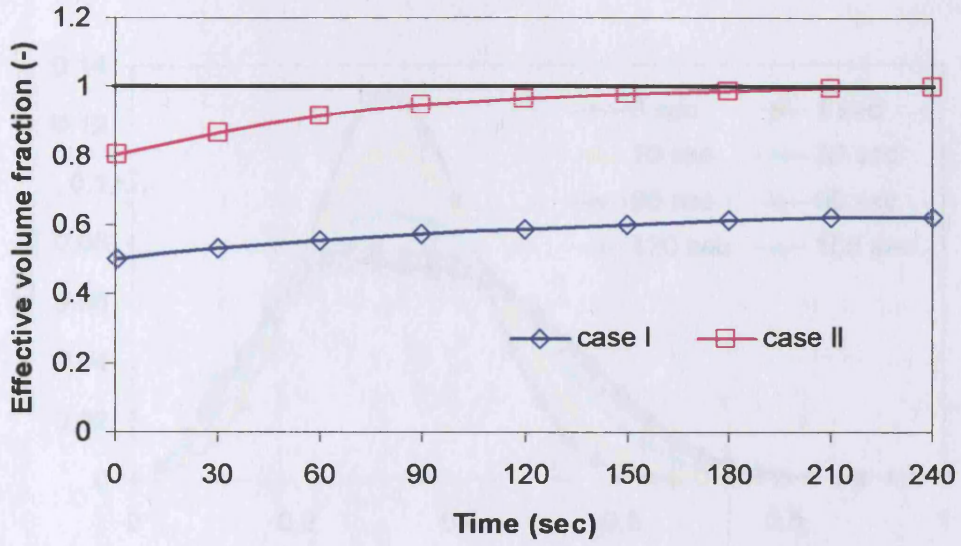

Figure 9.7: Evolution of the effective dispersed phase volume fraction, $\varphi_{eff} = \int_0^V N(V)VdV$, obtained for cases I and II listed in Table 9.1.

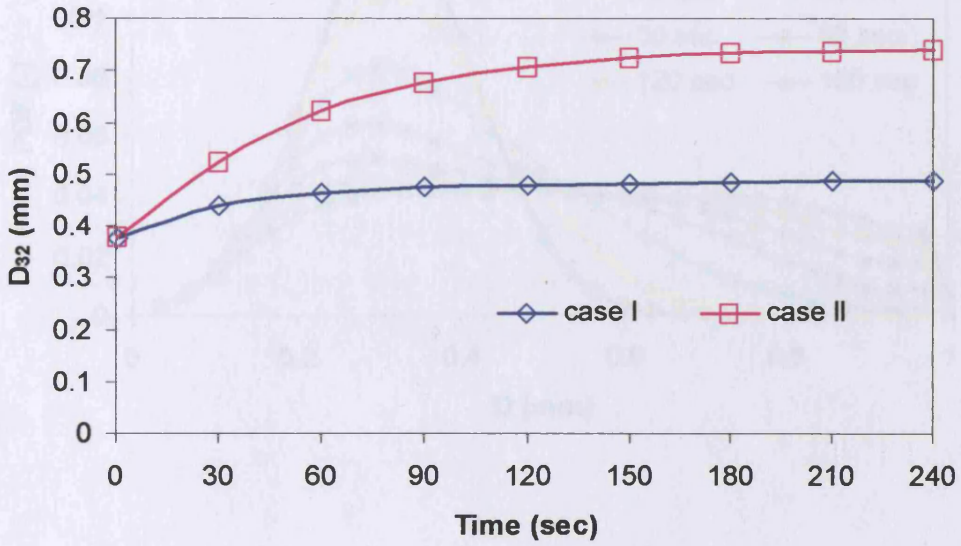

Figure 9.8: Evolution of the Sauter mean diameter (D_{32}) of host drops, obtained for cases I and II listed in Table 9.1.

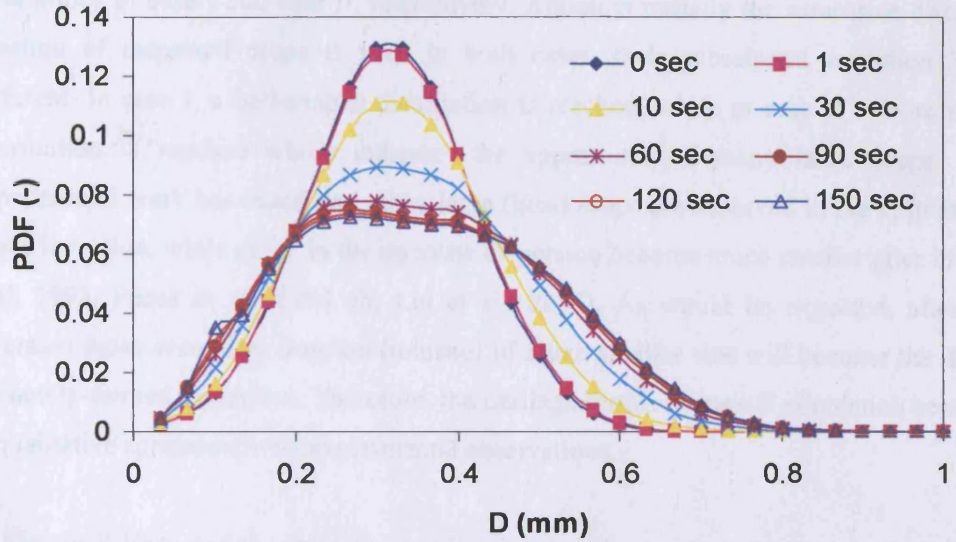

(a)

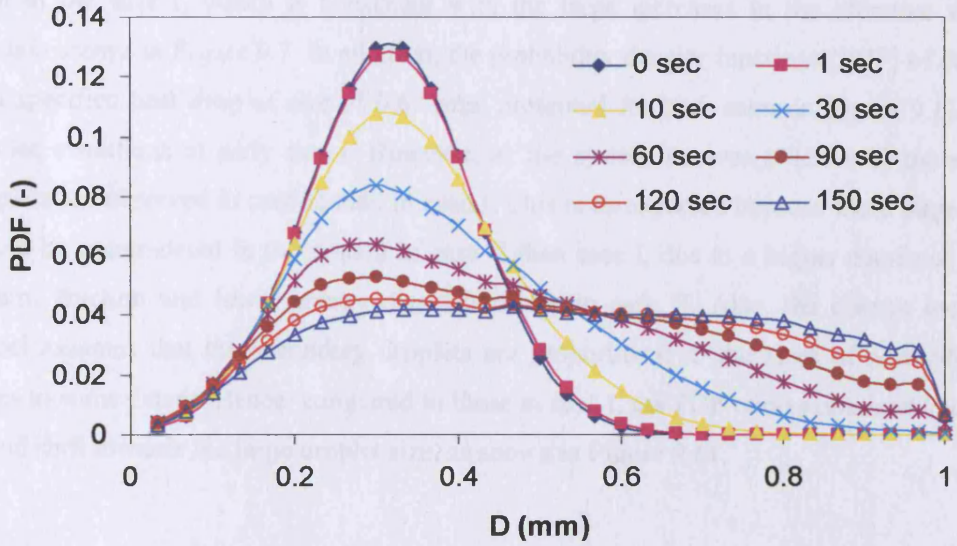

(b)

Figure 9.9: Evolution of (host) drop size distribution, obtained for (a) cases I and (b) II, listed in Table 9.1.

Figures 9.9(a) and (b) present the evolutions of (host) drop size distributions from the simulations of case I and case II, respectively. Although initially the same size distribution function of dispersed drops is used in both cases, their subsequent evolution is quite different. In case I, a bell-shaped distribution is reached, while in case II a more uniform distribution is reached which indicates the appearance of many large drops. Recent experimental work has found that many large (host) drops are observed in the system before phase inversion, while drops in the opposite dispersion become much smaller after inversion (Pal, 1993; Pacek et al., 1994 ab; Liu et al., 2005). As would be expected, after phase inversion those secondary droplets (toluene) of much smaller size will become the drops in the newly-formed dispersion. Therefore, the findings shown by case II simulation seem to be in qualitative agreement with experimental observations.

Figures 9.10(a) and (b) show the number density of secondary droplets in host drops of various sizes, predicted by the simulations of cases I and II, respectively. As illustrated, secondary droplets are gradually generated by coalescence of drops until an equilibrium state is reached where the rate of escape balances that of inclusion. Although the overall trends are the same for case II, the number of secondary droplets is higher by two orders of magnitude than in the case I, which is consistent with the large increases in the effective volume fraction shown in Figure 9.7. In addition, the probability density functions (PDF) of droplets in a specified host drop of size of 0.67 mm, presented for both cases in Figure 9.11, have similar evolutions at early times. However, as the system evolves (>120 sec) more large droplets are observed in case II than in case I. This is as expected because more large drops would be accumulated in the system of case II than case I, due to a higher dispersed phase volume fraction and lower energy dissipation rate in case II. Also, the current inclusion model assumes that the secondary droplets are proportional to the sizes of newly-formed drops to some extent. Hence, compared to those in case I, the PDF curves obtained in case II would shift towards the large droplet size, as shown in Figure 9.11.

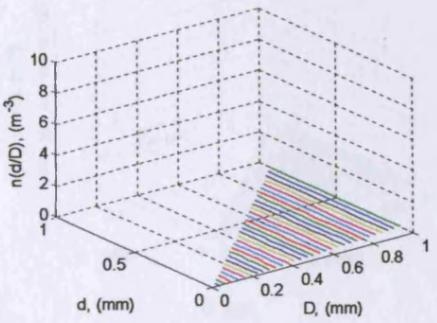

0 sec

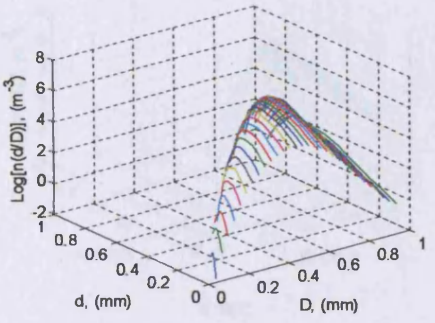

1 sec

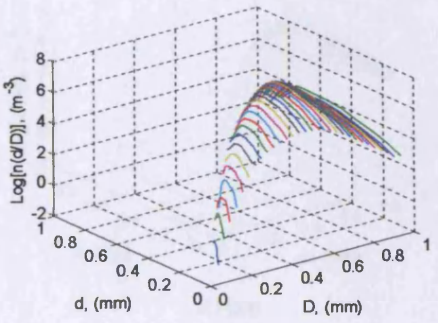

10 sec

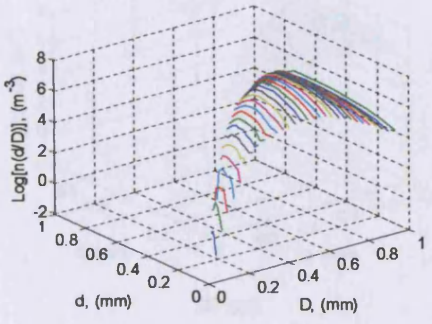

30 sec

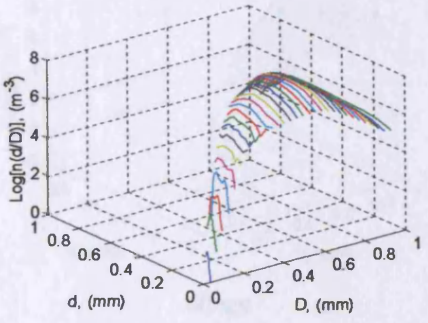

60 sec

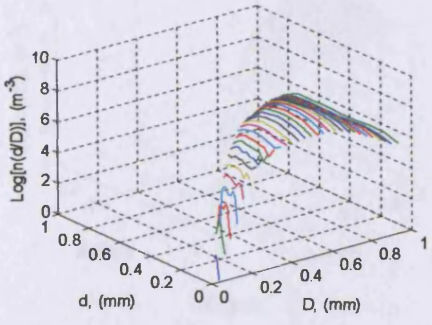

90 sec

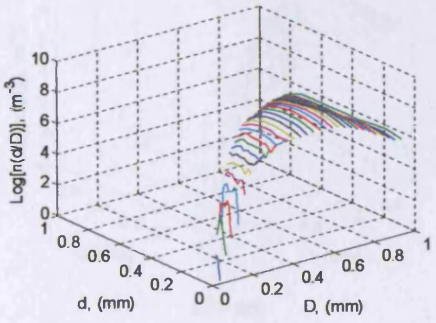

120 sec

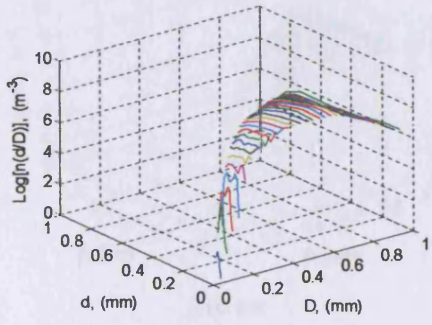

210 sec

(a)

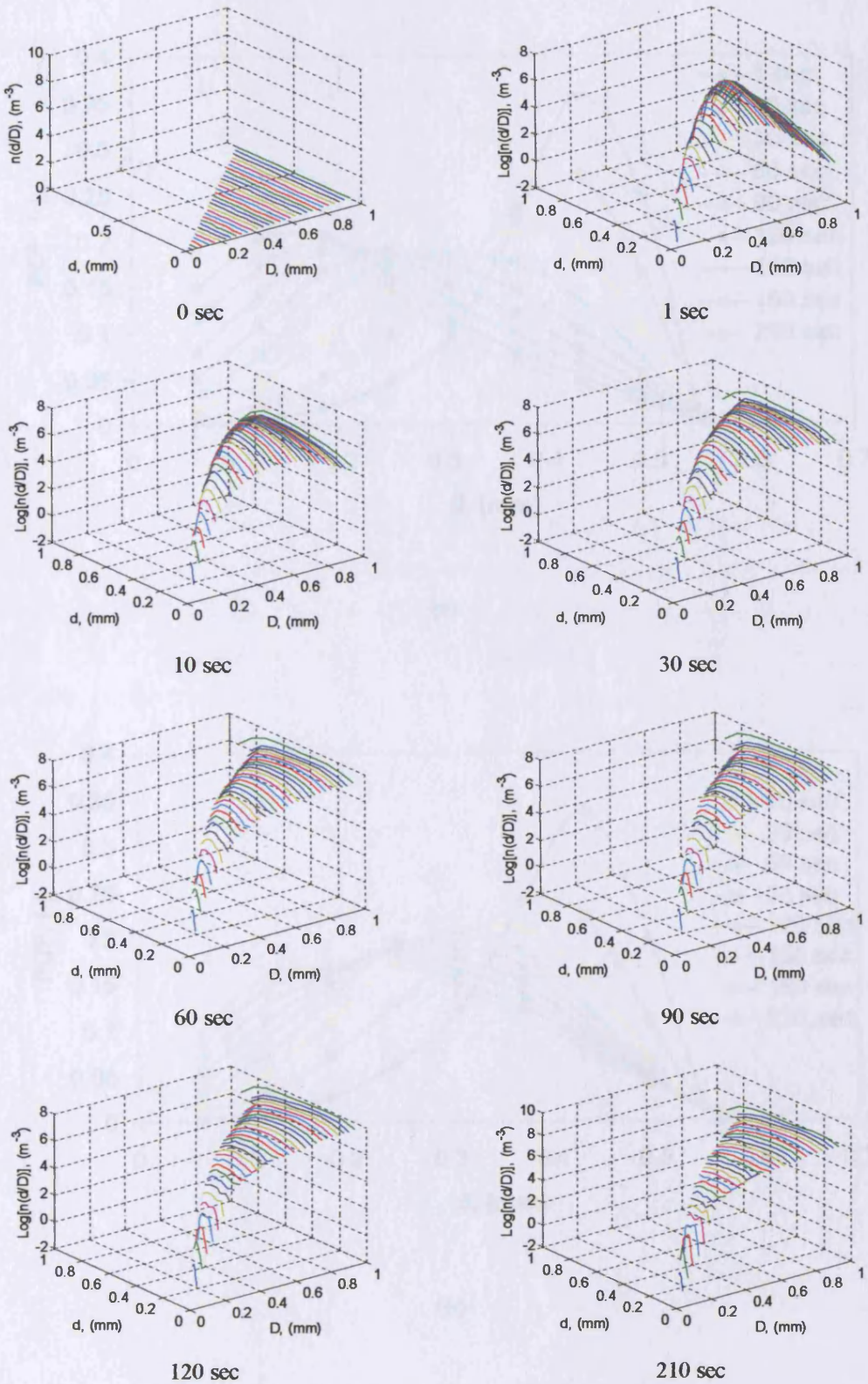

(b)

Figure 9.10: Evolution of the overall distribution of secondary droplets in host drops of given size, obtained for (a) cases I and (b) case II, listed in Table 9.1.

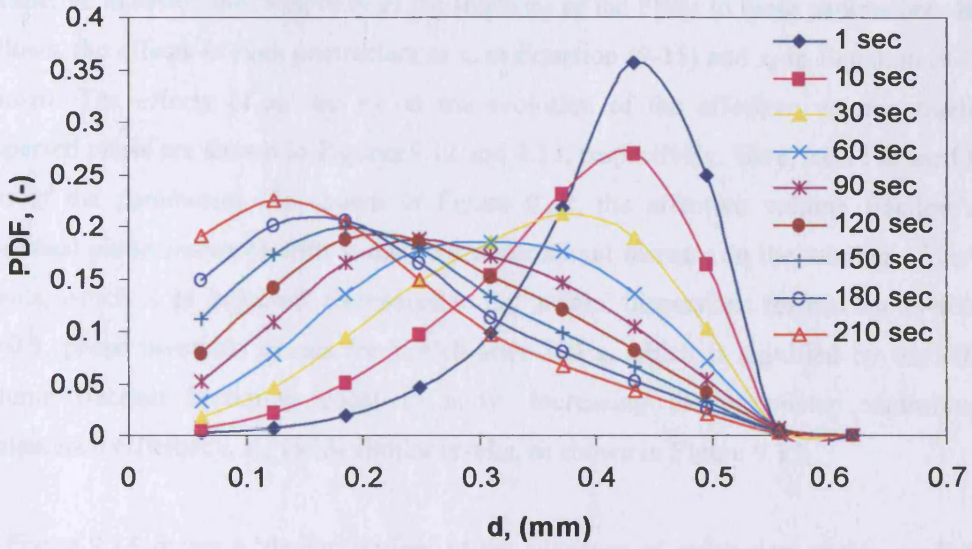

(a)

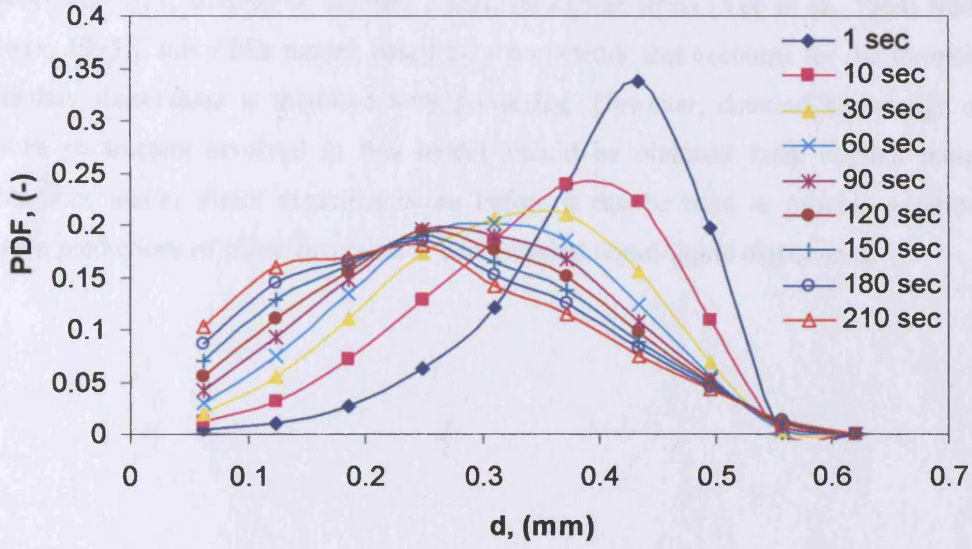

(b)

Figure 9.11: Evolution of the distribution of secondary droplets within a specific host drop of size (D = 0.67mm), obtained for cases I, (a), and II, (b), listed in Table 9.1.

Since the model derived contains a relatively large number of parameters, it proves instructive to assess the sensitivity of the solutions of the PBEs to these parameters. In what follows, the effects of such parameters as x_0 in Equation (9-15) and x_6 in Equation (9-18) are studied. The effects of x_0 and x_6 on the evolution of the effective volume fraction of dispersed phase are shown in Figures 9.12 and 9.13, respectively. Here, case I is used for the rest of the parameters. As shown in Figure 9.12, the effective volume fraction of the dispersed phase increases with x_0 due to a concomitant increase in the number of inclusion events, which is as expected. Compared to the 'stable' dispersions formed for x_0=0.05 and x_0=0.5, phase inversion occurs for x_0=5.0 after 200 s, which is signified by the effective volume fraction becoming equal to unity. Increasing the parameter controlling the coalescence efficiency, x_6, yields similar results, as shown in Figure 9.13.

Figure 9.14 shows a 'demonstration' of the existence of ambivalent region predicted by the PBEs model simulation with the case I parameter set. Based on the criterion that phase inversion occurs once the effective volume fraction reaches unity, an ambivalent region is clearly predicted by the proposed model. Since the prediction of an ambivalent region has not been successfully reported by means of other methods [e.g. equal system free energy (Fakhr-Din, 1971; Brauner & Ullman, 2002), zero shear stress (Yeh et al., 1964; Nädler & Mewes, 1995)], this PBEs model, based on a framework that accounts for the formation of secondary dispersions is therefore very promising. However, detailed knowledge of the various parameters involved in this model should be obtained from explicit numerical simulations and/or direct experimentation before it can be used to provide accurate and reliable predictions of phase inversion in concentrated liquid-liquid dispersions.

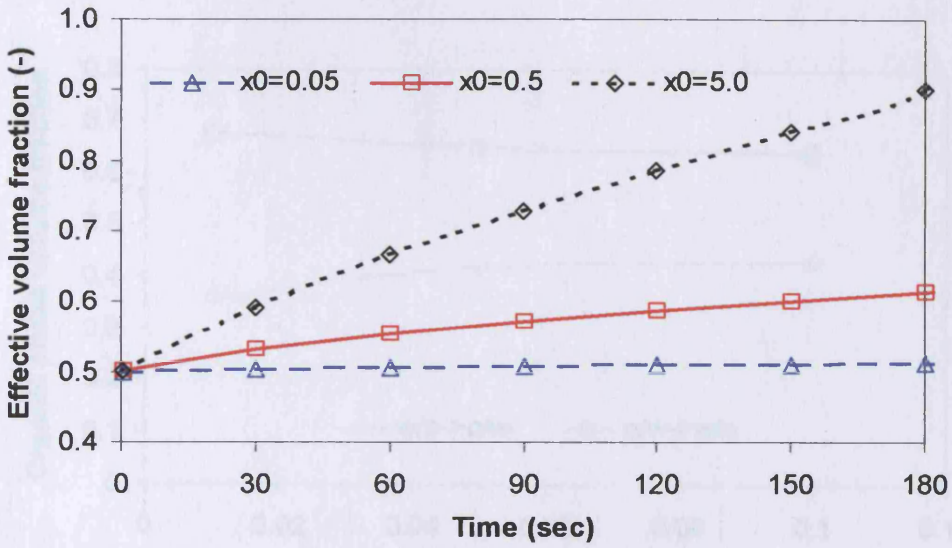

Figure 9.12: Effect of parameter x_0 on the evolution of the effective dispersed phase volume fraction (case I is used for the rest of the parameters).

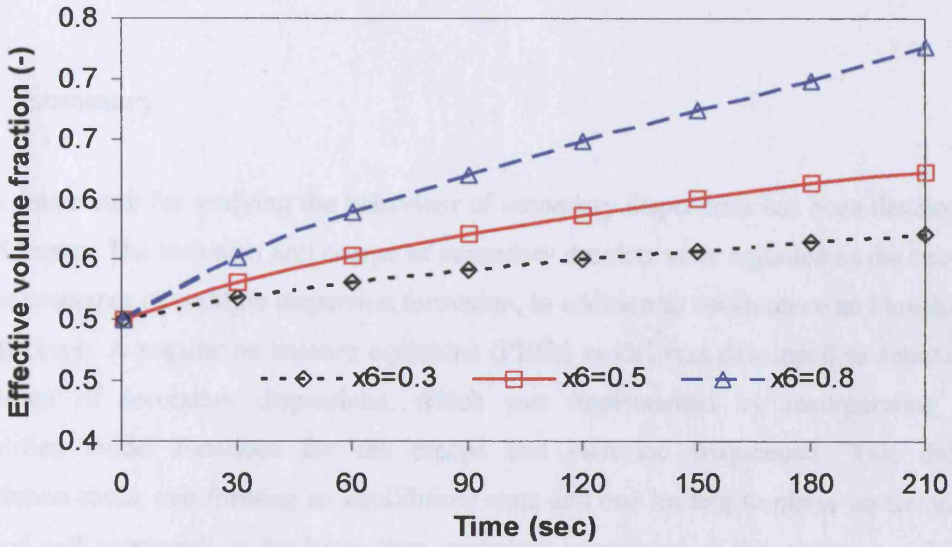

Figure 9.13: Effect of parameter x_6 on the evolution of the effective dispersed phase volume fraction (case I is used for the rest of the parameters).

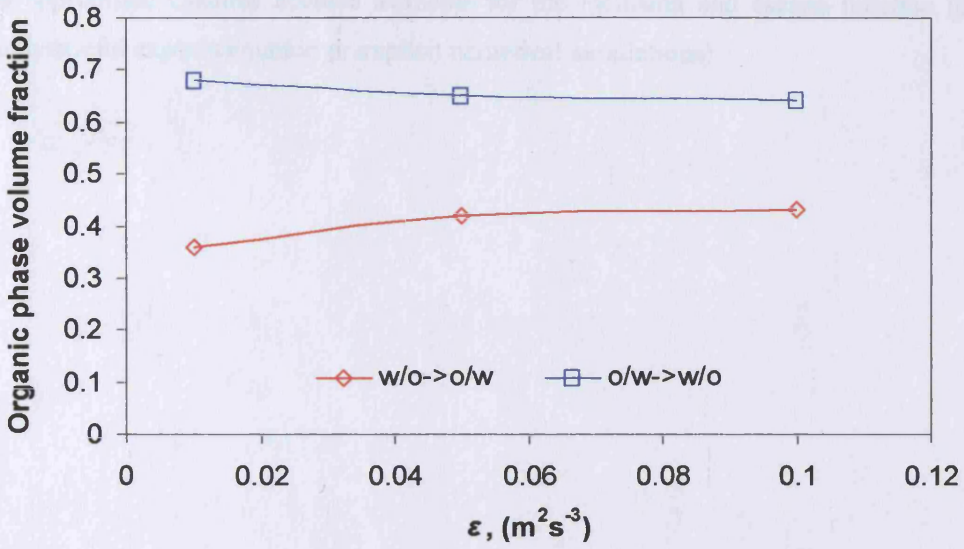

Figure 9.14: A demonstration of the ambivalent range predicted by the current model with parameters of case I.

9.5 Summary

A framework for studying the behaviour of secondary dispersions has been developed in this Chapter. The inclusion and escape of secondary droplets were regarded as the two other major processes in multiple dispersion formation, in addition to coalescence and breakage of (host) drops. A population balance equations (PBEs) model was developed to simulate the evolution of secondary dispersions, which was implemented by incorporating some simplified model functions for the escape and inclusion frequencies. Two different simulation cases, one forming an equilibrium state and one leading to phase inversion were studied and compared; in the latter case, complete entrapment of the continuous phase by dispersed drops was interpreted to result in phase inversion. Using the PBEs model, the evolution of the effective volume fraction, the distribution of host drops and secondary droplets are simulated and analysed for two cases. The predictions were in qualitative agreement with experimental findings. However, as the current understanding of inclusion and escape is rather limited, it is unrealistic at this stage for the PBEs model to produce accurate predictions of phase inversion. The objectives of this work are mainly focused on

developing a quantitative methodology capable of predicting phase inversion characteristics when appropriate closures become available for the inclusion and escape function (either through careful experimentation or explicit numerical simulations).

Chapter 10

Conclusions and Recommendations

This Chapter outlines the conclusions drawn from the present experimental and theoretical work and provides recommendations for future studies in this field. The main conclusions are presented in Section 10.1, and possible directions for future work are included in Section 10.2.

10.1 Conclusions

10.1.1 Conclusions from Experimental Investigations

The experimental work described in this thesis investigated phase inversion and associated phenomena (e.g. ambivalent region and turbulence modification) in oil-water pipeline flows. Experiments on oil-in-water (o/w) and water-in-oil (w/o) flows in the vertical upward, vertical downward and horizontal directions were carried out on the WOLF facility at Department of Chemical Engineering, University College London. Phase inversion was detected by means of several techniques, i.e. conductivity probe, glue-on hot-film probe and visualization. Two inversion routes (w/o to o/w and o/w to w/o, respectively) were followed to elucidate the hysteresis effect in pipeline flows. Investigations of parameters such as pressure drop, drop size, holdup, mean and turbulence velocity, were accordingly conducted to observe their behaviour at increasing dispersed phase fractions that lead to inversion and beyond. An advanced instrument, the hot-film anemometer (HFA), commissioned on the WOLF rig, was employed for measuring turbulence structures and modifications of the continuous phase in oil-water dispersed flows. Also, an improved analytical method was developed to derive stable drop size distributions (DSD) from the distributions of chord lengths (CLD), measured by a dual-impedance probe. The effect of biased sampling towards

larger drops was included while smoothing equations were introduced to eliminate the negative DSD values that can arise from the direct backward transformation of CLD. Both forward and backward transforms were shown to be in good agreement with ideal data and with data obtained from Monte-Carlo simulations. A method for choosing an appropriate smoothing factor was also suggested.

Phase inversion in co-current upward and downward vertical flows were investigated by two types of experiments: constant mixture velocity (type I experiments) and increasing mixture velocity with the superficial velocity of one of the phases fixed (type II experiments). A conductivity probe at the pipe centre and a glue-on HFA probe at the pipe wall indicated that phase inversion initially takes place at the pipe centre with the formation of complex structures, before it reaches the wall. The input oil fraction at which inversion is detected at the wall, defined as the complete phase inversion point, signifies that the new continuous phase has spread over the whole pipe cross section.

In summary, the main experimental conclusions ensuing from the work described in this thesis are as follows:

- No obvious ambivalent region is found in both type I (constant mixture velocity) and type II experiments (with an increasing mixture velocity) in vertical flows. There is however, a narrow range of input phase fractions ($\Delta\epsilon_o$<4%- 6%) where the flow is unstable and complex structures are formed.

- The results from type I experiments in both upward and downward flows indicate that frictional pressure gradient reaches a *minimum* at the complete phase inversion point. Drag reduction as well as the effect of drop size on mixture viscosity are suggested as possible reasons for this behaviour, which contrasts with the maximum pressure gradient near phase inversion often observed in horizontal flows.

- The phase inversion point is found by the type II experiments to depend on mixture velocity at low and medium mixture velocities.

- The phase inversion points were found to be different in upward and downward vertical flow respectively. However, the velocity ratios where complete inversion appeared, had close to the same constant value in both flow directions, apart from at the lowest velocity investigated.

- In contrast to the previously postulated phase inversion mechanisms, it was found, based on drop size measurements, that the interfacial energies of the dispersions just before and after phase inversion are not necessarily equal. Other phenomena, such as increased coalescence rate before inversion, probably related to the large drops observed in this region, could also be responsible for the appearance of the phenomenon.

- In o/w upward flow, the axial mean velocity profiles become flatter than single-phase flow and then change to centre peaked from as the input oil fraction increases; a flatter profile is seen in w/o upward flow. In downward flow, the presence of oil drops always tends to flatten the continuous phase velocity profile in o/w flows, while a profile with a slight centre peak is observed in all cases of w/o downward flows. In horizontal flows, the results for two-phase flows of both o/w and w/o dispersions show a more uniform distribution of the continuous phase velocity than occurs in single-phase flow of either phase. Previous studies (e.g. that of Iskandrani & Kojasoy, 2001), had suggested that effects such as the turbulent fluctuations of the dispersed phase and the local dispersed phase fraction (or population) could play a key role in influencing the continuous phase velocity; the present study shows that the local velocity of the dispersed phase is also important in this context.

- In downward flow, the velocity profile of oil drops in a continuous water phase was shown to be generally more flattened in the pipe core region than that for water drops in an oil continuous phase; both two-phase velocity profiles were flatter than that for a single-phase flow. The velocities of oil drops were found to be lower than those of water drops and this difference became more pronounced at the low velocity. There is no obvious difference on drop velocity profile between o/w and w/o flows in upward flows.

- The presence of a dispersed phase tends to flatten the turbulence intensity profile of the continuous phase and results in a more uniform distribution of the turbulent energy over the pipe cross-section. This finding is consistent with the observations in previous studies in air-water and oil-water bubbly/dispersed flows.

- In all cases investigated in vertical flows, the turbulence of the continuous phase is found to be enhanced in the pipe centre and attenuated close to the wall compared to that of a single-phase flow. Enhancement or attenuation of turbulence level of the continuous phase could depend on a number of parameters such as local dispersed phase concentration, drop size, flow direction and velocity. It is evident that high concentration and large drops of the dispersed phase are likely to increase local turbulence.

- Experimental observations on turbulence modulation in oil-water flows were compared with the postulated models by Hetsroni (1989) and Kenning & Crowe (1997) for particle-fluid systems. The present data did not agree with these models, indicating that a much more complex method of the dispersed phase/turbulence interaction is needed for droplet dispersions where interface deformation and breakup and coalescence would be expected to exert an influence.

- The experiments in oil-water horizontal pipe flows indicated that, in both o/w and w/o dispersions, the axial liquid mean velocity shows a more uniform distribution than that given by the $1/7^{th}$ power law. The turbulence levels in o/w and w/o generally increase with the input oil fraction. These findings are in agreements with those observed by Iskandrani & Kojasoy (2001) in air-water horizontal bubbly flows.

10.1.2 Conclusions from Theoretical Studies

A novel application of a population balance equations (PBEs) model in the prediction of phase inversion was developed and presented in this work. The application of the PBEs model aims to promote a better understanding of the influence of breakage and coalescence of dispersed drops on the process of phase inversion. Two PBEs models were developed for surfactant-free dispersions formed by two immiscible liquids for stirred vessels and pipeline flows, respectively. Also, modelling of phase inversion and the ambivalent region in stirred vessels with heterogeneous and homogeneous distribution of turbulent energy was considered. To achieve better predictions for systems in stirred vessels, a 'two-region' model was postulated which assumed that drop breakup and coalescence take place preferentially in the vicinity of the impeller and away from that region, respectively. Previous work (e.g. Groeneweg et al., 1998; Sajjadi et al., 2002) provides evidence that secondary dispersions play a key role in the phase inversion process; thus, the theoretical work was further extended to account for their presence. To this end, a framework incorporating inclusion and escape processes of secondary droplets was developed using as a basis the PBEs model. The evolution of secondary dispersions and its effect on phase inversion were evaluated.

In summary, the main theoretical conclusions and advances ensuing from the work described in this thesis are as follows:

- A combination of PBEs and phase inversion models was implemented for liquid-liquid dispersed systems in stirred vessels and in pipelines. For pipeline flow systems, a more advanced PBEs model was developed by taking into account the flow of the dispersion.

- The predicted distributions of drop sizes in stirred vessels by the PBEs model showed good agreement with the published experimental correlations for dilute dispersions. However, discrepancies appeared for dense dispersions, which were attributed to the less accurate predictions of coalescence efficiency and collision frequency in highly concentrated and closely packed dispersions.

- According to the PBEs simulations in pipeline flows, the steady state drop size distribution formed downstream of the inlet is independent of the initial and inlet conditions. The predictions of phase inversion points using the equal surface energy criterion, suggested by Brauner & Ullman (2002), showed good agreement with the experimental data observed in oil-water pipeline flows by Ioannou et al. (2004). In addition, the difference in the distance required to achieve the fully-developed state suggests the existence of an ambivalent region in terms of location rather than input oil fraction in pipeline flow; this location from inlet where inversion appears depends on initial conditions, mixture velocity and fluid physical properties.

- A two-region model is developed to predict the phase inversion volume fraction and the width of the ambivalent range of concentrated liquid-liquid dispersions in agitated vessels. This model is based on the assumption that rates of breakup and coalescence are relatively high in the impeller and circulation regions, in which the turbulence intensity is high and low, respectively. Phase inversion was assumed to take place when the drop coalescence rate in the circulation region exceeds that of breakup in the impeller region.

- The concept of a radial distribution function was used in order to extend the validity of the coalescence frequency expressions available in the literature which have been determined in dilute dispersions.

- The predictions from the two-region model in stirred vessels were found to be in good agreement with experimental observations by Norato et al. (1998), particularly for the upper curve of the ambivalent range (inversion from o/w to w/o). The agreement between the predictions of the lower ambivalent range curve (inversion from w/o to o/w) and experimental data, however, were not as good. This may be due to the formation of secondary dispersions, which have been observed experimentally to accompany the inversion from water-in-oil (w/o) to oil-in-water (o/w) dispersions (Pal, 1993; Pacek et al., 1994b; Liu et al., 2005).

- A framework of studying the behaviour of secondary dispersions was developed and incorporated into a PBEs model, by taking into account the inclusion and escape of secondary droplets. Two different simulation cases, one forming an equilibrium state and one leading to phase inversion were presented.

10.2 Recommendations

In this Section recommendations are put forward for future experimental and theoretical studies.

Experimental Studies

The following objectives are recommended for future experimental studies:

- In the present studies, experiments with only one pair of liquid phases (tap water and Exxol D140 oil) were performed. It is recommended that a wide range of fluids with different viscosity and interfacial tension should be investigated. Also, the effect of pipe wall wettability and surfactants on phase inversion should be studied. Examination of these aspects would extend the experimental data and further enhance understanding of the phenomena associated with phase inversion.

- The PBEs simulation suggested that, in oil-water pipeline flows, phase inversion may occur downstream of the pipe with a developing distance from the entrance and also that an ambivalent region in terms of pipe location may exist. It would therefore be interesting to verify the above suggestions experimentally and, if possible, study the factors that affect the location in the pipe where phase inversion appears.

- The experiments showed that occurrence of phase inversion seem to be accompanied by a constant slip velocity ratio between the phases; further investigation of the finding is recommended. To this end, a well-controlled entrance section which can provide known velocities and concentrations of both phases should be used.

- As the present PBEs model is capable of predicting the evolution of drop size distributions, it would be interesting to conduct experiments with a known distribution of dispersed drops introduced at the entrance and compare the simulated axial evolution with the experimental data.

- The work described in this thesis studied the modification of turbulence in the continuous phase in the presence of dispersed phase. Another issue which could be useful is to observe the fluctuating velocities of dispersed phase and study their behaviour around phase inversion.

Future work in investigating phase inversion behaviour should also take into consideration the role of secondary dispersions since the existence of secondary droplets within drops seems likely to be an important factor in the inversion process. In particular, due to limited information reported so far, future experiments should focus on providing information on secondary droplet size distribution, inclusion and escape rates.

Theoretical Studies

The following objectives are recommended for future analytical efforts:

- As mentioned previously in this thesis, most parameters appearing in the coalescence frequency functions are correlated from experimental data obtained in stirred vessels for dispersions of volume fraction less than 15%, whilst phase inversion is more likely to occur in dense dispersions. Therefore, developing improved parameters for a wide range of conditions (e.g. high concentrations and pipeline flow) is recommended.

- The present experiments and previous work by Liu et al. (2005) showed that phase inversion could occur locally and spread gradually to the rest of the system. Accordingly, studies of phase inversion combined with computed simulation of interface

behaviour, which might provide a more detailed view on flow structures would be interesting.

- Only limited studies have been carried out by considering secondary dispersions in the PBEs model in the present work. It is therefore recommended to extend the present framework to a more advanced model in future studies, by using reliable closure models for the inclusion and escape rate of secondary droplets (which might be obtained via explicit simulations and/or direct experimentation).

Bibliography

Abel, R., Resch, F. J. (1978). A method for the analysis of hot-film anemometer signals in two-phase flows, Int. J. Multiphase Flow, 4, 523–533.

Agterof, W.G.M., Vaessen, G.E.J., Haagh, G.A.A.V., Klahn, J.K., J.J.M. Janssen (2003). Prediction of emulsion particle sizes using a computational fluid dynamics approach. Colloids and Surfaces B: Biointerfaces, 31, 141–148.

Al-Deen, M.F.N., Hamad, F. A., Bruun, H.H. (1998). Kerosene/water two-phase flow in vertical and inclined pipes, 3rd International Conference on Multiphase Flow, ICMF'98, Lyon, France, June 8–12.

Al-Deen, M.F.N., and Bruun, H.H. (1997). A comparative study of single normal, X type and split-film anemometer probe measurements in kerosene/water two-phase flow. Meas. Sci. Technol. 8: 885–893.

Alopaeus, V., Koskinen, J., Keskinen, K.I. (1999). Simulation of the population balances for liquid-liquid systems in a nonideal stirred tank. Partl Description and qualitative validation of the model. Chem. Eng. Sci. 54: 5887–5899.

Alopaeus, V., Koskinen, J., Keskinen, K.I. (2002). Simulation of the population balances for liquid–liquid systems in a nonideal stirred tank. Part 2 parameter fitting and the use of the multiblock model for dense dispersions. Chem. Eng. Sci. 57: 1815–1825.

Angeli, P. (1996). Liquid – Liquid dispersed flows in horizontal pipes. PhD Thesis, University of London, London, UK.

Angeli, P., Hewitt, G. F. (1998). Pressure gradient in horizontal liquid-liquid flows. Int. J. Multiphase Flow, 24: 1183–1203.

Angeli, P., Hewitt, G. F. (2000a). Flow structure in horizontal oil-water flow, Int. J. Multiphase Flow, 26: 1117–1140.

Angeli, P., Hewitt, G. F. (2000b). Drop size distributions in horizontal oil-water dispersed flows. Chem. Eng. Sci., Vol. 55: 3133–3143.

Arashmid, M., Jeffreys, G. V. (1980). Analysis of the phase inversion characteristics of liquid-liquid dispersions. AIChE J., 26(1), 51–55.

Arirachakaran, S., Oglesby, K.D., Malinowsky, M. S., Shoham, O., Brill, J.P. (1989). An analysis of oil/water flow phenomena in horizontal pipes, Paper SPE 18836, Society of Petroleum Engineers, Oklahoma.

Augier, F., Guiraud, P., Masbernat, O. (2004). Fluctuating motion in a homogeneous liquid-liquid dispersed flow at high phase fraction. 5th International Conference on Multiphase Flow (ICMF 04), Yokohama, Japan, May30~June 4, paper No. 274.

Azzopardi, B. J., Teixeira, J. C. F. (1994a). Detailed measurements of vertical annular two-phase flow- Part I: Drop velocities and sizes. Transaction of ASME, 116, 792–795.

Azzopardi, B. J., Teixeira, J. C. F. (1994b). Detailed measurements of vertical annular two-phase flow- Part II: Gas core turbulence. Transaction of ASME, 116, 796–800.

Azzopardi, B. J. (1999). Turbulence modification in annular gas/liquid flow, Int. J. Multiphase Flow, 25, 945–955.

Bapat, P.M., Tavlarides, L.L., Smith, G.W. (1985). Monte Carlo simulation of mass transfer in liquid-liquid dispersions. Chem. Eng. Sci., 38, 2003–2013.

Barnea, E., Mizrahi, J. (1976). On the "effective" viscosity of liquid-liquid dispersions. Industrial and Engineering Chemistry Research Fundamentals. 15(2), 120–125.

Batchelor, G. K. (1956). The theory of homogeneous turbulence. Cambridge University Press, Cambridge.

Bedeaux, D. (1983). The effective shear viscosity for two-phase flow. Physics A, 121, 345–361.

Bearman, P.W. (1971). Corrections for the effect of ambient temperature drift on hotwire measurement in incompressible flow. Technical report, DISA report 11.

Brauner, N., Ullmann, A. (2002). Modelling of phase inversion phenomenon in two–phase pipe flow. Int. J. Multiphase Flow, 28(1), 55–68.

Brooks, W. B., Richmond, H. N. (1994a). Phase inversion in non–ionic surfactant-oil-water Systems – I. The effect of transitional inversion on emulsion drop sizes. Chem. Eng. Sci., 49(7): 1053–1064.

Brooks, W. B., Richmond, H. N. (1994b). Phase inversion in non-ionic surfactant—oil—water systems—II. Drop size studies in catastrophic inversion with turbulent mixing. Chem. Eng. Sci., 49(7): 1065–1075.

Brooks, W. B., Richmond, H. N. (1994c). Phase inversion in non-ionic surfactant—oil—water systems—III. The effect of the oil-phase viscosity on catastrophic inversion and the relationship between the drop sizes present before and after catastrophic inversion. Chem. Eng. Sci., 49(11): 1843–1853.

Brown, D.E. and Pitt, K. (1972). Drop size distribution of stirred non-coalescing liquid-liquid system. Chem. Eng. Sci., 27, 577–583.

Brown, P.N., Byrne, G.D., and Hindmarsh, A.C. (1989). VODE: A variable coefficient ODE solver. SIAM J. Sci. Stat. Comput., 10, 1038–1051.

Bruun H. H. (1995). Hot-wire anemometry: principles and signal analysis. Oxford University Press, Oxford.

Bruun H. H. (1996). Review article: hot-film anemometry in liquid flows. Meas. Sci. Technol. 7: 1301–1312.

Bruun H. H. (2004). Private communication.

Cartellier, A., Rivière, N. (2001). Bubble-induced agitation and microstructure in uniform bubbly flows at small to moderate particle Reynolds numbers. Phys. Fluids. 13(8): 2165–2181.

Charles, M. E., Govier, G. W., Hodgson, G. W. (1961). The horizontal pipeline flow of equal density oil-water mixtures. Can. J. Chem. Eng., 39: 27-36.

Chatzi, E. G., Garrielides, A. D., Kiparissides, C. (1989). Generalized model for prediction of the steady-size drop size distributions in batch stirred vessels. Ind. Eng. Chem. Res. 28: 1704–1711.

Chatzi, E. G., Kiparissides, C. (1992). Dynamic simulation of bimodal drop size distributions in low-coalescence batch dispersion systems. Chem. Eng. Sci., 47(2): 445–456.

Chesters, A. K. (1991). The modelling of coalescence processes in fluid-liquid dispersions: A review of current understanding. Chemical Engineering Research & Design, Transaction IChemE (Part A), 69, 259–270.

Chiang, C. J., Chen, C. M. (1994). Characteristics of phase inversion in a turbine-type agitator, J. the Chinese Institute Chem. Engineers, 25(6): 367–374.

Clarke, S. I., Sawistowski, H. (1978). Phase inversion of stirred liquid/liquid dispersions under mass transfer conditions. Trans. IChemE, 56: 50–55.

Clarke, N. N., and Turton, R. (1988). Chord length distributions related to bubble size distributions in multiphase flows, Int. J. Multiphase Flow, 14: 413–424.

Collins, S. B., Knudsen, J. G. (1970). Drop-size distributions produced by turbulent pipe flow of immiscible liquids, J. AIChE, 16(6), 1072–1080.

Coulaloglou, C. A. (1975). Dispersed phase interactions in an agitated flow vessel. PhD Thesis, Illinois Institute of Technology, Chicago.

Coulaloglou, C. A., Tavlarides, L. L. (1977). Description of interaction processes in agitated liquid-liquid dispersions. Chem. Eng. Sci., 32, 1289–1297.

Crowe, C. T. (2000). On models for turbulence modulation in fluid-particle flows, Int. J. Multiphase Flow, 26, 719–727.

Cui, Z., Fan, L. S. (2004). Turbulence energy distributions in bubbling gas-liquid and gas-liquid-solid flow systems, Chem. Sci. Eng., 59, 1755–1766.

Cutter, L.A. (1966). Flow and turbulence in stirred tank. A.I.Ch.E. J., 12, 35–45.

Das, P. K., Kumar, R., Ramkrishna, D. (1987). Coalescence of drops in stirred dispersion. A White noise model for coalescence, Chem. Sci. Eng., 42(2): 213–220.

Delichatsios, M. A., Prosbstein, R. F. (1976). The effect of coalescence on the average drop size in liquid-liquid dispersions. Industrial & Engineering Chemistry Fundamentals. 15: 134–138.

Deshpande, K. B., Kumar, S. (2003). A new characteristic of liquid-liquid systems–inversion holdup of intensely agitated dispersions. Chem. Eng. Sci., 58, 3829–3825.

Desnoyer, C., Masbernat, O., Gourdon, C. (2003). Experimental study of drop size distributions at high phase ratio in liquid-liquid dispersions. Chem. Eng. Sci., 58(7), 1353–1363.

Dong, J., Tsouris, C. (2001). Phase inversion of liquid-liquid dispersions under applied electric fields, J. Dispersion Sci. and Tech., 22(1): 57–60.

Doulah, M.S. (1975). An effect of holdup on drop sizes in liquid-liquid dispersions. Industrial and Engineering Chemistry Research Fundamentals, 14, 137–138.

Drubka, R. E., Nagib, H. M., Tan-Atichat, J. (1977). On temperature and yaw dependence of hot-wires. IIT, Chicago, USA.

Eastwood, C., Cartellier, A., lasheras, J.C. (2000) The break-up time of a droplet in a fully developed turbulent flow. In: Advanceds in Turbulence VIII, Proceedings of the Eight European Turbulence Conference. Barcelona, pp. 573–576.

El-Hamouz, A. M., Stewart, A. C. (1996). On-line drop size distribution measurement of oil-water dispersion using a Par-Tec M300 laser backscatter instrument, SPE Int. 36672, 1-14.

Fakhr-Din, S. M. (1973). Phase inversion and drop size measurements in agitated liquid-liquid systems. Ph.D. Thesis, University of Manchester.

Falco, J.W., Walker, R.D., Shah, D.O. (1974). Effect of phase-volume ratio and phase-inversion on viscosity of microemulsions and liquid crystals. AIChE J., 20(3), 510–514.

Farra, B., Bruun, H. H. (1996). A computer based hot-film technique used for flow measurements in a vertical kerosene-water pipe flow. Int. J. Multiphase Flow, Vol.22, No.4 : 733–751.

Farra, B., Samways, A. L., Ali, J., Bruun, H. H. (1995). A computer-based hot-film technique for two-phase flow measurements, Meas. Sci. Technol., 6, 1528-1537.

Fujiwara, A., Minato, D., Hishida, K. (2004). Effect of bubble diameter on modification of turbulence in an upward pipe flow. Int. J. Heat and Fluid Flow, 25, 481-488.

Furuse, J. (1972). Japanese Journal of Applied Physics, Part 1. 11(10), 1537.

Garnier, C., Lance, M., Marie, J.L. (2002). Measurement of local flow characteristics in buoyancy-driven bubbly flow at high void fraction. Experimental Thermal and Fluid Science, 26: 811–815

Gilchrist, A., Dyster, K. N., Moore, I. P. T., Nienow, A. W., Carpenter, K. J. (1989). Delayed phase inversion in stirred liquid-liquid dispersions, Chem. Eng. Sci., 44(10): 2381–2384.

Gillies, R. G., Sun, R., Shook, C. A. (2000). Laboratory investigation of inversion of heavy oil emulsions, The Canadian J. Chem. Eng., 78: 757–763.

Gnotke, O., Benk, H., Loth, R. (2003). Experimental study on the number density distribution function in turbulent bubbly flows with coalescence and break-up. Experimental Thermal and Fluid Science, 27 (7), 803–816.

Godfrey, J.C., Obi, F.I.N., Reeve, R.N. (1989). Measuring drop size in continuous liquid-liquid mixers. Chemical Engineering Progress, 85, 61–69.

Gore, R. A., Crowe, C. T. (1989). Effect of particle size on modulating turbulent intensity, Int. J. Multiphase Flow, 15(2), 279–285.

Govier, G.W., G.A., Sullivan, R.K., Wood (1961). The Upward Vertical Flow of Oil-water Mixtures. The Canadian J. Chem. Eng., 39: 27–36.

Groeneweg, F., Agterof, W. G. M., Jaeger, P., Janssen, J. J. M., Wieringa, J. A., Klahn, J. K. (1998). On the mechanism of the inversion of emulsions. Chemical Engineering Research & Design, Transaction IChemE (Part A), 76, 55–63.

Groetsch C.W. (1984). The theory of Tikhonov Regularization for Fredholm Equations of the First Kind. Pitman, London.

Guilinger, T. R., Grislingas, A. K., Erga, O. (1988). Phase inversion behaviour of water-kerosene dispersions. Industrial and Engineering Chemistry Research, 27(6), 978–982.

Guzhov, A. I., Grishin, A. D., Medredev, V. F., Medredeva, O. P. (1973). Emulsion formation during the flow of two liquids in a pipe. Neft Hhoz (in Russian), 8: 58–61.

Haam, S.J., Brodkey, R. S. (2000). Laser Doppler anemometry measurements in an index of refraction matched column in the presence of dispersed beads. Int. J. Multiphase Flow, 26: 1401–1418.

Hagesaether, L., Jakobsen, H.A., Svendsen, H.F. (2002). A model for turbulent binary break-up of dispersed fluid particles. Chem. Eng. Sci., vol. 57(16), pp.3251–3267.

Hagiwara, Y., Esmaeilzadeh, E., Tsutsui, H., Suzuki, K. (1989). Simultaneous measurement of liquid film thickness, wall shear stress and gas flow turbulence of horizontal wavy two-phase flow. Int. J. Multiphase Flow Vol.5, No.3: 421–431.

Hagiwara, Y., Takashina, Y., Tanaka, M. (1997). Direct numerical simulation of the basic phase-interactions in liquid turbulent channel flow with immiscible droplets. Nuclear Engineering and Design, 175, 49-57.

Hamad, F. A., Bruun, H. H. (2000). Evaluation of bubble/drop velocity and slip velocity by a single normal hot-film probe placed in a two-phase flow. Meas. Sci. Technol. 11: 11–19.

Hesketh, R.P., Etchells, W., Russell, T.W.F. (1991). Bubble breakage in pipeline flow. Chem. Eng. Sci. 46 (1): 1–9.

Hetsroni, G. (1982). Handbook of Multiphase Systems. Hemisphere Publishing Corp., New York.

Hetsroni, G. (1989). Particles-turbulence interaction. Int. J. Multiphase Flow, 15(5), 735-746.

Hibiki, T., Hogsett, S., Ishii, M. (1998). Local measurement of interfacial area, interfacial velocity and liquid turbulence in two-phase flow. Nuclear Engineering and Design, 184: 287–304

Hibiki, T., Ishii, M. (1998). Effect of flow-induced vibration on local flow parameters of two-phase flow. Nuclear Engineering and Design, Volume 185, 2–3:113–125.

Hinze, J.O. (1955). Fundamentals of the hydrodynamic mechanism of splitting dispersion processes. AIChE J. 1, 289–295.

Hinze, J. O. (1959). Turbulence. McGraw-Hill, New York.

Hobbel, E.R., Davies, R., Rennie, F.W., Allen, T., Butler, L.E., Waters, E. R., Smith, J. T., Sylvester, R. W. (1991). Modern methods of on-line size analysis for particulate process streams. Part. Part. Syst. Charact. 8: 29–34.

Hogsett, S., Ishii, M. (1997). Local two-phase flow measurements using sensor techniques. Nuclear Engineering and Design, Volume 175 (1-2): 15–24.

Howarth, W. J. (1967). Coalescence of drops in turbulent flow field. Chem. Eng. Sci., 19: 33–38.

Hsia, M.A., Tavlarides, L. L. (1980). A simulation model for homogeneous dispersion in stirred tanks. Chem. Eng. J., vol. 20: 225–236.

Hu, B., Stewart, C., Hale, C.P., Lawrence, C.J., Hall, A.R.W., Zwiens, H., Hewitt, G.F. (2005). Development of an X-ray computed tomography (CT) system with sparse sources: application to three-phase pipe flow visualization. Experiments in Fluids. In press.

Hussain, S.A. (2004). Experimental and Computational Studies of Liquid-liquid Dispersed Flows. PhD Thesis, University of London, London, UK.

Hutchinson, P, Hewitt, G.F., Dukler, A.E. (1971). Deposition of liquid or solid dispersions from turbulent gas streams: A stochastic model. Chem. Eng. Sci., 26, 419–439.

Ioannou, K., B., Hu, O.K., Matar, G.F., Hewitt, P., Angeli (2004). Phase Inversion in Dispersed Liquid-liquid Pipe Flows, 5th Int. Conference on Multiphase Flow, Yokohama, Japan.

Ioannou, K., O.J., Nydal, P., Angeli (2005). Phase inversion in dispersed liquid-liquid flows. Exp. Thermal and Fluid Sci., 29(3): 331–339.

Iskandrani, A., Kojasoy, G. (2001). Local void fraction and velocity field description in horizontal bubbly flow. Nuc. Eng. Design 204: 117–128.

Jeffreys G. V., Davies G. A. (1971). Coalescence of liquid droplets and liquid dispersion. Recent Advances in Liquid-Liquid Extraction, ed. C. Hanson, 495. New York: Pergamon.

Jones, O. C., Zuber, N. (1978). Use of a cylindrical hot-film anemometer for measurement of two-phase void and volume flux profiles in a narrow rectangular channel. AIChE Symp. Series, 74, 191–204.

Juswandi, J. (1995). Simulation of the oil-water inversion process. M.S. Thesis, Oklahoma State University.

Karabelas, A. J. (1978). Droplet size spectra generated in turbulent pipe flow of dilute liquid/liquid dispersions. AIChE J. 24, 170–180.

Kennard, E. H. (1938). Kinetic theory of gases. McGraw-Hill, New York.

Kenning, V. M., Crowe, C. T. (1997). On the effect of particles on carrier phase turbulence in gas-particle flows. Int. J. of Multiphase Flow, 23, 403–408.

Kim, S, Lee, K. B., Lee, C. G. (2005). Theoretical approach on the turbulence intensity of the carrier fluid in dilute two-phase flows. Int. Communications in Heat and Mass Transfer, 32, 435-444.

Klahn, J.K., Janssen, J.J.M., Vaessen, G.E.J., deSwart, R., Agterof, W.G.M. (2002). On the escape process during phase inversion of an emulsion. Colloids and Surfaces A: Physicochemical Engineering Aspects, 210, 167–181.

Konno, M., Aoki, M., Saito, S. (1983). Scale effect on break-up process in liquid-liquid agitated tanks. J. Chem. Eng. Jpn. 16: 312–319.

Kostoglou, M., Dovas, S., Karabelas, A.J. (1997). On the steady-state size distribution of dispersions in breakage processes. Chem. Eng. Sci., Volume 52 (8): 1285–1299.

Kostoglou, M., Karabelas, A.J. (1998). On the attainment of steady state in turbulent pipe flow of dilute dispersions. Chem. Eng. Sci. 53 (3): 505–513.

Kostoglou, M., Karabelas, A.J. (2001). A contribution towards predicting the evolution of droplet size distribution in flowing dilute liquid/liquid dispersions. Chem. Eng. Sci. 56: 4283–4292.

Kubie J., Gardner G. C. (1977). Drop sizes and drop dispersion in straight horizontal tubes and in helical coils. Chem. Eng. Sci., 32, 195–202.

Kumar, S., Kumar, R., Gandhi, K. S. (1991). Influence of the wetting characteristics of the impeller on phase inversion. Chem. Eng. Sci., 46(9), 2365–2367.

Kumar, S. (1996). On Phase Inversion Characteristics of Stirred Dispersions. Chem. Eng. Sci., 51(5), 831–834.

Kuboi, R., Komasawa, I., Otake, T. (1972a). Behaviour of dispersed particles in turbulent liquid flow. J. Chem. Eng. Japan, 5: 349.

Kuboi, R., Komasawa, I., Otake, T. (1972b). Collision and coalescence of dispersed drops in turbulent liquid flow. J. Chem. Eng. Japan, 5: 423.

Kulkarni, A. A., Joshi, J. B., Ramkrishna, D. (2004). Determination of bubble size distributions in bubble columns using LDA. AIChE J., 50(12), 3068–3084.

Kurban, A.P.A. (1997). Stratified Liquid-Liquid Flow. PhD Thesis, Imperial College London, London, UK.

Laity D. S., Treybal R E. (1957). Dynamics of liquid agitation in the absence of an air-liquid interface. AIChE J., 3, 176–180.

Lance, M., Bataille, J. (1991). Turbulence in the liquid phase of a uniform bubbly air-water flow. J. Fluid Mech., 222: 95–118.

Langston, P.A., Burbidge, A.S., Jones., T.F., and Simmons, M.J.H. (2001). Particle and droplet size analysis from chord measurements using Bayes' theorem, Powder Tech., Vol. 116: 33–42.

Lasheras, J. C., Eastwood, C., Martinez-Bazan, C., Montanes, J. L. (2002). A review of statistical models for the break-up of an immiscible fluid immersed into a fully developed turbulent flow. Int. J. Multiphase Flow, 28, 247–278.

Laufer, J. (1954). The structure of turbulence in fully developed pipe flow, NACA Report No. 1174.

Lee, C.H., Erickson, L.E., Glasgow, L.A. (1987). Dynamics of bubble size distribution in turbulent Gas-liquid dispersions. Chem. Eng. Commun. Vol.61: 181–195.

Levich, V. G. (1962). Physicochemical Hydrodynamics. Prentice-Hall, Englewood Cliffs, New Jersey.

Liu, L. (2005). Optical and Computational Studies of Liquid-liquid Flows. PhD Thesis, University of London, London, UK.

Liu, T. J., Bankoff, S. G. (1993a). Structure of air-water bubbly flow in a vertical pipe – I. Liquid mean velocity and turbulence measurements. Int. J. Heat Mass Transfer Vol.36(4): 1049–1060.

Liu, T. J., Bankoff, S. G. (1993b). Structure of air-water bubbly flow in a vertical pipe – II. Void fraction, bubble velocity and bubble size distribution. Int. J. Heat Mass Transfer. Vol.36(4): 1061–1072.

Liu, S., Li, D. (1999). Drop coalescence in turbulent dispersions. Chem. Eng. Sci., Volume 54, Issue 23, 5667–5675.

Liu W., Clark N. N. (1995). Relationships between distributions of chord lengths and distributions of bubble sizes including their statistical parameters. Int. J. Multiphase Flow, 21, 1073–1089.

Liu W., Clark N.N., Karamavruc A.I. (1998). Relationship between bubble size distributions and chord-length distribution in heterogeneously bubbling systems. Chem. Eng. Sci., 53(6), 1267–1276.

Liu, L., Matar, O.K., Perez de Ortiz, E.S., Hewitt, G.F. (2004). Experimental Methodology for Investigating Concentrated Liquid-liquid Dispersions. 5th International Conference on Multiphase Flow, ICMF'04, Yokohama, Japan, May 30–June 4. Paper No. 230.

Liu, L., O.K., Matar, E.S., Perez de Ortiz, G.F., Hewitt (2005). Experimental investigation of phase inversion in a stirred vessel using LIF. Chem. Eng. Sci., 60, 85–94.

Luhning, R.W., Sawistowski, H. (1971). Phase inversion in stirred liquid-liquid systems. Proceeding of the International Solvent Extraction Conference, The Hague, 873–887, Society of Chemical Industry, London.

Luo, H., Svendsen, H.F. (1996). Theoretical model for drop and bubble break up in turbulent dispersions. A.I.Ch.E. J. 42, 1225–1233.

Luo, Y.S., T.K., Chen, J.Y., Cai (1997). Frictional pressure loss and phase inversion point for oil-water emulsion in vertical tube", Proceedings of Int. Symposium on Multiphase Fluid non- Newtonian Fluid& Physico-Chemical Fluid Flows, 3.53–3.58.

Ljus, C., Johansson, B., Almstedt, A. (2002). Turbulence modification by particles in a horizontal pipe flow. Int. J. Multiphase Flow. 28: 1075–1090.

Lovick, J. (2004). Horizontal oil-water flows in the dual continuous flow regime. Ph.D. thesis, University College London, UK.

Madsen, N.K., Sincovec, R.F. (1979). PDECOL – collocation software for partial differential equations. ACM-TOMS, 5 (3), 326–351.

Maggioris, D., Goulas, A., Alexopoulos, A.H., Chatzi, E.G., Kiparissides, C. (2000). Prediction of particle size distribution in suspension polymerization reactors: Effect of turbulence nonhomogeneity. Chem. Eng. Sci., 55, 4611–4627.

Martínez-Bazán, C., Montanes, J.L., Lasheras, J.C. (1999). On the break-up of an air bubble injected into a fully developed turbulent flow. Part II: Size pdf of the resulting daughter bubbles, J. fluid mech., vol. 401: 183–207.

McClarey, M. J., Mansoori, G. A. (1978). Factors affecting the phase inversion of dispersed immiscible liquid-liquid mixtures. AIChE Symposium Series, 74(173): 134–139.

McQuarrie (2000). Statistical Mechanics. University Science Books, 2nd edition, ISBN 1-891389-15-7.

Michiyoshi, I., Serizawa, A. (1986). Turbulence in two-phase bubbly flow. Nucl. Eng. Des., 95, 253–267.

Mizukami, M., Parthasarathy, R. N., Faeth, G. M. (1992). Particle generated turbulence in homogeneous dilute dispersed flows. Int. J. Multiphase Flow, 18: 397–412.

Nädler, M., Mewes, D. (1995). Intermittent three-phase flow of oil, water and gas in horizontal pipes. Proc. 5th Int. Offshore and Polar Eng. Conf., pp. 72–80.

Nädler, M., Mewes, D. (1997). Flow induced emulsification in the flow of two immiscible liquids in horizontal pipes. Int. J. Multiphase Flow, 23(1): 55–68.

Narsimham, G., Gupta, J.P., Ramkrishna, D. (1979). A model for transitional breakage probability of droplets in agitated lean liquid-liquid dispersions. Chem. Eng. Sci. 47: 1989–3002.

Nguyen Y. T., Vu T. D., Wong H. K., Yeow Y. L. (1999). Solving the inverse problem of capillary viscometry by Tikhonov regularization. Journal of Non-Newtonian Fluid Mechanics, 87, 103–116.

Nienow, A. W., Pacek, A. W., Moore, I. P. T., Homer, J. (1994). Fundamental studies of phase inversion in a stirred vessel. Proc. Euro. Conf. on Mixing, IChemE Symposium Series, 136: 171–178.

Nishikawa, M., Mori, F., Fujieda, S. (1987). Average drop size in a liquid-liquid phase mixing vessel. Journal of Chemical Engineering of Japan, 20, 82–88.

Nisisako, T., Okushima, S., Torii, T. (2005). Controlled formulation of monodisperse double emulsions in a multiple-phase microfluidic system. Soft Matter, 1, 23–27.

Norato, M. A., Tsouris, C., Tavlarides, L. L. (1998). Phase inversion studies in liquid-liquid dispersions. Can. J. Chem. Eng., 76: 486–494.

Oolman, T. O., Blanch, H. W. (1986). Bubble Coalescence in Stagnant Liquids, Chem. Eng. Comm., 43, 237–261.

Pacek, A. W., Moore, I. P. T., Nienow, A. W. (1994a). Video technique for measuring dynamics of liquid-liquid dispersion during phase inversion. AIChE J., 40(12): 1940–1949.

Pacek, A. W., Nienow, A. W., Moore, I. P. T. (1994b). On the structure of turbulent liquid-liquid dispersed flows in an agitated vessel. Chem. Eng. Sci., 49(20): 3485–3498.

Pacek, A. W., Nienow, A. W. (1995). A problem for the description of turbulent dispersed liquid-liquid systems. Int. J. Multiphase Flow, Vol 21(2): 323–328.

Pacek, A.W., Man, C.C., Nienow, A.W. (1998). On the Sauter mean diameter and size distributions in turbulent liquid/liquid dispersions in a stirred vessel. Chem. Eng. Sci., Volume 53 (11), 2005–2011.

Pal, R., S.N., Bhattacharya, E., Rhodes (1986). Flow behaviour of oil-in-water emulsions. Can. J. Chem. Eng., 64: 3–10.

Pal, R. (1993). Pipeline flow of unstable and surfactant-stabilised emulsions. AIChE J., 39(11): 1754–1764.

Pan, L. (1996) High pressure three-phase (gas/liquid/liquid) flow. Ph.D. Thesis, University of London, London, UK.

Pan, L., Jayanti, S., Hewitt, G.F. (1995). Flow patterns, phase inversion and pressure gradient in air-oil-water flow in horizontal pipe. 2nd ICMF, Kyoto, Japan, April 3-7.

Parthasarathy, R. N., Faeth, G. M. (1990). Turbulence modulation in homogeneous dilute particle-laden flows. J. Fluid Mech. 220: 485–514.

Perry, A. E. (1982). Hot-wire anemometry. Oxford university press, Oxford, UK.

Pilehvari, A., Saddevandi, B., Halvaci, M., Clark, P. E. (1988). Oil/water emulsions for pipeline transport of viscous crude oils. Paper SPE 18218, SPE Annual Technical Conference and Exhibition, Houston.

Placek, J., and Tavlarides, L.L. (1985). Turbulent flows in stirred tanks. Part I: turbulent flow in the turbine impeller region. AIChE J., 31,1113–1120.

Prince, M., Blanch, H. W. (1990). Bubble coalescence and break-up in air-sparged Bubble columns. AIChE J., 36(10): 1485–1499.

Quinn, J. A., Sigloh, D. B. (1963). Phase inversion in the mixing of immiscible liquids. Can. J. Chem. Eng., 41: 15–18.

Reeve, R.N., Godfrey, J. C. (2002). Phase inversion during liquid-liquid mixing in continuous flow, pump-mix, agitated tanks. Transaction IChemE, part A, 80, 864–871.

Ribeiro, L. M., Regueiras, P., Guimarães, M., Madureira C. N., Cruz-Pinto, J. (1995). The dynamic behaviour of liquid-liquid agitated dispersions. I - The hydrodynamics. Computers & Chemical Engineering (19):333–343.

Rodger, W. A., Trice, Jr., V. G., Rushton, J. H. (1956). The effect of fluid motion on interfacial area of dispersions. Chemical Engineering Progress, 52(12), 515–520.

Rose, S. C., Marsden Jr, S. S. (1970). The flow of north slope crude oil and its emulsions at low temperatures. Paper SPE 2996, SPE 45th Annual Fall Meeting and Exhibition, Houston.

Rotta, J. C. (1972): Turbulente Strömungen. B. G. Teubner, Stuttgart.

Russell, T.W.F., Hodgsen, GW., Govier, GW. (1959), Horizontal pipeline flow of mixtures of oil and water. Can. J. Chem. Eng., 37:9–17.

Saffman, P.G., Turner, J.S. (1956). On the collision of drops in turbulent clouds. J. Fluid Mech., 1, 16–30.

Sajjadi, S., Zerfa, M., Brooks, B. W. (2002). Dynamic behaviour of drops in oil/water/oil dispersions. Chem. Eng. Sci., 57(4), 663–675.

Samways, A., Ali, J., Al-Deen, M. F. N., Bruun, H. H. (1994). The calibration and measurements with cylindrical hot-film probes in water flows. Meas. Sci. Technol. 5: 1551–1559.

Sanchez, L. E., Zakin, J. L. (1994). Transport of viscous crudes as concentration oil-in-water emulsions. Ind. Engng Chem. Res. 33: 3256–3261.

Santana, D., Macías-Machín, A. (2000). Local bubble-size distribution in fluidized beds. J. AIChE, 46(7), 1340-1347.

Sato, Y., Sekoguchi, K. (1975). Liquid velocity distribution in two-phase bubble flow. Int. J. Multiphase Flow, 2, 79-95.

Schwartzberg, H. G., Treybal, R.E. (1968). Fluid and particle motion in turbulent stirred tanks. Industrial and Engineering Chemistry Research Fundamentals, 7, 1–6.

Selker, A. H., Sleicher, Jr., C. A. (1965). Factors affecting which phase will disperse when immiscible liquids are stirred together. Canadian Journal of Chemical Engineering, 43, 298–301.

Serizawa, A., Kataoka, I. & Michiyoshi, I. (1975a). Turbulence structure of air-water bubbly flow. parts I: Measuring techniques. Int. J. Multiphase Flow 2: 221–233.

Serizawa, A., Kataoka, I. & Michiyoshi, I. (1975b). Turbulence structure of air-water bubbly flow. parts II: Local properties. Int. J. Multiphase Flow 2: 235–246.

Serizawa, A., Kataoka, I. & Michiyoshi, I. (1975c). Turbulence structure of air-water bubbly flow. parts III: Transport properties. Int. J. Multiphase Flow 2: 247–259.

Shaha, J. (1999). Phase interactions in transient stratified flow. Ph.D. Thesis, Department of Chemical Engineering and Chemical Technology, Imperial College of London.

Sharma, S., Lewis, S., Kojasoy, G. (1998). Local studies in horizontal gas-liquid slug flow. Nucl. Eng. Des. 184:305–318.

Shinnar, R. (1961). On the behaviour of liquid dispersions in mixing vessels. Journal of Fluid Mechanics, 10, 259–275.

Simmons, M.J.H., Langston, P.A., and Burbidge, AS. (1999). Particle and droplet size analysis from chord distributions. Powder Tech., Vol. 102: 75–83.

Simmons, M. J. H., Azzopardi, B.J. (2001). Drop size distributions in dispersed liquid-liquid pipe flow. Int. J. Multiphase Flow, 27: 843–859.

Soleimani, A. (1999). Phase distribution and associated phenomena in oil-water flows in horizontal tubes, PhD Thesis, Imperial College London, UK.

Sovová, H. (1981). Breakage and coalescence of drops in a batched stirred vessel - II. Comparison of model and experiments. Chem. Eng. Sci., 36(9): 1567–1573.

Sun, X., Kim, S., Smith, T. R., Ishii, M. (2002). Local liquid velocity measurements in air-liquid bubbly flow. Exp. In Fluids. 33: 653–662.

Sun, X., Paranjape, S., Kim, S., Ozar, B., Ishii, M. (2004). Liquid velocity in upward and downward air-water flows. Annals of Nuclear Energy, 31, 357-373.

Taylor, G.I. (1932). The viscosity of a fluid containing small drops of another fluid. Proceedings of the Royal Society of London Series A, 138, 41–48.

Theofanous, T. G., Sullivan, J. (1982). Turbulence in two-phase dispersed flows. J. Fluid Mech., 116: 343–362.

Tidhar, M., Merchuk, J. C., Sembira, A. N., Wolf, D. (1986). Characteristics of a motionless mixer for dispersion of immiscible fluids- Phase inversion of liquid-liquid systems. Chem. Eng. Sci., 41(3), 457–462.

Trabold, T.A., Kumar, R. (2000). Vapour core turbulence in annular two-phase flow. Experiments in Fluids 28: 187–194.

Trallero, J. L. (1995). Oil water flow patterns in horizontal pipes. PhD Thesis, University of Tulsa. Israel.

Tsouris, C., Dong, J. (2000). Effects of electric fields on phase inversion of liquid–liquid dispersions, Chem. Eng. Sci., 55(17): 3571–3574.

Tsouris, C., Tavlarides, L. L. (1994). Breakup and coalescence models for drops in turbulent dispersions. AIChE J., 40(3), 395–406.

Vaessen, G.E.J., Visschers, M., Stein, H.N. (1996). Predicting catastrophic phase inversion on the basis of droplet coalescence kinetics. Langmuir, 12: 875–882.

Valentas, K.J., Bilous, O., Amundson, N.R. (1966). Analysis of breakage in dispersed phase systems. Ind. Eng. Chem. Fundamentals, 5: 271–279.

Vermuelen, T., Williams, G.M., Langlois, G.E. (1955). Interfacial area in liquid-liquid and gas-liquid agitation. Chemical Engineering Progress, 51(2), 85–94.

Wang, G., Ching, C.Y. (2001). Measurement of multiple gas-bubble velocities in gas-liquid flows using hot-film anemometry. Exp. In Fluids 31: 428–439.

Wang, S. K., Lee, S. J., Jones JR, O. C., Lahey JR, R. T. (1987). 3-D turbulence structure and phase distribution measurements in bubbly two-phase flows. Int. J. Multiphase Flow, 13 (3), 327-343.

Wilson, C. (1989). Two mechanisms for drag reduction. Proc. 4th Int. Conf. Drag Reduction, Davos, Switzerland, July 31- August 3.

Wynn, E. J. W. (2003). Relationship between particle-size and chord-length distributions in focused beam reflectance measurement: Stability of direct inversion and weighting. Powder Technology, 133: 125–133.

Yarin, L.P., Hetsroni, G. (1994). Turbulence intensity in dilute two-phase flows- 3 The particle-turbulence interaction in dilute two-phase flow. Int. J. Multiphase Flow, 20(1), 27-44.

Yeh, G. C., Haynie, Jr., F. H., Moses, R. A. (1964). Phase-volume relationship at the point of phase inversion in liquid dispersions. AIChE J., 10(2), 260–265.

Yeo, L. Y., Matar, O. K., Perez de Ortiz, E. S., Hewitt, G. F. (2002). Simulation studies of phase inversion in agitated vessels using a Monte-Carlo technique. Journal of Colloid and Interface Science, 248, 443–454.

Yeo, L. Y. (2002). Modelling of phase inversion and associated phenomena in liquid-liquid systems. PhD Thesis, University of London, London, UK.

Yeo, L. Y., Matar, O. K., Perez de Ortiz, E. S., Hewitt, G. F. (2000). Phase inversion and associated phenomena. Multiphase Science and Technology, 12(1), 51–116.

Yeow Y. L., Nguyen Y. T., Vu T. D., Wong H. K. (2000). Processing the capillary viscometry data of fluids with yield stress. Rheol Acta. 39, 392-398.

Yuan, Z., Michaelides, E. E. (1992). Turbulence modulation in particulate flows- a theoretical approach, Int. J. Multiphase Flow, 18(5), 779-785.

Yuge, T., Hagiwara, Y. (2004). The modifications of near-wall turbulence structure and heat transfer by immiscible droplets in turbulent liquid-liquid two-phase flow, Int. J. Multiphase Flow, 25, 471-480.

Zhou, G., Kresta, S.M. (1998). Correlation of mean drop size and minimum drop size with the turbulence energy dissipation and the flow in an agitated tank, Chem. Eng. Sci., vol.53(11): 2063–2079.

Appendix A

Photographs of O/W and W/O Dispersed Flows

Figure A.1 (a-h) shows the photographs of dispersion at various input oil fractions taken by a high speed camera from 1.5 m/s mixture velocity in downward flow. The complete phase inversion point is found to be 75%, according to the glue-on hot-film probe. Figure A.2 illustrates the complex flow (like plug) observed in 1.0 m/s 80% input oil fraction.

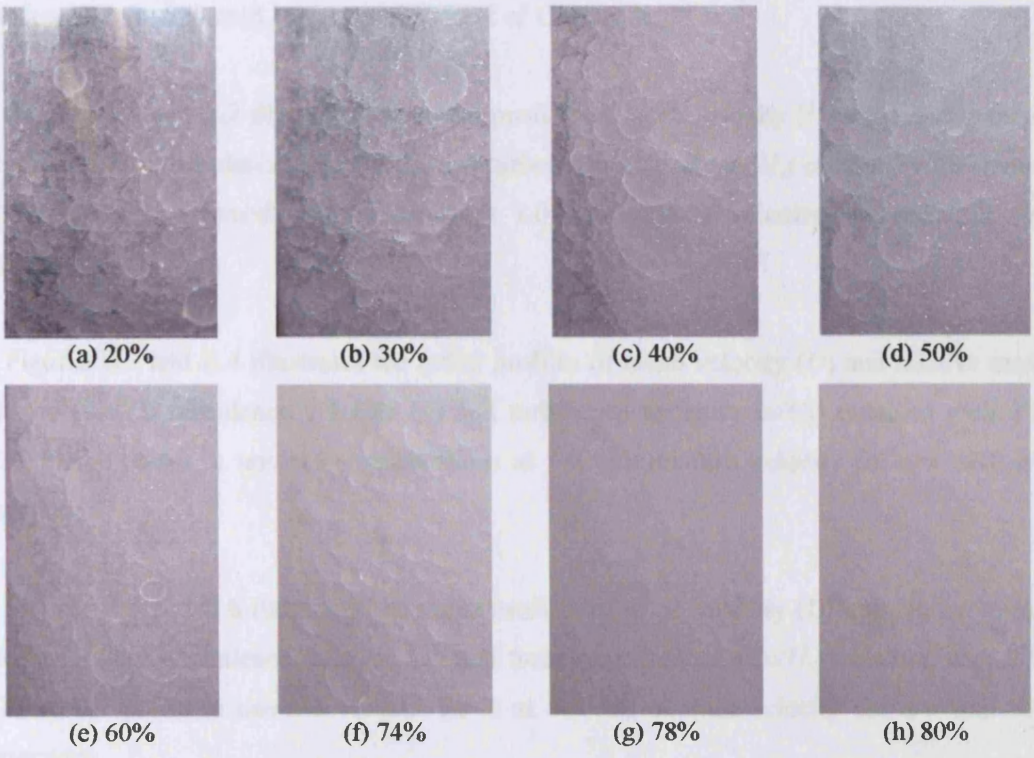

Figure A.1: Photographs of the dispersion taken at various input oil fractions from 1.5 m/s mixture velocity in downward flow (not to scale).

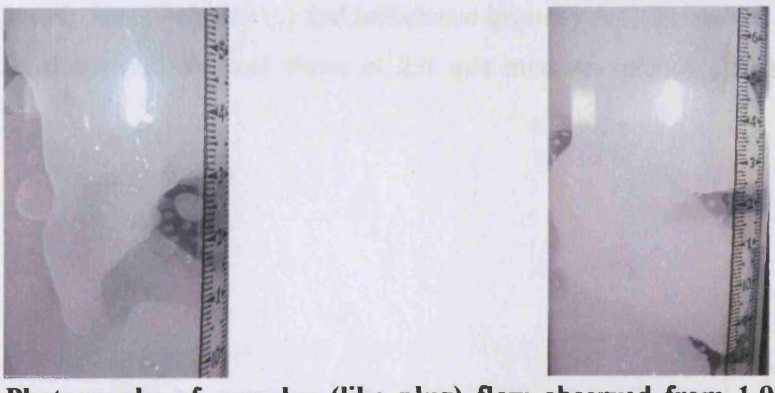

Figure A.2: Photographs of complex (like plug) flow observed from 1.0m/s mixture velocity at 80% input oil fraction in downward flow (not to scale).

Appendix B

Mean Velocity and Turbulence Fluctuation Velocity in Vertical Pipeline Flows

Appendix B shows the experimental data obtained from oil-water vertical pipeline flows which were not presented in the main context of Chapter 6.

Figures B.1 and B.2 illustrates the radial profiles of mean velocity (U) and relative mean velocity (U/U_c), turbulence velocity (u) and turbulence intensity (u/U_c) obtained with Dantec 55R14 probe in upward vertical flows at 1.0 m/s mixture velocity for o/w and w/o dispersions.

Figures B.3 and B.4 illustrates the radial profiles of mean velocity (U) and relative mean velocity (U/U_c), turbulence velocity (u) and turbulence intensity (u/U_c) obtained with TSI 1276-10AW probe in upward vertical flows at 1.0 m/s mixture velocity for o/w and w/o dispersions.

Figures B.5 and B.6 illustrates the radial profiles of mean velocity (U) and relative mean velocity (U/U_c), turbulence velocity (u) and turbulence intensity (u/U_c) obtained with TSI 1276-10AW probe in upward vertical flows at 1.5 m/s mixture velocity for o/w and w/o dispersions.

Figures B.7 and B.8 illustrates the radial profiles of mean velocity (U) and relative mean velocity (U/U_c), turbulence velocity (u) and turbulence intensity (u/U_c) obtained with Dantec 55R14 probe in downward vertical flows at 2.0 m/s mixture velocity for o/w and w/o dispersions.

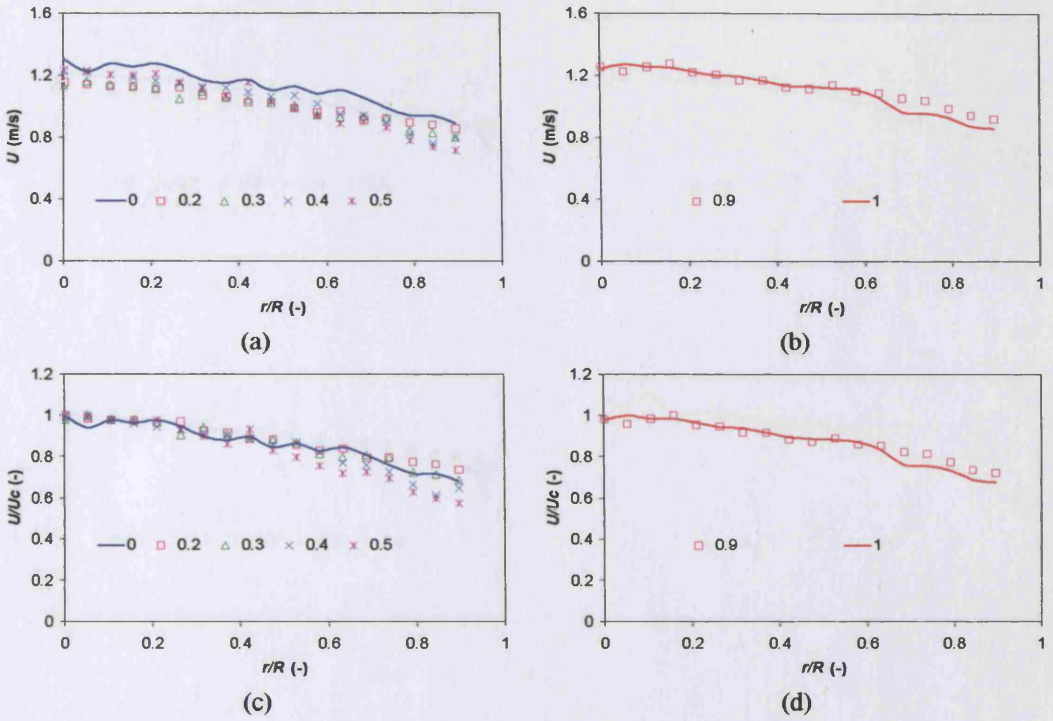

Figure B.1: Mean and relative velocity profiles of the continuous phase at different input oil fractions measured with Dantec 55R14 probe at 1.0 m/s mixture velocity in upward flow. (a) & (c): water continuous, (b) & (d): oil continuous.

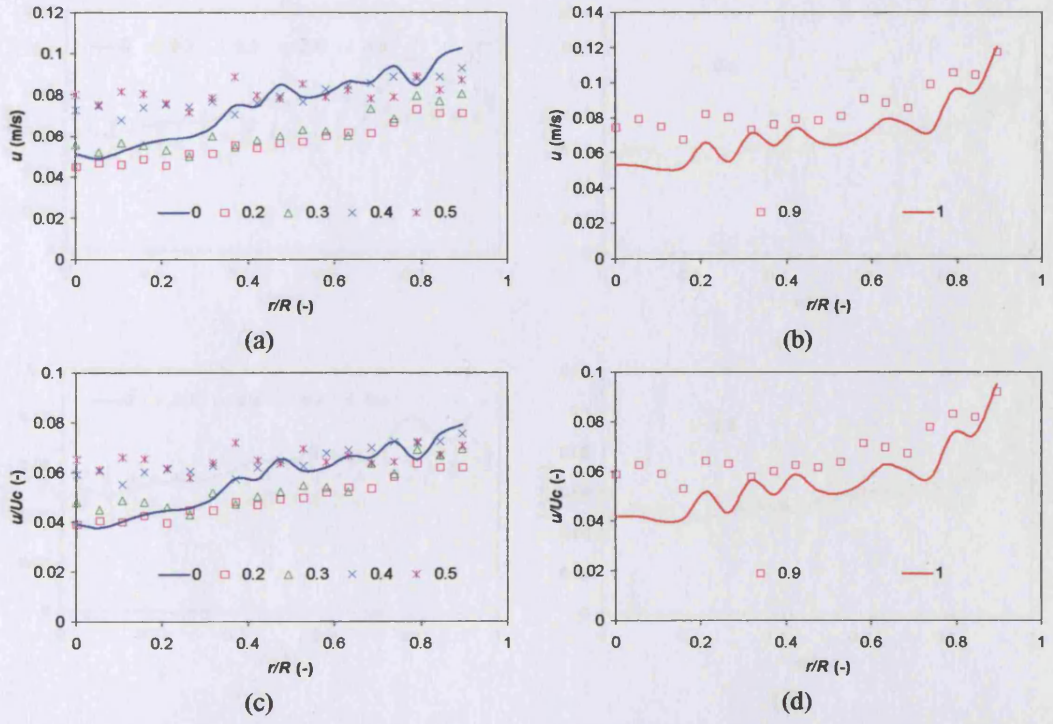

Figure B.2: Turbulence velocity and intensity profiles of the continuous phase at different input oil fractions measured with Dantec 55R14 probe at 1.0 m/s mixture velocity in upward flow. (a) & (c): water continuous, (b) & (d): oil continuous.

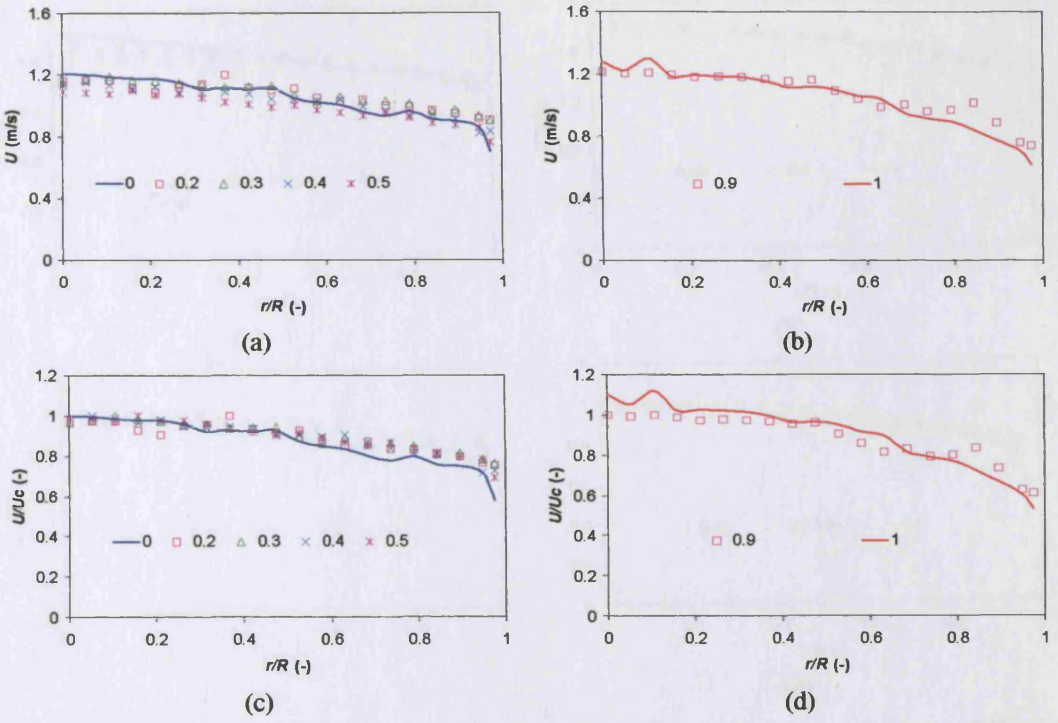

Figure B.3: Mean and relative velocity profiles of the continuous phase at different input oil fractions measured with TSI 1276-10AW probe at 1.0 m/s mixture velocity in upward flow. (a) & (c): water continuous; (b) & (d): oil continuous.

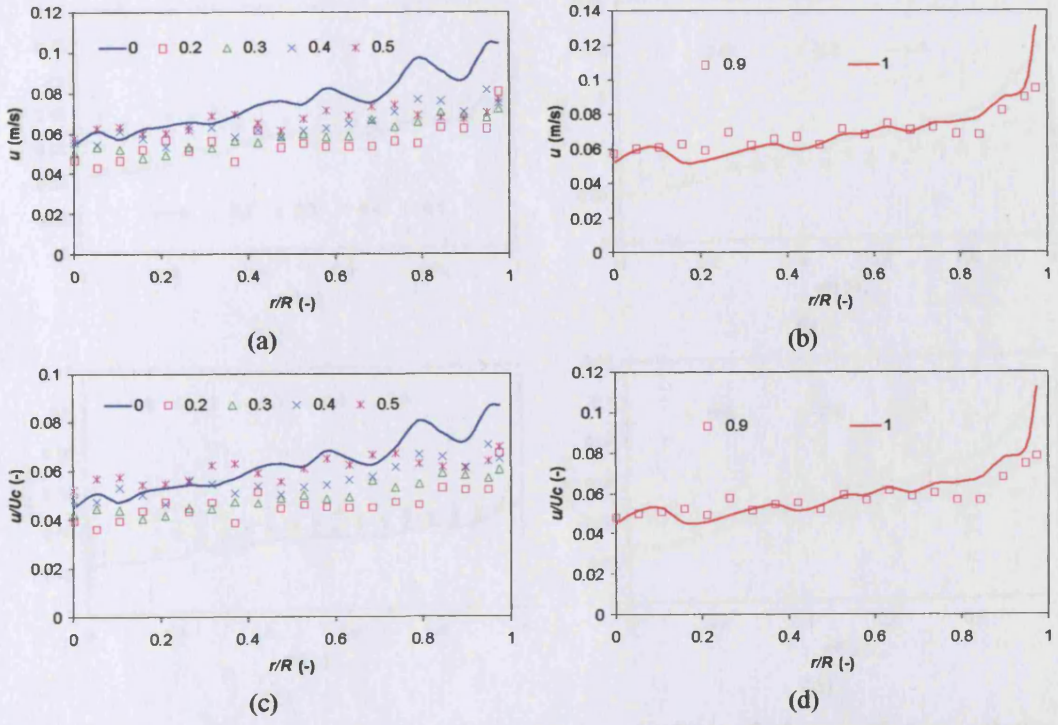

Figure B.4: Turbulence velocity and intensity profiles of the continuous phase at different input oil fractions measured with TSI 1276-10AW probe at 1.0 m/s mixture velocity in upward flow. (a) & (c): water continuous, (b) & (d): oil continuous.

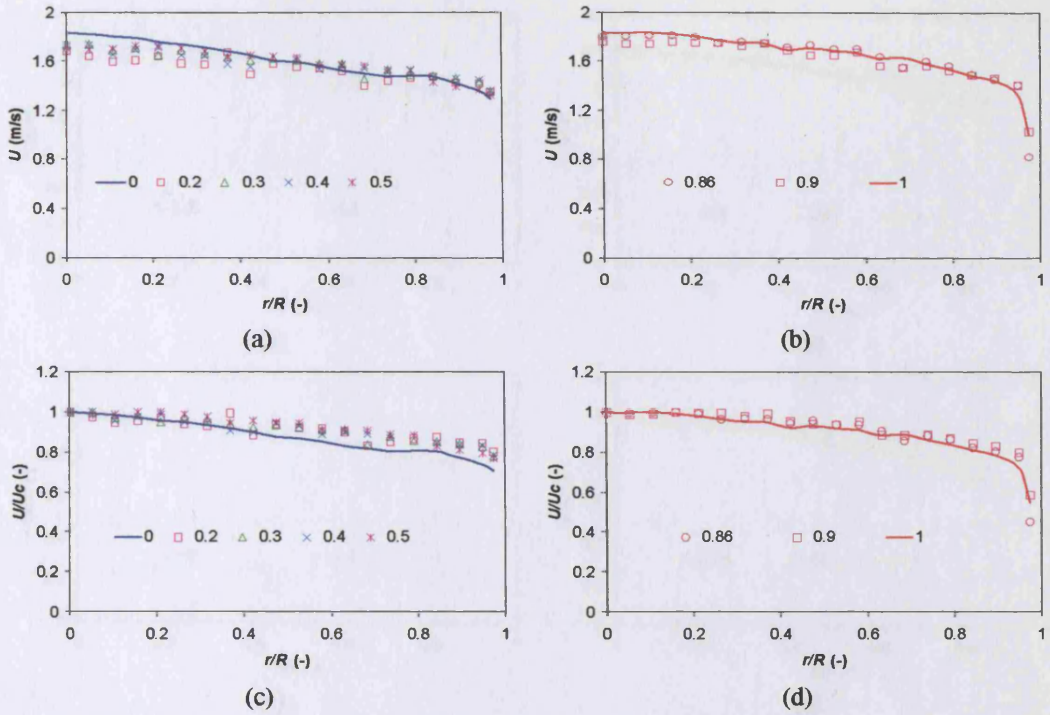

Figure B.5: Mean and relative velocity profiles of the continuous phase at different input oil fractions measured with TSI 1276-10AW probe at 1.5 m/s mixture velocity in upward flow. (a) & (c): water continuous; (b) & (d): oil continuous.

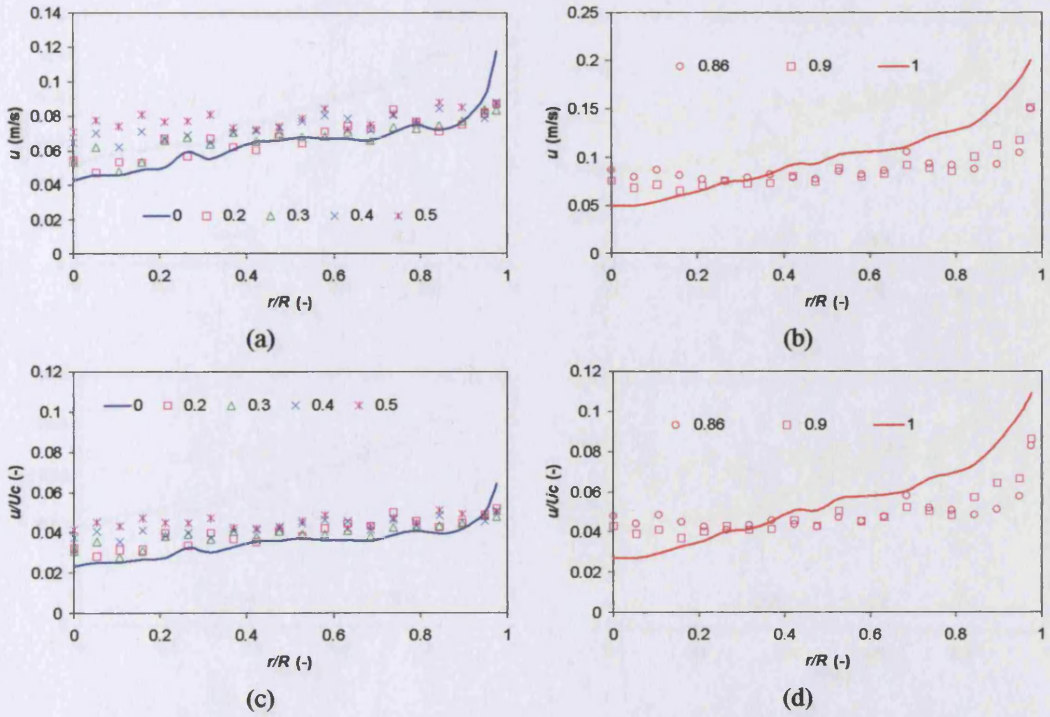

Figure B.6: Turbulence velocity and intensity profiles of the continuous phase at different input oil fractions measured with TSI 1276-10AW probe at 1.5 m/s mixture velocity in upward flow. (a) & (c): water continuous, (b) & (d): oil continuous.

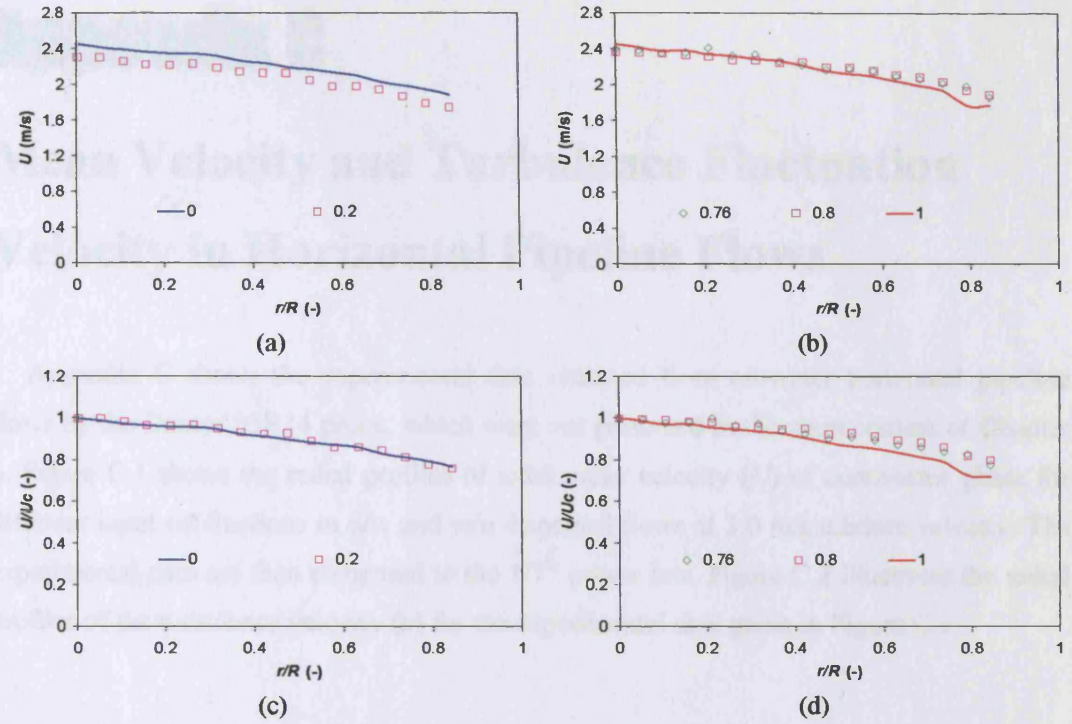

Figure B.7: Mean and relative velocity profiles of the continuous phase at different input oil fractions measured with Dantec 55R14 probe at 2.0 m/s mixture velocity in downward flow. (a) & (c): water continuous; (b) & (d): oil continuous.

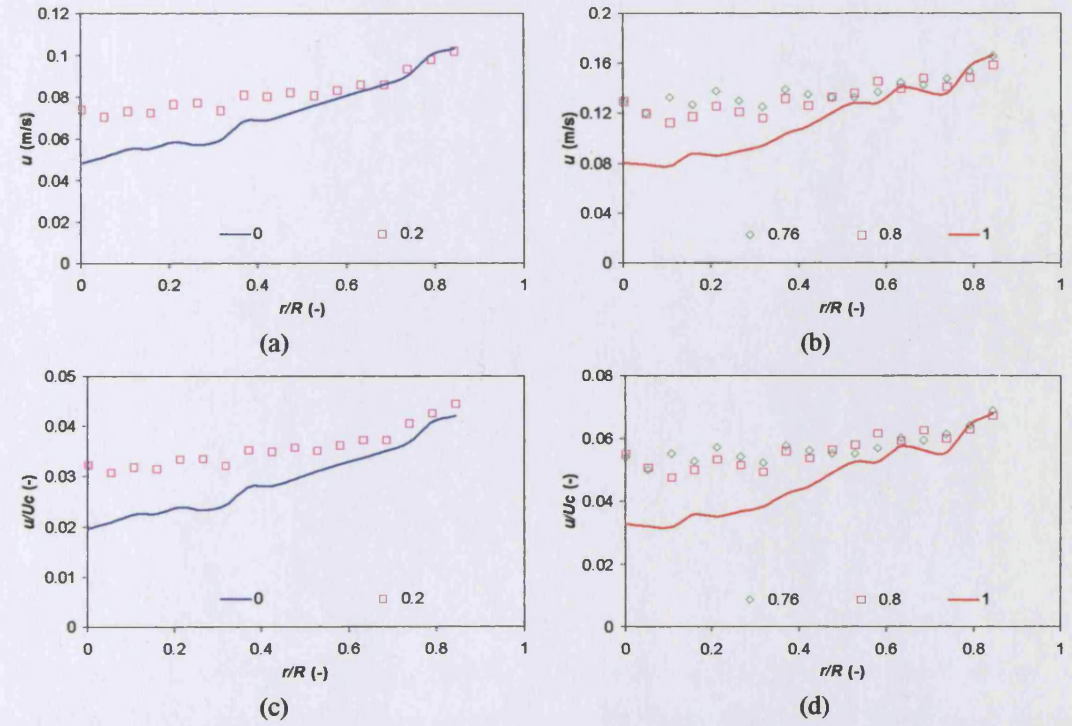

Figure B.8: Turbulence velocity and intensity profiles of the continuous phase at different input oil fractions measured with Dantec 55R14 probe at 2.0 m/s mixture velocity in downward flow. (a) & (c): water continuous, (b) & (d): oil continuous.

Appendix C

Mean Velocity and Turbulence Fluctuation Velocity in Horizontal Pipeline Flows

Appendix C shows the experimental data obtained from oil-water horizontal pipeline flows by the Dantec 55R14 probe, which were not presented in the main context of Chapter 6. Figure C.1 shows the radial profiles of axial mean velocity (U) of continuous phase for different input oil fractions in o/w and w/o dispersed flows at 3.0 m/s mixture velocity. The experimental data are then compared to the $1/7^{th}$ power law. Figure C.2 illustrates the radial profiles of the turbulence velocity (u) for the experimental data given in Figure C.1.

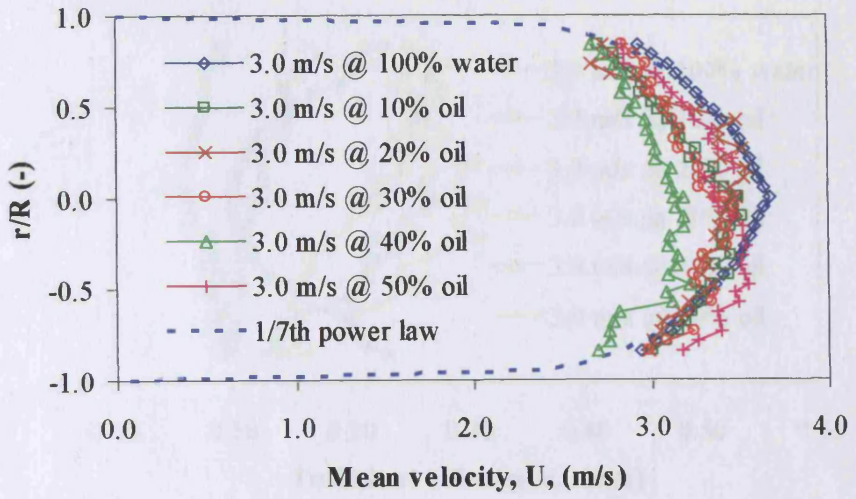

(a)

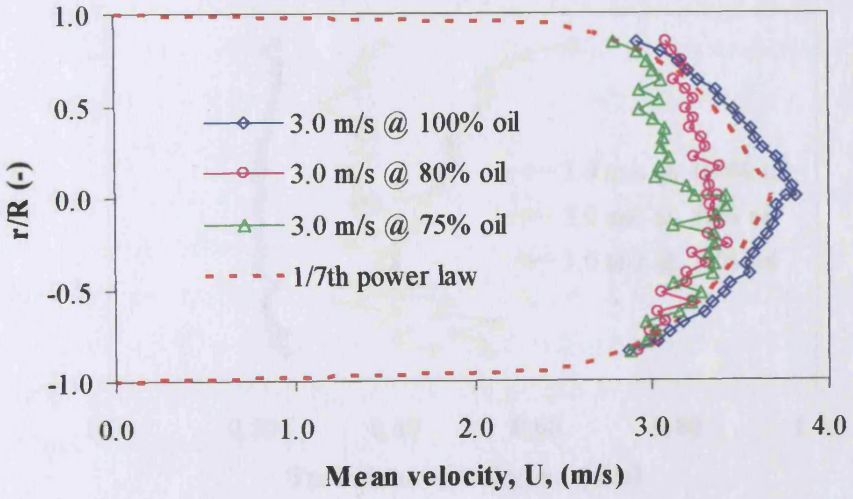

(b)

Figure C.1: Axial mean velocity (*U*) profiles of the continuous phase at different input oil fractions measured with Dantec 55R14 probe at 3.0 m/s mixture velocity in horizontal flow, in comparisons with the 1/7th Power law (dot line). (a): water continuous and (b): oil continuous

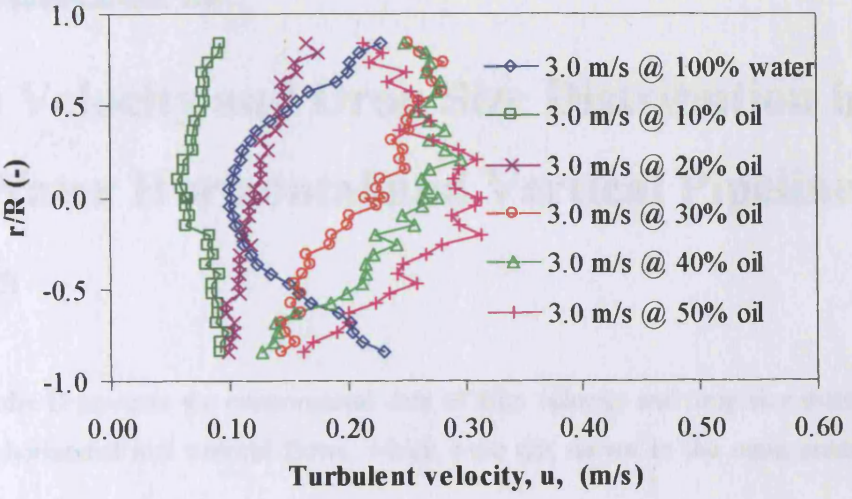

(a)

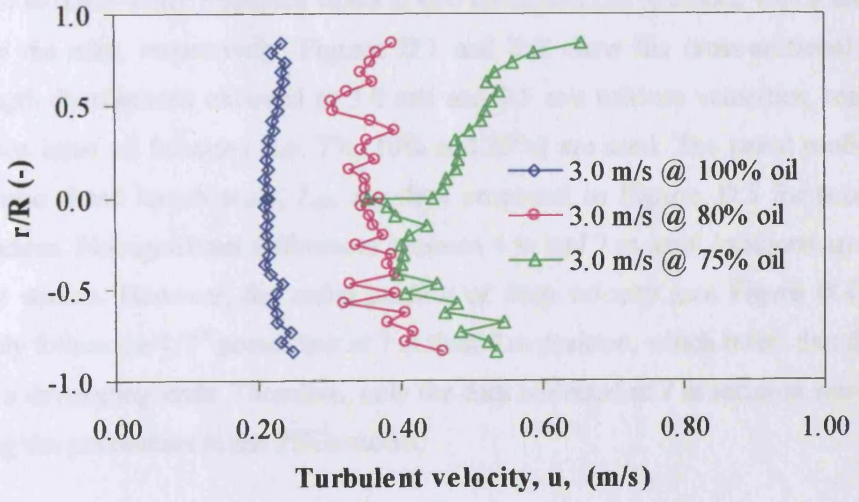

(b)

Figure C.2: Axial turbulence velocity (u) profiles of the continuous phase at different input oil fractions measured with Dantec 55R14 probe at 3.0 m/s mixture velocity in horizontal flow. (a): water continuous and (b): oil continuous

Appendix D

Drop Velocity and Drop Size Distribution in Oil-Water Horizontal and Vertical Pipeline Flows

Appendix D presents the experimental data of drop velocity and drop size distribution in oil-water horizontal and vertical flows, which were not shown in the main context of the Thesis.

One of the purposes to study the drop size distribution in horizontal flows is to correlate the coefficients appeared in the PBEs model, in particular in the coalescence kernel where most of the constant coefficients were reported for stirred vessel system. Experiments were carried out in oil-in-water dispersed flows at two different axial locations which are 4 m and 7 m from the inlet, respectively. Figures D.1 and D.2 show the cross-sectional averaged chord length distributions obtained at 3.0 m/s and 3.5 m/s mixture velocities, respectively, where three input oil fractions (i.e. 7%, 10% and 20%) are used. The radial profiles of the characteristic chord length scale, L_{32}, are then presented in Figures D.3 for two different axial locations. No significant differences between 4 m and 7 m axial locations are observed in current studies. However, the radial profiles of drop velocity (see Figure D.4) seem to more likely follow the $1/7^{th}$ power law at 7 m than 4 m position, which infers that the flow at 4 m is in a developing state. Therefore, only the data collected at 7 m location were used for correlating the parameters in the PBEs model.

Figures D.5 and D.6 illustrate the cross-sectional averaged chord length distributions measured in upward vertical flows at 1.5 m/s and 2.0 m/s mixture velocities, respectively. Figure D.7 then shows the cross-sectional averaged chord length distributions obtained in downward vertical flows at 1.5 m/s mixture velocity.

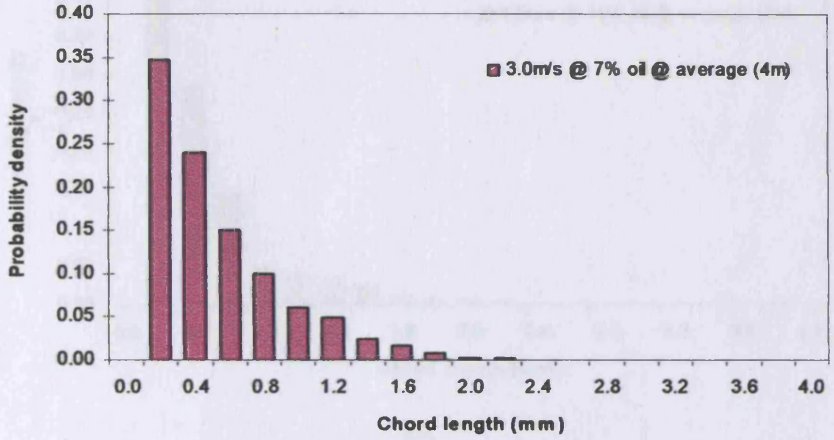
3.0m/s @ 7% oil @ average (4m)
Probability density
0.40
0.35
0.30
0.25
0.20
0.15
0.10
0.05
0.00
0.0 0.4 0.8 1.2 1.6 2.0 2.4 2.8 3.2 3.6 4.0
Chord length (mm)

(a)

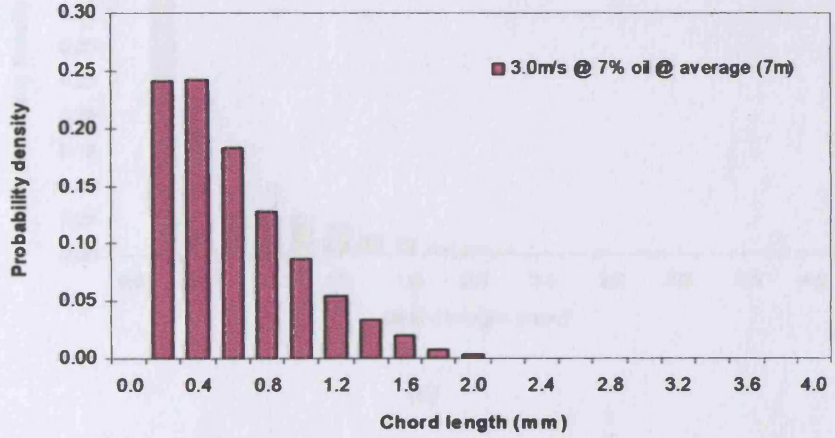
3.0m/s @ 7% oil @ average (7m)
Probability density
0.30
0.25
0.20
0.15
0.10
0.05
0.00
0.0 0.4 0.8 1.2 1.6 2.0 2.4 2.8 3.2 3.6 4.0
Chord length (mm)

(b)

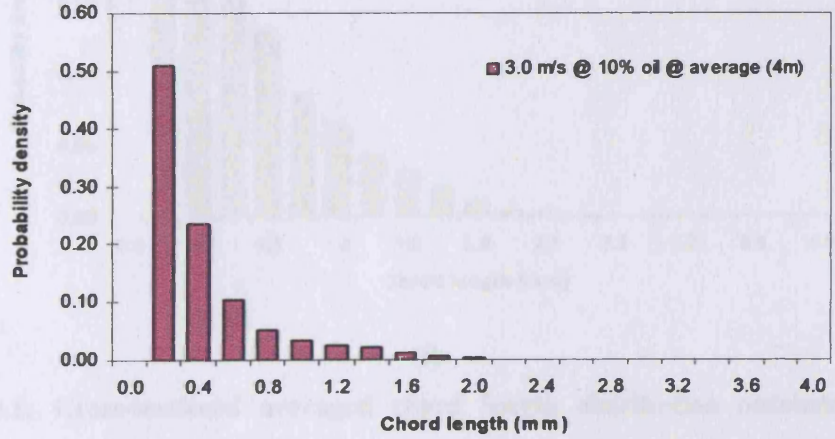
3.0 m/s @ 10% oil @ average (4m)
Probability density
0.60
0.50
0.40
0.30
0.20
0.10
0.00
0.0 0.4 0.8 1.2 1.6 2.0 2.4 2.8 3.2 3.6 4.0
Chord length (mm)

(c)

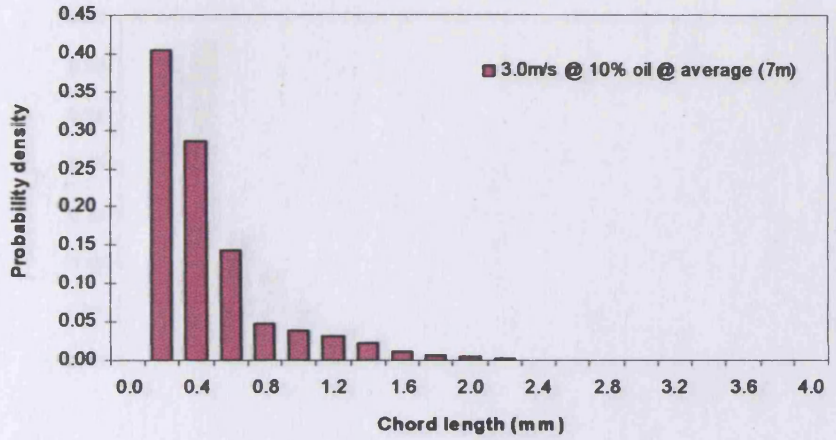

(d)

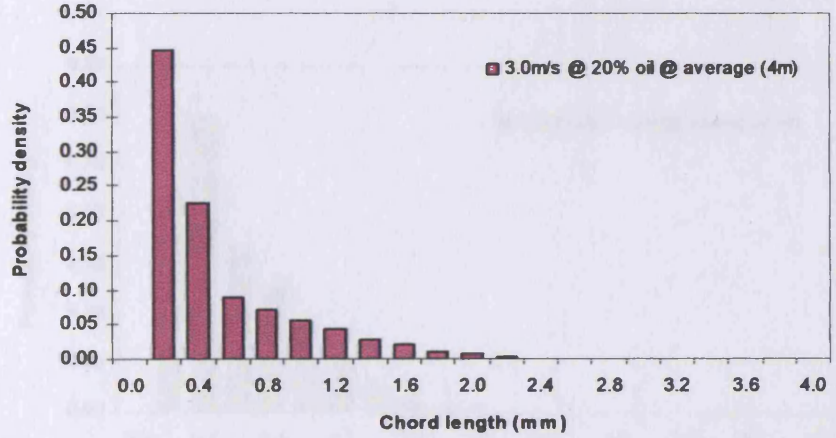

(e)

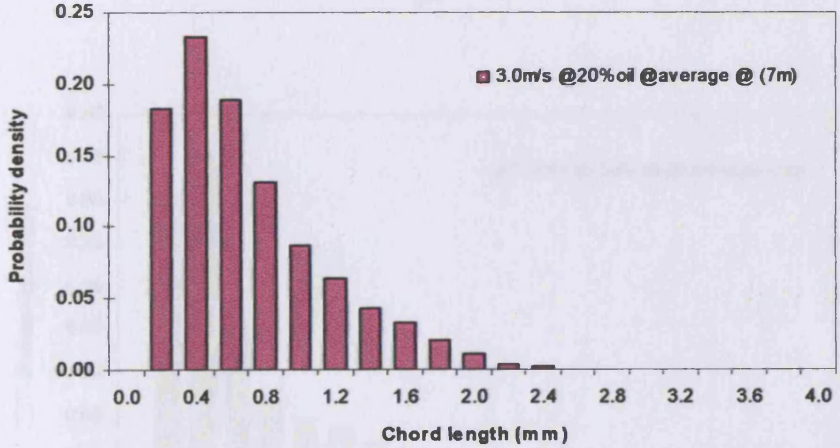

(f)

Figure D.1: Cross-sectional averaged chord length distribution obtained at axial positions of 4 m and 7 m (from the inlet) at 3.0 m/s mixture velocity in oil-in-water horizontal flows with 7%, 10% and 20% input oil fractions.

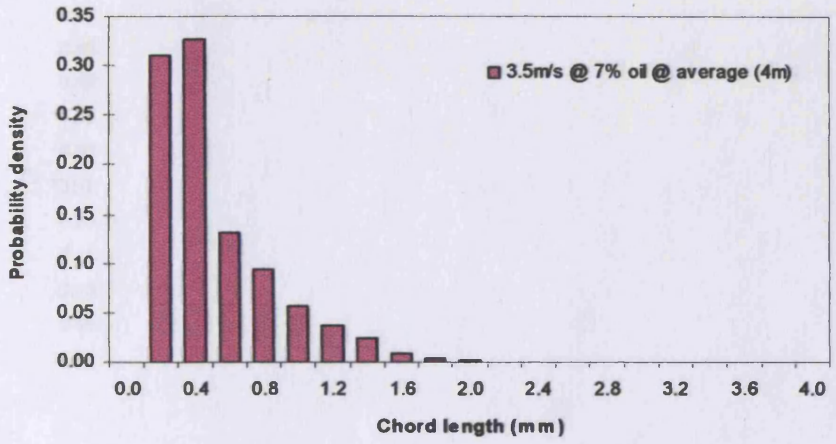
3.5m/s @ 7% oil @ average (4m)
Probability density
0.35
0.30
0.25
0.20
0.15
0.10
0.05
0.00
0.0 0.4 0.8 1.2 1.6 2.0 2.4 2.8 3.2 3.6 4.0
Chord length (mm)

(a)

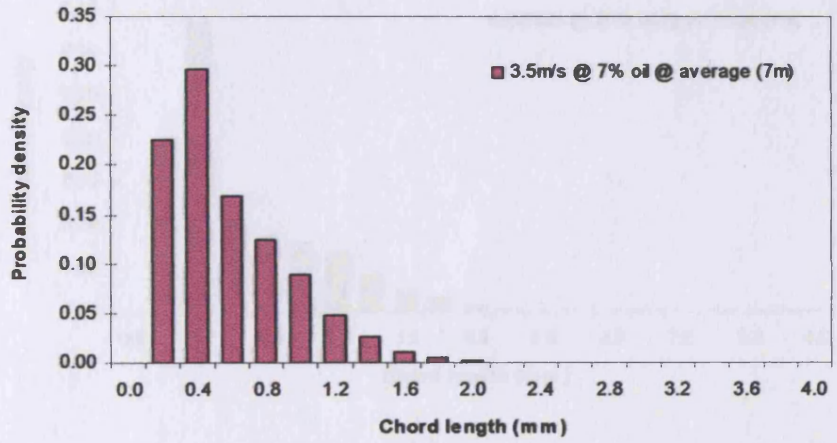
3.5m/s @ 7% oil @ average (7m)
Probability density
0.35
0.30
0.25
0.20
0.15
0.10
0.05
0.00
0.0 0.4 0.8 1.2 1.6 2.0 2.4 2.8 3.2 3.6 4.0
Chord length (mm)

(b)

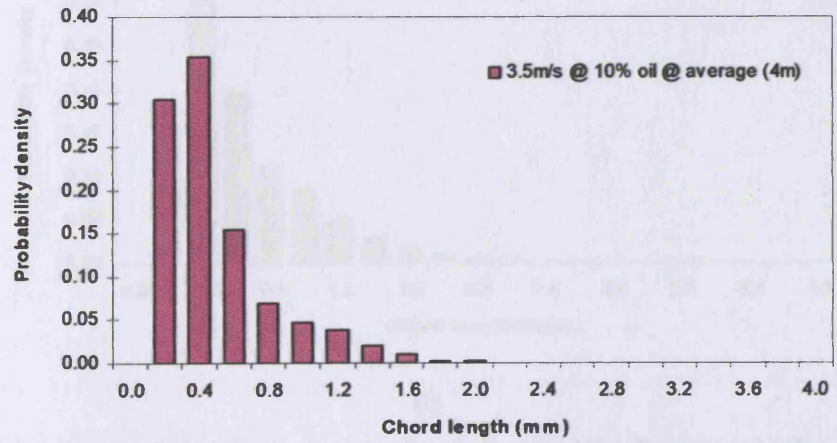
3.5m/s @ 10% oil @ average (4m)
Probability density
0.40
0.35
0.30
0.25
0.20
0.15
0.10
0.05
0.00
0.0 0.4 0.8 1.2 1.6 2.0 2.4 2.8 3.2 3.6 4.0
Chord length (mm)

(c)

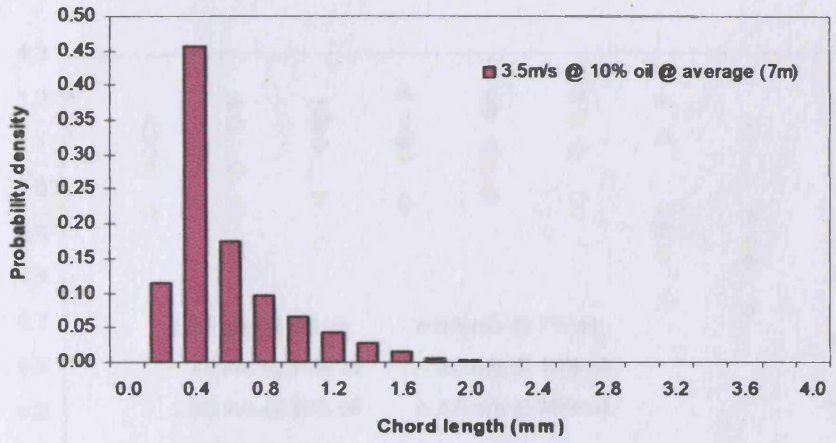

(d)

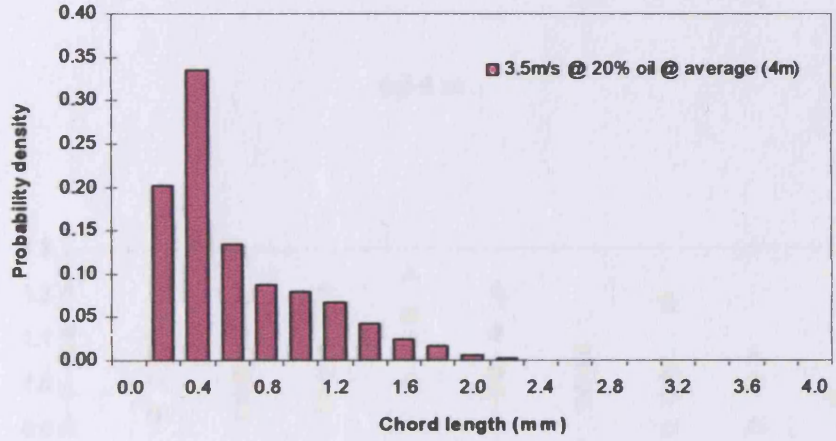

(e)

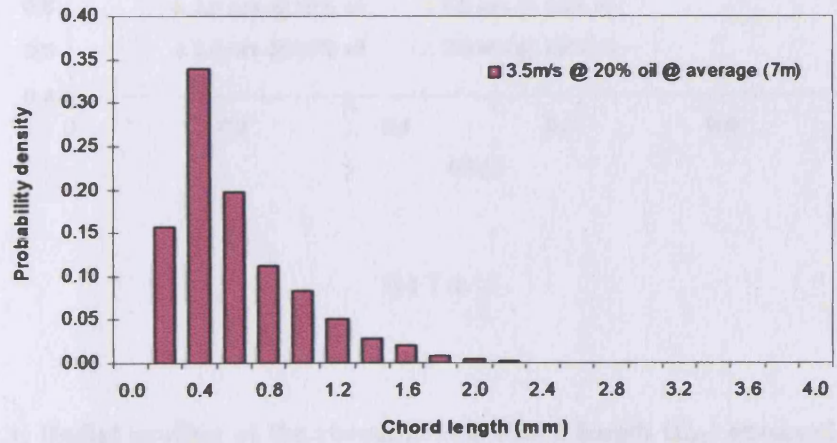

(f)

Figure D.2: Cross-sectional averaged chord length distribution obtained at axial positions of 4 m and 7 m (from the inlet) at 3.5 m/s mixture velocity in oil-in-water horizontal flows with 7%, 10% and 20% input oil fractions.

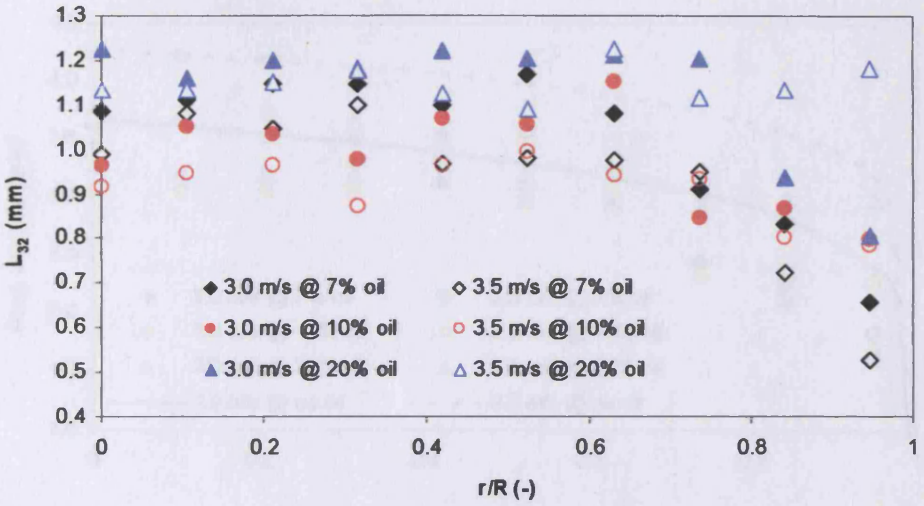

(a) 4 m

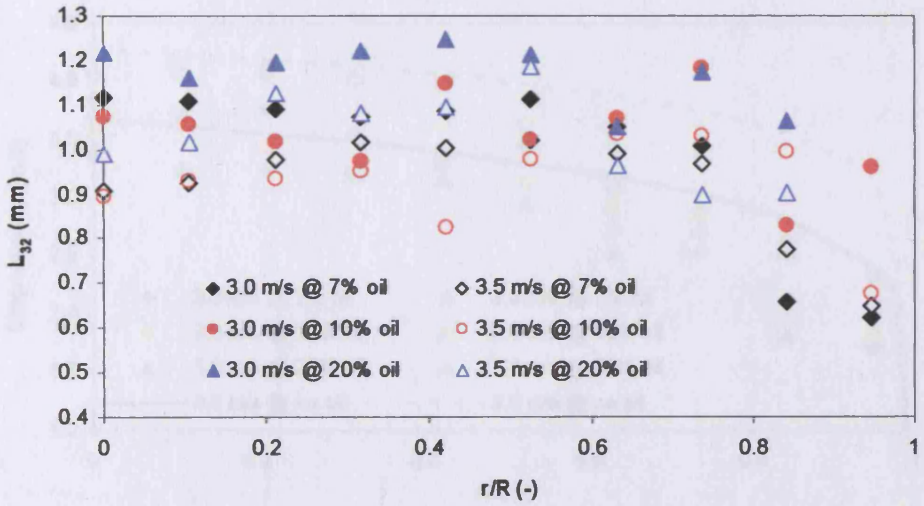

(b) 7 m

Figure D.3: Radial profiles of the characteristic chord length (L_{32}) obtained at 3.0 m/s and 3.5 m/s mixture velocities in o/w horizontal dispersed flows at positions of 4 m (a) and 7 m (b) from the inlet.

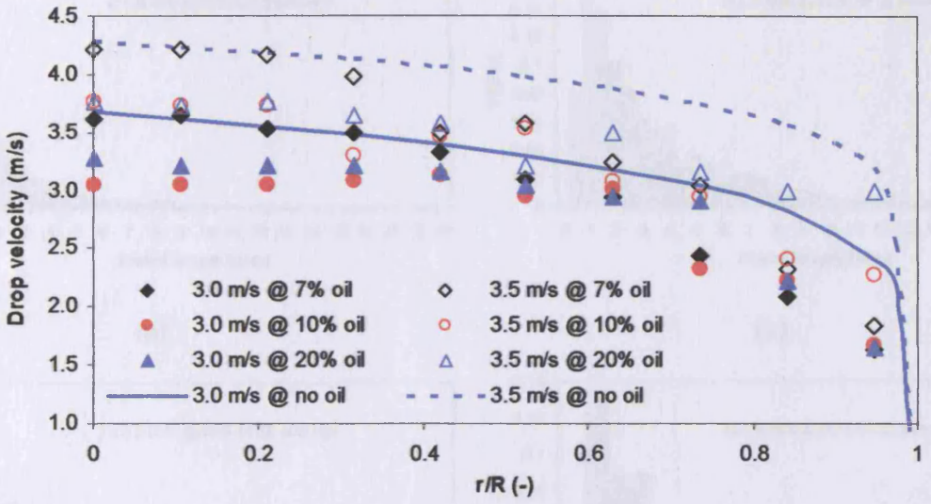

(a) 4 m

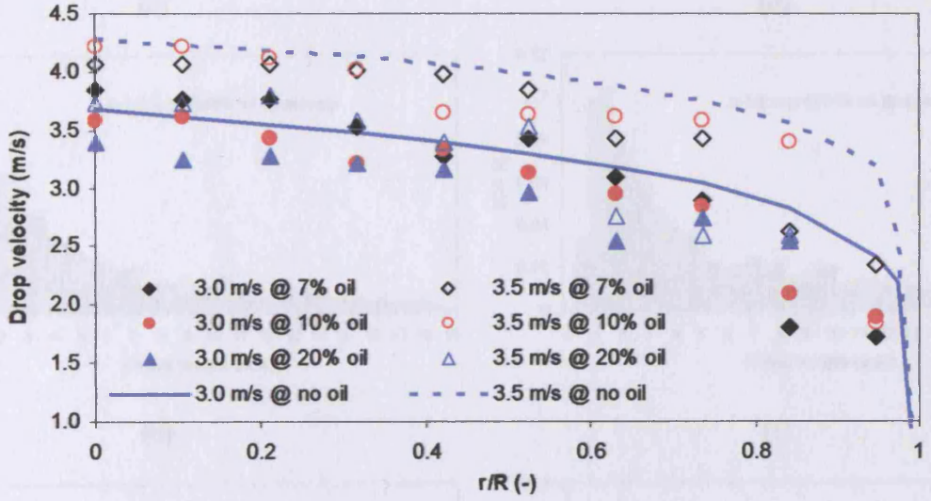

(b) 7 m

Figure D.4: Radial profiles of drop velocities obtained at 3.0 m/s and 3.5 m/s mixture velocities in horizontal o/w dispersed flows at positions of 4 m (a) and 7 m (b) from the inlet, in comparison with the 1/7th power law (see lines).

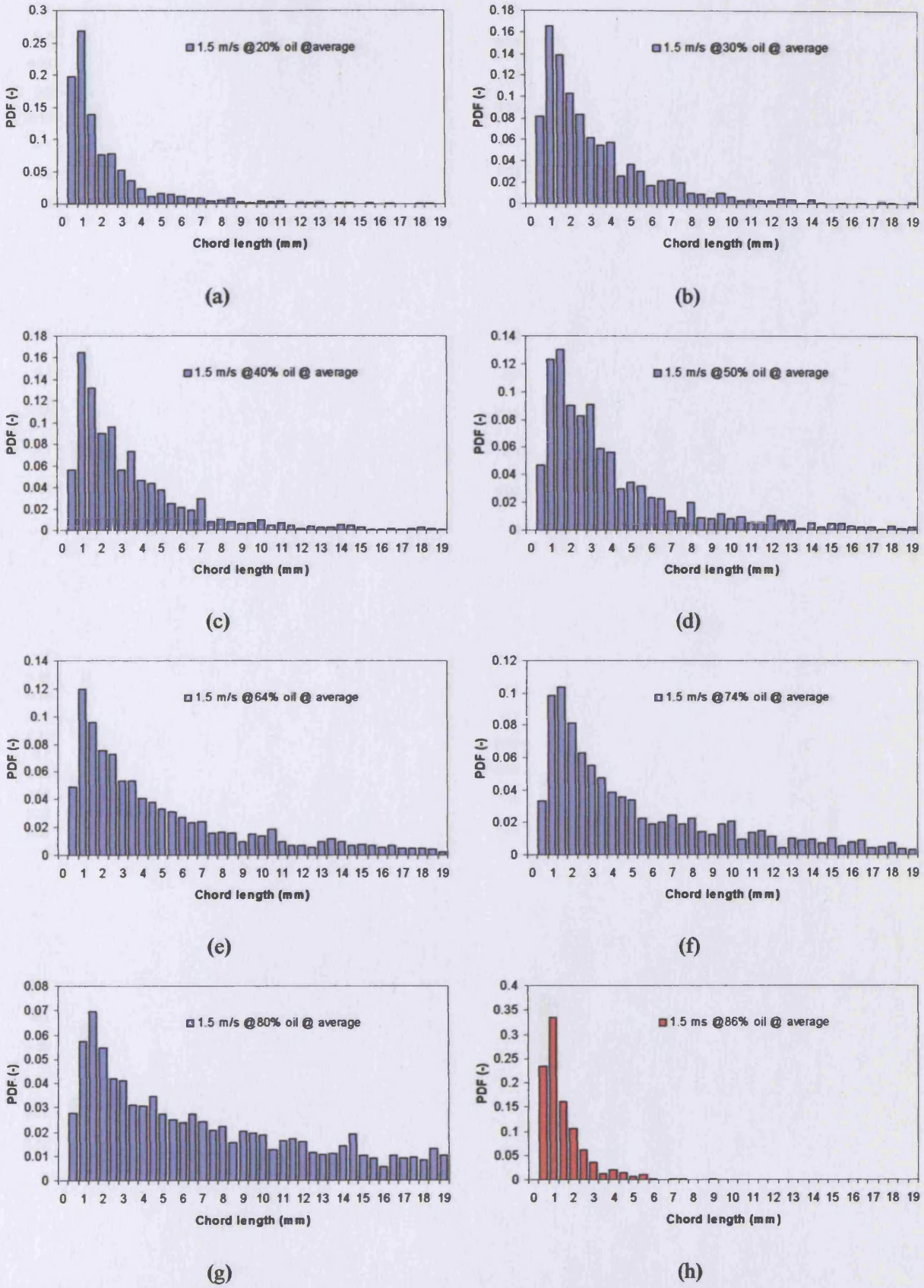

Figure D.5: Cross-sectional averaged chord length distributions obtained at 1.5 m/s mixture velocity in upward flows for o/w (blue) and w/o (red) dispersions.

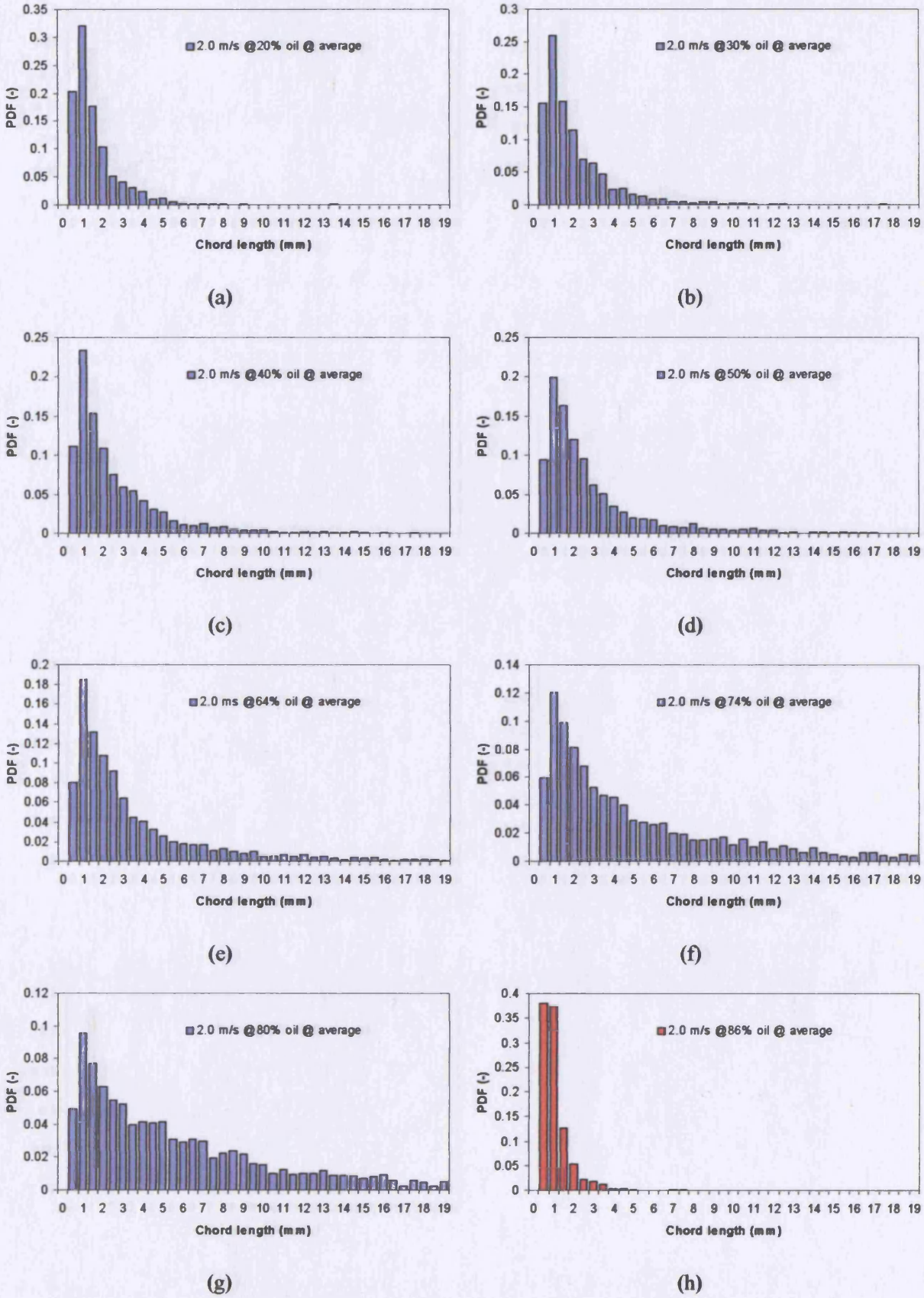

Figure D.6: Cross-sectional averaged chord length distributions obtained at 2.0 m/s mixture velocity in upward flows for o/w (blue) and w/o (red) dispersions.

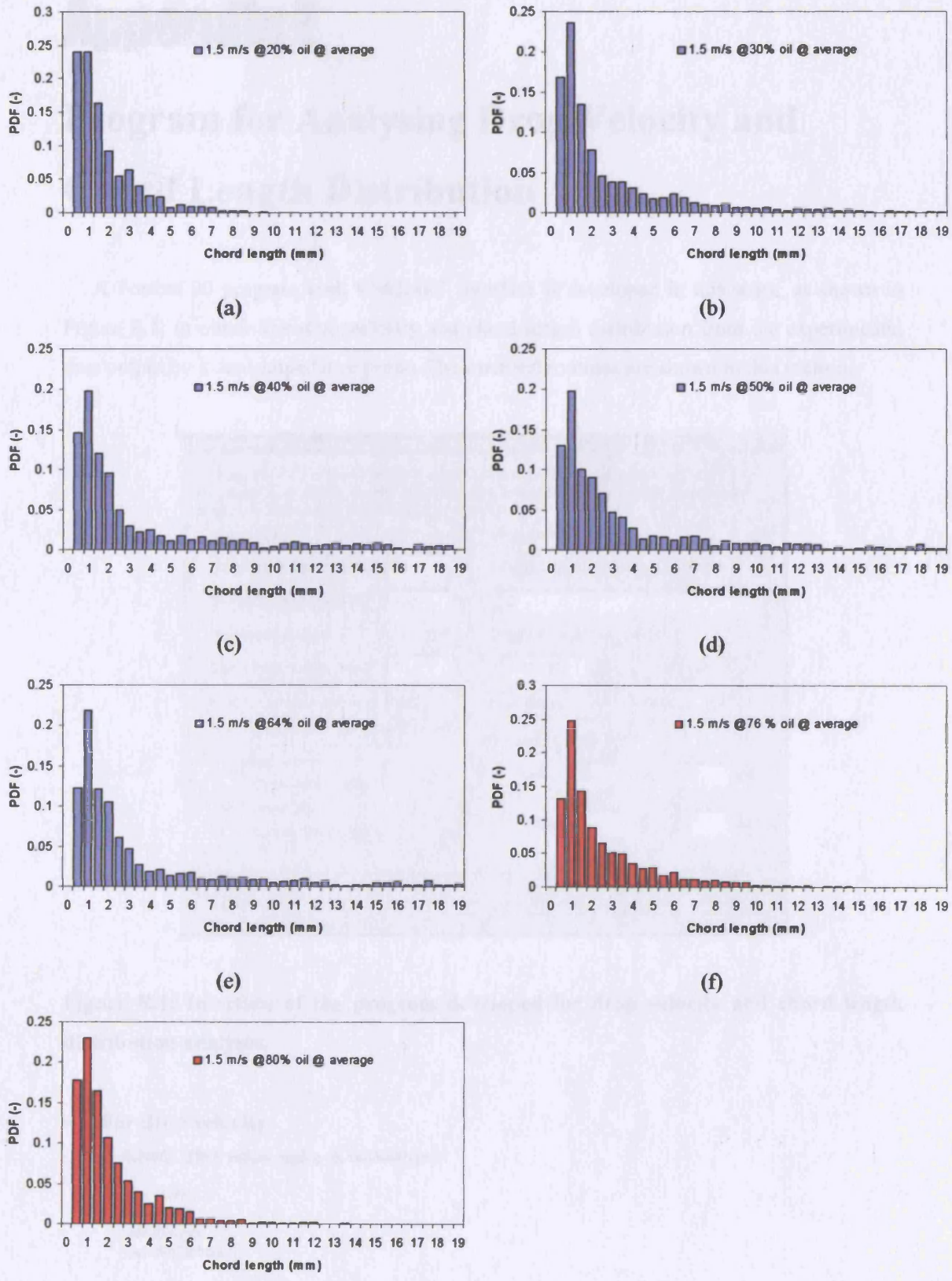

Figure D.7: Cross-sectional averaged chord length distributions obtained at 1.5 m/s mixture velocity in downward flows for o/w (blue) and w/o (red) dispersions.

Appendix E

Program for Analysing Drop Velocity and Chord Length Distribution

A Fortran 90 program with Windows® interface is developed in this work, as shown in Figure E.1, to obtain the drop velocity and chord length distribution from the experimental data output by a dual-impedance probe. The main subroutines are shown in this section.

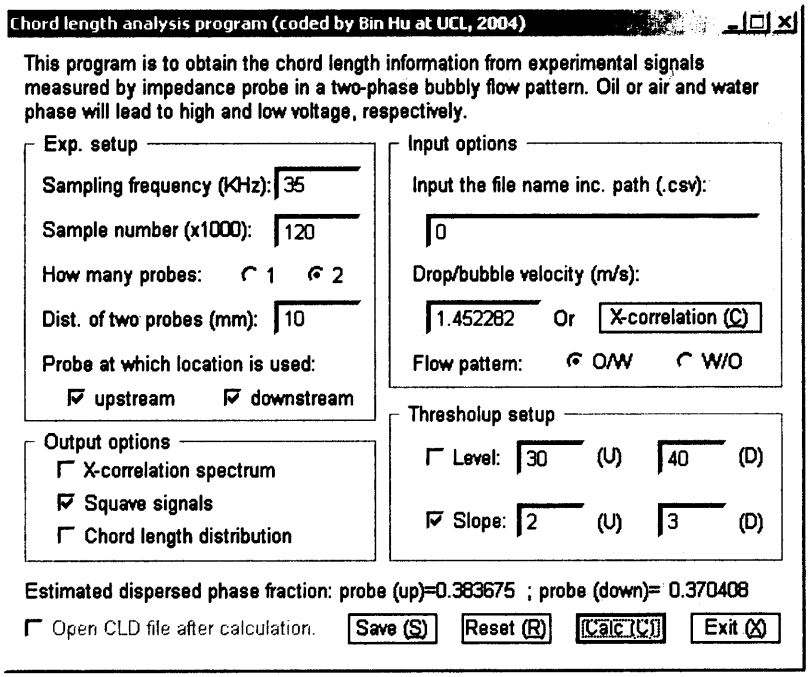

Figure E.1: Interface of the program developed for drop velocity and chord length distribution analyses.

- **For drop velocity**

```
SUBROUTINE xcSub( mgdlg, id, callbacktype )

use user32
use msflib
use dflogm
use cldGlobals

implicit none
include 'resource.fd'

type (dialog) mgdlg
integer id, callbacktype
integer*4 lret
character*100 filepath,ctemp
```

```
 integer,allocatable :: indexs(:)

 real, allocatable :: t(:),X(:),Y(:),ans(:),ansout(:)
 real   xmean,ymean,xstd,ystd,lagtime
 logical ylagsx

 ylagsx=.TRUE.

 if (callbacktype == dlg_clicked) then
call DlgSetTitle(mgdlg,'Program is running...')
call getDialog(mgdlg)
!check validity
if(SN_C == "")then
    lret = MessageBox(NULL, "Sample number cannot be NULL!"C, &
                      "Error"C, MB_OK)
    return
else
    read(SN_C,*)num
    num=num*1000
endif
if(SF_C == "")then
    lret = MessageBox(NULL, "Sampling frequency cannot be NULL!"C, &
                      "Error"C, MB_OK)
    return
else
    read(SF_C,*)sf
    sf=sf*1000.0
endif
if(dist_C == "")then
    lret = MessageBox(NULL, "distance between 2 probes cannot be NULL!"C, &
                      "Error"C, MB_OK)
    return
else
    read(dist_C,*)dist
    dist=dist/1000.0
endif
!allocate variables
if(num>=30000)then
    num=32768
elseif (num>8000)then
    num=8192
else
    num=2048
endif
allocate(t(1:num),X(1:num),Y(1:num),ans(1:2*num),ansout(1:num/2))
allocate(indexs(1:num/2))
!file path and name
I=len_trim(filename)
if(I>=5.and.filename(I-3:I)==".csv")then
    filepath=filename
else
    filepath=trim(filename)//".csv"
endif
!read data
Open(66,File=trim(filepath),STATUS="OLD",ERR=999,IOSTAT=Istatus)
IF(Istatus.GT.0)GOTO 999
I=0

DO 10 WHILE(.NOT.EOF(66).AND.I.LE.num-1)
    I=I+1
    READ(66,*) t(I),X(I),Y(I)
10  END    DO

Close(66)
!mean
DO I=1, num
    Xmean=Xmean+X(I)
    Ymean=Ymean+Y(I)
END DO

Xmean=Xmean/Num
Ymean=Ymean/Num
!standard deviation
DO I=1, Num
    Xstd=(X(I)-Xmean)**2.0+Xstd
    Ystd=(Y(I)-Ymean)**2.0+Ystd
```

```
END DO

Xstd=(Xstd/(Num-1))**0.5
Ystd=(Ystd/(Num-1))**0.5
!normalization
DO I=1, Num
    X(I)=(X(I)-Xmean)/Xstd
    Y(I)=(Y(I)-Ymean)/Ystd
ENDDO
ans=0.0
!xcorrelation calc...
CALL   correl(X,Y,num,ans)
DO I=1,num/2
    IF(ylagsx)THEN
        ansout(I)=ans(num+1-I)/(num/2)
    ELSE
        ansout(I)=ans(I)/(num/2)
    ENDIF
ENDDO
DEALLOCATE(X,Y,ans)
!output x-correlation
IF(OUT_XC) THEN
    filepath=trim(filepath)
    OPEN(88,FILE=filepath(1:Len(Trim(filepath))-4)//"cc.csv")
    DO I=1,num/2
        write(88,*)1.0/sf*I,',',ansout(I)
    ENDDO
    Close(88)
ENDIF
!sorting the results
call indexx(num/2,ansout,indexs)
!drop velocity
lagtime=indexs(num/2-1)*1.0/sf
dropU=dist/lagtime
!printing on the dialog
OPEN(99,FILE="~.tmp")
write(99,"(F8.6)")dropU
REWIND(99)
READ(99,'(A30)')ctemp
CLOSE(99)
lret=DlgSet(gdlg,IDC_DROP_U, trim(ctemp))
  lret=DELFILESQQ("~.tmp")

 endif
call DlgSetTitle(mgdlg,'Chord length analysis program (coded by Bin Hu at UCL, 2004)')
 return

999 &
lret = MessageBox(NULL, "Error finding the source file"C, &
            "Error"C, MB_OK)
END SUBROUTINE xcSub


!x-correlation function

    SUBROUTINE correl(data1,data2,n,ans)
    INTEGER n,NMAX
    REAL data1(n),data2(n)
    COMPLEX ans(n)
    PARAMETER (NMAX=131072)
!CU   USES realft,twofft
    INTEGER i,no2
    COMPLEX fft(NMAX)
    call twofft(data1,data2,fft,ans,n)
    no2=n/2
    do 11 i=1,no2+1
     ans(i)=fft(i)*conjg(ans(i))/float(no2)
11   continue
    ans(1)=cmplx(real(ans(1)),real(ans(no2+1)))
    call realft(ans,n,-1)
    return
    END
!C  (C) Copr. 1986-92 Numerical Recipes Software v%1jw#<0(9p#3.


    SUBROUTINE realft(data1,n,isign)
```

```
      INTEGER isign,n
      REAL data1(n)
!CU   USES four1
      INTEGER i,i1,i2,i3,i4,n2p3
      REAL c1,c2,h1i,h1r,h2i,h2r,wis,wrs
      DOUBLE PRECISION theta,wi,wpi,wpr,wr,wtemp
      theta=3.141592653589793d0/dble(n/2)
      c1=0.5
      if (isign.eq.1) then
       c2=-0.5
       call four1(data1,n/2,+1)
      else
       c2=0.5
       theta=-theta
      endif
      wpr=-2.0d0*sin(0.5d0*theta)**2
      wpi=sin(theta)
      wr=1.0d0+wpr
      wi=wpi
      n2p3=n+3
      do 11 i=2,n/4
       i1=2*i-1
       i2=i1+1
       i3=n2p3-i2
       i4=i3+1
       wrs=sngl(wr)
       wis=sngl(wi)
       h1r=c1*(data1(i1)+data1(i3))
       h1i=c1*(data1(i2)-data1(i4))
       h2r=-c2*(data1(i2)+data1(i4))
       h2i=c2*(data1(i1)-data1(i3))
       data1(i1)=h1r+wrs*h2r-wis*h2i
       data1(i2)=h1i+wrs*h2i+wis*h2r
       data1(i3)=h1r-wrs*h2r+wis*h2i
       data1(i4)=-h1i+wrs*h2i+wis*h2r
       wtemp=wr
       wr=wr*wpr-wi*wpi+wr
       wi=wi*wpr+wtemp*wpi+wi
11    continue
      if (isign.eq.1) then
       h1r=data1(1)
       data1(1)=h1r+data1(2)
       data1(2)=h1r-data1(2)
      else
       h1r=data1(1)
       data1(1)=c1*(h1r+data1(2))
       data1(2)=c1*(h1r-data1(2))
       call four1(data1,n/2,-1)
      endif
      return
      END
!C  (C) Copr. 1986-92 Numerical Recipes Software v%1jw#<0(9p#3.


      SUBROUTINE four1(data0,nn,isign)
      INTEGER isign,nn
      REAL data0(2*nn)
      INTEGER i,istep,j,m,mmax,n
      REAL tempi,tempr
      DOUBLE PRECISION theta,wi,wpi,wpr,wr,wtemp
      n=2*nn
      j=1
      do 11 i=1,n,2
       if(j.gt.i)then
        tempr=data0(j)
        tempi=data0(j+1)
        data0(j)=data0(i)
        data0(j+1)=data0(i+1)
        data0(i)=tempr
        data0(i+1)=tempi
       endif
       m=n/2
1      if ((m.ge.2).and.(j.gt.m)) then
        j=j-m
        m=m/2
       goto 1
```

```
      endif
      j=j+m
11    continue
      mmax=2
2     if (n.gt.mmax) then
      istep=2*mmax
      theta=6.28318530717959d0/(isign*mmax)
      wpr=-2.d0*sin(0.5d0*theta)**2
      wpi=sin(theta)
      wr=1.d0
      wi=0.d0
      do 13 m=1,mmax,2
       do 12 i=m,n,istep
        j=i+mmax
        tempr=sngl(wr)*data0(j)-sngl(wi)*data0(j+1)
        tempi=sngl(wr)*data0(j+1)+sngl(wi)*data0(j)
        data0(j)=data0(i)-tempr
        data0(j+1)=data0(i+1)-tempi
        data0(i)=data0(i)+tempr
        data0(i+1)=data0(i+1)+tempi
12      continue
       wtemp=wr
       wr=wr*wpr-wi*wpi+wr
       wi=wi*wpr+wtemp*wpi+wi
13     continue
      mmax=istep
      goto 2
      endif
      return
      END
!C  (C) Copr. 1986-92 Numerical Recipes Software v%1jw#<0(9p#3.


      SUBROUTINE twofft(data1,data2,fft1,fft2,n)
      INTEGER n
      REAL data1(n),data2(n)
      COMPLEX fft1(n),fft2(n)
!CU   USES four1
      INTEGER j,n2
      COMPLEX h1,h2,c1,c2
      c1=cmplx(0.5,0.0)
      c2=cmplx(0.0,-0.5)
      do 11 j=1,n
       fft1(j)=cmplx(data1(j),data2(j))
11    continue
      call four1(fft1,n,1)
      fft2(1)=cmplx(aimag(fft1(1)),0.0)
      fft1(1)=cmplx(real(fft1(1)),0.0)
      n2=n+2
      do 12 j=2,n/2+1
       h1=c1*(fft1(j)+conjg(fft1(n2-j)))
       h2=c2*(fft1(j)-conjg(fft1(n2-j)))
       fft1(j)=h1
       fft1(n2-j)=conjg(h1)
       fft2(j)=h2
       fft2(n2-j)=conjg(h2)
12    continue
      return
      END
!C  (C) Copr. 1986-92 Numerical Recipes Software v%1jw#<0(9p#3.

      SUBROUTINE indexx(n,arr,indx)
      INTEGER n,indx(n),M,NSTACK
      REAL arr(n)
      PARAMETER (M=7,NSTACK=50)
      INTEGER i,indxt,ir,itemp,j,jstack,k,l,istack(NSTACK)
      REAL a
      do 11 j=1,n
       indx(j)=j
11    continue
      jstack=0
      l=1
      ir=n
1     if(ir-l.lt.M)then
       do 13 j=l+1,ir
```

```
      indxt=indx(j)
      a=arr(indxt)
      do 12 i=j-1,1,-1
        if(arr(indx(i)).le.a)goto 2
        indx(i+1)=indx(i)
12      continue
      i=0
2     indx(i+1)=indxt
13    continue
    if(jstack.eq.0)return
    ir=istack(jstack)
    l=istack(jstack-1)
    jstack=jstack-2
   else
    k=(l+ir)/2
    itemp=indx(k)
    indx(k)=indx(l+1)
    indx(l+1)=itemp
    if(arr(indx(l+1)).gt.arr(indx(ir)))then
      itemp=indx(l+1)
      indx(l+1)=indx(ir)
      indx(ir)=itemp
    endif
    if(arr(indx(l)).gt.arr(indx(ir)))then
      itemp=indx(l)
      indx(l)=indx(ir)
      indx(ir)=itemp
    endif
    if(arr(indx(l+1)).gt.arr(indx(l)))then
      itemp=indx(l+1)
      indx(l+1)=indx(l)
      indx(l)=itemp
    endif
    i=l+1
    j=ir
    indxt=indx(l)
    a=arr(indxt)
3    continue
      i=i+1
    if(arr(indx(i)).lt.a)goto 3
4    continue
      j=j-1
    if(arr(indx(j)).gt.a)goto 4
    if(j.lt.i)goto 5
    itemp=indx(i)
    indx(i)=indx(j)
    indx(j)=itemp
    goto 3
5    indx(l)=indx(j)
    indx(j)=indxt
    jstack=jstack+2
    if(jstack.gt.NSTACK)pause 'NSTACK too small in indexx'
    if(ir-i+1.ge.j-l)then
      istack(jstack)=ir
      istack(jstack-1)=i
      ir=j-1
    else
      istack(jstack)=j-1
      istack(jstack-1)=l
      l=i
    endif
   endif
   goto 1
   END
!C  (C) Copr. 1986-92 Numerical Recipes Software v%1jw#<0(9p#3.
```

- For chord length distribution

```
SUBROUTINE cldCalc(x,y,N)

use cldGlobals
implicit none

real     X(num),Y(num),diamin
integer      K,N,N1,N2,Nmin
logical      switch

N=0
Nmin=0
alpha=0.0
alpha2=0.0
diamin=250*10.0**(-6.0)

!threshold options
if(level_L.AND..NOT.slope_L)then            !only level
    goto    101
elseif(.NOT.level_L.AND.slope_L)then        !only slope
    goto    102
elseif(level_L.AND.slope_L)then             !slope and level
    goto    103
endif
!only level method
!upstream probe
101 N1=0
N2=0
if(oildrop)then
    switch=.false.
elseif(waterdrop)then
    switch=.true.
endif

if(upstream)then
    do k=1,num
            if(X(k).GE.level.AND..NOT.switch)then
                switch=.true.
                N1=k
            elseif(X(K).LE.level.AND.switch)then
                switch=.false.
                N2=k
            endif
            if(oildrop.AND.N2.GT.N1)then
                !output values of oil drop as 1
                do i=N1,N2
                    square(i,1)=1.0
                enddo

                N=N+1
                chord(N,1)=N
                chord(N,2)=N2-N1
                chord(N,3)=1.0E3*(N2-N1)/sf*dropU
                N1=N2+1
                alpha=chord(N,2)+alpha
            elseif(waterdrop.AND.N2.LT.N1)then
                !output values of water drop as 0
                do i=N1,N2
                    square(i,1)=0.0
                enddo

                N=N+1
                chord(N,1)=N
                chord(N,2)=N1-N2
                chord(N,3)=1.0E3*(N1-N2)/sf*dropU
                N2=N1+1
                alpha=chord(N,2)+alpha
            endif

    enddo
endif
alpha=alpha/num
!downstream probe
N1=0
```

```
N2=0
if(oildrop)then
    switch=.false.
elseif(waterdrop)then
    switch=.true.
endif

if(downstream)then
    do k=1,num
        if(Y(k).GE.level2.AND..NOT.switch)then
            switch=.true.
            N1=k
        elseif(Y(K).LE.level2.AND.switch)then
            switch=.false.
            N2=k
        endif
        if(oildrop.AND.N2.GT.N1)then
            !output values of oil drop as 1
            do i=N1,N2
                square(i,2)=1.0
            enddo

            N=N+1
            chord(N,1)=N
            chord(N,2)=N2-N1
            chord(N,3)=1.0E3*(N2-N1)/sf*dropU
            N1=N2+1
            alpha2=chord(N,2)+alpha2
        elseif(waterdrop.AND.N2.LT.N1)then
            !output values of water drop as 0
            do i=N1,N2
                square(i,2)=0.0
            enddo

            N=N+1
            chord(N,1)=N
            chord(N,2)=N1-N2
            chord(N,3)=1.0E3*(N1-N2)/sf*dropU
            N2=N1+1
            alpha2=chord(N,2)+alpha2
        endif
    enddo
endif
alpha2=alpha2/num
return

!only slope method
!upstream probe
102 N1=0
N2=0
switch=.false.
Nmin=int(diamin/dropU*sf)

if(oildrop)then
    level=minval(x)+2.0
    level2=minval(y)+2.0
elseif(waterdrop)then
    level=maxval(x)-2.0
    level2=maxval(y)-2.0
endif


if(upstream)then
    do k=1,num-1
        if(oildrop)then
            if(X(k+1)-X(k).GE.slope.AND..NOT.switch.AND.X(k).GE.level)then
                switch=.true.
                N1=k+1
            elseif(X(k)-X(k+1).GE.slope.AND.switch.AND.X(k+1).GE.level)then
                switch=.false.
                N2=k
            elseif(X(k).LT.X(N1)-1.AND.switch.AND.X(k+1).GE.level)then
                switch=.false.
                N2=k
            endif
```

```
            elseif(waterdrop)then
                if(X(k)-X(k+1).GE.slope.AND..NOT.switch.AND.X(k).LE.level)then
                    switch=.true.
                    N1=k+1
                elseif(X(k+1)-X(k).GE.slope.AND.switch.AND.X(k+1).LE.level)then
                    switch=.false.
                    N2=k
                elseif(X(k).GT.X(N1)+1.AND.switch.AND.X(k+1).LE.level)then
                    switch=.false.
                    N2=k
                endif
            endif

            if(N2>N1+Nmin)then
                N=N+1
                !output values of oil drop as 1, or water drop as 0
                do i=N1,N2
                    if(oildrop)then
                        square(i,1)=1.0
                    else
                        square(i,1)=0.0
                    endif
                enddo

                chord(N,1)=N
                chord(N,2)=N2-N1
                chord(N,3)=1.0E3*(N2-N1)/sf*dropU
                N1=N2+1
                alpha=chord(N,2)+alpha
            endif
        enddo
    endif
    alpha=alpha/num


    !downstream probe
    N1=0
    N2=0
    switch=.false.

    if(downstream)then
        do k=1,num-1
            if(oildrop)then
                if(Y(k+1)-Y(k).GE.slope2.AND..NOT.switch.AND.Y(k).GE.level2)then
                    switch=.true.
                    N1=k+1
                elseif(Y(k)-Y(k+1).GE.slope2.AND.switch.AND.Y(k+1).GE.level2)then
                    switch=.false.
                    N2=k
                elseif(Y(k).LT.Y(N1)-1.AND.switch.AND.Y(k+1).GE.level2)then
                    switch=.false.
                    N2=k
                endif

            elseif(waterdrop)then
                if(Y(k)-Y(k+1).GE.slope2.AND..NOT.switch.AND.Y(k).LE.level2)then
                    switch=.true.
                    N1=k+1
                elseif(Y(k+1)-Y(k).GE.slope2.AND.switch.AND.Y(k+1).LE.level2)then
                    switch=.false.
                    N2=k
                elseif(Y(k).GT.Y(N1)+1.AND.switch.AND.Y(k+1).LE.level2)then
                    switch=.false.
                    N2=k
                endif
            endif

            if(N2>N1+Nmin)then
                !output values of oil drop as 1, or water drop as 0
                do i=N1,N2
                    if(oildrop)then
                        square(i,2)=1.0
                    else
                        square(i,2)=0.0
                    endif
                enddo
```

```
            N=N+1
            chord(N,1)=N
            chord(N,2)=N2-N1
            chord(N,3)=1.0E3*(N2-N1)/sf*dropU
            N1=N2+1
            alpha2=chord(N,2)+alpha2
        endif

    enddo
endif
alpha2=alpha2/num
return

!level and slope method
!upstream probe
103 N1=0
N2=0
switch=.false.
Nmin=int(diamin/dropU*sf)

if(upstream)then
    do k=1,num-1
        if(oildrop)then
            if(X(k+1)-X(k).GE.slope.AND..NOT.switch.AND.X(k).GE.level)then
                switch=.true.
                N1=k+1
            elseif(X(k)-X(k+1).GE.slope.AND.switch.AND.X(k+1).GE.level)then
                switch=.false.
                N2=k
            elseif(X(k).LT.X(N1)-1.AND.switch.AND.X(k+1).GE.level)then
                switch=.false.
                N2=k
            endif

        elseif(waterdrop)then
            if(X(k)-X(k+1).GE.slope.AND..NOT.switch.AND.X(k).LE.level)then
                switch=.true.
                N1=k+1
            elseif(X(k+1)-X(k).GE.slope.AND.switch.AND.X(k+1).LE.level)then
                switch=.false.
                N2=k
            elseif(X(k).GT.X(N1)+1.AND.switch.AND.X(k+1).LE.level)then
                switch=.false.
                N2=k
            endif
        endif

        if(N2>N1+Nmin)then
            N=N+1
            !output values of oil drop as 1, or water drop as 0
            do i=N1,N2
                if(oildrop)then
                    square(i,1)=1.0
                else
                    square(i,1)=0.0
                endif
            enddo

            chord(N,1)=N
            chord(N,2)=N2-N1
            chord(N,3)=1.0E3*(N2-N1)/sf*dropU
            N1=N2+1
            alpha=chord(N,2)+alpha
        endif
    enddo
endif
alpha=alpha/num


!downstream probe
N1=0
N2=0
switch=.false.

if(downstream)then
```

```
    do k=1,num-1
        if(oildrop)then
            if(Y(k+1)-Y(k).GE.slope2.AND..NOT.switch.AND.Y(k).GE.level2)then
                switch=.true.
                N1=k+1
            elseif(Y(k)-Y(k+1).GE.slope2.AND.switch.AND.Y(k+1).GE.level2)then
                switch=.false.
                N2=k
            elseif(Y(k).LT.Y(N1)-1.AND.switch.AND.Y(k+1).GE.level2)then
                switch=.false.
                N2=k
            endif

        elseif(waterdrop)then
            if(Y(k)-Y(k+1).GE.slope2.AND..NOT.switch.AND.Y(k).LE.level2)then
                switch=.true.
                N1=k+1
            elseif(Y(k+1)-Y(k).GE.slope2.AND.switch.AND.Y(k+1).LE.level2)then
                switch=.false.
                N2=k
            elseif(Y(k).GT.Y(N1)+1.AND.switch.AND.Y(k+1).LE.level2)then
                switch=.false.
                N2=k
            endif
        endif

        if(N2>N1+Nmin)then
            !output values of oil drop as 1, or water drop as 0
            do i=N1,N2
                if(oildrop)then
                    square(i,2)=1.0
                else
                    square(i,2)=0.0
                endif
            enddo

            N=N+1
            chord(N,1)=N
            chord(N,2)=N2-N1
            chord(N,3)=1.0E3*(N2-N1)/sf*dropU
            N1=N2+1
            alpha2=chord(N,2)+alpha2
        endif

    enddo
endif
alpha2=alpha2/num
return


END SUBROUTINE cldCalc
```

Appendix F

Program for Separating HFA Signals in Two-Phase Flow

According to the algorithm suggested by Liu & Bankoff (1993a,b), a Matlab® program is written to attain the HFA output signals for the continuous phase.

- For oil-in-water dispersed flow

```
clear all;
close all;
clc;
%load the signals into a 2-D array
out=load('2.txt');%give sampling frequency Hz
tcorrection=0;
calibration=1;
%temperature setup
tref=25.05;
toverheat=21.63;
twire=tref+toverheat;
%calibration curve Power law fit
a=  11.430622;
b=  6.712339;
n=  0.224063;
%despatch into time and voltage
time=out(:,1);
vol=out(:,2);
volc=vol;
temperature=out(:,3);
tambient=mean(temperature)*30;
clear out;
clear temperature;
%setup level threshold
levelmin=4.282; %c-coeff*d;
levelmax=4.35;
%setup slop threshold
slope=0.001;
J=1;
for I=2:length(vol)-2
% for the case in that there are at least two points in water
%   if (vol(I)>level && vol(I+1)>level)||(vol(I)>level && vol(I-1)>level)
    Pb=vol(I)-vol(I-1); %backward slop
    Pf=vol(I)-vol(I+1); %forward slop
    Rb=abs(Pb);       %backward slop magnitude
    Rf=abs(Pf);       %forward slop magnitude
  if(vol(I)>levelmin && vol(I)<levelmax) %larger than the level value, in water
    if(Rb<slope && Rf<slope)
                %it's in water
      water(J,1)=time(I);
      water(J,2)=vol(I);
      J=J+1;
    elseif(Rb<slope && Pf>slope)
      water(J,1)=time(I);
      water(J,2)=vol(I);
      J=J+1;
        %entering oil or dispersed phase
    elseif(vol(I)>levelmin && vol(I)<levelmax && Pb>slope && Rf<slope)
      water(J,1)=time(I);
      water(J,2)=vol(I);
      J=J+1;
            %entering into the water
```

```
    elseif(Pf<0 && Pb<slope && Pf<1.5*slope && abs(vol(I+2)-vol(I+1))>slope)
      %in liquid, just having a overshoot
      water(J,1)=time(I);
      water(J,2)=vol(I);
      J=J+1;

    elseif(vol(I-1)<levelmin && vol(I+1)>levelmin && Pf>0 && Pb>slope && Rf<1.5*slope)
      %overshooting due to detaching of bubble, in water
      water(J,1)=time(I);
      water(J,2)=vol(I);
      J=J+1;
    % add by Hu Bin apart from Liu & Bankoff
    elseif( vol(I+1)>levelmin && vol(I+1)<levelmax && Pf>0 && Pb>slope && Rf<1.5*slope)
      %overshooting due to detaching of bubble, in water
      water(J,1)=time(I);
      water(J,2)=vol(I);
      J=J+1;
    else
      volc(I)=0;     %in oil or dispersed phase
    end

  else          %less than the level value, in dispersed phase
      volc(I)=0;     %in oil or dispersed phase
  end
end

if(tcorrection)
  water(:,2)=water(:,2)*((twire-tref)/(twire-tambient))^0.5;
end

if(calibration)
  water(:,2)=((water(:,2).^2-a)/b).^(1/n);
end

figure, plot(time(1:5000), volc(1:5000),'xr','markersize',2,'linestyle','none' );
hold on;
plot(time(1:5000), vol(1:5000)-1,'linestyle','-');
m(1)=mean(water(:,2));
m(2)=std(water(:,2),1);
m(3)=1-J/length(vol)
m(4)=levelmax;
m(5)=levelmin;
m(6)=slope;
m(7)=tambient;
clear time;
clear volc;
clear vol;
%csvwrite('0v.csv',water);
plot(water(1:1000,1), water(1:1000,2),'.g','markersize',2,'linestyle','none' );
hold off;
%subplot(2,1,1), plot(time(1:5000), vol(1:5000),'marker','.','markersize',2,'linestyle','none');
%subplot(2,1,2), plot(time(1:5000), volc(1:5000),'marker','.','markersize',2,'linestyle','-');
%plot(water(90:110,1),water(90:110,2),'marker','*','markersize',2,'linestyle','none')
```

- For water-in-oil dispersed flow

```
clear all;
close all;
clc;
%load the signals into a 2-D array
out=load('19.txt');%give sampling frequency Hz
tcorrection=1;
calibration=1;
%temperature setup
tref=31.85;
toverheat=22.39;
twire=tref+toverheat;
%calibration curve Power law fit
a=  6.400499;
b=  4.534054;
n=  0.610000;
%despatch into time and voltage
time=out(:,1);
vol=out(:,2);
```

```
volc=vol;
temperature=out(:,3);
tambient=mean(temperature)*30;
clear out;
clear temperature;

%setup level threshold
levelmin=3.2; %c-coeff*d;
levelmax=3.5;

%setup slop threshold
slope=0.001;

J=1;
for I=2:length(vol)-2

    Pb=vol(I)-vol(I-1); %backward slop
    Pf=vol(I)-vol(I+1); %forward slop
    Rb=abs(Pb);       %backward slop magnitude
    Rf=abs(Pf);       %forward slop magnitude

 if(vol(I)<levelmax && vol(I)>levelmin) %less than the level value, in oil

    if(Rb<slope && Rf<slope)
                %it's in oil
      oil(J,1)=time(I);
      oil(J,2)=vol(I);
      J=J+1;
    elseif(Rb<slope && -Pf>slope)
      oil(J,1)=time(I);
      oil(J,2)=vol(I);
      J=J+1;
        %entering water or dispersed phase

    elseif(vol(I+1)<levelmax && vol(I+1)>levelmin && -Pb>slope && Rf<slope)
      oil(J,1)=time(I);
      oil(J,2)=vol(I);
      J=J+1;
    % add by Hu Bin apart from Liu & Bankoff
    elseif( vol(I+1)<levelmax && vol(I+1)>levelmin && -Pf>0 && -Pb>slope && Rf<1.5*slope)
      %overshooting due to detaching of bubble, in oil
      oil(J,1)=time(I);
      oil(J,2)=vol(I);
      J=J+1;
    else
      volc(I)=0;     %in water or dispersed phase
    end

  else         %less than the level value, in dispersed phase
      volc(I)=0;     %in water or dispersed phase
  end
end
if(tcorrection)
  oil(:,2)=oil(:,2)*((twire-tref)/(twire-tambient))^0.5;
end
if(calibration)
  oil(:,2)=((oil(:,2).^2-a)/b).^(1/n);
end
figure, plot(time(1:5000), volc(1:5000)-1,'xr','markersize',2,'linestyle','none' );
hold on;
plot(time(1:5000), vol(1:5000),'linestyle','-');
m(1)=mean(oil(:,2));
m(2)=std(oil(:,2),1);
m(3)=1-J/length(vol)
m(4)=levelmax;
m(5)=levelmin;
m(6)=slope;
m(7)=tambient;
clear time;
clear volc;
clear vol;
%csvwrite('0v.csv',water);
plot(oil(1:500,1), oil(1:500,2),'.g','markersize',2,'linestyle','none' );
hold off;
```

Appendix G

Program for the PBEs Model in Stirred Vessels

```
Program Main

USE     Properties
IMPLICIT NONE
DOUBLE PRECISION    OPTIME, TMark
DOUBLE PRECISION    Re
DOUBLE PRECISION    vT      !Tank volume (m^3)
DOUBLE PRECISION    f       !friction factor
DOUBLE PRECISION    T, TOUT
DOUBLE PRECISION    Vol,D3,D2
DOUBLE PRECISION    RTOL
DOUBLE PRECISION    ATOL, RPAR, RWORK
DOUBLE PRECISION,   ALLOCATABLE    :: Y(:)
DOUBLE PRECISION    G,Birth,B, CR
DIMENSION           ATOL(KC)

DOUBLE PRECISION    beita,X1,X2, test1,test2, test(100)
INTEGER     IWORK
INTEGER     NEQ             !Nums of Equations
INTEGER     I, K, NLOOP, NL
INTEGER     IOUT
INTEGER     ITASK
INTEGER     ISTATE
INTEGER     IOPT
INTEGER     LRW
INTEGER     LIW
INTEGER     MF
INTEGER     ITOL
INTEGER     IPAR
INTEGER     ML, MU

INTEGER     IV
INTEGER     ITR             !Transient switch
INTEGER     Organic
EXTERNAL    FEX, JEX, G, B

ALLOCATABLE :: RWORK(:), IWORK(:)

ALLOCATE (CN(KC),Y(KC),GA(KC),DA(KC,KC),CRA(KC,KC),g12(KC,KC),
  &     CRATemp(KC,KC) )

!/-------------------------------------------------------------------------------------!
PipeFlow=.FALSE. !.FALSE.

BModel=4            !1 -- Coulaloglou & Tavlarides 1977
                    !2 -- Tsouris & Tavlarides 1994
                    !3 -- Prince and Blanch 1990
                    !4 -- Luo and Svendsen 1996

DKernel=1           !1 -- Vella Alpaneus, 1999
                    !2 -- Lars Hagesaether 2002

DModel=8            !1 -- Coulaloglou & Tavlarides 1977, Normal dist.
                    !2 -- Hsia & Tavlarides 1983, Beta Dist.
                    !3 -- Lee 1987
                    !4 -- Konno et al. 1980
                    !5 -- Prince & Blanch 1990, Uniform dist.
                    !6 -- Tsouris & Tavlarides 1994
                    !7 -- Luo and Svendsen 1996
                    !8 -- Kostoglou 1997, U-shaped beta dist.

CModel=1            !1 -- Coulaloglou & Tavlarides 1977
                    !2 -- Tsouris & Tavlarides 1994
                    !3 -- Ville Alopaeus, 1999, 2001
```

```
Organic=0                !0 -- O/W -> W/O
                         !1 -- W/O -> O/W
!/-------------------------------------------------------------------------------------!
IF(Organic.EQ.1)THEN
    rhoC=867.0D0
    rhoD=996.0D0
    muC=0.57D0*10.0**(-3.0)
    muD=0.96D0*10.0**(-3.0)
ELSEIF(Organic.EQ.0)THEN
    rhoC=996.0D0
    rhoD=867.0D0
    muC=0.96D0*10.0**(-3.0)
    muD=0.57D0*10.0**(-3.0)
ENDIF

sigma=0.0323D0
pi=DACOS(-1.0D0)

!For pipeflow
usC=3.5*0.93D0
usD=3.5*0.07D0
dia=0.038D0
umix=usC+usD

dI=0.05D0
tV=0.102    !2.0*dI
hV=0.102    !2.0*dI
rpm=900.0D0
alpha=0.20D0

NLOOP=200
NTot=1D0             !Total drop numbers
MeanInit=0.0005D0    !Mean drop size, m

DMax=0.0010D0        !The upper limitation of drop dia., m
lmax=1

OPTime=2D0               !Output time interval
TMark=0.0D0

!/---------5-----------------------------------------------------------------------------!
!Density and Viscosity
rhoM=(1-alpha)*rhoC+alpha*rhoD
IF(CModel.EQ.3)THEN
muM=muC/(1-alpha)*(1.0+1.5*alpha*muD/(muC+muD))    !Ville Alopaeus 1999
ELSE
muM=muC*(1+2.5*alpha*((muD+0.4*muC)/(muD+muC)))
ENDIF

muM=muC*(1+2.5*alpha*((muD+0.4*muC)/(muD+muC)))  !Taylor (1932)
c    muM=muC/(1D0-alpha)*(1D0+1.5*alpha*muD/(muD+muC))    !Vernuelen (1955)
nI=rpm/60.0

!Calculate Energy Dissipation Rate
IF (PipeFlow) THEN
    Re=rhoC*dia*umix/muC
    f=0.079*Re**(-0.25)
    e=2.0*f*umix**3.0/dia
ELSE
    Web=(nI**2.0*dI**3.0*rhoM)/sigma
    vT=pi*tV**2.0*hV/4.0
    !e=5.1*nI**3.0*dI**5.0/vT
    e=0.99*nI**3.0*dI**2.0
ENDIF

!Dampling influence on energy dissip.
e=e*(muC*rhoM/(muM*rhoC))**3D0

!Kolmogroff microscale (m)
xkmg=(muC**3D0/(rhoC**3D0*e))**0.25D0

!Critical Maximum Stable Drop Size, Dc, (m)
IF(PipeFlow) THEN
    WebCrit=10.00
    para1=sigma**0.6/(rhoC**0.3*rhoD**0.2*muC**0.1)
```

```
    dc=1.38*WebCrit**0.6*(para1)*dia**0.5/umix**1.1
ELSE
    Web=(nI**2.0*dI**3.0*rhoC)/sigma
    vi=1+2.5*alpha*((muD+0.4*muC)/(muD+muC))    !Taylor (1932)
    cm=0.125D0
    dc=cm*Web**(-0.6)*dI*vi**1.2
ENDIF

dDia=(DMax-xkmg)/KC


CALL  NInit(CN,Y,MeanInit)

!Write the initial volume in a file
Vol=0D0
DO I =1, KC
    Vol=Vol+Y(I)*pi/6D0*(1000D0*CN(I))**3D0
ENDDO

!Calculate the total drop number
NTot=alpha/(Vol*10D0**(-9.0))
Y=NTot*Y
Vol=NTot*Vol

OPEN (11, File="C:\result.xls")
OPEN (12, File="C:\volume.xls")

WRITE(11,'(F14.5,<KC>F14.6)')0.0,(CN(K)*1000,K=1,KC)
WRITE(11,'(F14.5,<KC>F14.6)')0.0,(Y(K)/NTot,K=1,KC)

WRITE(*,20)T,Vol

!Fill out the look up table
DA=0D0
CRA=0D0
GA=0D0

DO K=1,KC
    GA(K)=G(K)
    !GA(K)=B(K,50)
ENDDO

DO K=1,KC
    DO I=1,K-1
        DA(I,K)=B(I,K)
    ENDDO
ENDDO

DO K=1,KC
    DO I=1,KC
        CRA(K,I)=CR(K,I)
    ENDDO
ENDDO
open (13, File="C:\d.xls")
    DO I=1, KC
    write(13,'(2F12.8)')CN(I),DA(I,KC)
ENDDO


   NEQ = KC
   T = 0.0D0
   TOUT = 0.04D0
   ITOL = 2
   RTOL = 1.D-8
DO 15 I =1, KC
    ATOL(I)=1.D-8
15  END DO

   ITASK = 1
   ISTATE = 1
   IOPT = 0
   MF =22
ML=1        !FOR JACOBIAN
MU=2        !FOR JACOBIAN

IF(MF.EQ.10)THEN
```

```
      ALLOCATE(RWORK(20+16*NEQ),IWORK(30))
      LRW = 20+16*NEQ
    LIW = 30
  ELSEIF(MF.EQ.21.OR.MF.EQ.22)THEN
      ALLOCATE(RWORK(22+9*NEQ+2*NEQ**2),IWORK(30+NEQ))
      LRW = 22+9*NEQ+2*NEQ**2
    LIW = 30+NEQ
  ELSEIF(MF.EQ.24.OR.MF.EQ.25)THEN
      ALLOCATE(RWORK(22+11*NEQ+(3*ML+2*MU)*NEQ),IWORK(30+NEQ))
       IWORK(1) = ML
       IWORK(2) = MU
      LRW = 22+11*NEQ+(3*ML+2*MU)*NEQ
    LIW = 30+NEQ
  ENDIF


  ALLOCATE(D32(1:NLOOP))

666  DO 40 IOUT = 1,NLOOP
      ITASK = 1
      IOPT = 0
      ISTATE = 1
      T=0D0
      TOUT=OPTIME

      CALL DVODE(FEX,NEQ,Y,T,TOUT,ITOL,RTOL,ATOL,ITASK,ISTATE,
     &          IOPT,RWORK,LRW,IWORK,LIW,JEX,MF,RPAR,IPAR)

      !Total number
      NTot=0D0
      !Output Sum(D^3) here
      Vol=0D0
      D3=0D0
      D2=0D0

      DO I =1, KC
          NTot=NTot+Y(I)
          Vol=Vol+Y(I)*pi/6D0*(1000D0*CN(I))**3D0
          D3=D3+Y(I)*CN(I)**3D0
          D2=D2+Y(I)*CN(I)**2D0
      ENDDO
      D32(IOUT)=D3/D2
      Imax=D3/D2

      !radial distribution
      beita=D2*pi/6.0

      IF(DABS((TOUT*IOUT-TMark)/OPTIME).GT.0.999D0)THEN
          WRITE(11,'(F14.5,<KC>F14.6)')TOUT*IOUT,(Y(K)/NTot,K=1,KC)
          TMark=TOUT*IOUT
      ENDIF

      !Compare break up rate and coalescence rate
      BRK=0D0
      COA=0D0

      DO I =1, KC
          BRK=BRK+Y(I)*GA(I)
          DO K =1,KC
              COA=COA+Y(I)*Y(K)*CRA(I,K)
          ENDDO
      ENDDO
          COA=COA/2D0

      WRITE(12,*) Tout*Iout,D32(IOUT)*10**6.0   !Vol
      WRITE(*,20)Tout*Iout,Vol,COA/BRK
20        FORMAT(' At t (sec)=',D12.4,';Total Volume (mm^3) =',D14.6    !)
     &          ,';C/B=',F8.5)

    IF (ISTATE .LT. 0) GO TO 80

40   END DO

  CLOSE (11)
  WRITE(*,60) IWORK(11),IWORK(12),IWORK(13),IWORK(19),
     &          IWORK(20),IWORK(21),IWORK(22)
```

```
60   FORMAT(/' No. steps =',I4,'  No. f-s =',I4,
     &     '  No. J-s =',I4,'  No. LU-s =',I4/
     &     ' No. nonlinear iterations =',I4/
     &     ' No. nonlinear convergence failures =',I4/
     &     ' No. error test failures =',I4/)

WRITE(*,85)ISTATE
85   FORMAT(///'ISTATE =',I3)

IF(ISTATE.NE.2)PAUSE
STOP

80   WRITE(*,90)ISTATE
90   FORMAT(///' Error halt: ISTATE =',I3)

IF(ISTATE.NE.2)PAUSE

     END

DOUBLE PRECISION   FUNCTION B_D (N,Y)
!Birth rate and Death rate of size D
!Due to breakage and coalescence

USE Properties
IMPLICIT NONE
DOUBLE PRECISION   DN              !Drop diameter of N, m
DOUBLE PRECISION   VN              !Volume of N, m^3
DOUBLE PRECISION   V0              !Volume of Max(N&Stable), m^3
DOUBLE PRECISION   Y(*)
DOUBLE PRECISION   D0              !Max(dc,d)
DOUBLE PRECISION   B               !Daughter distribution function
DOUBLE PRECISION   G               !Breakage frequency function
DOUBLE PRECISION   DK,VK,DJ,VJ         !VK+VJ->X*VN+(1-X)*VN-1
DOUBLE PRECISION   DN1,VN1             !D(N-1), V(N-1)
DOUBLE PRECISION   DN2,VN2             !D(N+1), V(N+1)
DOUBLE PRECISION   CR              !Coalescence rate of VK & VJ
DOUBLE PRECISION   X1,X2
DOUBLE PRECISION   CTemp1,CTemp2

INTEGER   N                        !Size Class
INTEGER   K,J
INTEGER   IClass
INTEGER   NDaughter                !=2 for binary breakage
INTEGER   IV                       !External Function
INTEGER   IHalfV                   !Index of V/2
INTEGER   IComp                    !Index of Compensary Part of V1
INTEGER   IStore

EXTERNALB
EXTERNALG
EXTERNALIV
EXTERNALCR

DN=CN(N)
VN=pi*DN**3D0/6D0

NDaughter=2
B_D=0.0D0

C    GOTO 25
!Birth rate due to larger drop breakage
IF(DKernel.EQ.1)THEN
    DO K=N+1,KC        !OR IClass+1,KC
        B_D=B_D+BX*NDaughter*DA(N,K)*GA(K)*Y(K)
    ENDDO

ELSEIF(DKernel.EQ.2)THEN
    DO K=N+1,KC        !OR IClass+1,KC
        B_D=B_D+NDaughter*DA(N,K)*GA(K)*Y(K)
    !need to think about.....
    ENDDO

ENDIF

!Death rate to this class drop breakage
```

```
B_D=B_D-GA(N)*Y(N)

C   Return

!Death rate due to drop coalecence with this class
25  DO 20 K=1, KC
    IF(K.EQ.N)THEN
    B_D=B_D-2.0*CRA(N,K)*Y(N)*Y(K)
    ELSE
    B_D=B_D-CRA(N,K)*Y(N)*Y(K)
    ENDIF
20  ENDDO

!Birth rate due to smaller drop coalescence

IF(N.EQ.1) THEN
    CTemp1=0D0
    VK=VN
    DJ=CN(2)
    VJ=pi*DJ**3D0/6D0
    X1=(VJ-2D0*VK)/(VJ-VK)
    CTemp1=X1*CRA(1,1)*Y(1)*Y(1)
    B_D=B_D+CTemp1
RETURN
ENDIF

DN1=CN(N-1)
VN1=pi*DN1**3D0/6D0
CTemp1=0D0

DO 40 K=1,N-1
    DK=CN(K)
    VK=pi*DK**3D0/6D0
    DO 30 J=1,N-1
        DJ=CN(J)
        VJ=pi*DJ**3D0/6D0
        IF(VK+VJ.GT.VN1.AND.VK+VJ.LE.VN)THEN
            X1=(VK+VJ-VN1)/(VN-VN1)
            IF(J.EQ.K)THEN
                CTemp1=CTemp1+2D0*X1*CRA(K,J)*Y(K)*Y(J)
            ELSE
                CTemp1=CTemp1+X1*CRA(K,J)*Y(K)*Y(J)
            ENDIF
        ENDIF
30      ENDDO
40  ENDDO

B_D=B_D+0.5D0*CTemp1

IF(N.EQ.KC)THEN
    CTemp2=0D0
    DO 60 K=1,N
        DK=CN(K)
        VK=pi*DK**3D0/6D0
        DO 50 J=1,N
            DJ=CN(J)
            VJ=pi*DJ**3D0/6D0
            IF(VK+VJ.GT.VN)THEN
                X2=(VK+VJ)/VN
                IF(J.EQ.K)THEN
                    CTemp2=CTemp2+2D0*X2*CRA(K,J)*Y(K)*Y(J)
                ELSE
                    CTemp2=CTemp2+X2*CRA(K,J)*Y(K)*Y(J)
                ENDIF
            ENDIF
50          ENDDO
60      ENDDO
    CTemp2=CTemp2

ELSE
    DN2=CN(N+1)
    VN2=pi*DN2**3D0/6D0
    CTemp2=0D0

    DO 80 K=1,N
        DK=CN(K)
```

```
            VK=pi*DK**3D0/6D0
            DO 70 J=1,N
               DJ=CN(J)
               VJ=pi*DJ**3D0/6D0
               IF(VK+VJ.GT.VN.AND.VK+VJ.LE.VN2)THEN
                  X2=(VN2-VK-VJ)/(VN2-VN)
                  IF(J.EQ.K)THEN
                     CTemp2=CTemp2+2D0*X2*CRA(K,J)*Y(K)*Y(J)
                  ELSE
                     CTemp2=CTemp2+X2*CRA(K,J)*Y(K)*Y(J)
                  ENDIF
               ENDIF
70          ENDDO
80       ENDDO

ENDIF

B_D=B_D+0.5D0*CTemp2

100 END    FUNCTION B_D

MODULE Properties
DOUBLE PRECISION   rhoC
DOUBLE PRECISION   rhoD
DOUBLE PRECISION   rhoM
DOUBLE PRECISION   muC
DOUBLE PRECISION   muD
DOUBLE PRECISION   muM
DOUBLE PRECISION   sigma
DOUBLE PRECISION   dia
DOUBLE PRECISION   usC
DOUBLE PRECISION   usD
DOUBLE PRECISION   umix
DOUBLE PRECISION   alpha
DOUBLE PRECISION   dc              !Maximum stable drop size, m

!For Impeller
DOUBLE PRECISION   tV              !Diameter of Vessle, m
DOUBLE PRECISION   dI              !Impeller diameter, m
DOUBLE PRECISION   hV              !Height of the tank, m
DOUBLE PRECISION   pi
DOUBLE PRECISION   Web
DOUBLE PRECISION   nI              !Impeller speed, 1/s
DOUBLE PRECISION   rpm             !Impeller speed, rpm
DOUBLE PRECISION   vi              !Viscosity damping
DOUBLE PRECISION   cm              !Coefficient for dc
DOUBLE PRECISION   WebCrit         !Critical Web number
DOUBLE PRECISION   para1
DOUBLE PRECISION   xkmg            !Komogorov length,m

DOUBLE PRECISION   NTot
DOUBLE PRECISION   MeanInit        !
DOUBLE PRECISION,  ALLOCATABLE     :: CN(:)
DOUBLE PRECISION   DMax            !Max. drop diamter, m
DOUBLE PRECISION   dDia
DOUBLE PRECISION,  ALLOCATABLE     :: GA(:) !Breakage Array storing G(I)
DOUBLE PRECISION,  ALLOCATABLE     :: DA(:,:)   !Daughter Dist. Array
DOUBLE PRECISION,  ALLOCATABLE     :: CRA(:,:)  !Coalecscence Rate Array
DOUBLE PRECISION,  ALLOCATABLE     :: D32(:)!Sauter mean diameter
DOUBLE PRECISION,  AllOCATABLE ::    g12(:,:)!radial distribution
DOUBLE PRECISION,  AllOCATABLE :: CRATemp(:,:)!temp. matrix for coa

DOUBLE PRECISION   VolIncr
DOUBLE PRECISION   e               !Energy dissipation, m^2/s^3
DOUBLE PRECISION   TV1,TV2,BX
DOUBLE PRECISION   BRK                 !Breakage rate, 1/s
DOUBLE PRECISION   COA                 !Coalescence rate, 1/s
DOUBLE PRECISION   ep              !
DOUBLE PRECISION   lmax            !maximum eddy size

INTEGER, PARAMETER :: KC=40

INTEGER   BModel         !Breakage model choice
INTEGER   DModel         !Daughter Distribution Model
INTEGER   CModel         !Coalescence Model
INTEGER   DKERNEL            !Kernel to conserve mass due to breakage
```

```
LOGICAL   PipeFlow

END MODULE PROPERTIES

DOUBLE PRECISION FUNCTION gammp(a,x)
DOUBLE PRECISION a,x
C    USES gcf,gser
!    Returns the incomplete gamma function P(a, x).
DOUBLE PRECISION gammcf,gamser,gln
DOUBLE PRECISION temp1
if(x.lt.0.D0.or.a.le.0.D0)  pause "bad arguments in gammp"
if(x.lt.a+1.D0)then !Use the series representation.
call gser(gamser,a,x,gln)
gammp=gamser
else !Use the continued fraction representation
call gcf(gammcf,a,x,gln)
gammp=1.-gammcf !and take its complement.

endif

temp1=gammln(a)
gammp=(1D0-gammp)*DExp(temp1)
return
END


**==gammln.spg  processed by SPAG 4.04J  at 17:18 on 28 Jul 1998
    DOUBLE PRECISION FUNCTION GAMMLN(Xx)
    IMPLICIT NONE
    DOUBLE PRECISION Xx
    INTEGER j
    DOUBLE PRECISION ser , stp , tmp , x , y , cof(6)
    SAVE cof , stp
    DATA cof , stp/76.18009172947146D0 , -86.50532032941677D0 ,
   &    24.01409824083091D0 , -1.231739572450155D0 ,
   &    .1208650973866179D-2 , -.5395239384953D-5 ,
   &    2.5066282746310005D0/
    x = Xx
    y = x
    tmp = x + 5.5D0
    tmp = (x+0.5D0)*DLOG(tmp) - tmp
    ser = 1.000000000190015D0
    DO 100 j = 1 , 6
      y = y + 1.D0
      ser = ser + cof(j)/y
100  CONTINUE
    GAMMLN = tmp + DLOG(stp*ser/x)
    RETURN
    END


**==gser.spg  processed by SPAG 4.04J  at 17:18 on 28 Jul 1998

    SUBROUTINE GSER(Gamser,A,X,Gln)
    IMPLICIT NONE
    INTEGER ITMAX
    DOUBLE PRECISION A , Gamser , Gln , X , EPS
    PARAMETER (ITMAX=10000,EPS=3.E-7)
CU   USES gammln
    INTEGER n
    DOUBLE PRECISION ap , del , sum , GAMMLN
    Gln = GAMMLN(A)
    IF ( X.LE.0.D0 ) THEN
      IF ( X.LT.0.D0 ) PAUSE 'x < 0 in gser'
      Gamser = 0.D0
      RETURN
    ENDIF
    ap = A
    sum = 1.D0/A
    del = sum
    DO 100 n = 1 , ITMAX
      ap = ap + 1.
      del = del*X/ap
      sum = sum + del
      IF ( DABS(del).LT.DABS(sum)*EPS ) GOTO 200
```

```
100  CONTINUE
     PAUSE 'a too large, ITMAX too small in gser'
200  Gamser = sum*DEXP(-X+A*DLOG(X)-Gln)
     RETURN
     END



**==gcf.spg  processed by SPAG 4.04J  at 17:18 on 28 Jul 1998
C  (C) Copr. 1986-92 Numerical Recipes Software *1(.~[)!-7k'(4.

c$debug
     SUBROUTINE GCF(Gammcf,A,X,Gln)
     IMPLICIT NONE
     INTEGER ITMAX
     DOUBLE PRECISION A , Gammcf , Gln , X , EPS , FPMIN
     PARAMETER (ITMAX=10000,EPS=3.E-7,FPMIN=1.E-30)
CU   USES gammln
     INTEGER i
     DOUBLE PRECISION an , b , c , d , del , h , GAMMLN
     Gln = GAMMLN(A)
     b = X + 1. - A
     c = 1D0/FPMIN
     d = 1D0/b
     h = d
     DO 100 i = 1 , ITMAX
       an = -i*(i-A)
       b = b + 2.
       d = an*d + b
       IF ( DABS(d).LT.FPMIN ) d = FPMIN
       c = b + an/c
       IF ( DABS(c).LT.FPMIN ) c = FPMIN
       d = 1./d
       del = d*c
       h = h*del
       IF ( DABS(del-1D0).LT.EPS ) GOTO 200
100  CONTINUE
     PAUSE 'a too large, ITMAX too small in gcf'
200  Gammcf = DEXP(-X+A*DLOG(X)-Gln)*h
     RETURN
     END

!----
SUBROUTINE   NInit(DropSize,DropN,Mean)

USE Properties
IMPLICIT NONE

INTEGER   I

DOUBLE PRECISION   DropSize(1:KC)  !Drop Size Class
DOUBLE PRECISION   DropN(1:KC)         !Drop Number

DOUBLE PRECISION   Mean              !Mean dia, m
DOUBLE PRECISION   Dev               !Deviation of dia, m
DOUBLE PRECISION   XN1                   !Temporary variant
DOUBLE PRECISION   XN2                   !Temporary variant

Dev=Mean/4D0

DO 10 I=1, KC

    DropSize(I)=xkmg+I*dDia     !dDia*I
    XN1=DEXP(-0.5*((DropSize(I)-Mean)/Dev)**2.0)
   &              /(DSQRT(2.0*pi)*Dev)
    XN2=DEXP(-0.5*(((I-1)*dDia-Mean)/Dev)**2.0)
   &              /(DSQRT(2.0*pi)*Dev)


    DropN(I)=(XN1+XN2)*0.5*dDia*NTot
!       DropN(I)=1D0/KC*NTot

10   END DO
```

```
END SUBROUTINE NInit


!----
DOUBLE PRECISION   FUNCTION G(I)!Breakage frequency

USE Properties
IMPLICIT NONE

DOUBLE PRECISION   D              !Drop size diameter, m
DOUBLE PRECISION   v              !Drop volume, m^3
DOUBLE PRECISION   K1             !Coefficient for G
DOUBLE PRECISION   K2             !Coefficient for G
DOUBLE PRECISION   ei             !Energy dissipation in impeller region
DOUBLE PRECISION   DF             !Dampling factor
DOUBLE PRECISION   dk
DOUBLE PRECISION   Demin
DOUBLE PRECISION   X
DOUBLE PRECISION   D1,D2
DOUBLE PRECISION   ec             !breakage efficiency
DOUBLE PRECISION   eddy           !average eddy energy
DOUBLE PRECISION   p1,p2,c1
DOUBLE PRECISION   c4,tm,b0,b1
DOUBLE PRECISION   beta,cf
DOUBLE PRECISION   Dson           !daughter drop size,m
DOUBLE PRECISION   Gtemp          !Temp. variable
DOUBLE PRECISION   fbv
DOUBLE PRECISION   xk,xkmax,dkx   !Prince & Blanch, =k
DOUBLE PRECISION   xkmin          !Prince & Blanch, =k
DOUBLE PRECISION   lmax0

DOUBLE PRECISION   gammp

EXTERNAL           gammp

INTEGER            Integral    !Integrate step num.
INTEGER            I           !Mother drop
INTEGER            J           !Daughter Drop

D=CN(I)
v=pi*D**3.0/6.0

IF(D.LE.DC)THEN
C       G=0D0
C       RETURN
ENDIF


IF(BModel.EQ.1) THEN              !Coulaloglou & Tavlarides 1977

    IF(PipeFlow)THEN
        K1=0.005
        K2=0.62
    ELSE
        K1=0.00487          !0.287      !0.00487
        K2=0.0552           !0.0252     !0.0552
    ENDIF

    G=K1*e**(1.0/3.0)/((1D0+alpha)*D**(2D0/3D0))*DExp((-K2*sigma*
   &        (1D0+alpha)**2D0)/(rhoD*D**(5.0/3.0)*e**(2D0/3D0)))

ELSE IF (BModel.EQ.2) THEN        !Tsouris & Tavlarides 1994

    DF=(1D0+2.5D0*alpha*(muD+0.4*muC)/(muD+muC))**2D0
    Demin=0.5*dc
    Integral=1000
    dk=(2D0/Demin-2D0/D)/Integral
    ei=5.16*e

    IF(I.EQ.1)THEN !Maximum daughter drop size
        D1=CN(1)   !Dmin1(dc,0.99*D)              !CN(1,1)
    ELSE
        D1=CN(I-1)
    ENDIF
```

```
      D2=(D**3D0-D1**3D0)**(1D0/3D0)
      Ec=0.5*pi*sigma*(2.0*(D/1.2599)**2.0+D2**2.0+D1**2.0-2.0*D**2.0)

      c1=1.3D0                    !From T&T 1994
      G=0.0D0
      DO 10 X =2D0/D, 2D0/Demin, dk

          eddy=17.16*rhoC*ei**(2D0/3D0)*X**(-11D0/3D0)
          p1=(2D0/X+D)**2D0*(8.2D0*X**(-2D0/3D0)+1.07D0*
     &            D**(2D0/3D0))**0.5D0*X**2D0
          p2=DEXP(-Ec/(c1*eddy))
          G=G+DMax1(p1*p2*dk,0.0D0)

10        END DO

      G=0.0118*DF*ei**(1.0/3.0)*G         !0.0118

  ELSE IF(BModel.EQ.3) THEN               !Prince & Blanch 1990

      xkmax=10D0*pi/D !0.5*(rhoC**3D0*e/(muC**3D0))**0.25D0  !
      xkmin=2D0*pi/D
      dkx=xkmax/1000D0
      G=0D0

      DO 20 xk=1,xkmax,dkx
      Gtemp=0D0
      Gtemp=DEXP(-1.18D0*sigma*xk**(2D0/3D0)/((2D0*pi)**(2D0/3D0)
     &          *rhoC*D*e**(2D0/3D0)))*xk**2D0*e**(1D0/3D0)*(D**(2D0/3D0)+
     &          (2D0*pi/xk)**(2D0/3D0))**0.5D0
     &         *0.14D0*pi*(D+2D0*pi/xk)**2D0/16D0
      G=G+Gtemp*dkx
20        END DO

  ELSE IF (BModel.EQ.4) THEN              !Luo & Svendsen 1996

      c4=0.923
      beta=2.0466

      G=0D0
      DO 50 J=1,I-1
      Gtemp=0D0
      Dson=CN(J)

      cf=(Dson/D)**2D0+(1-(Dson/D)**3D0)**(2D0/3D0)-1

      b1=12D0*cf*sigma/(beta*rhoC*e**(2D0/3D0)*d**(5D0/3D0))
      !maximum eddy size
      lmax0=DMin1(lmax,d)
      b0=b1*(lmax0/d)**(-11D0/3D0)
      !end on maximum eddy size

      tm=b1*(xkmg/d)**(-11D0/3D0)

      Gtemp=(Gammp(8D0/11D0,tm)-Gammp(8D0/11D0,b0))+
     &     2D0*b1**(3D0/11D0)*(Gammp(5D0/11D0,tm)-Gammp(5D0/11D0,b0))
     &     +b1**(6D0/11D0)*(Gammp(2D0/11D0,tm)-Gammp(2D0/11D0,b0))

      Gtemp=-3D0*c4*(e/d**2D0)**(1D0/3D0)/(11D0*b1**(8D0/11D0))*Gtemp

      Gtemp=Dmax1(0D0,Gtemp)
!         G=G+Gtemp*dDia
!         G=G+Gtemp*pi/2D0*Dson**2D0*dDia
!         G=G+Gtemp*(CN(J+1)**3D0-Dson**3D0)/D**3D0          !From Luo's
      G=G+Gtemp*3D0*Dson**2D0*dDia/D**3D0                   !From Luo's

50        END DO
      G=G*0.5D0*(1-alpha)

  ELSE IF(BModel.EQ.5) THEN

  ENDIF

  END FUNCTION G

  !----
  DOUBLE PRECISION FUNCTION B(N,M)
```

```
!Daughter drop size distribution

USE Properties
IMPLICIT NONE

DOUBLE PRECISION Dd                 !Daughter drop size, m
DOUBLE PRECISION Dm                 !Mother drop size, m
DOUBLE PRECISION Vd                 !Daughter drop volume, m3
DOUBLE PRECISION Vm                 !Mother drop volume, m3
DOUBLE PRECISION TempA, TempB, TempC
DOUBLE PRECISION c1,c2              !Lee's PDF
DOUBLE PRECISION Gammln
DOUBLE PRECISION Dx1,Dx2,Dx0  !T & T
DOUBLE PRECISION Dxi                !T & T
DOUBLE PRECISION c4,tm
DOUBLE PRECISION beta,cf,b1
DOUBLE PRECISION Gtemp,Gammp

INTEGER             M               !Mother Drop Class
INTEGER             N               !Daughter Drop Class
INTEGER             I

External Gammp

Dd=CN(N)
Dm=CN(M)
Vd=pi*Dd**3.0/6.0
Vm=pi*Dm**3.0/6.0

IF(DModel.EQ.1)THEN             !C&T 1977
    B=2.4/Vm*DExp(-4.5*(2.0*Vd-Vm)**2.0/Vm**2.0)
    B=B*pi/2D0*Dd**2D0*dDia

ELSEIF(DModel.EQ.2) THEN    !Hsia &T    1983

    B=90.0*Dd**2D0/Dm**3D0*(Dd/Dm)**6D0*(1D0-Dd**3D0/Dm**3D0)**2D0
    B=B*dDia   !B*3D0*Dd**2D0*dDia

ELSEIF(DModel.EQ.3)THEN     !Lee 1987
    c1=2D0
    c2=2D0
    B=DEXP(Gammln(c1+c2))*(Vd/Vm)**(c1-1)*(1D0-Vd/Vm)**(c2-1)
  &         /(DEXP(Gammln(c1))*DEXP(Gammln(c2))*Vm)
    B=B*pi/2D0*Dd**2D0*dDia
ELSEIF(DModel.EQ.4)THEN     !Konno 1980
    B=DEXP(Gammln(12D0))*(Dd/Dm)**8D0*(1-Dd/Dm)**2D0
  &         /(DEXP(Gammln(3D0))*DEXP(Gammln(9D0))*Dm)
    B=B*dDia

ELSEIF(DModel.EQ.5)THEN     !Prince & Blanch 1990
    B=1D0/(Vm)
    B=B*pi/2D0*Dd**2D0*dDia !pi/6D0*(CN(N+1)**3D0-CN(N)**3D0)

ELSEIF(DModel.EQ.6) THEN    !T &T 1994

    Dx1=CN(1)
    Dx2=(Dm**3D0-Dx1**3D0)**(1D0/3D0)
    Dx0=(0.5D0)**(1D0/3D0)*Dm
    Dxi=(Dm**3D0-Dd**3D0)**(1D0/3D0)

    TempA=Dx1**2D0+Dx2**2D0+2D0*Dx0**2D0-Dm**2D0-Dd**2D0-Dxi**2D0
    TempB=(M-1)*(Dx1**2D0+Dx2**2D0+2D0*Dx0**2D0-2D0*Dm**2D0)

    TempC=0D0
    DO I=1,M-1
        TempC=TempC+CN(I)**2D0+(Dm**3D0-CN(I)**3D0)**(2D0/3D0)-Dm**2D0
    ENDDO

    B=TempA/(TempB-TempC)

ELSEIF(DModel.EQ.7)THEN     !Luo & Svendsen 1996

C       open(3, File="d:\n.xls")

C       DO c1=0.0001D0,0.019D0,0.0001D0
    Gtemp=0.0
```

```
C       Dd=c1  !**(1D0/3D0)*Dm

      c4=0.923
      beta=2.0466

      cf=(Dd/Dm)**2D0+(1-(Dd/Dm)**3D0)**(2D0/3D0)-1

      b1=12D0*cf*sigma/(beta*rhoC*e**(2D0/3D0)*Dm**(5D0/3D0))

      tm=b1*(xkmg/Dm)**(-11D0/3D0)

      Gtemp=(Gammp(8D0/11D0,tm)-Gammp(8D0/11D0,b1))+
     &     2D0*b1**(3D0/11D0)*(Gammp(5D0/11D0,tm)-Gammp(5D0/11D0,b1))
     &     +b1**(6D0/11D0)*(Gammp(2D0/11D0,tm)-Gammp(2D0/11D0,b1))

      Gtemp=-3D0*c4*(e/Dm**2D0)**(1D0/3D0)/(11D0*b1**(8D0/11D0))*Gtemp

      IF(GA(M).NE.0D0)THEN
          B=Gtemp/(GA(M)*Vm)        !Need some work here
          B=B*pi*Dd**2D0*dDia/2.0
      ENDIF

C       Write(3,'(2F14.8)') c1,B
C       enddo

ELSEIF(DModel.EQ.8)THEN      !Kostoglou, 1997, U shaped beta dist.
      c1=0.01
      c2=1.0
      TempA=0.5D0*c1/(2D0*c2*(1.0+c2)*(1.0-c1))
      TempB=0.5/(DLOG(1D0+c2)-DLOG(c2)+(TempA-1D0)/(c2+0.5D0))
      B=(1D0/(Vd/Vm+c2)+1D0/(1D0-Vd/Vm+c2)+2D0*(TempA-1D0)/
     &          (c2+0.5D0))*TempB/Vm
      !B=B*pi/2D0*(Dd**2D0*dDia)
      B=B*pi/6D0*((Dd+0.5*dDia)**3D0-(Dd-0.5*dDia)**3D0)
      !B=B*Vm          !For plot beta curve
ENDIF
END FUNCTION B


!!!!
SUBROUTINE FEX(NEQ, T, Y, YDOT, RPAR, IPAR)

      USE     Properties

DOUBLE PRECISION RPAR, T, Y, YDOT
DIMENSION Y(NEQ), YDOT(NEQ)

DOUBLE PRECISION   d1
DOUBLE PRECISION   B_D
DOUBLE PRECISION   G
DOUBLE PRECISION   NDrop
INTEGER   I,K,J

TV1=0D0
DO K=1,KC
      TV1=TV1+(pi*CN(K)**3/6D0)*GA(K)*Y(K)
ENDDO

TV2=0D0
DO K=1,KC-1
      DO I=K+1,KC
      TV2=TV2+(pi*CN(K)**3/6D0)*DA(K,I)*2*GA(I)*Y(I)
      ENDDO
END DO

BX=TV1/TV2

DO 40 I =1, NEQ
      YDOT(I)=B_D(I,Y)
40    END DO


RETURN

END
```

```
!----
SUBROUTINE JEX ()        !Dummy Jacobian Function

END

!----
INTEGER   FUNCTION IV(V)   !Find out the index of drop of vol. V

    USE    Properties
IMPLICIT NONE

DOUBLE PRECISION   V              !Volume m^3
DOUBLE PRECISION   D              !Diameter, m
INTEGER            I

D=(6D0*V/pi)**(1D0/3D0)

IF(D.GT.CN(KC))THEN
    IV=KC
    RETURN
ENDIF

DO 10 I=1,KC
    IF(D.LT.CN(1)+0.5*dDia)THEN
        IV=1
        RETURN
    ELSEIF(D.GT.CN(I)+0.5*dDia.AND.D.LE.CN(I+1)+0.5*dDia)THEN
        IV=I+1
    ENDIF

10  END DO

END FUNCTION IV


!----
DOUBLE PRECISION   FUNCTION CR(I,J)  !Coalescence Rate of I & J 1I+1J

    USE    Properties
IMPLICIT NONE

DOUBLE PRECISION   D1             !Dia. of Class I
DOUBLE PRECISION   D2             !Dia. of Class J
DOUBLE PRECISION   Re
DOUBLE PRECISION   f              !friction factor
DOUBLE PRECISION   vT
DOUBLE PRECISION   C1             !Coeff. of Collision Freq.
DOUBLE PRECISION   C2             !Coeff. of Coalecence Efficiency
DOUBLE PRECISION   CF             !Collision Frequency of I & J
DOUBLE PRECISION   CE             !Coalescence Efficience of I & J
DOUBLE PRECISION   H1,H2
DOUBLE PRECISION   Q,Temp1,Temp2
DOUBLE PRECISION   C3,C4,CE1,CE2

INTEGER   I, J

D1=CN(I)
D2=CN(J)

IF(CModel.EQ.1)THEN               !Coulaloglou & Tavlarides 1977
    C1=2.0*10D0**(-3D0)   !1.9*10D0**(-3D0)  !2.17*10D0**(-4D0)
    C2=2.28*10D0**13      !2.0*10D0**13      !2.28*10D0**13

    CF=C1*e**(1D0/3D0)/(1+alpha)*(D1+D2)**2D0*
   &        (D1**(2D0/3D0)+D2**(2D0/3D0))**(1D0/2D0)

    CE=DEXP(-C2*muC*rhoC*e*(D1*D2/(D1+D2))**4D0/
   &    (sigma**2D0*(1D0+alpha)**3D0))
ELSEIF(CModel.EQ.2)THEN           !2 -- Tsouris & Tavlarides 1994
    C1=28.1!28.1D0
    H1=0.1*(0.5*D1*D2/(D1+D2))
    H2=0.0  !500.0*10D0**(-10D0)
    Q=(muC/muD)*(0.5*D1*D2/(D1+D2))**0.5D0
    Temp1=(H1**0.5+1.378*Q)/(H2**0.5+1.378*Q)
```

```
      Temp2=(H1**0.5+0.312*Q)/(H2**0.5+0.312*Q)
      C2=1.872*DLOG(Temp1)+0.127*DLOG(Temp2)

      CF=0.2586*pi*e**(1D0/3D0)*(D1+D2)**2D0*
     &        (D1**(2D0/3D0)+D2**(2D0/3D0))**(1D0/2D0)

      CE=DEXP(-6D0*pi*muC*C1*C2*31.25*nI*dI/(rhoC*e**(2D0/3D0)*
     &        (D1+D2)**(2D0/3D0)*(tV**2D0*hV)**(1D0/3D0)))

  ELSEIF(CModel.EQ.3)THEN
      C1=1712*28.1D0     !1712*3.44D0
      C2=-C1*muC/(rhoC*5D0**(1D0/3D0)*e**(1D0/3D0)*(D1+D2)**
     &        (2D0/3D0)*DI**(2D0/3D0))

      CF=0.2586*pi*e**(1D0/3D0)*(D1+D2)**2D0*
     &        (D1**(2D0/3D0)+D2**(2D0/3D0))**(1D0/2D0)
      CE=(0.26144*muD/muC+1.0)**C2

  ELSEIF(CModel.EQ.4)THEN
      C1=2.17*10D0**(-4D0)  !1.9*10D0**(-3D0)  !2.17*10D0**(-4D0)
      C2=2.28*10D0**13      !2.0*10D0**13      !2.28*10D0**13

      CE1=DEXP(-C2*muC*rhoC*e*(D1*D2/(D1+D2))**4D0/
     &     (sigma**2D0*(1D0+alpha)**3D0))

      C3=28.1!28.1D0
      H1=0.1*(0.5*D1*D2/(D1+D2))
      H2=0.0  !500.0*10D0**(-10D0)
      Q=(muC/muD)*(0.5*D1*D2/(D1+D2))**0.5D0
      Temp1=(H1**0.5+1.378*Q)/(H2**0.5+1.378*Q)
      Temp2=(H1**0.5+0.312*Q)/(H2**0.5+0.312*Q)
      C4=1.872*DLOG(Temp1)+0.127*DLOG(Temp2)

      CF=0.2586*pi*e**(1D0/3D0)*(D1+D2)**2D0*
     &        (D1**(2D0/3D0)+D2**(2D0/3D0))**(1D0/2D0)

      CE2=DEXP(-6D0*pi*muC*C3*C4*31.25*nI*dI/(rhoC*e**(2D0/3D0)*
     &        (D1+D2)**(2D0/3D0)*(tV**2D0*hV)**(1D0/3D0)))

      CE=2.0*CE1*CE2/(CE1+CE2)

  ENDIF

  IF((D1**3D0+D2**3D0).GT.CN(KC)**3D0)THEN
      CR=CF*CE
  ELSE
      CR=CF*CE
  ENDIF

  END FUNCTION CR
```

Appendix H

Program for the PBEs Model in Pipeline Flows

```
PROGRAM MAIN
USE SHARE
IMPLICIT NONE

INTEGER,  PARAMETER:: NPDE=20, LWORK=100000, LIWORK=30000
INTEGER,  PARAMETER:: NINT=20              !NUMBER OF LENGTH INTERVAL
DOUBLE PRECISION, PARAMETER:: TFINAL=5D0 !FINAL TIME SCALE, SEC

DOUBLE PRECISION XLEFT,DTUSED,XBKPT(NINT+1),U(NPDE,NINT+1),
+          SCTCH(NINT+1),WORK(LWORK),T0,TOUT,DT,EPS,DX
DOUBLE PRECISION PLENGTH
DOUBLE PRECISION RE                !REYNOLD NUMBER
DOUBLE PRECISION FRICTION          !FRICTION FACTOR
DOUBLE PRECISION PARA1
DOUBLE PRECISION WEC           !CRITICAL WEBER NUMBER
DOUBLE PRECISION D3(NINT+1)        !CRITICAL WEBER NUMBER
DOUBLE PRECISION D2(NINT+1)        !FOR D32=D3/D2
DOUBLE PRECISION UTOT(NINT+1)   !FOR MAXIMUM DROP NUMBER AT X
DOUBLE PRECISION V_IN          !OVERALL INJET VOLUME OF DROPS
DOUBLE PRECISION V_OUT             !OVERALL OUTLET VOLUME OF DROPS
DOUBLE PRECISION V_PIPE(2)     !OVERALL PIPE VOLUME OF DROPS
DOUBLE PRECISION dispHoldup        !DISPERSED PHASE INPUT FRACTION

INTEGER NQ,NSTEPS,NF,NJ,IWORK(LIWORK),NPTS,KORD,NCC,MF,I,K,INDEX, ISTEP
INTEGER   NOC                      !ORGANIC CONTINUOUS IF NOC=1
COMMON /ENDPT/ XLEFT
COMMON /GEAR0/ DTUSED,NQ,NSTEPS,NF,NJ
DOUBLE PRECISION BREAKAGE, DDRPD, COA
EXTERNALBREAKAGE, DDRPD, COA
!/*****************************************************************************************
ISTEP = 5              !STEP NUMBERS FROM 0(SEC) TO TFINAL

NOC=0
dispHoldup=0.30D0
usC=3.0*(1-dispHoldup)
usD=3.0*dispHoldup
dia=0.038D0
umix=usC+usD

PI=DACOS(-1D0)
PLENGTH =15.0     !UMIX*TFINAL     !PIPE LENGTH, M
MEAN=0.001D0
DEV =0.0002D0
DMAX=0.0020D0
C
C    DDIA=0.000254777  !DMAX/NPDE

ALLOCATE(DSIZE(1:NPDE),GT(1:NPDE),DDT(1:NPDE,1:NPDE))
ALLOCATE(COAT(1:NPDE,1:NPDE))

IF(NOC.EQ.1)THEN
    rhoC=828.0D0
    rhoD=998.0D0
    muC=5.5D0*10.0**(-3.0)
    muD=1.17D0*10.0**(-3.0)
ELSE
    rhoC=998.0D0
    rhoD=828.0D0
    muC=1.17D0*10.0**(-3.0)
    muD=5.5D0*10.0**(-3.0)
ENDIF

sigma=0.025D0
V_IN=0D0
```

```
V_OUT=0D0
V_PIPE=0D0
!/*****************************************************************************************
!SUPPOSE THERE IS NO SLIP BETWEEN DISPERSED DROP AND CONTINUOUS PHASE
ALPHA=USD/UMIX
!Density and Viscosity
rhoM=(1-alpha)*rhoC+alpha*rhoD
muM=muC*(1+2.5*alpha*((muD+0.4*muC)/(muD+muC)))

RE=rhoM*dia*umix/muM
FRICTION=0.079*RE**(-0.25)
E=2.0*FRICTION*UMIX**3.0/dia

!Dampling influence on energy dissip.
E=E*(MUC*RHOM/(MUM*RHOC))**3D0

!Kolmogroff microscale (m)
xkmg=(muM**3D0/(rhoM**3D0*E))**0.25D0

!ALLOCATE DROP SIZE FOR CLASS I
DDIA=(DMAX-xkmg)/NPDE
DO I=1,NPDE
    DSize(I)=xkmg+DDIA*I
C       DSize(I)=0D0+DDIA*I
ENDDO

!CALC MAXIMUM STABLE DROP SIZE ACCORDING TO CRITICAL WEBER NUMBER
WeC=1.10
para1=sigma**0.6/(rhoC**0.3*rhoD**0.2*muC**0.1)
dc=1.38*WeC**0.6*(para1)*dia**0.5/umix**1.1
C   DC=0.0015D0

!INITIAL CONDITION CALL
CALL   NUMBER(NPDE,NINT+1,PLENGTH)
WRITE(*,*)"TOTAL DROPS=",NTOT
!FILL OUT THE BREAKAGE TABLE AND DAUGHTER DROP SIZE TABLE
GT=0D0
DDT=0D0
COAT=0D0

DO I=1,NPDE
    GT(I)=BREAKAGE(I)
ENDDO

DO K=1,NPDE
    DO I=1,K-1
        DDT(I,K)=DDRPD(I,K)
    ENDDO
ENDDO

!FILL OUT THE COALESCENCE RATE TABLE
DO K=1,NPDE
    DO I=1,NPDE
        COAT(K,I)=COA(K,I)
    ENDDO
ENDDO

OPEN(888,FILE="PROFILES.dat")
OPEN(889,FILE="D32.dat")
OPEN(890,FILE="X.dat")
OPEN(891,FILE="Y.dat")
!/*****************************************************************************************
KORD=4                  !KORD=SPLINE ORDER + 1, FOR CUBIC, SET KORD = 4

   NPTS = NINT + 1      !NUMBER OF POINTS
   NCC = 2              !NUMBER OF CONTINUITY CONDITIONS
C   THE NUMBER OF CONTINUITY CONDITIONS, NCC, TO BE IMPOSED ACROSS ALL OF
C   THE BREAKPOINTS IS THE LAST PIECE OF USER SUPPLIED DATA WHICH IS
C   REQUIRED TO UNIQUELY DETERMINE THE DESIRED PIECEWISE POLYNOMIAL
C   SPACE.  FOR EXAMPLE, NCC = 2 WOULD REQUIRE THAT THE APPROXIMATE
C   SOLUTION (MADE UP OF THE SEPARATE POLYNOMIAL PIECES) AND ITS FIRST
C   SPATIAL DERIVATIVE BE CONTINUOUS AT THE BREAKPOINTS AND HENCE ON
C   THE ENTIRE DOMAIN (XLEFT,XRIGHT).  NCC = 3 WOULD REQUIRE THAT THE
C   APPROXIMATE SOLUTION AND ITS FIRST AND SECOND SPATIAL DERIVATIVES
C   BE CONTINUOUS AT THE BREAKPOINTS, ETC.
   T0 = 0D0             !THE INITIAL VALUE OF T(USED ONLY ON FIRST CALL)
```

```
      TOUT = 0D0              !THE VALUE OF T AT WHICH OUTPUT IS DESIRED NEXT
      DT = 1.0D-12          !THE INITIAL(MAXIMUM) STEP SIZE IN T FOR INDEX=1(3)
      EPS = 1.0D-4          !THE RELATIVE TIME ERROR BOUND
      MF = 22                 !BACKWARD DIFFERENTIATION FORMULAS+NO JACOBIAN
      INDEX = 1               !THE FIRST CALL TO USE SOLVER
      IWORK(1) = LWORK
      IWORK(2) = LIWORK       !NCPTS*(NPDE + 1)

      WRITE(*,9000)NINT,KORD,EPS

      DX=PLENGTH/DBLE(NPTS-1)   !THE INTERVAL LENGTH
C     WRITE DOWN THE INITIAL VALUES

   20 DO I=1,NPTS
        XBKPT(I) = 1D0*(I-1)*DX
      ENDDO

      XLEFT = XBKPT(1)  !DEFINE THE LEFT POINTS (X=0)

      CALL PDECOL(T0,TOUT,DT,XBKPT,EPS,NINT,KORD,NCC,NPDE,MF,INDEX,
     &       WORK,IWORK)

      IF(INDEX.NE.0)THEN
           WRITE(*,9500) INDEX
        WRITE(*,*)"INPUT ERROR, PLEASE CHECK AGAIN!"
        PAUSE
        STOP
      ENDIF

      CALL VALUES(XBKPT,U,SCTCH,NPDE,NPTS,NPTS,0,WORK)

C     OUTPUT RESULTS HERE
      WRITE(*,9200) TOUT,DTUSED,NSTEPS

C     CHECK THE MASS BALANCE
      UTOT=0D0
      V_PIPE(2)=0D0
      DO K=1,NPTS
         D3(K)=0D0
         D2(K)=0D0
         DO I=1,NPDE
            UTOT(K)=U(I,K)+UTOT(K)

            D3(K)=U(I,K)*DSIZE(I)**3D0+D3(K)
            D2(K)=U(I,K)*DSIZE(I)**2D0+D2(K)
         ENDDO

C           CALCULATE THE DROP VOLUME IN PIPE
         V_PIPE(2)=V_PIPE(2)+PI/6D0*D3(K)

C           OUTPUT THE D32 AT ALL POSITIONS
         WRITE(889,*)XBKPT(K),D3(K)/D2(K)

         IF(TOUT.EQ.0D0) THEN
            WRITE(890,*)XBKPT(K)     !OUTPUT X AXIAL POSITION
            V_PIPE(1)=V_PIPE(1)+PI/6D0*D3(K)
         ENDIF

         WRITE(*,8900)K,PI/6D0*D3(K)
      ENDDO

      V_IN=V_IN+UMIX/DX*PI/6D0*D3(1)*TFINAL/ISTEP
      V_OUT=V_OUT+UMIX/DX*PI/6D0*D3(NPTS)*TFINAL/ISTEP
      WRITE(*,9100) V_IN-V_OUT+V_PIPE(1)-V_PIPE(2)
      DO K = 1,NPDE
            IF(TOUT.EQ.0D0)WRITE(891,*)DSIZE(K)    !OUTPUT Y AXIAL POSITION
         WRITE(888,9400)(U(K,I)/UTOT(I),I=1,NPTS)
      ENDDO
      TOUT=TOUT+TFINAL/ISTEP
      IF(TOUT.LE.TFINAL) GOTO 20
      OPEN (892,FILE="D2.DAT")
      WRITE(892,9600)(D2(K),K=1,NPTS)
      CLOSE(888)
      CLOSE(889)
      CLOSE(890)
      CLOSE(891)
```

```
CLOSE(892)

9000 FORMAT('NO. OF SUBINTERVALS = ',I3,'  KORD = ',I2,
   *' EPS = ',D10.2)
8900 FORMAT(' VOLUME  (',I4,')=',F12.8)
9100 FORMAT(' VOLUME INCREASE (M^3) =',F12.8)
9200 FORMAT(' T = ',E10.3,' DT = ',E10.3,' TOTAL STEPS = ',I6)
9300 FORMAT(10X,'PDE COMPONENT = ',I3)
9400 FORMAT(10X,<NPTS>(F12.8,','))
9500 FORMAT('  INDEX = ',I3)
9600 FORMAT(10X,<NPTS>(E12.4,','))
C    PAUSE "CALCULATION FINISHED!"
END

SUBROUTINE BNDRY(T,X,U,UX,DBDU,DBDUX,DZDT,NPDE)
C
C    THIS ROUTINE SPECIFIES THE BOUNDARY CONDITION EQUATIONS.
C
C     USE SHARE
 INTEGER NPDE
 REAL*8 T,X,U(NPDE),UX(NPDE),DZDT(NPDE),
    *            DBDU(NPDE,NPDE), DBDUX(NPDE,NPDE),
    *            XLEFT
 INTEGER I
 COMMON /ENDPT/ XLEFT
 IF ( X .NE. XLEFT ) GO TO 10

 DO I=1,NPDE
      DBDU(I,I)=1D0
      DBDUX(I,I)=0D0
      DZDT(I)=0D0
 ENDDO


 RETURN
 10 CONTINUE
 C       DBDU(1,1) = U(2)*COS(U(1)*U(2))
 C       DBDUX(1,1) = 1.0
 C       DZDT(1) = 0.0
 DO I=1,NPDE
      DBDU(I,I)=0D0
      DBDUX(I,I)=1D0
      DZDT(I)=0D0
 ENDDO

    RETURN

    END

    SUBROUTINE DERIVF(T,X,U,UX,UXX,DFDU,DFDUX,DFDUXX,NPDE)
C
C    THIS IS THE OPTIONAL ROUTINE PROVIDED IF THE USER WISHES TO
C    SUPPLY AN ANALYTIC JACOBIAN.
C
    INTEGER NPDE
    REAL*8 T,X,U(NPDE),UX(NPDE),UXX(NPDE)
    RETURN
    END

DOUBLE PRECISION FUNCTION BREAKAGE(I)

USE SHARE
IMPLICIT NONE
INTEGER I,J
REAL*8 K1,K2,DS,K3,BETA,GTEMP,DSON,B1,TM,CF
REAL*8 GAMMP

DS=DSIZE(I)
BREAKAGE=0D0

GOTO 10

K1=0.00487          !0.00487
K2=0.0552       !0.0552
```

```
BREAKAGE=K1*e**(1.0/3.0)/((1D0+alpha)*DS**(2D0/3D0))*
   &        DExp((-K2*sigma*(1D0+alpha)**2D0)/
   &        (rhoD*DS**(5.0/3.0)*e**(2D0/3D0)))

RETURN

10  CONTINUE

C   K3=0.0223
k3=0.923
beta=2.0466

DO 50 J=1,I-1
    Gtemp=0D0
    DSON=DSIZE(J)

    cf=(Dson/DS)**2D0+(1-(Dson/DS)**3D0)**(2D0/3D0)-1D0

    b1=12D0*cf*sigma/(beta*rhoC*e**(2D0/3D0)*DS**(5D0/3D0))

    tm=b1*(xkmg/DS)**(-11D0/3D0)

    Gtemp=(Gammp(8D0/11D0,tm)-Gammp(8D0/11D0,b1))+
   &        2D0*b1**(3D0/11D0)*(Gammp(5D0/11D0,tm)-Gammp(5D0/11D0,b1))
   &    +b1**(6D0/11D0)*(Gammp(2D0/11D0,tm)-Gammp(2D0/11D0,b1))

    Gtemp=-3D0*K3*(e/DS**2D0)**(1D0/3D0)/(11D0*b1**(8D0/11D0))*Gtemp

    Gtemp=Dmax1(0D0,Gtemp)
    BREAKAGE=BREAKAGE+Gtemp*3D0*DSON**2D0*dDia/DS**3D0                    !From Luo's
50  END DO
BREAKAGE=BREAKAGE*0.5D0

END FUNCTION BREAKAGE

REAL*8     FUNCTION COA(I,J)
USE SHARE
IMPLICIT NONE
INTEGER   I,J
DOUBLE PRECISION C1,C2
DOUBLE PRECISION CF,CE
DOUBLE PRECISION D1,D2

D1=DSIZE(I)
D2=DSIZE(J)

C2=2.28*10**8
C1=0.0033*alpha**(-1.3404)

CF=C1*e**(1D0/3D0)/(1+alpha)*(D1+D2)**2D0*
   &        (D1**(2D0/3D0)+D2**(2D0/3D0))**(1D0/2D0)

CE=DEXP(-C2*muC*rhoC*e*(D1*D2/(D1+D2))**4D0/
   &    (sigma**2D0*(1D0+alpha)**3D0))

COA=CF*CE

END FUNCTION COA

REAL*8     FUNCTION DDRPD(I,K)

USE SHARE
IMPLICIT NONE
INTEGER   I,K
REAL*8     C1,C2,TEMPA,TEMPB,VD,VM,DD,DM
c    real*8 tem(100)
c    integer l
DD=DSIZE(I)
DM=DSIZE(K)
Vd=pi*DSIZE(I)**3.0/6.0
Vm=pi*DSIZE(K)**3.0/6.0
c1=0.1        !0.3
c2=1.0        !0.5
TempA=0.5D0*c1/(2D0*c2*(1.0+c2)*(1.0-c1))
TempB=0.5/(DLOG(1D0+c2)-DLOG(c2)+(TempA-1D0)/(c2+0.5D0))
DDRPD=(1D0/(Vd/Vm+c2)+1D0/(1D0-Vd/Vm+c2)+2D0*(TempA-1D0)/
```

```
     &          (c2+0.5D0))*TempB/Vm
  DDRPD=DDRPD*3D0*Dd**2D0*dDia
  RETURN
  10  DDRPD=90.0*Dd**2D0/Dm**3D0*(Dd/Dm)**6D0*(1D0-Dd**3D0/Dm**3D0)**2D0
  DDRPD=DDRPD*3D0*Dd**2D0*dDia

  END FUNCTION DDRPD

     SUBROUTINE F(T,X,U,UX,UXX,FVAL,NPDE)
  C
  C    THIS IS THE USER SUPPLIED SUBROUTINE TO SPECIFY THE DIFFERENTIAL
  C    EQUATIONS.
  C
  USE SHARE
  IMPLICIT NONE
  INTEGER I,J,K,NPDE,NDTER
  REAL*8 U(NPDE),UX(NPDE),UXX(NPDE),FVAL(NPDE),T,X
  REAL*8 B1      !BIRTH DUE TO LARGER DROP BREAKAGE
  REAL*8 D1      !DEATH DUE TO ITSELF BREAKAGE
  REAL*8 B2      !BIRTH DUE TO SMALLER DROP COALESCENCE
  REAL*8 D2      !DEATH DUE TO COALESCENCE WITH OTHER DROPS
  REAL*8 BX      !BREAKGE MASS BALANCE COEFFICIENT
  REAL*8 V1,V2
  REAL*8 DK,VK,DJ,VJ        !VK+VJ->X*VN+(1-X)*VN-1
  REAL*8 DN,VN
  REAL*8 DN1,VN1
  REAL*8 DN2,VN2
  REAL*8 CTEMP1,CTEMP2
  REAL*8 X1,X2
  NDTER=2            !NUMBER OF DAUGHTER DROPS
  V1=0D0
  V2=0D0
  C    CALCUALTE THE BREAKGE MASS BALANCE COEFFICIENT,BX ~O(1)
  DO K=1,NPDE
      V1=V1+DSIZE(K)**3D0*GT(K)*U(K)
  ENDDO

  DO K=1,NPDE-1
      DO I=K+1,NPDE
      V2=V2+DSIZE(K)**3*NDTER*DDT(K,I)*GT(I)*U(I)
      ENDDO
  END DO
  BX=V1/V2
  DO I=1,NPDE
  C    CALCULATE THE SOURCE TERMS FROM DROP BREAKING
      B1=0D0
      DO K=I+1,NPDE
          B1=B1+BX*NDTER*DDT(I,K)*GT(K)*U(K)
      ENDDO
  D1=GT(I)*U(I)
  C    CALCULATE THE SOURCE TERMS FROM DROP COALESCENCE
      !Death rate due to drop coalecence with this class
      D2=0D0
      DO K=1, NPDE
          IF(K.EQ.I)THEN
          D2=D2+2.0*COAT(I,K)*U(I)*U(K)
          ELSE
          D2=D2+COAT(I,K)*U(I)*U(K)
          ENDIF
      ENDDO

      !Birth rate due to smaller drop coalescence
      B2=0D0

      IF(I.EQ.1) THEN          !FOR THE MINIMUM DROP CLASS

          DN=DSIZE(I)
          VN=pi*DN**3D0/6D0
          VK=VN
          DJ=DSIZE(2)
          VJ=pi*DJ**3D0/6D0
          X1=(VJ-2D0*VK)/(VJ-VK)
          B2=X1*COAT(1,1)*U(1)*U(1)

      ELSE
```

```
      DN=DSIZE(I)
      VN=pi*DN**3D0/6D0
      DN1=DSIZE(I-1)
      VN1=pi*DN1**3D0/6D0
      CTEMP1=0D0
      DO K=1,I-1      !WHEN VK+VJ<VN
        DK=DSIZE(K)
        VK=pi*DK**3D0/6D0
        DO J=1,I-1
          DJ=DSIZE(J)
          VJ=pi*DJ**3D0/6D0
          IF(VK+VJ.GT.VN1.AND.VK+VJ.LE.VN)THEN
            X1=(VK+VJ-VN1)/(VN-VN1)
            IF(J.EQ.K)THEN
              CTEMP1=CTEMP1+2D0*X1*COAT(K,J)*U(K)*U(J)
            ELSE
              CTEMP1=CTEMP1+X1*COAT(K,J)*U(K)*U(J)
            ENDIF
          ENDIF
        ENDDO
      ENDDO
      CTEMP1=CTEMP1*0.5  !DELETE THE DUPLICATE CASES FOR (K,J) AND (J,K)

      CTEMP2=0D0      !WHEN VK+VJ>VN
      IF(I.NE.NPDE) THEN    !FOR DROPS ARE NOT IN 1ST AND LAST CLASS

        DN2=DSIZE(I+1)
        VN2=pi*DN2**3D0/6D0
        DO K=1,I
          DK=DSIZE(K)
          VK=pi*DK**3D0/6D0
          DO J=1,I
            DJ=DSIZE(J)
            VJ=pi*DJ**3D0/6D0
            IF(VK+VJ.GT.VN.AND.VK+VJ.LE.VN2)THEN
              X2=(VN2-VK-VJ)/(VN2-VN)
              IF(J.EQ.K)THEN
                CTEMP2=CTEMP2+2D0*X2*COAT(K,J)*U(K)*U(J)
              ELSE
                CTEMP2=CTEMP2+X2*COAT(K,J)*U(K)*U(J)
              ENDIF
            ENDIF
          ENDDO
        ENDDO

      ELSEIF(I.EQ.NPDE)THEN   !FOR MAXIMUM DROP CLASS

        DO K=1,I
          DK=DSIZE(K)
          VK=pi*DK**3D0/6D0
          DO J=1,I
            DJ=DSIZE(J)
            VJ=pi*DJ**3D0/6D0
            IF(VK+VJ.GT.VN)THEN
              X2=(VK+VJ)/VN
              IF(J.EQ.K)THEN
                CTEMP2=CTEMP2+2D0*X2*COAT(K,J)*U(K)*U(J)
              ELSE
                CTEMP2=CTEMP2+X2*COAT(K,J)*U(K)*U(J)
              ENDIF
            ENDIF
          ENDDO
        ENDDO

      ENDIF
      CTEMP2=CTEMP2*0.5  !DELETE THE DUPLICATE CASES FOR (K,J) AND (J,K)

      B2=CTEMP1+CTEMP2
    ENDIF

C   OVERALL INFLUENCES FROM BREAKAGE AND COALCESCENCE

    FVAL(I) = -UMIX*UX(I)+B1-D1+B2-D2
C       FVAL(I) = B2-D2    !+B1-D1
 ENDDO
   END
```

```
      SUBROUTINE UINIT(X,U,NPDE)
C
C     UINIT GIVES THE INITIAL CONDITIONS AT T=T0.
C
 USE SHARE
      INTEGER NPDE
      REAL*8 X,U(NPDE),UTEMP(15)
c     REAL*8 UCONST(200)
 INTEGER  I
 REAL*8 XN1,XN2
 DO I=1,NPDE
      XN1=DEXP(-0.5*((DSize(I)-Mean)/Dev)**2.0)
     &              /(DSQRT(2.0*pi)*Dev)
      XN2=DEXP(-0.5*(((I-1)*dDia-Mean)/Dev)**2.0)
     &              /(DSQRT(2.0*pi)*Dev)
      U(I)=(XN1+XN2)*0.5*dDia*NTot
C         U(I)=1D0/NPDE*NTOT
C         UCONST(I)=U(I)
 ENDDO
      RETURN
      END
C     CALCULATE THE TOTAL DROP NUMBER IN EACH CROSSSECTION

 SUBROUTINE NUMBER(NPDE,NPTS,LENGTH)
 USE SHARE
 IMPLICIT NONE
 INTEGER I,NPDE,NPTS
 REAL*8 XN1,XN2,U(NPDE),VOL,LENGTH,UTEMP(15)
 NTOT=1
 DO I=1,NPDE
      XN1=DEXP(-0.5*((DSize(I)-Mean)/Dev)**2.0)
     &              /(DSQRT(2.0*pi)*Dev)
      XN2=DEXP(-0.5*(((I-1)*dDia-Mean)/Dev)**2.0)
     &              /(DSQRT(2.0*pi)*Dev)
      U(I)=(XN1+XN2)*0.5*DDia*NTot
C         U(I)=1D0/NPDE*NTOT
 ENDDO
 Vol=0D0
 DO I =1, NPDE
      Vol=Vol+U(I)*pi/6D0*DSIZE(I)**3D0
 ENDDO
 !Calculate the total drop number
 NTot=alpha/Vol

 END SUBROUTINE NUMBER

 MODULE SHARE
 DOUBLE PRECISION   rhoC
 DOUBLE PRECISION   rhoD
 DOUBLE PRECISION   rhoM
 DOUBLE PRECISION   muC
 DOUBLE PRECISION   muD
 DOUBLE PRECISION   muM
 DOUBLE PRECISION   sigma
 DOUBLE PRECISION   dia
 DOUBLE PRECISION   usC
 DOUBLE PRECISION   usD
 DOUBLE PRECISION   umix
 DOUBLE PRECISION   alpha
 DOUBLE PRECISION   dc          !Maximum stable drop size, m
 DOUBLE PRECISION   Mean        !
 DOUBLE PRECISION   DEV
 DOUBLE PRECISION   PI
 DOUBLE PRECISION   DMAX        !Max. SPECTRUM drop diamter, m
 DOUBLE PRECISION   DDIA
 DOUBLE PRECISION   E           !ENGERGY DISSIPATION RATE
 DOUBLE PRECISION   xkmg        !Komogorov length,m
 DOUBLE PRECISION   NTOT        !TOTAL DROP NUMBER, IN PIPE OF LENGTH
 DOUBLE PRECISION,  ALLOCATABLE    :: DSIZE(:)
 DOUBLE PRECISION,  ALLOCATABLE    :: GT(:) !BREAKAGE TABLE
 DOUBLE PRECISION,  ALLOCATABLE    :: DDT(:,:)   !DAUGHTER DROP SIZE TABLE
 DOUBLE PRECISION,  ALLOCATABLE    :: COAT(:,:)!COALESCENCE RATE TABLE

 END MODULE
```

Appendix I

Program for the Two-Region Model

```
Program Main

USE Properties
IMPLICIT NONE

integer oINw, I, K
double precision we,e,vT
double precision rpm,nx,nxc
double precision nb,nc,d32,xf, d32c
double precision break,coal
double precision a0,a1,cm,vi,dc,vvi
double precision re,Z, x(6)

double precision g,cr
external g,cr
open(888,File="c:\pi.xls")

oINw=1                    !0 -- O/W -> W/O
!Test
IF(oINw.EQ.1)THEN
    !water in oil
    rhoC=996.0D0
    rhoD=996.0D0
    muC=5.0D0*10.0**(-3.0)
    muD=1.0D0*10.0**(-3.0)
ELSEIF(oINw.EQ.0)THEN
    !oil in water
    rhoC=996.0D0
    rhoD=996.0D0
    muC=0.6D0*10.0**(-3.0)
    muD=1.0D0*10.0**(-3.0)
ENDIF
sigma=0.0323D0
goto 20

!Toluene+Water
IF(oINw.EQ.1)THEN
    !water in oil
    rhoC=867.0D0
    rhoD=996.0D0
    muC=0.57D0*10.0**(-3.0)
    muD=0.96D0*10.0**(-3.0)
ELSEIF(oINw.EQ.0)THEN
    !oil in water
    rhoC=996.0D0
    rhoD=867.0D0
    muC=0.96D0*10.0**(-3.0)
    muD=0.57D0*10.0**(-3.0)
ENDIF
sigma=0.0323D0
goto 20
!MIVB+WATER
                          !1 -- W/O -> O/W
IF(oINw.EQ.1)THEN
    !water in oil
    rhoC=805.0D0
    rhoD=977.0D0
    muC=0.61D0*10.0**(-3.0)
    muD=1.02D0*10.0**(-3.0)
ELSEIF(oINw.EQ.0)THEN
    !oil in water
    rhoC=977.0D0
    rhoD=805.0D0
    muC=1.02D0*10.0**(-3.0)
```

```
      muD=0.61D0*10.0**(-3.0)
ENDIF
sigma=0.0089D0

c     goto 20

!Benzene+water
IF(oINw.EQ.1)THEN
      !water in oil
      rhoC=870.0D0
      rhoD=977.0D0
      muC=0.61D0*10.0**(-3.0)
      muD=1.0D0*10.0**(-3.0)
ELSEIF(oINw.EQ.0)THEN
      !oil in water
      rhoC=977.0D0
      rhoD=870.0D0
      muC=1.0D0*10.0**(-3.0)
      muD=0.61D0*10.0**(-3.0)
ENDIF
sigma=0.03D0


20    pi=DACOS(-1.0D0)


dI=0.05D0
tV=0.102     !2.0*dI
hV=0.102     !2.0*dI

DO 100 K=1,6

rpm=200.0+K*200.0 !1200.0D0
nI=rpm/60D0

a0=0.05
a1=0.95
I=0


DO 10 WHILE (ABS(a1-a0)/a0.GT.0.0005)

alpha=(a0+a1)/2.0
I=I+1
!Density and Viscosity
rhoM=(1-alpha)*rhoC+alpha*rhoD

muM=muC/(1-alpha)*(1.0+1.5*alpha*muD/(muC+muD))
C     muM=muC*(1+2.5*alpha*((muD+0.4*muC)/(muD+muC)))

We=(nI**2.0*dI**3.0*rhoM)/sigma
vT=pi*tV**2.0*hV/4.0
!e=5.1*nI**3.0*dI**5.0/vT
e=0.99*nI**3.0*dI**2.0
e=e*(muC*rhoM/(muM*rhoC))**3D0

eb=e*5.16
ec=e*0.26
xf=0.15

!Kolmogroff microscale (m)
xkmg=(muM**3D0/(rhoM**3D0*eb))**0.25D0

!D32

nxc=-1.0*alpha**2.0+0.1625*alpha+0.5962
nx=-0.425*alpha+0.598

IF(oInw.EQ.1)THEN
nx=Max(3.0/8.0,nx)
nxc=Max(3.0/8.0,nxc)
nx=nxc
ELSE
nx=0.6
ENDIF
```

```
C    d32c=0.06*(1.0+10.0*alpha)*we**(-nxc)*dI*(muD/muC)**0.25 !test

IF(oInw.Eq.0)THEN
d32=0.08*(1.0+4.0*alpha)*we**(-nx)*dI*(muD/muC)**0.25!oil in water
ELSE
d32=0.08*(1.0+0.3*alpha)*we**(-nx)*dI*(muD/muC)**0.25!water in oil
ENDIF


!Weinstein & Treybal 1973
vi=1+2.5*alpha*((muD+0.4*muC)/(muD+muC))     !Taylor (1932)
cm=0.125D0
dc=cm*We**(-0.6)*dI*vi**1.2

c    d32=Dmax1(d32,dc)

!drop number
ntotal=6D0*alpha/(pi*d32**3D0)
C    xf=0.15
nc=(1-xf)*vT*ntotal
nb=xf*vT*ntotal

break=nb*g(d32)!*(1.0*D32**3D0)
coal=nc*nc*CR(d32,d32) !*(1.0*D32**3D0)

if(break.LT.coal)then
     a1=alpha
else
     a0=alpha
endif

IF(I.GT.100)Pause
10  continue
x(K)=alpha
write(*,'(F10.5,5x,F10.5,5x,F10.5,5x,F10.5,5x,F10.5)')
   +rpm,x(K),d32*1000000D0,nx,nxc
write(888,'(F10.5,5x,F10.5,5x,F10.5)') rpm,x(K),d32*1000000D0
100 CONTINUE
Pause

End

!----
DOUBLE PRECISION    FUNCTION CR(D1,D2)  !Coalescence Rate of I & J 1I+1J

     USE     Properties
IMPLICIT NONE

double precision  d1,d2
double precision  c1,c2,cf,ce,radial,beita
double precision  h1,h2,temp1,temp2,Q
INTEGER   I, J

C    GOTO 100
C1=2.17*10D0**(-4D0)  !1.9*10D0**(-3D0)   !2.17*10D0**(-4D0)
C2=2.28*10D0**13      !2.0*10D0**13       !2.28*10D0**13

CF=C1*ec**(1D0/3D0)/(1+alpha)*(D1+D2)**2D0*
   &          (D1**(2D0/3D0)+D2**(2D0/3D0))**(1D0/2D0)

CE=DEXP(-C2*muC*rhoC*ec*(D1*D2/(D1+D2))**4D0/
   &     (sigma**2D0*(1D0+alpha)**3D0))

!Radial distribution
beita=ntotal*D1**2D0*pi/6.0

radial=1D0/(1-alpha)+3D0*D1*D2/(D1+D2)*beita/(1D0-alpha)**2D0+
   +2D0*(D1*D2/(D1+D2))**2D0*beita**2D0/(1D0-alpha)**3D0
!Radial distribution
!    CR=CF*radial*CE
CR=CF*radial**(1.5*CE*muD/muC)*CE
!    CR=CF*CE
return
!---------------------
!Radial distribution
100 beita=ntotal*D1**2D0*pi/6.0
```

```
radial=1D0/(1-alpha)+3D0*D1*D2/(D1+D2)*beita/(1D0-alpha)**2D0+
   +2D0*(D1*D2/(D1+D2))**2D0*beita**2D0/(1D0-alpha)**3D0
!Radial distribution

C1=3.4D0
H1=0.1*(0.5*D1*D2/(D1+D2))
H2=0.0  !500.0*10D0**(-10D0)
Q=(muC/muD)*(0.5*D1*D2/(D1+D2))**0.5D0
Temp1=(H1**0.5+1.378*Q)/(H2**0.5+1.378*Q)
Temp2=(H1**0.5+0.312*Q)/(H2**0.5+0.312*Q)
C2=1.872*DLOG(Temp1)+0.127*DLOG(Temp2)

CF=0.2586*pi*ec**(1D0/3D0)*(D1+D2)**2D0*
   &          (D1**(2D0/3D0)+D2**(2D0/3D0))**(1D0/2D0)

CE=DEXP(-6D0*pi*muC*C1*C2*31.25*nI*dI/(rhoC*ec**(2D0/3D0)*
   &          (D1+D2)**(2D0/3D0)*(tV**2D0*hV)**(1D0/3D0)))

CR=CF*radial*CE
!    CR=CF*CE

END FUNCTION CR
```

Appendix J

Program for Simulation of Secondary Dispersion within a PBEs Model

```
PROGRAM MAIN

USE    Properties
IMPLICIT NONE

INTEGER, PARAMETER ::  NLoop=1200
INTEGER       IWORK, I, J, K, IOUT,M
INTEGER    ITASK, ISTATE, IOPT, LRW, LIW, MF, ITOL, IPAR, ML, MU
INTEGER       NEQ

DOUBLE PRECISION   TOUT, T, sumtemp
DOUBLE PRECISION, PARAMETER :: DT=0.5D0
DOUBLE PRECISION   Vol, D3, D2, Vole
DOUBLE PRECISION   RTOL
DOUBLE PRECISION    RPAR, RWORK
DOUBLE PRECISION   G,B, CR, JEX, FEX, Es

DOUBLE PRECISION,  ALLOCATABLE    :: ATOL(:),Y(:)
DOUBLE PRECISION,  ALLOCATABLE    :: Z2(:,:)
LOGICAL, PARAMETER ::  OinW=.FALSE.

ALLOCATABLE :: RWORK(:), IWORK(:)
EXTERNALG,B,CR, JEX, FEX, Es
!-------
ALLOCATE (CN(KC),GA(KC),DA(KC,KC),CRA(KC,KC),g12(KC,KC),
  &    CRATemp(KC,KC)  )

IF(OinW)THEN
    rhoC=996.0D0
    rhoD=867.0D0
    muC=0.96D0*10.0**(-3.0)
    muD=0.57D0*10.0**(-3.0)
ELSE
    rhoC=867.0D0
    rhoD=996.0D0
    muC=0.57D0*10.0**(-3.0)
    muD=0.96D0*10.0**(-3.0)
ENDIF
sigma=0.0323D0
pi=DACOS(-1.0D0)
e=0.1D0
alpha=0.65D0            !effective volume fraction
alphaD=0.65D0           !dispersed phase volume fraction

MeanInit=0.0004D0          !Mean drop size, m
DMax=0.0010D0              !The upper limitation of drop dia., m
rhoM=(1-alpha)*rhoC+alpha*rhoD
muM=muC*(1+2.5*alpha*((muD+0.4*muC)/(muD+muC)))
xkmg=(muC**3D0/(rhoC**3D0*e))**0.25D0  !Kolmogroff microscale (m)
Ntot=1
dDia=DMax/KC
lmax=1D0                   !maximal eddy length

!---- 2nd dispersion
a2nd=alpha-alphaD              !2nd droplets volume fraction
NEQ=KC+K2nd*KC
    ALLOCATE(ATOL(NEQ),Y(NEQ),C2nd(KC,K2nd),Z2(KC,K2nd))

CALL   NInit(CN,Y,MeanInit)
```

```
Vol=0D0
DO I =1, KC
    Vol=Vol+Y(I)*pi/6D0*(1000D0*CN(I))**3D0
ENDDO

!Calculate the total drop number
NTot=alpha/(Vol*10D0**(-9.0))
Y=NTot*Y
Vol=NTot*Vol

CALL   N2ndInit(C2nd,Z2,Y)

OPEN (11, File="C:\result.xls")
OPEN (12, File="C:\volume.xls")
OPEN (13, File="C:\result2nd.xls")

WRITE(11,'(F14.5,<KC>F14.6)')0.0,(CN(K)*1000,K=1,KC)
WRITE(11,'(F14.5,<KC>F14.6)')0.0,(Y(K)/NTot,K=1,KC)
DO I=1,KC
    WRITE(13,'(F14.5,<K2nd>E12.5)')0.0,(C2nd(I,K),K=1,K2nd)
ENDDO

DO I=1, KC
    DO J=1, K2nd
        Y((I-1)*K2nd+J+KC)=Z2(I,J)
    ENDDO
END DO

!Fill out the look up table
DA=0D0
CRA=0D0
GA=0D0

DO K=1,KC
    GA(K)=G(K)
ENDDO

DO K=1,KC
    DO I=1,K-1
        DA(I,K)=B(I,K)
    ENDDO

    sumtemp=0D0
    DO I=1,K-1
        sumtemp=sumtemp+2D0*DA(I,K)*CN(I)**3D0
    ENDDO

    IF(sumtemp.GT.0D0)THEN
        sumtemp=CN(K)**3D0/sumtemp
    ELSE
        sumtemp=sumtemp
    ENDIF

    DO I=1,K-1
        DA(I,K)=DA(I,K)*sumtemp
    ENDDO

ENDDO



DO K=1,KC
    DO I=1,KC
        CRA(K,I)=CR(K,I)
    ENDDO
ENDDO

!   lmax=es(0.0006D0,0.001D0)

   ITOL = 2
   RTOL = 1.D-4
DO I =1, NEQ
    ATOL(I)=1.D-4
END DO
```

```
      ITASK = 1
      ISTATE = 1
      IOPT = 0
      MF =10
ML=1        !FOR JACOBIAN
MU=2        !FOR JACOBIAN

IF(MF.EQ.10)THEN
      ALLOCATE(RWORK(20+16*NEQ),IWORK(30))
      LRW = 20+16*NEQ
    LIW = 30
ELSEIF(MF.EQ.21.OR.MF.EQ.22)THEN
      ALLOCATE(RWORK(22+9*NEQ+2*NEQ**2),IWORK(30+NEQ))
      LRW = 22+9*NEQ+2*NEQ**2
    LIW = 30+NEQ
ELSEIF(MF.EQ.24.OR.MF.EQ.25)THEN
      ALLOCATE(RWORK(22+11*NEQ+(3*ML+2*MU)*NEQ),IWORK(30+NEQ))
       IWORK(1) = ML
       IWORK(2) = MU
      LRW = 22+11*NEQ+(3*ML+2*MU)*NEQ
    LIW = 30+NEQ
ENDIF

T=0D0
DO IOUT = 1,NLOOP

      TOUT=IOUT*DT

      CALL DVODE(FEX,NEQ,Y,T,TOUT,ITOL,RTOL,ATOL,ITASK,ISTATE,
    &         IOPT,RWORK,LRW,IWORK,LIW,JEX,MF,RPAR,IPAR)

    IF (ISTATE .LT. 0) GO TO 80

      DO I=1, K2nd
!           K=KC+(KC-1)*K2nd+I
!           Y(KC)=Y(KC)-Y(K)*C2nd(KC,I)**3D0/CN(KC)**3D0
!           Y(K)=0D0
      ENDDO


      Vol=0D0
      D3=0D0
      D2=0D0
      NTot=0D0

      DO I =1, KC
          IF(Y(I).LT.0D0)THEN
              IF(I.GT.1)THEN
                  sumtemp=0D0
                  DO K=1,K2nd
                      M=KC+(I-1)*K2nd+K
                      sumtemp=sumtemp+Y(M)*C2nd(I,K)**3D0
                  ENDDO
                  Y(I-1)=Y(I-1)+(Y(I)*CN(I)**3D0+sumtemp)/CN(I-1)**3D0
              ELSE
                  sumtemp=0D0
                  DO K=1,K2nd
                      M=KC+(I+1-1)*K2nd+K
                      sumtemp=sumtemp+Y(M)*C2nd(I,K)**3D0
                  ENDDO
                  Y(I+1)=Y(I+1)+(Y(I)*CN(I)**3D0+sumtemp)/CN(I+1)**3D0
              ENDIF
              Y(I)=0D0
              DO K=1,K2nd
                  Y((I-1)*K2nd+K+KC)=0D0

              ENDDO
          ENDIF

          NTot=NTot+Y(I)
          Vol=Vol+Y(I)*pi/6D0*(CN(I))**3D0
          D3=D3+Y(I)*CN(I)**3D0
          D2=D2+Y(I)*CN(I)**2D0
      ENDDO

      Vole=Vol
```

```
      DO I=1,KC
         DO K=1, K2nd
            Vol=Vol-pi/6D0*C2nd(I,K)**3D0*Y((I-1)*K2nd+K+KC)
         END DO
      ENDDO

!        WRITE(11,'(F14.5,<KC>E14.6)')dt*IOUT,(Y(K)/NTot,K=1,KC)
      WRITE(11,'(F14.5,<KC>E14.6)')dt*IOUT,(Y(K),K=1,KC)
      !WRITE(11,'(F14.5,<KC>E14.6)')dt*IOUT,(Y(K),K=1,KC)

      WRITE(12,'(F14.5,2E14.6)')dt*IOUT,D3/D2*1000,Vole

      DO J=1,KC
      I=(J-1)*K2nd+KC
!        I=(16-1)*K2nd+KC
      WRITE(13,'(F14.5,<K2nd>E12.5)')dt*IOUT,(Y(I+K),K=1,K2nd)
      ENDDO

      WRITE(*,'(4F12.8)')DT*IOUT, VOL, Vole, D3/D2


   END DO


   CLOSE (11)
   CLOSE (13)

   Pause

   WRITE(*,60) IWORK(11),IWORK(12),IWORK(13),IWORK(19),
     &         IWORK(20),IWORK(21),IWORK(22)
20       FORMAT(' At t (sec)=',D12.4,';Total Volume (mm^3) =',D14.6    !)
     &         ,';C/B=',F8.5)

60    FORMAT(/' No. steps =',I4,'  No. f-s =',I4,
     &     '  No. J-s =',I4,'  No. LU-s =',I4/
     &     ' No. nonlinear iterations =',I4/
     &     ' No. nonlinear convergence failures =',I4/
     &     ' No. error test failures =',I4/)

   WRITE(*,85)ISTATE
85    FORMAT(///'ISTATE =',I3)


   IF(ISTATE.NE.2)PAUSE
   STOP

80    WRITE(*,90)ISTATE
90    FORMAT(///' Error halt: ISTATE =',I3)

   IF(ISTATE.NE.2)PAUSE
   END PROGRAM MAIN

   DOUBLE PRECISION FUNCTION    Es (d2nd,D)

   USE PROPERTIES
   IMPLICIT NONE

   DOUBLE PRECISION    d2nd, D
   DOUBLE PRECISION    mtot, Ca, Ah
   DOUBLE PRECISION    temp1,temp2, tc, alphaCr, temp3,sr

   sr=20D0

   temp2=2.22+1.51*(muD/muC)**(-0.57)
   alphaCr=1D0-dexp(-temp2*d2nd/D)

   Ca=0.5*D*muC*sr/sigma

   if (Ca>10.7D0)Then
      pause
   endif

   temp2=muD/muC
   mtot=(1+temp2)/(temp2*(1+temp2))**0.5+95.0*temp2*(19.0*temp2+16.0)
```

```
   +/(4.0*((19*temp2)**2D0+(20.0/Ca)**2D0))*(5D0-
   +(1D0+temp2)*(25D0*temp2**2D0+50*temp2-31D0)/(5D0*(
   +temp2*(temp2+2D0))**1.5))

!    temp1=mtot
!    tc=4D0*pi/(1D0-temp1**2D0)**0.5D0/(e**(1.0/3.0)*D**(-2D0/3D0))
!    tc=4D0*pi*mtot/(e**(1.0/3.0)*D**(-2D0/3D0))
tc=4D0*pi*mtot/sr


Ah=4.88*10D0**(-21.0)

temp3=((pi*sigma*0.25*d2nd**2D0)/(2.0*Ah))**(-4.0*(1.0+temp2)/
   +(9.0*pi*mtot))
!Es=2.0*temp3*alphaCr/tc
Es=2.0*temp3/tc*1.0

END FUNCTION    Es

DOUBLE PRECISION    FUNCTION Es_Inc (I,J,Y,DYtemp)
!Birth rate and Death rate of 2nd droplets
!Due to escape and inclusion

USE Properties
IMPLICIT NONE

INTEGER    I,J,K,N1
DOUBLE PRECISION    Y(KC+KC*K2nd)
DOUBLE PRECISION    V1,V2,Vij
DOUBLE PRECISION    VTemp,Vol2nd,DYtemp


DOUBLE PRECISION    ES
EXTERNALES

K=KC+(I-1)*K2nd+J
Es_Inc=-es(C2nd(I,J),CN(I))*Y(K)

VTemp=0D0

DO N1=1,K2nd
    K=KC+(I-1)*K2nd+N1
    VTemp=Y(K)*C2nd(I,N1)**3D0+VTemp
ENDDO

c    Vol2nd=VTemp/(Y(I)*CN(I)**3D0)

Vol2nd=VTemp/Y(I)
!    DYTEMP=Es_Inc*C2nd(I,J)**3D0/(CN(I)**3D0)   !-Vol2nd)
IF(Y(K)/Y(I).LE.0D0)THEN
    DYTEMP=0D0
ELSE
    DYTEMP=Es_Inc/(Y(K)/Y(I))
ENDIF

IF(I.EQ.1)   THEN
DYTEMP=0D0
Es_Inc=0D0
ENDIF

END FUNCTION Es_Inc

DOUBLE PRECISION    FUNCTION Inclusion (N,Y)
!Birth rate and Death rate of size D
!Due to breakage and coalescence

USE Properties
IMPLICIT NONE
DOUBLE PRECISION    DN              !Drop diameter of N, m
DOUBLE PRECISION    VN              !Volume of N, m^3
DOUBLE PRECISION    V0              !Volume of Max(N&Stable), m^3
DOUBLE PRECISION    Y(*)
DOUBLE PRECISION    D0              !Max(dc,d)
DOUBLE PRECISION    B               !Daughter distribution function
DOUBLE PRECISION    G               !Breakage frequency function
DOUBLE PRECISION    DK,VK,DJ,VJ         !VK+VJ->X*VN+(1-X)*VN-1
```

```
DOUBLE PRECISION  DN1,VN1          !D(N-1), V(N-1)
DOUBLE PRECISION  DN2,VN2          !D(N+1), V(N+1)
DOUBLE PRECISION  CR               !Coalescence rate of VK & VJ
DOUBLE PRECISION  X1,X2
DOUBLE PRECISION  CTemp1,CTemp2

INTEGER  N                         !Size Class
INTEGER  K,J
INTEGER  IClass
INTEGER  NDaughter                 !=2 for binary breakage
INTEGER  IV                        !External Function
INTEGER  IHalfV                    !Index of V/2
INTEGER  IComp                     !Index of Compensary Part of V1
INTEGER  IStore

EXTERNALB
EXTERNALG
EXTERNALIV
EXTERNALCR

DN=CN(N)
VN=pi*DN**3D0/6D0

NDaughter=2
Inclusion=0.0D0

!Death rate due to drop coalecence with this class
25  DO 20 K=1, KC
    IF(K.EQ.N)THEN
    Inclusion=Inclusion-2.0*CRA(N,K)*Y(N)*Y(K)
    ELSE
    Inclusion=Inclusion-CRA(N,K)*Y(N)*Y(K)
    ENDIF
20  ENDDO

!Birth rate due to smaller drop coalescence

IF(N.EQ.1) THEN
    CTemp1=0D0
    VK=VN
    DJ=CN(2)
    VJ=pi*DJ**3D0/6D0
    X1=(VJ-2D0*VK)/(VJ-VK)
    CTemp1=X1*CRA(1,1)*Y(1)*Y(1)
    Inclusion=Inclusion+CTemp1
RETURN
ENDIF

DN1=CN(N-1)
VN1=pi*DN1**3D0/6D0
CTemp1=0D0

DO 40 K=1,N-1
    DK=CN(K)
    VK=pi*DK**3D0/6D0
    DO 30 J=1,N-1
        DJ=CN(J)
        VJ=pi*DJ**3D0/6D0
        IF(VK+VJ.GT.VN1.AND.VK+VJ.LE.VN)THEN
            X1=(VK+VJ-VN1)/(VN-VN1)
            IF(J.EQ.K)THEN
                CTemp1=CTemp1+2D0*X1*CRA(K,J)*Y(K)*Y(J)
            ELSE
                CTemp1=CTemp1+X1*CRA(K,J)*Y(K)*Y(J)
            ENDIF
        ENDIF
30      ENDDO
40  ENDDO

Inclusion=Inclusion+0.5D0*CTemp1

IF(N.EQ.KC)THEN
    CTemp2=0D0
    DO 60 K=1,N
        DK=CN(K)
        VK=pi*DK**3D0/6D0
```

```
        DO 50 J=1,N
            DJ=CN(J)
            VJ=pi*DJ**3D0/6D0
            IF(VK+VJ.GT.VN)THEN
                X2=(VK+VJ)/VN
                IF(J.EQ.K)THEN
                    CTemp2=CTemp2+2D0*X2*CRA(K,J)*Y(K)*Y(J)
                ELSE
                    CTemp2=CTemp2+X2*CRA(K,J)*Y(K)*Y(J)
                ENDIF
            ENDIF
50          ENDDO
60      ENDDO
    CTemp2=CTemp2

ELSE
    DN2=CN(N+1)
    VN2=pi*DN2**3D0/6D0
    CTemp2=0D0

    DO 80 K=1,N
        DK=CN(K)
        VK=pi*DK**3D0/6D0
        DO 70 J=1,N
            DJ=CN(J)
            VJ=pi*DJ**3D0/6D0
            IF(VK+VJ.GT.VN.AND.VK+VJ.LE.VN2)THEN
                X2=(VN2-VK-VJ)/(VN2-VN)
                IF(J.EQ.K)THEN
                    CTemp2=CTemp2+2D0*X2*CRA(K,J)*Y(K)*Y(J)
                ELSE
                    CTemp2=CTemp2+X2*CRA(K,J)*Y(K)*Y(J)
                ENDIF
            ENDIF
70          ENDDO
80      ENDDO

ENDIF

Inclusion=Inclusion+0.5D0*CTemp2

100 END    FUNCTION INCLUSION

!----
SUBROUTINE  NInit(DropSize,DropN,Mean)

USE Properties
IMPLICIT NONE

INTEGER   I

DOUBLE PRECISION   DropSize(1:KC)  !Drop Size Class
DOUBLE PRECISION   DropN(1:KC)     !Drop Number

DOUBLE PRECISION   Mean            !Mean dia, m
DOUBLE PRECISION   Dev             !Deviation of dia, m
DOUBLE PRECISION   XN1                 !Temporary variant
DOUBLE PRECISION   XN2                 !Temporary variant

Dev=Mean/3D0

DO 10 I=1, KC

    DropSize(I)=dDia*I  !xkmg+I*dDia
    XN1=DEXP(-0.5*((DropSize(I)-Mean)/Dev)**2.0)
   &            /(DSQRT(2.0*pi)*Dev)
    XN2=DEXP(-0.5*(((I-1)*dDia-Mean)/Dev)**2.0)
   &            /(DSQRT(2.0*pi)*Dev)


    DropN(I)=(XN1+XN2)*0.5*dDia*NTot
!       DropN(I)=1D0/KC*NTot

10  END DO

END SUBROUTINE NInit
```

```
!-----
SUBROUTINE  N2ndInit(DS2nd,DN2nd,Y)

USE Properties
IMPLICIT NONE
DOUBLE PRECISION   DS2nd(KC,K2nd)        !2nd Drop Size Index
DOUBLE PRECISION   DN2nd(KC,K2nd)
DOUBLE PRECISION   Y(KC+K2nd*KC)
DOUBLE PRECISION   Dd2, Vd2
INTEGER   K,J

DO K=1, KC
    DS2nd(K,K2nd)=fv2nd**(1D0/3D0)*CN(K)
    Dd2=DS2nd(K,K2nd)/K2nd
    DO J=1, K2nd
        DS2nd(K,J)=Dd2*J
    ENDDO
ENDDO

DN2nd=0D0

DO K=1, KC
    Vd2=0D0
    DO J=1, K2nd
        Vd2=Vd2+DS2nd(K,J)**3D0
    ENDDO

    DO J=1, K2nd
        DN2nd(K,J)=a2nd/alpha*Y(K)*CN(K)**3D0/Vd2
    ENDDO

ENDDO

!   DN2ND=a2nd/Vd2

END SUBROUTINE N2ndInit

MODULE Properties
DOUBLE PRECISION   rhoC
DOUBLE PRECISION   rhoD
DOUBLE PRECISION   rhoM
DOUBLE PRECISION   muC
DOUBLE PRECISION   muD
DOUBLE PRECISION   muM
DOUBLE PRECISION   sigma
DOUBLE PRECISION   usC
DOUBLE PRECISION   usD
DOUBLE PRECISION   alphaD, alpha
DOUBLE PRECISION   dc              !Maximum stable drop size, m

!For Impeller
DOUBLE PRECISION   pi
DOUBLE PRECISION   Web
DOUBLE PRECISION   vi              !Viscosity damping
DOUBLE PRECISION   cm              !Coefficient for dc
DOUBLE PRECISION   WebCrit         !Critical Web number
DOUBLE PRECISION   xkmg            !Komogorov length,m

DOUBLE PRECISION   NTot, BX
DOUBLE PRECISION   MeanInit        !
DOUBLE PRECISION,  ALLOCATABLE     :: CN(:)
DOUBLE PRECISION   DMax            !Max. drop diamter, m
DOUBLE PRECISION   dDia
DOUBLE PRECISION,  ALLOCATABLE     :: GA(:) !Breakage Array storing G(I)
DOUBLE PRECISION,  ALLOCATABLE     :: DA(:,:)    !Daughter Dist. Array
DOUBLE PRECISION,  ALLOCATABLE     :: CRA(:,:)   !Coalecscence Rate Array
DOUBLE PRECISION,  ALLOCATABLE     :: D32(:)!Sauter mean diameter
DOUBLE PRECISION,  AllOCATABLE :: g12(:,:)!radial distribution
DOUBLE PRECISION,  AllOCATABLE :: CRATemp(:,:)!temp. matrix for coa

DOUBLE PRECISION   e               !Energy dissipation, m^2/s^3
DOUBLE PRECISION   lmax            !maximum eddy size

INTEGER, PARAMETER :: KC=30, BModel=4, DModel=8, CModel=1
```

```
!2nd dispersion
INTEGER, PARAMETER :: K2nd=10
DOUBLE PRECISION,  ALLOCATABLE    :: C2ND(:,:) !2nd drop size catogories
DOUBLE PRECISION, PARAMETER :: fv2nd=0.8D0      !maximum 2nd size interms of volume
DOUBLE PRECISION, PARAMETER :: Espara=1D0       !maximum 2nd size interms of volume
!   DOUBLE PRECISION   Espara
DOUBLE PRECISION   a2nd             !2nd drop total volume fraction
DOUBLE PRECISION, PARAMETER :: coa2nd=0.5D0     !parameter of 2nd droplet coalesence
END MODULE PROPERTIES

DOUBLE PRECISION   FUNCTION B_D (N,Y)
!Birth rate and Death rate of size D
!Due to breakage and coalescence

USE Properties
IMPLICIT NONE
DOUBLE PRECISION   DN              !Drop diameter of N, m
DOUBLE PRECISION   VN              !Volume of N, m^3
DOUBLE PRECISION   V0              !Volume of Max(N&Stable), m^3
DOUBLE PRECISION   Y(*)
DOUBLE PRECISION   D0              !Max(dc,d)
DOUBLE PRECISION   B               !Daughter distribution function
DOUBLE PRECISION   G               !Breakage frequency function
DOUBLE PRECISION   DK,VK,DJ,VJ        !VK+VJ->X*VN+(1-X)*VN-1
DOUBLE PRECISION   DN1,VN1            !D(N-1), V(N-1)
DOUBLE PRECISION   DN2,VN2            !D(N+1), V(N+1)
DOUBLE PRECISION   CR              !Coalescence rate of VK & VJ
DOUBLE PRECISION   X1,X2
DOUBLE PRECISION   CTemp1,CTemp2

INTEGER   N                        !Size Class
INTEGER   K,J
INTEGER   IClass
INTEGER   NDaughter                !=2 for binary breakage
INTEGER   IV                       !External Function
INTEGER   IHalfV                   !Index of V/2
INTEGER   IComp                    !Index of Compensary Part of V1
INTEGER   IStore

EXTERNALB
EXTERNALG
EXTERNALIV
EXTERNALCR

DN=CN(N)
VN=pi*DN**3D0/6D0

NDaughter=2
B_D=0.0D0

C   GOTO 25

!Birth rate due to larger drop breakage
DO K=N+1,KC
    B_D=B_D+BX*NDaughter*DA(N,K)*GA(K)*Y(K)
ENDDO

!Death rate to this class drop breakage
B_D=B_D-GA(N)*Y(N)

C   Return

!Death rate due to drop coalecence with this class
25  DO 20 K=1, KC
    IF(K.EQ.N)THEN
    B_D=B_D-2.0*CRA(N,K)*Y(N)*Y(K)
    ELSE
    B_D=B_D-CRA(N,K)*Y(N)*Y(K)
    ENDIF
20  ENDDO

!Birth rate due to smaller drop coalescence

IF(N.EQ.1) THEN
    CTemp1=0D0
    VK=VN
```

```
      DJ=CN(2)
      VJ=pi*DJ**3D0/6D0
      X1=(VJ-2D0*VK)/(VJ-VK)
      CTemp1=X1*CRA(1,1)*Y(1)*Y(1)
      B_D=B_D+CTemp1
RETURN
ENDIF

DN1=CN(N-1)
VN1=pi*DN1**3D0/6D0
CTemp1=0D0

DO 40 K=1,N-1
      DK=CN(K)
      VK=pi*DK**3D0/6D0
      DO 30 J=1,N-1
            DJ=CN(J)
            VJ=pi*DJ**3D0/6D0
            IF(VK+VJ.GT.VN1.AND.VK+VJ.LE.VN)THEN
                  X1=(VK+VJ-VN1)/(VN-VN1)
                  IF(J.EQ.K)THEN
                        CTemp1=CTemp1+2D0*X1*CRA(K,J)*Y(K)*Y(J)
                  ELSE
                        CTemp1=CTemp1+X1*CRA(K,J)*Y(K)*Y(J)
                  ENDIF
            ENDIF
30          ENDDO
40    ENDDO

B_D=B_D+0.5D0*CTemp1

IF(N.EQ.KC)THEN
      CTemp2=0D0
      DO 60 K=1,N
            DK=CN(K)
            VK=pi*DK**3D0/6D0
            DO 50 J=1,N
                  DJ=CN(J)
                  VJ=pi*DJ**3D0/6D0
                  IF(VK+VJ.GT.VN)THEN
                        X2=(VK+VJ)/VN
                        IF(J.EQ.K)THEN
                              CTemp2=CTemp2+2D0*X2*CRA(K,J)*Y(K)*Y(J)
                        ELSE
                              CTemp2=CTemp2+X2*CRA(K,J)*Y(K)*Y(J)
                        ENDIF
                  ENDIF
50                ENDDO
60          ENDDO
      CTemp2=CTemp2

ELSE
      DN2=CN(N+1)
      VN2=pi*DN2**3D0/6D0
      CTemp2=0D0

      DO 80 K=1,N
            DK=CN(K)
            VK=pi*DK**3D0/6D0
            DO 70 J=1,N
                  DJ=CN(J)
                  VJ=pi*DJ**3D0/6D0
                  IF(VK+VJ.GT.VN.AND.VK+VJ.LE.VN2)THEN
                        X2=(VN2-VK-VJ)/(VN2-VN)
                        IF(J.EQ.K)THEN
                              CTemp2=CTemp2+2D0*X2*CRA(K,J)*Y(K)*Y(J)
                        ELSE
                              CTemp2=CTemp2+X2*CRA(K,J)*Y(K)*Y(J)
                        ENDIF
                  ENDIF
70                ENDDO
80          ENDDO

ENDIF

B_D=B_D+0.5D0*CTemp2
```

```
100 END    FUNCTION B_D

!!!!
SUBROUTINE FEX(NEQ, T, Y, YDOT, RPAR, IPAR)

    USE    Properties
IMPLICIT NONE
INTEGER   NEQ,IPAR,NDAUGHTER
DOUBLE PRECISION RPAR, T, Y, YDOT
!   DOUBLE PRECISION   TV1,TV2
DIMENSION Y(NEQ), YDOT(NEQ)

DOUBLE PRECISION   d1
DOUBLE PRECISION   B_D
DOUBLE PRECISION   G
DOUBLE PRECISION   NDrop,DYTEMP
DOUBLE PRECISION   Dtemp1, temp2,BR, te3, temp3, sumtemp
DOUBLE PRECISION   DK,FK, FK2, F2nd,F2ndJ, df2nd, Pv2nd
DOUBLE PRECISION   dk2nd
DOUBLE PRECISION   FB, Pmean, Pdev, Pdis(1:K2nd)
INTEGER   I,K,J,M,N,L,H,Iv

DOUBLE PRECISION   Es_Inc
EXTERNALEs_Inc

YDOT=0D0

!   go to 60
!   breakage of mother drops which have secondary droplets inside
NDaughter=2
DO I=1, KC
    !death due to itself breakage
    YDOT(I)=YDOT(I)-GA(I)*Y(I)
    FB=DMin1(GA(I),0.5D0)          !***
    DO J=1,K2nd
        K=KC+(I-1)*K2nd+J
        YDOT(K)=YDOT(K)-FB*Y(K)
    ENDDO

    !Birth rate due to larger drop breakage
!       DO K=I+1,KC
!           YDOT(I)=YDOT(I)+NDaughter*DA(I,K)*GA(K)*Y(K)

    DO K=1,I-1
        YDOT(K)=YDOT(K)+NDaughter*DA(K,I)*GA(I)*Y(I)
    ENDDO

    !2nd increase due to breakage of big drops
    DO J=1,I-1
        BR=Ndaughter*DA(J,I)*CN(J)**3D0/CN(I)**3D0       !----????


        DO K=1,K2nd
            L=KC+(I-1)*K2nd+K
            IF(C2nd(I,K).LT.C2nd(J,K2nd))THEN
                M=1
                DO WHILE(C2nd(I,K).GT.C2nd(J,M))
                    M=M+1
                ENDDO
                N=KC+(J-1)*K2nd+M-1
                YDOT(N)=YDOT(N)+BR*FB*Y(L)*C2nd(I,K)**3D0/C2nd(J,M-1)**3D0
            ELSEIF(C2nd(I,K).GE.C2nd(J,K2nd))THEN
!                   sumtemp=0D0
!                   DO M=1,K2nd
!                       sumtemp=sumtemp+C2nd(J,M)**3D0
!                   ENDDO
!                   DO M=1,K2nd
!                       N=KC+(J-1)*K2nd+M
!                       YDOT(N)=YDOT(N)+BR*FB*Y(L)*C2nd(I,K)**3D0
! +                                 /Sumtemp
!                   ENDDO


!               N=KC+(J-1)*K2nd+K2nd
!               YDOT(N)=YDOT(N)+BR*FB*Y(L)*C2nd(I,K)**3D0/C2nd(J,K2nd)**3D0
```

```
!                       YDOT(N)=YDOT(N)+BR*FB*Y(L)*C2nd(I,K)**3D0/C2nd(J,K2nd/2)**3D0
!                       sumtemp=sumtemp+BR*FB*Y(L)*C2nd(I,K)**3D0
                    YDOT(J)=YDOT(J)-BR*FB*Y(L)*C2nd(I,K)**3D0/CN(J)**3D0
                ENDIF
            ENDDO


        ENDDO

    ENDDO

!   return
!   go to 60
!   escape of secondary droplets


160 DO I=1,KC
        DO J=1,K2nd
        K=KC+(I-1)*K2nd+J
        DYTEMP=0D0

        te3=0D0

        IF(Y(I).LE.0D0)THEN
            YDOT(K)=0D0
            YDOT(I)=0D0
            GOTO  50
        ELSEIF(Y(K).LE.0D0)THEN
            Y(K)=0D0
            GOTO  50
        ELSE
            te3=Es_Inc(I,J,Y,DYtemp)
            YDOT(K)=te3+YDOT(K)
            YDOT(I)=EsPara*DYTEMP+YDOT(I)
        ENDIF

!           Dtemp1=(CN(I)**3D0-C2nd(I,J)**3D0)**(1D0/3D0)
        Dtemp1=(CN(I)**3D0-Y(K)/Y(I)*C2nd(I,J)**3D0)**(1D0/3D0)

        IF(Dtemp1.LE.CN(1))THEN
!                   YDOT(1)=-(Espara-1.0)*DYTEMP*CN(I)**3D0/CN(1)**3D0+YDOT(1)
            YDOT(1)=(-DYTEMP*CN(I)**3D0+te3*C2nd(I,J)**3D0)/CN(1)**3D0+YDOT(1)
        ELSE
            M=1
            DO WHILE(CN(M)<Dtemp1.AND.M<KC)
                M=M+1
            ENDDO
            IF(M>1)THEN
                FK=(Dtemp1**3D0-CN(M)**3D0)/(CN(M-1)**3D0-CN(M)**3D0)

!                   YDOT(M)=-(Espara-1.0)*DYTEMP*CN(I)**3D0/CN(M)**3D0+YDOT(M)
                YDOT(M-1)=FK*(-DYTEMP*CN(I)**3D0+te3*C2nd(I,J)**3D0)
     &                  /CN(M-1)**3D0+YDOT(M-1)
                YDOT(M)=(1-FK)*(-DYTEMP*CN(I)**3D0+te3*C2nd(I,J)**3D0)
     &                      /CN(M)**3D0+YDOT(M)
            ELSE
                YDOT(M)=(-DYTEMP*CN(I)**3D0+te3*C2nd(I,J)**3D0)/CN(M)**3D0
     &              +YDOT(M)
            ENDIF
        ENDIF


50      ENDDO
    ENDDO

!   return
!coalescence

60  DO I =1, KC
        DO J=1, I
        !for class I
            YDOT(I)=YDOT(I)-CRA(I,J)*Y(I)*Y(J)

            !future consideration
            IF(CRA(I,J).LE.0D0)THEN
                F2nd=0D0
```

```
            ELSE
                F2nd=Dmin1(CRA(I,J)*Y(I)*Y(J)/Y(I)*1.0,0.99D0)
            ENDIF

            DO K=1,K2nd
                M=KC+(I-1)*K2nd+K    !Y2nd index
                YDOT(M)=YDOT(M)-F2nd*Y(M)
            ENDDO

        !for class J
            YDOT(J)=YDOT(J)-CRA(I,J)*Y(I)*Y(J)

            !future consideration on the fraction of secondary droplets going with mother drop
            IF(CRA(I,J).LE.0D0)THEN
                F2ndJ=0D0
            ELSE
                F2ndJ=Dmin1(CRA(I,J)*Y(I)*Y(J)/Y(J)*1.0,0.99D0)
            ENDIF

            DO K=1,K2nd
                M=KC+(J-1)*K2nd+K    !Y2nd index
                YDOT(M)=YDOT(M)-F2ndJ*Y(M)
            ENDDO
        !the fraction of creating secondary droplets
            temp2=CN(I)*CN(J)/(CN(I)+CN(J))    !relevant diameter
            df2nd=1.0-Dexp(-0.50*(e*temp2)**
     +      (1D0/3D0)*(muD/muC)**0.2/sigma**1.0)

            df2nd=df2nd*coa2nd

!!      If there is no secondary droplets created

            !careful for this when having inclusion
            DK=(CN(I)**3D0+CN(J)**3D0)**(1D0/3D0)

            IF(DK.GE.CN(KC))THEN          ! if formed drop > largest drop
                YDOT(KC)=YDOT(KC)+(1-df2nd)*CRA(I,J)*Y(I) !*
     +              *Y(J)*DK**3D0/CN(KC)**3D0
                DO K=1,K2nd

                    !for droplets from Ith mother drop
                    M=KC+(I-1)*K2nd+K
                    IF(C2nd(I,K).LE.C2nd(KC,1))THEN
                        N=KC+(KC-1)*K2nd+1
                        YDOT(N)=YDOT(N)+(1-df2nd)*F2nd*Y(M)*C2nd(I,K)**3D0  !*
     +                          /C2nd(KC,1)**3D0
                    ELSE
                        L=1
                        DO WHILE(C2nd(I,K).GT.C2nd(KC,L))
                            L=L+1
                        ENDDO
                        N=KC+(KC-1)*K2nd+L

                        !split the droplet
                        FK2=(C2nd(I,K)**3D0-C2nd(KC,L)**3D0)/
     +                      (C2nd(KC,L-1)**3D0-C2nd(KC,L)**3D0)

                        YDOT(N-1)=YDOT(N-1)+(1-df2nd)*F2nd*Y(M)*FK2
                        YDOT(N)=YDOT(N)+(1-df2nd)*F2nd*Y(M)*(1D0-FK2)

                    ENDIF

                    !for droplets from Jth mother drop
                    M=KC+(J-1)*K2nd+K
                    IF(C2nd(J,K).LE.C2nd(KC,1))THEN
                        N=KC+(KC-1)*K2nd+1
                        YDOT(N)=YDOT(N)+(1-df2nd)*F2ndJ*Y(M)*C2nd(J,K)**3D0 !*
     +                          /C2nd(KC,1)**3D0
                    ELSE
                        L=1
                        DO WHILE(C2nd(J,K).GT.C2nd(KC,L))
                            L=L+1
                        ENDDO
                        N=KC+(KC-1)*K2nd+L

                        !split the droplet
```

```
                FK2=(C2nd(J,K)**3D0-C2nd(KC,L)**3D0)/
+                   (C2nd(KC,L-1)**3D0-C2nd(KC,L)**3D0)

                YDOT(N-1)=YDOT(N-1)+(1-df2nd)*F2ndJ*Y(M)*FK2
                YDOT(N)=YDOT(N)+(1-df2nd)*F2ndJ*Y(M)*(1D0-FK2)
            ENDIF

        ENDDO
    ELSE                !if formed drop is < largest

        H=1
        DO WHILE(CN(H).LE.DK)
            H=H+1
        ENDDO

        !careful for this when having inclusion
        FK=(DK**3D0-CN(H)**3D0)/(CN(H-1)**3D0-CN(H)**3D0)


    YDOT(H-1)=YDOT(H-1)+(1-df2nd)*FK*CRA(I,J)*Y(I)*Y(J)                    !*
    !for drop H-1 from Ith

        !2nd droplets re-distribution
        DO K=1,K2nd

            !for droplets from Ith mother drop
            M=KC+(I-1)*K2nd+K
            IF(C2nd(I,K).LE.C2nd(H-1,1))THEN
                N=KC+(H-1-1)*K2nd+1
                YDOT(N)=YDOT(N)+(1-df2nd)*F2nd*Y(M)*C2nd(I,K)**3D0  !*
+                       *FK/C2nd(H-1,1)**3D0
            ELSE
                L=1
                DO WHILE(C2nd(I,K).GT.C2nd(H-1,L))
                    L=L+1
                ENDDO
                N=KC+(H-1-1)*K2nd+L

                !split the droplet
                FK2=(C2nd(I,K)**3D0-C2nd(H-1,L)**3D0)/
+                   (C2nd(H-1,L-1)**3D0-C2nd(H-1,L)**3D0)

                YDOT(N-1)=YDOT(N-1)+(1-df2nd)*F2nd*Y(M)*FK2*FK
                YDOT(N)=YDOT(N)+(1-df2nd)*F2nd*Y(M)*(1D0-FK2)*FK
            ENDIF
        ENDDO
    !for drop H-1 from Jth
        DO K=1,K2nd
            !for droplets from Jth mother drop
            M=KC+(J-1)*K2nd+K
            IF(C2nd(J,K).LE.C2nd(H-1,1))THEN
                N=KC+(H-1-1)*K2nd+1
                YDOT(N)=YDOT(N)+(1-df2nd)*F2ndJ*Y(M)*C2nd(J,K)**3D0 !*
+                       *FK/C2nd(H-1,1)**3D0
            ELSE
                L=1
                DO WHILE(C2nd(J,K).GT.C2nd(H-1,L))
                    L=L+1
                ENDDO
                N=KC+(H-1-1)*K2nd+L

                !split the droplet
                FK2=(C2nd(J,K)**3D0-C2nd(H-1,L)**3D0)/
+                   (C2nd(H-1,L-1)**3D0-C2nd(H-1,L)**3D0)

                YDOT(N-1)=YDOT(N-1)+(1-df2nd)*F2ndJ*Y(M)*FK2*FK
                YDOT(N)=YDOT(N)+(1-df2nd)*F2ndJ*Y(M)*(1D0-FK2)*FK
            ENDIF

        ENDDO

    YDOT(H)=YDOT(H)+(1-df2nd)*(1-FK)*CRA(I,J)*Y(I)*Y(J)          !*
    !for drop H from Ith

        !2nd droplets re-distribution
        DO K=1,K2nd
```

```
                !for droplets from Ith mother drop
                M=KC+(I-1)*K2nd+K
                IF(C2nd(I,K).LE.C2nd(H,1))THEN
                    N=KC+(H-1)*K2nd+1
                    YDOT(N)=YDOT(N)+F2nd*Y(M)*C2nd(I,K)**3D0*        !*
     +                  (1-df2nd)*(1-FK)/C2nd(H,1)**3D0
                ELSE
                    L=1
                    DO WHILE(C2nd(I,K).GE.C2nd(H,L))
                        L=L+1
                    ENDDO
                    N=KC+(H-1)*K2nd+L

                    !split the droplet
                    FK2=(C2nd(I,K)**3D0-C2nd(H,L)**3D0)/
     +                  (C2nd(H,L-1)**3D0-C2nd(H,L)**3D0)

                    YDOT(N-1)=YDOT(N-1)+F2nd*Y(M)*FK2*(1-df2nd)*(1-FK)
                    YDOT(N)=YDOT(N)+F2nd*Y(M)*(1D0-FK2)      !*
     +                  *(1-df2nd)*(1-FK)
                ENDIF
            ENDDO

        !for drop H from Jth

            DO K=1,K2nd
                !for droplets from Jth mother drop
                M=KC+(J-1)*K2nd+K
                IF(C2nd(J,K).LE.C2nd(H,1))THEN
                    N=KC+(H-1)*K2nd+1
                    YDOT(N)=YDOT(N)+F2ndJ*Y(M)*C2nd(J,K)**3D0
     +                  *(1-df2nd)*(1-FK)/C2nd(H,1)**3D0        !*
                ELSE
                    L=1
                    DO WHILE(C2nd(J,K).GT.C2nd(H,L))
                        L=L+1
                    ENDDO
                    N=KC+(H-1)*K2nd+L

                    !split the droplet
                    FK2=(C2nd(J,K)**3D0-C2nd(H,L)**3D0)/
     +                  (C2nd(H,L-1)**3D0-C2nd(H,L)**3D0)


                    YDOT(N-1)=YDOT(N-1)+F2ndJ*Y(M)*FK2
     +                  *(1-df2nd)*(1-FK)        !*
                    YDOT(N)=YDOT(N)+F2ndJ*Y(M)*(1D0-FK2)
     +                  *(1-df2nd)*(1-FK)        !*
                ENDIF

            ENDDO
        ENDIF

!!  Coalescence when creating secondary droplets

!           distribution of secodnary droplets included by coalescence
        temp3=0D0
        Pmean=(0.5D0)**(1D0/3D0)*DMax1(C2nd(I,K2nd),C2nd(J,K2nd))
        Pdev=1D0/3D0*Pmean
        DO Iv=1,K2nd
            dk2nd=DMax1(C2nd(I,K2nd),C2nd(J,K2nd))*Iv/K2nd   !2nd droplet size
            Pdis(Iv)=DEXP(-0.5D0*((dk2nd-Pmean)/Pdev)**2D0)
     &          /(DSQRT(2D0*pi)*Pdev)
            Pdis(Iv)=Pdis(Iv)*DMax1(C2nd(I,K2nd),C2nd(J,K2nd))/K2nd
            temp3=Pdis(Iv)+temp3
        ENDDO
        !normaliz the distribution make sure sum to 1
        DO Iv=1,K2nd
            Pdis(Iv)=Pdis(Iv)/temp3
        ENDDO

        !careful for this when having inclusion

        DO 55 Iv=1,K2nd
```

```
            Pv2nd=Pdis(Iv)
            dk2nd=DMax1(C2nd(I,K2nd),C2nd(J,K2nd))*Iv/K2nd   !2nd droplet size

            DK=(CN(I)**3D0+CN(J)**3D0+dk2nd**3D0)**(1D0/3D0)

            IF(DK.GE.CN(KC))THEN          ! if formed drop > largest drop

                YDOT(KC)=YDOT(KC)+df2nd*CRA(I,J)*Y(I)     !*
     +              *Y(J)*DK**3D0/CN(KC)**3D0*Pv2nd
                DO K=1,K2nd

                    !for droplets from Ith mother drop
                    M=KC+(I-1)*K2nd+K
                    IF(C2nd(I,K).LE.C2nd(KC,1))THEN
                        N=KC+(KC-1)*K2nd+1
                        YDOT(N)=YDOT(N)+df2nd*F2nd*Y(M)*C2nd(I,K)**3D0 !*
     +                      /C2nd(KC,1)**3D0*Pv2nd
                    ELSE
                        L=1
                        DO WHILE(C2nd(I,K).GT.C2nd(KC,L))
                            L=L+1
                        ENDDO
                        N=KC+(KC-1)*K2nd+L


                        !split the droplet
                        FK2=(C2nd(I,K)**3D0-C2nd(KC,L)**3D0)/
     +                      (C2nd(KC,L-1)**3D0-C2nd(KC,L)**3D0)

                        YDOT(N-1)=YDOT(N-1)+df2nd*F2nd*Y(M)*Pv2nd*FK2
                        YDOT(N)=YDOT(N)+df2nd*F2nd*Y(M)*Pv2nd*(1d0-FK2)



!                           YDOT(N)=YDOT(N)+df2nd*F2nd*Y(M)*C2nd(I,K)**3D0 !*
!    +                          /C2nd(KC,L)**3D0*Pv2nd
                    ENDIF

                    !for droplets from Jth mother drop
                    M=KC+(J-1)*K2nd+K
                    IF(C2nd(J,K).LE.C2nd(KC,1))THEN
                        N=KC+(KC-1)*K2nd+1
                        YDOT(N)=YDOT(N)+df2nd*F2ndJ*Y(M)*C2nd(J,K)**3D0     !*
     +                      /C2nd(KC,1)**3D0*Pv2nd
                    ELSE
                        L=1
                        DO WHILE(C2nd(J,K).GT.C2nd(KC,L))
                            L=L+1
                        ENDDO
                        N=KC+(KC-1)*K2nd+L

                        !split the droplet
                        FK2=(C2nd(J,K)**3D0-C2nd(KC,L)**3D0)/
     +                      (C2nd(KC,L-1)**3D0-C2nd(KC,L)**3D0)

                        YDOT(N-1)=YDOT(N-1)+df2nd*F2ndJ*Y(M)*Pv2nd*FK2
                        YDOT(N)=YDOT(N)+df2nd*F2ndJ*Y(M)*Pv2nd*(1D0-FK2)

!                           YDOT(N)=YDOT(N)+df2nd*F2ndJ*Y(M)*C2nd(J,K)**3D0     !*
!    +                          /C2nd(KC,L)**3D0*Pv2nd
                    ENDIF

                ENDDO

            !secondary droplets created from I+J coalescence into KC
                IF(dk2nd.LE.C2nd(KC,1))THEN
                    N=KC+(KC-1)*K2nd+1
                    YDOT(N)=YDOT(N)+df2nd*CRA(I,J)*Y(I)    !*
     +                  *Y(J)*dk2nd**3D0/C2nd(KC,1)**3D0*Pv2nd

                ELSE
                    L=1
                    DO WHILE(dk2nd.GT.C2nd(KC,L).AND.L.LT.K2nd)
                        L=L+1
                    ENDDO
                    N=KC+(KC-1)*K2nd+L
```

```
            !split the droplet
            FK2=(dk2nd**3D0-C2nd(KC,L)**3D0)/
     +           (C2nd(KC,L-1)**3D0-C2nd(KC,L)**3D0)

            YDOT(N-1)=YDOT(N-1)+df2nd*CRA(I,J)*Y(I)    !*
     +          *Y(J)*Pv2nd*FK2
            YDOT(N)=YDOT(N)+df2nd*CRA(I,J)*Y(I)    !*
     +          *Y(J)*Pv2nd*(1D0-FK2)
        ENDIF

    ELSE                !if formed drop is < largest

        H=1
        DO WHILE(CN(H).LE.DK)
            H=H+1
        ENDDO

        !careful for this when having inclusion
        FK=(DK**3D0-CN(H)**3D0)/(CN(H-1)**3D0-CN(H)**3D0)


    YDOT(H-1)=YDOT(H-1)+df2nd*FK*CRA(I,J)*Y(I)*Y(J)*Pv2nd          !*
    !for drop H-1 from Ith

        !2nd droplets re-distribution
        DO K=1,K2nd

            !for droplets from Ith mother drop
            M=KC+(I-1)*K2nd+K
            IF(C2nd(I,K).LE.C2nd(H-1,1))THEN
                N=KC+(H-1-1)*K2nd+1
                YDOT(N)=YDOT(N)+df2nd*F2nd*Y(M)*C2nd(I,K)**3D0 !*
     +              *FK/C2nd(H-1,1)**3D0*Pv2nd
            ELSE
                L=1
                DO WHILE(C2nd(I,K).GT.C2nd(H-1,L))
                    L=L+1
                ENDDO
                N=KC+(H-1-1)*K2nd+L

                !split the droplet
                FK2=(C2nd(I,K)**3D0-C2nd(H-1,L)**3D0)/
     +              (C2nd(H-1,L-1)**3D0-C2nd(H-1,L)**3D0)

                YDOT(N-1)=YDOT(N-1)+df2nd*F2nd*Y(M)*FK2 !*
     +              *FK*Pv2nd
                YDOT(N)=YDOT(N)+df2nd*F2nd*Y(M)*(1D0-FK2)   !*
     +              *FK*Pv2nd
            ENDIF
        ENDDO
    !for drop H-1 from Jth
        DO K=1,K2nd
            !for droplets from Jth mother drop
            M=KC+(J-1)*K2nd+K
            IF(C2nd(J,K).LE.C2nd(H-1,1))THEN
                N=KC+(H-1-1)*K2nd+1
                YDOT(N)=YDOT(N)+df2nd*F2ndJ*Y(M)*C2nd(J,K)**3D0     !*
     +              *FK/C2nd(H-1,1)**3D0*Pv2nd
            ELSE
                L=1
                DO WHILE(C2nd(J,K).GT.C2nd(H-1,L))
                    L=L+1
                ENDDO
                N=KC+(H-1-1)*K2nd+L

                !split the droplet
                FK2=(C2nd(J,K)**3D0-C2nd(H-1,L)**3D0)/
     +              (C2nd(H-1,L-1)**3D0-C2nd(H-1,L)**3D0)

                YDOT(N-1)=YDOT(N-1)+df2nd*F2ndJ*Y(M)*FK2    !*
     +              *FK*Pv2nd
                YDOT(N)=YDOT(N)+df2nd*F2ndJ*Y(M)*(1D0-FK2) !*
     +              *FK*Pv2nd
            ENDIF
        ENDDO
```

```
      !secondary droplets created from I+J coalescence into H-1
          IF(dk2nd.LE.C2nd(H-1,1))THEN
              N=KC+(H-1-1)*K2nd+1
              YDOT(N)=YDOT(N)+df2nd*FK*CRA(I,J)*Y(I)    !*
     +            *Y(J)*dk2nd**3D0/C2nd(H-1,1)**3D0*Pv2nd

          ELSE
              L=1
              DO WHILE(dk2nd.GT.C2nd(H-1,L).AND.L.LT.K2nd)
                  L=L+1
              ENDDO
              N=KC+(H-1-1)*K2nd+L

              !split the droplet
              FK2=(dk2nd**3D0-C2nd(H-1,L)**3D0)/
     +                (C2nd(H-1,L-1)**3D0-C2nd(H-1,L)**3D0)

              YDOT(N-1)=YDOT(N-1)+df2nd*FK*CRA(I,J)*Y(I)    !*
     +            *Y(J)*Pv2nd*FK2
              YDOT(N)=YDOT(N)+df2nd*FK*CRA(I,J)*Y(I)    !*
     +            *Y(J)*Pv2nd*(1D0-FK2)
          ENDIF


      YDOT(H)=YDOT(H)+df2nd*(1-FK)*CRA(I,J)*Y(I)*Y(J)*Pv2nd          !*
      !for drop H from Ith

          !2nd droplets re-distribution
          DO K=1,K2nd

              !for droplets from Ith mother drop
              M=KC+(I-1)*K2nd+K
              IF(C2nd(I,K).LE.C2nd(H,1))THEN
                  N=KC+(H-1)*K2nd+1
                  YDOT(N)=YDOT(N)+F2nd*Y(M)*C2nd(I,K)**3D0*          !*
     +                    df2nd*(1-FK)/C2nd(H,1)**3D0*Pv2nd
              ELSE
                  L=1
                  DO WHILE(C2nd(I,K).GE.C2nd(H,L))
                      L=L+1
                  ENDDO
                  N=KC+(H-1)*K2nd+L

                  !split the droplet
                  FK2=(C2nd(I,K)**3D0-C2nd(H,L)**3D0)/
     +                (C2nd(H,L-1)**3D0-C2nd(H,L)**3D0)

                  YDOT(N-1)=YDOT(N-1)+F2nd*Y(M)*FK2          !*
     +                    *df2nd*(1-FK)*Pv2nd
                  YDOT(N)=YDOT(N)+F2nd*Y(M)*(1D0-FK2)        !*
     +                    *df2nd*(1-FK)*Pv2nd
              ENDIF
          ENDDO

      !for drop H from Jth

          DO K=1,K2nd
              !for droplets from Jth mother drop
              M=KC+(J-1)*K2nd+K
              IF(C2nd(J,K).LE.C2nd(H,1))THEN
                  N=KC+(H-1)*K2nd+1
                  YDOT(N)=YDOT(N)+F2ndJ*Y(M)*C2nd(J,K)**3D0
     +                    *df2nd*(1-FK)/C2nd(H,1)**3D0*Pv2nd    !*
              ELSE
                  L=1
                  DO WHILE(C2nd(J,K).GT.C2nd(H,L))
                      L=L+1
                  ENDDO
                  N=KC+(H-1)*K2nd+L

                  !split the droplet
                  FK2=(C2nd(J,K)**3D0-C2nd(H,L)**3D0)/
     +                (C2nd(H,L-1)**3D0-C2nd(H,L)**3D0)


                  YDOT(N-1)=YDOT(N-1)+F2ndJ*Y(M)*FK2
```

```
     +                    *df2nd*(1-FK)*Pv2nd          !*
                      YDOT(N)=YDOT(N)+F2ndJ*Y(M)*(1D0-FK2)
     +                    *df2nd*(1-FK)*Pv2nd          !*
                  ENDIF

              ENDDO

            !secondary droplets created from I+J coalescence into H
              IF(dk2nd.LE.C2nd(H,1))THEN
                  N=KC+(H-1)*K2nd+1
                  YDOT(N)=YDOT(N)+df2nd*(1-FK)*CRA(I,J)*Y(I)    !*
     +                *Y(J)*dk2nd**3D0/C2nd(H,1)**3D0*Pv2nd

              ELSE
                  L=1
                  DO WHILE(dk2nd.GT.C2nd(H,L).AND.L.LT.K2nd)
                      L=L+1
                  ENDDO
                  N=KC+(H-1)*K2nd+L

                  !split the droplet
                  FK2=(dk2nd**3D0-C2nd(H,L)**3D0)/
     +                    (C2nd(H,L-1)**3D0-C2nd(H,L)**3D0)

                  YDOT(N-1)=YDOT(N-1)+df2nd*(1-FK)*CRA(I,J)*Y(I)    !*
     +                *Y(J)*Pv2nd*FK2
                  YDOT(N)=YDOT(N)+df2nd*(1-FK)*CRA(I,J)*Y(I)    !*
     +                *Y(J)*Pv2nd*(1D0-FK2)
              ENDIF

            ENDIF
55          ENDDO

!--------------
        ENDDO
    ENDDO
    RETURN
    END
```